

Formation and decomposition processes  
of CO<sub>2</sub> hydrates  
at conditions relevant to Mars

Dissertation  
zur Erlangung des Doktorgrades  
der Mathematisch-Naturwissenschaftlichen Fakultäten  
der Georg-August-Universität zu Göttingen

vorgelegt von

**Andrzej Falenty**

aus Pruszków, Polen

Göttingen 2008

D 7

Referentin/Referent: Prof. Dr. W. F. Kuhs

Korreferentin/Korreferent: Prof. Dr. J. Hoefs

Tag der mündlichen Prüfung:

# TABLE OF CONTENTS

<b>ABSTRACT</b> .....	I
<b>ZUSAMMENFASSUNG</b> .....	II
<b>CHAPTER 1 – Gas Hydrate</b> .....	1
<b>1.1. General introduction</b> .....	1
<b>1.1.1. History</b> .....	1
<b>1.1.2. Crystal structure and chemical composition of hydrates</b> .....	3
<b>1.1.3. Crystal structure of Ih and Ic water ice</b> .....	8
<b>1.1.4. Thermodynamic stability boundaries of CO<sub>2</sub> hydrates</b> .....	10
<b>1.1.5. Kinetics of gas hydrates</b> .....	12
<b>1.1.5.1. Nucleation and driving force</b> .....	13
<b>1.1.5.2. Formation</b> .....	15
<b>1.1.5.3. Decomposition</b> .....	17
<b>1.1.5.4. Formation and decomposition in porous media</b> .....	17
<b>1.2. Occurrence of gas hydrates</b> .....	20
<b>1.2.1. Earth</b> .....	21
<b>1.2.2. Solar system</b> .....	28
<b>CHAPTER 2 – Mars</b> .....	31
<b>2.1. History of Mars exploration</b> .....	31
<b>2.2. Mars in numbers and figures</b> .....	35
<b>2.3. Mars’ surface and internal structure</b> .....	37
<b>2.3.1. Core</b> .....	37
<b>2.3.2. Mantle</b> .....	38
<b>2.3.3. Crust</b> .....	40
<b>2.4. Magnetic field</b> .....	43
<b>2.5. Volatiles and Martian climate evolution</b> .....	45
<b>2.5.1. Blue Mars</b> .....	46
<b>2.5.2. White Mars</b> .....	62
<b>2.6. Clathrate on Mars</b> .....	66
<b>2.6.1. Polar caps</b> .....	67
<b>2.6.2. The regolith</b> .....	71
<b>2.6.3. Environmental impact of clathrate decomposition</b> .....	72
<b>CHAPTER 3 – Methods and instrumentation</b> .....	75
<b>3.1. Kinetics investigations</b> .....	75
<b>3.1.1. X-rays and neutrons</b> .....	75
<b>3.1.2. In-situ time-resolved neutron powder diffraction</b> .....	77
<b>3.1.3. pVT and ex-situ X-ray diffraction</b> .....	80
<b>3.1.4. In-situ neutron powder diffraction or pVT / ex-situ X-ray diffraction</b> .....	82
<b>3.2. Custom build setups and experimental cells</b> .....	84
<b>3.2.1. Experimental cells</b> .....	84
<b>3.2.2. High/low pressure systems</b> .....	88
<b>3.3. Scanning electron microscopy (SEM)</b> .....	93
<b>3.3.1. Introduction to the electron microscopy</b> .....	93
<b>3.3.2. LEO 1530 Gemini and FEI Quanta 200 FEG</b> .....	97
<b>3.4. Brunauer-Emmett-Teller method (BET)</b> .....	98
<b>3.4.1. Principles of the BET</b> .....	98
<b>3.4.2. In-house BET setup</b> .....	102

3.5. Excess fugacity – driving force.....	105
3.6. Clathrate formation – Powder 4 model.....	106
3.6.1. Theoretical background.....	107
3.6.2. Formation from frost – “Frost” module.....	111
<b>CHAPTER 4 – CO<sub>2</sub> hydrates: kinetics of formation and decomposition at Martian conditions.....</b>	<b>113</b>
4.1. Excess fugacity.....	113
4.2. Formation.....	114
4.2.1. Starting material and sample preparation.....	115
4.2.2. Nucleation and growth stage – interrupted runs.....	117
4.2.3. Formation’s kinetics at low T.....	124
4.2.4. Modelling with Powder 4 – Frost Module.....	128
4.3. Decomposition.....	134
4.3.1. Starting material and sample preparation.....	136
4.3.2. Decomposition kinetics at Martian surface pressure.....	138
4.3.3. Cubic and defective hexagonal ices formation.....	147
4.3.4. Decomposition kinetics within Martian regolith pressure range.....	153
4.3.5. “Self-preservation” phenomenon.....	163
4.3.6. Kinetic inhibition.....	171
<b>CHAPTER 5 – Possible role of clathrates on Mars and other planetary bodies.....</b>	<b>173</b>
5.1. Clathrates on Mars.....	173
5.1.1. Polar regions.....	173
5.1.2. Regolith.....	177
5.1.3. Environmental impact of the formation and decomposition of gas hydrates.....	180
5.2. Gas hydrates in the Solar System.....	191
<b>SUMMARY OF THE PROJECT AND OUTLOOK.....</b>	<b>193</b>
<b>INDEX.....</b>	<b>195</b>
<b>APPENDICES.....</b>	<b>223</b>



# Abstract

From a thermodynamic point of view there is no argument against the existence of CO<sub>2</sub> hydrates in the Martian regolith close to the surface. It was postulated, that CO<sub>2</sub> hydrates may occur in the ice layers of the north and the south polar caps. On this basis, many suggestions linking decomposition of CO<sub>2</sub> hydrates to morphological features like chaotic terrains, some outflow channels or gullies have been put forward. Another group of theories discusses the possibility that releases gases may have an environmental impact such as causing a climate change (greenhouse effect) or alter the isotopic ratios in the atmosphere.

At present days and possibly also in the past p-T conditions the most likely formation reaction to take place between gaseous CO<sub>2</sub> and water ice. Both components are available on the surface. Lately, also H<sub>2</sub>O has been found to be abundant in Martian regolith. However, the discussions in a large number of publications didn't reach a final conclusion, because of the lack of elementary knowledge about the formation and decomposition kinetics of this particular gas hydrates, yet. The investigations presented here provide the required information.

To achieve a physicochemical basis for these ideas, a series of CO<sub>2</sub> hydrate formation and decomposition experiments at Martian surface and sub-surface conditions were performed, using p-V-T methods as well as in-situ neutron diffraction at ILL Grenoble.

The experiments indicate that the formation time is directly related to the accessible surface area of the ice grains as well as temperature and CO<sub>2</sub>-pressure. At p-T conditions close to the Martian poles CO<sub>2</sub> hydrates are thermodynamically stable at the surface. Despite this fact the results show that at these low temperatures slow kinetics and nucleation difficulties prevent any significant formation of clathrates. However, there is still a fair chance to find CO<sub>2</sub> hydrates deeper in the regolith at different latitudes (given a pressure sealing of the overburden layers e.g. by water ice). Higher temperatures and pressures create much more favorable conditions. Additionally, climate variations on longer time-scales provide a conceivable scenario for hydrate decomposition and perhaps formation cycles as long as suitable conditions can be created. Gases from dissociating clathrates might be able to affect isotopic ratios in the atmosphere. Larger releases could also potentially cause episodes of warmer climate. The experimental decomposition runs in a temperature interval from about 240 to 273 K, have firmly established a behavior, called "self-preservation" (or "anomalous preservation"), which may preserve CO<sub>2</sub> hydrates for geologically long time scales. Self-preservation is a complex micro-structural process related to changes on the surface of decomposing hydrates. Small (up to 20µm) ice crystals formed upon decomposition create a layer, which due to annealing of ice defects and grain coarsening drastically slows down the out-diffusion of gas molecules and thus preventing decomposition. Below this temperature regime the "self-preservation" also occurs in the narrow p-T range. The sealing is less effective and is governed by the microstructure of an ice film. The destruction of this fragile, mechanically or by reaching the ice melting temperature achieved state may lead to the rapid gas release from decomposing clathrates. Sudden increase of pore pressure in the regolith may trigger the formation of large geomorphologic features like chaotic terrains thus letting pressurized liquids escape to the surface.

# Zusammenfassung

Von einem thermodynamischen Gesichtspunkt aus gibt es kein Argument gegen die Existenz von CO<sub>2</sub> Hydraten im Marsregolith nahe der Oberfläche. Es wurde bereits postuliert, dass CO<sub>2</sub> Hydrate in den Eisschichten des Nordens sowie den polaren Südkappen existieren könnten. Auf dieser Basis wurden Vorschläge, die Zersetzung von CO<sub>2</sub> Hydrat betreffend, in Verbindung mit morphologischen Eigenschaften, vorgebracht. Ein weiterer Ideenbereich behandelt den Einfluss den die Zersetzung von CO<sub>2</sub> Hydraten auf die Umwelt, hinsichtlich einer möglichen Klimaveränderung (Greenhouse-Effekt) oder der Modifizierung von Isotopenverhältnissen in der Atmosphäre, haben könnte.

Heutzutage und wahrscheinlich auch in der Vergangenheit bestimm(t)en Druck und Temperatur, dass die wahrscheinlichste Bildungsreaktion für CO<sub>2</sub> Hydrate zwischen gasartigem CO<sub>2</sub> und Wassereis stattfindet. Beide Bestandteile sind an der Oberfläche des Mars verfügbar. Kürzlich wurde zudem entdeckt, dass auch Wasser (H<sub>2</sub>O) häufig im Marsregolith vorkommt. Jedoch führten bislang alle Diskussionen bezüglich dieser Möglichkeit zu keinem Ergebnis, da es an elementaren Kenntnissen der Bildungs- und Zersetzungskinetik dieser besonderen Gashydrate mangelt.

Um eine physikochemische Grundlage für diese Ideen zu schaffen, wurde eine Reihe von CO<sub>2</sub> Hydrat Bildungs- und Zersetzungsexperimenten sowohl unter Marsoberflächenbedingungen als auch unter unterirdischen Marsbedingungen mit p-V-T-Methoden und in-situ Neutronbeugung an der ILL Grenoble, durchgeführt.

Die Experimente haben gezeigt, dass die Bildungsdauer der CO<sub>2</sub> Hydrate direkt mit der zugänglichen Eiskornoberfläche, den herrschenden Temperaturen und dem CO<sub>2</sub> Druck zusammenhängt. Unter p-T Bedingungen die an der Marsoberfläche nahe den Polen herrschen ist CO<sub>2</sub> Hydrat thermodynamisch stabil. Trotz dieser Tatsache zeigen die Ergebnisse, dass bei sehr niedrigen Temperaturen die langsame Kinetik sowie Schwierigkeiten die Nukleation der Hydrate betreffend, jede signifikante Bildung von Klathraten verhindern. Dennoch bleibt eine gute Chance CO<sub>2</sub> Hydrate tiefer im Regolith aufgrund vorliegender Druck-Versiegelung durch überliegende Schichten (z.B. Wassereis) zu finden. Höhere Temperaturen und höherer Druck schaffen günstigere Bedingungen für die Bildung von CO<sub>2</sub> Hydraten. Zusätzlich stellen Klimaschwankungen ein denkbares Szenario für die Hydrat-Zersetzung und mögliche Bildungszyklen dar, sofern passende Stabilitätsbedingungen geschaffen werden können. Durch die Zersetzung von Gashydraten können Gase freigesetzt werden, die im Stande sind die Isotopenverhältnisse der Atmosphäre zu verändern. Die Freisetzung größerer Gasmengen könnte eine potentielle Ursache wärmerer Klimaepisoden darstellen. Die experimentellen Zersetzungsvorgänge, in einem Temperaturbereich zwischen etwa 240 und 273 Kelvin begründen einen Prozess, welcher auch als "Selbsterhaltung" bezeichnet wird. Dieser ist in der Lage, CO<sub>2</sub> Hydrat über einen geologisch bedeutsamen Zeitraum stabil zu halten. Der Prozess der Selbsterhaltung, der besonders die Mikrostruktur von Hydraten betrifft, ist sehr kompliziert und steht in Verbindung mit Veränderungen auf der Oberfläche der sich zersetzenden Hydrate. Sehr kleine Gashydratkristalle (Durchmesser bis zu 20µm) erzeugen bei ihrer Zersetzung eine Schicht, die durch das Verheilen oder Ausheilen von Defekten im Eisgitter sowie Kornvergrößerungsprozessen zu einer Ausbreitung der Gasmoleküle und somit zu einer drastischen Verlangsamung des Zersetzungsprozesses führt. Unterhalb dieses Temperaturregimes findet der "Selbsterhaltungsprozess" auch in einem sehr schmalen P-T-Bereich statt. Die Versiegelung ist hier weniger wirksam und wird durch die Mikrostruktur des Eisfilms geregelt. Die Zerstörung dieses mechanisch oder durch das Erreichen des Schmelzpunktes von Eis erlangten metastabilen Zustandes kann zu einer sehr schnellen Gasfreisetzung aufgrund der Zersetzung von Gashydraten führen. Die plötzliche Zunahme des Porendrucks im Regolith kann die Bildung von großen geomorphologischen Phänomenen, wie z.B. 'chaotic terrains' bewirken und so unter Druck stehende Fluide an die Oberfläche lassen.

# Chapter 1 – Gas Hydrates

The first part of this chapter is meant to give the reader an introduction to the history, physics, crystallography and chemistry of gas hydrates, which is indispensable for the full understanding of the experimental section and following conclusions. Briefly also two ice structures are reviewed. The second part of the chapter lives laboratory to present environments, favorable for gas hydrate formation and stability in nature on Earth and other possible places in the Solar system.

## 1.1 General introduction

### 1.1.1 History

Gas hydrates have been known for more than 200 years, and as it is with many discoveries, they have been found actually by accident. Between XVIII and XIX century a number of different gases like oxygen or carbon and sulfur dioxide have been recognized. Right after it, scientists were probing them for their chemical and physical properties. In



**Fig. 1)** The discoverer of CO<sub>2</sub> hydrates – the Polish scientist, Zygmunt Florenty Wróblewski.

one of such experiments the English philosopher and naturalist Joseph Priestley presumably obtained the hydrate of sulfur dioxide (Makogon, 1997). Priestley, who was performing cold experiments with vitriolic acid air (SO<sub>2</sub>) and water, observed ice like material formed during the reaction. This information is dated on 1778 and was officially published in “Versuche und Beobachtungen über verschiedene Gattungen der Luft” between 1778 and 1780. About 32 years later (1810), another British scientist, Sir Humphrey Davy formed chlorine hydrate by cooling an aqueous solution saturated with chlorine gas below 9°C. Since Priestley's experiment was performed below freezing point of water (-8.3°C) there is no unambiguous proof that the hydrate phase was really present. Therefore some authors (e.g. Sloan, 1998) suggest Davy as the

discoverer of gas hydrates. Few years later his apprentice, Michael Faraday, successfully repeated the experiment in 1823. The trace of gas hydrate research leads also to Göttingen where Friedrich Wöhler, known also as a pioneer in high-pressure research, obtained hydrogen sulfide hydrate under elevated pressure in 1840. CO<sub>2</sub> hydrates, which are the cornerstone of present PhD, have been discovered in 1882 by the Polish chemist and physicist, Zygmunt Florenty Wróblewski (Fig. 1) while studying carbonic acid. In the next years a series of new gas hydrates have been obtained e.g. CH<sub>4</sub>, C<sub>2</sub>H<sub>6</sub>, C<sub>2</sub>H<sub>4</sub>, N<sub>2</sub>O (Villard, 1888), C<sub>3</sub>H<sub>8</sub> (Villard, 1890), Ar (Villard, 1896), Kr (de Forcrand, 1925). Although gas hydrates, from their discovery, were treated more like interesting curiosity for about 150 years, researchers were still investigating these systems using different gases or gas mixtures. In this short history review a large part of the thermodynamic considerations has been skipped to not distract the reader from the main story. The sudden interest in gas hydrates arose with the development of oil and gas industry in early XX century. The transportation of pressurized gas and oil on the long distances via pipelines was haunted by solid plugs in autumn and spring time. As the reader may easily guess, it was caused by gas hydrate growth from “wet” hydrocarbons. But yet, at that time water ice was pointed as the cause for the blockages. Finally in 1934, American chemist E. G. Hammerschmidt concluded that the p-T conditions in the pipelines were favorable for gas hydrate formation and they were to blame for the plugs. This small but remarkable discovery opened a new chapter in gas hydrate research related to industrial applications. That was the time when first investigations on methods of avoiding or inhibiting gas hydrate growth were undertaken. Academic research was directed more in to the chemistry and molecular structure problematic. Commonly used light polarization microscopy allowed distinguishing gas hydrated from water ice by lack of polarization effect; it points to cubic symmetry but without any further details. Prior to the first X-ray diffraction experiments on clathrates, Russian scientist B. A. Nikitin (1936-1940) suggested, for the first time, a cage like structure of gas hydrates for inert gases. Moreover, he stated that single species or complex gas hydrates are crystalline non-stoichiometric compounds made of hydrogen bonded water molecules that form cages filled by gas molecules. This very important theory has been confirmed by X-ray diffraction experiments of H. M. Powell in 1948 that introduced the term: Clathrate. One year later the German scientist von Stackelberg and his group (1949-1958), also by means of X-ray diffraction, established two cubic crystal structures (Structure I and II). Many years later, in 1987, a third, hexagonal structure (Structure H) was found (Ripmeester et al. 1987).

The section above, not without a reason, discussed exclusively the history of synthetic gas hydrates. Natural clathrates were not known for a long time. Although their existence was suggested, by Russian Prof. I. N. Strizhev, already in 1946, first cores containing gas hydrates (mostly methane hydrates) were extracted in 1967 during the exploratory drilling in permafrost of Yakutiya and Messoyakhia fields in western Siberia (Makogon, 1972). About one year after the Russians, the Americans found air hydrates in drilling cores extracted from 2164m at the Station Byrd in West Antarctica. Later on a series of new sites on the continental shelves, in river deltas and permafrost of Russia and North America has been found. It is worth to notice that already at that time scientists started to consider gas hydrates as a constituent of icy bodies like comets (Delsemme and Miller, 1970), (Mendis and Ip, 1974), (Makogon, 1987), planetary rings (Pang et al. 1983) or other planets e.g. Mars (Milton, 1974). These pivotal hypotheses opened, for gas hydrates (also very exotic for Earth), a new field of research in planetology science (Chapter 2). Among them are CO<sub>2</sub> hydrates in Martian environment, which are in the focus of this work.

### 1.1.2 Crystal structure and chemical composition of gas hydrates

Gas hydrates form large family of crystalline solids composed from two main components: a host lattice and guest molecules. Although theoretically a large number of different crystal lattices is possible (Jeffrey, 1984), (Dyadin et al. 1991), (Komarov et al. 2005), up to now, only a few types of crystal structures have been recognized. The most common are: cubic structure I (sI) (Fig. 3), cubic structure II (sII) (Fig. 4) and hexagonal

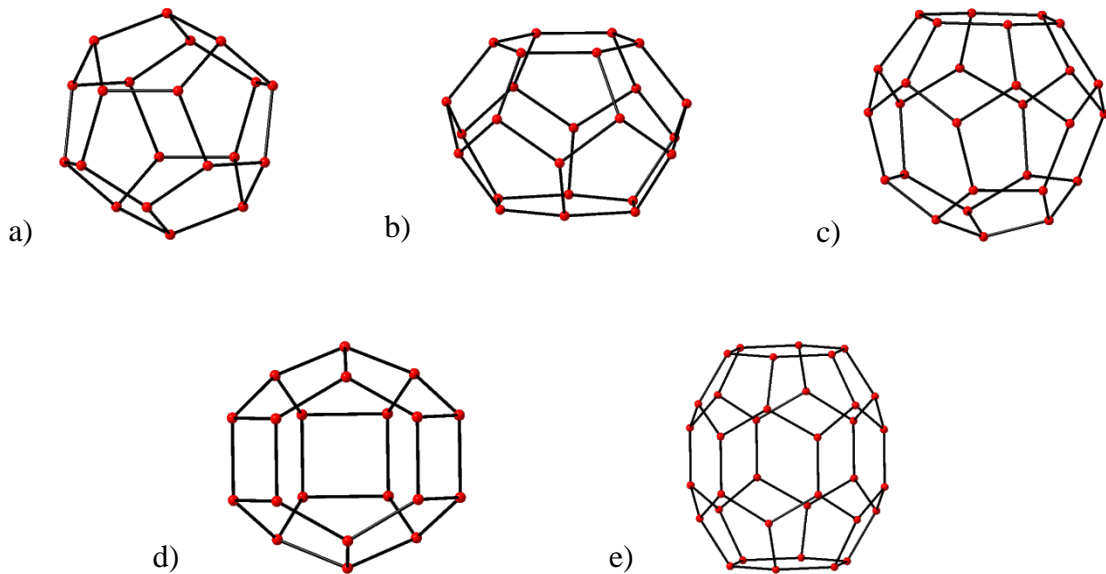


**Fig. 2)** Five types of cages commonly found in gas hydrates: a) Pentagonal dodecahedra ( $5^{12}$ ), b) Tetrakaidecahedron ( $5^{12}6^2$ ), c) Hexakaidechedron ( $5^{12}6^4$ ), d) Irregular Dodecahedron ( $4^35^66^3$ ), e) Icosahedron ( $5^{12}6^8$ ).

structure H (sH) (Fig. 5). The building blocks for these structures are polyhedrons made of hydrogen bonded water molecules. Commonly used description  $n^i k^j$  (Jeffrey, 1984) of these cages use the number of edges (i,j,...) for each face type (n,k,...) e.g.  $4^3 5^6 6^3$  describes irregular dodecahedron with twelve faces; 3-squares, 6-pentagons and 3-hexagons. The origin of this notation comes from earlier work (King, 1972) on water clusters where polyhedra with different structures are temporarily formed. As the reader may see later on in this section, the elements building cages are pentagons, squares and hexagons. The reason for it is fundamental for the formation and stability of cavities. The O-O-O angle between hydrogen bounded water molecules forming pentagons are  $108^\circ$ . The strains are very low as the opening angle is very close to the natural one in free water molecules ( $104.5^\circ$ ) or the tetragonal angle in ice Ih ( $109.5^\circ$ ). Larger strains exist within hexagons ( $120^\circ$ ) or squares ( $90^\circ$ ) and additional conditions for polyhedrons stabilization are required (Belosludov et al. 1991). Faces with even larger strains like heptagons ( $128.6^\circ$ ) or octagons ( $135^\circ$ ) are not stable in gas hydrate structures.

In the following section the reader will find a detailed description of the five common cages (Makogon, 1997), (Sloan, 1998):

Pentagonal dodecahedra ( $5^{12}$ ) (Fig. 2 a). This cavity, often referred to as a small cage, exists in both cubic structures (sI and sII) and the hexagonal one (sH). The cage is composed from twelve pentagonal faces, which makes it almost spherical. The average radius is of  $3.95\text{\AA}$  (sI) and  $3.91\text{\AA}$  (sII). The average radius in sH structure is assumed to be close to the one in sII. Low strains in such structures allow them to form naturally in supercooled water (Anglell, 1982) and possibly also in quasi-liquid layer on the ice surface. In 1959 Pauling suggested even that water might be composed of complexes of  $5^{12}$  cages with a water molecule as a guest.

Tetrakaidecahedron ( $5^{12} 6^2$ ) (Fig. 2 b) is composed from two hexagonal faces separated by twelve pentagonal faces. The oblate shape makes it considerably non-spherical with large O-O-O angle variations. Effectively, fairly large strains require a guest molecule to stabilize the cavity. In hydrate structure I, often referred as a large cage, plays main stabilization role (to many empty cages will collapse the structure). Short lived  $5^{12} 6^2$  cavities may be formed within a liquid film on ice surface but also here the stabilization by a guest molecule is necessary. The average radius is of  $4.33\text{\AA}$ .

Hexakaidehedron ( $5^{12} 6^4$ ) (Fig. 2 c) is the most spherical cage from the five. It is constructed from four hexagonal and twelve pentagonal faces so that no two hexagons share the same edge. In structure sII, as a large cage, plays main stabilization role

(similarly to  $5^{12}6^2$  cavities in sI). The size of the cage is sufficient to encase considerably large molecules like propane or iso-butane.

Irregular Dodecahedron ( $4^35^66^3$ ) (Fig. 2 d) is rather unusual cage. Among all five common cages only this particular one has square faces. In combination with hexagonal faces internal strains are noticeably high. The average radius was calculated as 4.06Å.

Irregular Icosahedron ( $5^{12}6^8$ ) (Fig. 2 e) is also unique as exists only in structure sH. It is composed from two 6-elements pentagonal belts separated by 6-elements hexagonal belt. Hexagonal faces finish both ends. Such construction create indeed enormous cage capable of encasing such molecules like methylcyclohexane. Although the average radius has been estimated to about 5.17Å, the cage is highly non-spherical. Therefore the shape and the position of a guest molecule in the cavity start to play an important role.

Three dimensional arrangements of selected cages create several crystallographic lattices. Although CO<sub>2</sub> hydrates mainly crystallize in structure type I and it will be the main subject of the next section, other structures will be also introduced. The reader should be aware that it would be merely a touch of this vast field of research. High pressure phases will be also included. Even if up to now there are no published high pressure data on CO<sub>2</sub> hydrates, it is possible that some of these structures may occur also in their case.

Structure I (sI) belongs to the primitive cubic space group Pm3n with pentagonal dodecahedra placed in the center of symmetry (Fig. 2). Large cavities ( $5^{12}6^2$ ) share hexagonal faces and the spaces between so created columns form small cavities ( $5^{12}$ ) (Fig. 3). The unit cell contains 46 water molecules in two small ( $5^{12}$ ) and six large cages ( $5^{12}6^2$ ). The average lattice parameter is of 12Å. X-ray and neutron diffraction experiments on CH<sub>4</sub> hydrate indicate that the lattice constant decreases slightly with the rising pressure up to several MPa. (Klapproth et al. 2003). The effect is negligible small, for CO<sub>2</sub> hydrates discussed in this work as the pressure range is far too small. In this case, more interesting is how the lattice constant and the volume of cages change with temperature. Again neutron diffraction comes into hand. Cage volume

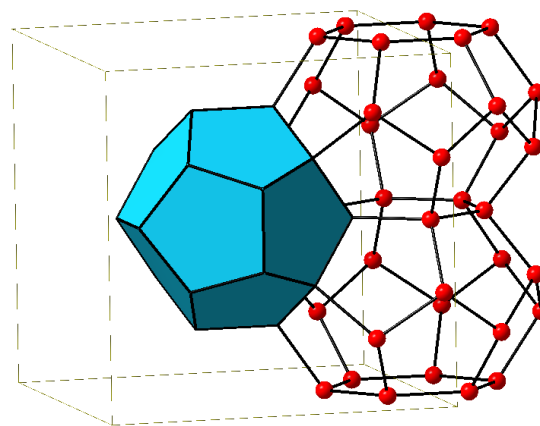


**Fig. 3)** The arrangement of cages in cubic structure sI. Gray dashed line outlines the elementary unit.

measurements of several gas hydrates, among others CO<sub>2</sub> hydrate, between 4 and 180K (Chakoumakos et al. 2003), shows strong correlation with the guest specie. CO<sub>2</sub> fits relatively tightly (Fig. 6) into small (5<sup>12</sup>) cages, in comparison to methane, living very little room for volume reduction. The volume change for large cages is somewhat greater but still relatively small in comparison to other hydrates. Although most of the guest molecules enter into the small and large cages (CH<sub>4</sub>, CO<sub>2</sub>, H<sub>2</sub>S, Xe), a handful of large species can stabilize sI structure only by occupying large voids (C<sub>2</sub>H<sub>6</sub>, c-C<sub>3</sub>H<sub>6</sub>). The cage filling is non-stoichiometric (also in other structures). Generally for all hydrates, excluding high pressure phases (Vos et al. 1993), (Hirai et al. 2002), (Loveday et al. 2003), (Alavi et al. 2006), N<sub>2</sub> (Kuhs et al. 1997), Ar (Itoh et al., 2001) and O<sub>2</sub> hydrate (Chazallon and Kuhs, 2002) the average number of guest molecules in the voids do not exceed unity. It is accepted that the occupancy follow a Langmuir isotherm with increasing pressure; fugacity (van der Waals and Platteuw, 1959). The degree of filling changes also with the type of the guest molecule. The neutron diffraction experiments (Klapproth et al. 2003) performed on synthetic CO<sub>2</sub> hydrates show almost complete filling of (5<sup>12</sup>6<sup>2</sup>) cages over the wide pressure range. The percentage of occupied small cages oscillates around 55%. The average formula for CO<sub>2</sub> clathrate is assumed to be close to: CO<sub>2</sub> x 5.75H<sub>2</sub>O (Stern et al. 2001). Due to the presence of guest molecules in the host lattice the total density of hydrates is greater than of water but in order to accommodate e.g. gas molecules the water framework must expand. For instance, when at 250K CO<sub>2</sub> and water ice (1.02g/cm<sup>3</sup>) form clathrates (1.188g/cm<sup>3</sup>) the density of the empty hydrogen bond frame falls (0.89g/cm<sup>3</sup>) to make a room for carbon dioxide. The same effect is true for all clathrates.

Structure II (sII) has a diamond type lattice and belongs to the cubic Fd3m space group. Similarly to sI also contains small and large cavities. By sharing pentagonal faces between small (5<sup>12</sup>) cages a new type of cages (5<sup>12</sup>6<sup>4</sup>) with 4 hexagonal faces are created (Fig. 4). The ideal unit cell contains 136 water molecules shared by sixteen pentagonal dodecahedra (5<sup>12</sup>) and eight hexakaidehedrons. Two distinct groups of guest species crystallize in this

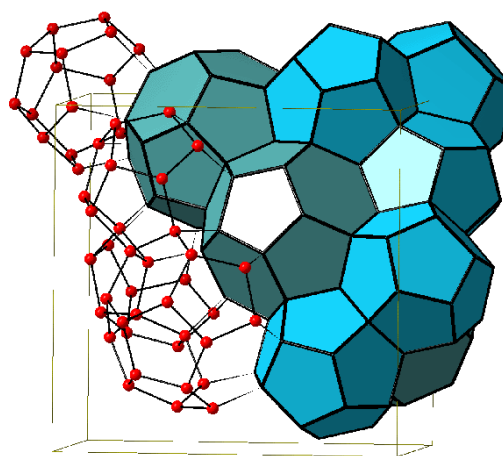


**Fig. 4)** Three dimensional visualization of cubic structure sII. Gray dashed line outlines the elementary unit.



structure. Molecules from the first group with the diameter between 3.8Å (Ar) and 4.2Å (O<sub>2</sub>) occupy small and large cages. The second group includes large molecules, with diameter 6.1-6.5Å, entering only in large cavities (Fig. 6). Lately, a structure sII CO<sub>2</sub> hydrate has been formed in pure D<sub>2</sub>O CO<sub>2</sub> system (Klapproth et al. 2003). Yet, the phase was metastable and after quick formation recrystallized into the stable structure sI. Similar behavior is observed for ethane hydrate (M. M. Murshed, private communication).

Structure H (sH) was discovered relatively recently (Ripmeester et al. 1987) and still is a subject of investigations (Tse, 1990), (Ohmura et al. 2005), (Okano and Yasuoka, 2006). In contrary to the previous two structures sH belongs to the primitive hexagonal P6/mmm space group. The unit cell is of moderate size ( $a = 12.26\text{\AA}$ ,  $c = 10.17\text{\AA}$ ) and contains 36 water molecules shared by one large cavity ( $5^{12}6^8$ ), two medium size

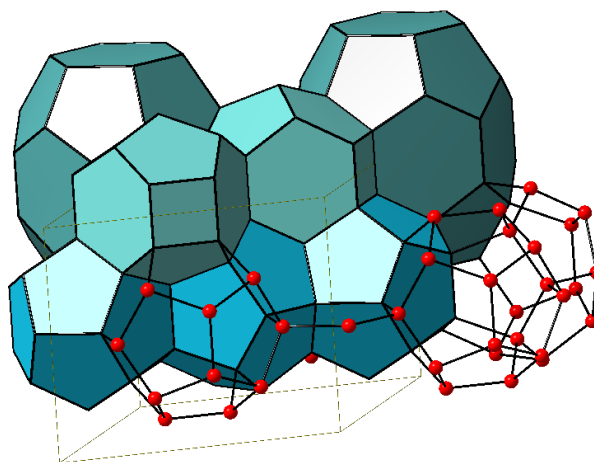


**Fig. 5** 3D model of structure H formed by three different types of cages. Gray dotted line outlines the elementary unit.

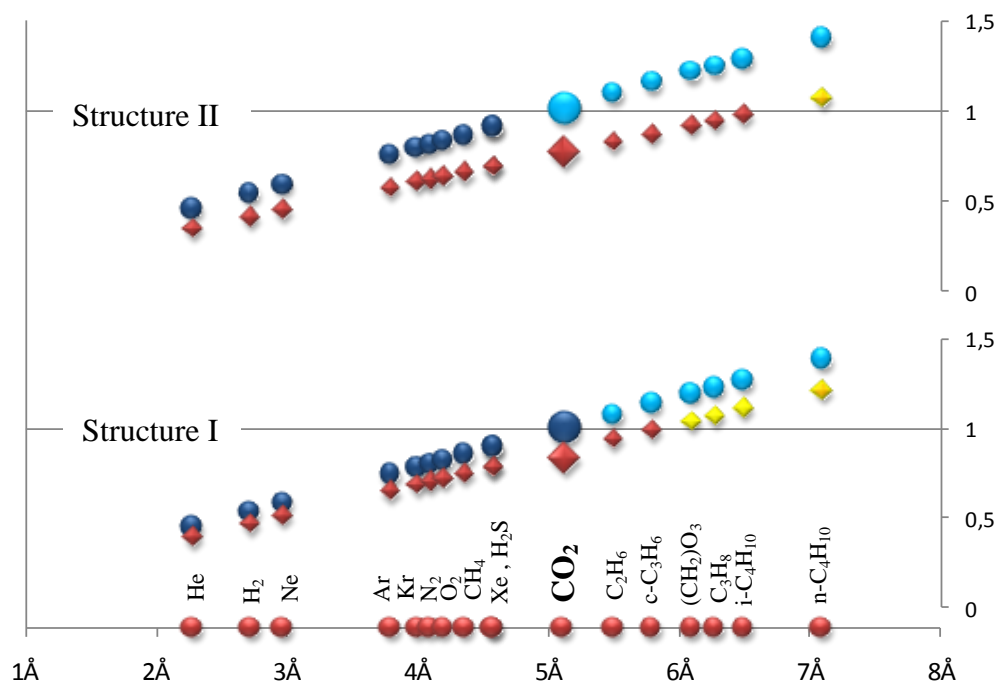


**Fig. 6** Guest's molecular diameters to cavity diameters excluding (1.4Å water radii) for structure sI and sII (small cage - dots, large cage - diamonds). Ratio above 1 means that a guest molecule is too big to fit into a small cage (light blue) or large cage (yellow). X-axis at the bottom - guest diameters of the most common guest molecules (after Sloan, 1998).

( $4^35^66^3$ ) and three small cages ( $5^{12}$ ) (Fig. 5). The large cavity can accommodate molecules of diameters between 7.1 and 9 Å (Fig. 6). The complexity of this structure requires guest molecules of two sizes (e.g. n-butane and methane) to stabilize it at atmospheric pressure.

High pressure phases are the subject of intense research for the last two decades driven by purely academic (Londono et al. 1992), (Larionov et al. 2005), planetologic (Kurnosov et al. 2006), (Machida et al. 2006) and industrial interest e.g. for hydrogen storage. At least six high pressure phases, including structure sH and sII, are recognized. Up to now, the best explored systems are of noble gases and methane, which are relatively easy to compress. As an example, initial compression of argon hydrate, which forms structure sII at ambient pressure, leads to the tetragonal structure sT at about 9kbar (Hirai et al. 2002). Although there are some indications for a transient structure sH between them (4.5-7.2kbar) with at least four Ar molecules in big cages (Manakov et al 2001), the reproducibility of these results was found to be difficult. The tetragonal structure belongs to the  $P4_2/mnm$  space group and it is supposed to be made of 14-hedra ( $4^25^86^4$ ) with two argon atoms in each cage. Further increase of pressure, to about 20kbar, transforms structure sT into orthorhombic lattice also known from  $CH_4$  hydrate (Loveday et al. 2001b). Due to the very strong similarities to ice  $I_h$  it is often named as a “filled ice” structure (Loveday et al. 2003).

Molecules with the small diameter like hydrogen or helium were assumed (Sloan, 1997) to not create common hydrate structures (sI, sII, sH) presented in this section. It was accepted that, the small size allows them only to enter in open channels of ices  $I_h$  and  $I_c$ , (Londono et al. 1992), (Dyadin et al.1999). Yet, high pressure experiments on such gas filled ices led to the discovery of two new types of gas hydrate structures resembling ice II and ice VII (Vos et al. 1993). Relatively recently also a structure sII hydrogen hydrate has been formed under moderate pressure of 20 MPa (Mao et al. 2002).

### 1.1.3 Crystal structures of $I_h$ and $I_c$ water ice

Before the reader will be introduced to the thermodynamic and kinetics of clathrates, especially at low temperatures relevant to this work, it is essential to clarify what crystalline structures of water one might expect upon formation and decomposition. Up to now, at least thirteen different crystalline structures have been established and the list is still not closed (Petrenko, and Whitworth, 1999). For our purpose only two of them will be discussed as the most relevant to the pT conditions expected to exist on Mars:  $I_h$  and  $I_c$ .

Ice Ih – is the most common form of water ice on Earth. In spite of its chemical simplicity, or in fact because of it, in the early work on the crystal structure, where X-rays were used only oxygen positions could be defined. Unfortunately this method is not very useful for precise mapping of hydrogen that has only one electron to scatter an incoming beam. In the middle of XX century neutron diffraction on D<sub>2</sub>O samples (Wollan et al. 1949)

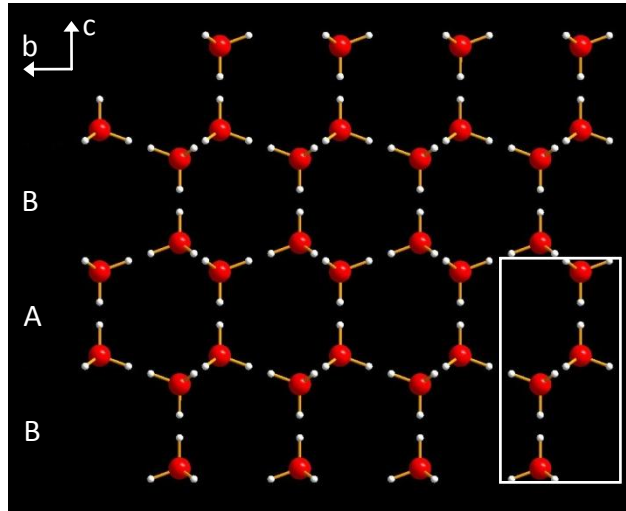


**Fig. 7)** Ice Ih crystal structure along [0001] axis with ABABA stacking. White solid line outlines the elementary unit.

subsequently confirmed by single crystal neutron diffraction eight years later (Peterson and Levy, 1957) finally solved the structure. It turned out that ice Ih belongs to the hexagonal primitive group P6<sub>3</sub>/mmc. Molecules localized in planes perpendicular to the [0001] axis are stacked together in the sequence ABABA (Fig. 7). The crystal structure is build up from tetrahedrons with oxygen in central position and other four connected through two covalently bounded hydrogen atoms two hydrogen bonds. In the ideal structure tetragonal O-O-O angle is 109.5°. The molecules are orientationally disordered which in turn translates into 2 possible positions for H along the O...O H-bond. Ih ice forms by water freezing or through cold deposition of water vapor. In the second case, the minimum temperature is somewhat unclear but commonly assumed to extend from 173K to 190K (Petrenko, and Whitworth, 1999). It can be formed also from other water ices by annealing or/and recrystallization above mentioned minimal temperature and appropriate pressure.

Ice Ic – is a metastable form of ice that in many ways resembles previous hexagonal structure. Although the ideal structure is cubic (Fd3m), it is also constructed from tetrahedrons and has virtually identical hydrogen disorder. In contrary to hexagonal form, cubic ice has different stacking that is denoted as ABCABCA (Fig. 8). The quality or defectiveness of the crystal depends strongly on the way of its preparation e.g. (Kuhs et al. 1987). This in turn, is responsible for a wide variation in Ic diffraction patterns and severe problems in a refinement. Ice Ic can be formed from in several ways: (1) from high pressure phases of ice (II-IX) by low-T pressure release, (2) by annealing of amorphous

ice, (3) cold deposition of water vapor, (4), hyperquenching of liquid water (Mayer and Hallbrucker, 1987), (5) crystallization in confined porous spaces e.g. (Steytler et al. 1983) or (6) decomposition of gas hydrates (Kuhs et al. 2004) (Chapter 4). Lately it turned out also that cubic ice can be formed in clouds of upper Earth's atmosphere (Murray et al. 2005), (Murray and Bertram, 2007). In all cases very low temperatures are required (from about 130 to 190K) but thermodynamic boundaries are not sharp. Ice Ic that upon warming transforms into Ih cannot be recovered in backward process.

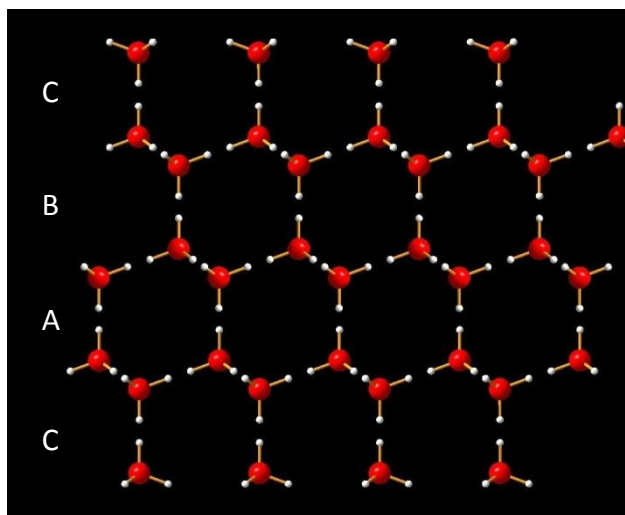


**Fig. 8)** Cubic crystal structure of Ice Ic along c axis with characteristic ABC stacking.

#### 1.1.4 Thermodynamic stability boundaries of CO<sub>2</sub> hydrates

The research on thermodynamics of these particular clathrates is divided in two distinct fields (Fig. 9). The first, relatively narrow one in the temperature scale is placed above liquid water point of water and pressure up to ~5MPa. The second one is greatly extended below melting point of water ice down to about 121K and 0.1mbar. For the last couple of decades, investigators were concentrating almost exclusively on exploration of CO<sub>2</sub> hydrate stability in the first p-T region (Fig. 10). In comparison to this, only a handful of publications (Miller and Smythe, 1970), (Falabella, 1975 after Sloan, 1998) is dedicated to the low temperature part. Recently, an extensive theoretical study on CO<sub>2</sub> clathrate (Longhi, 2005) brought a series of small modifications to the CO<sub>2</sub>-H<sub>2</sub>O system. Although most of the changes have no mathematical description (A curve fitting of the phase boundaries), two new equations to calculate a higher and lower temperature part of CO<sub>2</sub>(V) H H<sub>2</sub>O (S) - CO<sub>2</sub>(V) H<sub>2</sub>O (S) boundary has been introduced. The division on two parts is meant to decrease an absolute deviation from the experimental points, which becomes apparent for extended temperature range. Indeed, the expression, for the interval 254-271K, fits available data very well (deviation below 0.2%). Surprisingly, the equation for lower temperature part of the CO<sub>2</sub>(V) H H<sub>2</sub>O (S) - CO<sub>2</sub>(V) H<sub>2</sub>O (S) boundary shows great misfit in the order of 2000MPa (possibly a typo error). The same author has calculated,

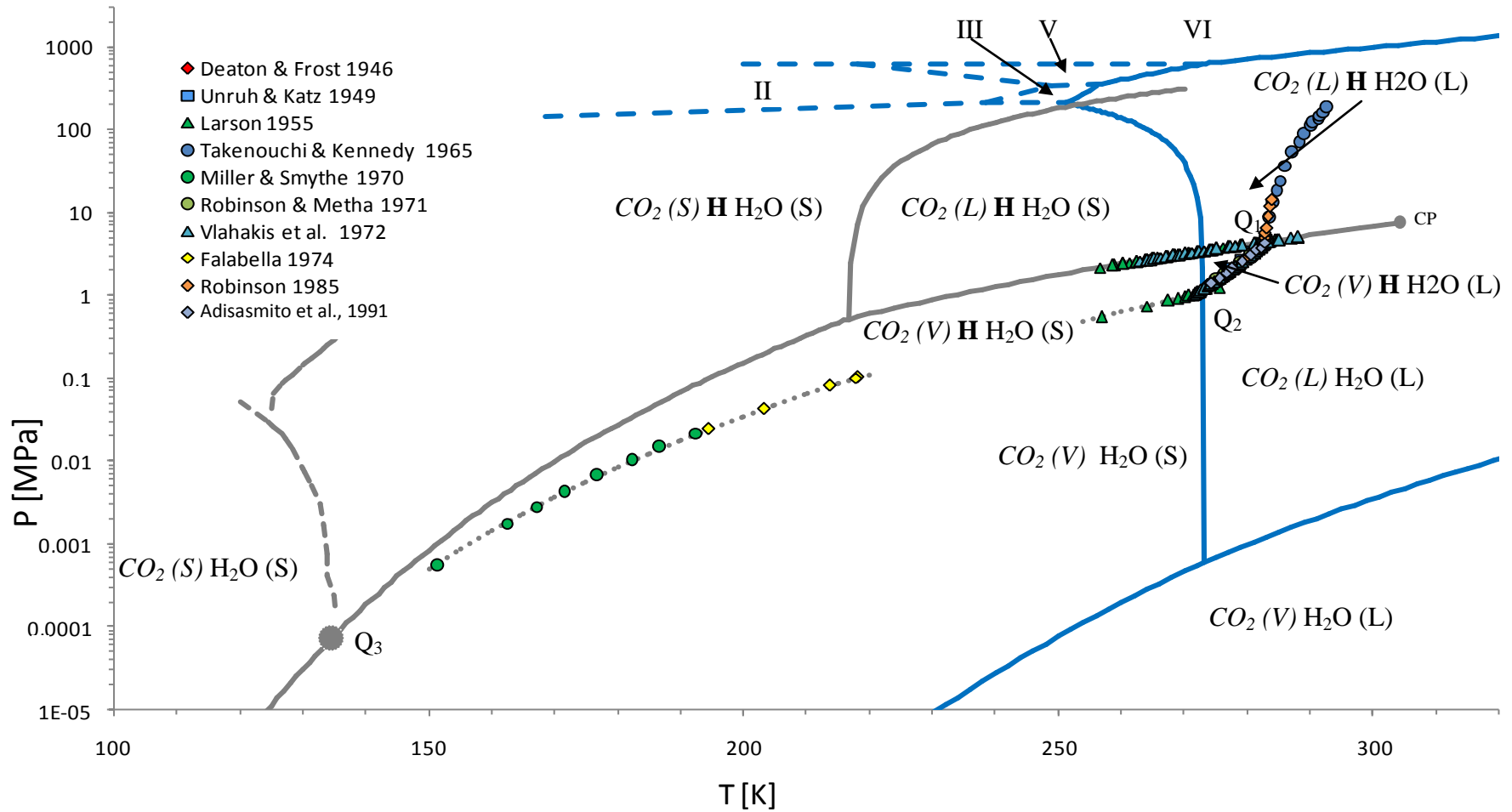


**Fig. 9)** Binary phase diagram of  $CO_2$  -  $H_2O$  system. Blue solid lines –  $H_2O$  phase boundaries (Wagner and Pruss, 1993), (Wagner et al. 1994). Blue dashed lines – water ice polymorphs stability boundaries. Gray solid line -  $CO_2$  phase boundaries (Span and Wagner, 1996). Gray dashed line -  $CO_2(S) \text{ H}_2O(S)$  -  $CO_2(S) \text{ H H}_2O(S)$  boundary (Longhi, 2005). Gray dotted lines - calculated  $CO_2(V) \text{ H H}_2O(S)$  -  $CO_2(V) \text{ H}_2O(S)$  boundary for lower T (Sloan, 1998) and higher T (Longhi, 2005). Experimental points after (Sloan, 1998).  $Q_1$ ,  $Q_2$ ,  $Q_3$  – quadruple points. CP – critical point of  $CO_2$ .

$\underline{CO_2 (S) H_2O (S)-CO_2 (S) H H_2O (S)}$  boundary (Fig. 8), that was previously unconstrained. It is interesting to note that an extrapolation of this data in lower pressures intersects the  $CO_2$  solid/gas boundary in virtually the same place as  $\underline{CO_2 (V) H H_2O (S)}$  -  $\underline{CO_2 (V) H_2O (S)}$  curve. On this basis an existence of the new quadruple point ( $Q_3$ ) has been proposed but without detailed p-T coordinate. Although this is an interesting finding, one has to keep in mind that these are only theoretical predictions that are not confirmed by any experimental studies.

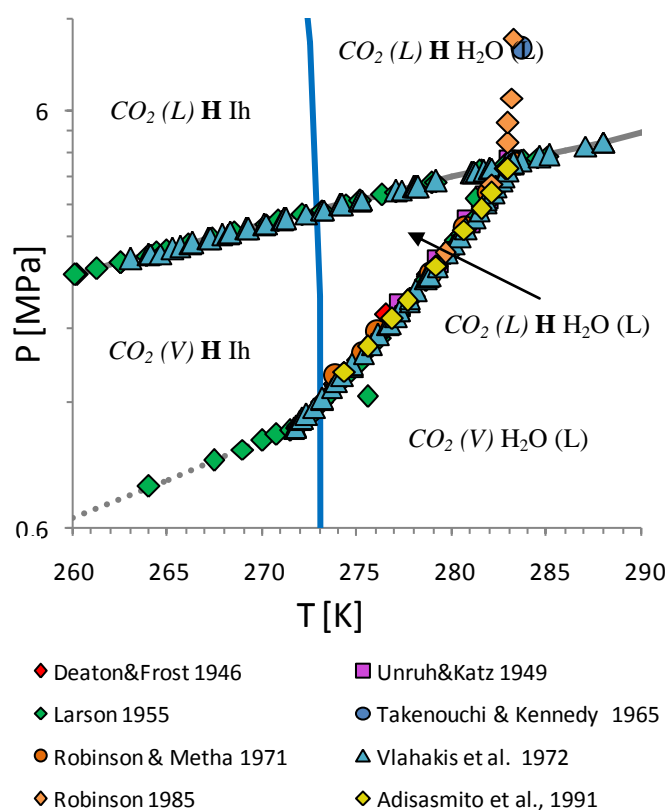


**Fig. 10)**  $CO_2$  hydrate stability field (**H**) close to melting point of ice. Experimental points after (Sloan, 1998). Blue line –  $H_2O$  melting curve. Gray solid line –  $CO_2$  liquefy curve. Gray dotted line – higher T part of H- $CO_2$  (V) Ih boundary.

### 1.1.5 Kinetics of gas hydrates

The kinetics of the formation and decomposition of gas hydrates is extensively studied by a number of experimental techniques like NMR and IR spectroscopy, X-ray and neutron diffraction or gas consumption. In spite of greatly extended p-T stability field that creates a number of technical difficulties (e.g. thick pressure cells, seals, absorbing materials), they were successfully applied to study almost all stages of reaction except the nucleation. This still mysterious and elusive process is very difficult to investigate in experimental way. Nowadays, molecular dynamic (MD) calculations stepped forward to investigate this no man's land. Unfortunately, very often, small box size, unrealistic boundary conditions or short time frame dramatically decrease the reliability of a simulation and one should be careful while dealing with such results.

### 1.1.5.1 Nucleation and driving force

The liquid water – ice phase transition boundary, crossing through the CO<sub>2</sub> hydrate stability field, greatly influence the nucleation of gas hydrates. As the reader may already guess, two different states of water force a reaction to follow two different kinetic pathways. One is related to very low temperatures and almost vacuum and another one to liquid-liquid or liquid-gas mixtures at moderate pressure. The driving force, that governs the reaction, may be defined in different ways (Sloan, 1998). The most general definition of it is the change in molar Gibbs free energy. In the thermodynamic equilibrium, it may be expressed as a super saturation, which is a difference between chemical potentials between phases in binary (Kashchiev and Firoozabadi, 2002a) or multi component systems (Anklam and Firoozabadi, 2004) that take part in the reaction. This term can be rewritten into a gas fugacity. For detailed mathematical description the reader may refer to mentioned papers or PhD thesis of A. Klapproth from 2002 (in German). For gas/solid interaction investigated in this work, it is related to the gas overpressure in the system as well as to temperature that is tightly related to the chemical potential. It is worthwhile to notice that the crystallization does not start immediately after reaching suitable conditions, even with high driving force. This delay in time is commonly called, an induction or incubation period (Kashchiev and Firoozabadi, 2003) and will be discussed later in Chapter 4. The stochastic nature of this process is influenced by a number of factors like: temperature, pressure, history of starting material, a presence of certain gases/chemical compounds or agitation of the system (Sloan, 1998), (Takeya et al. 2000), (Moudrakovski et al. 2001). The nucleation and growth is still a subject of research and a number of theories have been formulated to provide its physico-chemical description. Unfortunately, they are often in contradiction with each other or lacking a confirmation in experimental data. Following previous considerations, a division in two main groups is observed.

The tendency to form short-lived (Miyazaki and Yasuoka, 2002) clusters in pure liquid water suggests that embryos might be formed in the bulk. At this basis the labile cluster hypothesis has been formulated (Sloan, 1998). A nucleus is to be formed by an association of local clusters formed due to spontaneous arrangement of water molecules in the first coordination shell around guest molecule that stabilize the cage. Molecular dynamic (MD) calculations on methane clathrates (Belosludov et al. 2002) suggest that at the first step the most stable, small cages (5<sup>12</sup>) are formed. Yet, short lifetime of such clusters and low solubility of guest molecules in water (excluding CO<sub>2</sub> and H<sub>2</sub>S, whose solubility is considerably higher (Sloan, 1998) than e.g. hydrocarbons) create a significant barrier for so

interpreted nucleation. A change of the nucleation place from the bulk of water to the liquid-liquid or liquid-gas interface (Kvamme, 2002) increases considerably a probability of nucleus formation as the guest solubility problem is greatly reduced. It is also in accordance to the experimental observations where a hydrate film usually starts to grow at the interface of two phases (Mori and Mochizuki, 1998), (Takeya et al. 2000). Also an extensive mathematical description, for the ideas mentioned above, can be found in the literature (Kashchiev and Firoozabadi, 2002b). Yet, modern MD calculations show that the labile clusters can be easily formed only in much diluted solutions (Radhakrishnan and Trout 2002). Additionally, a closer analysis indicates that polyhedra tend to disintegrate rather than cluster together as the free surface energy of the growing embryo increases rapidly with the size. Eventually, the formation of critical size nuclei becomes very difficult. To overcome this problem a new model, “the local structuring mechanism”, has been proposed (Radhakrishnan and Trout 2002), (Anderson et al. 2007). It explains the nucleation as a phenomenon caused by a certain arrangement of guest species. The authors claim that a thermal fluctuation can distribute a group of the gas molecules in configuration resembling the one known from clathrates. Water molecules in the surrounding would automatically adjust their positions to form cages. So created clusters would be temporal and only if the number of building units exceeds the critical value a nucleus will be stabilized. The critical size has been calculated to be between 9.6 and 14.5Å, which is considerably less than 32Å obtained with the classical nucleation theory (Larson and Garside, 1986 after Radhakrishnan and Trout, 2002). An independent MD simulation (Hirai et al. 1997) of an aqueous solution with CO<sub>2</sub> molecules held fixed at the positions comparable to those known from the crystalline structure sI, seems to confirm the assumptions of local structuring hypothesis. Similar conclusions came out of *ab-initio* calculations of the stability of (5<sup>12</sup>) and (5<sup>12</sup>6<sup>2</sup>) empty and argon filled buckyball water clusters (Chihaiia et al. 2005).

The nucleation below the melting point of water is relatively simpler, in comparison to the previous case, as it can occur only at the ice/gas or ice/liquid interface. Also direct estimations of the nucleation density and their localization are possible, as it will be shown in Chapter 4. Imperfections (cracks, impurities, lattice defects) at the surface are most likely places where the growth starts (Moudrakovski et al. 2001). The quasi liquid layer (QLL) closer to the melting point of ice might also promote the nucleation (Hwang et al., 1990). An existence of this distorted layer on the ice surface has been found, with the help of NMR, as far as down to ~173K (Mizuno and Hanafusa, 1987), but already at about



223K the effect is negligibly small (Petrenko, and Whitworth, 1999).

### 1.1.5.2 Formation

As the hydrate formation above the freezing point of water is not a subject of this work and only a general picture will be presented. For further information, the reader may refer to a number of publications that deal with various scenarios in this p-T region e.g. (Lekvam and Ruoff, 1993), (Makogon, 1997), (Sloan, 1998). From the other side, formation below the melting point of ice, as a part of this thesis, will be more broadly discussed later on in this work (Chapter 4). Even though, before the reader reaches that point an elementary knowledge about the growth and its possible stages is necessary.

An initial growth, above melting point of ice, is rapid that proceeds mostly along the interface (Fig. 11). The growth in volume is considerably slower than at the surface because gas/water molecules transport limitation. When the available contact surface is completely transformed the reaction changes to a largely diffusion limited one (Fig. 12). Even then, high mobility of molecules at this temperature range carries on the transformation at reasonably high rate. Also in low temperature formation, two general stages can be distinguished. After an induction period, a surface exposed to gas molecules is relatively rapidly transformed into hydrate. A significant slowdown is observed when the hydrate layer is thick enough to reduce gas/water molecules transport through the shell (Barrer and Ruzicka, 1962). In case of xenon hydrate, the critical thickness varies between 20 and 100 unit cells, which assuming  $12\text{\AA}$  per unit cell, give  $240\text{-}1200\text{\AA}$  (Moudrakovski et al. 2001). The hydrate barrier changes the growth mechanism to diffusion limited one, which greatly affects the reaction rate. With temperature decrease, the already slow reaction is retarded even more. Mechanical grinding of the initial hydrate shell can be used to restore high transformation rate (Barrer and Ruzicka, 1962) but reaching full

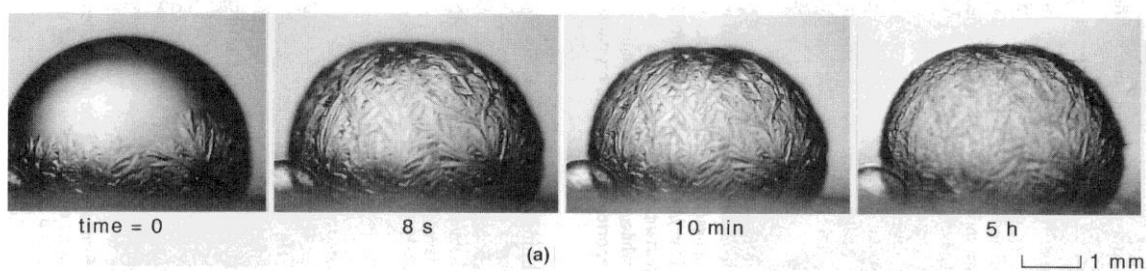


**Fig. 11)** Clathrate film developing on the water droplet. On closer inspection one can notice a characteristic dendritic like branching on the coating (Sloan, 1998).

transformation in reasonably short time requires crossing the melting point of ice in the later stages of the formation (Circone et al. 2004).

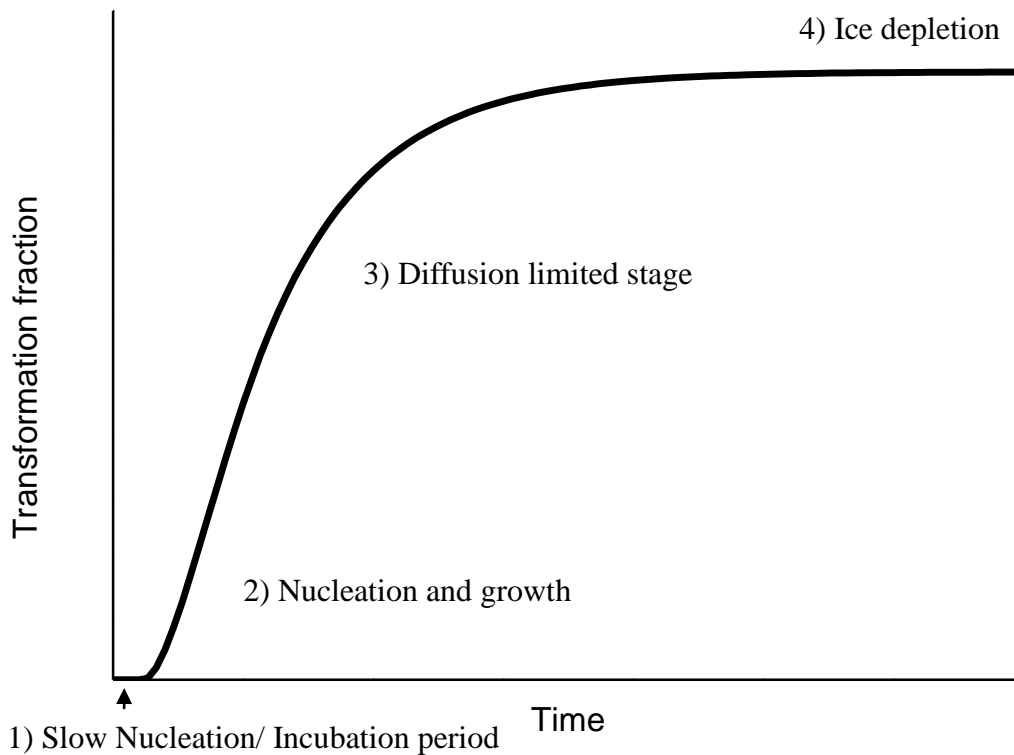


**Fig. 12)** Simulated formation curve (Powder 4 - Chapter 4) for the transformation of water ice and gas into CO<sub>2</sub> clathrate. 1) Initial fragment that do not show any reaction corresponds to a slow nucleation or incubation period. 2) The later lift off marks the moment where the nucleation limitation is overcome and clathrates beginning grow rapidly. 3) As the reaction proceeds gas/water diffusion starts to govern the formation. 4) Depletion of ice terminates the formation.

The formation of clathrates, like any other crystallization process, leads to an isotopic fractionation. Unfortunately, available information on this interesting process is very scarce. Presently the best explored is the ability of has hydrates to fractionate oxygen and deuterium from liquid water. Values for  $\Delta\delta^{18}\text{O}$  and  $\Delta\delta\text{D}$  measured close to the freezing point of water (Davidson et al., 1983), (Maekwa, 2004) are very close to those found for water ice. This similarity is most likely caused by the large similarities between both structures in terms of bond length and O-O-O angle. Much less explored is the ability to fractionate gas guest molecules. In fact the only work on this issue known to me was publishes very recently analyses of natural methane and ethane clathrates from lake Baikal (Hachikubo et al. 2007) accompanied by a laboratory studies on synthetic methane hydrates (Kosaka et al. 2007). In the first case one could observe a small enrichment of

hydrates in lighter carbon ( $\Delta\delta^{13}\text{C} \sim -57\%$ ) if compared to gas dissolved in water ( $\Delta\delta^{13}\text{C} \sim -55\%$ ). Slightly stronger effect was found for ethane (Hydrate =  $\Delta\delta^{13}\text{C} \sim -28\%$ , Dissolved gas =  $\Delta\delta^{13}\text{C} \sim -25\%$ ). In laboratory formed clathrates the enrichment was very small ( $\alpha \sim -0.0024$ ). It should be noted that all these experimental work was performed at temperatures close to the freezing point of water and higher.

#### 1.1.5.3 Decomposition

Above the freezing point of water, destabilized hydrates dissolve quickly to free gas and water e.g. (Rehder et al. 2004). Though, there is one exception where reaction may be abruptly halted just after short period of rapid decomposition close to 273K. Gas liberated from the cage structure absorb large amount of heat from the surrounding that is required to move molecules away from the collapsing crystal. This phenomenon, called the latent heat of reaction, very effectively lowers local temperature temporarily conserving clathrates in frozen water. In practice, thanks to it, not pressurized drilling cores containing gas hydrates may be excavated (Tulk et al. 1999).

Much more complicated processes governing the decomposition below melting point of ice will be discussed in details later on in this thesis (Chapter 4). Water molecules from destroyed cages crystallize at the surface forming a layer of ice crystals. After the end of previous section, the reader should be already aware of the difficulties caused by ice coating. This barrier can be overcome only by outward diffusive transport of gas molecules through imperfections in the ice shell. The total time necessary for complete transformation often exceeds days, weeks or even months. In extreme cases the decomposition may lead to, so called, “self preservation” e.g. (Stern et al. 2001), (Takeya et al, 2002), (Circone et al. 2003), (4.3.5) where gas hydrates virtually stop decomposing.

#### 1.1.5.4 Formation and decomposition in porous media

Natural gas hydrates often occupy empty voids in sediments and fractured rocks where thermodynamic and kinetics properties substantially differ from the one known from bulk accumulations e.g. (Clennell et al. 2000), (Anderson et al. 2003). A large diversity of natural sediments makes simulation in laboratory very tedious and in some cases leads to unique results. Yet, within a broad array of publications discussing this complex issue, one can distinguish three main trends in research concentrated around: (1) pore size and distribution, (2) mineral composition of a host rock, (3) ions and organic compounds dissolved in water.

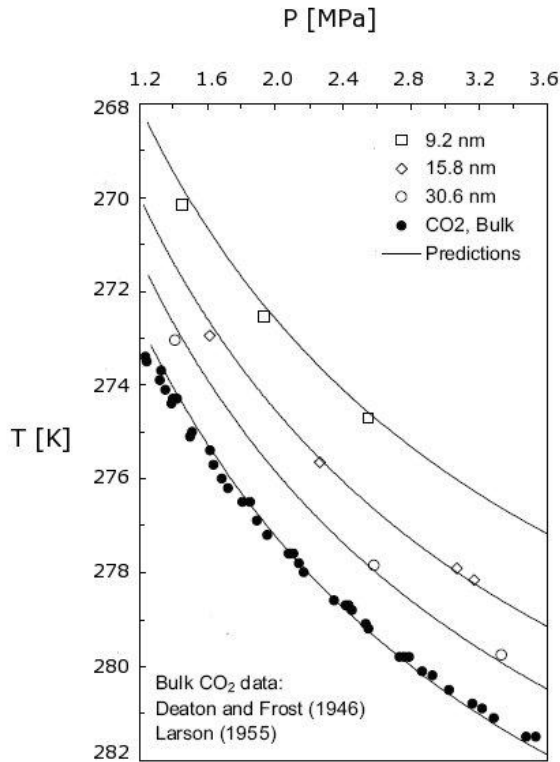


**Fig. 13)** Dissociation curves of CO<sub>2</sub> clathrates in porous silica with different mean pore diameter in comparison to bulk data. Experimental data in porous media after (Anderson et al. 2003). Theoretical prediction (solid line) after (Llamedo et al. 2004).

A use of glass or porous silica beads with known pore size distribution provides information of inhibiting capillary pressure effect on small voids/channels (Handa and Stupin, 1992), (Smith et al. 2002), (Uchida et al. 2002), (Anderson et al. 2003), (Llamedo et al. 2004), (Uchida et al. 2004), (Aladko et al. 2006). An analysis of existing data shows relationship between the reciprocal pore diameter and dissociation temperature /pressure (Fig. 13). The limitation of present predictive models oscillates around 3-6nm (Uchida, et al. 2002), (Llamedo et al. 2004) where bulk properties hold no longer. Along with porosity, another issue has been researched, namely position and development of gas hydrates in mineral framework (Tohidi et al, 2001), (Spangenberg et al. 2005), (Spangenberg

and Kulenkampff, 2006), (Schicks et al. 2007). Preliminary visual observation of growing clathrates in glass porous media by (Tohidi et al, 2001) comes to the conclusion that natural hydrates of poorly dissolvable gases (e.g. methane) may have no cementing properties. Indeed, in contrast to clay minerals, silicates like quartz, a thin layer of water

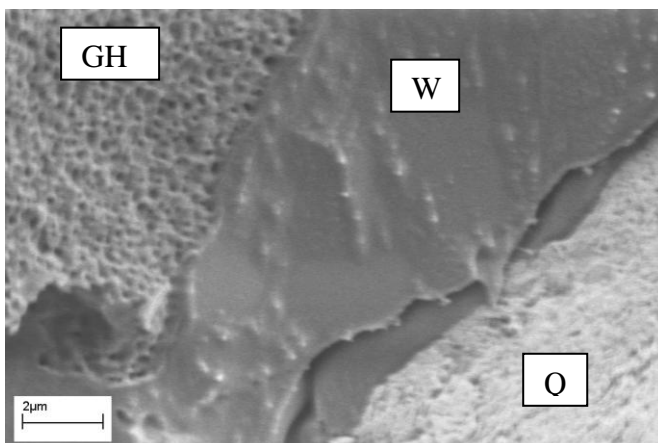


**Fig. 14)** Cryo-SEM image of natural methane hydrate from Malik research well. Between hydrate (GH) and quartz grain (Q) there is a clearly visible layer of frozen water (W) (Techmer et al. 2002).

film separates hydrates from pore walls (Fig. 14), thus hindering cementation process at low hydrate concentration. Nevertheless, a large concentration eventually leads to almost completely filled pore spaces and the cementation is unavoidable (Fig. 15). For more information the reader may go to the following publications: (Rempel and Buffett, 1997), (Xu and Ruppel, 1999), (Clennell et al. 2000), (Spangenberg and Kulenkampff, 2006).

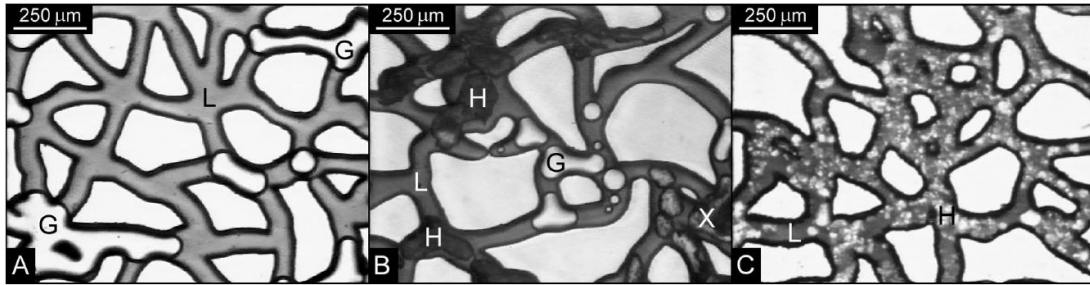


**Fig. 15)** Micromodel of nucleation and growth of methane clathrate within glass mesopore network (Tohidi et al. 2001). **A)** Starting system with liquid water (L) and free methane bubbles (G). **B)** Initial hydrate growth (H). Some bubbles show hydrate film formed at the gas-water interface (X). **C)** System after 2 days of reaction where pores are essentially filled with fine hydrate crystals.

Much more complex effect on decomposition conditions is observed in sediments containing clay minerals (Cha et al. 1988), (Uchida et al. 2004), (Chuvilin et al, 2005), (Chuvilin et al, 2007), (Klapproth, et al. 2007). An influence of these fine phyllosilicates is studied with two major representatives: kaolinite (1:1) and montmorillonite (2:1). Both of the materials typically occur in form of tiny plate crystals (Meunier, 2005) that effectively shift pore size distribution to lower values and thus contributing to the inhibiting effect (Uchida et al. 2004). Kaolinite having only very weak swelling properties binds H<sub>2</sub>O molecules on the crystal surfaces that in turn might reduce available water for clathrate formation in closed systems (Fig. 16), (Chuvilin et al. 2007). Similar effect, in case of montmorillonite, is even more drastic. An unbalanced charge on molecular plates that attracts ions/water between the packets leads to an adsorption of even larger amount of water molecules; the expansion of interplate distance may be as big as 18.8Å (Meunier, 2005). Yet, so preorganised water molecules might simultaneously promote hydrate nucleation even at the interplate faces. This phenomenon is expressed in reported shift of dissociation curve to higher temperatures (Cha et al. 1988), (Uchida et al. 2004). Yet, one should be aware that neither the nucleation promotion effect nor the temperature shift is firmly established as the mentioned results was found difficult to reproduce (Englezos and Hall, 1994), (Lee et al. 2002).

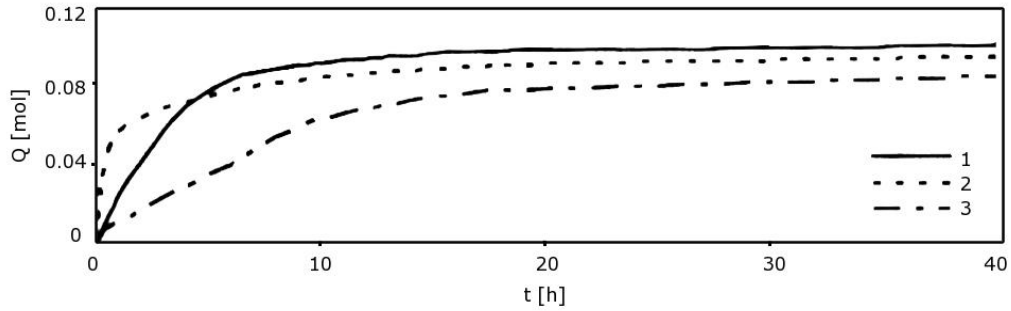


**Fig. 16)** CO<sub>2</sub> consumption curves in simulated soil with 10% of H<sub>2</sub>O. 1) pure sand sample, 2) sand with 7% of kaolinite, 3) sand with 7% of montmorillonite (Chuvilin et al. 2007). Both sediments containing clay minerals show lower gas consumption after 40h than pure sand sample possibly caused by decreased availability of water.

The salinity influence on clathrate stability seems to be less complicated but still carries many open questions. Even if the inhibition effect is confirmed in a number of publications

e.g. (Sloan, 1998), (Clennell et al. 2000), also regarding porous media (Fig. 17), (Østergaard et al. 2002), (Llamedo et al. 2004), it is still not know how particular salts stimulate the inhibition. It is especially important for sediments containing considerable amount of clay swelling minerals that host very broad variety of exchangeable ions. Also it is not clear how the inhibiting effect changes with an increasing concentration of salts in rest fluid during clathrate formation, which may be significant in no or weakly permeable sediments.

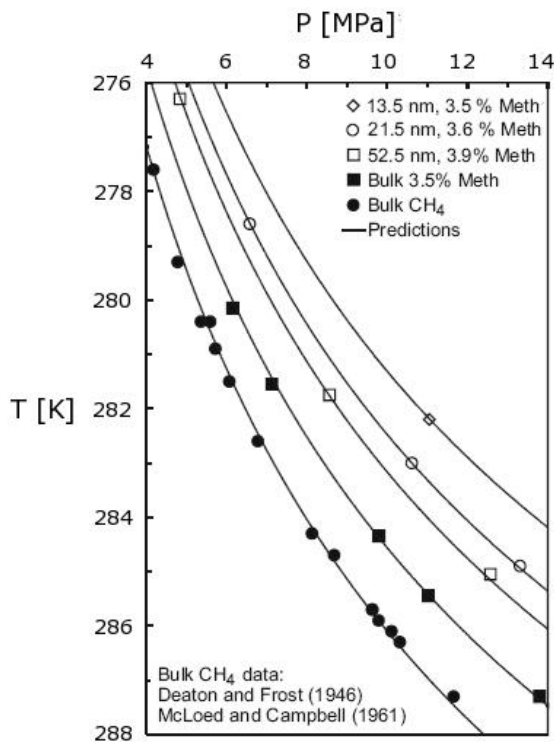


**Fig. 17)** An influence of organic compounds (3.5% methanol) on dissociation curves of CO<sub>2</sub> clathrates in porous silica with different mean pore diameter in comparison to bulk data. Theoretical prediction (solid line) after (Llamedo et al. 2004).

## 1.2 Occurrence of gas hydrate

Gas hydrates are formed on Earth and presumably also in other planetary bodies (e.g. comets, icy moons, planets) whenever suitable conditions are met. Terrestrial environments that favor clathrate crystallization are relatively easily accessible. The situation looks

differently for alien worlds in Solar System and beyond it. Nowadays, there is no direct or indirect method that would unquestionably determine existence of clathrate compounds anywhere outside Earth. This natural limitation drives authors to study extraterrestrial geological environments through laboratory simulations or by finding Earth analogs.

### 1.2.1 Earth

After the discovery of natural deposits of gas hydrates (see section 1.1), in over 40 years numerous sites in permafrost and continental margins have been successfully probed all around the world (Fig. 19). In these environments hydrates lie at different depths in a zone known as GHSZ (Gas Hydrate Stability Zone) (Sloan, 1998). Its position in vertical profile is controlled by lithostatic or hydrostatic pressure and temperature gradients. In Arctic Ocean, at depth ~300m and temperature close to 0°, GHSZ extends from the sea bottom to about 1100m into sediments. In permafrost this zone extends from 150 to 2000m below the surface (Buffett and Archer, 2004). The downward extension of GHSZ is often marked by, so called, BSR (Bottom Simulating Reflector) (Sloan, 1998) on seismic profiles, where clathrates border with sediments most likely filled with free gas and water (Fig. 18). The most common hosts for clathrates are permeable or semi permeable sediments. An overlying cover of poorly permeable layers additionally helps to saturate pore fluids in gas molecules. Depending on the host, hydrates may crystallize in various forms and shapes (Fig. 20). The most common are four types (Malone, 1985): (1) small quantities dispersed in sediments (Fig. 20A), (2) nodular agglomerations of few centimeter size separated by sediments (Fig. 20B), (3) Interlayer hydrates with sediments (Fig. 20C), (4) massive accumulations, even few meter thick (Fig. 20D). The chemical composition of natural

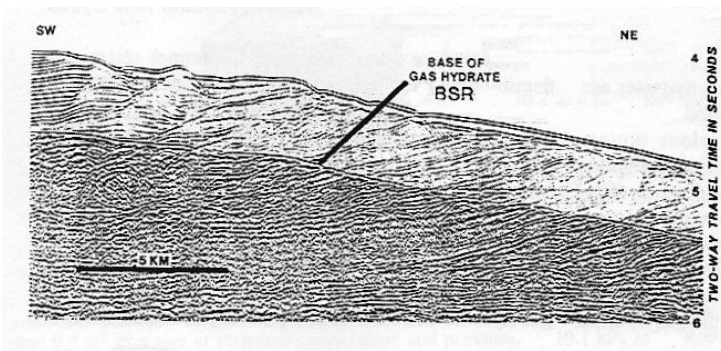


**Fig. 18)** Seismic profile through the HGSZ zone with clearly visible (BSR) bottom simulating reflector (Kvenvolden, 1993 after Shipley et al, 1979).



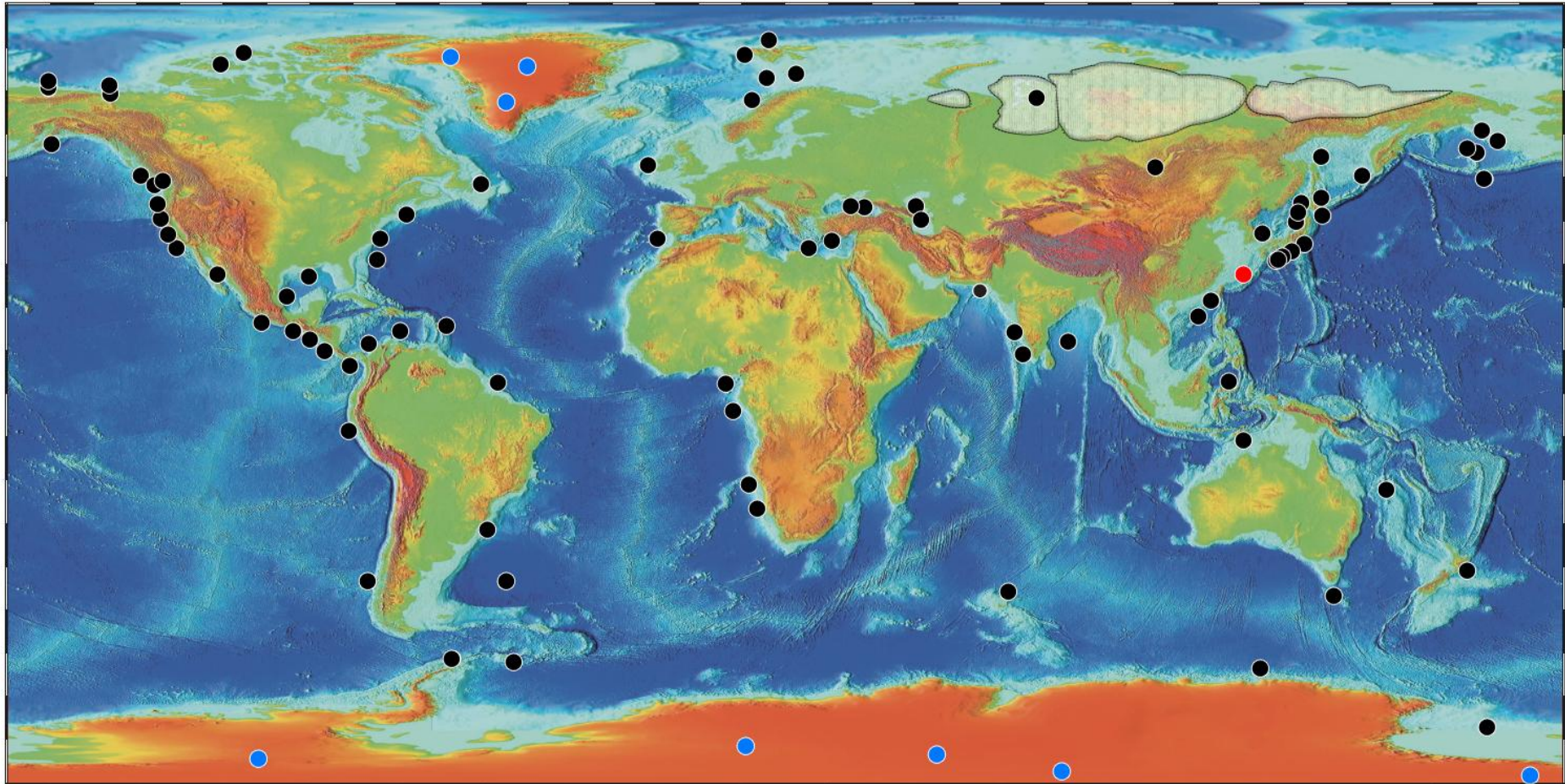


**Fig. 19)** Global occurrence of natural gas hydrates. Black dots: clathrate of hydrocarbons (mostly methane hydrates) (Kvenvolden, 2000), (Koh and Sloan, 2007). Red dot: known occurrence of CO<sub>2</sub> hydrates (Sakai et al. 1990). Blue dots: locations of ice deep wells (below 900m) with air hydrates (Thorsteinsson, 1996). White fields point o a possible existence of gas hydrates in Russian permafrost region.

Map source: USGS poster: A global Inventory of Natural Gas Hydrate Occurrence- Kvenvolden and Lorenson (2000).



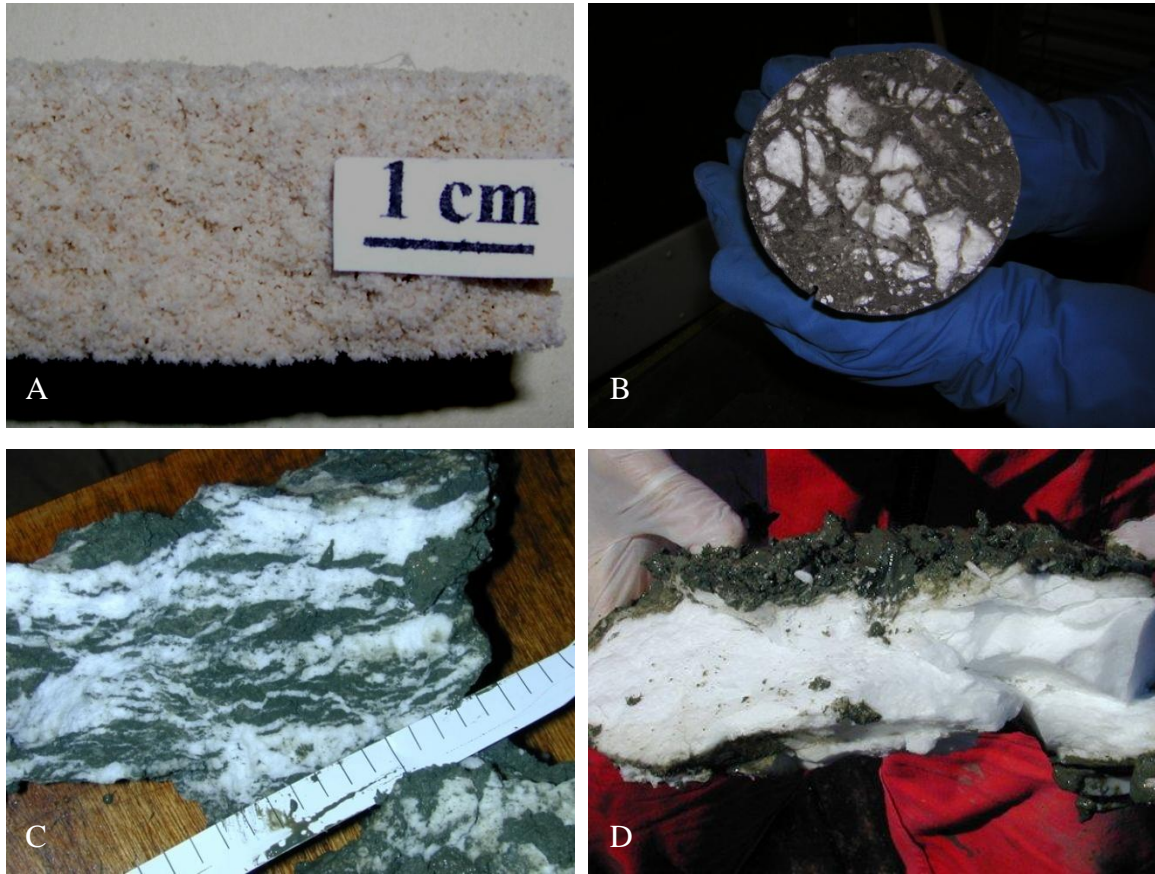


**Fig. 20)** Typical forms of clathrates within sediments. A) Dispersed crystals (laboratory grown clathrates in quartz sand), B) Nodular agglomeration, C) Layers of clathrates separated by sediment, D) Massive accumulation (approximately 10cm thick). Images: A) E.M Chuvilin, Moscow State University, Moscow, Russia. B-D) G. Bohrmann, Research Center Ocean Margins/Marum, Bremen, Germany.

clathrates varies from one place to another one but in almost all cases the dominating gas is methane. Aside from this main component, these natural hydrates contain also minor amounts of higher hydrocarbons (mostly: ethane, propane and butane), CO<sub>2</sub> and H<sub>2</sub>S. The percentage of additional gases depends on the source; (1) bacterial metabolism and (2) thermogenic exhalations are the most common (Sloan, 1998). While gas hydrates of organic origin are almost pure methane clathrates rich in light isotope <sup>12</sup>C (**Table 1**), the

Site	δ <sup>13</sup> C	C <sub>1</sub>	C <sub>2</sub>	C <sub>3</sub>	C <sub>4</sub>	C <sub>4</sub>	CO <sub>2</sub>	<b>Table 1)</b> Characteristic samples from biogenic and thermogenic sources (Gulf of Mexico and Caspian Sea) with striking difference in isotopic and chemical composition (After Sloan, 1998).
Biogenic Clathrate Samples								
Orca Basin	-71.3	99.1	0.34	0.28	-	-	0.24	
Green Canyon-257	-69.2	99.7	-	-	-	-	0.26	
Thermogenic Clathrate Samples								
Green Canyon-204	-56.5	61.9	9.2	22.8	4.5	1.3	0.2	
Buzdag (Caspian)	-44.8	74.7	17.4	2.4	0.4	1.1	3.6	

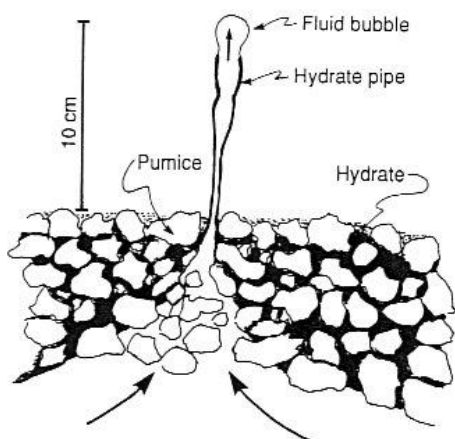


**Fig. 21)** Graphical interpretation of the occurrence of CO<sub>2</sub> hydrates in Mid-Okinawa hydrothermal system (Sakai et al. 1990).

non-organic are more diverse. Clathrates of other gases, like CO<sub>2</sub>, rarely exist as separate agglomerations. As the reader may see from the examples in Table 1 the average amount of CO<sub>2</sub> in natural gas hydrates is very small. Similarly looks water saturation in this oxide. Even if the p-T conditions are favorable, CO<sub>2</sub> hydrates tend to dissolve than accumulate (Teng et al. 1997), (Rehder et al. 2004). Therefore CO<sub>2</sub> hydrates, in general, are not stable on Earth and can be formed only in unusual geological context. Up to now, only one such place, associated with hydrothermal

system of the Mid-Okinawa trough back arc basin (Fig. 19), has been identified (Sakai et al. 1990) where CO<sub>2</sub> hydrates crystallize from CO<sub>2</sub> saturated pore water thus cementing overlying sediments. In some places, fluids are able to penetrate this impermeable layer and reach seawater. At the water/fluid interface, around the vents a thin layer of hydrate is also formed (Fig. 21). Although, this example may help to understand the formation of CO<sub>2</sub> clathrates in local environment, one should be cautious in direct application to other geological settings.

Apart from the occurrences discussed above, another kind of clathrate, namely air hydrate is worth mentioning. These compounds were recovered during deep drilling projects on Antarctica and the Greenland ice caps (Fig. 19). The transition zone (Fig. 22), where this particular hydrates are formed, extends from depth of about 800m to around 1200m where air trapped in bubbles is completely consumed (Miller, 1969). Some drillings shows exception from this theoretical consideration where hydrates occur (but are not necessarily stable) above e.g. (Craig et al. 1994), (Narita et al. 1999) or below predicted

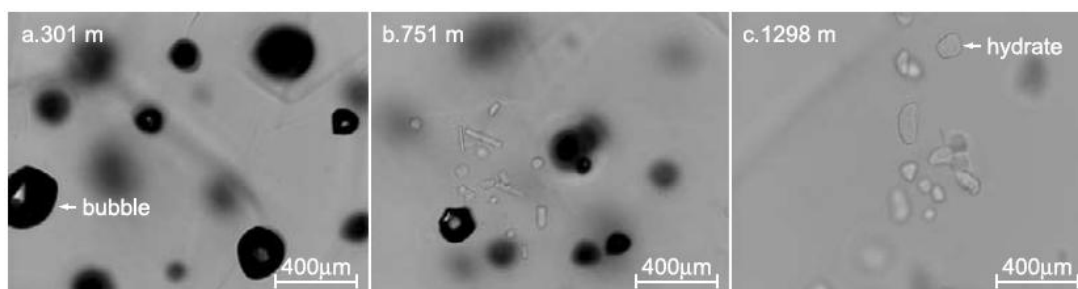


**Fig. 22)** Micrographs from three depths showing the transition from air bubble to air hydrate in the Dome F core (Ohno et al. 2004).

upper boundary e.g. (Kipfstuhl et al. 2001), (Lipenkov, 2000). Crystals have various shapes (e.g. spherical, graupel-like, rod-like, regular with well developed faces) with size do not exceeding 2mm (Narita et al. 1999), (Kipfstuhl et al. 2001). Air clathrates are not only a potential carriers of gases to the base of the ice cap but also a promising indicator of climate changes expressed in a number, mean size and crystal shape (Narita et al. 1999), (Lipenkov, 2000).

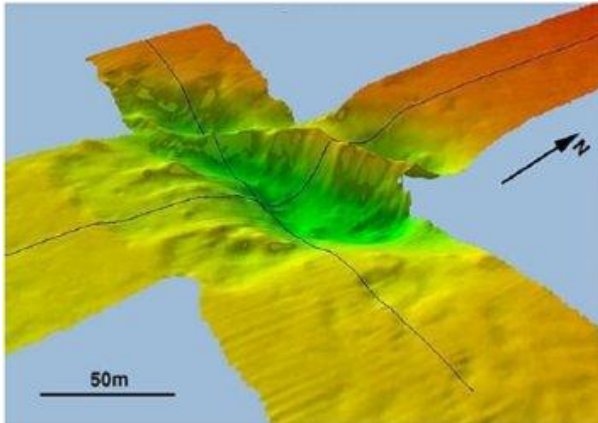


**Fig. 23)** Oblique view on one of the pockmark from Nyegga complex, off mid Norway with approximate depth of 9.5m (Hovland et al. 2005).

Along with growing economic and scientific interest in natural gas hydrates, scientists became aware also of possible geohazards that are related to these materials. They are often referred as a source of underwater landslides (Kayen and Lee, 1991 after Kenvolden, 1993), (Hanumantha Rao et al. 2002), marine fluid vents (Mazurenko and Soloviev, 2003), gas outbursts (Yakushev and Chuvilin, 2000) or even considerably large craters called pockmarks (Fig. 23)

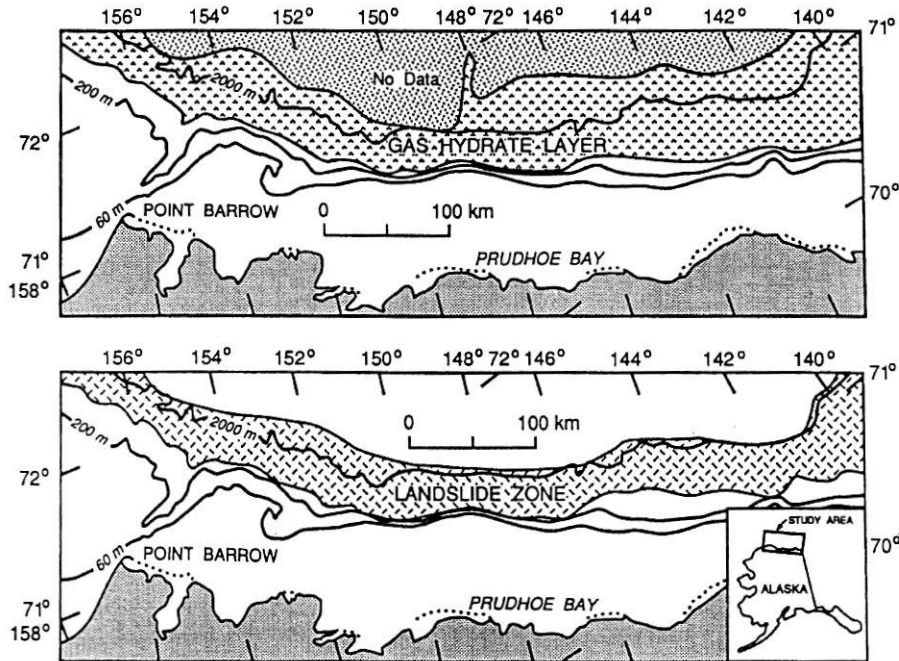


**Fig. 24)** Strikingly overlapping gas hydrate occurrence and landslide zone (Kvenvolden, 1993 after Kayen and Lee, 1991).



e.g. (Kelly et al. 1994), (Vogt et al. 1994), (Hovland et al. 2005), (Ondréas et al. 2005), (Gay et al. 2006). Indeed, any vertical shift of GHSZ causes decomposition, which may lead to the formation of previously mentioned structures. In marine settings, below the lower p-T boundary, sediments that may be saturated in gas-water mixture, behave similarly to water silt/sand mixture commonly called running ground. As a consequence slopes, rich in such material, are very susceptible to generate landslides (Fig. 24) triggered by e.g. seismic activity, turbidity flows or another landslides. Also an exploration of sea bottom containing gas hydrates is exposed to considerable hazard. Clathrates act as a seal to underlying sediments containing free gas and breaking this no permeable layer during a drilling may lead to gas blowups or uncontrollable leakages (Grauls, 2001). Gas hydrates trapped within permafrost are characterized by yet another unique property, already mentioned- self-preservation (Yakushev and Istomin, 1992), (Ershov and Yakushev, 1992), (4.3.5). This bizarre mechanism is capable of halting clathrate decomposition even if favorable p-T conditions for stabilization are long gone. So preserved gas hydrates are highly unstable, and can spontaneously decompose if this fragile state would have been destroyed. At the surface, it is expressed as natural gas releases or dangerous ejections of

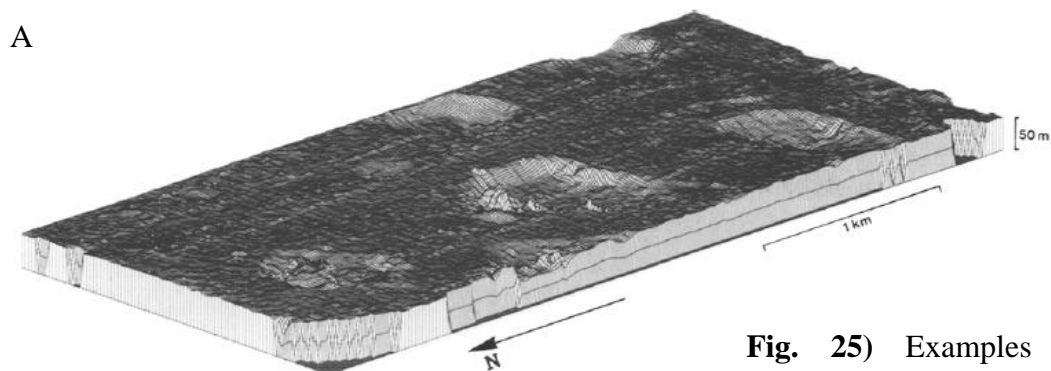
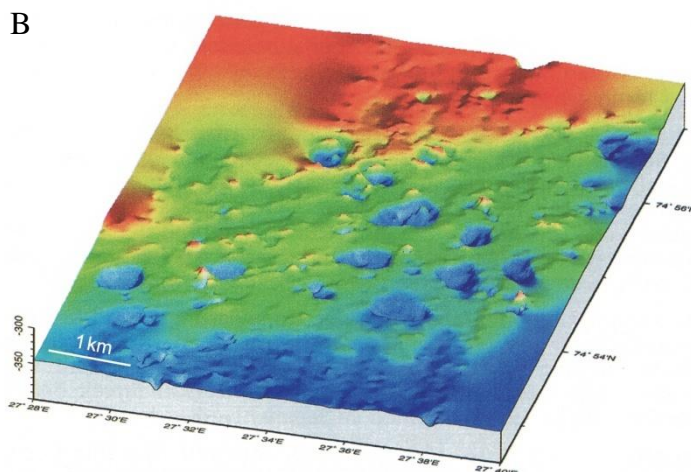


**Fig. 25)** Examples of cratered fields from the Barrens Sea bottom:



A) A section of sea bottom with close to 1km size and about 15m deep craters (Solheim and Elverhoi 1993).

B) Craters reaching 700m in diameter and depth up to 50m (Bohrmann and Suess, GEOMAR, Kiel).

volatiles during exploration drillings after new oil/gas deposits (Yakushev and Chuvilin, 2000). Possibly the most extreme example of destructive force related to decomposing hydrates can be found at the junction of two environments described above, namely flooded permafrost. Such bizarre geological settings have been created after last great glaciations in Pleistocene when global sea level raised for approximately 100m flooding lower placed old permafrost regions. Self-preserved hydrates trapped within ice layers that are in constant retreat (Rachold et al. 2007 EOS), with time, are exposed directly to seawater and thus causing violent decompositions. If free gas were trapped below the decomposing clathrate, such force would be increased even more. Releases in short time period, may be sufficient to form even hundred meters (Solheim and Elverhoi 1993) to a few kilometers (Prior et al. 1989) large craters (Fig. 25) on the sea bottom.

Aside from these local geohazards, there is another, global, aspect related to hydrate decomposition. Variations of global sea level or/and water temperature are very likely to affect the global position of GHSZ in vertical profile (Kenvolden, 1993). Gas hydrates driven outside stability field would feed Earth's atmosphere with methane and CO<sub>2</sub>; well known greenhouse gases. Yet, mentioned changes alone are not enough to have a significant impact on Earth's climate. Very important is the time scale of a transition (Buffet and Archer, 2004). Slow decomposition would lead to dissolution and oxidation of methane to carbon dioxide and water in oceans and seas. Small volumes of free gas that would escape to the atmosphere are not able to have any significant impact on the climate. Fast changes, destabilizing large volumes of hydrates in geologically short period of time, are the ones that pose real threat to the climate. In a still controversial concept, known as "the clathrate gun hypothesis" (Kennett et al. 2003), rapid releases that occur through fracturing or slumping of continental margins are related to a number of global warming events in Earth's past. Geologically recently, during the last ice age in Pleistocene some of the interglacials are associated to a series of large methane releases (Maslin et al. 2004). Also the end of this cold period, about 14ka ago, is sometimes linked to clathrate decomposition (Kenvolden, 1993). Going further in the past, active role of gas hydrates decomposition is suggested for the latest Paleocene warm period (Dickens et al. 1997), mass extinctions from Cretaceous-Tertiary boundary (Max et al. 1999) and possibly the greatest annihilation of life on Earth at Permian-Triassic boundary (Benton and Twitchett, 2003).

### 1.2.2 Solar System

The presence of clathrate hydrates in planetary systems is a subject of long debate but up to now no direct proof of their existence has been provided. From existing publications discussing this issue, two distinct groups emerge: (1) The first one is linked to the primordial material formed with the Solar system. (2) The second one considers an existence of gas hydrates in evolved, mature bodies (Chapter 2, 5).

Successive cooling of the nebula during the accretion eventually pushed the temperature sufficiently down to bind water vapor and other volatiles in form of ices. Yet, presently observable differences in chemical and isotopic composition of volatiles in different parts of the Solar System cannot be explained by simple condensation and the form in which water and other volatiles occur have to be taken into consideration (Delsemme, 1983), (Notesco et al. 1999), (Notesco et al. 2002), (Iro et al. 2003), (Mousis and Alibert, 2006), (Alibert and Mousis, 2007). Among different hypothesis explaining mentioned inhomogeneity, a theory of clathrate formation from condensation (Lunine and Stevenson, 1985) has been postulated. Based on thermodynamic calculations and handful of experimental results, authors suggested that gas hydrates may be formed directly from condensing water and gas (e.g. CH<sub>4</sub>, CO, Ar, Kr, Xe) within temperatures as low as 60K. One has to be aware that available formation experiments by deposition at 82K (Barrer and Ruzicka, 1962) or from water ice at 90K (Delsemme and Wenger, 1970) were not even close to postulated minimal temperature. Such approach already at that time caused serious doubts (Lewis and Prinn, 1980), since the hydrate formation is an activated process and great kinetic barrier at so low temperatures is to be expected. In spite of this obvious limitations a number of authors still consider this theory as a plausible scenario of trapping gases at very low temperatures during accretion of the outer Solar System e.g. (Iro et al. 2003), (Mousis and Alibert, 2006), (Alibert and Mousis, 2007). In course of time a theory of gas adsorption in amorphous ice has been postulated (Owen and Bar-Nun, 1995) that do not suffers from the very low temperature inhibition and can reasonably well reproduce binding properties of clathrates. Even if competitive in many ways to the gas hydrates condensation hypothesis, it does not completely neglect clathrate existence in extraterrestrial ices (Jenniskens et al, 1995). An annealing of amorphous ice in presence of sufficient amount of gas or mixture of gases at higher temperatures, about 130K (Richardson et al. 1985), (Blake et al. 1991), (Jenniskens et al, 1995) may eventually transform into gas hydrates, which makes this mechanism useful for larger icy moons or wandering bodies like comets. Even so, small planetismals orbiting at the frigid outskirts

of our Solar System would stay unaffected. Lately, even this process has been questioned (Notesco and Bar-Nun, 2000).

More evolved bodies, like icy moons and planets create another group of possible locations for clathrate hydrates. A unique environment and chemical composition of volatiles in each case requires a new scenario for the formation process. Large icy moons belonging to the Saturnian and Jovian systems may be a good example. Europa's shell of substantial thickness and underlying deep ocean of liquid water as it is generally accepted e.g. (Kargel et al. 2000a) theoretically create suitable environment for clathrates formation of gases such as O<sub>2</sub>, SO<sub>2</sub>, CO<sub>2</sub>, CH<sub>4</sub> (Crawford and Stevenson, 1988), (Prieto-Ballestros et al. 2005), (Hand et al. 2006). Although, the existence of these hydrates stay essentially as unconfirmed speculation, O<sub>2</sub> deserves here for special attention. Molecular oxygen is formed during radiolysis of water in a proximity to the surface and essentially contributes to the moon's thin atmosphere and Jovian plasma (Hand et al. 2006). Even though, in infrared spectra it is found to be in the solid form (Spencer and Calvin, 2002). It is particularly puzzling since the temperature of the first few meters into the icy regolith is too high (70-130K) for O<sub>2</sub> ice to be stable. Although there are attempts to explain this fact by O<sub>2</sub> mechanically trapped in ice (Johnson and Jesser, 1997), up to now the only plausible explanation might be found only in mixed clathrate cages (Hand et al. 2006). Next broadly discussed moon, in terms of clathrate occurrence, is Titan where within thick nitrogen dominated atmosphere, a considerable amount of methane has been detected during Voyager 1 flyby (Hanel et al. 1981) and lately firmly constrained by Cassini-Huygens mission (Niemann et al. 2005), (Waite et al. 2005). CH<sub>4</sub> as highly susceptible to photolysis would not be able to survive longer than 10-100 million years e.g. (Atreya et al. 2006) without a replenishing mechanism. At this place several theories step forward but there are still controversies around them (see Atreya et al. 2006 for full review). Among others e.g. (Niemann et al. 2005), (Kress and McKay, 2004), (McKay and Smith, 2005), a source of methane were pointed in the accretion of the moon from planetismals containing methane clathrate (Alibert and Mousis, 2007). Yet, in light of present knowledge, it is rather doubtful scenario. Apart from the gas origin, the present (and dominating) view on the composition of Titan's present crust and mantle also takes CH<sub>4</sub> hydrates into consideration as a plausible reservoir harboring methane (Loveday et al. 2001a), (Loveday and Nelmes, 2003), (Osegovic and Max, 2005), (Atreya et al. 2006), (Tobie et al. 2006). Along with studies of Titan, a new interest in another Saturn's satellite arose, namely Enceladus. This small moon shows evidences of an active cryo-volcanism or venting system that feeds

Saturn's E ring with icy material (Porco et al. 2006). The peculiarity of this phenomenon lies in its unknown source and mechanism. Aside from ideas involving boiling liquid water exposed to vacuum (Porco et al. 2006), a rapid decomposition of clathrate by sudden decompression (Kieffer et al. 2006) has been suggested. Presently, both warm and cold theories are extensively discussed (Kerr, 2006), (Huford et al. 2007), (Matson et al. 2007), (Nimmo et al. 2007), (Spencer and Grinspoon, 2007), but scarce data prevent from reaching the final conclusions.



# Chapter 2 – Mars

A proper understanding of the results coming from this work require from the reader some basic knowledge about the present and past Martian environment. Unfortunately, the popularity of the Red Planet in the modern planetary science is also its curse. A countless number of publications make a comprehensive review very difficult to write. From the point of view of this thesis, the most important is the history of Martian water and CO<sub>2</sub>. Yet those elements are tightly entangled with the rest of Martian environment

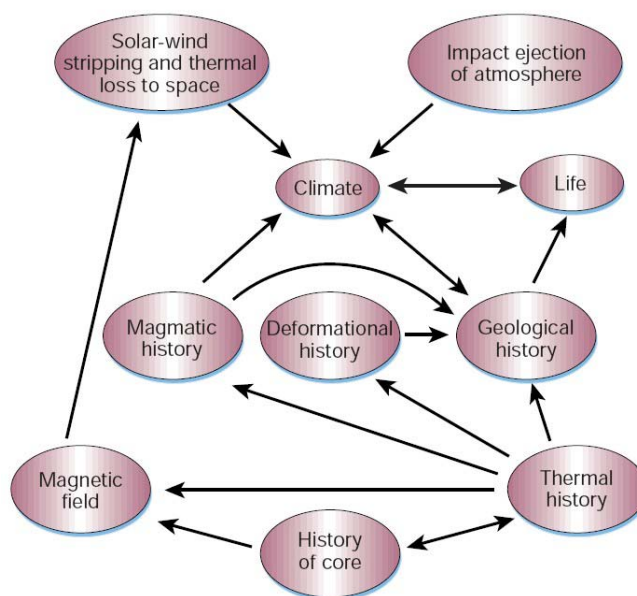


**Fig. 26)** Schematic graph of dependences between various elements of the Martian realm (Jakosky and Phillips, 2001).

through such variables like e.g. initial content of water and gases, accretion and out gassing, the lifetime of the global magnetic field or atmosphere stripping (Fig. 26). Therefore, a broader introduction is indispensable. In the first part, the reader will find a short review of Mars exploration. Extended version this fascinating story one can find in a numerous books on Mars e.g. (Sheehan, 1996). Next subchapters present results from the past and present missions. The last part will contain a compilation of ideas and hypothesis concerning presence of gas hydrates on the Red Planet and their possible role in the environment.

## 2.1 History of Mars exploration

Mars is one of the planets that is known from ancient times thanks to its very high brightness (-2,9 magnitude) on the night sky, that is surpassed only by Venus, Moon and sometimes Jupiter. Its present name, after the Roman god of war, comes from hematite dust that gives it a characteristic reddish or bloody color well visible with naked eye. It is interesting to note that the idea of planet's divine patron related to fire or war is much older than Roman civilization. In ancient Babylon, a name of the Red Planet was *Nergal* from their god of war, fire and destruction. It was probably adopted by Mediterranean

civilizations like Egyptian (*Hr-Dšr* – Horus the Red), Hebrew (*Ma'adim* – the one who blushes) or Greek (Ares) and later on brought to Rome and again renamed to Mars. It is not clear how strong relations were between ancient civilizations but a similar pattern can be observed all around the world (Hindu: Mangala/Bhauma/Angaraka- “one who is red in color”, Chinese, Japanese, Korean and Vietnamese: 火星 – “fire star”). Numerous observations of Mars’ passages were recorded through centuries in Europe (among others by Aristotle, Galileo), far east (e.g. in Babylon), India and East Asia. There are also hints that South American civilizations possessed considerable observational knowledge about Mars but a great deal of it has been lost forever during conquests.

A new era in observations has been opened by a development of first advanced optical devices, in the XIX century. In September 1877, during a perihelic opposition of Mars, the Italian astronomer Giovanni Schiaparelli constructed a first “detailed” maps of Martian surface (Fig. 27), within the limits of resolution. Several features introduced in Schiaparelli’s creation, survived till modern times (e.g. Tharsis, Elysium, Syrtis Major) giving a birth to present Martian nomenclature. Also in that time, a network of controversial *canali*, observed on Mars, ignited a vigorous discussion about the extraterrestrial life that goes on even now (see section 1.5). In course of time increasing

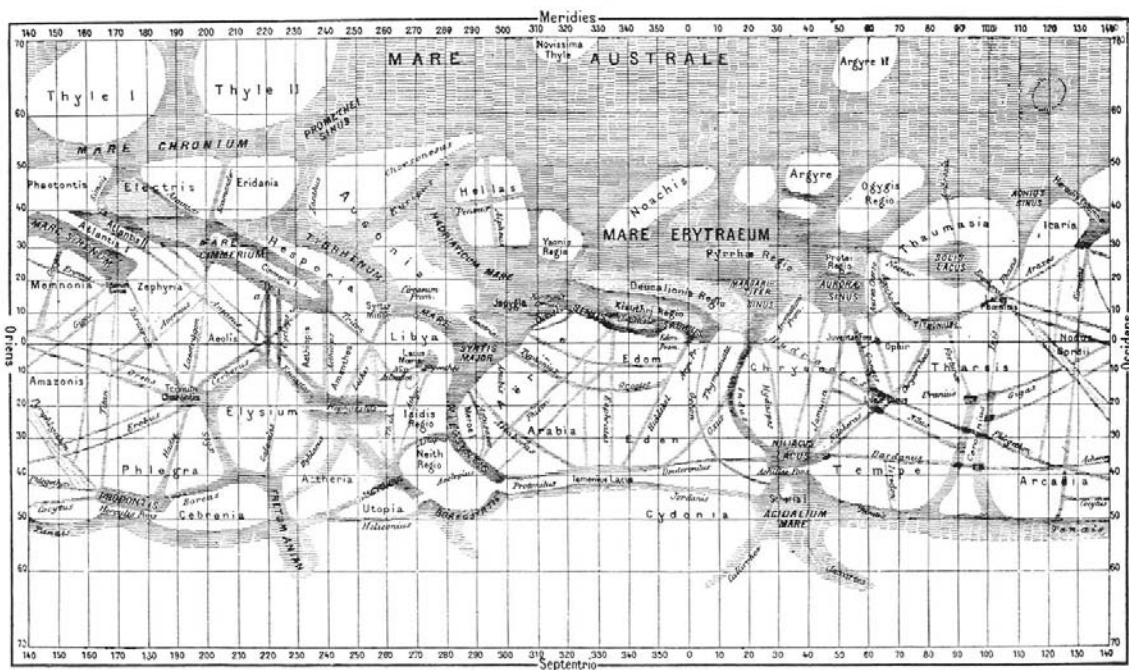


**Fig. 27)** Giovanni Schiaparelli's map of Mars (1877-1886), with famous channels. Reproduction from "Flammarion, La Planhte Mars" 1888. North of the map points downward (Source: NASA).

resolution of ground based telescopes allowed for revision and considerable reconstruction of older Martian maps.

The next great leap in our knowledge about Mars is dated on early 1960s with the first space exploration programs that were launched in the atmosphere of a space race between USA and Soviet Union (presently Russia). An early politics of these two countries was based on multiple missions of twin probes lunched one after another one in a narrow time window. Therefore the reader should not be surprised by indeed enormous list of Martian space missions, found in the literature, surpassed only by Earth and Moon related programs. Yet, among 46 spacecrafts/landers sent to Mars (including two Phobos probes) only 19 reached the planet and conducted the planned tasks. This great discordance is often termed as a Martian curse or Martian Bermuda triangle. The first attempts were made by Russians with a series of six probes: Marsinik 1, 2 (Mars 1960A, Mars 1960B), Mars 1, Sputnik 22, 24 (Mars 1962A, Mars 1960B) and Zond 1964A. None of them ever reached Mars (to be precise only Mars 1 succeeded in leaving Earth's orbit). Also the first

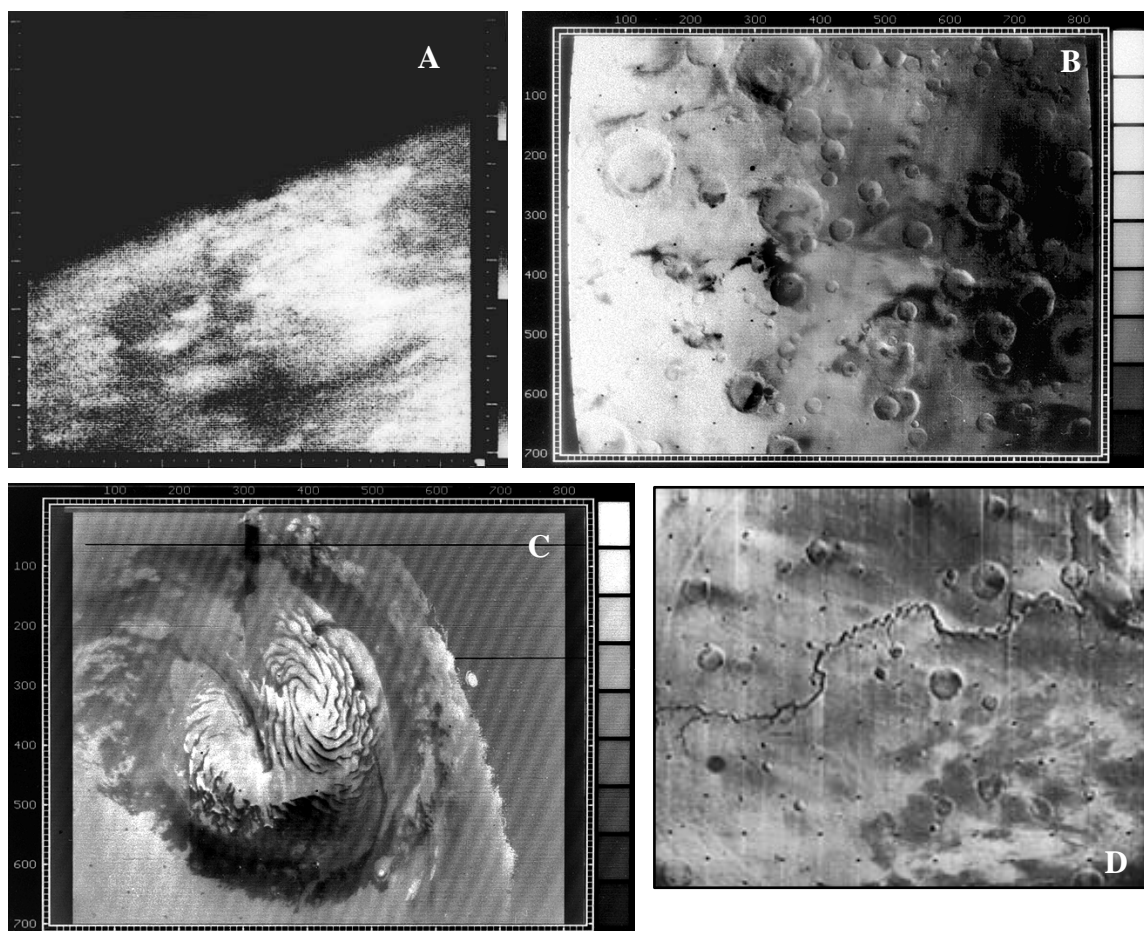


**Fig. 28)** Images of the Mars' surface from the early missions: A) The very first close-up of Mars - Mariner 4, B) Promethei Sinus - Mariner 9, C) The north polar cap - Mariner 9, D) Flow features-Nirgal Vallis-Mariner 9 (Courtesy NASA/JPL-Caltech and NSSDC).

American attempt, Mariner 3, shared the same fate. In spite of this failure, in 1965 its twin spacecraft, Mariner 4, successfully passed the Red Planet in a close flyby and transmitted the first close-ups of Martian surface (Fig. 28 A). These images, although of a limited quality, confirmed what was suspected already for a long time; Mars was a cold and dry planet with water locked at the poles (Fig. 28 B, C). Subsequent successful flybys in 1969 (Mariner 6, 7) and later missions additionally grounded this image but also provided first evidences for past water or other liquid activity on Mars (Fig. 28 D). A next step, in the exploration, has been made by orbiters and first attempts to settle automated landers and rovers on the surface. The first probe successfully placed on the orbit around Mars belonged to USA (Mariner 9 in 1971). It arrived on Mars two weeks before a Russian probe, Mars 2 that carried also a lander module. An attempt to deploy the device ended with a crash that came into history as the first human made parts that touched the Martian surface. For the first truly successful landing one had to wait till famous Viking twin mission in 1976 that that provided first images of barren Martian desert covered with basaltic blocks (Fig. 29). Both landers were functional for extended period of time (Viking 1 till 1982) providing priceless data on Martian weather. In spite of this obvious success Mars was deserted for nearly 13 years. A great impact on this pause had the collapse of Soviet Union in early 1990s that brought the space race to an abrupt end. A next successful mission (MGS-Mars Global Surveyor) arrived to Mars as late as in 1996 and was followed, a year later, by Mars Pathfinder, the first successful rover mission. Presently there are three orbiter missions operating over the planet (Mars Odyssey, Mars Express and MRO-Mars Reconnaissance Orbiter) and two rovers on the surface (Spirit and Opportunity). It is also worthwhile to mention that the newest lander mission (Phoenix Lander) was launched in 4<sup>th</sup> of August of this year (2007) safely reach Mars, and already sends data.

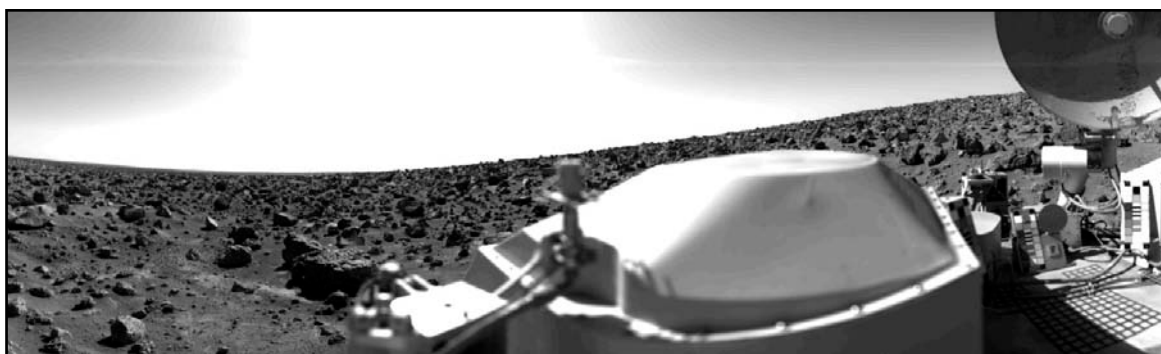


**Fig. 29)** Rocky desert on Utopia Planitia landing site, northern plains – Viking 2 lander. (Courtesy NASA/JPL-Caltech).

## 2.2 Mars in numbers and figures

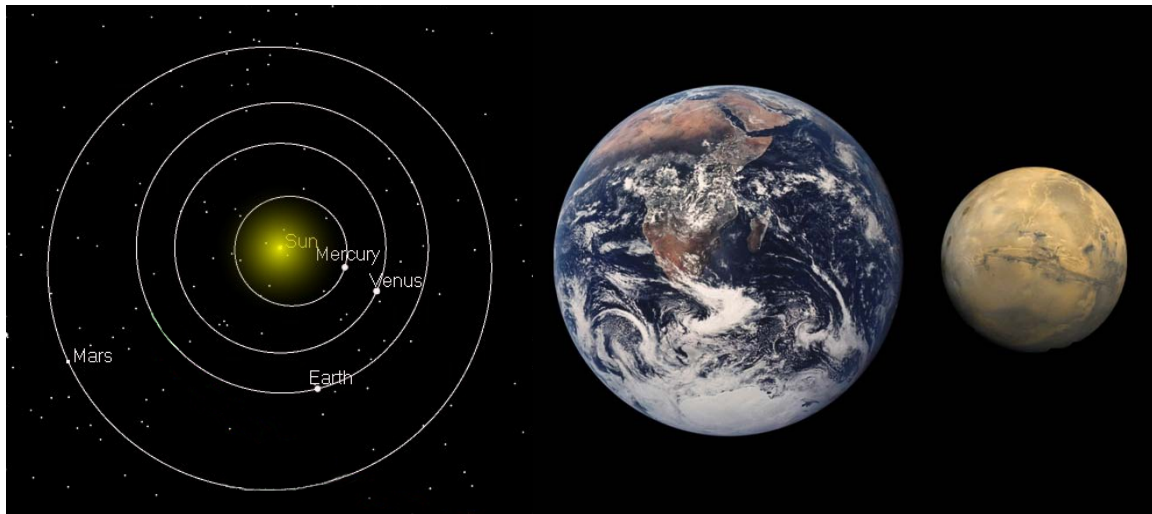


**Fig. 30)** Model of the inner Solar System (left) with well visible eccentricity of Mars' orbit. Earth and Mars size comparison (right) (Courtesy NASA/JPL-Caltech).

Mars, the fourth planet in the Solar system, is often referred as very similar planet to Earth (see comparison in Table 2) (Read and Lewis, 2004). The distance from the Sun is on average close to 1.5AU but due to the considerably big eccentricity of Mars' almost ideally circular orbit (Fig. 30) the real distance varies from 1.66AU (aphelion) to 1.38AU (perihelion). As a consequence of the greater distance from the Sun, Martian orbital period takes 686.98 terrestrial days, which is nearly two times (1.88) longer than Earth needs to complete the orbit. Mars rotates around its axis with the period of 24h 40min (1sol), which

	Earth	Mars
Mean orbital radius ( $10^{11}$ m)	1.5	2.28
Distance from Sun (AU)	0.98-1.02	1.38-1.67
Orbital eccentricity	0.017	0.093
Planetary obliquity	23.93°	25.19°
Rotaiton rate ( $10^{-5}$ /s)	7.294	7.088
Solar day (s)	86.4	88.775
Year length (sol)	365.24	668.6
Year length (Earth days)	365.24	668.98
Equatorial radius ( $10^6$ m)	6.378	3.396
Surface gravity ( $m/s^2$ )	9.81	3.72
Surface pressure (Pa)	101300	600 (variable)

**Table 2)** Similarities and differences between Earth and Mars (Read and Lewis, 2004).

is close to 23h 56min long Earth day. The tilt of the axis is again similar, 25.19° against terrestrial 23.93°. As it will be also discussed later (see 2.5) this close agreement is coincidental. Martian obliquity (tilt) was changing in a very broad range between 10 and 40° on a 10<sup>5</sup> year time scale reaching even 60° on a 10<sup>7</sup> year time scale. Projection of those changes, on the distant past, beyond ~10Myr is hindered by large uncertainties in orbital parameters. The tilt of Earth's spin axis is greatly stabilized by a mass of Moon (Laskar and Robutel, 1993), (Touma and Wisdom, 1993). The same cannot be said for the Red Planet that is encircled by two small natural satellites: Phobos (11.1km mean radius) and Deimos (6.3km mean radius). Their non-spherical size and low density (~2.0 g/cm<sup>3</sup>) suggest that those bodies are in fact captured asteroids, most likely of carbonaceous chondrite composition. The planet's average radius is close to 3400km, which is about twice less than our planet (Fig.30). With the smaller size, and the mean density of 3.934 g/cm<sup>3</sup> Martian gravity is about 38% of the terrestrial. Present atmosphere is composed almost entirely from CO<sub>2</sub> with small amount of nitrogen and argon. The rest of gases do not exceed 1% (Table 3). An average atmospheric pressure at the surface is very low in comparison to Earth and varies around 6mbar (0.6kPa) (Read and Lewis, 2004). Such tenuous atmosphere cannot support elevated surface temperatures that extend from ~140K at the pools to ~295K in equatorial region. The average amount of atmospheric water vapor is very low but stays close to saturation. It is usually represented by a global layer of ~10µm thickness (Read and Lewis, 2004), (Fouchet et al. 2007). Any liquid water exposed to the atmosphere would boil off or freeze as it is thermodynamically unstable e.g. (Haberele et al. 2001).

#### Atmospheric constituents

CO <sub>2</sub>	95.32 %	H <sub>2</sub> O	210 ppm
N <sub>2</sub>	2.7 %	NO	100 ppm
Ar	1.6 %	He	2.5 ppm
O <sub>2</sub>	0.13 %	HDO	850 ppb
CO	0.08 %	Kr	300 ppb
		CH <sub>2</sub> O*	130 ppb
		Xe	80 ppb
		CH <sub>4</sub> **	10 ppb

**Table 3)** Composition of the Martian atmosphere (Williams, 2004), \*(Formisano V, public information), \*\* (Formisano et al. 2004).

## 2.3 Mars' surface and internal structure

Present knowledge about the internal structure is based largely on remote sensing techniques, landers and meteorites (SNC): shergottites, nakhlites, and chassigny (commonly believed as fragments of Martian crust ejected during large impacts – e.g. Nyquist et al. 1979 , Jagoutz, 1991, Head et al. 2002). On this basis, it has been generally accepted that Mars, perhaps like other planets from the inner Solar System, have a differentiated interior where core, mantle and crust can be distinguished (Fig. 31). The segregation in layers gives a rise for thermally or/and chemically driven convection that eventually might lead to a global magnetic field generation (see 2.4).

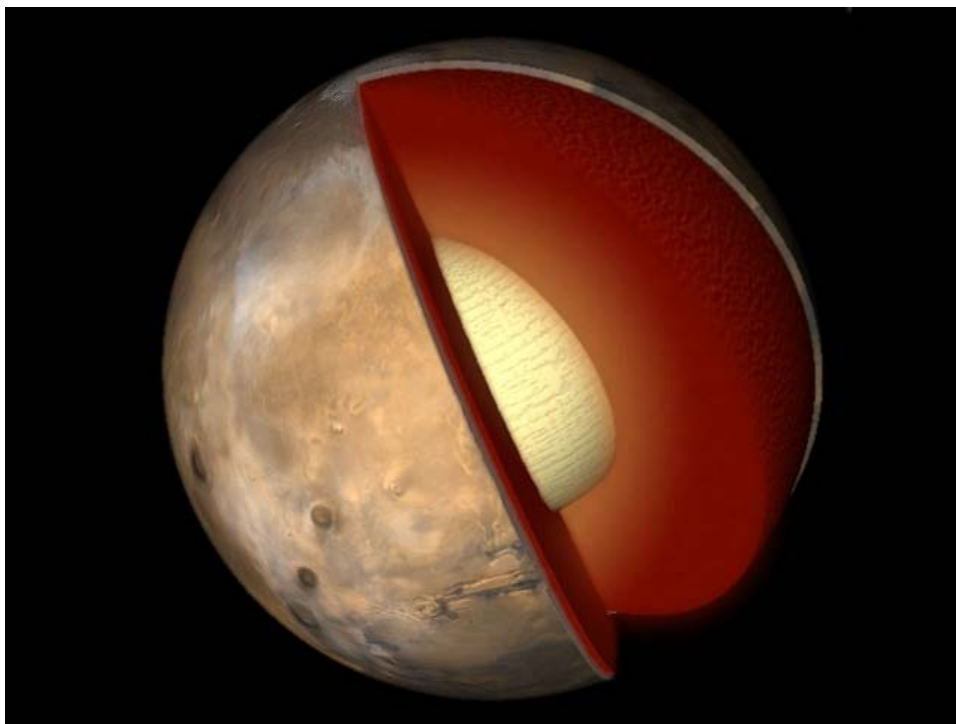


**Fig. 31)** Model of Mars' interior. A) Core, B) Mantle, C) Crust (Source: PSN National Science Center, Malaysia, [www.psn.gov.my](http://www.psn.gov.my)).

### 2.3.1 Core

The mean density and moment of inertia that can be measured by probes from the orbit suggest large similarities to a scaled Earth model (Stevenson, 2001). Following this assumption, the core has been formed due to a gravitational differentiation of immiscible iron and silicates at the early stage of planet's accretion. Based on  $^{146}\text{Sm}$ ,  $^{182}\text{Hf}$ ,  $^{142}\text{Nd}$ ,  $^{182}\text{W}$  e.g. (Harper et al. 1995), (Lee and Halliday, 1997), (Kleine et al. 2004), (Foley et al. 2005), derived from SNC meteorites, the time for core-mantle separation was very short. The



presently accepted value is 10 - 12My years after the formation of the Solar System (Blichert-Toft et al. 1999), (Shih et al. 1999), (Kleine et al. 2004), but even a shorter period has been suggested (Yin et al. 2002), (Jacobsen, 2005). Heat needed for an extensive melting and possibly formation of magma ocean e.g. (Elkins-Tanton et al. 2005a), (Elkins-Tanton et al. 2005b), (Médard and Grove, 2006), could have been provided through the kinetic energy of impacting bodies e.g. (Wetherill, 1990), (Agnor et al. 1999). An influence of decaying radioactive elements, like  $^{26}\text{Al}$ , seems to be insignificant at this early stage of evolution (Elkins-Tanton et al. 2005a). Recently refined moment of inertia (Sohl et al. 2005) and tidal deformations data (Yoder et al. 2003) allow for the core radius estimation, with considerable precision, between 1520 and 1840km taking 3390km as a mean planetary radius (Stewart et al. 2007). Although, there are indications (Yoder et al. 2003) for a still relatively hot and at least partially molten core, it is still unclear if a solid inner core is developed. Evolutionary models propose several solutions e.g. (Stevenson, 2001), (Fei and Bertka, 2005), (Sohl et al. 2005), (Stewart et al. 2007) that are strongly correlated with core's chemical composition. The most often invoked constituents in terrestrial planets are iron with small amount of nickel and some light element like sulfur or silicon (Gessmann et al. 2001), (Li and Agee, 2001), (Sohl et al. 2005), (Stewart et al. 2007).

### 2.3.2 Mantle

The mantle is even less understood. Additionally to a large variation in possible chemical composition (see review in Médard and Grove, 2006), difficulties arise also from the history of mantle formation. Possibly, the most widely accepted chemical composition model (Dreibus and Wänke, 1985), derived from SNC meteorites, seems to confirm a hypothesis of two distinct sources that took a part in terrestrial planets accretion (Ringwood, 1977), (Wänke, 1981). Proposed components are: A) chondrites with reduced chemical components (e.g. enstatite chondrites), B) volatile rich carbonaceous chondrites (Dreibus and Wänke, 1985). Quick, homogenous accretion from such elements would cause partial oxidation of more reduced components thus binding them before segregation could take a place. Fe, Cr and Mn enrichment in SNC meteorites seems to be in accordance with this scenario (Dreibus and Wänke, 1985). Moreover, high volatile content in component B would effectively support partial melting by lowering solidus temperature (Médard and Grove, 2006) that eventually lead to magma ocean formation and homogenization of upper 700-1500km of Mars (Richter et al. 1998), (Elkins-Tanton et al. 2005a), (Elkins-Tanton et al. 2005b). Even though, close analyses of SNC meteorites



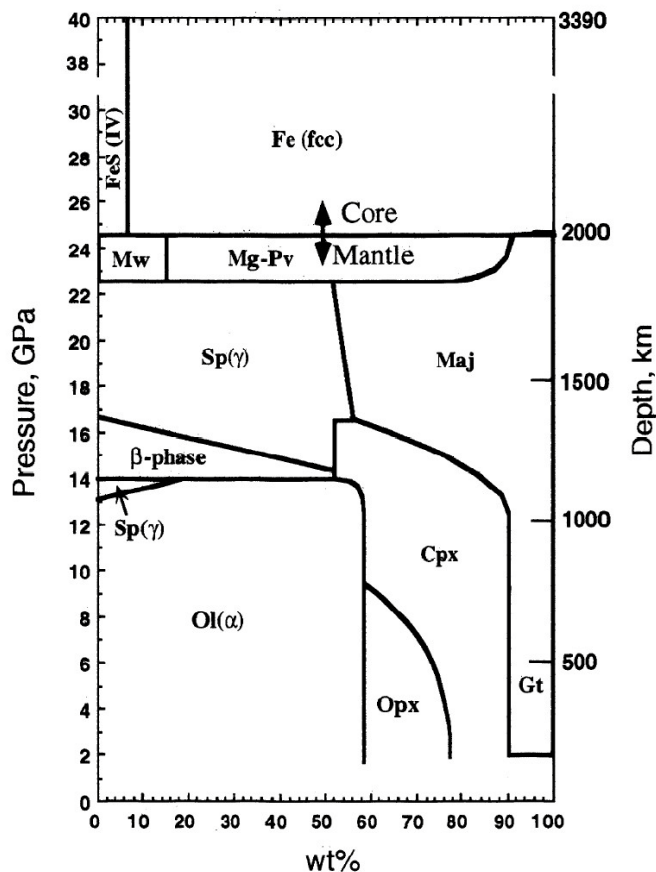


**Fig. 32)** Mineralogical model of the Martian mantle. Ol - olivine, Sp ( $\gamma$ ) – ringwoodite,  $\beta$ -phase – wadsleyite, Opx – orthopyroxene, Cpx – clinopyroxene, Gt - garnet, Maj – majorite, Mw – magnesiowüstite, Mg-Pv – magnesium perovskite (Bertka and Fey, 1997).

yield similar mineralogical assemblages e.g. (Bertka and Fei, 1997). Upper Martian mantle is thought to be dominated by olivine, (ortho- and clino-) pyroxens and garnet (Fig. 32). At about 9GPa, orthopyroxene become unstable. Close to 13.5GPa, due to high Fe content, olivine transforms partially to ringwoodite marking the beginning of the Martian transition zone (in Earth’s upper mantle olivine transforms to wadsleyite and later to ringwoodite). A small increase in pressure, to 14GPa, causes transformation of olivine and ringwoodite into wadsleyite accompanied by clinopyroxene and high pressure garnet (majorite). From about 15GPa, ringwoodite is formed in expense of wadsleyite and clinopyroxene. The last one is completely consumed at about 17GPa. In Martian conditions, where pressure increases much slower with depth than in Earth’s mantle, the phase transitions between  $(\text{Fe,Mg})\text{SiO}_4$  polymorphs are likely to form diffusive boundaries. Close to the core/mantle boundary another transition that marks the beginning of the lower mantle is predicted. If the

suggest that some parts of the mantle could retained heterogeneous domains (Foley et al. 2005) that were later on magma sources for shergottites, nakhlites, and chassigny. Although present Martian mantle is “dry”, it cannot be excluded that at the early stage of evolution it contained appreciable amount of water (Médard and Grove, 2006) that supports thermal convection by decreasing melt’s viscosity. Presently, a minor amount of water (several ppm) from homogeneous accretion might be still bound in nominally anhydrous crystal phases (Médard and Grove, 2006). High pressure experimental studies on present Martian mantle compositional models, although based on different assumptions,

temperature is high enough and if current values for the core radius (Sohl et al. 2005) are close to the reality, an existence of the lower mantle becomes plausible. The assemblage of ringwoodite and partially majorite is replaced by magnesiowüstite, perovskite and majorite.

### 2.3.3 Crust

Unlike the core and mantle, Martian crust is much easier subject of investigation. Gravimetric and topographic data (Fig. 33 A) defines the maximum crustal thickness on not greater than 150km (Sohl et al. 2005) with the average value between 30 and 80km (McGovern et al. 2002), (Wieczorek and Zuber, 2004). These results are consistent with geochemical data retrieved from the SNC meteorites (Norman, 1999) and in-situ measurements (McLennan, 2001). Generally, younger surfaces overlay regions with thinner crust. Older surfaces match closely to the regions with thicker crust (Fig. 33 A, B). The lowest crustal thickness marks old, large impact basins (e.g. Hellas, Utopia, Isidis) (Fig. 33 A, C). A large volcanic province, Tharsis, with four large shield volcanoes (Olympus Mons, Arsia, Pavonis, Ascreaus) (see Appendix 1) marks another characteristic feature of the Martian surface where the thickest crust has been detected. The considerably large thickness on southern hemisphere rapidly decreases while moving to the northern hemisphere. The division is often referred as Martian dichotomy. Its origin is widely discussed (see review: Zuber, 2001, Solomon et al. 2005) but no conclusions have been reached yet. What is also intriguing, the dichotomy is not only in crustal thickness and age but also in hypsometry (Fig. 33 C) as well as in chemical composition. The bulk of crust is generally composed from basalts and possibly basaltic andesites. Old southern heavily cratered highlands are most likely composed from products of primitive magmas. Products of more evolved magma, andesitic rocks are suspected to build the relatively smooth younger northern plains. A presence of the basaltic andesites is still a subject of debate (Bandfield et al. 2000), (Wyatt and McSween, 2002), (Rogers and Christensen, 2003), (Chevrier and Mathé, 2007), (Karunatillake et al. 2007), since the formation process would have required an environment similar to the one in a terrestrial subduction zone. This analogy supports an idea of plate tectonics that perhaps was present at the early stage of

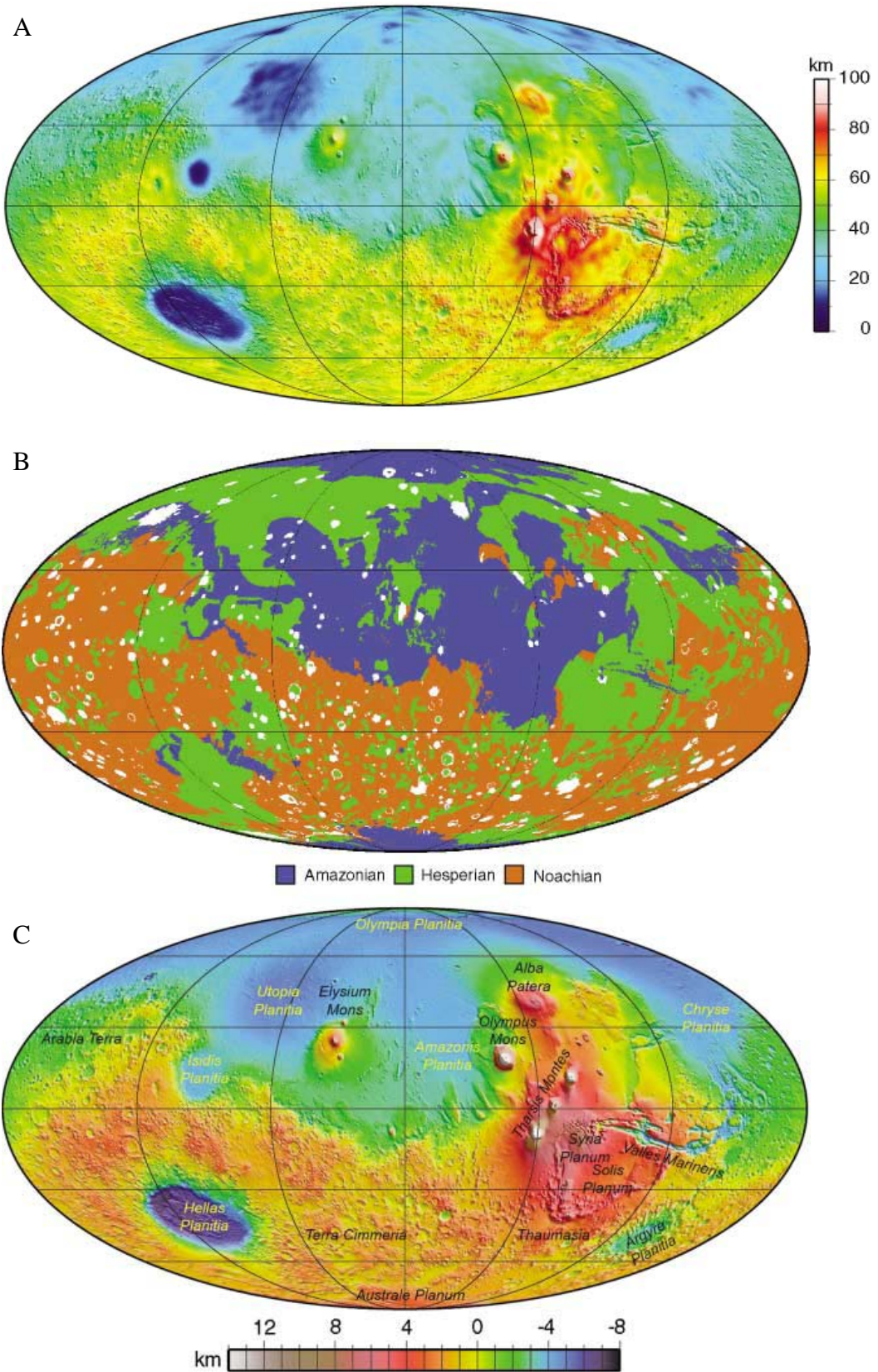


**Fig. 33)** A) Martian crustal thickness, B) Approximate surface ages, C) Topography map with major regions marked (Solomon et al. 2005). More detailed shaded relief map in Appendix 1.

Martian evolution (Sleep, 1994), (Fairén and Dohm, 2004), (Lenardic et al. 2004). This very much intriguing hypothesis neatly explains water transport into the mantle thus supporting partial melting and more evolved magmas generation. Plate tectonics is also a very effective interior cooling mechanism that stimulates mantle and core convection. Although such short activity cannot be completely rejected in the early Martian history e.g. (Nimmo and Stevenson, 2000), surface dating at least for southern hemisphere, based on a crater counting method (Hartmann and Neukum, 2001) seems to diminish its extent. Retrieved ages are close to a value obtained from ALH84001 meteorite that is considered as a fragment of an ancient crust (4-4,5Gyr –Nyquist et al. 2001, Weiss et al. 2002). Shergottites, that crystallized much later (0.15-1.3Gyr- Chen and Wasserburg 1986, Jagoutz, 1991), show only a little change in geochemical markers. This line of evidences suggests that the crustal recycling, if ever existed, was strongly limited. Presently Mars is assumed to be a single plate planet (Solomatov, 1995), (Grasset and Parmentier, 1998), (Spohn et al. 2001) covering a dry, low viscosity mantle where subduction is not possible. Although, rifting related magmatism is very unlikely in the stagnant lid convection regime, it does not mean that there was no volcanic activity on Mars in later periods. The most prominent example is, as already mentioned, Tharsis related volcanism. Although, a mechanism that lead to such a focused magmatism, remains a mystery, it is reasonable to assume its plume affinities even if present models cannot reproduce this feature (see review: Solomon et al. 2005). Recurring throughout the time a volcanic activity emplaced an old crust (Arkani-Hamed, 2004), (Johnson and Phillips, 2005), with 20-30km thick lava layers covering about 25% of the total planet's surface (Anderson et al. 2001).

The surface mineralogy, although dominated by olivine, pyroxenes and mafic feldspars, shows also products of alteration (Fig. 34). Initial determination by landers (Viking 1 and 2, Pathfinder) and orbital spectroscopy e.g. (TES-MGS, THEMIS-Mars Odyssey, OMEGA-Mars Express) has been significantly refined by the recent rover missions (Spirit, Opportunity) (see review: Chevrier and Mathé, 2007). In the investigated areas rovers found weathering products of mafic minerals (e.g. talc, iddingsite), clay minerals (e.g. nontronite, montmorillonite), sulfates (e.g. jarosite, gypsum, kiserite) and iron compounds (e.g. hematite, goethite). All those findings provide important clues for water activity and ancient climate reconstruction leading to the current state (see 2.5).



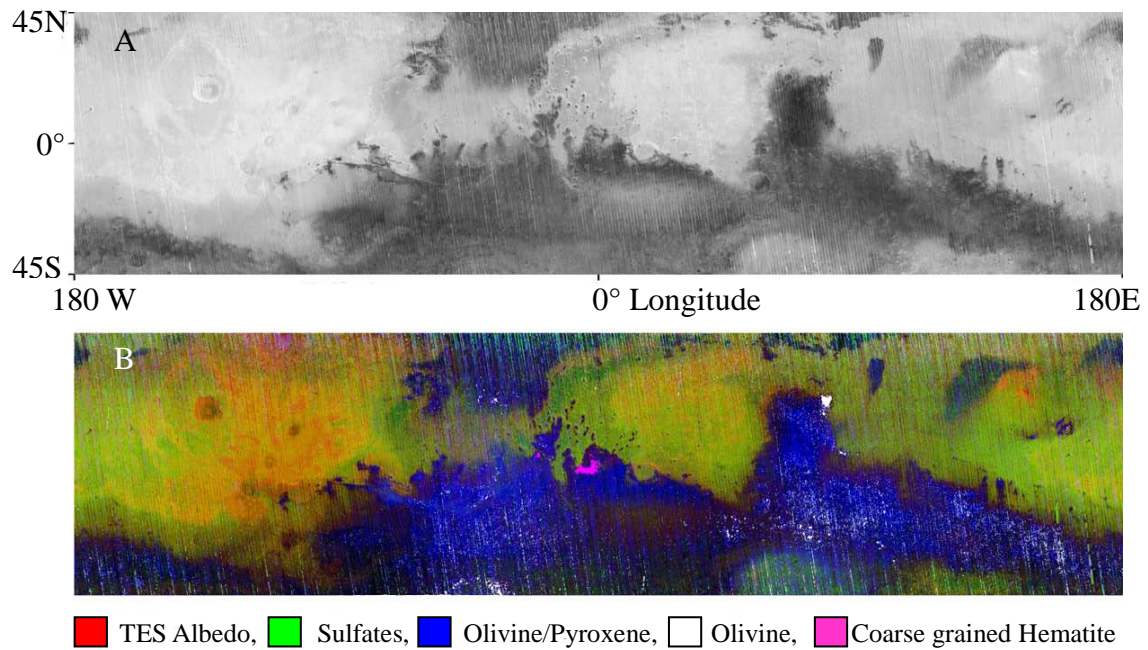


**Fig. 34** A) TES-MGS albedo map, B) Surface mineralogy of Mars. Older terrains are richer in mafic minerals (blue/white) in contrary to younger units that show signs of aqueous alterations (green) (Modified after Clark and Hoefner, USGS, <http://speclab.cr.usgs.gov>).

## 2.4 Magnetic field

Presently, Mars do not possess an intrinsic global magnetic field (see review Connerney et al. 2004). Even though MGS detected and mapped (Fig. 35) a strong remnant magnetization of the crust (Acuña et al. 1998), (Acuña et al. 1999). Its extent coincides mostly with the old southern highlands. It is commonly believed that these magnetic anomalies have been formed through magnetization of iron bearing minerals like magnetite, hematite or pyrrhotite e.g. (Kletetschka et al. 2000), (Arkani-Hamed, 2005)

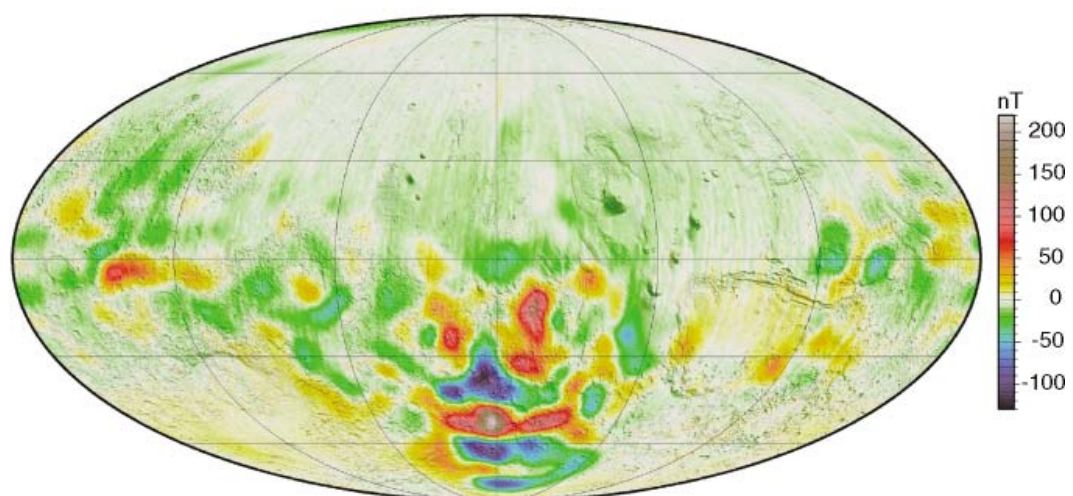


**Fig. 35)** Map of remnant crustal magnetism at an altitude of  $400 \pm 30$ km (Solomon et al. 2005).

when the core dynamo was still active e.g. (Arkani-Hamed, 2004). Large impact basins, young Tharsis volcanic province and almost whole northern plains (Fig. 35) are free from coherent magnetization. This observation requires that Martian dynamo ceased to operate before the mentioned features have been formed. A precise estimation of this particular moment is of key importance for Martian atmosphere evolution and thus volatile (e.g H<sub>2</sub>O and CO<sub>2</sub>) abundance calculations (see 2.5). Therefore, important questions are: how did the dynamo start to operate and how or when turned off? A magnetic field is generated by a convective flow of electric-conducting liquid metal in a core e.g. (Connerney et al. 2004). The convection can be initiated by a thermal or chemical contrast (Fig. 36). Either an initial core temperature must be higher than the one in the mantle or an inner core has to grow e.g. (Breuer and Spohn, 2003), (Breuer and Spohn, 2006). In order to support convection with a resulting magnetic field, mantle cooling must be efficient. Heat removal depends on: 1) planet's tectonic regime (plate tectonic or stagnant lid), 2) size of the planet, 3) amount of volatiles in the mantle, 4) thickness of the mantle. In light of present knowledge, Mars most likely possessed an early thermally driven dynamo. Due to increasing difficulties in heat removal through a dehydrated stiff mantle and stagnant lid, it ceased to operate after hundreds of millions of years. From that event the Red Planet remains in a transient stage to a chemically driven dynamo generation (Fig. 36). It is worthwhile to notice that either thermally or chemically based model allow for a short period of plate tectonic also inferred by other authors (see 2.3.3). Recent analyses of magnetic anomalies (Arkani-Hamed, 2001), (Arkani-Hamed and Boutin, 2004), (Hood et al. 2005) aside from revealing magnetic field reversals, allow establishing an approximate

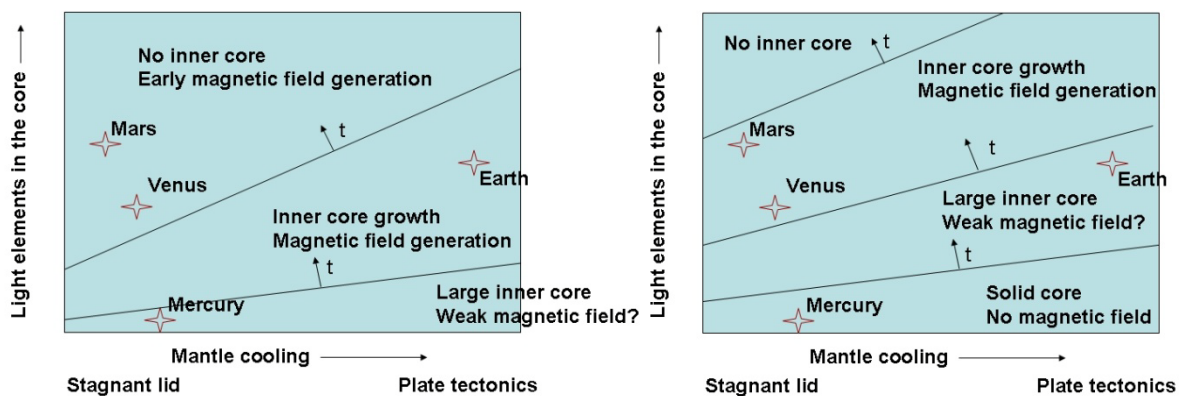


**Fig. 36)** Simplified evolutionary model of the Martian core with an early thermally driven dynamo (left) and theoretical future chemically driven on (right) in comparison to other terrestrial planets (Courtesy Doris Breuer).

position of ancient global magnetic pools. If one assumes that there was no significant plate movement and the magnetic dipole is roughly aligned with the planetary spin axis, similarly to Earth, Mercury, Jupiter or Saturn, localization of Martian ancient pools become feasible. The positions, although still imprecise, has been determined between present Mars' spin axis and Olympus Mons (Hood et al. 2005). The shift to the present position is approximately 50-60 degrees. This result is in close agreement with paleopole estimations prior to Tharsis gravity anomaly formation (Melosh, 1980).

## 2.5 Volatiles and Martian climate evolution

The image of Mars underwent a significant change since the beginning of the era of space flights. Initial barren, cold desert world has been gradually replaced by geologically still active planet with an intriguing history shaped by impacts, lavas and liquids under a CO<sub>2</sub> dominated atmosphere (Fig.37). Dating methods (crater counting and superimposition relations) implemented on the surface established three distinct epochs (Noachian, Hesperian and Amazonian) in the surface evolution (Hartmann and Neukum, 2001). In order to explain the observed features two contradictory evolutionary concepts have been proposed. The first one that is presently favored and proposes a warm young Mars where liquid water was and perhaps still is an active agent in the surface processes. This model

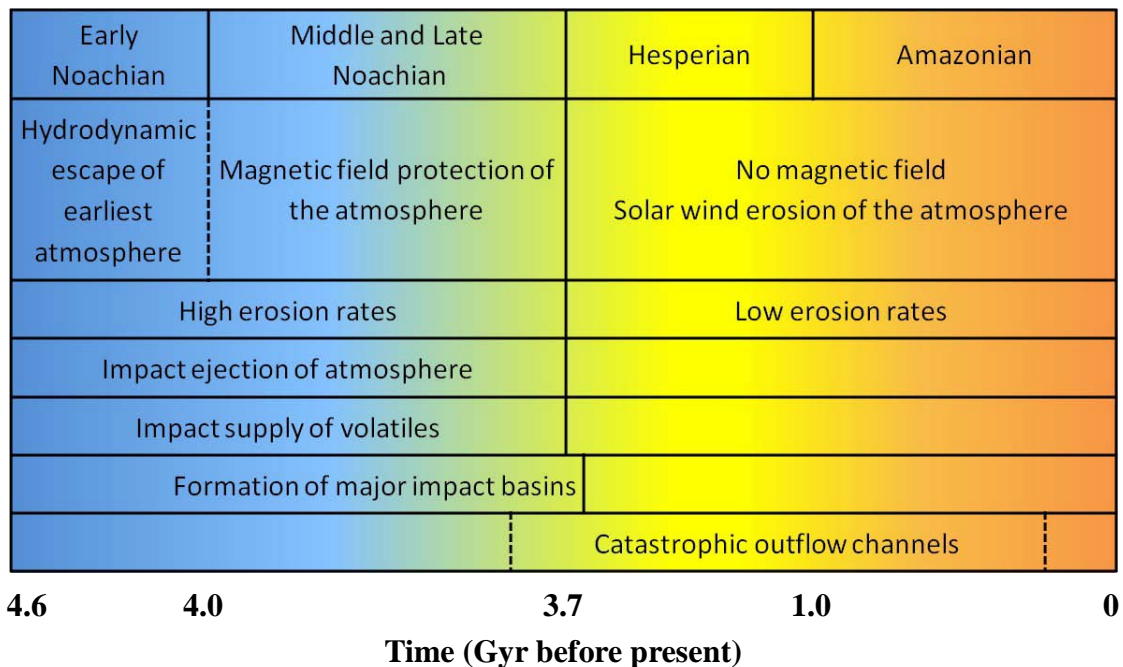


**Fig. 37)** Evolutionary timeline for Mars with three main geological epochs. The youngest, glacial and fluvial features are not included (modified after Jakosky and Phillips, 2001).

here is referred as the “Blue Mars” hypothesis. The second one, known as the “White Mars” hypothesis, assumes cryogenic conditions on Mars from the accretion till now. In this scenario, the liquid that left clear marks on the surface is not water but liquid CO<sub>2</sub> and gas supported density flows. Even if in light of present knowledge, this scenario is rather unlikely, it touches a several interesting points that are difficult to explain by the “Blue Mars” model. Although both evolutionary pathways include clathrates into discussion (see 2.6), this subchapter will only introduce possible environments where those compounds could be formed and/or decompose.

### 2.5.1 Blue Mars

Numerous images of river networks from the southern highlands, massive outflow channels and other flow features have been interpreted as relicts of flowing water e.g. (Baker, 2001), (Masson et al. 2001), (Kargel, 2004). In several publications, authors discuss also an existence of long standing bodies of water or even an ocean e.g. (Lucchitta et al. 1986), (Parker et al. 1989), (Baker et al. 1991), (Carr, 2000), (Kargel, 2004).

Such hypotheses demand a climate much different from the one observed now. With an initial solar heat flux ~ 20-30% weaker than now (Newman and Rood 1977), surface liquid water had to be stabilized by a thick and warming primordial atmosphere. The role of such efficient greenhouse gases like NH<sub>3</sub>, CH<sub>4</sub> was most likely strongly limited by their short lifetime under the strong UV radiation (Pollack et al. 1987), (Kasting, 1991) from very young Sun. In such a situation the reader should not be surprised that most of the climate evolution models relay on CO<sub>2</sub>, water vapor and the radiative effect of clouds as warming agents (Pollack et al. 1987), (Kasting, 1991), (Haberle et al. 1994), (Pepin, 1994), (Carr, 1999), (Colaprete and Toon, 2003), (Manning et al. 2006). Other primordial components like H<sub>2</sub>, N<sub>2</sub> and noble gases essentially do not participate in warming effect. Moreover, light gases like He or H<sub>2</sub> were quickly lost through a thermal and hydrodynamic escape (Fig. 37). The limits of the atmospheric pressure vary strongly for different models but do not exceed 10bar (1MPa) e.g. (Haberle et al. 1994), (Manning et al. 2006). Under such an atmosphere, liquid water could be indeed stable at most of the surface. Dendritic river networks (Fig. 38) with characteristic V-shaped valleys from this period bear a close resemblance to those formed by runoff of water on Earth. Yet, a lower number of tributaries e.g. (Carr and Clow, 1981), (Cabrol and Grin, 2001) cast some doubts on the means of water supply that might be different from terrestrial analogs where precipitation is the most widespread mechanism. In Martian case the most often invoked are seepages of



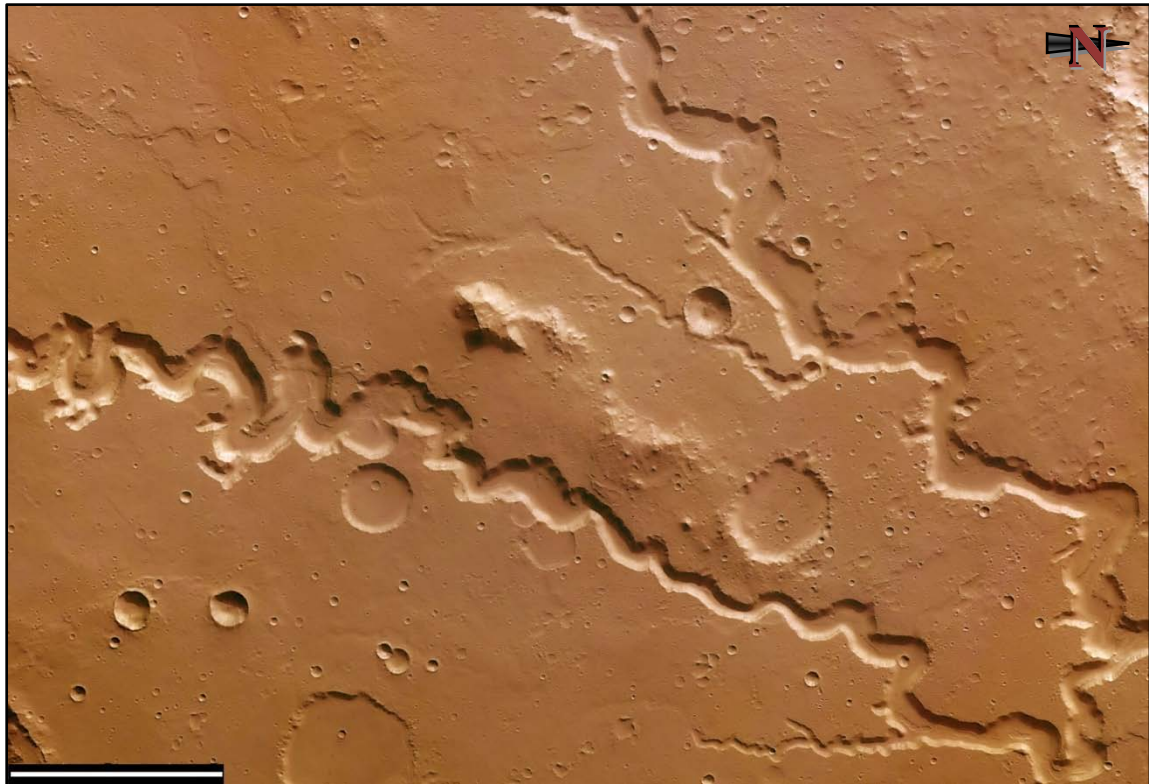


**Fig. 38)** Fragment of Nanedi Valles (Xanthe Terra) most likely formed by a continuous flow of liquid. Observed meandering valleys are 0.8-0.5km deep with steep walls and flat floor. Scale bar - 20km (Source: ESA/DLR/FU Berlin/G. Neukum).

water from underground sources replenished by the basal melting of the polar caps (Clifford, 1987) and/or juvenile water (Carr, 1983). Recent analysis of MGS laser altimetry (MOLA) data shows some evidences for smaller tributary valley systems that are barely recognizable on surface images (Kargel, 2004). This finding might add at least limited precipitation to the list of recharging mechanisms and thus shift Martian river pattern closer to the one we know from Earth. Such an extensive surface water system might have been connected to long standing bodies of water like lakes or even a sea e.g. (Lucchitta et al. 1986), (Parker et al. 1989), (Baker et al. 1991), (Parker et al, 1993), (Carr, 2000), (Clifford and Parker, 2001). Up to now a numerous craters, valleys and depressions have been proposed to be standing water reservoirs (Cabrol and Grin, 1999). The greatest reservoirs of surface liquid water have been suggested to exist on the Northern Plains and/or Hellas Basin including the most extreme variant, so called Oceanus Borealis (Parker et al. 1989). Its existence is a subject of long standing discussion starting in the middle of 80's (see Kargel, 2004). Based on imagery of the planet, an interpretation of certain surface features as paleo shorelines (Fig. 39) e.g. (Lucchitta et al. 1986), (Parker et al. 1993), (Clifford and Parker, 2001) became a main proof for the globally extended water reservoir. Reexamination of the hypothetic coastline structures with MOLA data do not provide the

final answer but seem to negate the existence of certain shorelines (Malin and Edgett, 1999) and show the inconsistency in the constant geopotential surface between the features (Head et al. 1998), (Head et al. 1999).

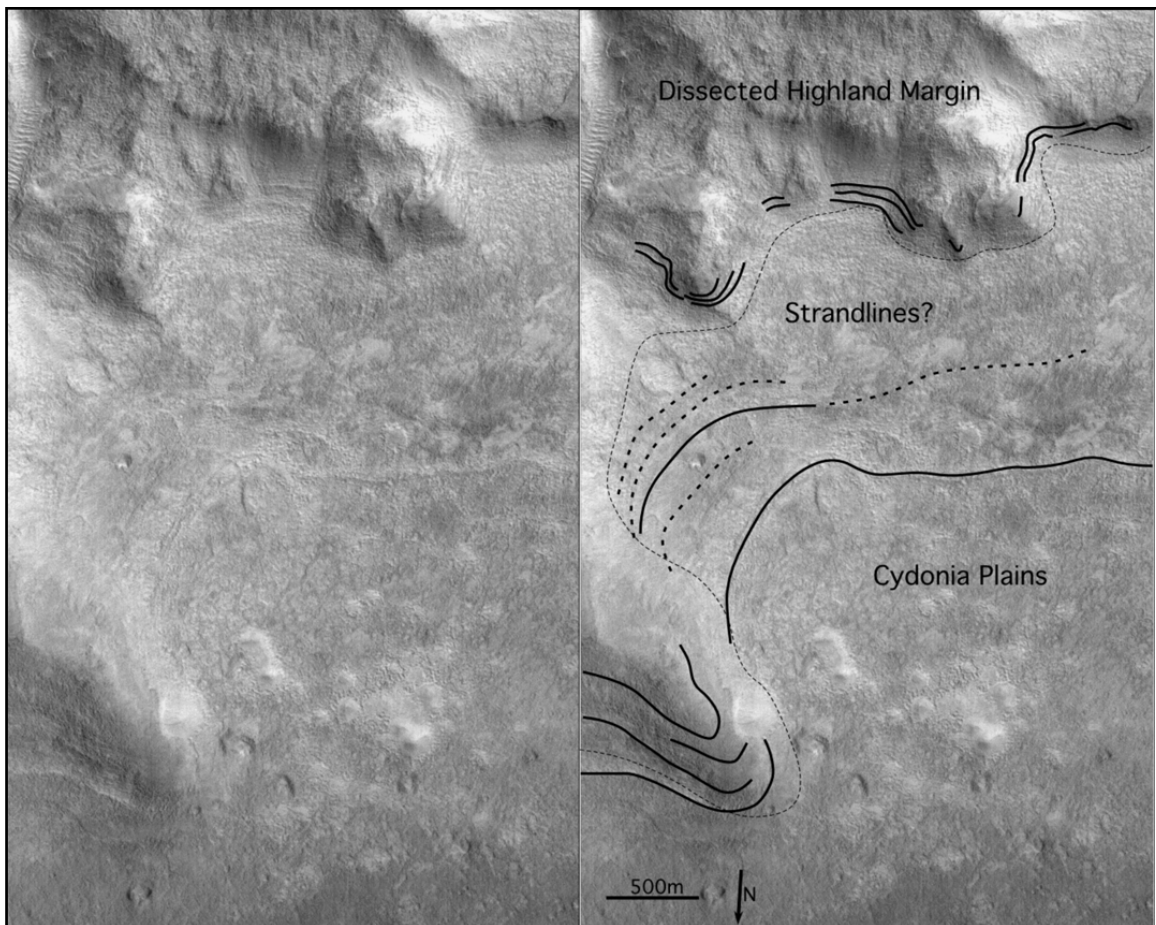


**Fig. 39)** Fragment of “Arabia Shoreline” east of Cydonia Mensae (36.35°N, 9.14°W) with a number of ridges parallel to the dissected highlands. The difference between the lowest and highest terrace is about 300m (Clifford and Parker, 2001).

The present pressure (~6mbar), which is much lower than in above assumptions, suggest that at some point of Martian history the Red Planet has been almost striped from its atmosphere thus reducing the greenhouse effect to barely ~5K (Pollack et al. 1987), (Hoffman, 2000a). The initial atmosphere has been strongly affected by a massive bombardment of dust and space debris through the Noachian period (Pavlov and Pavlov, 1998), (Hartmann and Neukum, 2001), (Kring and Cohen, 2002). The kinetic energy of larger asteroids was sufficient to jettison a considerable amount of gas into space upon numerous impacts (Melosh and Vickery, 1989). Estimated atmospheric losses suggest that 50-90% of the primordial atmosphere has been lost (Brain and Jakosky, 1998). Adsorptions in the regolith and formation of carbonates are other commonly proposed atmospheric sinks but in these cases CO<sub>2</sub> at certain conditions (temperature/pressure dissolution) may be recycled back to the atmosphere e.g. (Kahn, 1985), (Carr, 1999), (Manning et al. 2006).

The erosive effect of the solar wind probably through the greatest part of Noachian was minimized by a protective global magnetic field. The precise moment of its shut down is no clear but most likely it has happened close to the end of Noachian (~3,8Gyr) (Fig. 37), before the formation of large impact basins that are free from remnant magnetization (see 2.2.3). Not shielded atmosphere underwent gradual erosion through pick-up ions, thermal, non-thermal and hydrodynamic escape. Its effect is observed nowadays in the isotopic ratio of the atmospheric gases e.g. (Jakosky and Jones, 1997), (Jakosky and Phillips, 2001). The local heating upon impacts (Segura et al. 2002a), (Segura et al. 2002b), with a constant supply of gasses from volcanic sources (mostly Tharsis region) and space debris, was able at least to partially counterbalance the atmosphere stripping, could not stop the cooling. Progressive thinning of the atmosphere lead to its final collapse along with CO<sub>2</sub> ice polar caps formation e.g. (Haberle et al. 1994), (Yokohata et al. 2002), (Manning et al. 2006).

At the dawn of Noachian era, geomorphologic records show a change from the wet and warm climate to the cold, ice dominated one e.g. (Jakosky and Phillips, 2001), (Masson et al. 2001), (Kargel, 2004) accompanied by a rapid decrease of the erosion rates (Fig. 37) e.g. (Carr, 1996), (Kargel, 2004) and thickening of so called cryosphere e.g. (Clifford and Parker, 2001). This transition begins two subsequent eras in Martian history: Hesperian and Amazonian. Throughout those two periods Martian climate went through multiple cycles of climate excursions controlled mainly by the orbital and spin axis parameters (eccentricity, longitude of perihelion, obliquity) (Fig. 40) e.g. (Toon et al, 1980), (Laskar et al, 2004), (Armstrong, et al. 2004). An additional positive climatic

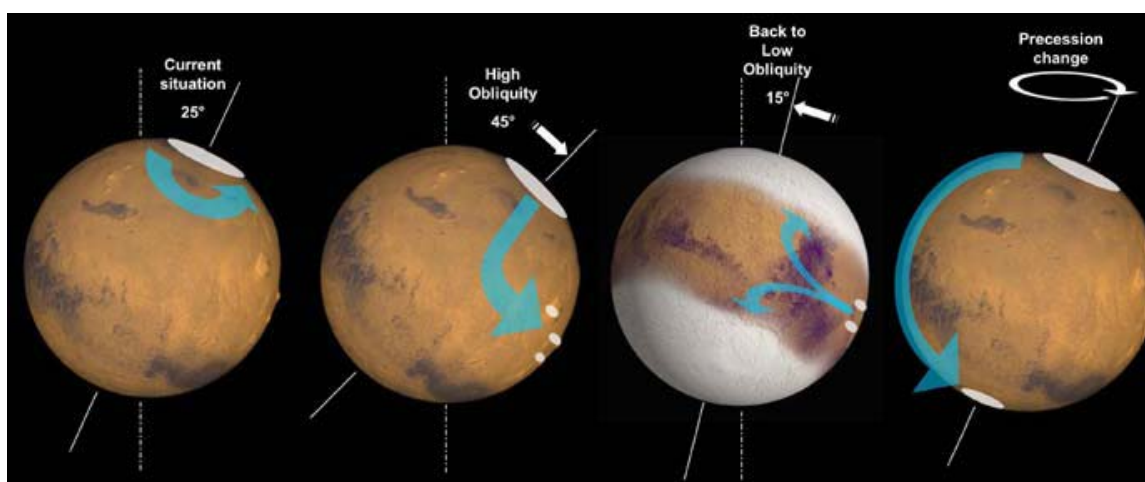


**Fig. 40)** A model of recent changes in the orbital parameters and their impact on the water distribution across the planet. Arrows mark directions of water transport (Montmessin, 2006).

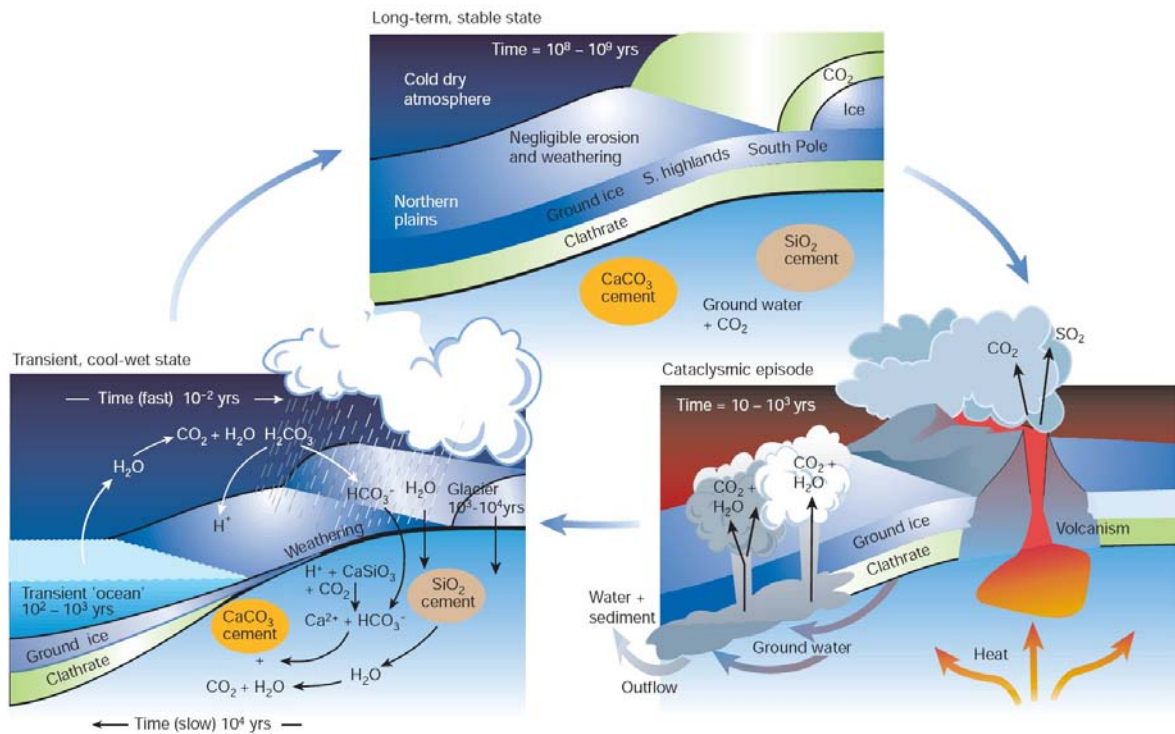


**Fig. 41)** A model of cyclic short-duration warmer and wetter periods caused by increased volcanic activity accompanied by release of CO<sub>2</sub> stored in the regolith. Catastrophic releases supplied liquid water to transient surface reservoirs (Baker, 2001).

feedback (Fig. 41) (Baker et al. 1991), (Gulick, 1997), (Baker, 2001) from the recurring volcanism (Berman and Hartmann, 2002), (Márquez et al. 2004), (Neukum et al. 2004) cannot be ruled out but its influence was decreasing with time. Hesperian climate was not too distant from the one observed now but the activity of liquid water was still significant.

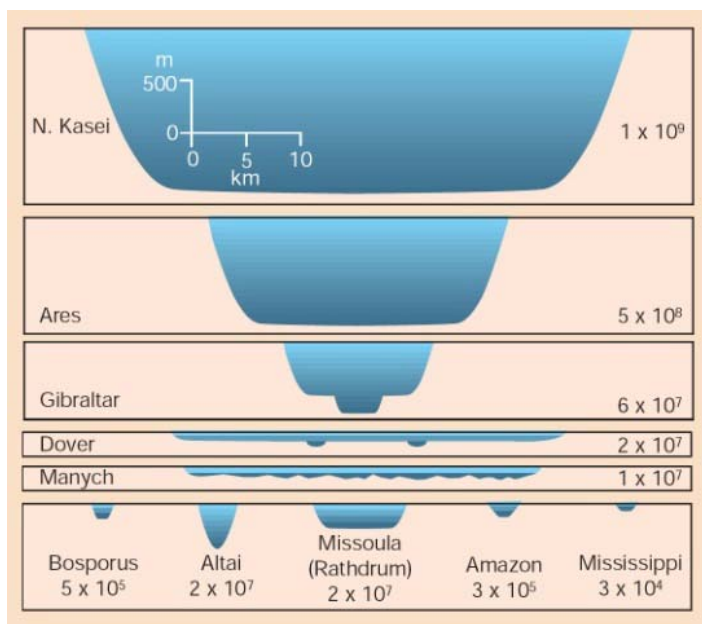


**Fig. 42)** Simplified cross-sections of two Martian outflow channels and Earth examples. Peak discharges are given in m<sup>2</sup>/s (Baker, 2001).

In the freezing conditions still a number of crater lakes were present (Cabrol and Grin, 1999). River systems have been greatly reduced and restricted to active volcanic centers e.g. (Carr, 1996), (Gulick, 1997), (Fassett and Head, 2006), (Fassett and Head, 2007) where accumulated ice/frost could undergo basal melting due to geothermal heating. Still such events produced only a fraction of total liquid water released to the



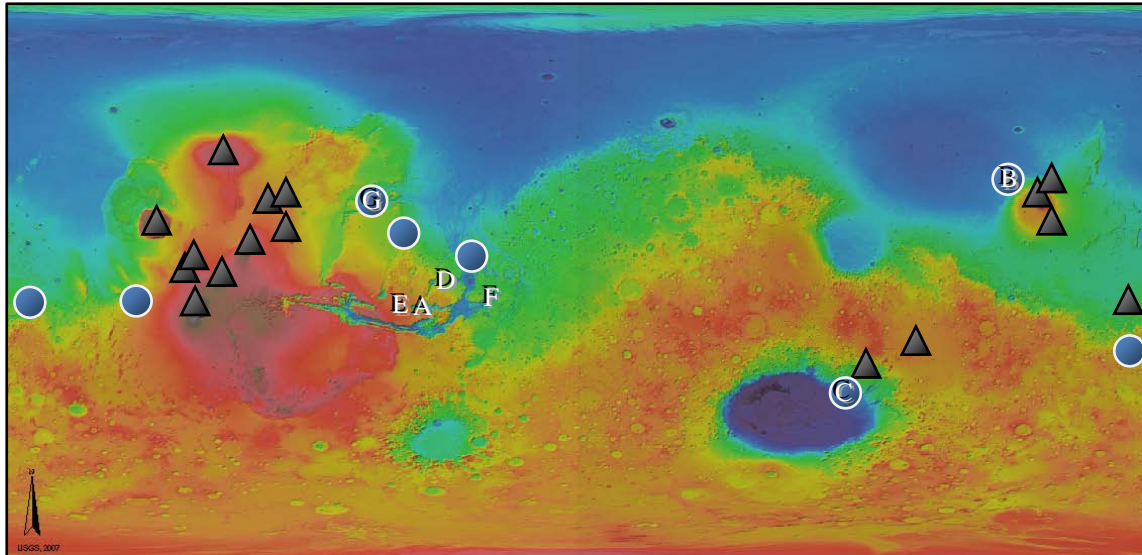


**Fig. 43)** Distribution of volcanoes (triangles) and outflow channels (circles) (After Carr, 1996). A-G– location of the images from Fig. 42. Background map - MOLA color shade relief and MDIM (Courtesy USGS Astrogeology Research Program, <http://astrogeology.usgs.gov>).

surface. Between the late Noachian and late Amazonian, with the peak activity in late Hesperian, Mars experienced a series of catastrophic releases of water on a scale often exceeding all known terrestrial analogs (Fig. 42) e.g. (Carr, 1996), (Clifford and Parker, 2001), (Masson et al. 2001), (Kargel, 2004), (Rodriguez et al. 2005), (Coleman et al. 2007). From the source regions, liquid water carved hundreds of kilometer long, tens of kilometer wide and up to a kilometer deep outflow channels that lead to the lower placed grounds like Hellas basin or the northern lowlands where eroded material have been deposited (Fig. 43G). Nearly all of those features are localized in close vicinity to the volcanic provinces in four main regions (Fig. 43) (Carr, 1996), (Clifford and Parker, 2001): Around the Chryse-Acidalia basin, Elysium Planitia, eastern part of Hellas Basin and southern margins of Amazonis Planitia. Fully-born channels start in impact craters (Fig. 44A), alcove-like walls (Fig. 44B, C), collapsed edges of cliffs (Fig. 44D), chasmae (linear extension structures) (Fig. 44E) or in chaotic terrains (blocky dissected ground with considerable loss of volume) (Fig. 44D, F). This and other differences in channel structure cannot be explained by one universal scenario. Since the formation of channels requires a sudden release of very large amounts of water several sources have been suggested, among others breaches of the water from lakes, global or local pressurized underground reservoirs (Clifford, 1987), (Clifford and Parker, 2001), (Carr, 2002), (Coleman et al. 2007), (Russell and Head, 2007). The first mechanism is proposed for high placed channels like Ganges Chasma, or neighboring Elaver and Allegheny Valles. Water supply for such reservoirs might be found in the melting of permafrost ice through geothermal heating or rainfalls

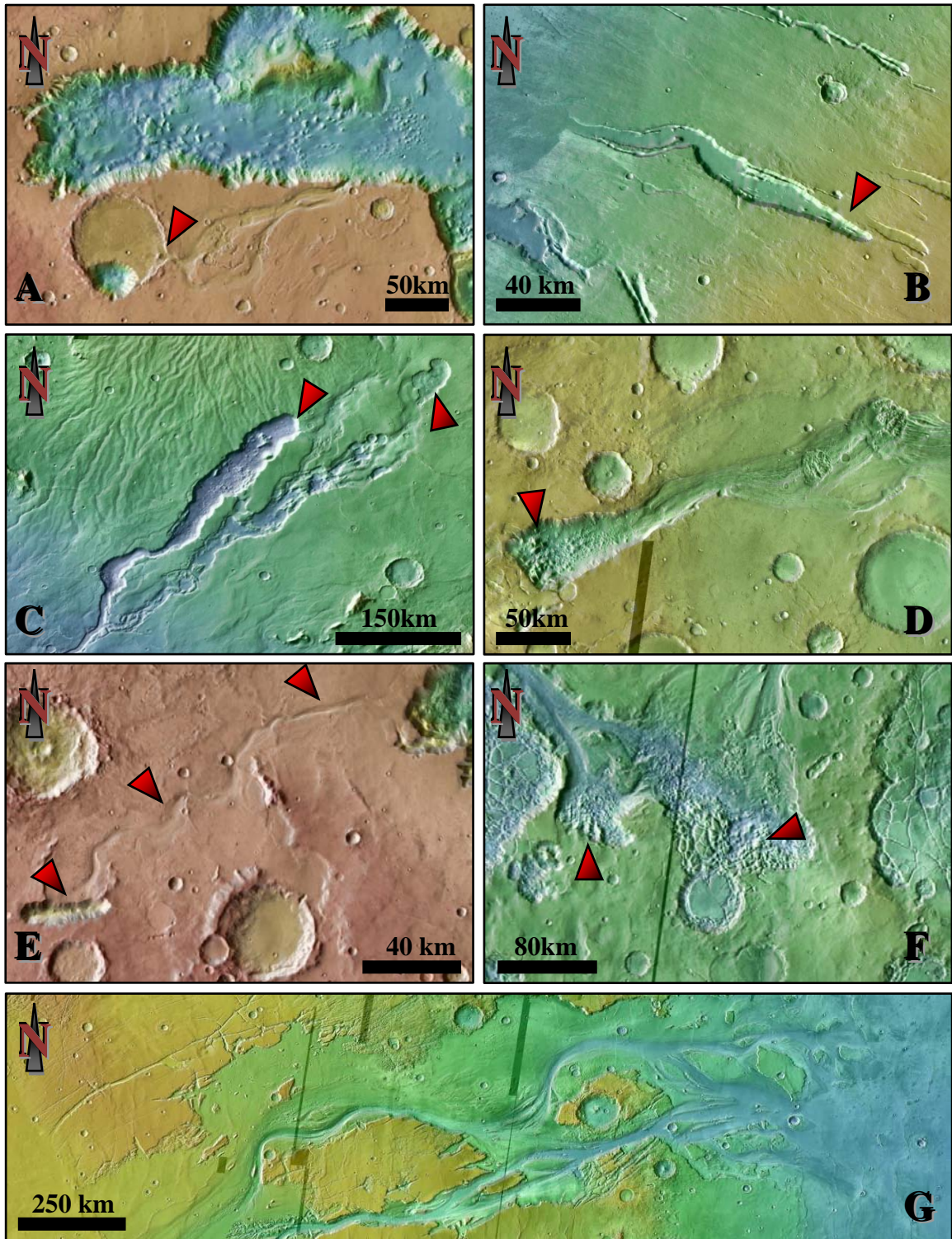


**Fig. 44)** Initial and terminal parts of outflow channels (Global localization: Fig. 41). **A)** Crater lake, Aurora Planum, **B)** Alcove like wall, Elysium Fossae, **C)** Alcove like wall, Dao and Niger Vallis, **D)** Collapsed edge of cliff/chaos, Arumatum Chaos, **E)** Chasma, Ophir Planum, **F)** Chaos, Aram Chaos. **G)** Kasei Valles outflow channel. Images – THEMIS daily IR and MOLA colored relief (*JMars*. Mars Space Flight Facility, Arizona State University, <http://jmars.asu.edu>). Dark strips – gaps in THEMIS data.



during short episodes of climate warming caused by gases released from volcanic centers (Baker et al. 1991), (Gulick, 1997), (Baker, 2001). The pressurized source model can be explained in several ways. Among the most often proposed are (see Baker, 2001; Clifford and Parker, 2001; Russell and Head, 2007): 1) Global scale thickening of the cryosphere that compress underlying water to some critical value at which it was able to breach the permafrost seal, 2) Localized or regional pressurization due to geothermal heating or cryosphere thickening, 3) Tectonic faulting. Large amount of water released upon each catastrophic event was sufficient to create persisting lakes or even a transient sea e.g. (Baker, 2001), (Clifford and Parker, 2001), (Carr and Head, 2003) that would not stay without an impact on the climate.

The activity of rivers and outflow channels has diminished through Amazonian and eventually stopped completely closing the period in Mars history where larger amounts of liquid water were existing on the planet's surface. Along with this process another class of surface activity started to gain in importance, namely permafrost and glacial processes. Although the cryosphere started to develop on global scale with the end of Noachian, presently observed features are relatively young or/and forming even now. According to the theoretical models e.g. (Leighton and Murray, 1966), (Clifford and Hillel, 1983), (Paige, 1992), (Mellon et al, 2004), (Schorghofer and Aharonson, 2005), (Schorghofer, 2007) confirmed by orbital gamma rays, neutron spectroscopy data and surface observations e.g. (Feldman et al. 2002), (Mitrofanov et al. 2002), (Boyton et al. 2002),

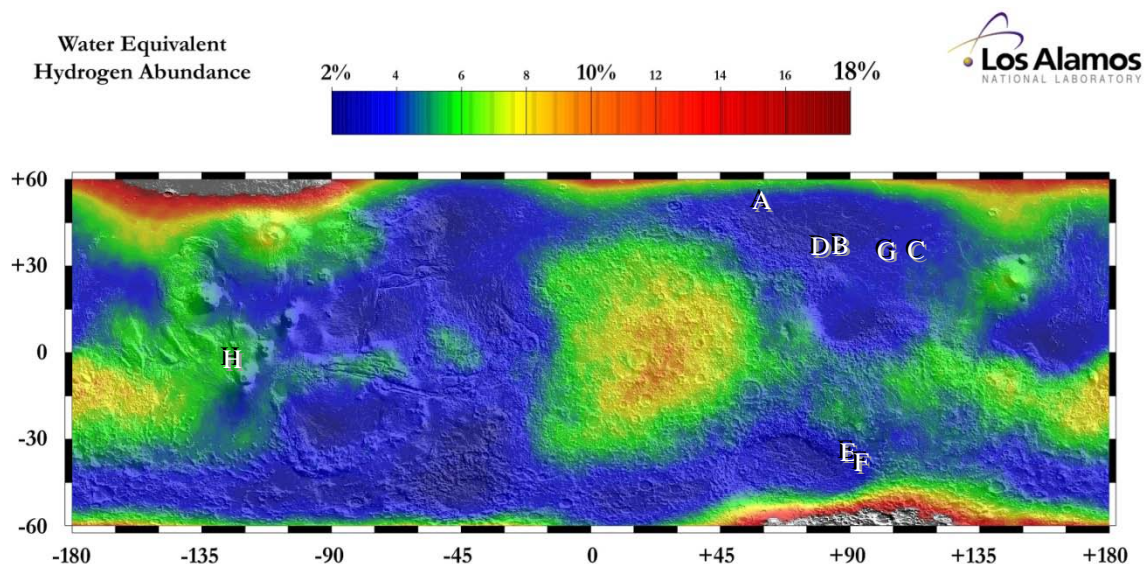


**Fig. 45)** Present distribution of water (hydrogen abundance) in the regolith up to 1m depth based on epithermal neutron count (Mars Odyssey). A-H localization of the images from Fig. 44. Data imposed on the shade relief MOLA topography map (© Copyright 2006 Los Alamos National Security, LLC All rights reserved).

(Mangold, et al. 2004), at present obliquity ground ice table stays in dynamic equilibrium with the atmosphere from 40°-60° (with the emphasis placed on the higher value) towards higher latitudes (Fig. 45). Indeed, a numerous images showed at higher latitudes a characteristic smoothening or softening of the surface caused by ice mantling (Fig. 46A) formed through the precipitation or frost accumulation. The layer has an average thickness of several meters/tens of meters (Mustard et al. 2001), (Morgenstern et al. 2007) but those values may vary due to local topography and differences in albedo. Yet, even if the present climate does not allow for frost/snow accumulation at lower latitudes, a discontinued mantling has been also found as low as to 30° on both hemispheres e.g. (Carr, 1996), (Mustard et al. 2001), (Morgenstern et al. 2007). In those areas numerous thermocarst features: e.g. scalloped (Fig. 46B) and fretted terrains, knobby features (Fig. 46C), large fields of patterned ground (e.g. polygons) (Fig. 46B, D), filled craters (Fig. 46E) have been observed. Aside from a deposition of commonly observed ice-dust mantle, at numerous slopes the accumulation had to be intensive enough to drive ice filled debris in motion (Fig. 46F, G, H). Linear grooves and ridges on top of the flowing masses as well as lobate debris or circular crater aprons bear a close resemblance to terrestrial alpine, piedmont or rock glaciers e.g. (Luchitta, 1980), (Squyres, 1989), (Colaprete and Jakosky, 1998), (Masson et al. 2001), (Neukum et al. 2004), (Head et al. 2005), (Shean et al. 2007). Moreover, glacial and permafrost features, covered by dust and rocky mantle, have been found also at low to “tropical” latitudes (mostly at the flanks of volcanoes) (Fig. 45, 46H). Those phenomena can be readily explained by cycles of sublimation of water vapor from the polar regions and condensation at lower latitudes during the high obliquity excursions (Fig. 40) e.g. (Clifford, 1993), (Jakosky et al. 1995), (Jakosky and Phillips, 2001), (Mustard et al. 2001), (Laskar et al. 2002), (Levrard et al. 2004), (Forget et al. 2006) or/and climate warming upon the volcanic activity (Baker et al. 1991), (Gulick, 1997), (Baker, 2001). Subsequent migration to lower obliquities would cause destabilization and sublimation of ice deposits. Theoretical models suggest that during ~100000 years long cycles, the maximum depth of the regolith that is affected by this process may reach up to a few meters e.g. (Mellon et al, 2004), (Jakosky et al. 2005) and strongly depend on the impurity content (e.g. dust, sand, rocks). Below this level one should expect much more stable ice trapped within the cryosphere that presently extends downward ~2.3-4.7km at the equator to ~6.5-13km at the poles (Clifford and Parker, 2001). Another line of evidences arguing for numerous climate changes is recorded in the one of the most intriguing Martian large scale features, namely polar layered deposits e.g.



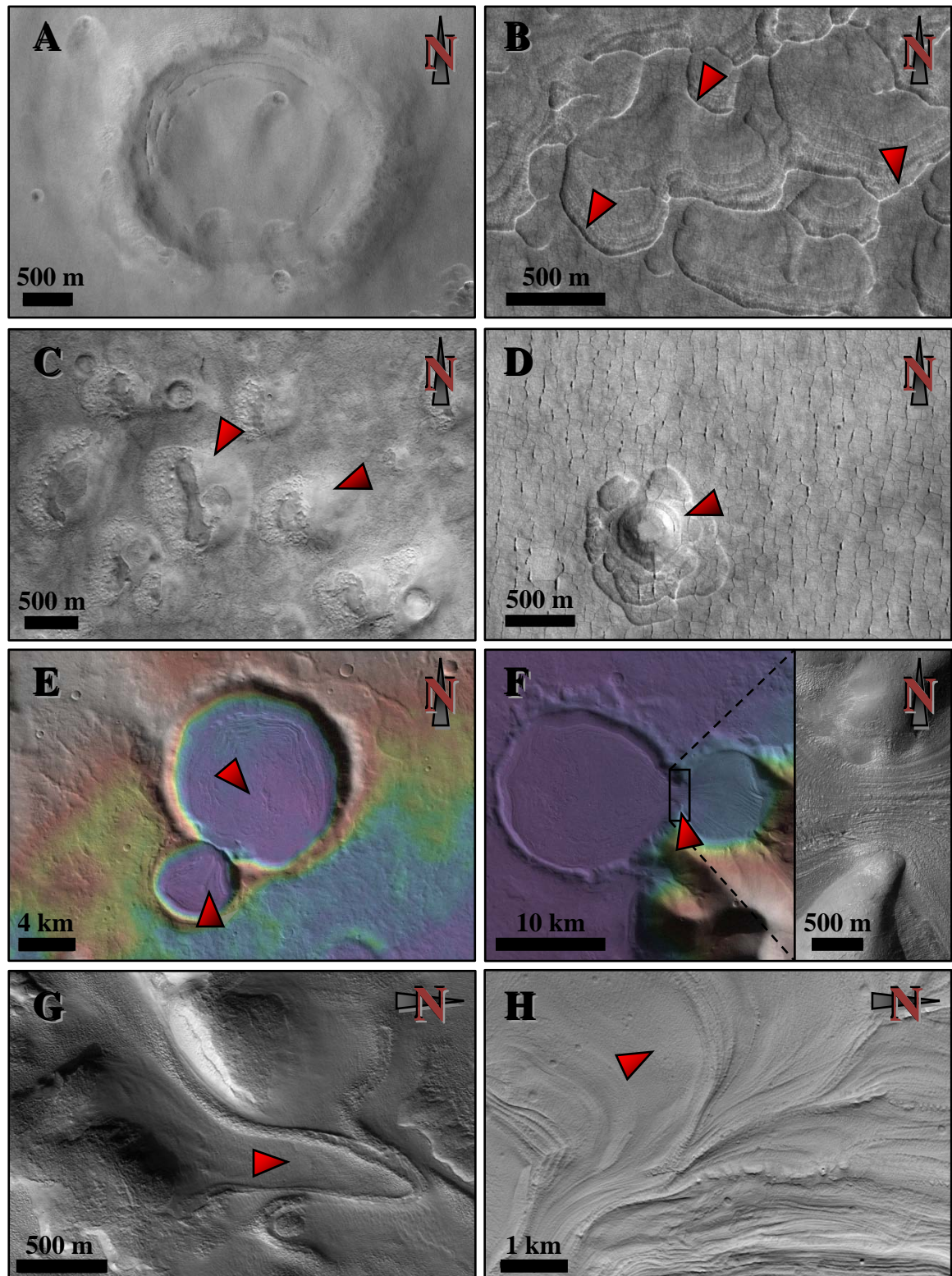


**Fig. 46)** **A)** Ice mantling over the crater, **B)** Scalped terrain with polygons, **C)** Partially excavated knobby, hill-like features, **D)** Polygonal ground with excavated crater surrounded by scalped features, **E)** Ice filled craters, **F)** “Hourglass glacier” (left). Flow lineation between the craters (right). **G)** Lobate apron in Hellas Planitia, **H)** Glacial-like features on the north-western flank of Arsia Mons. Images from MRO-HiRISE: A-D, F (right), G-H (NASA/JPL/University of Arizona). Images E-F (left): Elevation mode, HRSCView (*HRSCview*. Freie Universitaet Berlin and DLR Berlin, <http://hrscview.fu-berlin.de/>). Global localization: Fig. 43.

(Murray et al.1972), (Cutt and Lewis, 1982), (Milkovich and Head, 2005), (Tanaka, 2005), (Levrard et al. 2007), (Plaut et al. 2007), (Seu et al. 2007). These complexes of bright and dark lamellas are most prominent for northern hemisphere where they are exposed within scarps and walls of the spiraling grooves and troughs (Fig. 47). It is commonly believed that brighter belts are enriched in water ice in contrary to more dusty darker units. Computer simulations suggest that the polar caps might be completely removed during the high obliquity periods if not protected from sublimation by a dust mantling e.g. (Jakosky et al. 1995), (Laskar et al. 2002). If so, recently observed layered deposits most likely reflect all obliquity changes since the last high obliquity period. An average thickness of one unit has been estimated on ~30m e.g. (Milkovich and Head, 2005) but also thinner layers are found (Fig. 47). This abundance of lamellas is too greater to be explained only by orbital forcing and other mechanisms had to be included as well (Fenton and Herkenhoff, 2000), (Levrard et al. 2007). Among others, water an exchange with sources at different latitudes and dust storms activities have been proposed.

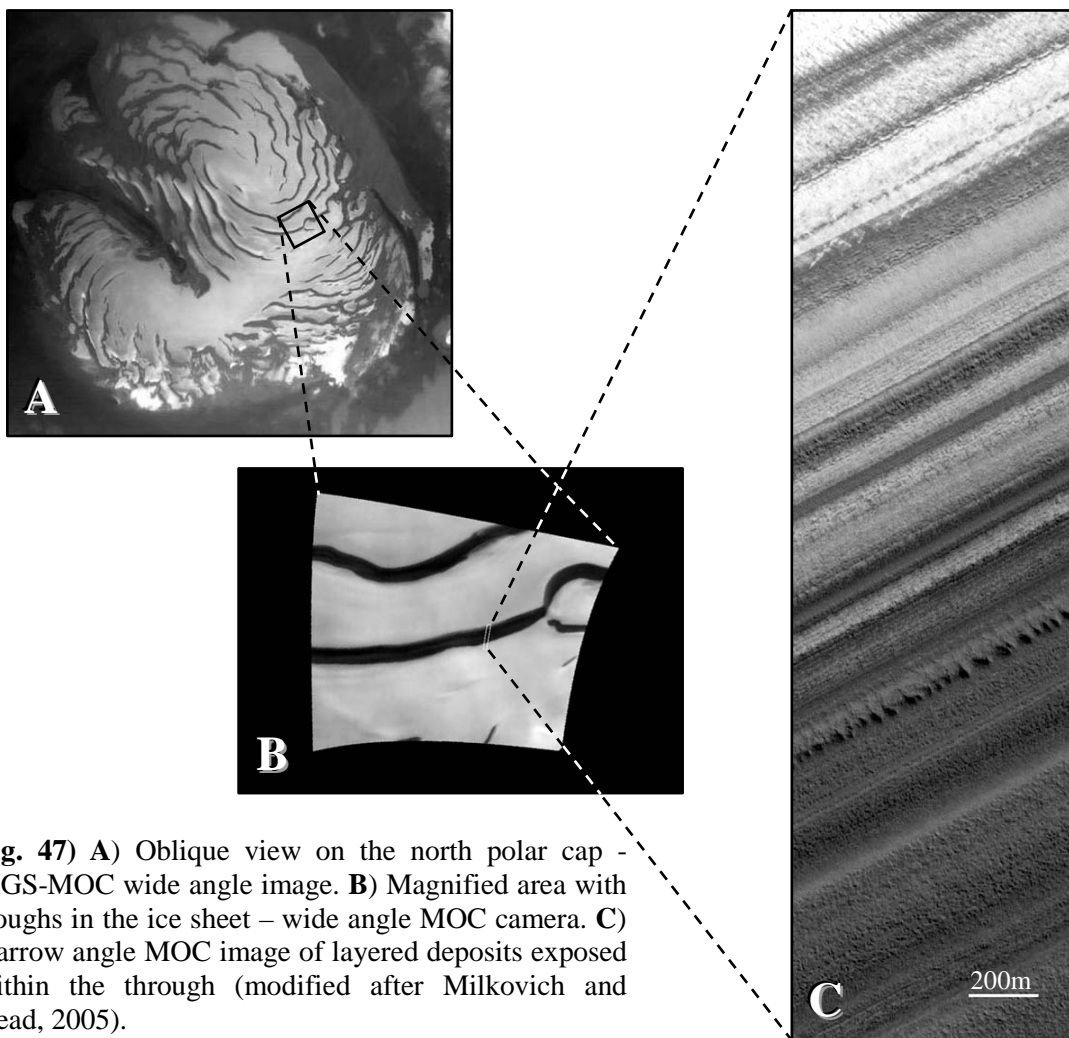


**Fig. 47)** A) Oblique view on the north polar cap - MGS-MOC wide angle image. B) Magnified area with troughs in the ice sheet – wide angle MOC camera. C) Narrow angle MOC image of layered deposits exposed within the through (modified after Milkovich and Head, 2005).



In polar regions, one can observe another periodic phenomenon but happening on much shorter scale, namely a condensation and sublimation of temporary dry ice caps e.g. (Thomas et al. 2000), (Smyth et al. 2001), (Mitrofanov et al. 2003). Their thickness on usually do not exceed a few tens of meters with an average value of 1.5-2m (Smyth et al. 2001). A higher insolation during warmer seasons the temporary dry ice sheet retreats toward higher latitudes but while at the northern polar caps it disappear completely, dry ice on the opposite cooler hemisphere is persistent during the whole year (Bibring et al, 2004) (see also 2.6.1). Interestingly, during the sublimation of solid CO<sub>2</sub> one can observe a formation of numerous seasonal dark spots, fans and blotches that mark centers of radially branching “spiders” cutting into underlying layered polar deposits (Fig. 48A, B) (Kieffer, 2000), (Piqueux et al., 2003), (Kieffer et al., 2006). An origin of those features has been proposed in a basal sublimation dry ice slab and ejection of pressurized CO<sub>2</sub> with dust particles on its surface. The mechanism requires a considerably clean ice that could be penetrated by a solar radiation to the bottom. CO<sub>2</sub> pressure would gradually rise until the overlaying ice would not be able to confine gathered gas (Fig. 48C).

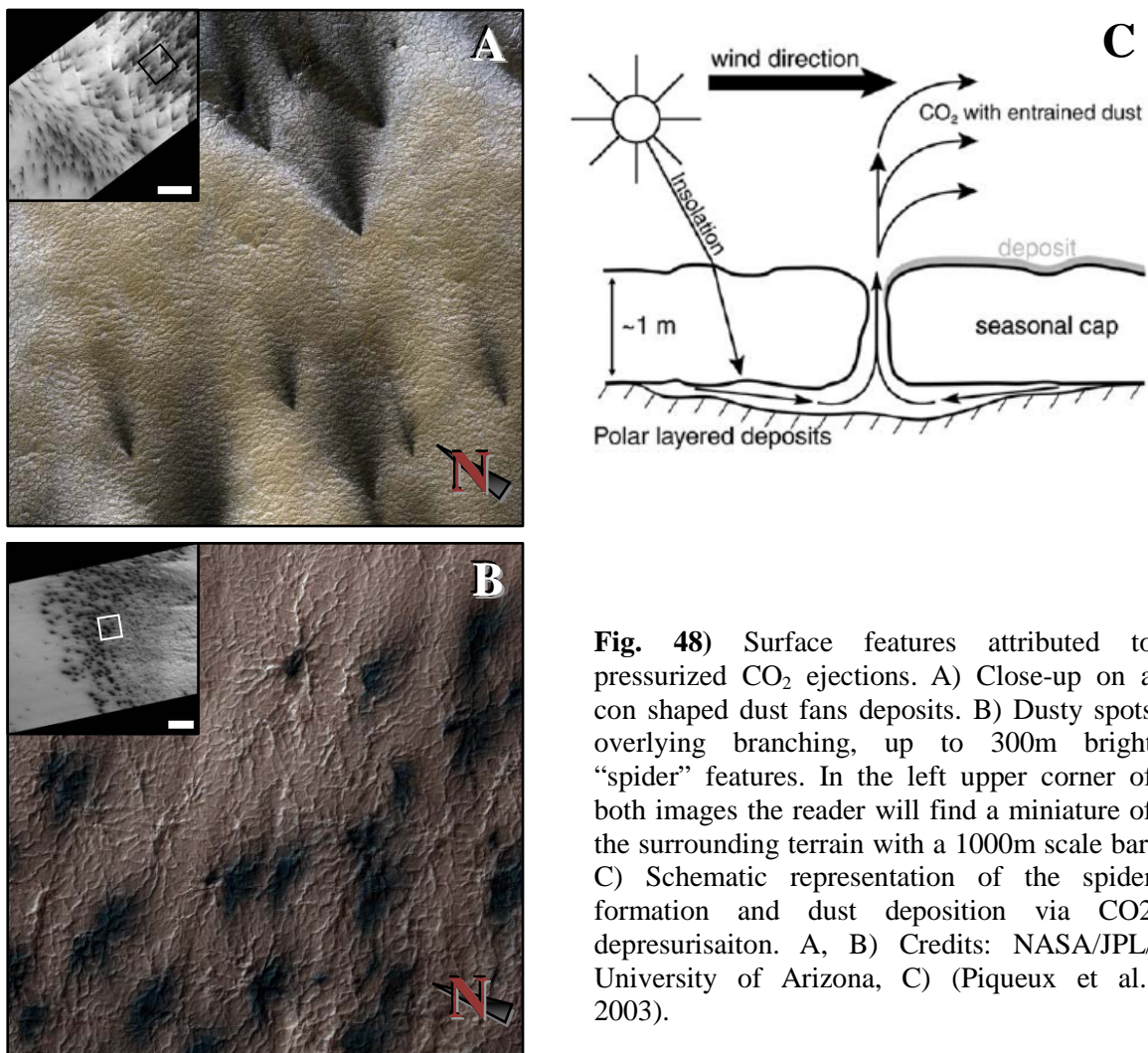


**Fig. 48)** Surface features attributed to pressurized CO<sub>2</sub> ejections. A) Close-up on a con shaped dust fans deposits. B) Dusty spots overlying branching, up to 300m bright “spider” features. In the left upper corner of both images the reader will find a miniature of the surrounding terrain with a 1000m scale bar. C) Schematic representation of the spider formation and dust deposition via CO<sub>2</sub> depressurisation. A, B) Credits: NASA/JPL/ University of Arizona, C) (Piqueux et al., 2003).

One could expect that in this ice dominated landscape controlled by quasi regular cycles of sublimation and deposition there is no place for liquid water close to the surface. Yet, high resolution images revealed a large number of gullies related most likely to the very recent activity of liquid water. Moreover, they are essentially identical to features observed in periglacial environments on Earth (Costard et al, 2001). Gullies have versatile appearance (Fig. 49) but most of these structures possess a complex morphology that can be divided on alcove (red arrow), channel (green arrow) and depositional apron (blue arrow) part that would require a considerable volume of liquid to be formed. Features start in alcoves seated in cliff faces, crater walls, dunes or knobby hills. From the base of incision emanate a single V-shape channel like conduit that may be from several tens of meters to a kilometer long (Fig. 49 G). The morphology of certain channels suggests multistage formation (Fig. 49C, D ,H)

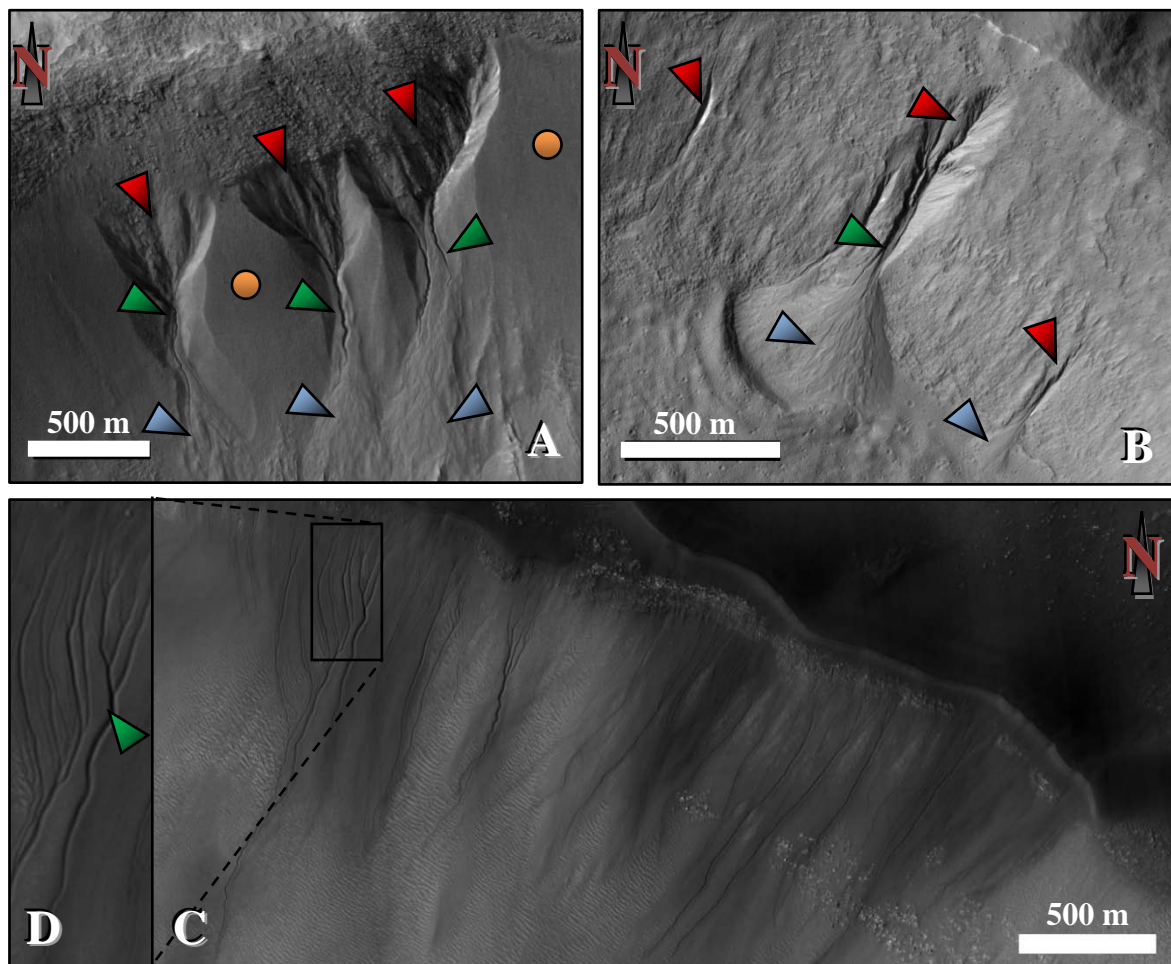


**Fig. 49)** A) Well developed gullies cutting through ice rich mantle (yellow dots) at the crater wall, B) Gully with very well developed sedimentary cone, C) Branched gullies with minimal alcoves and almost no aprons, D) Close-up on branched gully, E) Ice rich mantle (yellow dots) cut by immature gullies, F) Close-up on the gully with no channel, G) Swarm of crater wall gullies with branching and meandering long channels, H) Zoom in on one of the multistage channel. Images: MRO-HiRESE (NASA/JPL/University of Arizona). Global localization Fig. 47.



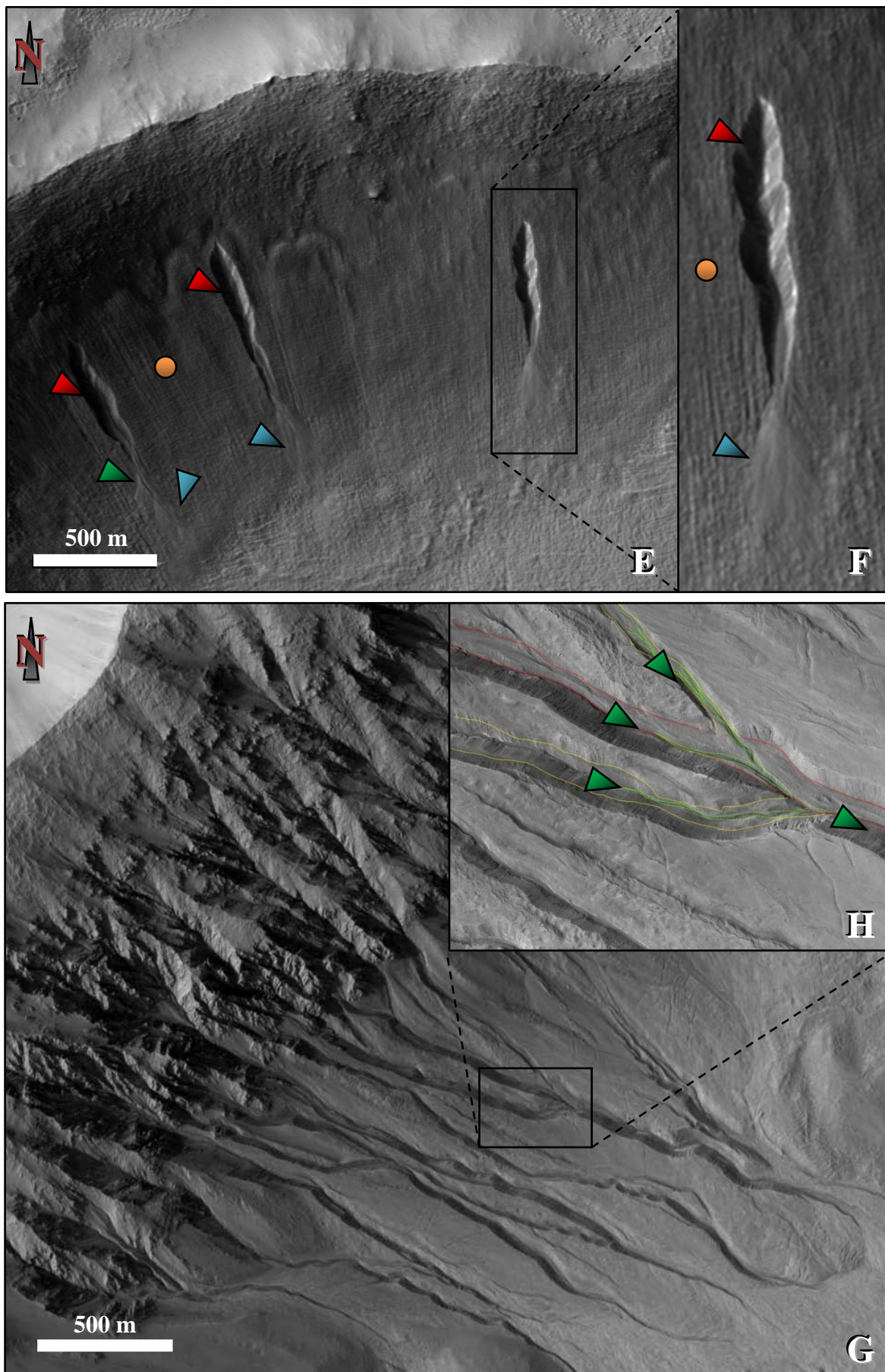
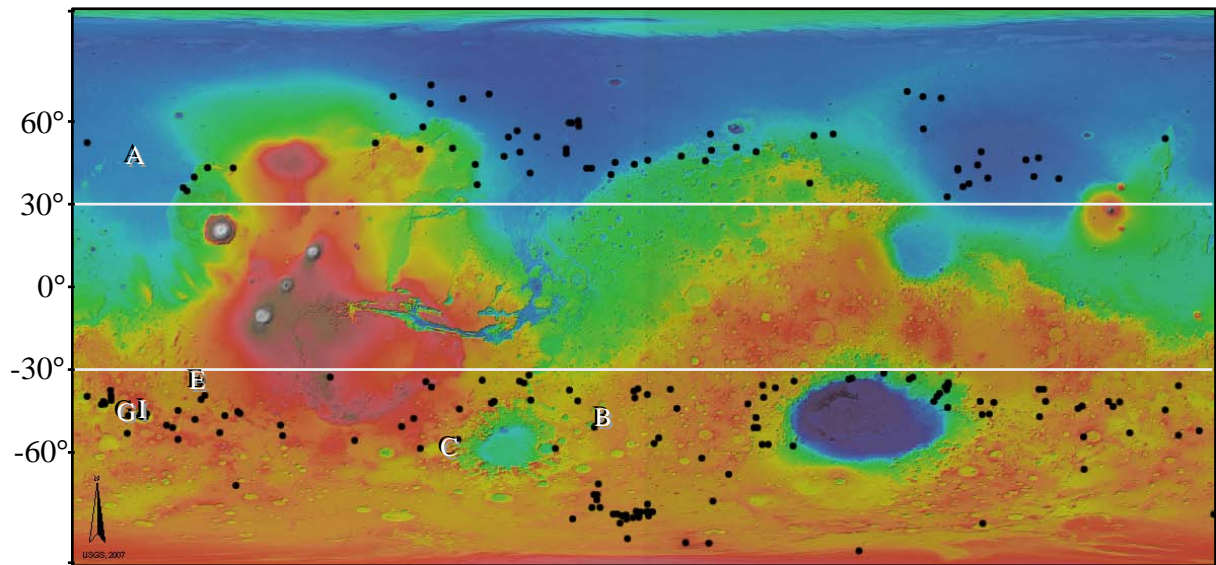
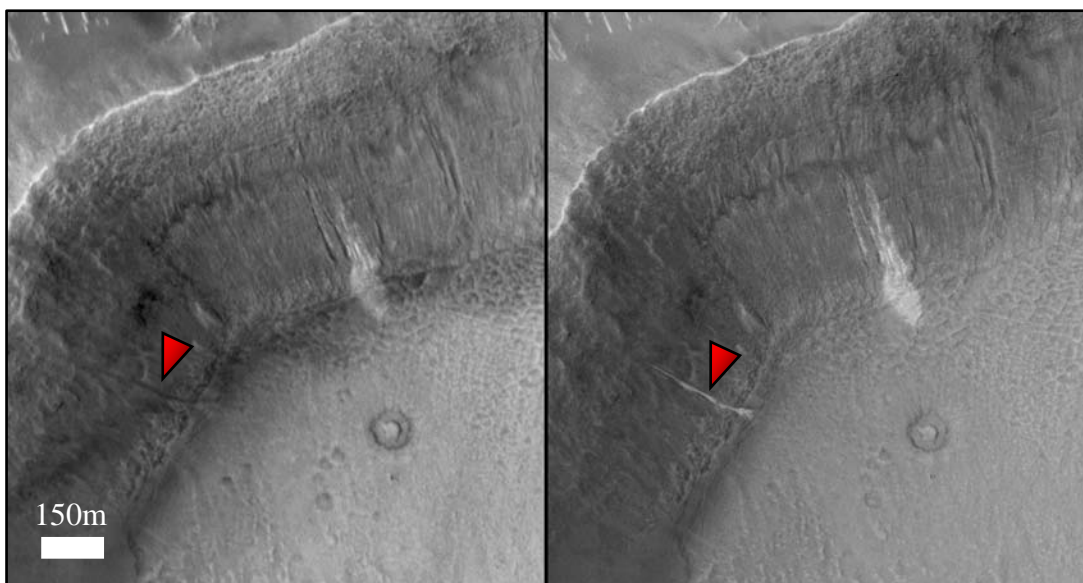


Fig. 49) Continuation.



**Fig. 50)** Global distribution of gullies (Malin and Edgett, 2000), (Bridges and Lackner, 2006). All identified gullies lay from 30° south and north toward higher latitudes. A-C, E, G - localisation of images from the Fig. 46. I – image from Fig. 48. Base map - MOLA color shade relief and MDIM (Courtesy USGS Astrogeology Research Program, <http://astrogeology.usgs.gov>).

(Bridges and Lackner, 2006) and meandering character of the flow (Malin and Edgett, 2000). Almost all conduits terminate in a sedimentary cone or prism. Detailed positioning and orientation measurements revealed yet another interesting information. Gullies are found almost exclusively between 45 and 72° latitude on both hemispheres Bridges and Lackner, 2006), mostly on pole facing slopes (see review Dickson et al. 2007). The paradox of flowing water in present climate is essentially still unsolved in spite of



**Fig. 51)** Spectacular MGS-MOC images (left-2001, right-2005) proofing that gullies are forming even now. Unnamed crater in Terra Sirenum (Courtesy NASA/JPL-Caltech).

several theories describing more or less plausible mechanisms like granular flow (Treiman, 2003), release of pressurized liquefier in shallow (Malin and Edgett, 2000t), (Mellon and Phillips, 2001), (Heldmann and Mellon, 2003) or deep reservoirs (Gaidos, 2001), geothermal melting (Hartmann, 2001), ice blanket melting, percolation and transport of non equilibrium water in porous media (Márquez et al. 2005), outflow of brines (Knauth and Burt, 2002) or accumulation and subsequent melting of surface snowpack (Fig. 49A, E, F) (Costard et al. 2002), (Christensen, 2003), (Balme et al. 2006), (Bridges and Lackner, 2006), (Dickson et al. 2007). From this wide array of hypotheses the last one gained the greatest attention but also meet difficulties in explanation how certain gullies can be formed in the present climate without apparent ice mantling (Fig. 51).

Although, the Blue Mars model describes the evolution of Mars in many ways unquestionably well, it also faces certain unexplained paradoxes. Most of them are concentrated around the early period where according to the theory Mars should be warm and considerably wet. A first problem appears already for the estimation of Martian initial CO<sub>2</sub> reservoir. Fast accretion (see 2.3) would tend to release most of gases to the primordial atmosphere. Simple scaling of Earth and Venus inventories that oscillate around 60-90 bars (6-8MPa) of CO<sub>2</sub> suggests 10-30 bars for Mars (Pollack et al. 1987), (Hoffman, 2000a). If such approach is correct then thermal instability would cause Martian atmosphere to condensate at the poles (Kasting, 1991) leaving a few bars of CO<sub>2</sub> in equilibrium with dry ice. It was also claimed that even considerably thick CO<sub>2</sub> atmosphere (up to ~5bar / 0.5MPa) might not be sufficient to provide greenhouse warming intense enough to compensate for the initially weaker Sun and stabilize liquid water at the surface. Models with thicker atmosphere that cross 5bar are most likely to introduce another potential liquid acting on the surface, namely liquid CO<sub>2</sub> (Chapter 1, Fig. 10), (Hoffman, 2000a), (Kargel, 2004). In order to avoid this scenario, essentially all publications considering this issue propose an extensive trapping of CO<sub>2</sub> in carbonates that readily form in a warm and wet environment. At this point another paradox comes into play. Up to now the highest amount of carbonates detected on Mars do not exceed 5% (Christensen et al, 2001), (Bandfield et al. 2003), (Christensen et al. 2004). This amount is far from the expected. A remedy for this obvious drawback can be a burial of carbonates deep into the regolith while overlying deposits were dissolved in acidic environment (Baker, 2001). Although, the final confirmation would require a deep drilling, the significant quantities of sulfates (Fig. 34) that have been found on the surface would at least partially support this explanation. The next significant issue of wet Mars is presence of olivine at the surface e.g.

(Hoefen et al. 2003). This mineral is highly unstable under wet climate and should transform into secondary phases through e.g. serpentinisation. Much later in the Martian history, other issues arise with the catastrophic water releases where pure water-based theories meet serious difficulties in providing enough fluid in a short period of time. It is especially apparent for the formation chaotic terrains (Hoffman, 2000a). In the discussion of this PhD (Chapter 5) a few additional problems will be shown.

### 2.5.2 White Mars

A number of inconsistencies in the “Blue Mars” model pushed some authors to search for different evolutionary pathways that could replicate present Martian surface features (Lambert and Chamberlain, 1978), (Hoffman, 2000a), (Hoffman, 2000b), (Hoffman, 2001a) (Jöns, 2001), (Parsons, 2001), (Tanaka et al. 2001), (Hoffman, 2002), (Kargel, 2004), (Rodriguez et al. 2006). The only reasonable alternative seems to be related to liquid CO<sub>2</sub> appearing above 5.11bar (0.51MPa) that may act under certain circumstances as liquid water. Moreover, some geomorphologic features can be better explained by decompression of CO<sub>2</sub> than by water outflow. Yet, in this view Mars most likely should have a greater starting CO<sub>2</sub> reservoir, 10-30bar (1-3MPa), than predicted by Blue Mars model and a climate that would have to be much colder. The reader should be aware that this approach met a serious resistance from followers of the warm Mars idea that do not hesitate to use doubtful arguments for criticism e.g. (Stewart and Nimmo, 2002), (see. 5.1.2). The name, “White Mars” itself, has been used for a standalone theory (Hoffman, 2000a) that represents the most extreme view among the hypotheses questioning warm Mars. For purpose of this thesis the “White Mars” concept will be extended to other publications that significantly diverge from the “Blue Mars” model in a similar spirit.

At low temperature and elevated pressures CO<sub>2</sub> may exist in liquid state, similarly to liquid ethane or methane on Titan, Saturn’s moon e.g. (Mitri et al, 2007), (Stofan et al. 2007). If Martian initial surface temperatures, under a thick atmosphere, did not exceed the melting point of ice then indeed liquid CO<sub>2</sub> might be considered as an alternative to water. In such case (Lambert and Chamberlain, 1978), (Hoffman, 2000a), (Hoffman, 2001b) CO<sub>2</sub> would exist in all three states within the regolith filling pore spaces similarly to water in the “Blue Mars” scenario (Fig. 52). Mirroring the water cycle, dry ice condensed at the poles at critical depths would undergo basal melting introducing liquid CO<sub>2</sub> into the regolith (Kurahashi-Nakamura and Tajika, 2006), (Longhi, 2006). Transported through the regolith



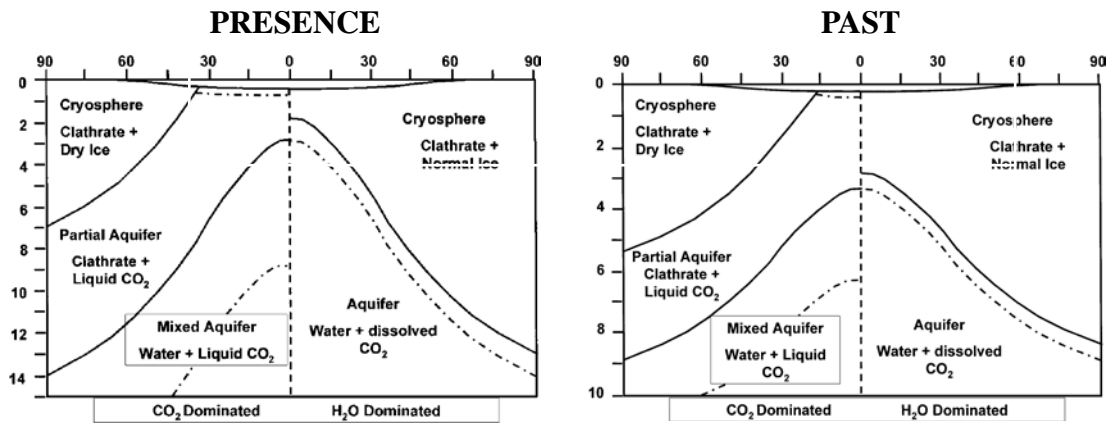


**Fig. 52)** A comparison between pore filling in “Blue” and “White Mars” model in two time windows. Present Mars model (left) is based on 10K/m thermal gradient. Past Mars variant includes twice higher heat flux (Hoffman, 2000a).

it could approach the surface at lower latitudes where the cryosphere should be the thinnest. Under suitable conditions liquid CO<sub>2</sub> would flow out on the surface and act similarly to water. In case of warmer climate or thinner atmosphere this process would be replaced by a violent decompression upon the phase change with gaseous CO<sub>2</sub> as a product. Following this idea an alternative mechanism for catastrophic outbursts and channel formation has been proposed (Fig. 53) (Hoffman, 2000a). Fracturing and slumping of CO<sub>2</sub> rich permafrost up to the liquid CO<sub>2</sub> depth would form a gas supported density flow (Hoffman, 2000a), (Hoffman, 2001a), (Hoffman, 2001c), (Hoffman, 2001d),

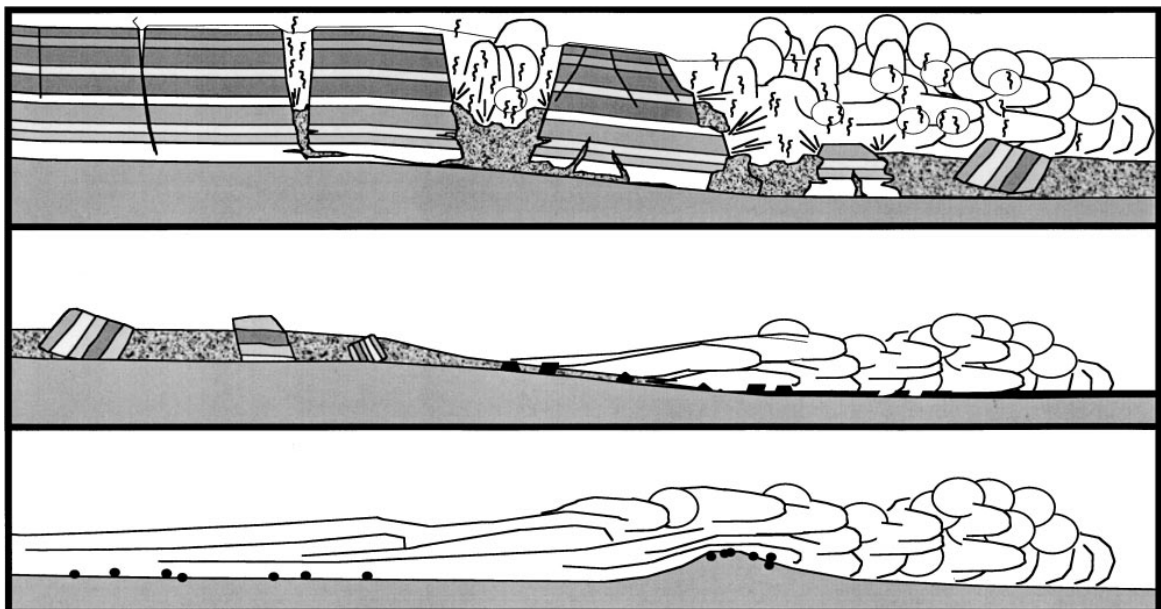


**Fig. 53)** Catastrophic outburst mechanism driven by liquid and gaseous CO<sub>2</sub>. Initial slumping produces a lubricated density flow. Subsequent grinding of carried debris is meant to supply the cryoclastic cloud in CO<sub>2</sub> (Hoffman, 2000a).

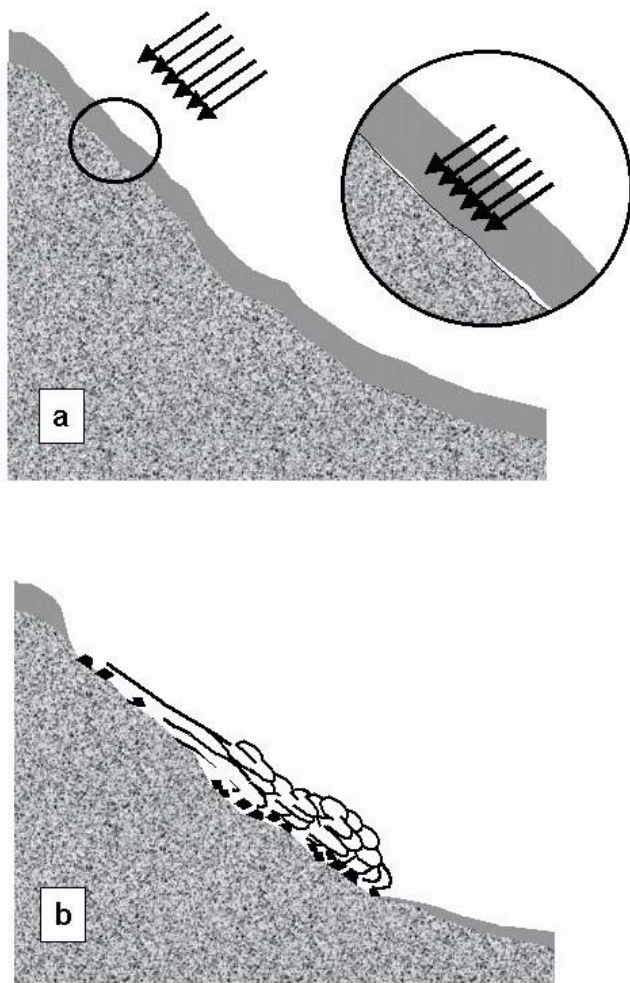


**Fig. 54)** CO<sub>2</sub> ice thaw model for gullies formation. A) Sun penetrates snowpack causing thawing at the base. CO<sub>2</sub> destabilizes ice layer and generates an avalanche. The flow is supported by sublimating dry ice (Hoffman, 2002).

(Tanaka et al. 2001), (Hoffman and Tanaka, 2002), (Rodriguez et al. 2006) that might be compared to terrestrial pyroclastic flows or turbidities. A constant supply of lubricating gas that sustains the movement is provided through grinding of CO<sub>2</sub> rich material carried within the cloud. Outbursts CO<sub>2</sub> have been adopted also at much smaller, local scale as an explanation for recent gullies formation (Hoffman, 2001e), (Musselwhite et al. 2001) even if the tenuous Martian atmosphere severely limits the stability of all CO<sub>2</sub> phases except the volatile one. To overcome this difficulty authors proposed CO<sub>2</sub> frost accumulation within the regolith just below poleward facing slopes, the most potential places for cold traps. Subsequent summer warming of deposited dry ice would lead to sublimation at the gas/solid contact and at greater lithostatic pressures to

liquid CO<sub>2</sub> formation. Eventually the dry ice barrier would be thinned enough to fail and release rapidly expanding liquid. According to a similar but more conservative model (Hoffman, 2002) gullies may be formed not by liquid but gaseous CO<sub>2</sub> (Fig. 54). The mechanism of this process is similar to the one proposed for dark spots and fans (Fig. 48) observed in the south polar regions of Mars (Kieffer, 2000a), (Kieffer et al, 2006). Solar radiation that penetrates a thin CO<sub>2</sub> snowpack may be absorbed by underlying rocks and due to a secondary radiation effect causes its thawing at the contact. CO<sub>2</sub> gas under pressure may disrupt the surface layer triggering an avalanche. Mechanical grinding of destabilized material is meant to provide additional CO<sub>2</sub> to lubricate a density supported

flow.

As the reader surely noticed, the “White Mars” scenario is rather a draft than a fully working hypothesis. Moreover a significant number of inconsistencies in the publications decreased its credibility as compared to the “Blue Mars” model. A choice of the early geothermal surface heat flow ( $20\text{mW/m}^2$ ) has been criticized as preferentially supporting the cold climate (Urquhart and Gulick, 2002). In comparison to  $30\text{mW/m}^2$  from “Blue Mars” it is indeed less but this difference can be easily explained by different thermal conductivities for water and dry ice and other species stored in pore spaces (see 2.6). Among others solid  $\text{CO}_2$  is likely to produce much steeper vertical thermal gradient that would decrease the amount of heat delivered to the surface. Yet, the stability of the  $\text{CO}_2$  inventory over the Martian history is probably the most often invoked issue of this concept. Noachian thick atmosphere can still support the “White Mars” scenario if the  $\text{CO}_2$  polar caps were partially compensating for the atmosphere stripping and still supporting the basal melting. Any presence of large surface liquid reservoirs, lakes or seas was not discussed at all in frame of the “White Mars” model. At some point Martian atmospheric pressure had to drop below the stability limits of liquid  $\text{CO}_2$  ( $\sim 5\text{bar} / 0.5\text{MPa}$ ) that terminated any river like activity. Yet, none of the papers explicitly state when it might have happened and whether it is possibly linked to the Noachian/Hesperian boundary. Later on, potential  $\text{CO}_2$  activity in the formation of chaos terrains and channels has been a subject of heavy criticism. Hypothetical Martian gas supported cryoclastic density flows may not possess any eroding properties that could allow for channels formation. Potential terrestrial analogs, pyroclastic flows or turbidities show that after violent blast or destabilization the mobilized masses tend to follow the preexisting depressions or channels with minor traces of erosion (Coleman, 2002). Moreover, the stability of dry ice and liquid  $\text{CO}_2$  from the past epoch under thin Hesperian and Amazonian atmosphere for geological timescales has been critically reviewed as impossible. The argumentation line was based on gas diffusion calculation through the porous regolith (Stewart and Nimmo, 2002), which strangely ignores any potential sealing effect of water ice, salts or clay minerals (Kargel, 2004). Effectively also an eventual accumulation of  $\text{CO}_2$  through magma outgassing has been described as improbable, as it was claimed, due to the imbalance between slow accumulation and an order of magnitude faster out diffusion. Another difficulty comes with the Martian early ocean. If such body of surface liquid ever existed it would require liquid water since the  $\text{CO}_2$  global budget might be too small. Gullies formation, one of the most controversial ideas within the “White Mars” scenario, also has not escaped from critical

comments. The accumulation mechanism of CO<sub>2</sub> was found to be insufficient to reproduce the observed features. Moreover, there is also a discrepancy between the maximum depths at which seasonal temperature changes might be observed. An ultimate proof against this hypothesis has been found in the calculated escape velocity of decompressed liquid CO<sub>2</sub> that is about two times faster than estimated for Martian gullies (Mangold et al. 2002), (Stewart and Nimmo, 2002).

## 2.6 Clathrate on Mars

Thermodynamic stability field of CO<sub>2</sub> hydrates fits very well in present and perhaps also in the past Martian realm (Fig. 55) e.g. (Longhi, 2000), (Longhi, 2001), (Longhi, 2006). Over the last several decades, hypotheses discussing the role of clathrates in different processes were strongly basing on this knowledge with little support from a work on kinetics. Certainly it is sufficient to start speculations but any time constrains or even feasibility of certain processes was impossible to determine. As a consequence a number of speculations appear supporting or negating clathrate existence or their possible impact on

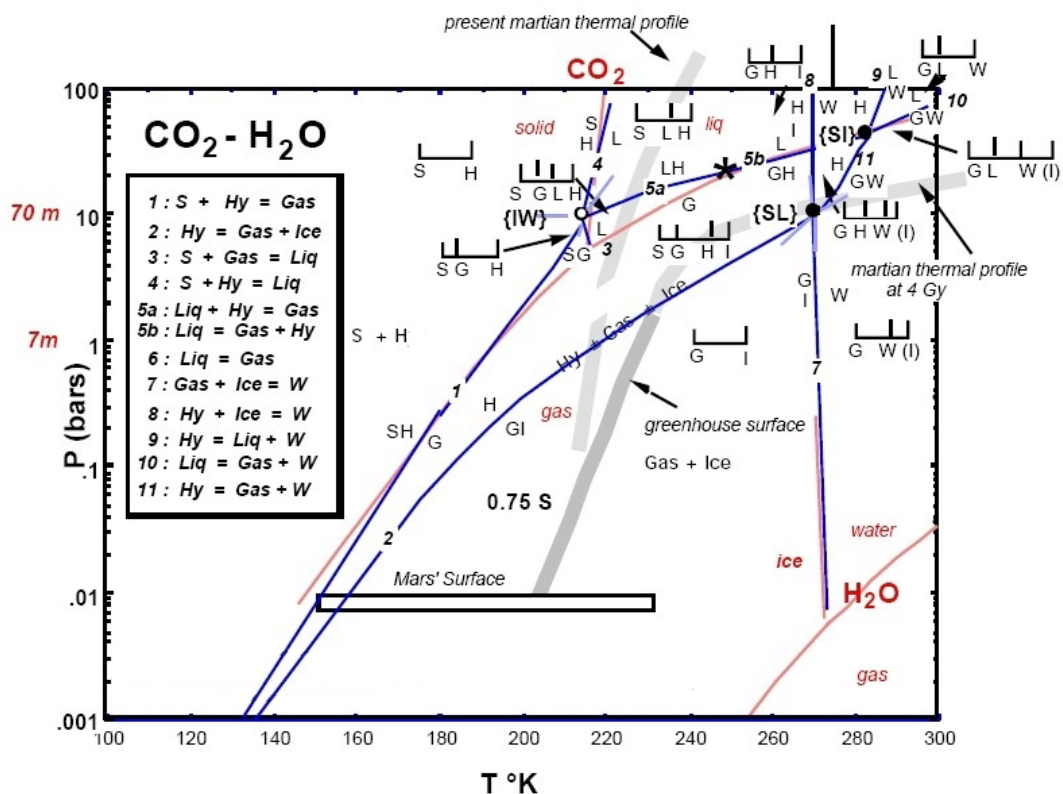


**Fig. 55)** CO<sub>2</sub>-H<sub>2</sub>O binary phase diagram relevant to Mars (Longhi, 2000). Blue lines – phase stability boundaries (see table for detailed description). Red lines – stability boundaries for pure CO<sub>2</sub> and pure H<sub>2</sub>O systems. SL, SI, IW – invariant points. Phases present in the diagram: S – solid CO<sub>2</sub>, L – liquid CO<sub>2</sub>, I – H<sub>2</sub>O ice, W – liquid H<sub>2</sub>O, G – CO<sub>2</sub> gas, H – CO<sub>2</sub> Hydrate.

the environment. This thesis attempts to deliver missing information, which can be used to verify most of the hypotheses (see Chapter 5). Yet, before the reader will read the final discussion it is out most important to be familiarized with a present state of knowledge. I have deliberately separated any information about clathrates from the above discussion on the Blue and White Mars to underline the main differences between them but the reader should be aware that clathrates appear in both concepts. This is in fact where the scientific beauty of gas hydrates lays. They are independent from discussed evolutionary models. In principle these compounds can be formed under The Blue or White Mars paradigm but different p-T and availability of CO<sub>2</sub> and H<sub>2</sub>O controls their abundance. As a natural consequence, the cold model richer in CO<sub>2</sub> favors clathrates while the warm one reduces their occurrence to several places including polar caps, perhaps regolith and even atmosphere.

### 2.6.1 Polar caps

Martian polar caps are presently the biggest reservoirs of surface water ice e.g. (Kieffer et al 1976), (Smith et al. 1999), (Bibring et al, 2004), (Plaut et al. 2007), (Zuber et al. 2007). Due to differences in present illumination, the northern polar cap (NPC) is slightly warmer than the southern one (SPC) e.g. (Kargel and Lunine, 1998). The mean annual temperature on the northern ice sheet stays around 170K but go as high as 200K during summer time. Winter temperatures drops below the condensation temperature of dry ice. This allows for a formation of few meters to tens of meters high seasonal solid CO<sub>2</sub> cap (Thomas et al. 2000), (Smyth et al. 2001), (Mitrofanov et al. 2003). Southern polar cap also poses dry ice cover that shows seasonal shrinking and growth (Fig. 56) e.g. (Paige et al. 1990), (Bibring et al, 2004) but it is much more stable due to lower annual temperatures (mean ~150K) that do not exceed 160-170K. On closer inspection, one will find all necessary components to form CO<sub>2</sub> clathrate on both caps. Moreover, the thermodynamic stability field of CO<sub>2</sub> clathrates spans almost over whole depth of polar caps. These facts have been noticed already in early 60's of XX century (Miller, 1961) and several years later confirmed by experimental work (Miller and Smythe, 1970). Even though, a direct proof of their existence was still missing at the time. Theoretically, temporary (NPC) or more permanent presence (SPC) of clathrates at the surface gave hope to detect them from the orbit. The most promising were places showing both CO<sub>2</sub> and H<sub>2</sub>O signal localized at the edges of the dry ice south polar cap (Fig. 56A, B). Unfortunately, it turned out that spectroscopically hydrates are very difficult to distinguish from water ice / dry ice

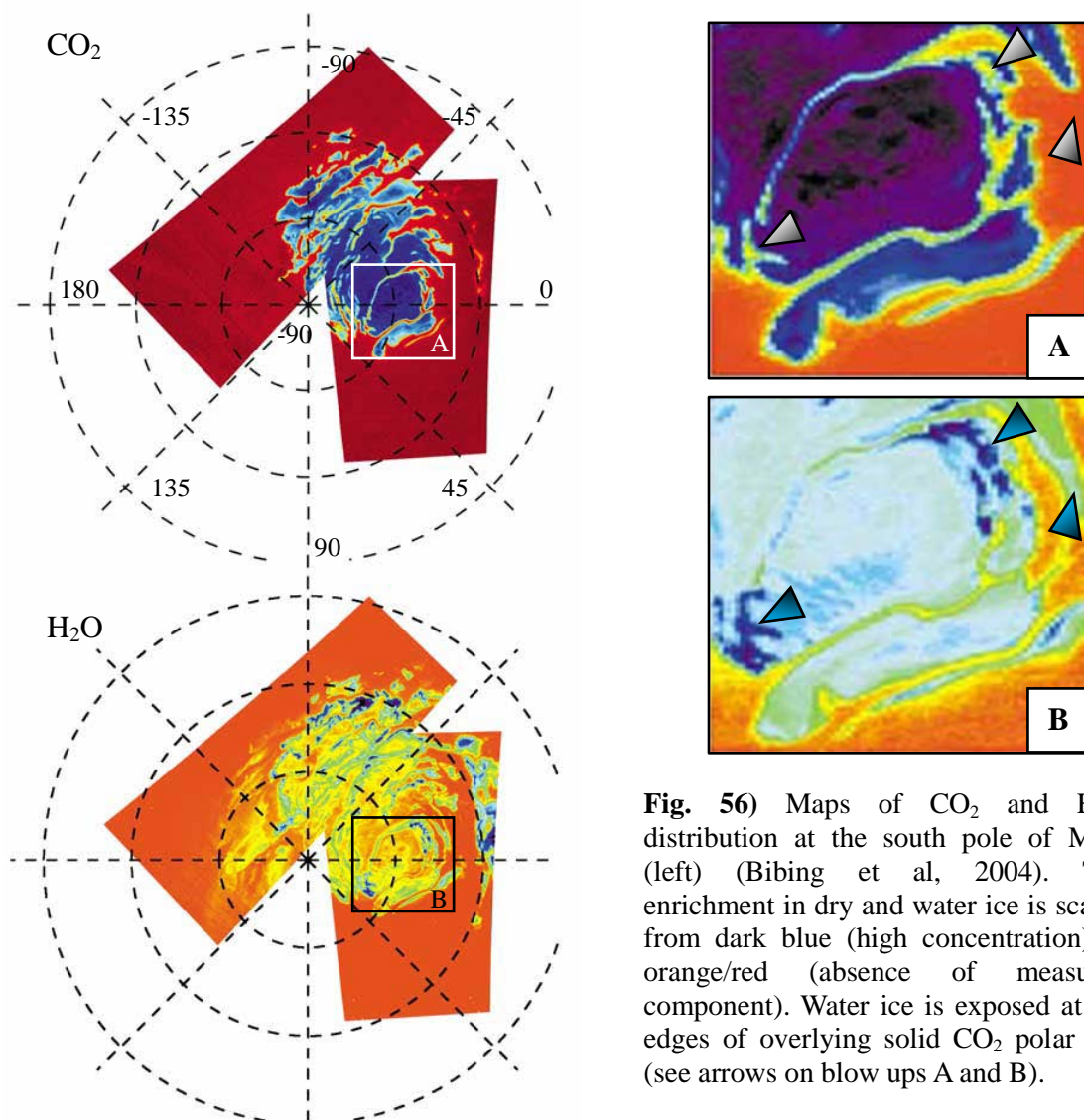


**Fig. 56)** Maps of CO<sub>2</sub> and H<sub>2</sub>O distribution at the south pole of Mars (left) (Bibing et al, 2004). The enrichment in dry and water ice is scaled from dark blue (high concentration) to orange/red (absence of measured component). Water ice is exposed at the edges of overlying solid CO<sub>2</sub> polar cap (see arrows on blow ups A and B).

mixture and better optical constants for hydrate are needed (Smythe, 1975), (Landry and England, 1994), (Schmitt, 2000). Not so long ago the hope was revived with the failure of Mars Polar Lander mission where eruption of CO<sub>2</sub> clathrates was used as one of the explanations (Koster van Groos and Guggenheim, 2000). Yet, this idea could not defend itself (Kieffer, 2000b) and Martian gas hydrates still remain unconfirmed. Laboratory experiments (Chapter 4) and terrestrial analogs suggest several plausible pathways for clathrates formation (see review Kargel et al. 2000). Small quantities can be formed by direct precipitation from the atmosphere but this reaction type is limited strongly by an availability of water vapor (see review Fouchet et al. 2007). Transformation of water ice at the surface, especially at the northern cap, is restricted by temperature excursion outside the stability field. Much more suitable p-T conditions are likely to be found deeper in polar ice where CO<sub>2</sub> gas or dry ice trapped in bubbles and inclusions are likely to react with



water ice (Mellon, 1996). An analogy could be drawn from terrestrial air hydrates (1.2.1) but in the Martian case transformation can start just from a few meters below the surface of water ice. The efficiency of this process is rather low and only a small volume of clathrates might be produced (Kargel et al. 2000). To support more extensive transformation at greater depths, an efficient source of CO<sub>2</sub> would be needed. It could be provided through a burial (Jakosky et al. 1995) and subsequent pressure melting of dry ice (Fig. 57A) e.g. (Kreslavsky and Head, 2002), (Hoffman, et al. 2002), (Longhi, 2006) or even basal melting of the thick dry ice cap (Fig. 57B) (Kurahashi-Nakamura and Tajika, 2006). While the first mechanism, related to obliquity variations, can be active over the Martian history, the last one is rather restricted to a collapse of the early thicker atmosphere. CO<sub>2</sub> clathrate similarly to its terrestrial methane counterpart is likely to incorporate also another species into its structure. Most likely candidates are N<sub>2</sub>, CO, O<sub>2</sub> and heavy noble gases: Xe, Kr, Ar. It is worthwhile to point out that during crystallization heavier gases are likely to be enriched but without altering their isotopic ratio (Musselwhite and Lunine, 1995), (Musselwhite and Swindle, 2001).

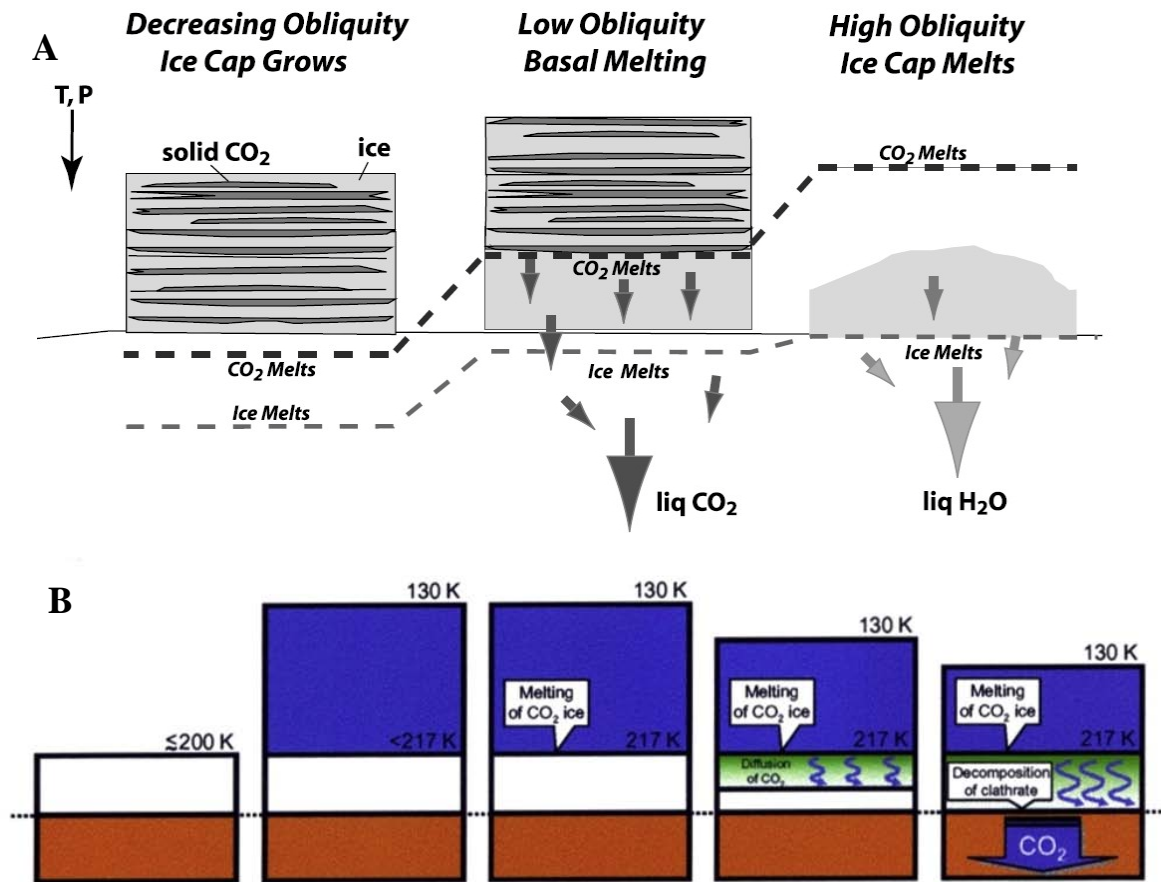


**Fig. 57)** Potential ways of CO<sub>2</sub> clathrate formation through the pressure melting of: **A)** Buried dry ice (Longhi, 2006), **B)** Thick CO<sub>2</sub> ice cap (Kurahashi-Nakamura and Tajika, 2006). Dissociation of clathrates at the base, above melting point of ice, will supply liquid water and CO<sub>2</sub> into the regolith.

The incorporation of clathrates in polar ices bears serious consequences for ice mechanics and thermal gradients within the caps due to their strong rheology and remarkably low thermal conductivity (Mellon, 1996), (Kargel, 1998), (Urquhart and Gulick, 2002). Since some of the properties are still not measured explicitly for CO<sub>2</sub> hydrates, some authors assumed that this value do not deviate much from other structure I clathrates e.g. (Mellon, 1996). Thermal conductivity has been found to be about 5 times lower than for water ice (~2.3 W/m K) and almost identical to dry ice (~0.5 W/m K). Adopting flow rates from methane clathrates, gas hydrates became the hardest among all ices building the Martian polar caps. Experiments on the rheology of CO<sub>2</sub> clathrates

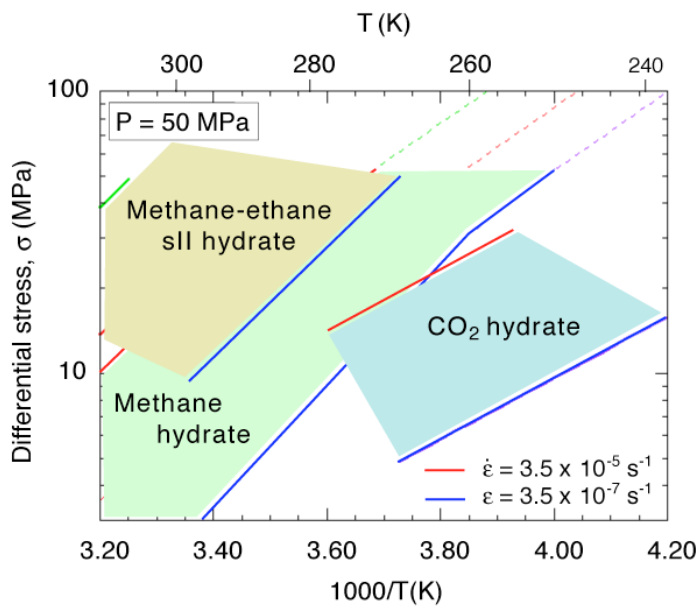


**Fig. 58)** Rheologies CO<sub>2</sub> hydrate in comparison to methane hydrate (sI) and mixed hydrate (sII) (Durham et al. 2003).

(Durham et al. 2003a) show a considerably big difference in flow rates from those measured in CH<sub>4</sub> clathrates (Fig. 58) Stern et al. 1996), (Durham et al. 2003b). Even though, CO<sub>2</sub> hydrate is still about two orders of magnitude more viscous than pure water ice (Durham, 1998). CO<sub>2</sub> ice, in comparison to water ice, is about ten times weaker e.g. (Durham, 1999).

Interlayered CO<sub>2</sub> hydrates with water ice and perhaps dry ice could well explain folding, boudinage or elastic flexural bulges commonly observed on the southern polar cap (Kargel and Tanaka, 2002), (Brightwell et al. 2003). Each component of the layered sequence will behave according to its mechanical strength. The hardest, CO<sub>2</sub> clathrates will tend to form boudins while other ices are likely to undergo plastic deformation. Even a small addition of clathrates to the polar ice is likely to reduce the flow rate and increase the temperature at the base of the ice sheet (Greve and Mahajan, 2004). In this way gas hydrates may actively control the maximum thickness of polar ices and thus basal melting (Mellon, 1996), (Kreslavsky and Head, 2002), (Longhi, 2004). Taking an average present Martian geothermal heat flux (~30mW/m<sup>2</sup>) and assuming that both polar caps do not undergo the basal melting, one could try to estimate the upper limit for gas hydrates locked in those ice



bodies. For the 4km thick northern polar ice this value has been calculated on 72% of the total volume. The southern ice sheet is about twice thinner and allowed to be constructed even from 100% of clathrates (Mellon, 1996). Even if the real values are lower from above predictions, the polar caps can be considered as a potential CO<sub>2</sub> storage. The maximum CO<sub>2</sub> content trapped in clathrates under favorable conditions may be as high as 112-200mbar (Jakosky et al. 1995), (Mellon, 1996) but also lower values are proposed (Dobrovolskis and Ingersoll, 1975).

### 2.6.2 The regolith

Although first two subsurface radar sounders (Mars Express-MARSIS, MRO-SHARAD) operating over the planet already delivered interesting information about a few regions (Picardi et al. 2005), (Plaut et al. 2007), (Seu et al. 2007), the structure of the Marian regolith is essentially one big unknown. Noachian heavy bombardment most likely turned a several kilometers of the upper crust in a fractured and porous mega-regolith. Theoretical porosity profiles through this layer show an exponential decay of free spaces to about 10-13km where hydraulic conductivity is almost completely halted (Clifford, 1993), (Clifford and Parker, 2001). Permeability above this depth stays as a subject of numerous presently unverifiable speculations. Depending on the model a globally interconnected network e.g. (Clifford, 1993), (Clifford and Parker, 2001) or limited regional conductivity (Dohm et al. 2001), (Chapman and Tanaka, 2002), (Kargel, 2004), (Russell and Head, 2007) is invoked. The present knowledge about eventual pore filling and distribution is also very sparse. Aside from the already discussed ground water ice (see 2.5.1), also liquid water, dry ice and liquid CO<sub>2</sub> are possible. Their occurrence is tightly correlated with poorly constrained p-T conditions in the regolith, confining pressures, thermal gradients and preferred evolutionary model. In such an unexplored environment a number of authors suspected clathrates to be formed e.g. (Milton, 1974), (Lambert and Chamberlain, 1978), (Hoffman, 2000a), (Longhi, 2000), (Longhi, 2001), (Longhi, 2006). As already shown (Fig. 55), the thermodynamic stability field of gas hydrates indeed allows for gas hydrate crystallization within the regolith but two crucial conditions must be met: 1) Water and gas must be provided, 2) An appropriate partial pressure of forming gas or gas mixture must be kept to stabilize the compound (Sloan, 1998). It is safe to assume that water ice and perhaps liquid water are abundant in the regolith. Both phases can be used as a substrate in the clathration process. Water ice closer to the surface may serve also as a tight seal that slows down out-diffusion to geological timescales. Efficient gas sources are more difficult

to define since they depend strongly on the poorly understood Martian history. Concerning this point literature discusses three possibilities: 1) Introduction of liquid CO<sub>2</sub> through the basal melting (Jakosky et al. 1995), (Kurahashi-Nakamura and Tajika, 2006), 2) Magma degassing (Baker et al. 1991), (Baker et al, 2000), (Baker, 2001), (Max and Clifford, 2001), (Pellenbarg et al. 2003) and 3) Microbial activity (Max and Clifford, 2000a), (Max and Clifford, 2001), (Pellenbarg et al. 2003), (Krasnopolsky et al. 2004). The last two processes enable also other gases, like methane that could potentially form clathrate or be incorporated as trace components in CO<sub>2</sub> hydrate. Gases that are likely to move buoyantly toward the surface will tend to concentrate at the bottom of such quasi-impermeable layers. Gradual thickening of the cryosphere could seal off some deposits forming lenses of gas hydrates distributed in water ice filled regolith (Pellenbarg et al. 2003). The highest concentration of these compounds should be expected in close proximity to possible gas sources. Although an estimation of the clathrate volume in the regolith seems to be impossible some authors still speculate that the amount of CO<sub>2</sub> deposited in this way may significantly exceed the one from both polar caps (Baker et al, 1991), (Kargel and Lunine, 1995), (Kargel, 2004).

### 2.6.3 Environmental impact of clathrate decomposition

As it was already discussed (see. 2.5.1) Mars even now is a considerably dynamic system where quasi-cyclic obliquity changes are very likely to cause a massive mobilization of ices. Rapid sublimation at high obliquity will at least partially excavate and destabilize polar deposits of clathrates thus releasing stored CO<sub>2</sub> to the atmosphere. A similar effect might perhaps be achieved by periods of intensive volcanic activity (Baker, 2001). An environmental effect of the degassing is difficult to assess, since exact volumes of stored CO<sub>2</sub> are not known, but even several mbar (tens of kPa) may result in somewhat warmer climate (Jakosky et al. 1995). CO<sub>2</sub> and other released gases (see 2.6.2) are likely to have isotopic signatures characteristic for Mars at the moment of deposition. If so, Martian atmosphere constantly enriched in heavier isotopes through various processes (see 2.5.1) will be partially overprinted by less evolved gases (Musslewhite and Swindle, 2001). What is very intriguing, at least one, or two such episodes might have been recorded in the Martian meteorites, Nakhhalites and ALH84001. Although anomalous isotopic ratios might find also alternative explanations (see review Musslewhite and Swindle, 2001), they suffer from a number of inconsistencies that the clathrate related hypothesis seems to handle well.

Dissociation of clathrates stored in the regolith is more difficult to trigger as it requires

thermal or pressure disturbances able to act at greater depths. Terrestrial analogs suggest an increase in local geothermal activity, volcanism, tectonics or removal of overlaying deposits as most likely candidates e.g. (Baker et al, 2000), (Baker, 2001), (Max and Clifford, 2000b), (Max and Clifford, 2001), (Prieto-Ballesteros et al. 2006), (Rodriguez et al. 2006). Aside from those triggers also an increase in salinity has been suggested as a possible way to destabilize clathrates (Bodnar, 2001), (Madden et al. 2007). An accumulation of dissociation products may cause an instability of the affected area that after reaching some critical value will lead to outgassing. Depending on the geological situation, the scale of this process may vary from slow venting to catastrophic release. This idea was applied on Mars for the first time in 70's of XX century (Milton, 1974) as an explanation for chaotic terrain formation. According to this hypothesis, sublimation of equatorial and low latitude ices at low obliquity periods was likely to destabilize buried clathrates. A decomposition of shallower deposits was suggested to led to catastrophic eruptions of gaseous CO<sub>2</sub> and liquid water through the shattered overlaying frozen ground. Morphologic correlation (Fig. 42) of those features with outflow channels suggest that very large volume of liquid has been released from disrupted regolith in a short period of time (Fig. 40). The amount of water obtained from decaying clathrates is far insufficient to explain the observed features alone e.g. (Max and Clifford, 2001). Additionally, decomposing hydrates cool down the environment (1.5.3), (Peale et al. 1975), which might reduce available water even more. This line of argumentation excludes the principal role of clathrates in explaining the outflow channels. Since another source of liquid is required, again two evolutionary models come into play. Extreme differences between them regulate the possible role of clathrates in catastrophic releases. The “White Mars” approach replaces liquid water with liquid and solid CO<sub>2</sub> that drives violent decompression. At this point it is necessary to point out that, most of H<sub>2</sub>O in this model is bound in clathrate structure. Yet, the role of these compounds in this process is reduced essentially to an environmental seal (Lambert and Chamberlain, 1978), (Hoffman, 2000a) and possible support of long lasting cryoclastic flows due to slow dissociation kinetics (Hoffman, 2000a). The “Blue Mars” approach the issue from the other end. The liquid that formed outflow channels is assumed to be pressurized water that was stored under the cryosphere. In the global megaregolith of a limited permeability, decomposing clathrates might lead to a regional or local CO<sub>2</sub> saturation of water, liquefaction of weaker layers and catastrophic depressurization (Komatsu et al, 2000), (Rodriguez et al. 2006). In more conservative approach with the global pressure buildup under the cryosphere, gas hydrates would serve only as a medium

that disrupts the cryosphere. Detection of methane in the atmosphere e.g. (Formisano et al. 2004) opened a discussion on a possible source of this unstable gas. Among others, dissociation of mixed CO<sub>2</sub>-CH<sub>4</sub> clathrate deposits or enclaves with CH<sub>4</sub> clathrates has been proposed e.g. (Pellenbarg et al. 2003), (Prieto-Ballstros et al, 2006), (Chastain and Chevrier, 2007), (McMenamin and McGill, 2007). Decomposition of clathrates has been also used as one of the explanation for so called pancake-domes in craters at sub polar latitudes (Cabrol et al. 1997). Yet, high resolution images gathered over the last few years attributed those features to dunes rejecting their hydrate related origin.

# Chapter 3 – Methods and instrumentation

In this chapter the reader will find information about equipment and techniques that were used to study CO<sub>2</sub> clathrates. Since my thesis is a continuation of the work started by Georgi Genov, a number of basic definitions and elementary knowledge will not be discussed here in detail and the reader should refer to cited textbooks or two previous PhD theses (Genov, 2005), (Staykova, 2004). I will concentrate mostly on improvements and a comparison between different methods showing their weaker and stronger sides.

## 3.1 Kinetics investigations

In frame of this thesis two already proved methods were used to explore the kinetics of forming or decomposing hydrates: 1) In-situ time-resolved neutron diffraction, 2) pVT (pressure, volume, temperature) combined with ex-situ X-ray diffraction.

### 3.1.1 X-rays and neutrons

During all formation as well as decomposition reactions presented in this thesis at each time step samples contain one or several crystalline phases that structurally differ from each other. This property can be explored with diffraction techniques that can efficiently and accurately detect and quantify crystalline phases also as a function of time. Basics of this phenomenon can be found in the previous PhD thesis (Genov, 2005) or

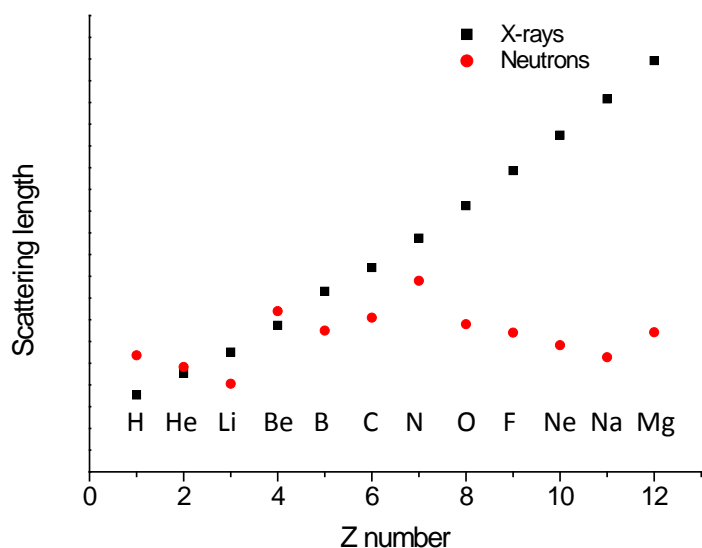


**Fig. 59)** Scattering length (amplitude) for X-rays and neutrons as a function the Z number (After: Parrish, 1992).

numerous textbooks e.g. (Als-Nielsen and McMoore, 2001). Photons and neutrons may scatter elastically, inelastically or be absorbed by an atom. For a standard diffraction and time-resolved kinetics studies the first listed type of interaction is used, while other contribute to unwanted effects like increased background or decreased

penetration depth. Generally X-rays and neutrons may be treated as equivalent but in certain cases one of them is more suitable than the other one (3.1.4). This difference is caused, among others, by the way of interaction with atoms and energy carried by a beam, availability of diffractometers and accessibility of beam time.

X-rays strongly interact with matter, scattering on electrons and its strength grows nearly linearly with the increasing Z number (atomic number) (Fig. 59). It also means that light elements (e.g. H, He, Li) will be underrepresented in a diffraction pattern in presence of heavier elements. Penetration depth increases for targets composed of elements with low Z number. Brilliance of even a several hundreds of keV, obtained on synchrotron beam

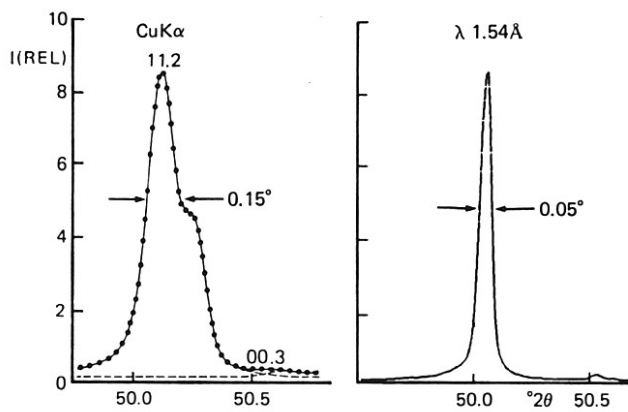


**Fig. 60)** Comparison of a quartz peak profile - FWHM (Full width at half maximum) for X-ray tube and synchrotron beam (After: Parrish, 1992).

lines, also increases penetration power in comparison to weaker X-rays generated by laboratory in-house tubes of about 5-17keV. Both types of sources differ also in beam shape. The parallel beam of the synchrotron, as opposed to the in-house X-ray tubes acting like point-like sources, considerably improves the maximum achievable resolution (Fig. 60).

In contrary to X-rays, neutrons interact with matter much weaker by scattering on nuclei. Since the core radius is much smaller than that of an atom, the penetration depth is usually considerably larger than that for photons. A probability of scattering on an atom is described by a neutron scattering cross section, which can be expressed as the area of a given nucleus as seen by the incident neutron. This parameter is unique for each isotope showing high dependence on a nuclear spin state and the structure of the nucleus. For this reason chemically identical isotopes of one element e.g. hydrogen and its heavier isotope, deuterium, may possess totally different neutron scattering cross sections. Moreover, within one isotope nucleons may be at different spin states which mean that the neutron scattering cross section is in fact a sum of coherent and incoherent component. The scattering power for different elements can be also defined using a scattering length ( $b$ ) that is related to the total scattering cross section ( $\sigma_s$ ) through the following expression:  $\sigma_s = 4\pi b^2$  (see e.g. Nielson, 1993). The scattering length is approximately on the same order

Element	Z	A	$b_c$	$b_i$	$\sigma_c$	$\sigma_i$	$\sigma_s$	$\sigma_a$
H	1	1	-3.7406(11)	25.217(6)	1.7583(10)	79.90(4)	81.67(4)	0.3326(7)
		2	6.71(4)	4.033(32)	5.592(7)	2.04(3)	7.63(3)	0.0000519(7)
C	6	12	6.6511(16)	0	5.559(3)	0	5.559(3)	0.00353(7)
O	8	16	5.803(4)	0	4.232(6)	0	4.232(6)	0.00016(1)
Al	13	27	3.449(5)	0.271(10)	1.495(4)	0.0092(7)	1.504(4)	0.231(3)
Mn	25	55	-3.72(2)	1.79(4)	1.75(2)	0.40(2)	2.15(3)	13.3(2)
Fe*	26		9.54(6)		11.44(14)	0.39(3)	11.83(14)	2.56(3)
Cu*	29		7.718(4)		7.486(8)	0.52(4)	8.01(4)	3.78(2)
Zn*	30		5.689(14)		4.067(20)	0.061(22)	4.128(10)	1.11(2)
Cd*	48		5.1(3)		3.3(4)	2.4(7)	5.7(6)	2520.(50)
Gd*	64		9.5(2)		34.5(5)	158.(4.)	192.(4.)	48890.(104.)

**Table 4)** Coherent ( $b_c$ ) and incoherent ( $b_i$ ) amplitudes, total scattering cross sections ( $\sigma_s$ ) with coherent and incoherent element ( $\sigma_c$ ,  $\sigma_i$ ) and absorption cross sections ( $\sigma_a$ ) for selected isotopes (first 6) and elements with their natural isotopic abundances (\*). Neutron cross sections here are presented in [barn]s where one unit corresponds to 100fm. Z-number of protons, A-number of neutrons (After: Sears. 1992)

of magnitude (Fig. 59) across the whole periodic table (with a few exceptions) that gives relatively even representation of light and heavy elements on a diffraction pattern. In certain cases neutron may be absorbed by the nucleus in a capture process. This probability is expressed by a neutron absorption cross section. For a several elements like cadmium or gadolinium it is exceedingly high (Table 4).

### 3.1.2 In-situ time-resolved neutron powder diffraction

For the clathrate formation and decomposition studies presented here neutron diffraction is nearly a perfect tool, among others due to: 1) Good penetration capabilities allowing for less complicated, thicker and cheaper cells that can withstand the required extreme conditions (see. 3.2), 2) Large beam cross section that allows for big samples and reduces the effect of grain statistics, 3) Strong interactions with deuterium atoms in clathrates and water ices (stronger than X-rays) giving much more complete structural information.

The greatest downside of the neutron-based methods is usually relatively low intensity of an incident beam that translates in longer acquisition times. In order to utilize above advantages and minimize this issue the diffractometer must be placed close to an intense neutron source trading an increased background noise for higher flux. Only a few neutron powder diffractometers all over the world meet all the above conditions. One such



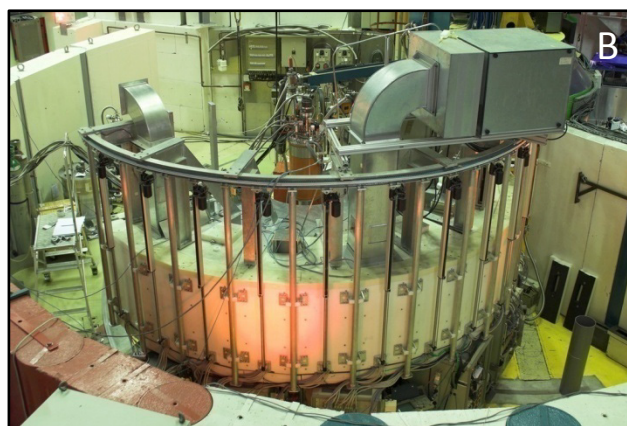
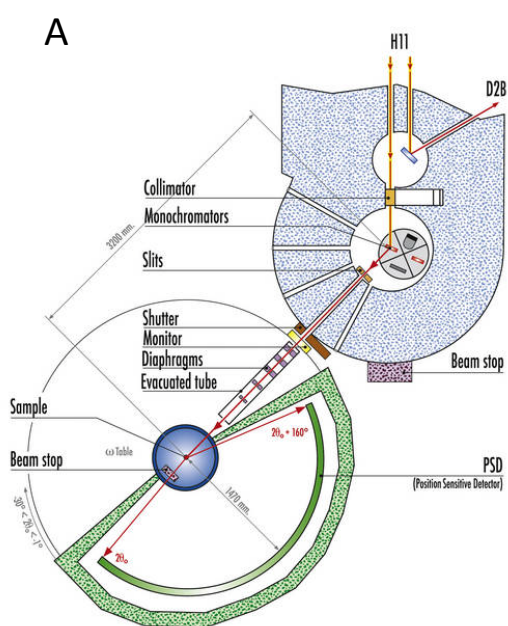


**Fig. 61)** Schematic drawing of the D20 powder diffractometer in the high flux configuration (A). View on the position sensitive detector embaing the "orange" cryostat. Source: ILL Yellow Book, (B). The installation is surrounded by a concrete anti-radiation wall.

instrument is D20 (Fig. 61). It is coupled to the fission reactor neutron source at Institute Laue Langevin (ILL) in Grenoble, France and has been successfully used by our group already for a number of years e.g. (Staykova, 2004), (Genov, 2005). This unique medium to high resolution 2-axis diffractometer operates at a thermal neutron beam line close to the 58.3MW reactor that provides very high flux at the sample position (max  $9.8 \times 10^7 \text{ n cm}^{-2} \text{ s}^{-2}$ ). A white beam is monochromatized on a pyrolytic graphite (002) monochromator that is the most suitable for the experiments presented here. The beam is vertically focused at the sample position, covering area of about  $5 \times 30\text{mm}$ . The greatest advantage of this particular diffractometer is its unique position-sensitive one dimensional detector composed of 1536 micro-strip cells filled with  $^3\text{He}$  and  $\text{CF}_4$  that cover a very impressive range of  $153.6^\circ$  with  $0.1^\circ$  resolution. What is even more interesting is that this detector is capable of an ultra fast simultaneous readout from all cells with a dead time between two frames as short as 20ns. This in turn enables acquisition time as short as a few seconds per frame but trading counting statistics and low intensities of Bragg reflections. Typical time steps used for this thesis were 30, 60 and 300s depending on the reaction rate. Keeping a good signal-to-noise ratio in short 30-60s frames makes it possible to follow fast, initial reactions commonly found during the decomposition of gas hydrates at higher temperatures. Utilizing already listed, high intensity, resolution and sensitivity,

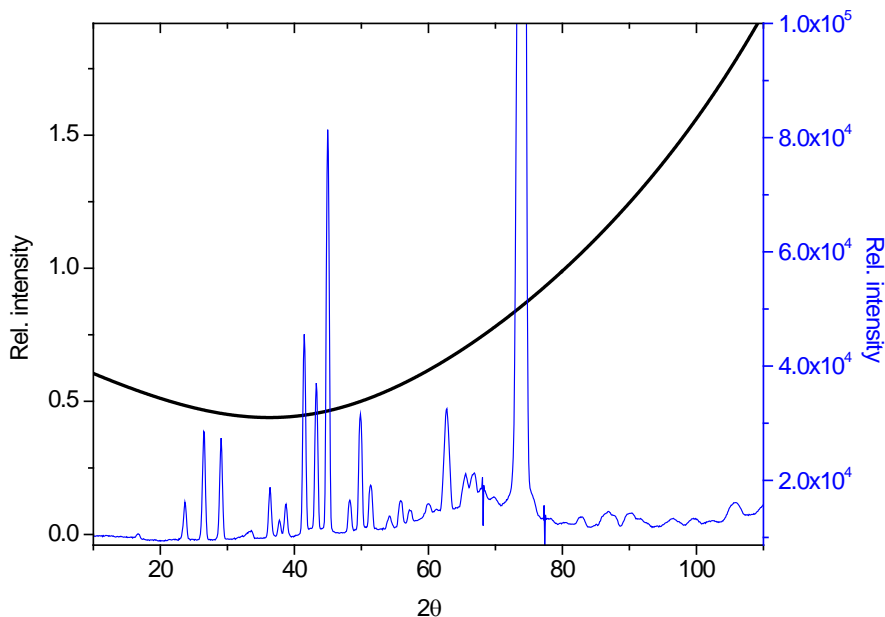


**Fig. 62)** D20 resolution curve (in black) plotted over a data set taken at the 185K and 6mbar (0.6kPa). Sharp Bragg reflections from the CO<sub>2</sub> clathrate and ice fall between 20 and 60 2θ. Towards higher angles peak broadening and intensities drop is observed. Strong reflections at ~63 and 75 2θ come from Al-precipitates in the experimental cell (see: 3.2.1).

D20 is capable of detecting newly formed phases even if their fraction is below 1% (~0.5%). This provides very detailed information on the early stage of a reaction and helps to explore such ambiguous issues like the incubation period (1.1.5.2) by reducing an uncertainty that comes from the instrument. The optimal resolution for D20 (Fig. 62) in the described configuration falls close to the 2θ region where the strongest ice and clathrate reflections appear. The resolution deteriorates rather quickly toward higher 2θ angles but reflections from that range are still useful for refinement. To improve the resolving power during the last campaign (see Chapter 4) a newly installed rocking oscillating collimator

was used (ROC) (see Appendix 2).

Low temperature control is

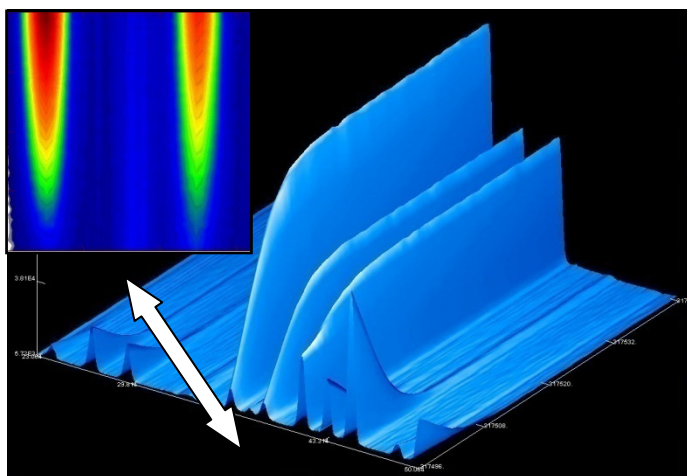


**Fig. 63)** Decomposition of CO<sub>2</sub> hydrates at 200K 6mbar (0.6kPa) in the 3D accumulation LAMP plot. Ice Bragg reflections grow with time while clathrate peaks diminish almost entirely. The reaction can be also displayed in a top 2D projection, which is shown here on the blow up for two ice reflections.

provided by the so called “orange” cryostat that operates between 1.7 K and 300 K. PID loop temperature controller regulates heating elements and cooling with He gas flowing between the cryostat and a sample stick. Although the precision of this system usually does not deviate much from 0.1K, in certain cases (rapid cooling/warming), equilibration with a given target temperature may take 30min. Data acquired during one frame can be quickly accessed via the LAMP software (Large Array Manipulation Program) that offers basic display functions as well as processing and exporting tools. It also enables to plot collected histograms as a function of time (Fig. 63) to trace eventual changes in the sample. This particular option has proven to be priceless in very low temperature runs presented here in the thesis (4.2.3). Later on, raw data can be converted to .gsa format for further processing in the GSAS (General Structure Analysis System) package.

Even if D20, in discussed configuration, is dedicated mostly to kinetics studies, it provides also limited structural information on investigated crystalline solids. Such parameters like thermal displacement factors and atomic positions, related to the higher  $2\theta$  angles, are beyond its reach but lattice constants or defectiveness of water ice can be successfully retrieved from lower  $2\theta$  angles. Cage fillings in clathrates also can be refined but some constrains must be applied (4.2.5).

### 3.1.3 pVT and ex-situ X-ray diffraction

Since clathrates upon formation consume a certain volume of gas it is possible to measure how fast it happens if the reaction volume is kept constant. Similar approach can be applied for decomposition reactions where gas release rate can be recorded. Yet closed systems have one serious flaw, namely non constant thermodynamic conditions over time. It means that e.g. even if upon formation clathrates will start to grow at desired pressure, the driving force expressed by reaction rate will diminish with time as gas is consumed until an equilibrium is achieved. Such style of reaction is not applicable for this thesis since all reactions are meant to be isobaric with a constant driving force. A way to go around the problem has been found in, rapid refills/releases. The oscillations in a narrow window around a targeted pressure create quasi constant thermodynamic conditions over a long time periods. Due to specific construction of experimental setups (see 3.2.2), during an initial stabilization as well as each refill in formation reactions a sample may be exposed to warm gas. This negative influence can be greatly reduced (see 3.2.2) but at the initial stage some artifacts may still occur. Typical collected data in a raw form look more like a jigsaw

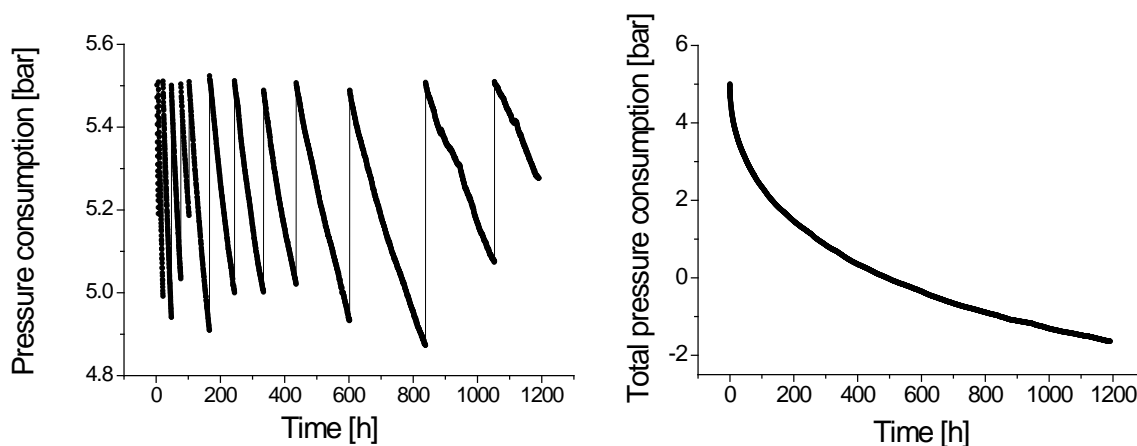


**Fig. 64)** Formation of CO<sub>2</sub> hydrates from spherical ice with the pVT method. Target pressure was set on 5.3bar (0.53MPa). The reaction curve registers each refill with a sharp pressure rise (left graph). Accumulation curve is reconstructed by adding all increments. Here, it has been done with the automated procedure.

(Fig. 64A) than a curve and need to be reworked. Short reactions can be processed manually but the same cannot be said about longer runs with multiple refill/release events. Such data are treated by software specially developed for this purpose by Georgi Genov. As a final result of pVT experiment one obtains the total accumulated or consumed pressure as a function of time (Fig. 64B). Individual data sets are valuable but very difficult to compare between each other due to differences in the initial volume of water and some way of normalization must be applied. The most suitable for this purpose is a hydrate fraction that can be easily determined by means of diffraction at the end of the experiment. For reasons discussed in the next section neutron diffraction cannot assist here and X-ray diffraction is used instead. Some preliminary analyses have been done on an in-house Philips X-PERT PW 3040 diffractometer in the modified (fixed sample position) Bragg-Brentano geometry (Parrish, 1992). A sample in a flat holder is sealed within a beryllium head and evacuated at LN<sub>2</sub> temperature. So obtained diffraction patterns suffer from a low resolution and low beam intensity that severely decrease the usefulness of the measured hydrate fraction below to 10% and extend the scanning time to several hours. Hard X-rays produced by synchrotron sources, successfully used by our group in the past e.g. (Staykova, 2004), offer much faster acquisition times (~90 seconds) and better resolution. Samples, kept at LN<sub>2</sub> temperature, were measured on BW5 experimental beam line at DESY-HASYLAB in Hamburg, Germany. The setup is equipped with a beryllium head and vacuum system similar to those of the in-house diffractometer. The instrument works in a transmission geometry (Fig. 65). The X-ray beam is monochromatised on

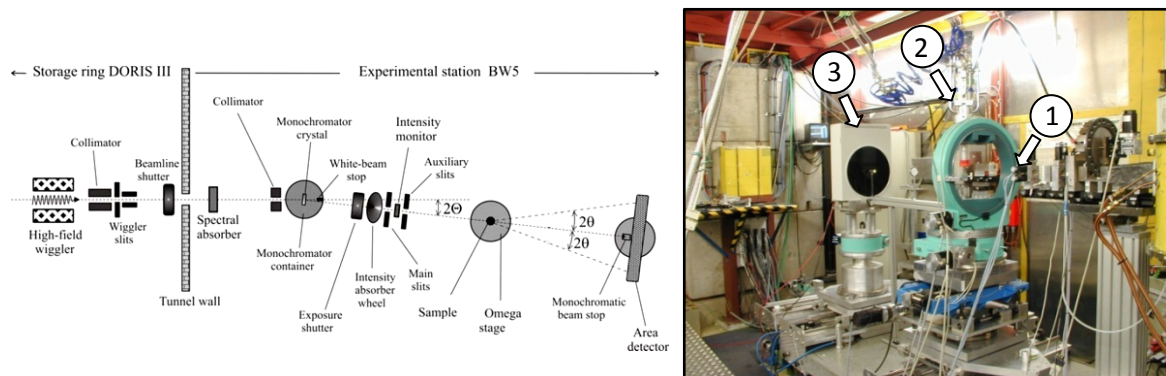


**Fig. 65)** BW5 experimental beam line at DORIS III storage ring, in Hamburg. To the left, a scheme of the installation. To the right, a view on an Euler cradle (1) equipped in the cold head (2) and the MAR image plate (3).

a SiGa or Silicon 111 crystal to about 100 keV ( $\sim 0.124 \text{ \AA}$ ) and collimated before reaching a sample. The spot size at this position is approximately  $2.25 \text{ mm}^2$ . A portion of X-rays that has been scattered on the investigated sample is recorded by a 2D MAR image plate located at the end of the setup. A part of the beam that passes unaffected through the sample is absorbed by a beam stopper before reaching the detector. Data presented here are stored with 1800 pixel vertical and horizontal resolution. The 2D images are processed in FIT2D software where after integration to 1D diffraction pattern can be exported to .gsa format and further refined with GSAS.

### 3.1.4 In-situ neutron powder diffraction or pVT / ex-situ X-ray diffraction

At first glance it might seem that both techniques, X-ray and neutron diffraction, give virtually the same output even though the way to obtain it differs very much. In reality, neutron diffraction and pVT method suffer from a number of shortcomings that effectively makes them complementary.

D20 in many ways is unquestionably an excellent diffractometer valued not only in standard kinetic studies but also in investigations of magnetic properties of different materials or ultra fast, stroboscopic experiments. This versatility makes D20 much desired tool, which consequently reduces available beam time per research group to at most 3 days per 6 month. To benefit from such a short time as much as possible and to cover the region where pVT method may be susceptible to experimental errors, D20 was used here to investigate only a few, several hour's long formation/decomposition processes at different p-T conditions. Some of the reactions can be completed even in so limited time frame but



runs at low temperatures and in “self-preservation” region that require at least several weeks or months are beyond given beam time and only initial stages can be recorded. In-house pVT method, which is accessible on demand, shows here its strength. Reactions may be carried out for even several months revealing the kinetics at later stages.

pVT is a suitable and by many ways easy method and certainly the only available option for long runs but it is highly susceptible, like the other volumetric methods, to temperature fluctuations (see 3.2.2). For this reason air conditioned rooms are indispensable. Another issue comes with a tightness of experimental setups, which becomes an increasing problem for several weeks or months long runs. Certainly the normalization to the hydrate fraction is the way to go around this problem but it also gives rise to a new set of issues related to the X-ray diffraction on BW5. This synchrotron installation, although not occupied as much as D20, also offers a limited beam time. A single measurement takes only about 30-60s and, consequently, most of the time is consumed by sample changes. In some cases two samples had to be loaded into one aluminum vial (Fig. 66) for higher efficiency. In comparison to neutron diffraction, synchrotron radiation illuminates very small sample volume. Only a small number of crystals is exposed to the beam leading to insufficient grain statistics and uneven intensity or even gaps in the Debye-Scherrer rings. Fairly large grains that sometimes also appear may create very intense spots on 2D images increasing the overall signal from affected planes. The problem can be partially solved by rotation of a sample around the omega axis but later, some areas must be masked (4.2.3) before integration into the final 1D histogram. The BW5 image plate, although fast in read out, inherently covers much smaller  $2\theta$  range in comparison to D20. It is still sufficient for phase fraction extraction but certain parameters like lattice constants, structural or thermal displacement parameters must be provided by other means.

Another difference between discussed techniques comes with a sample composition, or to be precise its isotopic characteristics. The pVT/X-ray technique accepts all samples but for neutron-based experiments it is strongly advised not to use isotopes with a high incoherent scattering length (Table 4) that is responsible for an elevated background noise (Staykova et al., 2003). For ices and clathrates this concerns the lightest form of hydrogen and therefore samples had to be deuterated. Although such substitution it is generally accepted it might not be necessarily identical in all aspects (e.g. cage filling in clathrates). Therefore, this matter requires further attention.

## 3.2 Custom build setups and experimental cells

The overwhelming majority of gas hydrates is not stable at ambient conditions. This obvious inconvenience can be overcome in ex-situ experiments by freezing investigated samples at the liquid N<sub>2</sub> temperature (3.1.3). In-situ reactions are much more demanding since usually elevated gas partial pressure and/or low temperatures are required. Such environment can be achieved with custom build systems. Usually the main difficulty in operating such experimental setups comes with their tightness and p-T regulation. For explosive/flammable gases like O<sub>2</sub> or CH<sub>4</sub> additional, costly safety measures are required. Adjustment to various analytical methods puts additional constraints. Neutron based techniques cause the activation of parts exposed to the beam and proper alloys must be used. Experimental cells placed in X-ray beam should interfere as little as possible with the incoming and scattered beam, which can be achieved by using very expensive, brittle and/or toxic materials like sapphire crystals or Be. These and other not mentioned restrictions call for designated custom build systems specific for different materials, types of the experiments and applied analytical methods. In the past years a number of such setups have been constructed in our group e.g. (Staykova, 2004), (Genov, 2005), (Kuhs et al., 2005) mostly designed to work at elevated pressures required for clathrates of such gases like CH<sub>4</sub>, O<sub>2</sub>, N<sub>2</sub> or Ne. The CO<sub>2</sub> clathrates case especially at the conditions relevant to Mars demands more complex approach of low and higher pressure systems or both merged in one, complex setup.

### 3.2.1 Experimental cells

The working horses of this thesis, experimental cells, have been manufactured from high strength aluminum alloy (Table 5). The experimental volume is sealed off from the surrounding by a Bridgman seal (hardened steel piston pressing on polymer/teflon rings) (Fig. 66). Chamber size, cell wall thickness and total length varies from cell to cell to meet the requirements of the different analytical methods.

Designation	Si	Fe	Cu	Mn	Mg	Cr	Zn	Ti	Other
Al 7075	0.4	0.5	1.2 - 2	0.3	2.1 - 2.9	0.18 - 0.25	5.1 - 6.1	0.2	0.05

**Table 5)** Chemical composition of the aluminum alloy used for cells and sample holders. Values are given in mass%. Aluminum makes the composition to 100%.

Neutron diffraction experiments put considerably high demand on the size, chemical composition and purity of the alloy used for cells construction (Genov, 2005). The most suitable metals for containers in neutron science are those of relatively small neutron absorption cross section like aluminum or vanadium (Table 4) allowing even for thick walled experimental pressure cells. Although capturing process is greatly reduced for given elements some atoms will be activated. Small amounts of additives present in the alloy (Table 5) will also contribute to this effect therefore their amount should be kept as low as possible. Most of the activation products of the high purity Al-alloy used for our cells dissipate usually in a few days and long term storage is not required. The iron alloy parts of the Bridgman seal contain also such elements like Mn, Zn and Cu that causes more serious problem as the half-life of the activation products is considerably longer. In order to protect this vulnerable part from being exposed a 0.5mm thick Cd plating has been mounted around the bottom part of the cell to shade this sensitive part from the incident beam (Fig. 66). Cadmium was chosen due to its extraordinarily large neutron absorption cross section, which makes it almost non transparent to the neutrons (Table 4). Aside from all above difficulties, the temperature control provided by the “orange cryostat” puts yet another very serious restriction. The overall cell size (cell + Bridgman) must be chosen so that it fits into a cryostat’s heat exchange volume. Unfortunately the last one may change from one experimental campaign to another and on-place adjustments are almost always needed. The



trade-off in the cell size affects also the Bridgman seal dimensions and consequently altered its ability to

**Fig. 66)** Experimental cells with Bridgman seals used in pVT (left most) and neutron diffraction (middle one with Cd plating) experiments. Aluminum vials (1) like the one from the right hand side were filled with a sample and inserted into the cells or mounted to the cold head on the BW5. For a few ex-situ X-ray diffraction experiments, some samples were transferred to smaller vials (2) and slipped into vials (1) with different samples.

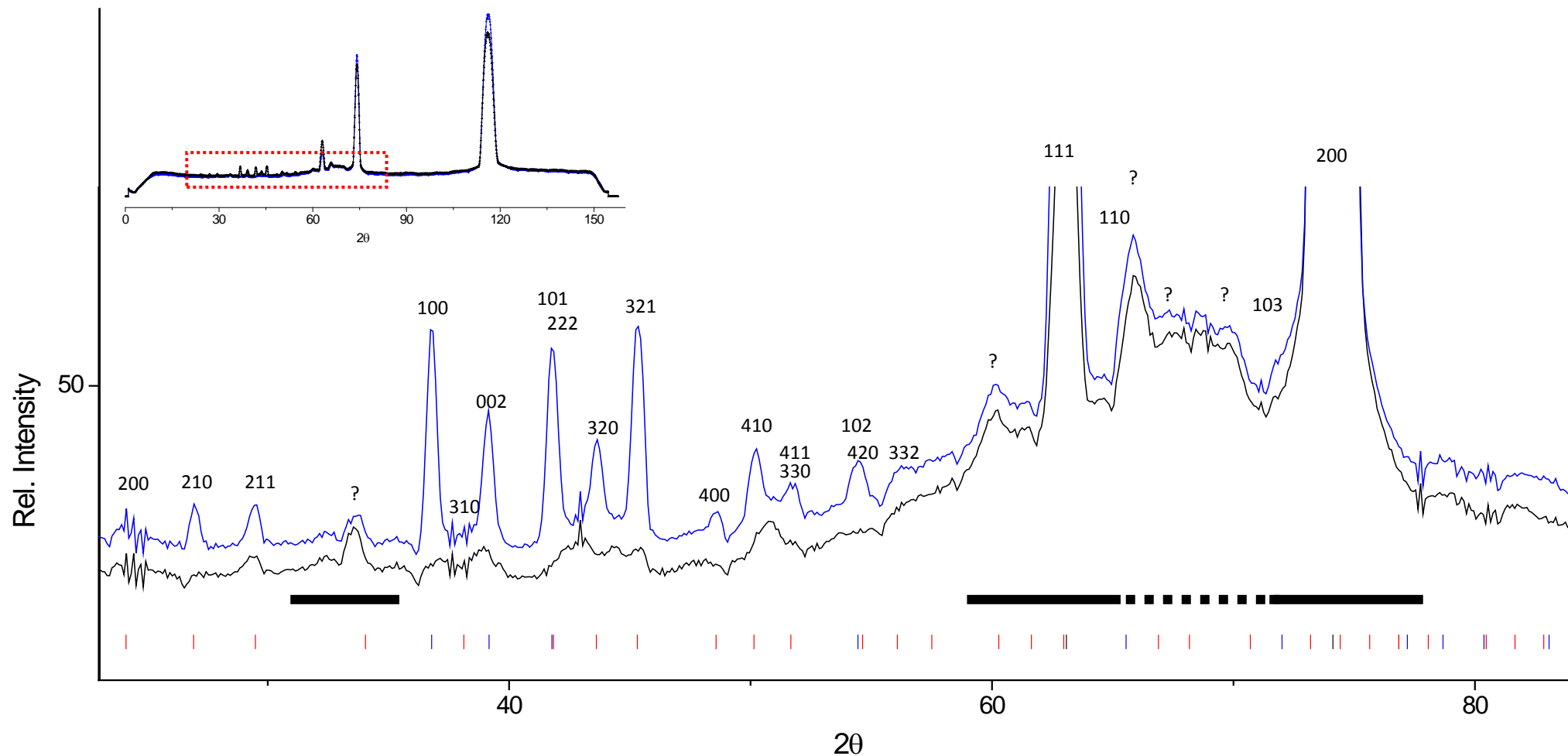


**Fig. 67)** Fragment of a diffraction pattern (full pattern in the upper left corner) from an incomplete formation experiment at 193K and 360mbar (36kPa) (in black) plotted over a pattern taken without the sample (in blue). In a several areas aluminum peaks (black tick marks) and other background features alter the peak shape of overlaying Bragg reflections from ice (blue tick marks) and clathrates (red tick marks). Higher angle data, from ~80 to 110 2θ are almost unaffected. Regions underlined with a thick black line were generally excluded from the refinement except a few cases where a background subtraction allowed treating the area between two aluminum peaks (thick black dotted line). hkl coordinates were given for identifiable reflections. Peaks marked with “?” come from unidentifiable phases.

hold targeted pressures at very low temperatures (<180K) where the Teflon seal slowly loses its elasticity. Another important factor concerning discussed experimental cells is their crystal structure and an orientation of crystals. The aluminum alloy and other cell components diffract a portion of the incident beam that is recorded along with clathrate and water ice reflections as a number of Bragg peaks and more diffused, broad features (Fig. 67). A large volume of the cell exposed to neutrons makes its contribution significant enough to hinder the refinement process. Therefore 2-theta regions where the influence of the cell is the greatest must be excluded from the treatment. Unfortunately it turned out that at least for some cells, alloy crystals show signs of preferred orientation and their contribution may change from one experiment to another one if the cell is rotated. Due to this effect it is necessary to adjust restricted areas for each run.

The pVT setups, as the least demanding, put virtually no constraints neither on the material used for construction nor the Bridgman sealing size. Larger aluminum cells equipped with a longer seal can be used. This small modification improves greatly the



**Fig. 68)** Experimental cell used to produce large volumes of clathrates for decomposition runs. Hydrate cores for powders (4.2.1) were prepared in the insert A. Consolidated samples were formed directly in the aluminum vials (insert B).

comfort of working, as well as the tightness of the system. The only limitation comes with the comparability to the cells in more constrained, neutron diffraction dedicated, system. This condition is met by keeping the sample volume constant in all above cells (Fig. 64).

Since this thesis is focusing on the decomposition experiments, large volumes of high quality CO<sub>2</sub> clathrates had to be produced beforehand. The use of small experimental cells was rather pointless due to their low efficiency. In such situation another type of cell had to be constructed (Fig. 68). Bridgman seal that serves well in previous designs for large reaction volume couldn't be used. Instead the cell is sealed by eight screws pressing a rubber o-ring. This solution makes opening and closing time considerably longer but still do not alter the quality of the obtained clathrates.



### 3.2.2 High/low pressure systems

High pressure setups used in this thesis is based on fully adjustable system of stainless steel tubing, connectors, fittings and manual valves provided by SITEC-Sieber Engineering AG. In a several cases semi-flexible high pressure cables were also used. Although all parts are designed to withstand severe pressure of at least a few kbars (a few hundreds of MPa), in all experiments and preparatory work the maximum CO<sub>2</sub> pressure has not exceeded 30bars (3MPa). Unfortunately sealant-free connections used here (Fig. 69A) are not very reliable under vacuum due to a high susceptibility to leaks.

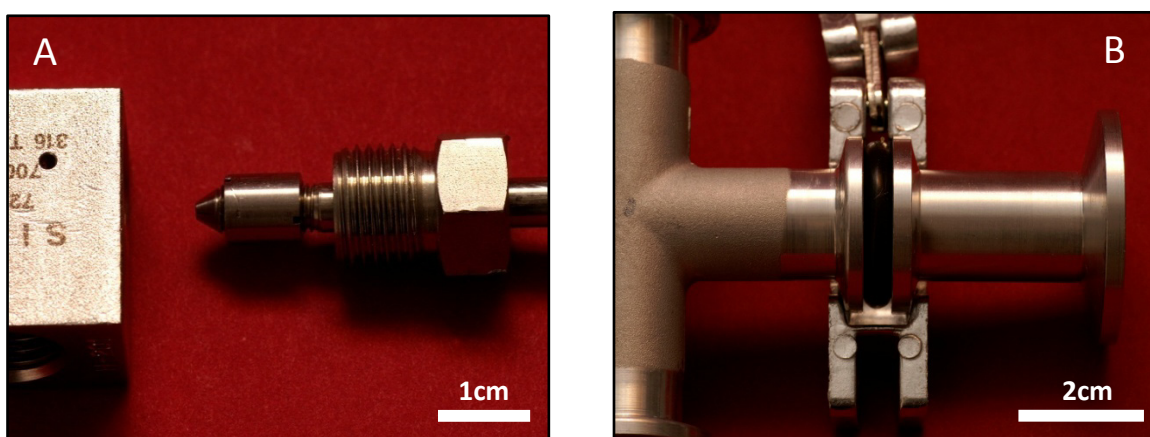


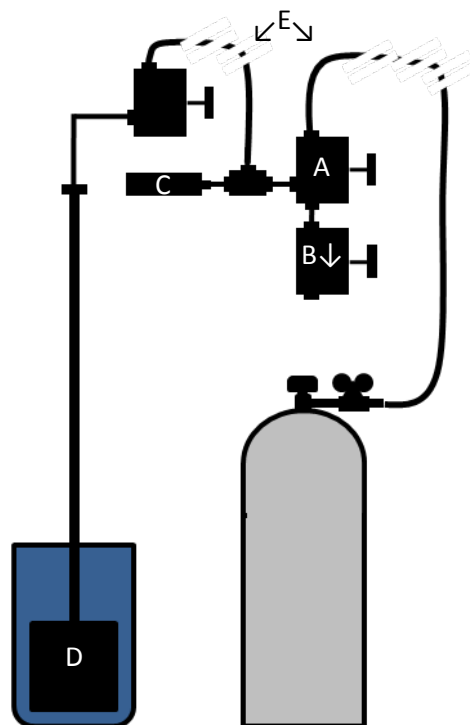
**Fig. 69)** Connections in high and low pressure systems. A) Conical, sealant free joint in the SITEC system tightened by a screw. B) Connection between the low pressure parts with a lubricated rubber o-ring in-between. Both metal pieces are held here in one half of a flange.

Low pressure setups have been constructed in ISO-K DN200 Pfeiffer Vacuum system of stainless steel/aluminum tubes, T- and crosspieces connected by flanges. Manual cut-off and precision valves were used to control the gas flow. The use of electro pneumatic valves was also attempted in one system. High tightness (vacuum down to  $10^{-11}$ bar/ $10^{-12}$ MPa) may be achieved with silicon paste lubricated rubber o-rings inserted between the pieces and tightened by the flanges (Fig. 69B). A downside of this o-ring based system is its limited reliability at elevated pressures. For the pieces used in our experimental setups the maximum given gas pressure is about 2-2.5 bar (0.2-0.25MPa).

The most basic and robust system operating under 25-30bar has been used to produce large volumes of CO<sub>2</sub> clathrates (up to a several hundreds of cm<sup>3</sup>) used later on as a

starting material (Fig. 70). The setup is composed of SITEC high pressure parts, semi-flexible high pressure cables and the large experimental cell attached to the modified experimental stick. Pressure is controlled on the ASHCROFT Pressure Reader connected to the 400bar (40MPa) ASHCROFT KXD linear gauge. Desired reaction temperature is provided by NESLAB RTE 140 cold bath filled with glycol coolant. Typical operation temperature was kept between 268 and 278K but the min reachable temperature goes down to ~233K (depending on water concentration in the liquid).

**Fig. 70)** Scheme of the experimental setup used to produce high quality H<sub>2</sub>O or D<sub>2</sub>O saturated CO<sub>2</sub> clathrates in large quantities. A) Gas inlet, B) Gas outlet/release valve, C) 400bar (40MPa) sensor, D) Large experimental cell, E) Semi flexible high pressure lines.



Neutron diffraction experiments in the range from a few mbar (Pa) to 2bar (0.2MPa) of CO<sub>2</sub> pressure have been performed in a complex setup (Fig. 71) composed of two parts. The first one, experimental stick with the sample cell, is inserted into the “orange” cryostat.

In order to avoid any unwanted CO<sub>2</sub> ice condensation and eventual blockage, the stick is equipped with heating elements that

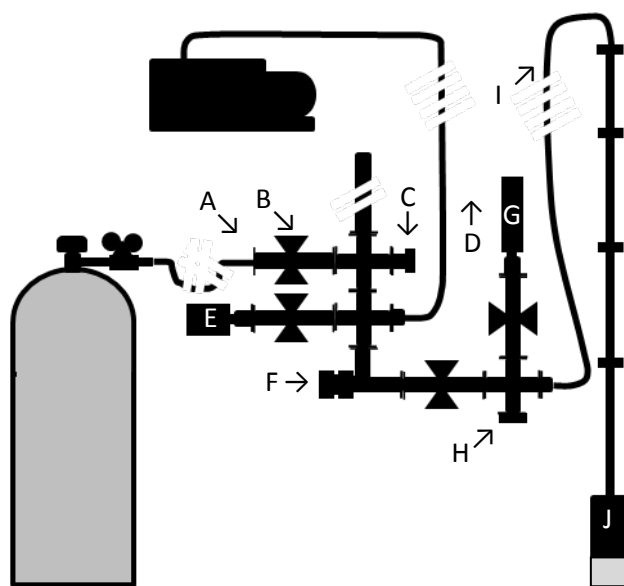


**Fig. 71)** Scheme of the low pressure experimental setup used in neutron diffraction studies. A) Gas inlet, B) Cut off valve, C) Release valve, D) Vacuum pump line, E) Pirani gauge, F) Fine dosing valve, G) 2bar (0.2MPa) Piezo gauge, H) Blind piece, I) PVC low pressure line, J) Small experimental cell with Cd shield (see Fig. 62).

shift the coldest spot to the reaction cell. Gas is transferred via a several meters long PVC line from the second part of the setup that stays behind a radiation barrier (Fig. 61B) where it can be safely operated. In frame of Pfeiffer Vacuum system tubes, a number of manual cut off valves and one Pfeiffer EVN 116 fine dosing valve provide good control on the pressure. Before each experiment the whole system was evacuated with a Pfeiffer Vacuum DUO 5 oil pump. At this stage pressure was controlled with a Pfeiffer Vacuum TPR 256 Compact Pirani Gauge operating between  $5 \times 10^{-4}$  ( $5 \times 10^{-8}$ ) and 1000mbar (0.1MPa). During each experiment another sensor has been used; Pfeiffer Vacuum APR 262 Piezo Gauge that shows linear change of pressure between 1 ( $1 \times 10^{-4}$ ) and 2000mbar (0.2MPa). In the formation experiments gas was supplied from a bottle to the system at controlled rate. In decomposition runs the situation is simpler as requires only evacuation at controlled rate by the vacuum pump.

The previously discussed setup was limited to 2bar (0.2MPa) of maximum pressure that excluded any reasonable experiments requiring clathrate stabilization and/or decomposition at higher T (above 230-240K). A new more sophisticated system merging low and high pressure parts overcome this limitation enabling higher pressure and temperature runs (Fig. 72). This approach, although not free from a number of issues like

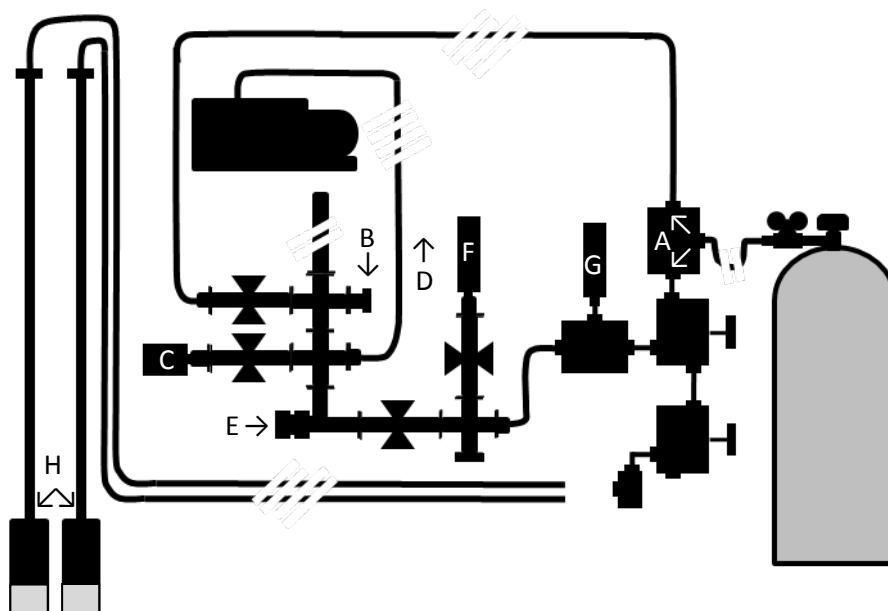
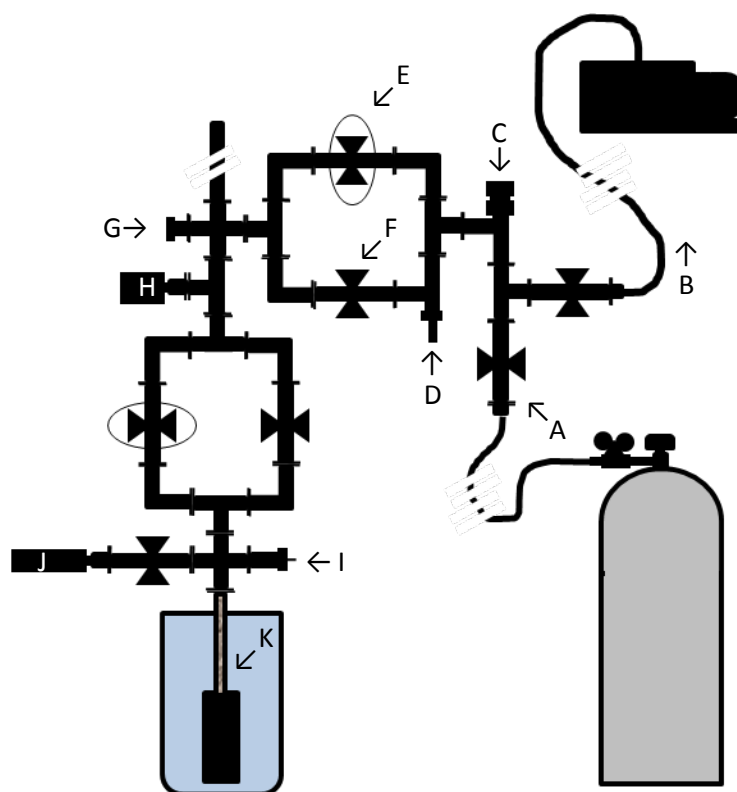


**Fig. 72)** Scheme of the low/high pressure experimental setup used in neutron diffraction studies. A) Gas inlet, B) Release valve, C) Pirani gauge, D) Vacuum pump line, E) Fine dosing valve, F) 2bar (0.2MPa) Piezo gauge, G) 60bar (6MPa) Piezo gauge, H) Experimental cell with Cd shield on high and low pressure sticks.

tightness or difficult fine pressure tuning at high pressure, serves well in neutron experiments and setup works nearly identically to the previously described design. CO<sub>2</sub> is supplied through allows for much greater flexibility than the earlier design. Low or high pressure sample stick is connected with the main system through the PVC or semi flexible pressure line depending on the experiment conditions. In low pressure formation/decomposition runs the high pressure part and semi flexible high pressure line into the already known section. Later on gas goes again through the high pressure part on the way to the stick with a sample. In decomposition runs there is virtually no difference between the systems. During experiments above 2bars (0.2MPa) the low pressure part is sealed off and pressure is controlled on RED LION pressure meter connected to 60bar (6MPa) ASHCROFT KXD linear gauge. In decomposition runs where stability of gas hydrates requires pressures higher than 2bars (0.2MPa) but target pressures are lower, both systems are applied. Prior to opening of the low pressure part, gas pressure must be quickly brought to 1bar (0.1MPa). Later on it may be safely evacuated to the required level with the vacuum pump.

pVT experiments in the range form a few mbar (Pa) to 2bar (0.2MPa) have been performed in the semi-automated setup constructed in ISO-K DN200 Pfeiffer Vacuum system (Fig. 73). Initial pressure and evacuation/refill rate is controlled with the Pfeiffer EVN 116 fine dosing valve. The system of

**Fig. 73)** Scheme of the low pressure in-house pVT experimental setup. A) Gas inlet, B) Vacuum pump line, C) Fine dosing valve, D) Adjustable volume rod insertion point, E) Electro pneumatic valve, F) Manual valve, G) Release valve 2bar, H) Pirani gauge, I) Thermocouple inlet, J) (0.2MPa) Piezo gauge, K) Tube filled with steel balls.



manual/SMC 110V-XLA-16G-M9 electro pneumatic cut off valves and adjustable volume element were meant to provide a good control on the setup at each automated evacuation/refill event. Volume between electro-pneumatic /manual valves and fine dosing valve can be adjusted by an aluminum rod inserted in to the setup. Opening and closure pressures of the electro pneumatic valves were set on a TPG 262 Pfeiffer Vacuum Dual Gauge reader. Signals between the valves and the reader are transmitted via a custom build relay box designed and manufactured by Georgi Genov. Before each experiment the setup was evacuated with the Pfeiffer Vacuum DUO 5 oil pump. Vacuum was controlled with the Pfeiffer Vacuum TPR 256 Compact Pirani Gauge connected to the first channel of the TPG 262 Pfeiffer Vacuum Dual Gauge reader. Reaction volume is divided in two parts. The lower one, experimental cell attached to the stainless steel tube, is almost completely submerged in 99% ethanol that can be cooled down to 193K with a NESLAB ULT-80 cold bath. The tube right above the cell is filled with 1mm steel balls to improve cooling rate of the introduced warm CO<sub>2</sub> that is crucial at the initial reaction stage. The other part lies above the cold bath at room temperature. Such design is very susceptible to temperature variations that appear mainly in summer time. Distortions caused by this effect, expressed as undulations in reaction curves, may be at least partially reduced with a High-Summer Correction introduced in the previous thesis (Genov, 2005). An EXTECH 421508 thermometer with a K-type thermocouple read has been used to record changes in a background temperature that later on are applied to the correction. Pressure drop/rise is registered by 2bar (0.2MPa) Pfeiffer Vacuum APR 262 Piezo Gauge connected to the second channel in the TPG 262 Pfeiffer Vacuum Dual Gauge reader. Data from the thermometer and the reader can be stored on PC through RS 232 serial interface using Windmill 5 software.

pVT experiments at higher temperatures that require more than 2bars (0.2MPa) of gas pressure for clathrate stabilization / decomposition were attempted in a setup constructed entirely from SITEC high pressure parts (Fig. 74). Like in the previous case, before each experiment the setup is evacuated. The vacuum build up is followed on the first channel of the TPG 262 Pfeiffer Vacuum Dual Gauge reader connected to the Pfeiffer Vacuum TPR 256 Compact Pirani Gauge. Initial pressure is controlled on the RED LION reader connected to the 60bar (6MPa) ASHCROFT KXD linear gauge. For target pressures that are higher than 2bars (0.2MPa) the same sensor is used to follow reactions. A set of cut off valves allows for relatively good pressure regulation. If target pressure is placed below

2bars (0.2MPa) more precise Pfeiffer VacuumAPR 262 Piezo Gauge working on the second channel of the TPG 262 Pfeiffer Vacuum Dual Gauge reader can be used. The reaction volume is much smaller than in the low pressure pVT setup. Its greater part is

submerged in the NESLAB ULT-80 cold bath filled with ethanol. The stainless steel tubing that stays at room temperature is covered with isolating foam.

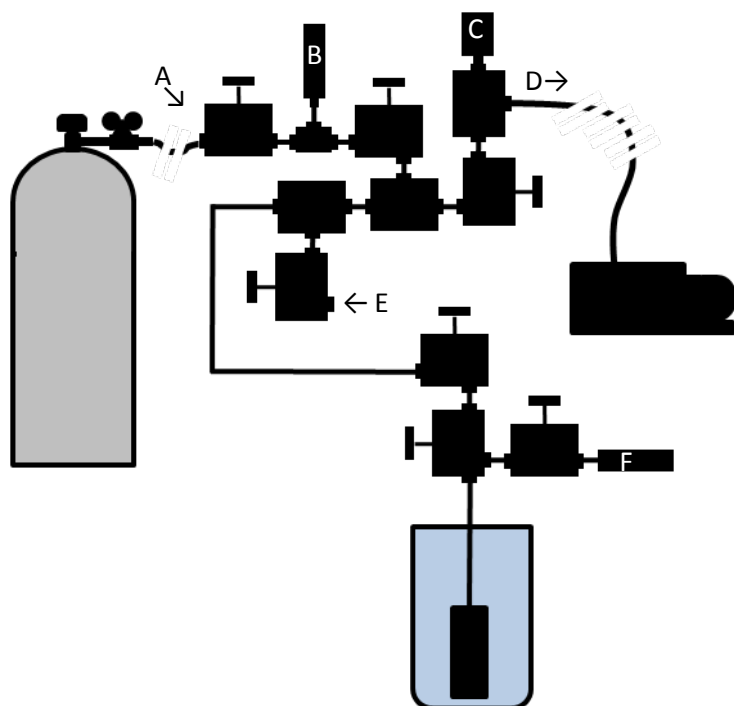


**Fig. 74)** Scheme of the higher pressure in-house pVT experimental setup. A) Gas inlet, B) 60bar (6MPa) Piezo gauge, C) Pirani gauge, D) Vacuum pump line, E) Release valve, F) 2bar (0.2MPa) Piezo gauge.

### 3.3 Scanning electron microscopy (SEM)

Diffraction and pVT methods provide generalized information on what is happening in a bulk sample during the transformation. This averaging over a volume helps to avoid eventual heterogeneities that might exist on a small scale. It is certainly useful for reactions governed by a single mechanism where reaction curves can be easily interpreted. Yet, if the situation is more complex, micro structural insight becomes indispensable to disentangle different processes that may act at the same time. Complicated kinetics that is frequently observed in the decomposition and formation reactions of the gas hydrates serves here as a good example. Scanning electron microscopy (SEM) that provides a frozen-in visualisation of investigated samples seems to be the best choice for providing missing data.

#### 3.3.1 Introduction to the electron microscopy

Electrons travelling in vacuum move in a straight line like visible light but have



much shorter wavelengths offering much higher magnification, even on an angstrom scale. Due to their magnetic momentum it is possible to model a beam shape with electrostatic and magnetic fields similarly to visible light on traditional lenses. Electron microscopy that utilises above property is presently a routine method that encompasses a large family of different modifications based on two main concepts. Transmission electron microscopy (TEM) with its high resolution option (HR-TEM) is applied to very thin, less than  $0.5\mu\text{m}$ , samples. Transmission microscopy usually requires considerably high acceleration voltage well exceeding 100kV. The other concept, scanning electron microscopy (SEM), is designed to study up to a several hundreds of nm thick upper layer of thick samples. Typical acceleration voltage in scanning microscopes stretches from  $\sim 0.2$  to 30-50kV.

The electron beam can be generated in two main ways. The first one, thermionic electron gun, is based on a sharp-tipped, hot wire or a needle (most often tungsten,  $\text{LaB}_6$  or  $\text{Ce}_6$ ) combined with an electric potential to direct and accelerate extracted electrons. At a few thousands of degrees, where electron production is the highest, a lifetime of the filament is greatly reduced. In return one obtains stable and low-noise beam. The second way, a cold field emission (FE) gun, is based on a quantum tunnelling phenomenon where electrons may lower their potential energy by moving away from atoms if very steep potential gradient is applied at the cathode surface. This can be achieved with a very large negative potential between electrodes. In this technique the filament is cold, which offers high brightness and low electron energy spread. Certain designs, like Schottky field emission gun, combine advantages both thermionic and field emission techniques allowing for high beam brightness but keeping low beam noise and high resistance to external vibrations at the same time. Since gas molecules can easily damage the cathode

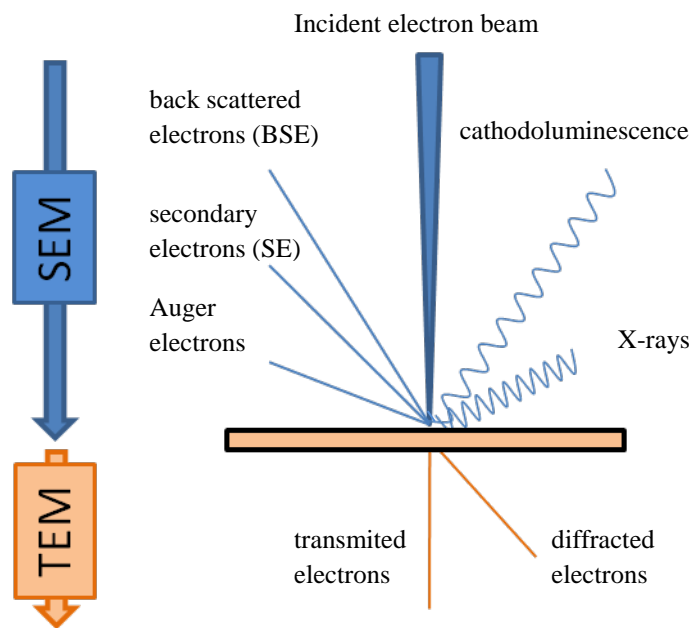


**Fig. 75)** Electron-sample interactions in the scanning and transmission microscopy.

and interfere with the beam, in all cases the source and guiding column must stay at ultra high vacuum ( $10^{-9}$  mbar,  $10^{-10}$  kPa). After extraction electrons are condensed at the negatively charged electrode and sent down toward a sample chamber. Under way, the beam is modelled by a set of electromagnetic and/or electrostatic lenses and focused at the sample.

The beam may interact with the target in a several ways (Fig. 75). Electrons colliding with a specimen's atom may be scattered  $180^\circ$  backward (BSE). Their production grows with the Z number, which is manifested on SEM images as a contrast if a difference between elements is high enough (Fig. 76A). For gas hydrates/water ice samples this effect is negligible small. Secondary electrons (SE) are ejected from the sample when incident electrons transfer some of their energy to lower electron shells (mostly K) while passing close to the atoms. Kinetic energy of liberated particles is very low  $\sim 5\text{eV}$  decreasing probing depth to a several, at most  $\sim 10\text{nm}$ . It makes them a perfect tool for studding surface microstructures (Fig. 76B). Imaging with the secondary electrons will be widely presented later in this thesis (Chapter 4). Emission of electrons from lower shells creates a vacancy that can be filled by a higher energy electron. This transition is accompanied with an emission of surplus energy in form of a photon. Its wavelength most often falls in the soft X-rays region. Energy emitted in this process is unique for each element and can be used to compositional characterisation with energy dispersive spectroscopy (EDS), or wavelength dispersive spectroscopy (WDS). Infrared, ultraviolet or visible light that can be also generated is used in a cathodoluminescence technique (CL). A fraction of released

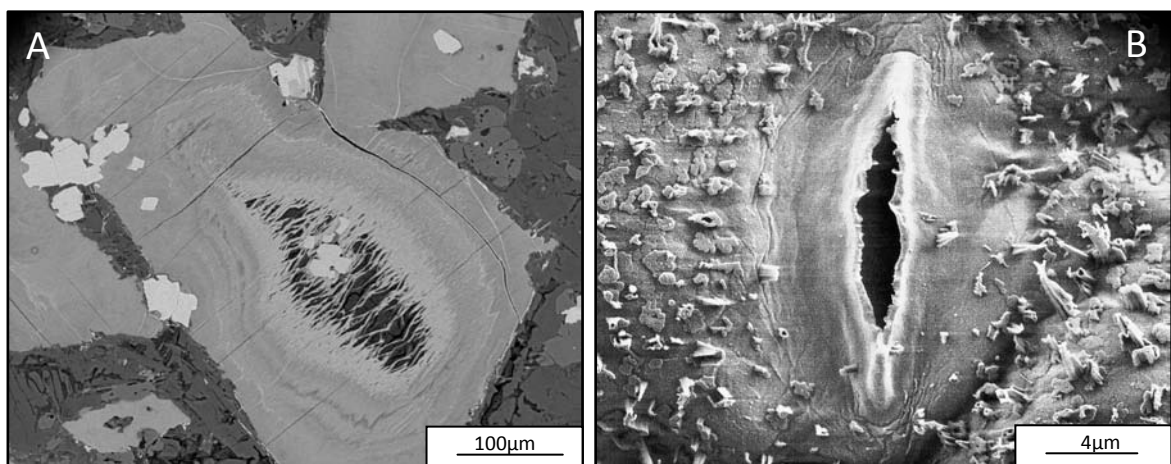


**Fig. 76** A SEM of images taken in different modes. (A) Trachite basalt thins section seen by backscattered electrons. Different mineral phases and metasomatic fronts are distinguishable due to the difference in Z-number. (B) A frozen-in image in secondary electrons of a breathing pore at a lower side of a leaf surrounded by wax nodes (© D. T. Heinrichs).

radiation can be used for outer electrons to escape. Liberated particles, Auger electrons, that are also unique for each element, can be used in compositional characterisation of the outermost specimen's layer up to 3 $\mu$ m deep. In TEM, electrons that pass through a thin sample may also undergo elastic and inelastic scattering or do not interact at all. While the first two phenomena can be used in studies of a local crystallography, the last one provides the sample thickness.

High resolution of electron microscopes is achieved by rising acceleration voltage. Scanning microscopes can reach a few nm at ~30kV. Transmission types go even to smaller, sub nm scales at 200-300kV. Although the resolving power increases, the beam becomes more and more destructive (Fig, 77A). It is well visible not only for fragile organic samples or gas hydrates but also in some cases also for some silicate minerals that are quickly etched by very fast HR-TEM electrons. Moreover, poorly conducting targets ( $R > 10^{10}\Omega$ ) like polymers, water ice or clathrates become quickly charged at higher acceleration voltages. Static electric fields that are formed at the sample deflect secondary electrons, which may distort output images (Fig. 77B). This effect may be reduced or completely eliminated by conducting coatings of Au, Pt, Pd or C but simultaneously another set of difficulties may appear (e.g. uneven coverage producing misleading surface features). Uncoated fragile samples require special approach. At relatively low acceleration voltage (~2-5kV) and high vacuum one can use standard SEM if the microscope is equipped with a cryo stage. This technique can be successfully applied for gas hydrates that do not decompose at LN<sub>2</sub> temperature even if stabilizing gas partial pressure is

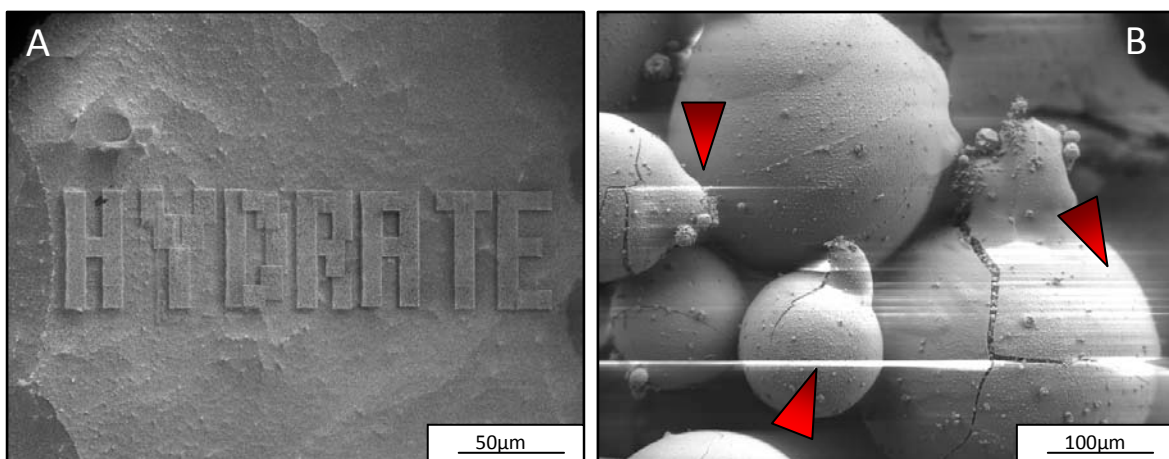


**Fig. 77)** Typical artifacts caused by an electron beam. (A) A surface of clathrate grain etched by a beam (first two letters), (B) Charging effect on an uncoated ice surface (arrows).

absent e.g.(Kuhs et al., 2000), (Kuhs et al., 2004), (Stern et al., 2004), (Bohrmann et al., 2007). Dynamic experiments like formation or decomposition of gas hydrates under limited gas/vapour pressure are also achievable but demand already specially designed for this purpose E-SEM - Environmental or Extended vacuum Scanning Electron Microscope (depending on a vendor). In this technique secondary electrons that escape from the specimen produce a new generation of electrons by hitting in gas/water vapour molecules. This cascade process amplifies the signal that is finally gathered in an in-lens detector. The maximum resolution in cryo or environmental mode may reach, in optimal conditions, about 3-10nm at 1kV but usually this value is about an order of magnitude smaller.

### 3.3.2 LEO 1530 Gemini and FEI Quanta 200 FEG

Images presented later on in this thesis (Chapter 4) were taken by two field emission scanning electron microscopes (FE- SEM), namely LEO 1530 Gemini and FEI Quanta 200 FEG equipped with Oxford Instruments EDX detectors and cryogenic systems including a preparation/transfer chamber and cryo stage, which allows for ex-situ investigations of gas hydrates. Both instruments utilize the ZrO/W (100) Schottky field emission guns which beside all advantages listed earlier, have additional zirconium oxide coating on the tungsten cathode that

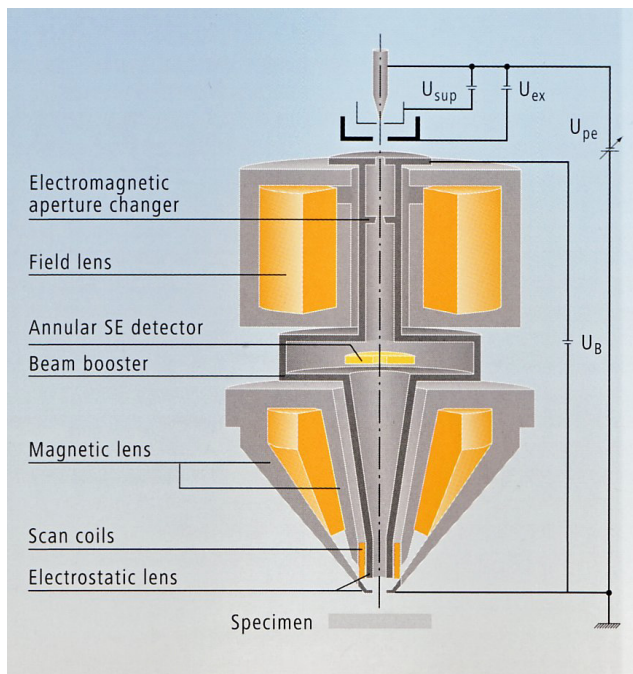


**Fig. 78)** A cross section through a SEM column based on the Gemini concept. Source: Carl Zeiss promotion brochure.

lowers ejection energy per electron. In LEO FE-SEM the beam is modeled by a set of Gemini electromagnetic and electrostatic lenses (Fig. 78). Its specific, non-crossover, construction greatly reduces stochastic interactions between electrons responsible for energy spread and consequently chromatic aberration. Additionally, a boosting element maintains electrons energy at 10kV throughout the column (Jakisch, 1996). Secondary electrons are gathered by an Everhardt-Thornley detector. Quanta

200 utilises high resolution field-emission SEM column with 45° objective lens geometry that provides results comparable to the previously described design. FEI SEM can also work under low vacuum 0.1-13mbar (10-130Pa) and in the E-SEM mode maintaining chamber pressure between 0.1 and 400mbar (10-4000Pa). Secondary electrons can be collected by three different detectors depending on the SEM mode. The classical Everhardt-Thornley detector is used only under high vacuum because of its distant position from the sample stage. This configuration has been used here for ex-situ gas hydrate/ice investigations. At low vacuum and in the environmental mode SE have to be collected close to the beam spot by a large field detector (LFD) or in-lens gaseous secondary electron detector (GSED). Unfortunately, because of details in the commissioning none of the methods could be used in this thesis.

### **3.4 Brunauer-Emmett-Teller method (BET)**

The reaction's rate during the nucleation and growth of gas hydrates/ice is very closely dependent on the available gas/sample interface (Chapter 1.5.2). The surface area (SA) generally increases with decreasing particle size but complicated, irregular grain shapes make it difficult to quantify. Several techniques may be used for this purpose but most of them suffer from large error bars. Granular materials can be approximated with regular shapes but eventual porosity, cracks or other additional surfaces are not taken into account. Similar problem appear for flat plate like materials where the surface area is estimated under an optical or electron microscope (Dominé et al. 2001). Moreover, at higher magnifications statistical errors may appear. Since the correct value of the surface area is crucial for kinetic studies and later also to constrain theoretical models, another method is necessary. Experimentally this can be achieved with gas adsorption at LN<sub>2</sub> temperature, which in spite of some limitations can measure surface areas with considerably good precision and reproducibility.

#### **3.4.1 Principles of the BET**

Volumetric Brunauer-Emmett-Teller (BET) method (Brunauer et al., 1938) is based on a physisorption phenomenon of gas molecules on solid bodies where they form a multi-layered film bounded by the Van der Waals forces. Measurements are performed at LN<sub>2</sub> temperature where the Ideal Gas Law can be applied without corrections. The adsorbed coating stays in a dynamic equilibrium with the surrounding gas and its thickness changes

with the gas pressure. At saturation pressure the number of layers is assumed to be infinite. An enthalpy of the first layer is assumed to correspond to the adsorption (heat of adsorption) while for the following layers to the liquefaction (heat of liquefaction). If exposed to low pressure/ vacuum, the adsorbed coating undergoes a gradual desorption and eventually disappears since the binding forces are relatively weak.

BET volumetric setups are divided in two known volumes. One serves as a gas reservoir (e.g. N<sub>2</sub>, CH<sub>4</sub>) here called initial volume and the other one, expansion volume, holds a specimen that is evacuated prior to an experiment. The sample is measured at LN<sub>2</sub> by opening of a valve between two volumes and registering pressure drop after the expansion. The first layer of molecules that is adsorbed at the surface corresponds to the searched SA. The process is repeated in a number of steps and new layers are formed until the saturation pressure for a given adsorbent is achieved. At the end of each experiment one obtains an adsorption isotherm that may be further analyzed.

Assuming that each gas molecule in the first layer occupies an equal area and the surface is tightly covered, the total surface area can be calculated just from the number of gas molecules. In simple cases where only one layer can be adsorbed, the result can be directly deduced from a slope of the isotherm by applying the Langmuir theory:

$$\theta = \frac{bp}{1 + bp} \quad (1)$$

$\theta$  represents here a fraction of the surface covered by adsorbed molecules,  $p$  stays for gas pressure,  $b$  is a constant assuming independence of the adsorption's enthalpy on  $\theta$ . Since  $\theta = V/V_m$ , where  $V$  is the volume of adsorbed molecules and  $V_m$  the volume needed for the total coverage, one can transform the first equation into:

$$\frac{p}{V} = \frac{p}{V_m} + \frac{b}{V_m} \quad (2)$$

The slope of the  $p/V$  as a function of pressure gives  $V_m$ , which can be used in the Ideal Gas Law to calculate the surface area of a measured sample:

$$N_{ads} = \frac{pV_m}{kT} \quad (3)$$

Here  $k$  is the Boltzman's constant,  $N_{ads}$  a number of adsorbed gas molecules and  $T$  the temperature. Multiplying  $N_{ads}$  by the surface of a single gas molecule gives the total surface area.

For clathrates and ices where more than one layer is adsorbed, Langmuir theory has



to be modified to account for this effect. It is done in the Brunauer-Emmett-Teller treatment (BET) that was shortly introduced at the beginning of this subchapter. Below, the reader will find the mathematical description of the whole procedure.

At the first step a number of moles of gas in the first volume are calculated. It will be later multiplied by the Avogadro number to get the number of adsorbed molecules  $N_{\text{ads}}$ :

$$n_1' = \frac{p_1' V_1}{RT_R} \quad (4)$$

Here  $n_1'$  is the number of moles of gas in the first increment,  $p_1'$  the introduction pressure in the initial volume  $V_1$ .  $R$  is the ideal gas constant and  $T_R$  room temperature. To reduce the deviation from the Ideal Gas Law  $p_1'$  must be kept small while  $V_1$  large. By opening the valve between the two volumes, pressure drops due to gas expansion and adsorption. The number of moles that remains in a gas phase  $n_1''$  is calculated as follows:

$$n_1'' = \frac{p_1'' (V_1 + V_{\text{ER}})}{RT_R} + \frac{p_1'' V_{\text{EL}}}{RT_L} \quad (5)$$

$p_1''$  is the pressure after the expansion. The sum  $V_1 + V_{\text{ER}}$  corresponds to the initial volume and the expansion volume that stays at room temperature.  $V_{\text{EL}}$  is the expansion volume kept under LN<sub>2</sub> temperature  $T_L$ . Since the number of moles adsorbed at the first increment  $n_{1 \text{ ads}}$  is a simple difference between  $n_1'$  and  $n_1''$  then:

$$n_{1 \text{ ads}} = (p_1' - p_1'') \frac{V_1}{RT_R} - p_1'' \left( \frac{V_{\text{ER}}}{RT_R} + \frac{V_{\text{EL}}}{RT_L} \right) \quad (6)$$

In the next increment one expands a portion of gas to the second part of the system that already contains a part of gas molecules from the first step. In such situation the number of adsorbed molecules after the second expansion is:

$$n_{2 \text{ ads}} = n_2' + n_{1 \text{ EV}}'' - n_2'' \quad (7)$$

The new expression  $n_{1 \text{ EV}}''$  describes a number of molecules that stayed in the second, expansion volume after the first increment. Following increments continue to build up the adsorbed film:

$$n_{n \text{ ads}} = \sum_{i=1}^n (p_i' - p_i'') \frac{V_i}{RT_R} + (p_n'' - p_1'') \left( \frac{V_{\text{ER}}}{RT_R} + \frac{V_{\text{EL}}}{RT_L} \right) \quad (8)$$

The equations presented above suffer from one serious misconception, namely two volumes at radically different temperatures are separated by a sharp boundary. Such situation in nature is highly unrealistic and a thermal gradient between them must be taken into consideration. For simplicity it will be described by a linear dependence that affects a

transition volume  $V_{ET}$  distinguished from the  $V_{ER}$ . Introducing a correction into (8) one obtains:

$$n_{n \text{ ads}} = \sum_{i=n}^n (p'_i - p''_i) \frac{V_i}{RT_R} - (p''_h - p''_i) \left( \frac{V_{ER}}{RT_R} + \frac{V_{ET} \ln \frac{T_R}{T_L}}{R(T_R - T_L)} + \frac{V_{EL}}{RT_L} \right) \quad (9)$$

The total number of adsorbed molecule after each increment is obtained by multiplying (9) with the Avogadro number  $A$  as it was already mentioned before. So calculated  $N_{\text{ads}}$  and consequently  $SA$  are essentially unique for every sample even for the same material, which needlessly to say is experimentally very inconvenient. This issue is eliminated by defining the number of molecules per mass unit called a specific surface area ( $SSA$ ). In the equation below  $N_{\text{ads}}$  is defined for a mass unit at each increment:

$$N_{n \text{ ads}} = \frac{\left[ \sum_{i=1}^n (p'_i - p''_i) \frac{V_i}{RT_R} - (p''_h - p''_i) \left( \frac{V_{ER}}{RT_R} + \frac{V_{ET} \ln \frac{T_R}{T_L}}{R(T_R - T_L)} + \frac{V_{EL}}{RT_L} \right) \right] A}{m} \quad (10)$$

After retrieving the number of adsorbed molecules at each increment, a next step will be to calculate how many gas molecules belong to the first layer that corresponds to the searched  $SSA$ . It is done using BET transform  $Y$  that is defined as:

$$Y_i = \frac{p''_i}{p_0 N_{n \text{ ads}} \left( 1 - \frac{p''_i}{p_0} \right)} \quad (11)$$

$p_0$  corresponds here to the saturation vapor pressure of an adsorbent at  $LN_2$ . Taking  $Y$  at each increment and plotting it against  $p''_i/p_0$  gives a BET transform isotherm that is used in a fitting procedure (Fig. 79). The isotherm is generally a curve with a linear part between 0.07-0.22 (Legagneux et al., 2002).

$$Y = S \frac{p''}{p_0} + I \quad (12)$$

$S$ , which is a slope of the function and an interception point  $I$  are used later to calculate the number of gas molecules  $N_m$  in the first layer:

$$N_m = \frac{1}{(S + I)} \quad (13)$$

Finally the  $SSA$  is obtained as follows:

$$SSA = N_m SA_{\text{gas}} \quad (14)$$

The  $N_m$  value and consequently  $SSA$  are prone to a number of experimental and systematic

errors (see 3.4.2) and the credibility of the measurements must be checked by calculating the mean heat of adsorption  $\Delta Q$ :

$$\Delta Q_{\text{gas}} = T_L R \ln \frac{(S + I)}{I} \quad (15)$$

The logarithm exponent in the equation (15) is often referred as a BET constant C.

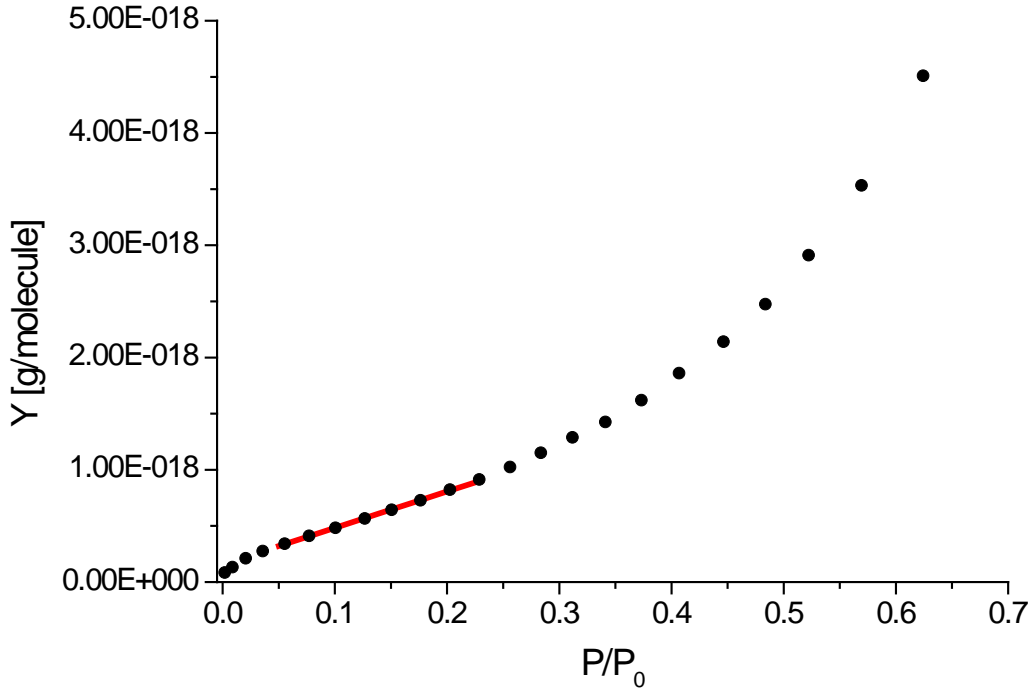


**Fig. 79)** BET isotherm recorded for the ice spheres (4.1.1) fitted in its linear part between 0.07-0.22. Slope of the trend line and the (S) intersection point with the Y axis (I) are used later in the SSA calculations.

### 3.4.2 In-house BET setup

Clathrates and ices are very difficult materials to study by BET. In order to protect hydrates from decomposition, samples must be kept at LN<sub>2</sub> from the moment of loading through the evacuation to the final measurement. The same procedure should be applied to ices where the surface area may still evolve if temperature is too high (Legagneux et al., 2002). Although commercial BET setups offer an easy way to measure SSA of a wide range of samples, the above condition is not met. For this reason, a custom build BET system has been constructed (Fig. 80) using high and low pressure parts described previously (3.2.2).

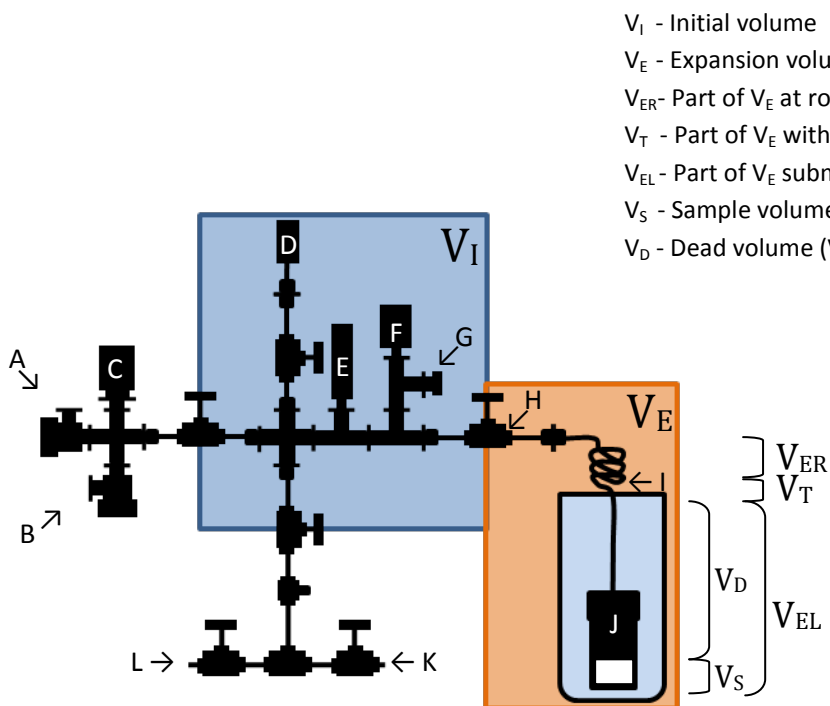


**Fig. 80)** Scheme of the in-house BET setup. A) Oil vacuum pump inlet, B) Turbo molecular pump inlet, C) Compact full range gauge, D) Compact capacitance gauge, E) 10bar (1MPa) Piezo gauge, F) Pirani gauge, G) Release valve, H) Valve between two volumes, I) Heating band, J) Experimental cell submerged in the Dewar, K) He inlet, L)  $CH_4$  inlet.

An experimental cell is attached to the system by a screw connector with a gasket ring in between. Vacuum is achieved by a preliminary evacuation with the Pfeiffer Vacuum DUO 5 oil pump to  $10^{-3}$ mbar ( $10^{-4}$ kPa) and later with a Pfeiffer Vacuum TMH 071P turbo molecular pump to  $\sim 10^{-5}$ mbar ( $10^{-6}$ kPa) where it is left for  $\sim 30$ min. Vacuum build up is followed on a Pfeiffer Vacuum Compact Full Range Gauge connected to the first channel of the TPG 262 pressure reader. For technical reasons discussed later the first set of sensors can be checked by the back-up pair. The initial and expansion volumes have been measured at room temperature with 10mbar (1kPa) of He gas that adsorb neither to the tubing nor to the eventual sample. Pressure drop has been recorded through the second channel of the TPG 262 with a Pfeiffer Vacuum Compact Capacitance Gauge operating in the range between  $10^{-3}$  and 10mbar ( $10^{-4}$  -1kPa). This approach essentially does not yield searched volumes unless a third, known volume is introduced. This is done using two empty experimental cells where the first one is twice larger than the second one. The volume difference can be very easily calculated and inserted into the set of two Ideal Gas Law equations with two unknowns. Consequently searched volumes have been established

on:  $V_I = 202.52\text{cm}^3$  and  $V_E = 194.54 / 258.16\text{cm}^3$  for the small and large cell respectively. A volume ratio of 1.04 for the system with the small cell and 0.78 with the large cell falls within the experimentally established frames for BET setups (0.5-2) (Legagneux et al., 2002). During surface area measurements the expansion volume is divided according to the temperature regimes in three sections (3.4.1). That must be known for data treatment. Unfortunately the construction of the setup does not allow for separation of each volume and they had to be calculated from their geometry:  $V_{ER} = 69.92\text{cm}^3$ ,  $V_{ET} = 15.28\text{cm}^3$ ,  $V_{EL} = 109.34 / 172.96\text{cm}^3$  (Fig. 80).

A sample loaded in the setup decreases the expansion volume, which has to be measured again by expanding  $\sim 10\text{mbar}$  (1kPa) of He gas. The procedure is repeated 3-4 times to account for better statistics. A sample volume  $V_S$  (Fig. 80), calculated from the difference is subtracted from the previously calculated  $V_{EL}$  giving a new volume submerged in  $\text{LN}_2$ . The result, a dead volume,  $V_D$  is inserted into (9). The system is again evacuated until a high vacuum in both volumes is established. At this point the valve between  $V_I$  and  $V_E$  is closed. The first volume is filled with a small portion of  $\text{CH}_4$  that serves here as an adsorbent. Consequently the valve between the volumes is reopened and the pressure drops due to the expansion and adsorption. The valve is closed again and another portion of gas is added to the initial volume. It was found to be sufficient to progress initially with a step of 0.3mbar (0.03kPa) until  $p'$  reaches about 5mbar (0.5kPa). At this point the adsorption curve should be already in its non linear part and the step can be increased to 0.5-1mbar (0.05-0.1kPa). The procedure is repeated until the  $p''$  approaches to the methane vapor saturation pressure  $p_0$  at  $\text{LN}_2$ , which has been established on 12.94mbar (1.294kPa) (Legagneux et al., 2002). So obtained adsorption isotherm (Fig. 79) may be further processed with the BET treatment. The final SSA is calculated from  $N_m$  multiplied by an area for a single  $\text{CH}_4$  molecule that was established on  $19.17 \times 10^{-20}\text{m}^2$  (Chaix et al., 1996). A precision of the measurement is controlled by a comparison of the experimentally calculated  $\Delta Q_{\text{CH}_4}$  to a published value of  $2240 \pm 100\text{ J/mol}$  (Domine et al. 2000).

The principles and the construction of a BET setup are fairly simple but from the technical point of view it is one of the most troublesome and tedious method from all presented here. The construction of the system used here inherited all the vacuum issues discussed previously (3.2.2). Aside from a number of small leakages coming from connections the biggest problems were found with a proper sealing of the experimental cell

submerged in LN<sub>2</sub>. The initially used Teflon ring gaskets were letting nitrogen gas into the system on random occasions spoiling the results. The situation has been greatly improved with a change to pure copper rings but the cell must be sealed before the gasket becomes too hard due to cooling. Another issue comes with pressure measurements. The Capacitance Gauge used for measurements is calibrated with the Compact Full Range Gauge, which is prone to misleading readings if not serviced regularly. The second set of sensors helps to detect a problem but cannot supplement the faulty one since the range they cover is not the same. The final results may be also affected by a non constant room temperature or changes of a LN<sub>2</sub> level in the Dewar during measurements. Although, both effects cannot be fully avoided, air conditioning with regular and frequent refills diminishes their impact to negligible levels.

### **3.5 Excess fugacity – driving force**

A fugacity of CO<sub>2</sub> or to be more precise its excess is one of the major components that influence observed reaction speed. Unfortunately derived fugacity/pressure ratios from a standard EOS equation (Angus et al., 1976) of CO<sub>2</sub> gas are limited rather to higher temperatures starting from 220K (10K step) with rather large pressure steps (5kPa for 10-100kPa, 50kPa for 100-1000kPa, 500kPa for 0.1-1MPa) (Fig. 81). To establish fugacity and finally driving force for the experiments emulating conditions relevant to Mars existing isobaric-isothermal data were fitted with a build-in Origin 6 Weibull2 function modified for this purpose. This approach proved to be quite reliable from almost vacuum conditions to about 2bars (0.2MPa). At the pressure of 6mbar (0.6kPa) the fugacity is assumed to be the same. A convenience of the fitting lays in its ability to plot fugacity/pressure ratios for intermediate pressure steps in a desired temperature region, but one has to keep in mind that calculated values below 220K are not confronted against experimental data and some divergence may occur. At higher pressures, the Weibull2 function is not very reliable in the region of interest (240-270K) and in order to avoid fitting errors in 2-10bars (0.2-1MPa) pressure region, values were retrieved with help of tabulated data (Angus et al., 1976).

The driving force used in this thesis has been empirically established in the previous studies at low pressures (Salamatin and Kuhs, 2002), (Staykova et al., 2003), (Genov et al., 2004). It is defined as a natural logarithm of ( $f/f_d$ ) where  $f$  corresponds to the fugacity during the experiment and  $f_d$  to the one at the stability boundary.



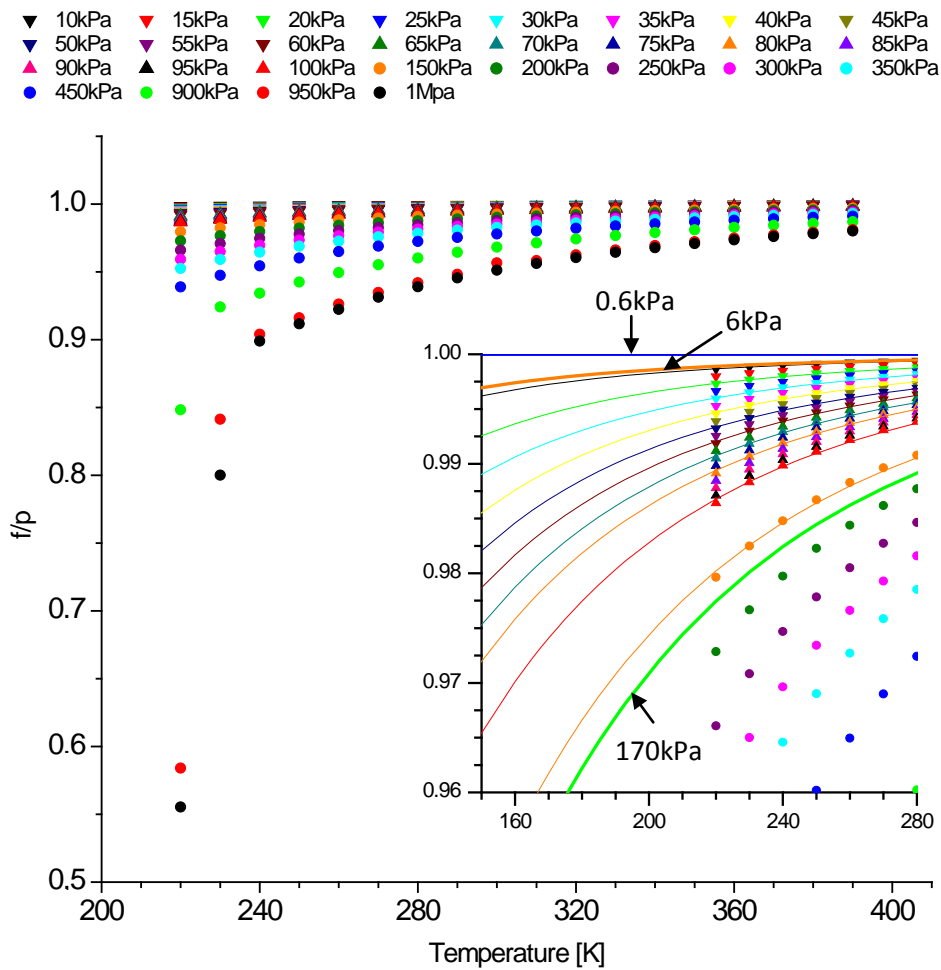


**Fig. 81)** Fugacity/ pressure ratio as a function of temperature (Angus et al., 1976). In the blow up chosen data are extended to lower temperatures through the fitting. Thick blue, orange and green curves (see arrows) are calculated for 0.6kPa, 6kPa and 170kPa, respectively.

### 3.6 Clathrate formation - Powder 4 model

“Powder 4” model presented below has been created in a group led by Prof. A. N. Salamatina<sup>1</sup> at the Kazan State University, Russia in cooperation with our department. It is still under development but can be already applied for mono dispersed spherical powders with a radius of a few  $\mu$  (frost). Ice spheres with a larger diameter can be also treated only in the initial part maximally up to 30-40 wt% where the reaction rate starts to be strongly dependent on a sample’s geometry. The treatment of the later part of the diffusion controlled transformation as well as polydispersivity is not yet implemented. Mathematical

<sup>1</sup> Department of Applied Mathematics, Kazan State University, Kazan 420008, Russia.

description of the transformation process is a synergy of already published phenomenological models (Salamatin and Kuhs, 2002), (Staykova et al., 2003), (Genov et al., 2004) and Johnson-Mehl-Avrami-Kolmogorv-Ginstling-Brounshtein concept (Genov, 2005). For details the reader may look into the previous PhD thesis (Genov, 2005) where both approaches were critically discussed.

### 3.6.1 Theoretical background

Powder 4 utilizes information on the nucleation and growth acquires during the latest interrupted runs (4.1.2). Previously considered case of the crack filling is still preserved if one feels a need to apply it. New data suggest that the initial surface coverage is in no longer limited by a nucleation rate but depends on a lateral growth of the clathrate film. Mathematically it is expressed with Johnson-Mehl-Avrami-Kolmogorv (JMAK) model that is modified for the spherical geometry. To account for observed heterogeneity of the nucleation (4.1.2) it is necessary to introduce a time dependent expression  $N_0 t^{\sigma-1}$  defining nucleation rate constant  $N_0$  at a moment  $\tau$  and a phenomenological exponent  $\sigma$  that ranges from 0 to 1 for instantaneous and uniform nucleation respectively. Consequently the nucleation rate  $\dot{N}$  per unit area of free ice surface is:

$$\dot{N} = N_0 \tau^{\sigma-1}$$

For an infinite 2D nucleation domain a single nucleus will increase its radius  $l$  from the moment of formation  $\tau$  to a moment  $t$  as follows:

$$l = 2G(t - \tau)^{\frac{m}{2}}$$

A new term  $G$  stands here for a nuclei growth rate constant. Parameter  $m$  is an empirical exponent that is related to a dimensionality of the growth varying between 1 and 3. Since in reality the growth seldom follows only one type (e.g.  $m=2$  for 2D), it is allowed to use real numbers (e.g.  $m=2.3$  for a mixed 2D/3D growth), (4.2.4). Modification introduced in Powder 4 limits above domain to the surface of a spherical particle:

$$S(t - \tau) = 4\pi \min\{r_{i0}^2, G^2(t - \tau)^m\}$$

The limitation of the nucleation domain causes the nucleation rate  $\dot{N}$  after a period of  $d\tau$  to be actually smaller since the available area of free ice decreases with time. In order to account for that, authors introduce a “phantom nuclei”  $\alpha_S \dot{N} d\tau$  which would have been created if the surface was free. This in turn leads to a fraction  $A_{ex}$  of the ice surface  $S$  that would have been coated by fictitious nuclei at a time  $t$ :

$$A_{ex} = \int_0^t S(t-\tau)\dot{N}(\tau)dt = 4\pi N_0 \int_0^t \min\{r_{i0}^2, G^2(t-\tau)^m\} \tau^{\sigma-1} dt$$

By definition a differential of  $A_{ex}$  is:

$$dA_{ex} = \frac{d\alpha_S}{1-\alpha_S} \equiv \Omega_S dt$$

A new terms  $\alpha_S$  and  $\Omega_S$  describe here a surface fraction coated by a new phase and rate of coating respectively. The rate of surface coating at a moment  $\tau$  will be then:

$$A_{ex} = \ln \frac{1}{1-\alpha_S} = \int_0^t \Omega_S(\tau) d\tau$$

The last part of the expression can be implemented into the exponent of the JMAK general equation as follows:

$$\alpha_S = 1 - e^{-\int_0^t \Omega_S(\tau) d\tau}$$

Refined JMAK approach gives the following parameterization:

$$\int_0^t \Omega_S(\tau) d\tau = \begin{cases} \varpi_s \int_0^t \left(\frac{\tau}{t_0}\right)^m (t-\tau)^{\sigma-1} d\tau, & t < t_0 \\ \varpi_s \int_0^{t_0} \left(\frac{\tau}{t_0}\right)^m (t-\tau)^{\sigma-1} d\tau + \frac{\varpi_s}{\sigma} (t-t_0)^\sigma, & t > t_0 \end{cases}$$

The rate of coating  $\Omega_S$  is here presented using a nucleation limited rate of hydrate formation  $\varpi_s = 4\pi r_{i0}^2 N_0$  for two different regimes defined by a typical time of the sphere coverage  $t_0 = \left(\frac{r_{i0}}{G}\right)^{\frac{2}{m}}$ . The first case,  $t < t_0$ , discusses a variant of a predominant nucleation in cracks, which presently seems to be not a valid scenario. The other one considers mentioned earlier case of a reaction where the initial surface coverage is in no longer limited by the nucleation rate but depends on the lateral growth of the clathrate film.

An expansion of the initial film into an ice particle generally follows a shrinking core concept introduced in previous phenomenological models e.g. (Salamatin and Kuhs, 2002). Knowing that clathrates have somewhat lower density (ignoring gas molecules in the structure) then a thickness of the initial hydrate film  $d_0$  can be written in the following form:

$$d_0 = \delta_0(1 + E)$$

$\delta_0$  describes a thickness of the ice layer converted during the initial mantling process.  $E$  is

a hydrate phase expansion coefficient defined as a ratio between the mole density of ice  $\rho_i$  and empty clathrate structure  $\rho_{kw}$  corrected for observed sub- $\mu$  porosity  $\varepsilon_h$  (see: 4.2.2):

$$E = \frac{\rho_i}{\rho_{kw}(1 - \varepsilon_h)}$$

The ice core radius after the initial coating  $\Delta(t)$  will undergo gradual consumption during the formation process. Sharp clathrate/ice interface will move toward the cores' center:

$$\frac{d\Delta}{dt} = -\frac{\omega_V}{\rho_i r_{i0}(1 + v_0^2)}, \Delta \geq 0$$

A new parameter  $\omega_V$  describes a number of ice moles transformed to clathrate in a unit of time and ice surface under the initial coating. Consequently ice radius is:

$$\Delta|_{t=0} = 1 - \frac{\delta_0}{r_{i0}(1 + v_0^2)}$$

The decrease of the ice core' radius in the period of time  $(t - \tau)$  leads to a fraction of clathrates in this increment:

$$d\alpha = [1 - \Delta^3(t - \tau)]d\alpha_S$$

$d\alpha_S$  defines here the fraction of a surface covered in the discussed time period. After integration over time one obtains the reaction degree  $\alpha$  in a time interval  $d\tau$ :

$$\alpha = \int_0^t [1 - \Delta^3(t - \tau)]d\alpha_S(\tau)$$

The typical time for coating  $t_0$  and the rates of the surface coating  $\omega_V$  as well as of the volume transformation  $\omega_V$  are related to a driving force defined as a supersaturation of the system in gas  $\ln \frac{f}{f_d}$  using fugacities  $f$  for the reaction pressure and  $f_d$  for decomposition pressure:

$$t_0 = \left( \frac{k_G}{r_{i0}} \ln \frac{f}{f_d} \right)^{-\frac{2}{m}}, \quad \omega_S = 4\pi r_{i0}^2 k_N \ln \frac{f}{f_d}, \quad \omega_V = \frac{k_R k_D}{k_R + k_D} \ln \frac{f}{f_d}$$

A set of new parameters:  $k_G$ ,  $k_N$ ,  $k_R$  are empirical constants used to tune the model. The  $k_D$  permeation constant is related to the gas/water transport through the hydrate shell. Since this process is tightly related to the geometry and packing of ice it must be also included in the model. The description of starting spheres follows published consideration (Staykova et al., 2003) on a random dense packing of monodispersed spheres. Generally each ice particle is represented as a truncated sphere of a radius  $r_h$  initially equal to  $r_{i0}$  that is surrounded by other particles. A number of contact, the coordination number  $Z$  can be expressed as a linear function of a relative hydrate shell radius  $R_h = \frac{r_h}{r_{i0}}$ :

$$Z = Z_0 + C(R_h - 1)$$

$Z_0$  and  $C$  are empirical values of the initial coordination number and the slope of the random density function respectively. For ice powders  $Z_0 \sim 7$  and  $C \sim 15.5$ . The specific surface of the starting material can be obtained experimentally (3.4) or through following equation:

$$S_{i0} = \frac{3}{r_{i0}\rho_i(1 + v_0^2)}$$

During the formation ice core radius  $r_{i0}$  decreases but the overall  $r_h$  in fact increases due to lesser density of clathrates. The normalized volume of the transforming particle is related to the reaction degree  $\alpha$  through a relative radius of the ice-hydrate interface  $R_i$ :

$$R_h^3 - \frac{Z_0}{4}(R_h - 1)^2(2R_h + 1) - \frac{C}{16}(R_h - 1)^3(3R_h + 1) = 1 + E(1 - R_i^3)$$

The fraction of the hydrate surface  $s$  in contact with gas is:

$$s = 1 - \frac{Z_0}{2} \frac{R_h - 1}{R_h} - \frac{C}{4} \frac{(R_h - 1)^2}{R_h}$$

Growing spheres improve contacts with surrounding particles and form new ones decreasing the porosity  $\varepsilon_m$  and total surface area of empty voids  $S_m$ :

$$\varepsilon_m = \varepsilon_{m0} - \alpha(1 - \varepsilon_{m0})E, \quad S_m = (1 - \alpha_S + \alpha_S R_h^2 s) S_{i0}$$

The normalized distance  $R$  from the center of an ice particle to an averaged contact plane is:

$$R = R_h \left[ 1 - \frac{2(1 - s)}{Z} \right]$$

Finally the permeation constant  $k_D$  is calculated as follows:

$$k_D = \frac{\rho_i D}{r_{i0}} \frac{\sqrt{s} R_h R}{\Delta [\sqrt{s} R_h (R - \Delta) + \Delta (R_h - R)]}$$

$D$  is the apparent gas/water mass transfer coefficient that changes with temperature. All four constants ( $k_G, k_N, k_R, k_D$ ) are assumed to be Arrhenius-type functions of temperature:

$$k_J = k_J^* e^{\left[ \frac{Q_J}{R_g} \left( \frac{1}{T_*} - \frac{1}{T} \right) \right]}, J = G, N, R, D$$

Again  $k_J$  and well as  $Q_J$  are constants at the reference temperature  $T_*$  and the activation energy of the J-type step of the hydrate formation. The gas constant is denoted here as  $R_g$ .

### 3.6.2 Formation from frost - “Frost” module

Frost particles create a special case of the general model described above, since a major volume of a few  $\mu\text{m}$  size ice is transformed already at the initial coating stage. Limited reaction volume sets the maximum size of a single nucleus to the  $\frac{4}{3}\pi r_{i0}^3$  and its evolution from the moment  $\tau$  to  $t$  can be written as:

$$V(t - \tau) = \frac{4}{3}\pi \min\{r_{i0}^3, G^3(t - \tau)^m\}$$

Defining the nucleation domain as a volume changes also the expression of the nucleation rate  $\dot{N}$ :

$$\dot{N} = 3 \frac{N_0 t^{\sigma-1}}{r_{i0}}$$

Consequently the general JMAK equation is also redefined:

$$\alpha = 1 - e\left(-\int_0^t \Omega_V(\tau) d\tau\right)$$

Similarly to the previous definition of  $\Omega_S$  a new term  $\Omega_V$  describes the rate of clathrate formation as a volume fraction of non reacted ice changed to hydrate in a time unit.

Refined JMAK approach gives:

$$\int_0^t \Omega_V(\tau) d\tau = \begin{cases} \bar{\omega}_s \int_0^t \left(\frac{\tau}{t_0}\right)^m (t - \tau)^{\sigma-1} d\tau, t < t_0 \\ \bar{\omega}_s \int_0^{t_0} \left(\frac{\tau}{t_0}\right)^m (t - \tau)^{\sigma-1} d\tau + \frac{\bar{\omega}_s}{\sigma} (t - t_0)^\sigma, t > t_0 \end{cases}$$

The only difference between the general theory in this case appear here in  $t_0 = \left(\frac{r_{i0}}{G}\right)^{\frac{3}{m}}$

The driving force and activation energy is calculated as previously.





# Chapter 4 – CO<sub>2</sub> hydrates: kinetics of formation and decomposition at Martian conditions

In this chapter the reader will find a detailed description of each group of experiments performed in frame of this thesis. The focus is placed on a number of previously unknown or poorly investigated processes that affect an overall kinetics of growing or decomposing clathrates seen on the reaction curves. The influence of each of them will be assessed with the help of experimental techniques from chapter 3 and theoretical models.

## 4.1 Excess fugacity

The excess fugacity, as it was already shortly discussed (1.5.1), reflects a tendency of a system to change from less stable thermodynamic state to more preferable one. A driving force defined in this way in case of discussed clathrates may have a positive or negative sign (Fig. 82). Values greater than zero describe a situation where the system is supersaturated in gas molecules and hydrates are likely to form if water or water ice is available. The driving force may be increased by adding gas to the system thus accelerating

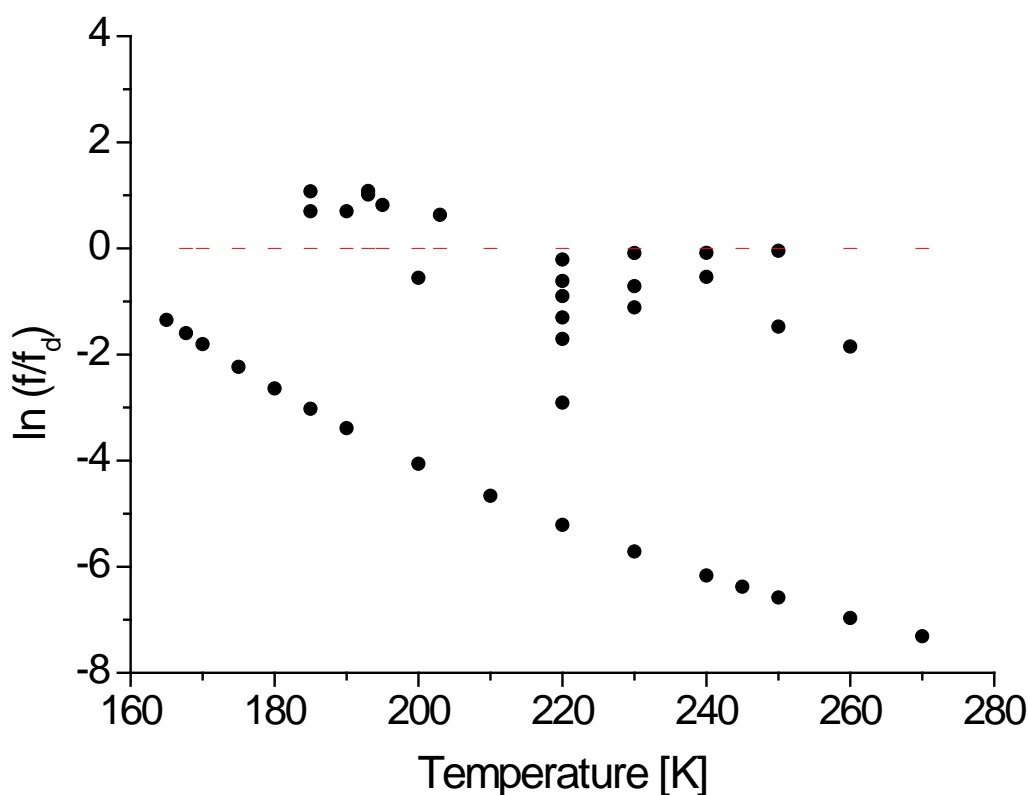


**Fig. 82)** Excess fugacity calculated for all successful runs presented in this thesis. Red dashed line divides decomposition and formation experiments (see Table 6, 8 for more details).

the transformation rate. Negative values of the excess fugacity indicate a lower chemical potential of CO<sub>2</sub> in the gas phase than in clathrates; consequently leading to the decomposition. While a driving force of the formation process may be increased rather freely as long as the p-T conditions remain in the stability field, negative excess fugacity reaches the limit at the theoretical perfect vacuum. An influence of the driving force or to be precise its size will be more broadly discussed in following subchapters.

## 4.2 Formation

The formation process for CO<sub>2</sub> but also for CH<sub>4</sub> hydrates, especially at higher temperatures, has been already well explored with the experimental techniques (see 1.5.2) and treated with a phenomenological model (Staykova et al., 2003), (Genov et al., 2004). Although the fitting procedure generally well covers data at the later, diffusion controlled stage, it usually deviates at the initial part of the reaction. This misfit was caused by a poor parameterization of this fragment and therefore an additional work was required. The issue will be assessed here in a series of short, interrupted runs that also may provide new information on the incubation period (1.5.1) or surface tension. In addition, two more formation runs at low temperatures (~190K) were performed to check a reproducibility with (Genov, 2005). The list of all runs can be found in Table 6. The new and previous

Nr.	T [K]	p (f) [kPa]	ln(f/f <sub>0</sub> )	Starting ice	Method	Duration [h]	Hydrate wt. frac. (sigmas)	SEM
1	190	36 (35.73)	0.69927	D <sub>2</sub> O frost	Neutrons	32.72	0.68 (0.003)	Yes
2	193	70 (69.07)	1.01463	H <sub>2</sub> O spheres	pVT+ X-rays	42.94 <sup>d</sup>	0.23 (0.003)	Yes
3	193*	75 (73.93)	1.08267	H <sub>2</sub> O spheres	pVT	0.25	0.007**	Yes
4	193*	75 (73.93)	1.08267	H <sub>2</sub> O spheres	pVT	0.56	0.01**	Yes
5	193*	75 (73.93)	1.08267	H <sub>2</sub> O spheres	pVT	1.49	0.03**	Yes
7	185	25 (24.86)	0.69972	D <sub>2</sub> O frost	Neutrons	25.29	0.26	Yes
8	190	36 (35.73)	0.69927	D <sub>2</sub> O frost	Neutrons	21.78	0.27	Yes
9	195	50 (49.53)	0.81761	D <sub>2</sub> O frost	Neutrons	15.1	0.80	Yes
10	203	80 (78.94)	0.63324	H <sub>2</sub> O spheres	pVT+ X-rays	93.97d	0.44	Yes

**Table 6)** List of the formation runs performed in frame of this thesis (1-5). Fugacity f is given in brackets for each experimental pressure. The duration of 193K run is given in days. The runs with \* mark the interrupted runs. \*\* denotes estimated values. The runs 6-10 come from the preceding thesis (Genov, 2005) but also appear here.

reaction curve at 190K along with older formation runs will be fitted with a current version of the phenomenological model (“Frost”) constrained with the data from the interrupted runs. At the end of this sub chapter the reader will find a first approximation on a degree of cage filling at low temperatures.

#### 4.2.1 Starting material and sample preparation

Ice powders used for the formation experiments were prepared using two slightly modified methods presented in the previous thesis (Genov, 2005).

Spherical material (Fig. 83A, B) of rather well defined lognormal distribution has been produced by spraying water into a dewar filled with LN<sub>2</sub>. The average diameter of the spheres obtained with this method was previously estimated with the help of SEM on ~55μm (Staykova, 2004). Present microscopy images are in a good agreement with this

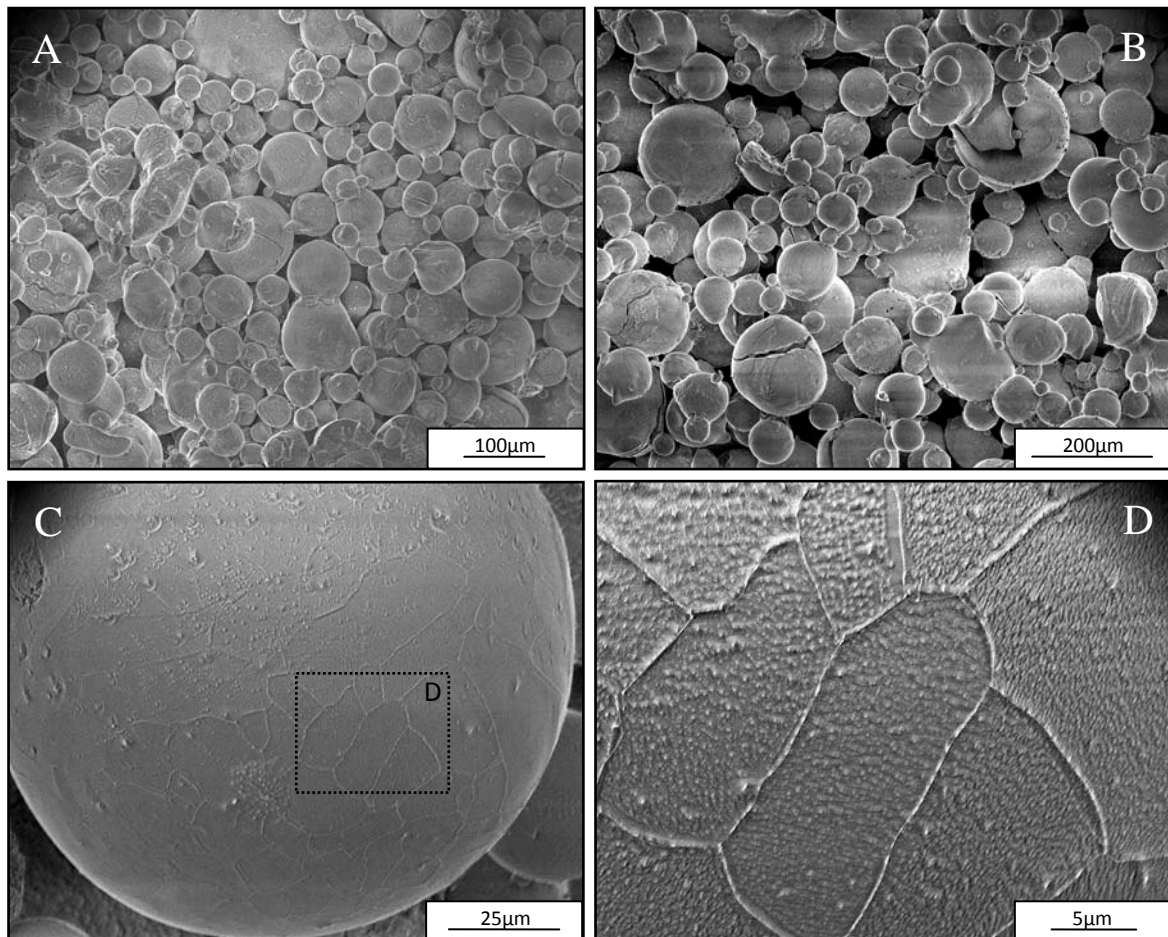


**Fig. 83** Two batches of sprayed ice spheres (A, B) prepared at different occasions. Some of the ice particles are cracked or spitted due to shock freezing. C) Polycrystalline ice sphere with well visible network of grain boundaries. D) Magnification of the ice sphere (C) showing filigree striation pattern. Images taken with FEI Quanta 200FEG. See also Appendix 3.

value. Moreover, they reveal a polycrystalline nature of the starting material (Fig. 83C, D). Ice crystals approximately 5-15 $\mu\text{m}$  in diameter are covered with a fine striation pattern (Fig. 83D) that depends on ice crystal orientation. Hydrogenated samples were prepared with demineralised H<sub>2</sub>O at ambient conditions. In such approach a buildup of frost condensate at a rim of the dewar is very difficult to avoid and some smaller, non spherical ice particles may fall into the LN<sub>2</sub>. Larger water droplets and some of the frost clumps are removed during sieving through 350 $\mu\text{m}$  mesh under LN<sub>2</sub>. In order to minimize an additional condensation at this final step, the procedure is performed in a cold room held at 263K. Unlike in previous experiments e.g. (Staykova, 2004), (Genov, 2005) ice powders were placed later in a storage dewar without an annealing period. This in order to keep the quality of ice identical for different batches. Deuterated samples were prepared with a 99.9% purity D<sub>2</sub>O delivered by SIGMA-ALDRICH GmbH. Spherical material has been produced in a sealed glow box under N<sub>2</sub> saturated atmosphere, to avoid possible contamination (and dilution) with atmospheric water. The sieving, performed later, has been done in the same way as for hydrogenated spheres. BET specific surface area (SSA) measurements of the material produced by spraying yield  $\sim 0.05\text{m}^2/\text{g}$  with  $\Delta Q_{\text{CH}_4} = 2200\text{J/mol}$  (Appendix 4) that corresponds to monodispersed spheres with a radius close to 60 $\mu\text{m}$ .

A second method was designed to produce much finer starting material than in the previous case. It is based on a water vapor deposition on a cold plate. Water is evaporated with a hot air gun and blown on a rotating copper plate that is submerged in LN<sub>2</sub> to about

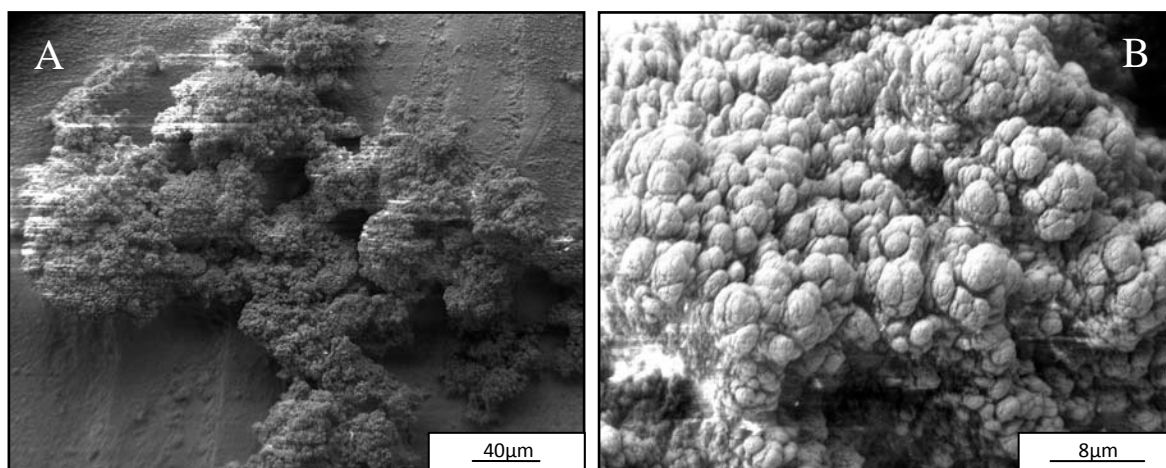


**Fig. 84)** A) Irregular frost particle produced by the cold deposition. High quality images are very difficult to obtain due to a strong charging effect on a rough surface. B) Magnification on one of the frost clumps composed of quasi-spherical particles. Images taken with LEO 1530 Gemini.

1/3 of its diameter. An accumulated frost is manually scratched down into the cooling liquid. The setup is mounted in a box that can be sealed if D<sub>2</sub>O is used. The efficiency of this method is very low and the ice material shows partial electrostatic charging. Agglomerates of the frost particles produced by the cold deposition are very irregular (Fig. 84A). An average diameter of a single ice-building unit has been estimated on ~5-15µm (Fig. 84B). An average SSA for this material was found to be ~1.9m<sup>2</sup> (ΔQ<sub>CH<sub>4</sub></sub>=2200J/mol), which is about two orders of magnitude higher than for sprayed material. Such surface corresponds to monodispersed spheres of 1.5µm radius. Poorly defined appearance is likely to cause difficulties during the data treatment with earlier theoretical models (Genov, 2005), (Kuhns et al., 2006) and the new one where spherical particles are assumed. Powders that are stored for an extended period of time under LN<sub>2</sub> must be dried before they can be loaded into aluminum vials (Fig. 66 [1]). It is especially crucial for frost that may easily shot out from the container upon warming. Leaving the material for a several minutes in the cold room at 267K or dry ice has proven to be a good method to avoid such surprises. Dried powders are gently compacted in vials and after loading sealed in plastic containers (Fig. 66) that can be again cooled down in LN<sub>2</sub>.

#### 4.2.2 Nucleation and growth stage – interrupted runs

The nucleation and initial growth of CO<sub>2</sub> hydrates on the ice surface has been studied

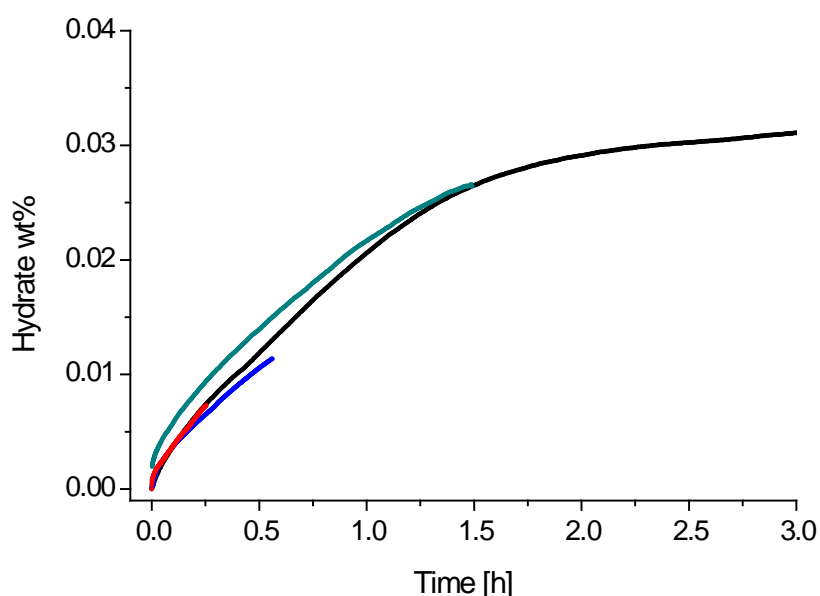


**Fig. 85)** Reaction curves of all three interrupted runs at 193K in comparison to a few month long experiment. Some inconstancies in the overall shape are likely to be caused by the introduction of not completely cooled gas at the very initial stage of the reaction.



using combination of gas consumption experiments and FE-SEM imaging. Spherical ice was reacted in the in-house pVT low pressure system (Fig. 73) at a constant temperature of 193K and applied pressure close to 750mbar (75kPa) for ~15, 30 and 90 min. Before each experiment samples were evacuated for several minutes to remove atmospheric gases introduced upon loading. At the end of the runs samples were quickly recovered and quenched in LN<sub>2</sub>. The transformation degree was roughly estimated with the help of a 43-days long reaction curve recorded at 193K and 700mbar (70kPa) (see 4.2.3). The reproducibility of the interrupted runs is not perfect as shown earlier (Fig. 85) but still

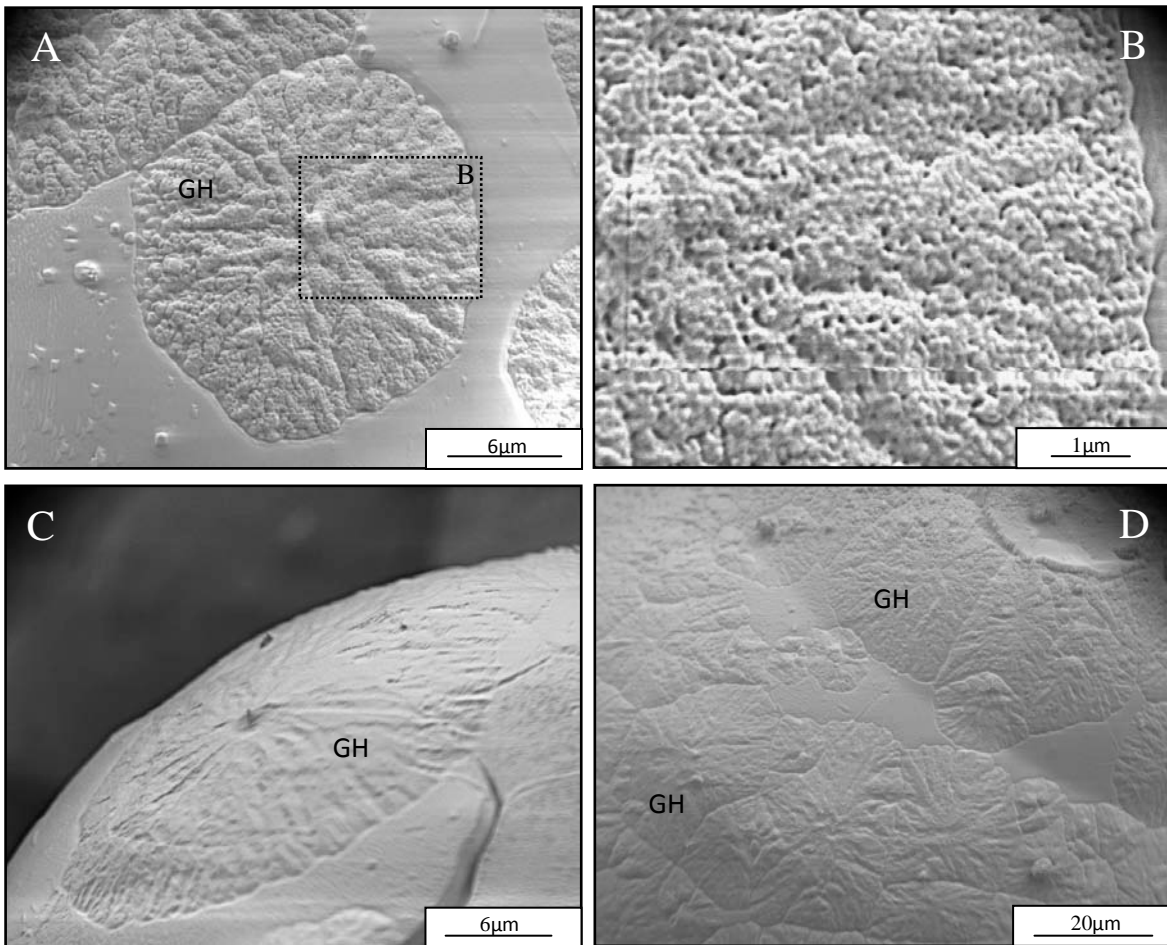


**Fig. 86)** Nucleation sites of hydrates on ice spheres after 15 (A, B) and 30min. (C, D). formation. A) Top view on a nucleation center with well developed spreading fronts. Rough clathrate surface is carrying some resemblance to concentrically growing dendrites. Surrounding ice-like smooth surface do not possess characteristic striation pattern, B) Magnification of the clathrate surface reveals characteristic small sub- $\mu\text{m}$  porosity. C) Oblique view on a clathrate crystallite that overgrows a fracture in the ice sphere. D) Ice particle covered by heterogeneously growing clathrates. Their size varies from 5 to 25 $\mu\text{m}$ . Between hydrates one can still observe icy smooth surface. Images A-C and D were taken with LEO 1530 Gemini and FEI Quanta 200FEG, respectively. Additional images can be found in the Appendix 5.

the general trend is preserved (Fig. 85).

SEM images of a sample reacted for 15 (~0.7 wt% of clathrates) (Fig. 86A, B) and 30min (~1.3 wt% of clathrates) (Fig. 86C, D) reveal clearly distinguishable nucleation sites and spreading fronts of clathrates growing on the icy surface. Up to now, similar but not identical features were observed only on a water/liquid  $\text{CF}_3\text{CH}_2\text{F}$  interface during some earlier formation experiments (Sloan, 1998). Nucleation sites are relatively flat, which suggests preferential 2D growth along the surface. An average diameter of the features is estimated on 10-15 $\mu\text{m}$ , which is within the limit of previous studies (Circone et al. 2003). Close-ups of the clathrate surface reveal a sub-micron size porous structure very characteristic for this phase (Fig.86B). One should point out that observed microstructure is characteristic for growth at the high super saturation. Formation experiments close to the

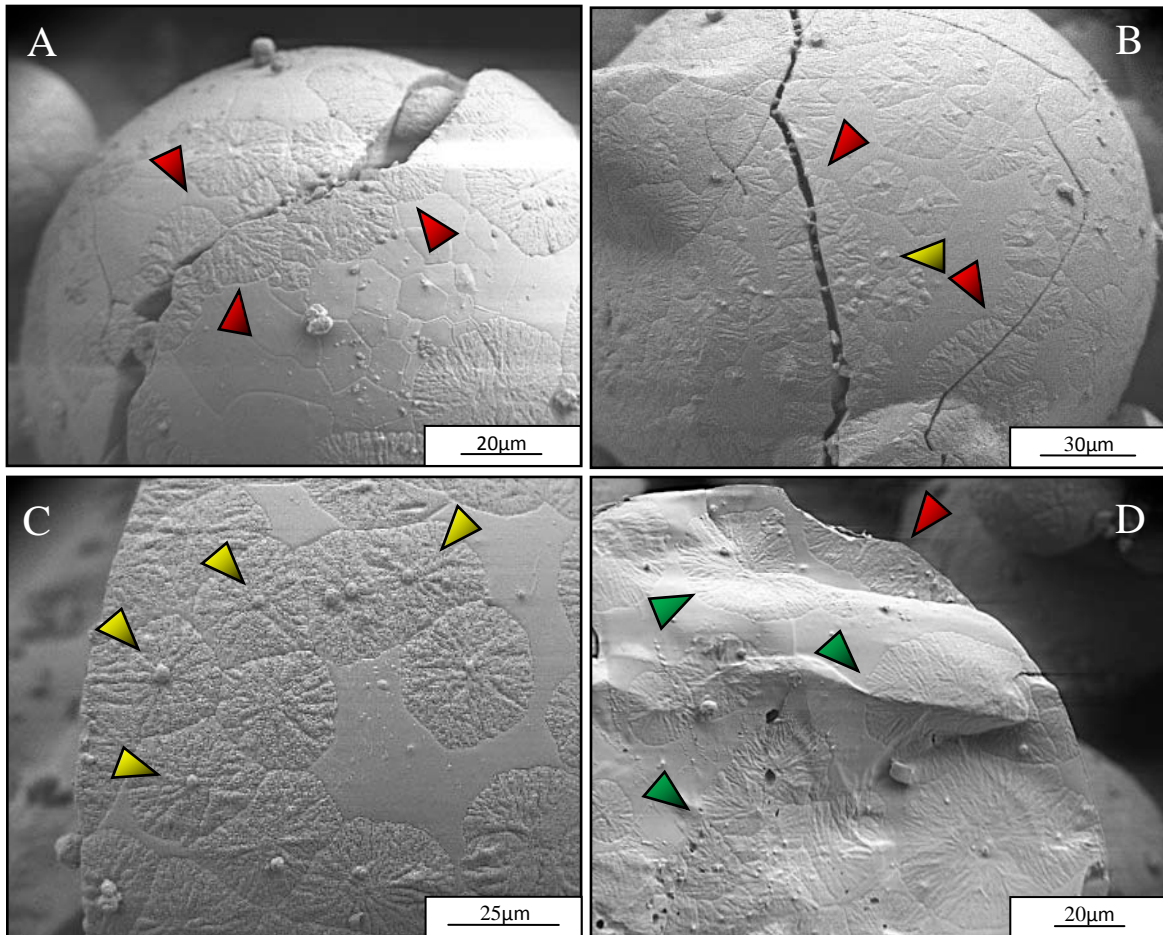


**Fig. 87)** Promotion of the nucleation on surface defects in 15 (C) and 30min (A, B, C) long runs. A, B) Clathrates preferentially growing along cracks and (red arrows), C) Hydrate crystallites initiated on small ice particles attached to sphere's surface during the preparation (yellow arrows). D) Uneven face of a broken sphere covered by patches of clathrates. Most of the crystallites are initiated on sharp edges or groves (green arrows). Images taken with LEO 1530 Gemini. Other examples can be found in the Appendix 5.

stability boundary are likely to form better developed 3D clathrate crystals. “Pancake like” shape of individual crystallites is also frequently related to heterogeneous nucleation (Lasaga, 1997). This observation is in accordance with an uneven distribution and different maturity of the clathrate cover in the discussed samples (Fig. 86D, 87B). Moreover, surface imperfections like cracks (Fig. 87A, B), small ice particles electrostatically attached to ice spheres (Fig. 87C) or other surface imperfections (Fig. 87D) seem to promote nucleation for a number of nucleation sites. Clathrate crystallites that tightly cover ice spheres form quite characteristic polygonal pattern resembling the one observed on a jackfruit (Fig. 88A, B). Assigning one center to one “jackfruit” area, the roughly estimated density of nucleation centers is about  $4.9-8.8 \cdot 10^3$  nuclei/mm<sup>2</sup>. Free icy surfaces, more common after the 15min long formation, are usually very smooth what is not typical for starting spherical ice where the striation pattern would be expected (Fig. 85D). Moreover, the resistance to etching by the electron beam in those areas seems to be somewhat decreased. On the other hand, EDX analyses do not show any elevated values for carbon, which would be consistent with a reacted surface. After 30min. icy surfaces become rare as the clathrate cover is closing to completion but still characteristic structures from the shorter run are well visible. In a several places boundaries between individual centers start to disappear and the original “jackfruit patterns” becomes less apparent. The surface in those areas is still undulated but the roughness is visibly decreased in comparison to the 15min long experiment. After seeing the reaction curve (Fig. 85) it is not very surprising that the

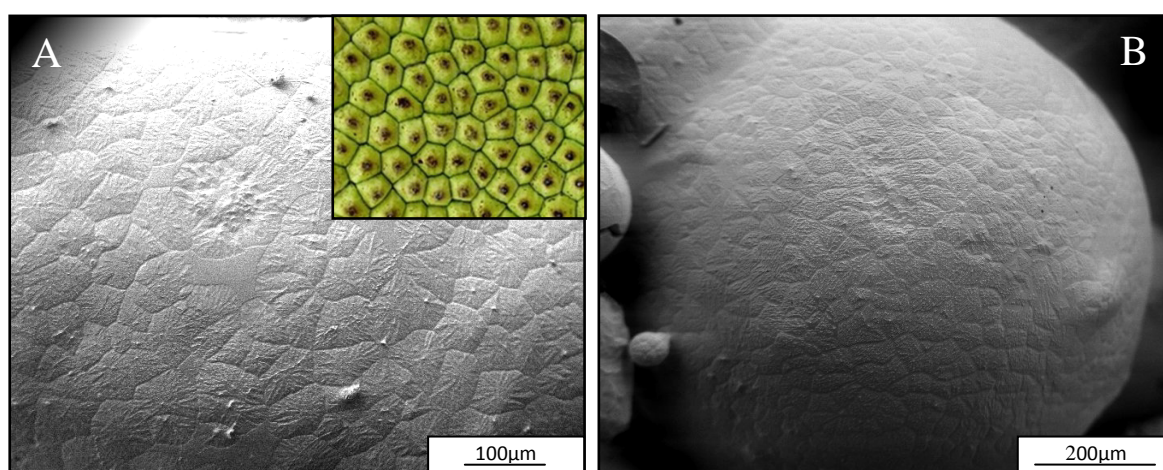


**Fig. 88)** Almost entirely A) and fully transformed B) surface of ice particles after 15min. long reaction. Clathrate crystallites form characteristic polygonal “jackfruit pattern” (A jackfruit skin in the right upper corner of A) image). Images taken with LEO 1530 Gemini. Other examples can be found in the Appendix 5.

microstructures after 15 and 30 min. do not differ much. Both samples lay on a steep part of the curve that in light of evidences presented above may be attributed to the surface coating process. Clearly visible alteration of observed features appear after a prolonged exposition to vacuum and the beam (Appendix 6). The surface becomes visibly coarser but clathrate crystallites are still recognizable. A considerable slow down of the reaction after approximately 90min suggest a transition to another formation regime. Indeed, the longest interrupted run that was stopped at the inflection point (~2.6 wt% of clathrates) seems to confirm this observation. The surface microstructure observed before is hardly recognizable. Ice spheres are coated by a continuous hydrate mantling (Fig. 89A, C, E) covered with a pattern of elevations and depressions that at the first glance might be mistaken with the water ice striation pattern (Fig. 89B). A careful analysis of those features reveals smoother and rounded edges that are untypical for ice (Fig. 89D, F). Additional evidences from EDX area scans, where a carbon signal is observed, confirm the presence of clathrates. Individual spheres become progressively cemented by hydrate necks at the contact points. Smaller fractures and cracks are partially or completely filled with sub-micron porous clathrates and expanding mantle (Fig. 89C, D, F). Although this process has been already observed in the previous studies (Genov et al., 2004), (Staykova, 2004) for CO<sub>2</sub> and CH<sub>4</sub> clathrates, its interpretation was different from the one presented here. Crack filling was considered to be a primary process that begins the formation, since slightly smaller activation energy necessary to initiate the nucleation in cracks might promote crystallization. Although, it is also partially in agreement with the present observations for 15 and 30min where some of the crystallites indeed grow on, in and out of the fractures (Fig. 87A, B), the overall picture that emerges from the present interrupted runs is somewhat opposite. The bridging and crack filling appears to be generally a consequence of the surface transformation and thickening of the clathrate coating. Apparently, the combination of volume expansion with the growth creates an effective mechanism for closing of the smaller cracks at least at the investigated p-T conditions. With this interpretation the crack filling stage (Genov et al., 2004) becomes essentially obsolete. The conclusions presented here shed also new light on the so called “incubation period”. This phenomenon is most often addressed as a period of a few hours/weeks after the beginning of the reactions below 200K where in spite of suitable p-T conditions the formation is not observed. It is still arguable though if this behavior is caused by an inhibition or it is just very slow start of reactions that follow a sigmoid-like pattern. The interrupted runs



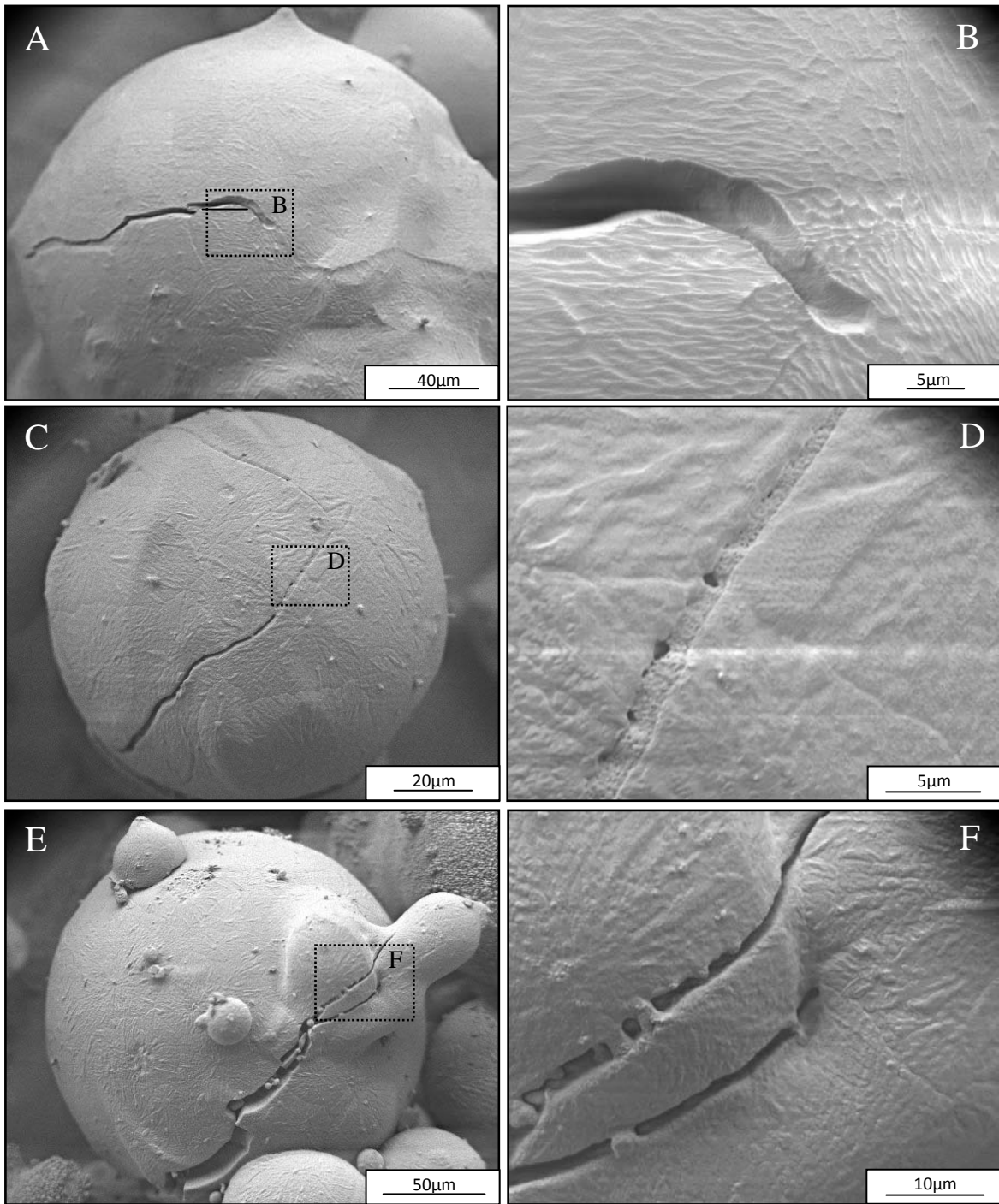


**Fig. 89)** Surface microstructures after 90min. long formation experiment. A) Ice sphere covered by a continuous clathrate mantle that under higher magnification (B) looks very similar to the striation pattern. C) Sphere with a crack partially cemented by clathrates. D) A blow up of the previous image revealing a fine sub-micron pores of the hydrate crack filling. E) Another cracked ice sphere where clathrate mantling is expanding into the fracture (F) bridging it in a several places. Hydrate surface is bruised and undulated resembling somewhat structures observed in the shorter runs. Pictures taken with LEO 1530 Gemini. Other images from this experiment can be found in the Appendix 7.

certainly cannot definitely solve this problem but they shift of the starting point closer to the beginning of the reaction suggest that at least in certain cases the second possibility may be correct. Though, it is necessary to point out that even if the nucleation and growth is initiated earlier it doesn't overrule the the incubation period that might still exist in much reduced form.

The interrupted runs presented here offer also an opportunity to measure two quite unique parameters that unfortunately could not be explored in frame of this thesis: wetting angle (surface tension) of clathrates on ice and a thickness of the initial hydrate coating formed at 190K. The first one is interesting from the clathrates thermodynamic point of view. The second one, thickness, is more significant for this thesis since it is one of the free parameters in the models presented in Chapter 3.

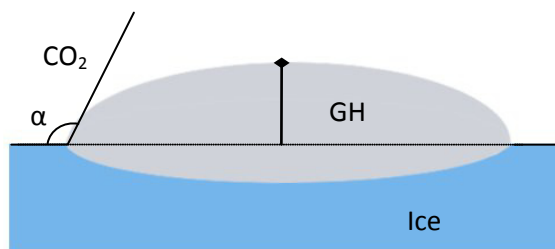


**Fig. 90)** Schematic cross section through a clathrate crystallite with the measurable thickness and wetting angle  $\alpha$ .

Clathrates crystallites that form pancakes or domes suggest that the growth is faster along the surface than in the inward direction (Fig. 90). If this interpretation is correct then one can safely assume that the maximum height of a single crystallite is more than half of the thickness of the initial clathrate coating. The surface tension between two phases can be derived from an angle created by a slope of clathrate surface with the ice interface. At

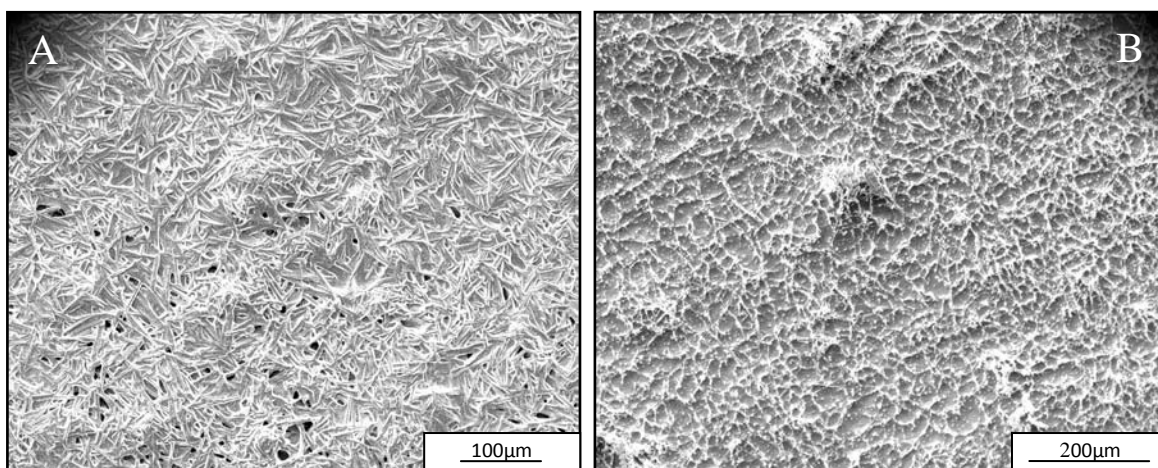


**Fig. 91)** Flat ice surface exposed to CO<sub>2</sub> for 15min. covered most likely by clathrate needles (A). Pancake like features observed on the spherical material are nowhere to be found. The coating was found to be very unstable and after about 2min. degraded entirely (B). Snapshots from FEI Quanta 200FEG.

the first glance a measurement of those parameters may seem to be quite simple but in the reality one has to face a number of pitfalls. First of all, the SEM microscopy used here cannot be of assistance since it doesn't offer scaling in Z direction. This problem could be overcome with an atomic force microscopy (AFM) or confocal laser scanning microscopy (CLSM) that provide 3D images but investigated area becomes restricted to at most a few  $\text{mm}^2$ . Moreover, ice surface should be relatively flat that is difficult to achieve with the powders used here. Preliminary attempts to reproduce observed features on a flat surface were unsuccessful (Fig. 91). Both microscopes are usually not equipped with an environmental conditions similar to those under SEM and hydrates cannot be measured directly. One of the ways to go around this problem is to use a replica method (Krokodylewski et al., 1994) widely used for fragile samples in the TEM microscopy. Sputtered coating can be thicker than typically used few nm since only a negative of the surface is required. Another, more direct way to approach the issue could be a combined FIB-cryo-SEM that allow for both in-situ cutting and visualization.

#### 4.2.3 Formation's kinetics at low T

Preparation of the starting material as well as experimental techniques are prone to experimental errors that may eventually cause irreproducibility of acquired data. Here the focus will be placed on the least well defined material (frost) and the reliability of the pVT method in a several months long reactions.

Formation experiment testing  $\text{D}_2\text{O}$  frost has been performed on  $\text{D}_2\text{O}$  at 190K and 360mbar (36kPa). During the 33h long experiment, individual diffraction patterns were taken in 5 minute-long steps. At the end the sample was recovered and preserved in  $\text{LN}_2$  for further investigations with the SEM. Raw data were imported to the GSAS Rietveld package and processed in a two phase refinement using an automated procedure described in details elsewhere (Staykova, 2004). Water ice Bragg reflections were fitted with a low temperature  $\text{D}_2\text{O}$  Ih ice structural model (Appendix 8) using lattice constants for 190K (Röttger et al., 1994).  $\text{CO}_2$  hydrate structure inserted into GSAS originates from an early work on a high temperature model (Klapproth, 2002) that was adapted for low temperatures by refining  $\text{CO}_2$  occupancy factors in both cages (4.2.5) and scaling down thermal displacement parameters. The last correction is somewhat arbitrary but still within the reason. Unfortunately,  $\text{D}_2\text{O}$   $2\theta$  range do not allow for an evaluation of those parameters. Missing information should be obtained from future experiments. Dimensions



of a clathrate lattice (D<sub>2</sub>O) were calculated from published third order polynomial function (Udachin et al. 2001). Both structural models can be found at the end of the thesis (Appendix 8). Results from the refinements are stored in a list file from where one can extract searched phase fraction of clathrates in each pattern and plot them against time. The transformation degree in the last pattern (Fig. 92) was ~36wt% (Table 6).

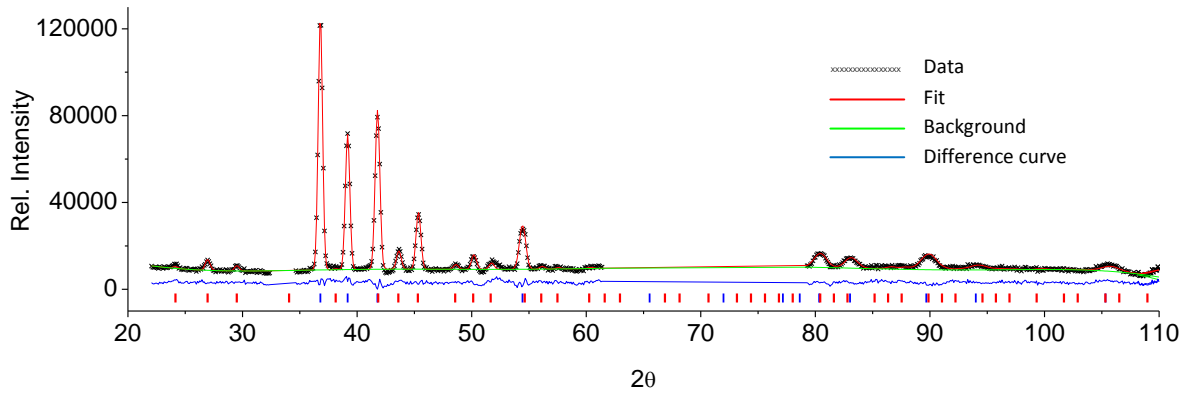


**Fig. 92)** The last pattern from the formation run at 190K and 360mbar (36kPa) (in black) fitted with GSAS (red line). Positions of reflections from both phases are showed in red (clathrate) and blue (ice) tick marks (see also Appendix 9).

A close comparison between the new and old experiment at 190K shows a very similar trend but one can notice a small deviation in the initial transformation rates that later become even more apparent (Fig. 93). The new run initiates slightly earlier, continue at similar rate than the previous one and after about 16h the rate becomes lower. This slight difference can be caused by a number of factors where the sample handling or differences

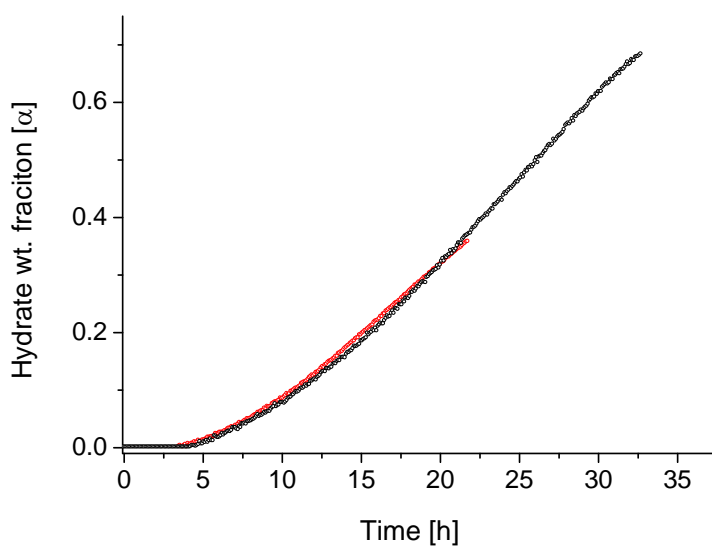


**Fig. 93)** New (in black) experiment at 190K plotted together with the earlier run (in red). Initial points where

in the initial SSA are the most probable. The last one is of particular importance at lower temperatures where variations in the surface area may greatly affect observed kinetics. What is worth to notice is the fact that the initial transformation is not observed until a relatively rapid lift off after about 3h. This rather surprising

behavior, observed also in the previous experiment at these conditions and other runs at 185K and 195K (4.1.4). At first glance it might be attributed to the incubation period. If this is indeed an inhibition then clathrate reflections should not be observed in this part of the formation. Yet, a close inspection of the raw data in a 2-theta region between 42.5 and 47.5 shows two of the strongest clathrate reflections (320, 321) slowly rising from the early minutes of the reaction (Fig. 94). Apparently the Rietveld refinement is somewhat less sensitive to the fraction that is well below 1% even if the diffractometer records the reaction.

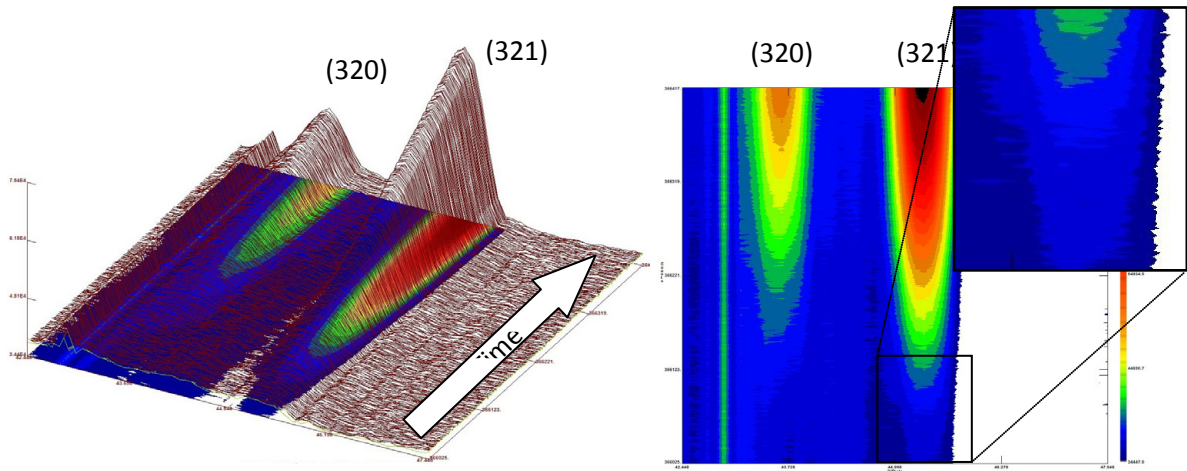


**Fig. 94)** Accumulated LAMP plots of the formation run at 190K 360mbar (36kPa) in a 2-theta region between 42.5 and 47.5. Raw data clearly indicate the reaction already in the initial diffraction patterns. It is particularly visible on the strongest (321).

The reproducibility of long term experiments in the low temperature pVT setup (Fig. 73) has been tested in a 23 days long run at 193K and pressure oscillating around 700mbar (70kPa). At the end of this period, the sample was recovered and quenched in LN<sub>2</sub>. The transformation degree was measured with hard X-rays at BW5 (3.1.3). The diffraction 2D image has been integrated to 1D pattern (Fig.94) and refined in GSAS. Ice peaks were fitted with a H<sub>2</sub>O structural model (Appendix 8) taking lattice constants at 77.2K from published data (Röttger et al., 1994). Hydrogenated CO<sub>2</sub> clathrate model was constructed from an empty frame of sI CH<sub>4</sub> hydrate that was filled with CO<sub>2</sub> molecules. Atomic positions for gas in cages were taken from the D<sub>2</sub>O model. Lattice dimensions at 77.2K were taken from the literature (Sloan and Koh, 2008). Relatively short 2θ range (Fig. 95) leaves only zero, scaling factors, peak shape profiles and background function to be refined. Other parameters were kept fixed. Retrieved hydrate fraction was close to 26wt%

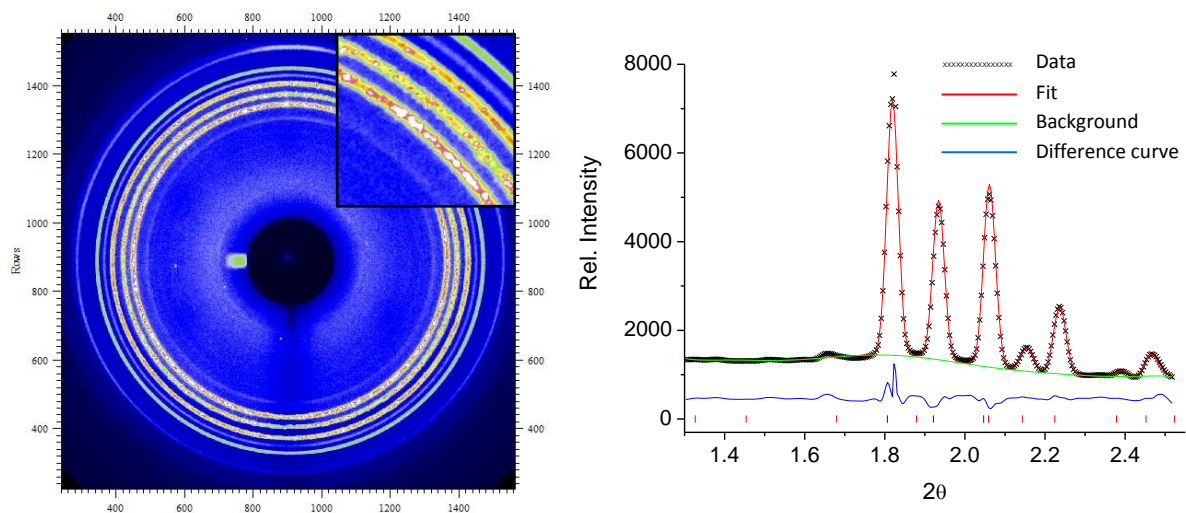


**Fig. 95)** 2D image from the MAR detector (to the left) integrated to 1D pattern and fitted in the GSAS (to the right. See also Appendix 9). Positions of reflections from both phases are marked by red (clathrate) and blue (ice) ticks. The misfit of the strongest ice peak is caused by an artifact from the integration of a spotty diffraction rings.

(Table 6). The new data set after normalization was plotted (Fig. 96) against the results from a 94 days long experiment at 203K and target pressure of 800mbar (80kPa) (Genov, 2005).

One of the first conclusions coming out from the comparison is a similar shape of both reaction curves at the later, diffusion controlled stage that seems to confirm a similar

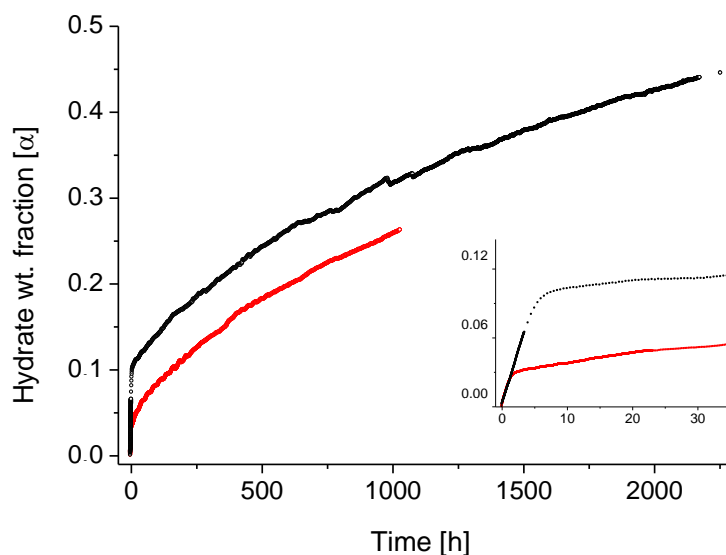


**Fig. 96)** Two long term pVT formation experiments at 193K (in red) and 203K (in black). The blow up of the first 35h in the right-bottom corner.

reliability of the low pressure pVT setup (Fig. 73). Both runs slowly diverge with time, which is most likely caused by a somewhat decreased transformation rate expected at the lower temperature. If this is the case one should expect also similar differences at the initial stage. Indeed, after about 1.5h of seemingly identical

reaction (Fig. 96), the 193K curve bends as discussed previously (4.1.2) while the 203K run continues further at similar rate until a gradual deceleration after about 4h. Since the diffusion controlled stage steps in after a longer period of time it is reasonable to assume that the maximum thickness of the initial coating is increased in comparison to the lower temperature (see also the following subchapter).

#### 4.2.4 Modeling with Powder 4 - Frost Module

The frost data from the neutron diffraction experiments were analyzed with a new “Frost” module. As it was discussed earlier (3.6.2) this approach considers a special case of the general Powder 4 model where the diffusion limitation is neglected due to a very small particle size. Fitted curves (Fig. 97) are obtained using six parameters from which the grain radius, excess fugacity  $\ln(f/f_d)$ , and nucleation exponent  $m$  could be constrained with help of SEM and BET methods. The nucleation rate  $k_N$  and grow rate  $k_G$  constants were used for a fine tuning. The growth exponent  $\sigma$  was kept fixed all cases (Table 7).

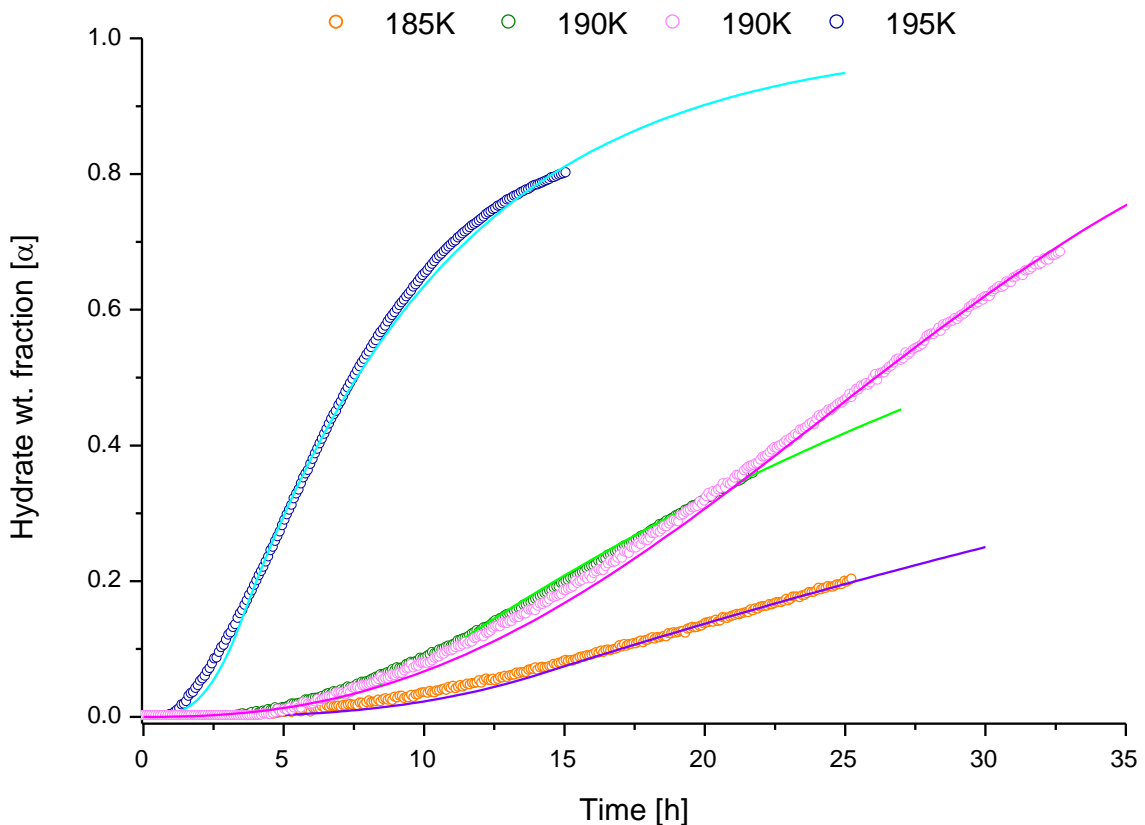


**Fig. 97)** Low temperature formation experiments with frost as a starting material (Table 6). The curves (open circles) are fitted (solid lines) with the “Frost” model.

The fits are quite satisfactory if one keeps in mind that the “Frost”-model assumes a monodispersed distribution of spherical particles. Since the starting ice particles (Fig. 84) have more complicated morphology and distribution it is not surprising that some misfit is observed. This issue is particularly pronounced at the initial and terminal stage. Larger particles that transform more readily initially enhance the transformation speed. A deceleration close to the end implies that only the smallest ice particles where the nucleation issue is the strongest still support the reaction. A good example for such behavior can be found here in curves where the wt. fraction  $\alpha$  exceeds 0.6 (195K and 33h long 190K. The fitting parameters returned by the model can be found below (Table 7).

T [K]	$\ln(f/f_d)$	Duration [h]	$\sigma$	$k_s/\sigma$ [1/h $^\sigma$ ]	m	$k_N$ [1/h $^\sigma$ m $^2$ ]	$k_G$ [m/h $^{m/3}$ ]	$t_0$
195	0.81761	15.01	1	0.190	2	$6.80 \cdot 10^9$	$9.55 \cdot 10^{-7}$	3.5
190	0.69927	21.78	1	0.044	2	$1.55 \cdot 10^9$	$4.30 \cdot 10^{-7}$	11.3
190	0.69928	32.72	1	0.133	1.4	$4.70 \cdot 10^9$	$4.13 \cdot 10^{-7}$	34.13
185	0.69972	25.29	1	0.017	2	$5.90 \cdot 10^8$	$3.65 \cdot 10^{-7}$	12.4

**Table 7)** Experimental conditions and kinetic parameters from the “Frost” model. The mean radius of the starting ice is 1.5 $\mu$ m. Grain nucleation constant  $k_s$  and typical time of grain coating  $t_0$  have been deduced from the fitted curves.

Although the SEM images (Fig. 86, 87) support 2D type of growth ( $m=2$ ) the older experiment at 190K could not be fitted with a correspondingly constrained parameter. After

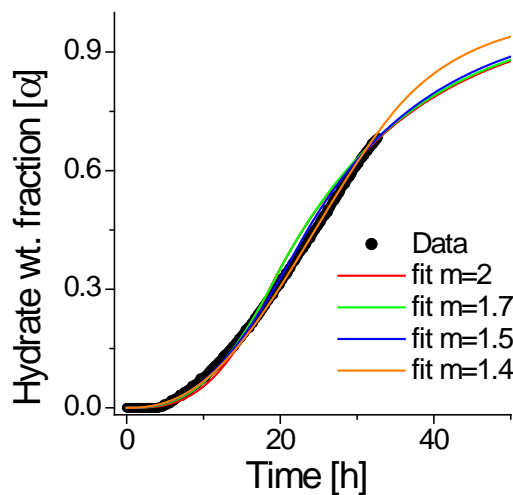


**Fig. 98)** Fitting curves for four different  $m$  plotted together with the 32.7h long formation run 190K and 360mbar (36kPa).

$k_s/\sigma$ [1/h $^\sigma$ ]	m	$k_N$ [1/h $^\sigma$ m $^2$ ]	$k_G$ [m/h $^{m/3}$ ]	$t_0$	SD
0.792	2	$2.80 \cdot 10^9$	$3.10 \cdot 10^{-7}$	18.2	0.025
0.081	1.7	$2.85 \cdot 10^9$	$3.10 \cdot 10^{-7}$	19.54	0.024
0.086	1.5	$3.05 \cdot 10^9$	$4.50 \cdot 10^{-7}$	22.72	0.015
0.133	1.4	$4.70 \cdot 10^9$	$4.13 \cdot 10^{-7}$	34.13	0.009

**Table 8)** Kinetic parameters for the fitting curves presented on the Fig. 98. SD-standard deviation.

a series of attempts (Fig. 98), (Table 8) a satisfactory solution was found for  $m=1.4$  that represents a mixed dendritic/2D growth. This solution is not totally unreasonable but difficult to explain if confronted with other three fits. The reason for this result might be searched in a different particle size of the starting material, its thermal history or/and fairly short experimental curves that leave some degree of freedom during the fitting procedure. On the other hand the dimensionality of growth might indeed be better represented by values between 1 and 2. Unfortunately, no conclusive answer has been found yet.

The discussion about the new modeling approach creates also a good opportunity to present some results from the Powder 4 used on data from the preceding thesis (Genov, 2005). A large set of kinetic parameters kindly provided by A. Salamatin (Table 9), gives an additional insight on the diffusion limited stage that gains considerable importance for larger particles ( $> \sim 2\mu\text{m}$ ). Moreover, it became possible to reexamine some earlier results concerning the nucleation rate exponent  $\sigma$  and the thickness of the initial clathrate film  $d_0$ .

No	T [K]	$p_d (f_d)$ Mpa	$\ln(f/f_d)$	Duration [h]	$\sigma$	$k_s/\sigma$ [1/h $^\sigma$ ]	$k_G$ [m/h]	$t_0$ [h]	D [m $^2$ /h]	$d_0$ [ $\mu\text{m}$ ]
1	272	20(19.7)	0.5558	18	1.0	1.6	-	0	$1.4 \cdot 10^{-11}$	7.8
2	263	10(9.3)	0.2699	18	0.5	1.54	0.002	0.074	$3.7 \cdot 10^{-12}$	6.7
3	253	10(9.1)	0.6190	23	0.62	1.25	-	0	$1.8 \cdot 10^{-12}$	3.6
4	230	3(2.9)	0.4441	26	0.34	0.78	0.0013	0.070	$3.6 \cdot 10^{-13}$	3.3
5	263	10(9.3)	0.2699	1128	0.49	1.24	0.00045	0.33	$1.6 \cdot 10^{-12}$	5.8
6	253	10(9.1)	0.6190	1128	0.64	0.70	-	0	$7.0 \cdot 10^{-13}$	3.3
7	233	5(4.9)	0.8473	1728	0.45	0.45	0.00028	0.09	$2.5 \cdot 10^{-13}$	3.0
8	223	1.95(1.9)	0.3950	240	0.7	0.73	-	0	$7.2 \cdot 10^{-14}$	2.5
9	218	1.95(1.88)	0.6413	288	0.8	0.66	-	0	$7.2 \cdot 10^{-14}$	2.0
10	213	1.5(1.47)	0.6729	185	0.79	0.54	-	0	$5.1 \cdot 10^{-14}$	1.6
11	203	0.89(0.88)	0.7161	2255	0.95	0.36	-	0	$2.5 \cdot 10^{-14}$	2.1
12	203	0.89(0.88)	0.7161	185	0.95	0.29	-	0	$2.45 \cdot 10^{-14}$	1.5
13	193	0.5(0.5)	0.8210	126	0.78	0.26	-	0	$3.2 \cdot 10^{-14}$	2.1

**Table 9)** Results from the fitting of the selected formation experiments (Genov, 2005) with the Powder 4 model. Datasets 1-4 and 5-13 come from the neutron diffraction and pVT runs, respectively. The growth exponent  $m = 2$ .

The parameters retrieved with help of the Powder 4 and Frost module follow Arrhenius behavior, which gives a possibility to extract activation energies for the  $Q_{k_s/\sigma}$ , nucleation  $Q_{k_N}$ , growth  $Q_{k_G}$  (Fig. 99) and in case of the Powder 4 also the diffusive transport of gas and water molecules through the clathrate layer  $Q_D$ . Interestingly, the first



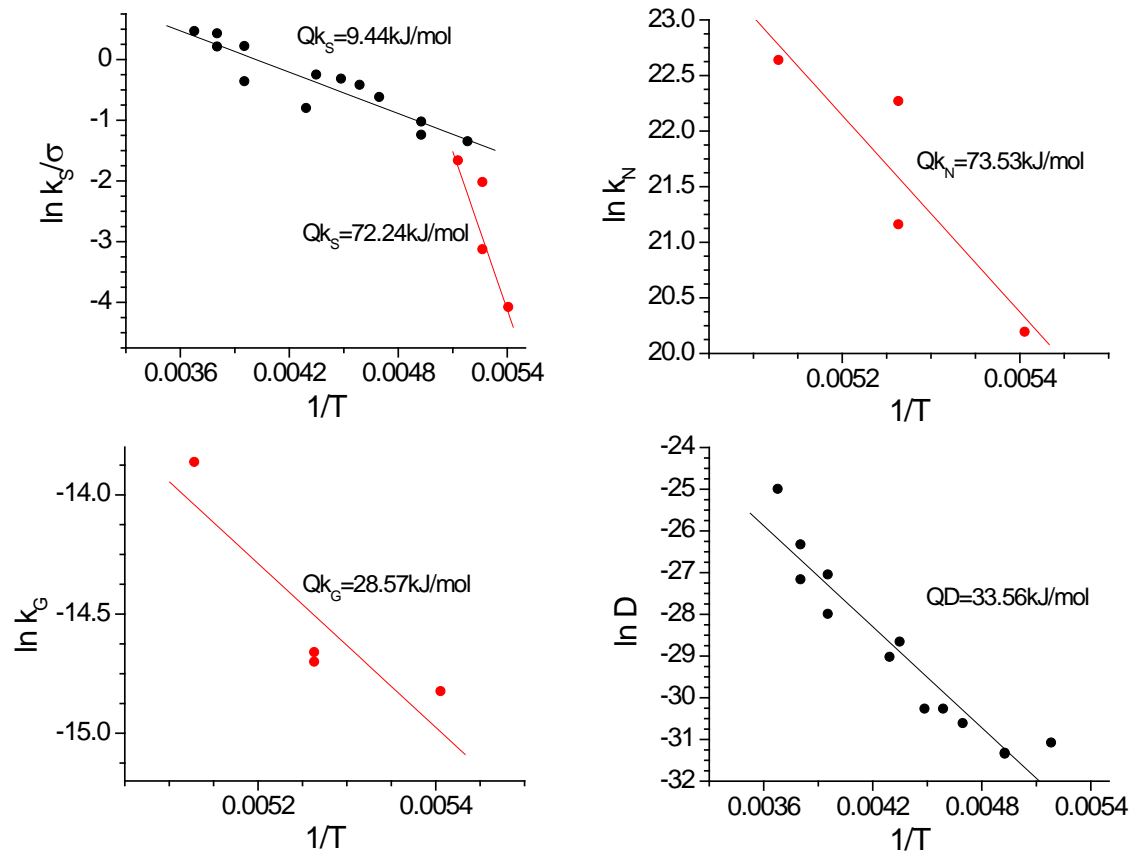


**Fig. 99)** Arrhenius plots of the kinetic parameters ( $k_N, k_G, k_S/\sigma, D$ ) from the Frost (red dots) and Powder 4 (black dots) modeling. For each trend line activation energy has been calculated.

process is apparently described by two values of  $Q_{k_S/\sigma}$ . The first one,  $Q_{k_S/\sigma} = 9.44 \text{ kJ/mol}$  is related to the experiments from 272 to 190K where a pivotal point is located. Towards even lower temperatures, down to 185K the activation energy switches to  $Q_{k_S/\sigma} = 72.24 \text{ kJ/mol}$ , which is almost identical to  $Q_{k_N} = 73.53 \text{ kJ/mol}$ . This significant change may indicate increasing difficulties in the nucleation, which find some confirmation on SEM images (4.2.2), shape of reaction curves (Fig.97) and evolution of the nucleation rate exponent  $\sigma \Rightarrow 1$  (Fig. 98). Interestingly,  $Q_{k_S/\sigma} = 9.44 \text{ kJ/mol}$  found between 272 and 190K is similar to the one calculated in previous studies ( $Q_{k_S} = 5.24 \text{ kJ/mol}$ ) for 225-193K temperature region (Genov et al. 2004). An extraction of the activation energy for the growth process met serious shortcomings in a number of available data point across the whole temperature region and presented  $Q_{k_G} = 28.57 \text{ kJ/mol}$  was calculated only for the data from the “Frost” module. In spite of a poor statistics the result is still comparable to the  $Q_r = 34 \text{ kJ/mol}$  obtained from the multistage model (Genov, 2005). Even better

agreement is achieved for the activation energy of the diffusion limited process  $Q_D = 33.56\text{kJ/mol}$  that is almost identical to the previous value  $Q_D = 36\text{kJ/mol}$  (Powder 2) (Genov, 2005). Both values are somewhat larger than activation energy of  $20\text{kJ/mol}$  and  $23.5\text{kJ/mol}$  acquired with JMAKGB (Genov, 2005) and in another independent study (Henning et al., 2000), respectively. This difference may originate in a less accurately defined diffusion limited stage incorporated into the other model, which might give some averaged value from all active processes (nucleation, growth and diffusion). Additionally to above parameters, the Powder 4 model delivers also valuable information on the character of the nucleation (instantaneous/uniform) and a maximum thickness of the initial clathrate film (Fig. 100). The first parameter show some scatter but still some trend toward more instantaneous nucleation at higher temperatures is visible. In the second case a trend line is much more apparent stretching from almost  $8\mu\text{m}$  at  $272\text{K}$  to  $\sim 2\mu\text{m}$  at about  $210\text{K}$ . This observation provides an additional argument for a treatment of small  $1.5\mu\text{m}$  frost particles with the “Frost” module that omits the diffusion limitation.

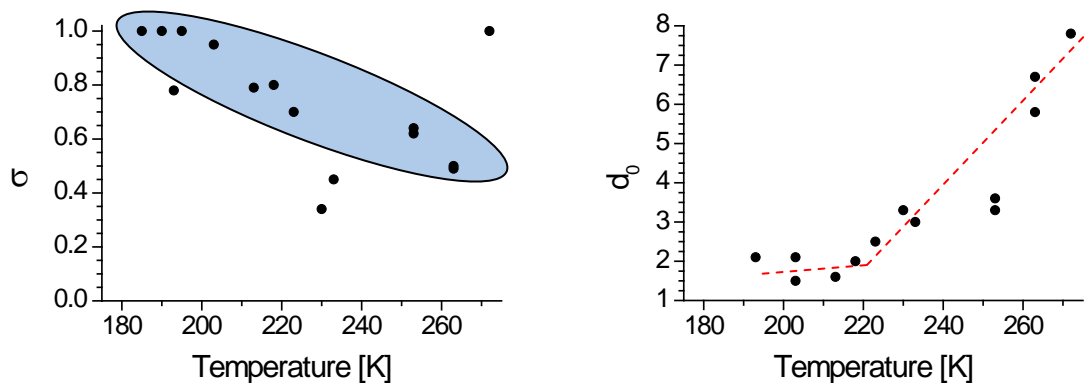


**Fig. 100)** Temperature dependent evolution of the nucleation rate exponent  $\sigma$  and the thickness of an initial clathrate film  $d_0$  retrieved from the Powder 4 model.

Through the activation energies the modeling gains a predictive power that can expand our knowledge on reaction rates at conditions that are not achievable in a laboratory. This is particularly important for temperatures below  $180\text{K}$  relevant to the Martian polar regions and/or larger ice particles where required reaction periods greatly exceed duration of a typical PhD studies, going very often into geological time scales (See Chapter 5).

#### 4.2.5 Cage occupancy

A volume of  $\text{CO}_2$  stored in hydrates, which might be of interest in the Martian case (2.6), is among others dependent on the degree of cage filling. Experimental studies

concerning this parameter are essentially limited to higher temperatures. CO<sub>2</sub> is particularly interesting here due to its radius that is similar to the one for cages already close to the melting point of ice (Fig. 6). In principle, as the lattice shrinks with decreasing temperatures the small cage occupancies may also decrease due to the tight fit of CO<sub>2</sub> molecule. A temperature effect for large cavities is speculative but it cannot be excluded that due to enhanced van der Waals interactions some small volume expansion may occur.

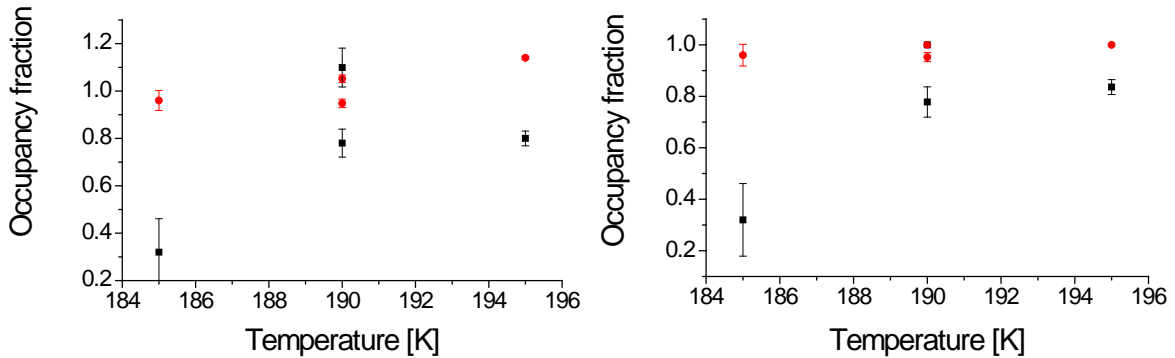


**Fig. 101)** Occupancy fractions for small (black) and large (red) cages from the runs at 185, 190 and 195K. The refinement of both cages (to the left) in certain cases returned values higher than one molecule per large cage. After fixing those values at one, the procedure was repeated (to the right).

At temperatures of ~180-190K this effect should be already detectable if the argumentation above is correct. Free refinement of both cage occupancies in most of the cases was leading to unrealistically high values (Table 10) for one of the cavities and had to be fixed at the highest filling degree. The results for large cages show some scatter (Fig.101) but generally indicate high occupancies. Values for smaller cavities are much less consistent (Table 10). Older experiments at 190K and 195K do not vary much between each other showing occupancies close to 80%. The new run at 190K after the background subtraction pushes this value to 100%. The formation run at 185K in contrary to other results shows only about 30% of CO<sub>2</sub> molecules in small cavities. Unfortunately, diagnostic reflections (200, 210, 221) for the cage filling are relatively weak in this case and at the hydrate fraction as low as 20% the influence of the background features from the cell is especially strong (Fig. 67). Information retrieved from this temperature should be taken with cautiousness until a higher quality data become available. Attempts to retrieve the occupancy fraction from the pVT experiment at 193K (4.2.3) were unsuccessful. Unfortunately, the diagnostic reflections on the BW5 were strongly affected by a structured background that increases toward the center of the MAR image plate.

T [K]	Small Cage	$\sigma_{SC}$	Large Cage	$\sigma_{LC}$	Hyd.Fraction	$\sigma_{frac}$
185	0.32	0.141	0.96	0.042	0.258	0.011
190	1.09 (1)	0.082	0.95 (0.95)	0.018	0.269 (0.018)	0.004
190	0.78 (0.78)	0.059 (0.059)	1.05 (1)	0.016	0.363	0.004
195	0.80 (0.84)	0.031 (0.029)	1.14 (1)	0.007	0.815	0.001

**Table 10)** Cage occupancy for the low temperature formation experiments presented in the Fig. 101. The results from the simultaneous refinement of both types of cages are given for each temperature. Values in brackets come from the refinement of one cage type while the second one is kept fixed at full occupancy.

### 4.3 Decomposition

CO<sub>2</sub> clathrates are stable at the Martian surface only in polar regions where temperature stays below 150K (Fig. 102). At lower latitudes, in contact with atmospheric

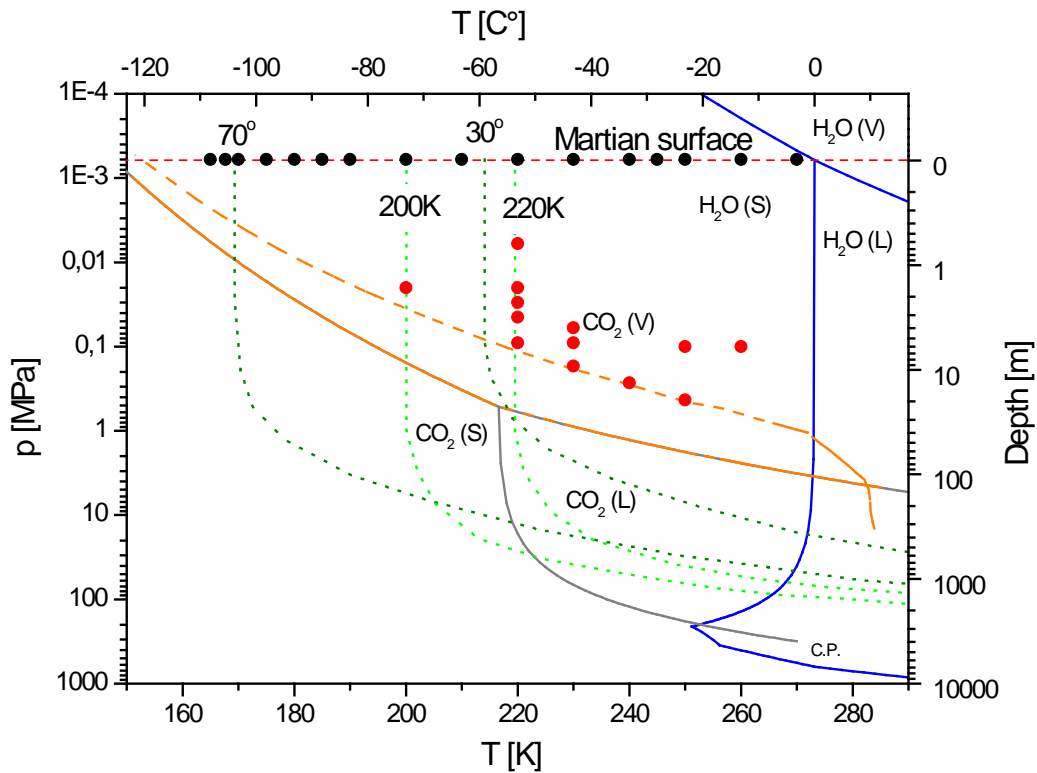


**Fig. 102)** H<sub>2</sub>O-CO<sub>2</sub> phase diagram in relation to the Martian surface and upper regolith. The red dashed line marks the averaged surface conditions. The orange field shows the p-T region where volatile CO<sub>2</sub> is in contact with ice or liquid water form CO<sub>2</sub> clathrate hydrates. Gas hydrates are stable also at greater depths in contact with solid CO<sub>2</sub> (dry ice) and liquid CO<sub>2</sub>. Dark and light green dashed lines show theoretical geotherms for selected latitudes (Kargel et al., 2000b) and temperatures (Steward and Nimmo, 2002). Black and red dots mark successful experiments that emulate decomposition at the surface and within the Martian regolith, respectively.

pressure clathrates will be destabilized. It must be clearly stated that gas hydrates most likely will decompose to water ice and free gas. Limited cases where liquid water is formed are not considered here for the reasons discussed previously (1.5.3). Most of the information presented below come from the neutron diffraction but for the same reason as in case of the formation runs additional in-house pVT experiments and interrupted runs were necessary to complete the picture (Table 11). The detailed studies of the decomposition kinetics reveal very complex behavior of reaction curves depending not only on targeted pT conditions but as well as on the duration of experiments and particle size of investigated powders. All above conditions eventually converge to one major parameter, namely the “quality” of ice cover formed from dissociating hydrates. This slightly enigmatic term encompasses crystallographic structure, stacking disorder, growth dimensionality and surface texture of ice. It is necessary to point out that all experiments were performed in a “clean” CO<sub>2</sub>-H<sub>2</sub>O system omitting the role of salts or other gases in the decomposition process.

Nr.	T [K]	p <sub>d</sub> (f) [kPa]	ln(f/f <sub>d</sub> )	Starting powder	Method	Duration [h]	Hydrate wt. frac.	SEM
1	165 <sub>ROC</sub>	0.6 (0.6)	-1.349	D <sub>2</sub> O 250μm	Neutrons	3.15	1	No**
2	167.7 <sub>ROC</sub>	0.6 (0.6)	-1.598	D <sub>2</sub> O 250μm	Neutrons	8.42	0.94	Yes
3	170	0.6 (0.6)	-1.805	D <sub>2</sub> O 250μm	Neutrons	16.34	0.66	Yes
4	175 <sub>ROC</sub>	0.6 (0.6)	-2.235	D <sub>2</sub> O 250μm	Neutrons	14.68	0.65	Yes
5	180	0.6 (0.6)	-2.641	D <sub>2</sub> O 250μm	Neutrons	12.18	0.85	Yes
6	185 <sub>ROC</sub>	0.6 (0.6)	-3.025	D <sub>2</sub> O 250μm	Neutrons	9.57	0.71	No
7	190	0.6 (0.6)	-3.387	D <sub>2</sub> O 250μm	Neutrons	10.26	0.26	No
8	200	0.6 (0.6)	-4.058	D <sub>2</sub> O 250μm	Neutrons	4.15	0.02	No
9	200 <sub>ROC</sub>	20 (19.93)	-0.555	D <sub>2</sub> O 250μm	Neutrons	1.77	0.21	No
10	210	0.6 (0.6)	-4.664	D <sub>2</sub> O 250μm	Neutrons	1.26	0.01	No
11	220	0.6 (0.6)	-5.211	D <sub>2</sub> O 250μm	Neutrons	0.80	0.02	No
11	220	6 (5.99)	-2.909	D <sub>2</sub> O 250μm	Neutrons	0.49	0.02	No
13	220*	6 (5.99)	-2.909	H <sub>2</sub> O 250μm	pVT	0.08	N/A	Yes
14	220*	6 (5.99)	-2.909	H <sub>2</sub> O 250μm	pVT	0.17	N/A	Yes
15	220	6 (5.99)	-2.909	D <sub>2</sub> O 350μm	Neutrons	0.35	0.02	No
16	220	20 (19.95)	-1.707	D <sub>2</sub> O 250μm	Neutrons	0.10	0.89	Yes
17	220 RE	20 (19.95)	-1.707	D <sub>2</sub> O 250μm	Neutrons	0.76	0.2	Yes
18	220*	20 (19.95)	-1.707	H <sub>2</sub> O 250μm	pVT	0.08	N/A	No
19	220*	20 (19.95)	-1.707	H <sub>2</sub> O 250μm	pVT	0.17	N/A	No
20	220	30 (29.88)	-1.303	H <sub>2</sub> O 350μm	pVT+ X-rays	72.32	N/A	No
21	220	45 (44.73)	-0.899	D <sub>2</sub> O 250μm	Neutrons	0.32	0.87	Yes
22	220	45 (44.73)	-0.899	H <sub>2</sub> O 350μm	pVT	72.57	N/A	No
23	220	60 (59.52)	-0.613	D <sub>2</sub> O 250μm	Neutrons	2.67	0.66	Yes

Nr.	T [K]	$p_d$ (f) [kPa]	$\ln(f/f_d)$	Starting powder	Method	Duration [h]	Hydrate wt. frac.	SEM
24	220*	60 (59.52)	-0.613	H <sub>2</sub> O 250 $\mu$ m	pVT	0.10	N/A	Yes
25	220*	60 (59.52)	-0.613	H <sub>2</sub> O 250 $\mu$ m	pVT	0.18	N/A	No
26	220	60 (59.52)	-0.613	H <sub>2</sub> O 350 $\mu$ m	pVT+ X-rays	106.73	0.33	Yes
27	220	60 (59.52)	-0.613	H <sub>2</sub> O 450 $\mu$ m	pVT	27.7d	AF	No
28	220	60 (59.52)	-0.613	H <sub>2</sub> O 750 $\mu$ m	pVT	9.26d	AF	No
29	220	90 (88.93)	-0.212	D <sub>2</sub> O 250 $\mu$ m	Neutrons	1.75	0.1	Yes
30	220*	90 (88.93)	-0.212	H <sub>2</sub> O 250 $\mu$ m	pVT	0.04	N/A	Yes
31	220*	90 (88.93)	-0.212	H <sub>2</sub> O 250 $\mu$ m	pVT	0.10	N/A	Yes
32	220*	90 (88.93)	-0.212	H <sub>2</sub> O 250 $\mu$ m	pVT	0.17	N/A	No
33	230	0.6 (0.6)	-5.713	D <sub>2</sub> O 250 $\mu$ m	Neutrons	0.18	0.02	No
34	230 <sub>ROC</sub>	60 (59.58)	-1.115	D <sub>2</sub> O 250 $\mu$ m	Neutrons	1.76	0.5	No
35	230 <sub>ROC</sub>	90 (89.06)	-0.510	D <sub>2</sub> O 250 $\mu$ m	Neutrons	1.22	0.78	Yes
36	230 <sub>ROC</sub> *	90 (89.06)	-0.510	D <sub>2</sub> O 250 $\mu$ m	Neutrons	1.47	0.75	Yes
37	230 <sub>ROC</sub>	170 (166.62)	-0.086	D <sub>2</sub> O 250 $\mu$ m	Neutrons	1.69	0.6	No
38	240	0.6 (0.6)	-6.167	D <sub>2</sub> O 250 $\mu$ m	Neutrons	0.15	0.03	No
39	240	0.6 (0.6)	-6.167	Cons.	pVT	23.19	N/A	No
40	240 <sub>ROC</sub>	170 (167.01)	-0.538	D <sub>2</sub> O 250 $\mu$ m	Neutrons	0.90	0.81	No
41	240	170 (167.01)	-0.538	H <sub>2</sub> O 250 $\mu$ m	pVT	48.39	N/A	No
42	240 <sub>ROC</sub>	270 (268.03)	-0.085	D <sub>2</sub> O 250 $\mu$ m	Neutrons	2.01	0.73	No
43	240	270 (268.03)	-0.085	H <sub>2</sub> O 250 $\mu$ m	pVT	161.65	N/A	No
44	245	0.6 (0.6)	-6.379	D <sub>2</sub> O 250 $\mu$ m	Neutrons	0.97	0.1	Yes
45	250	0.6 (0.6)	-6.582	D <sub>2</sub> O 250 $\mu$ m	Neutrons	0.77	0.09	Yes
46	250	0.6 (0.6)	-6.582	Cons.	pVT	23.17	N/A	No
47	250	0.6 (0.6)	-6.582	Cons.	pVT	499.27	N/A	No
48	250	100 (99.09)	-1.476	Cons.	pVT+ X-rays	356.04	N/A	Yes
49	250 <sub>ROC</sub>	430 (427.42)	-0.047	D <sub>2</sub> O 250 $\mu$ m	Neutrons	1.62	0.69	No
50	250	430 (427.42)	-0.047	H <sub>2</sub> O 250 $\mu$ m	pVT	28.20	N/A	No
51	250	430 (427.42)	-0.047	H <sub>2</sub> O 250 $\mu$ m	pVT	1.56	N/A	No
52	260	0.6 (0.6)	-6.967	D <sub>2</sub> O 250 $\mu$ m	Neutrons	3.19	0.07	Yes
53	260	0.6 (0.6)	-6.967	D <sub>2</sub> O 250 $\mu$ m	Neutrons	3.55	0.13	Yes
54	260	100 (99.2)	-1.851	D <sub>2</sub> O 250 $\mu$ m	Neutrons	6.41	0.69	Yes
55	270	0.6 (0.6)	-7.313	D <sub>2</sub> O 250 $\mu$ m	Neutrons	1.97	0.5	Yes

**Table 11)** List of all decomposition experiments performed in frame of this thesis. \* mark interrupted runs, \*\* denotes the sample that did not decompose at 165K and was later used in the 167.7K run. RE – repeated run, ROC- the rocking oscillating collimator was used during the experiment, d – day time scale, cons – consolidated sample. AF– Automatics failure. Electro pneumatic valves (Fig. 73) did not close the system leaving the sample exposed to vacuum.

#### 4.3.1 Starting material and sample preparation

Decomposition experiments were performed on two types of samples: well defined powders (distribution 100 $\mu$ m broad- width at the base) and “consolidated samples” of



cylindrical shape. The first type of the material was meant to deliver information about the clathrate kinetics in a broad pressure and temperature frame including particle size dependence. The natural analog for such powders could be found in more dispersed natural deposits. The second one was closing laboratory experiments to massive clathrate occurrences also found in nature. Both types were prepared from hydrogenated or deuterated ice that was crushed and sieved through 350 $\mu\text{m}$  mesh before loading into the experimental setup (3.2.2). A small particle size of starting material proved to give almost 100% transformation in a reasonably short period of time (about 2 weeks) even for large ice volume (up to  $\sim 158\text{cm}^3$ ). In order to avoid  $\text{H}_2\text{O}$  contamination of  $\text{D}_2\text{O}$  ice and consequently for deuterated clathrates the same precautions were taken as in case of formation runs (4.2.1).

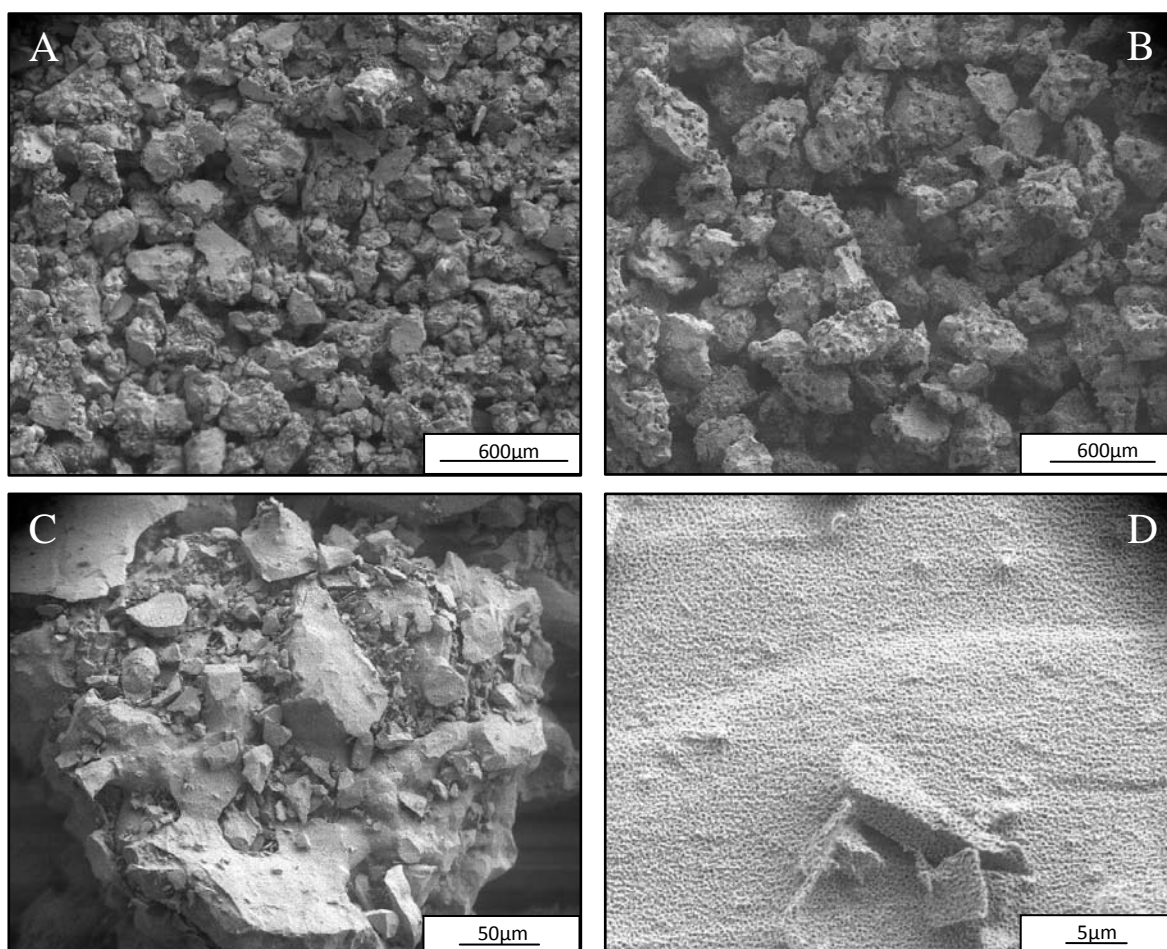


**Fig. 103)** Overview of the starting clathrate powders. A) 250 $\mu\text{m}$  fraction, B) 350 $\mu\text{m}$  fraction with the characteristic remnants of a pore network from starting ice. Images A and B are mosaics of a several snapshots to widen the field of view. C) Close up on a 250 $\mu\text{m}$  particle with a fine detritus attached to the surface, D) Clathrate sub- $\mu$  porosity well visible at higher magnification (250 $\mu\text{m}$ ) is also observed on other investigated particles. Images taken with LEO 1530 Gemini.

Powders were prepared from large clathrate cores by crushing in LN<sub>2</sub>. Grained material was sieved in a cold room under LN<sub>2</sub> through a set of meshes with a step of 100µm. For the experimental and preparatory convenience particles between 200 and 300µm (referred as 250µm) have been chosen as a standard powder. To explore grain size influence on the kinetics also a few other sizes were used (350, 450 and 750µm), (Table 11). SEM images of the powders show highly irregular particles as to be expected for crushed material (Fig. 103A, B). Porosity (diameter 20-50µm) partially visible in some particles (Fig.95B) is a remnant of a pore network in ice from the preparatory formation. The surface of individual grains is covered by small clathrate pieces (Fig. 103C) that are electrostatically charged during the sieving. This unavoidable bimodality in the particle size distribution unfortunately might influence decomposition rates at the initial stage. At higher magnifications one can clearly see, characteristic for clathrates, the sub- µm porosity (Fig. 103D).

So called “consolidated samples” (Fig. 104) similarly to previous studies (Genov, 2005) were prepared directly in aluminum vials (Fig. 68) and unfractured later used in decomposition experiments. Internal structure i.e. open and closed porosity, fracture system and finally effective a surface are of such cores is unfortunately poorly defined.

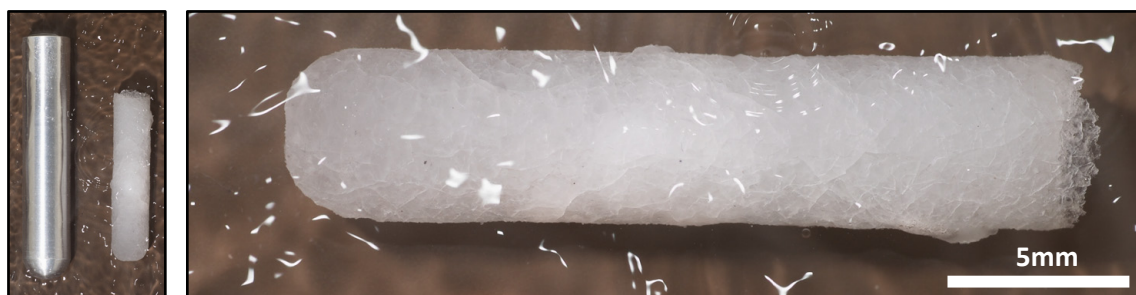


**Fig. 104)** Consolidated sample submerged in LN<sub>2</sub>. Even at this low magnification one can clearly see a network of small cracks across the consolidated core.

#### 4.3.2 Decomposition kinetics at Martian surface pressure

CO<sub>2</sub> hydrates are thermodynamically stable at the Martian surface essentially only in polar regions where temperature do not rises above ~150K (Fig.102). Towards warmer equatorial regions pressure of 6mbar (0.6kPa) is insufficiently low and clathrates become unstable in contact with the atmosphere. The kinetics of decomposition in this “unfriendly” region has been studied in a series of experiments spanning from 165 to 270K. A first look at all reaction curves (Fig. 105) reveals complicated kinetics across the whole temperature

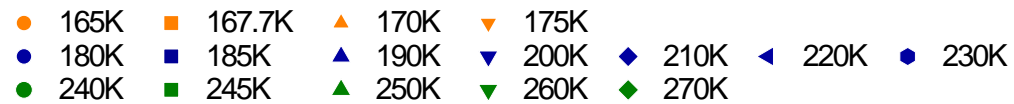
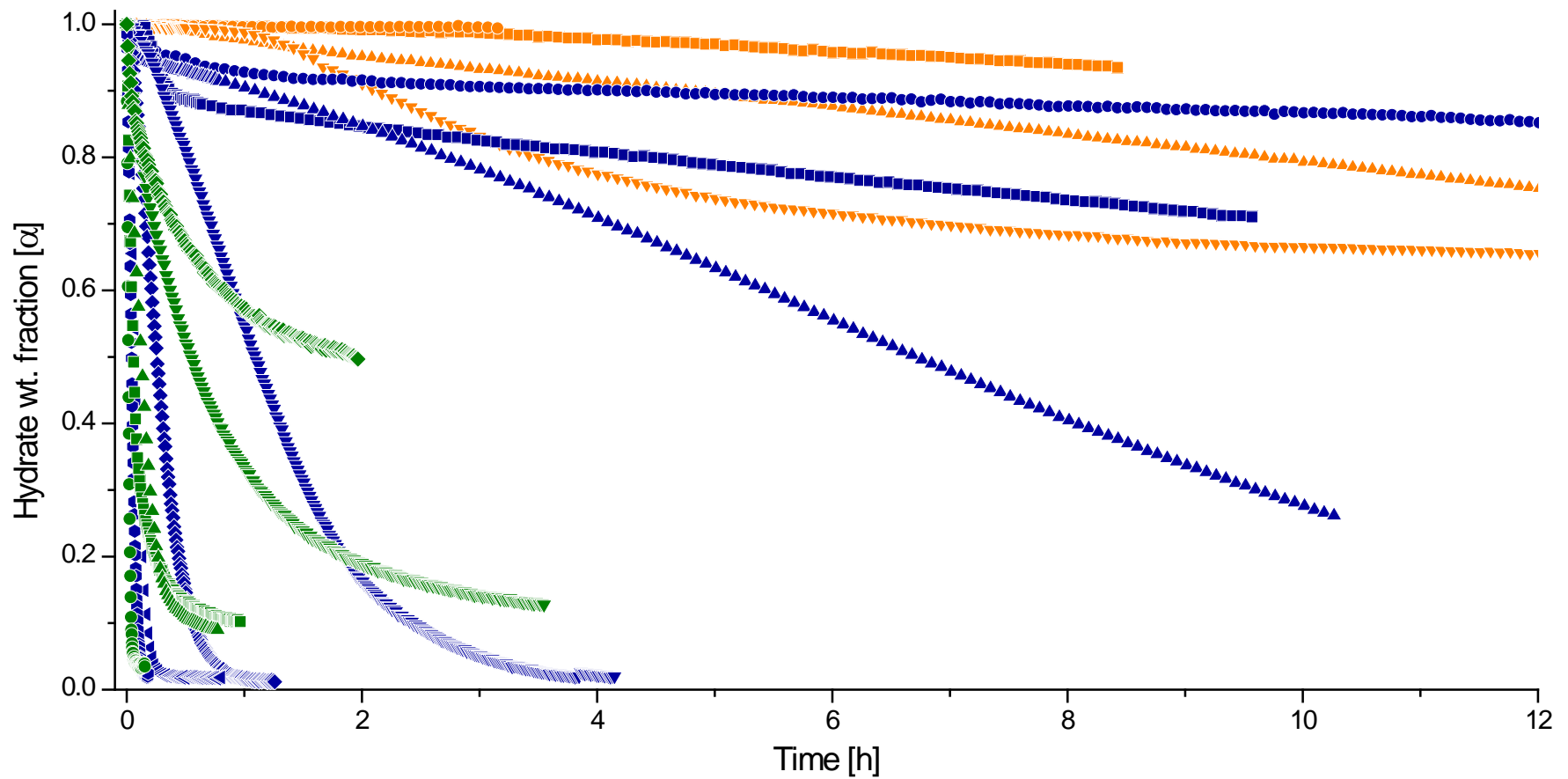
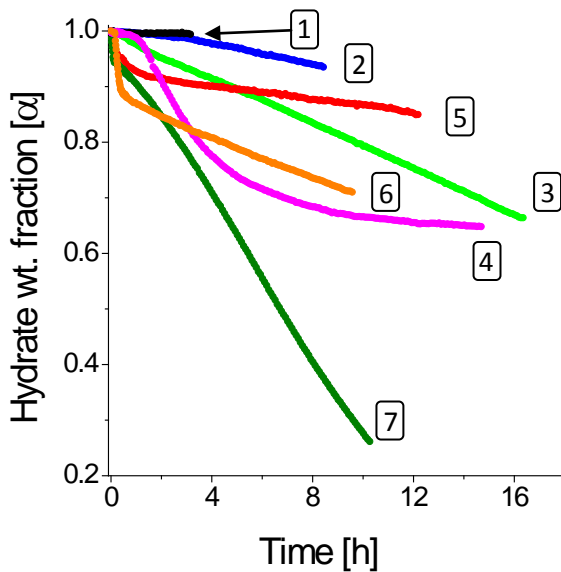


**Fig. 105)** Overview of the decomposition kinetics of CO<sub>2</sub> hydrates at the constant pressure of 6mbar (0.6kPa) relevant to Martian surface. Orange and green colors mark two regions where anomalous dissociation is observed (see text). All listed experiments were performed on 250μm powders.

range. While there is a general trend of an increase of the decomposition speed when going from 165 to 270K (Fig. 105), one can clearly see a number of anomalous curves at both ends of the investigated temperature region. To show clearly such a complex situation both groups will be presented separately. Yet, as will be shown in following subchapters (4.3.3 and 4.3.6) both phenomena have essentially the same origin.

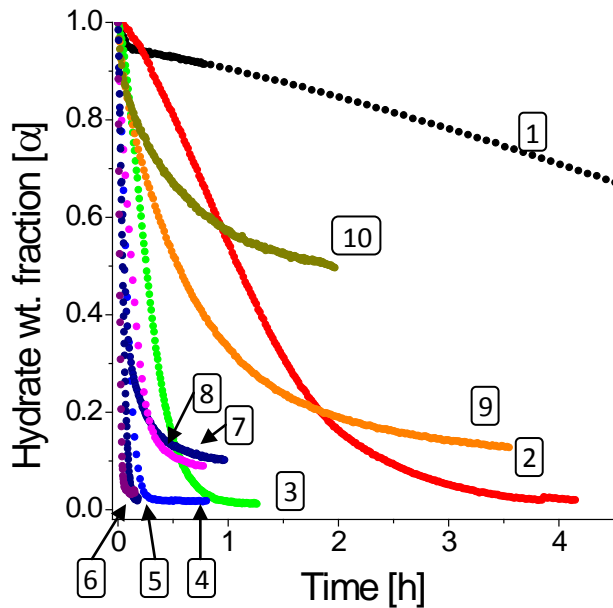
At the lower temperature end (Fig. 106) one can observe two interesting phenomena. The first one is a lack of decomposition at 165K in spite of staying outside the stability field for more than 3 hours. This rather surprising observation, which is also interesting in the Martian context, will be further analyzed in this sub-chapter 4.3.7. Since the reaction was not observed, the sample was brought back to the stability, heated up to 167.7K and destabilized again. This time clathrate weight fraction started to creep down. The second interesting, unexpected behavior of the reaction curves is observed between 170 and 180K where the decomposition at the lower temperature progresses generally faster than at the higher one. The run at 180K after a short period of rapid decomposition drastically slows



down while the one at 170K dissociate at quasi constant rate. The experiment at 175K shows a somewhat intermediate sigmoid like dissociation. Continuing from 180K towards higher temperatures the reactions accelerate as one could expect from the increasing driving force (Fig. 82). The shortest transformation period for the investigated powder samples was found at 220-230K but even then the refinement returns about 1-2% of remaining clathrates.

**Fig. 106)** Decomposition experiments emulating Martian surface conditions at higher latitudes. The runs were performed on 250 $\mu$ m CO<sub>2</sub> hydrate powders at the constant pressure of 6mbar (0.6kPa). In this temperature region one can observe two interesting phenomena; Lack of decomposition for over three hours at 165K and a transition from one dissociation regime to another one at about 185K. 1) 165K, 2) 167.7K, 3) 170K, 4) 175K, 5) 180K, 6) 185K, 7) 190K.

From about 240K the decomposition speed gradually decreases (Fig. 107). The



strongest retardation is observed at 270K where after two hours still about 50wt% of clathrates is present in the sample. This anomalous behavior is called the self-preservation that was already mentioned several times in Chapter 1. It will be discussed later more in detail (4.3.6), after presenting the whole line of observations that give an answer to its origin.

**Fig. 107)** Decomposition experiments on CO<sub>2</sub> hydrate powders of 250μm size at a constant pressure of 6mbar (0.6kPa). This set of the runs mimics the Martian surface conditions at lower latitudes. From ~240K towards higher temperatures some self-preservation is observed. 1) 190K, 2) 200K, 3) 210K, 4) 220K, 5) 230K, 6) 240K, 7) 245K, 8) 250K, 9) 260K, 10) 270K.

Evolution of the clathrate weight fraction with time provides a very useful bulk description on the decomposition process but fails to explain any of the observed anomalies. Since decomposition is a gradual consumption of clathrate particles by growing ice shell it is justified to assume that observed anomalous phenomena are related to the coating. Indeed, SEM images taken at different temperatures and stages of transformation reveal interesting details on the ice coating that forms from dissociating clathrates.

At the lowest decomposition temperature (167.7K) relatively well developed 3D ice crystals that grow at dissociating clathrates (Fig. 108A, B) indicate relatively sluggish transformation. It is in accordance with the small driving force in the system (Fig. 82) and observed decomposition speed (Fig. 106). At numerous places one can observe crystals with well visible faces (Fig. 108A-D) often marked with regular striation/kinks (Fig. 108C, D) that are a clear sign for defects in the crystal structure. The reaction was halted after reaching 6% of the transformation and the coating is far from being complete at this stage.



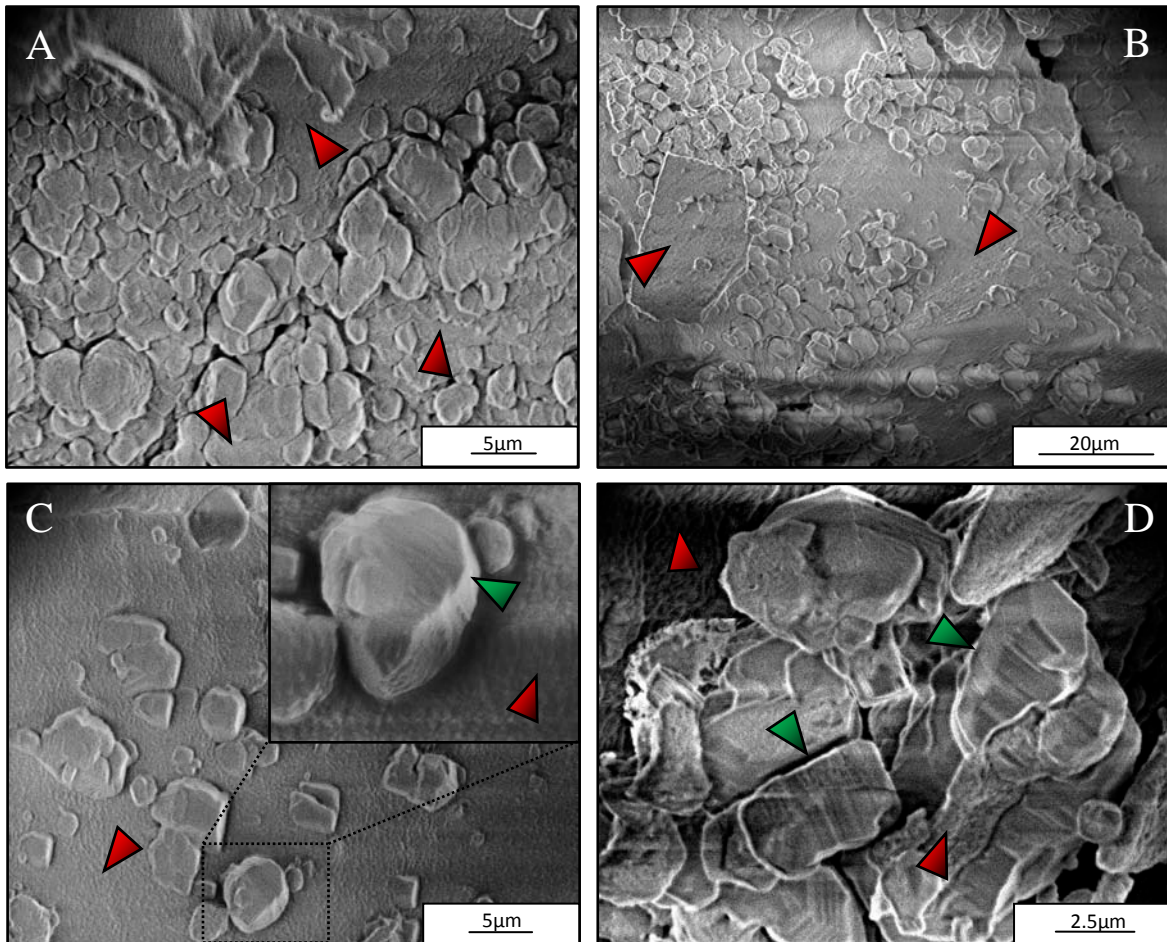


**Fig. 108)** Ice surface coating forming at 167.7K 6mbar (0.6kPa) after 8.4h. A-C) Clathrate surface (Red arrows-examples) between unevenly distributed, fairly well developed 3D ice crystals. At higher magnifications (C-left upper corner, D) One can clearly see multiple brighter and darker striation (Green arrows) on the crystal faces (most likely parallel to c axis). Snapshots from FEI Quanta 200FEG.

More evolved situation is observed at slightly higher temperature (170K) where the sample contains 34wt% of ice (Fig. 109). Fully developed ice coating is composed of a numerous small crystals with a diameter of 4-6µm (Fig. 109A). Strikingly the coverage instead of being continuous contains a large number of pores between individual ice crystals. Cross sections through broken particles indicate their presence also across the whole ice layer (Fig. 109B, C). Unfortunately, SEM as a local and surface method cannot really tell if those voids form a network or percolate to the clathrate surface on a regular basis. Even if not, the presence of empty spaces in the ice shell is likely to reduce a length of potential diffusion pathways. The thickening coating should lead to a gradual slow down of the dissociation but with such microstructure the sealing is likely to be still weak. Particles where the ice coating was mechanically removed during the sample loading show

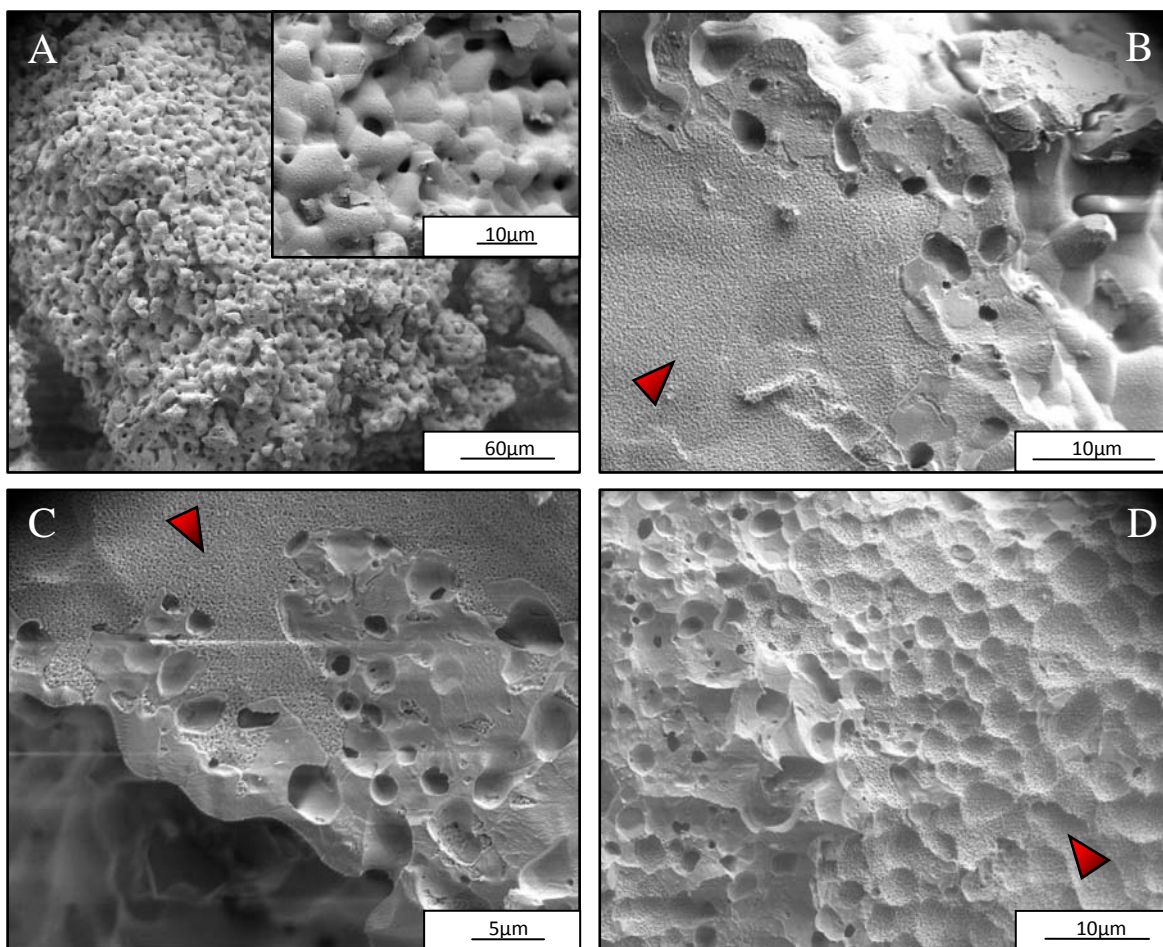


**Fig. 109)** Clathrates decomposed at 170K 6mbar (0.6kPa) after 16.3h. A) Powder particle completely covered by small ice crystals. One can clearly see a large number of pores in the coating (Yellow arrows). B, C) Images of broken surfaces that cut through the ice mantle and underlying micro porous clathrates (Red arrows), D) Clathrate surface exposed by mechanical removal of the ice coating during the sample handling. An inward growth of individual ice crystals forms characteristic depressions. Pictures taken with LEO 1530 Gemini.

a clear relief of inward growing ice crystals (Fig. 109D).

Looking at the reaction curves one would expect some differences in the ice coating that develops at 175K. Indeed, microstructures observed at lower temperatures are hardly recognizable even if the transformation degree is almost the same (Table 11). The first observable difference is found in much greater dispersion of crystal sizes. On closer inspection one can also notice that the ice film is in fact composed of two characteristic populations where smaller poorly developed crystals with a diameter of 2-3µm embay larger (6-10µm) and better shaped ones (Fig. 110A). The existence of such bimodality and its arrangement is in accordance with a behavior of the decomposition curve at this temperature. An initial considerably slow decomposition (Fig. 106) is associated to a slow



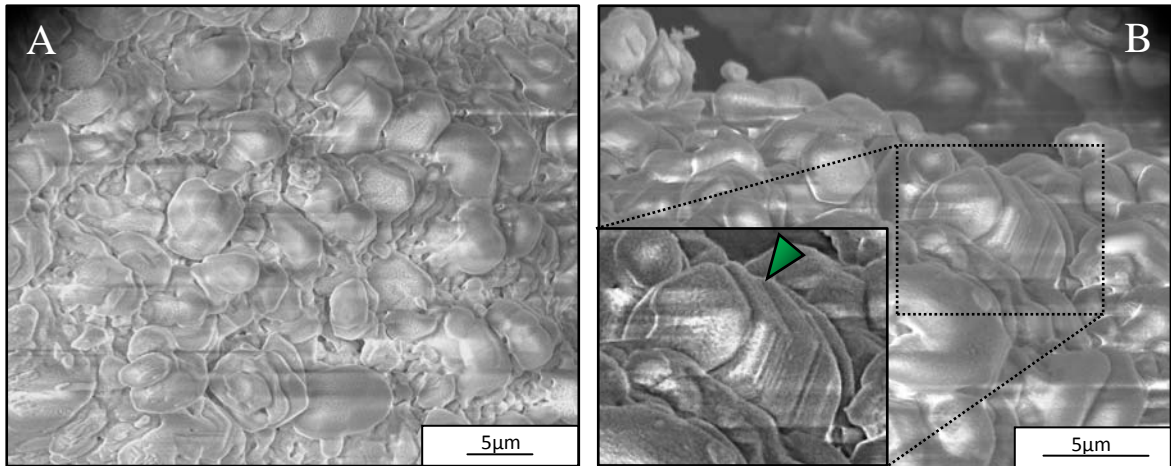


**Fig. 110)** Surface ice microstructure at 175K 6mbar (0.6kPa) after 14.7h. A) Fine, poorly developed generation of ice between larger better developed crystals. B) Ice crystals building the mantle show also signs of defects in the crystal network. Magnified section of the image has been enhanced by tuning sharpness and contrast to emphasize striation at the crystal faces. Snapshots from FEI Quanta 200FEG.

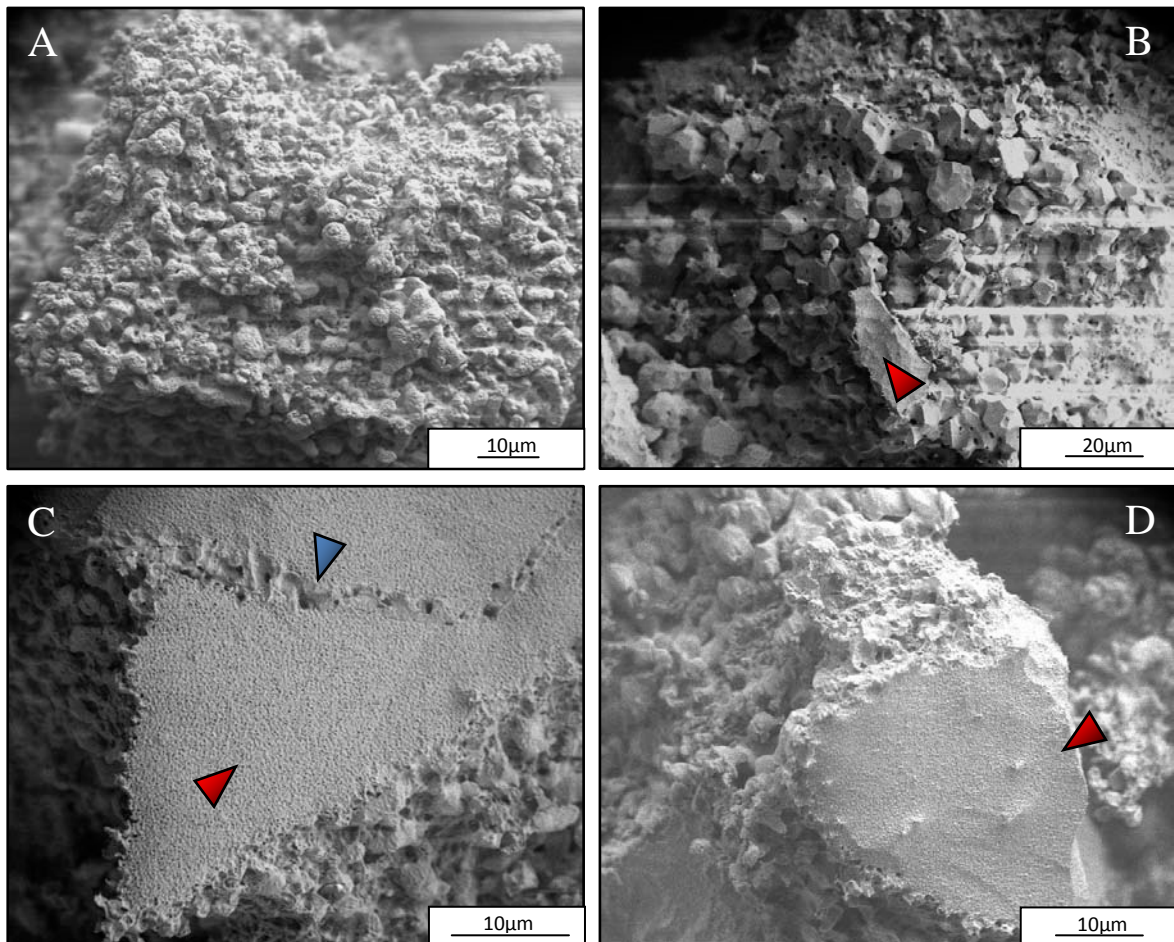


**Fig. 111)** Ice coverage formed at 180K 6mbar (0.6kPa) after 12.2h. A, B) Small, well developed ice crystals cover clathrate particles. C, D) Clathrates (Red arrows) exposed on broken faces. On the image C one can see the decomposition propagating along the fracture or grain boundary (Blue arrow). All images were taken with LEO 1530 Gemini.

growth of larger crystals like in case of the lower temperature runs. Consequently, the later gradual acceleration is reflected in the second population that apparently has formed more rapidly in free spaces of already existing coating. It is worth noticing that also in case of this sample ice crystals show signs of defects (Fig. 110B).

The experiment at 180K, which is already in a new decomposition regime, shows yet another surface microstructure. The sample was recovered at 15% of the transformation at which the coating is completed. Ice crystals that build it are fairly well developed reaching the diameter of  $\sim 3\mu\text{m}$  (Fig. 111A, B). Judging from the images of original and broken particles (Fig. 111C, D), the coverage is rather thin, quite coarse and with many voids. Exposed clathrate surface was observed only on broken faces. Since the reaction curve still indicates progressing dissociation, some way of gas out transport must be available. Unfortunately SEM imaging fails to identify the mechanism.

Microscopy images from the temperature region where another anomalous decomposition appear show much different microstructures to those discussed above. Ice crystals that build the coating tend to be larger and flatter (Fig. 112, 113). The coverage is generally tight and visibly improves with rising temperature. Starting from 245K one can already notice characteristic dome like features covering powder particles (Fig. 112A). The average diameter of those ice crystals oscillates around  $10\mu\text{m}$ . Interestingly in numerous places the surface is covered with a large number of  $1-3\mu\text{m}$  voids. They are also observed on broken surfaces cutting through the particles. The micro porosity, characteristic for clathrates, has been found on a few places where the original ice coating was fractured upon the sample preparation. At slightly higher temperature (250K) voids that were previously observed in the smooth surfaces (Fig. 112B) are less frequent but broken powder particles reveal foam-like structure beneath the upper layer of ice (Fig. 112C). Again SEM images fail to determine if individual voids are connected in the form of a network. Clathrate-like micro porous spots and islands were found to be dispersed in the ice matrix (Fig. 112D). Experiments performed at higher temperatures (260-270K) (Fig. 112E) show large similarities to the coating observed at 250K. Ice forms also a continuous mantle but a size of individual crystals visibly increases to  $\sim 40\mu\text{m}$  for the highest investigated temperature (Fig. 112F). The inner structure also evolves showing smaller number of voids and larger agglomerations of clathrates surrounded by ice (Fig. 112). The sample at 270K is the most extreme example where massive chunks of clathrates are located just below the thin ice surface layer (Fig. 113).

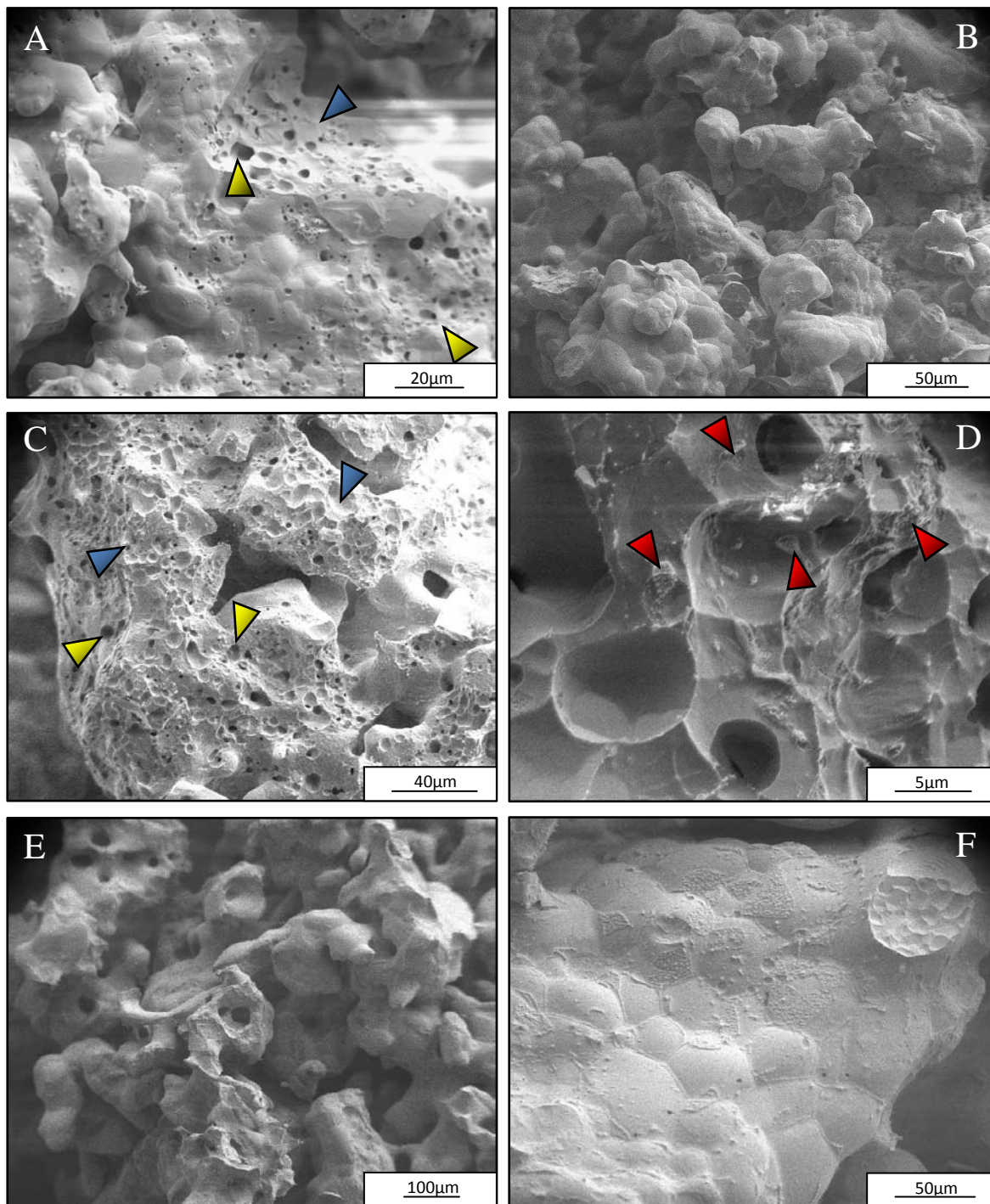


**Fig. 112)** Evolution of the ice coating during isobaric dissociation at 6mbar (0.6kPa) in the high temperature anomalous decomposition region. A) Former clathrate particle almost completely converted to ice at 245K after 1h. Smooth surface ice is covered with numerous pores (Yellow arrows). Broken surface created during the sample loading (Blue arrow) reveals also high abundance of voids within the particle, B) Ice coating at 250K after ~45min. and C) Crushed particle show similar foam-like internal structure like at 245K under the continuous ice film, D) Remaining clathrates form inclusions (Red arrows) in the ice matrix, E) Continuous surface ice mantle at 270K after ~2h, F) Ice crystals separated by well visible grain boundaries reach a diameter of 40µm. The images presented here were taken with LEO 1530 Gemini.



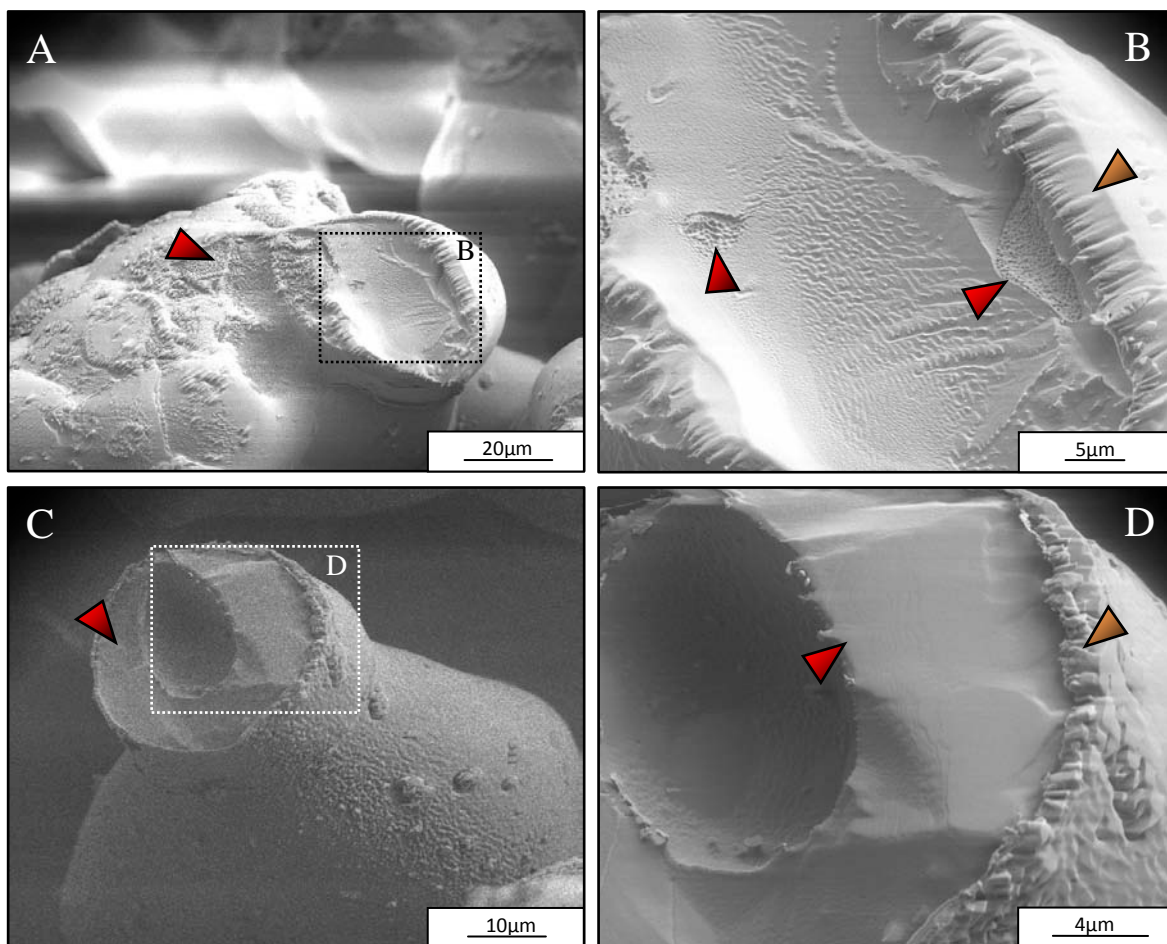


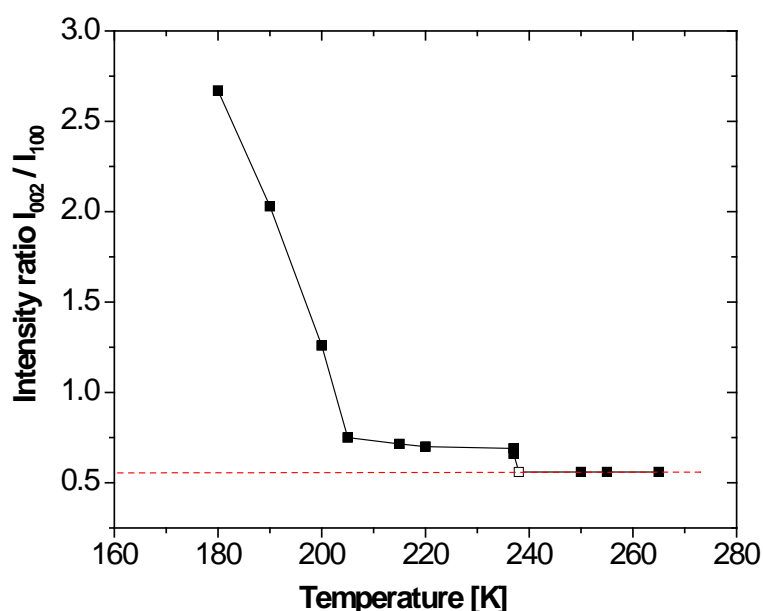
**Fig. 113)** Ice mantle developed after ~2h long decomposition at 270K 6mbar (0.6kPa). A) Clathrate particle with fractured ice coating. In places where ice has been chipped off one can observe sub- $\mu$  porous clathrates (Red arrows), B) Magnification of the previous image, aside from better resolved clathrate patches, shows also an edge of  $\sim 3\mu\text{m}$  thick ice coating (Orange arrows), C) Broken clathrate particle that shows a sharp boundary between hydrates and ice, D) Fragment of the previous image zoomed on the broken face. Unlike on the other pictures, clathrate sub- $\mu$  porosity here is very poorly visible. Observed ice film is about  $1\mu\text{m}$  thick. Images were taken with LEO 1530 Gemini.

#### 4.3.3 Cubic and defective hexagonal ices formation

SEM images presented in the previous subchapter provide an interesting correlation between the decomposition speed and microstructure of the ice coating but some observations still find no explanation. It is well visible for the low temperature anomaly where in spite of fully developed coatings the dissociation progresses quite rapidly. On the other end also unanswered remains how the thin ice film can retard decomposition so effectively. Even those questions remain, the presented observations suggest that the “quality” of the ice coverage plays principal role here.

Closer analysis of the SEM images (Fig. 108, 110) suggest that ice crystals formed at

lower temperature are contain a large number of planar faults perpendicular to the *c* axis (seen as the striation/kinks) most likely related to stacking faults (discussion of stacking faults: Petrenko and Whitworth, 1999). CO<sub>2</sub> is likely to use these imperfections in the crystal network for a quick transportation making even thicker, complete coatings semi permeable to gas molecules (Kuhs et al., 2004). Additionally, the rather small crystals and coarse coating makes diffusion even easier. Interestingly, the presence of the stacking faults in the hexagonal ABABAB sequence (Fig. 7) gives a rise to another ordering, ABCABC, which is characteristic for cubic ice (Fig. 8). If this interpretation of the SEM images is correct then the product of the decomposition is in fact a mixture of two ice phases, cubic and hexagonal. A conclusive argument for such situation is provided by preliminary results from neutron diffraction on dissociating CO<sub>2</sub> and CH<sub>4</sub> clathrates (Kuhs et al., 2004). A robust and quick diagnostic tool for stacking faults in the bulk was found in a ratio of the integrated intensities of two Ih ice Bragg reflections, namely 100 and 002. An ideal value for the hexagonal structure, although temperature dependent, is close to 0.55. The presence of the cubic stacking is reflected in somewhat higher ratios due to a 111 reflection from the cubic lattice that coincides with the 100 peak (Kuhs et al., 1987). As it was also shown, cubic stacking density quickly recovers to the hexagonal structure upon



warming (Fig. 114), which is in accordance with the SEM images presented above. The experimental annealing shows that stacking faults are persistent until about 240K that coincides with the beginning of the high temperature kinetic anomaly.

**Fig. 114)** Evolution of the  $I_{002}/I_{100}$  intensity ratio during the annealing of cubic ice. Quick annealing into the hexagonal phase is recorded from 180 to 200K but some stacking faults still remain until ~240K is reached. The ideal Ih ice ratio is shown by the dashed red line (Kuhs et al., 2004).

This thesis makes another two steps forward in the above analysis by showing the evolution of the cubic stacking density with time for the investigated temperatures from 167.7 to 250K and the first results from a modeling of the diffraction patterns developed by T. Hansen<sup>1</sup> in collaboration with our group (Hansen et al, 2008a), (Hansen et al, 2008b).

The evolution of stacking fault density and the type of stacking during the decomposition of clathrates is a complex phenomenon where two processes compete between each other. In the first on, “fresh” cubic or highly defective hexagonal ice is constantly formed at the rate corresponding to the dissociation of clathrates. The second one, the annealing, is driven by a thermally activated mobility of water molecules that visibly increases upon warming (Fig. 114). The interplay between above processes is approximately displayed in the curves of the  $I_{002}/I_{100}$  ratio ported against time (Fig. 115).

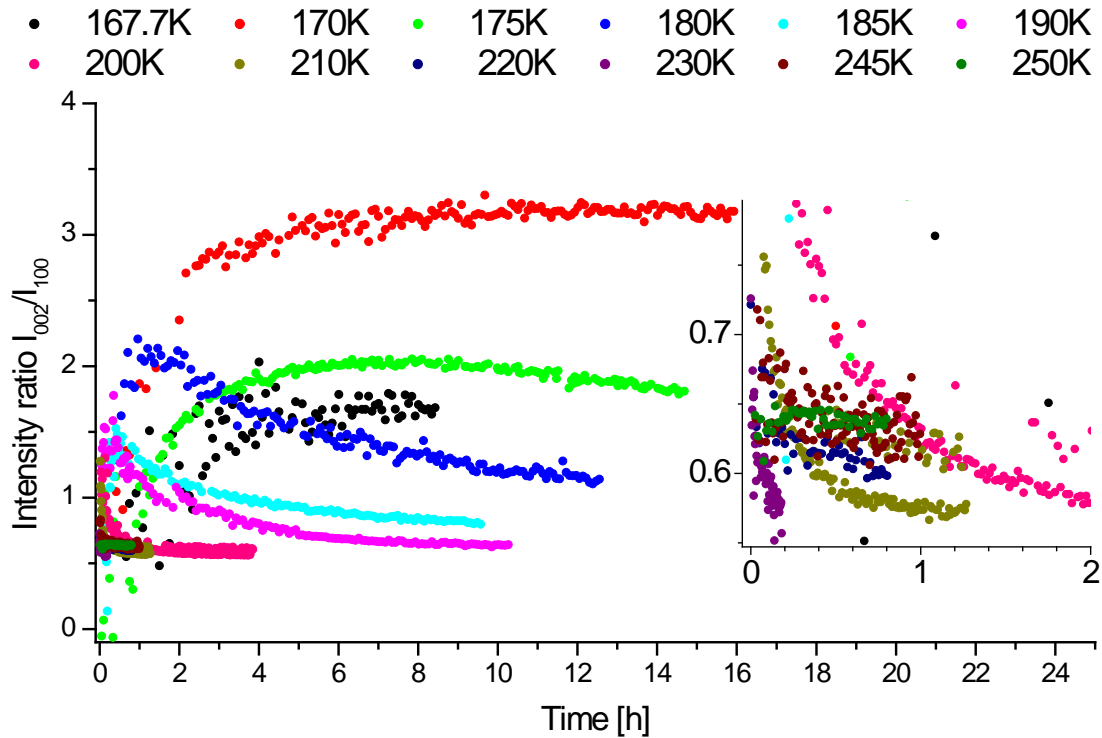


**Fig. 115)**  $I_{002}/I_{100}$  ratio for selected decomposition runs at 6mbar (0.6kPa) plotted as a function of time. Cubic sequences clearly accumulate between 167.7 and 170K. 175K run shows already an effect of the progressing annealing at the later stages. From 180K toward higher temperatures stackings formed in the initial rapid decomposition quickly recovers to the less defective ice. The highest temperature runs (210-250K) still indicate a presence of a minor cubic phase. Data scattering is caused by a fitting technique used to extract the peak intensities.

<sup>1</sup> Institut Laue-Langevin, 6 rue Jules Horowitz 38000 Grenoble, France



Starting from 167.7K the data show some scattering but the accumulation of the cubic component is clearly visible. The maximum ratio for this sample reaches about 1.6 when the annealing starts to counterbalance the further increase. Rapidly dissociating clathrates combined with a still slow annealing at the temperature just a few degrees higher (170K) deliver even more stacking faulty, cubic ice that shifts the  $I_{002}/I_{100}$  intensity ratio as high as to 3.2. Interestingly, the next sample at 175K marks already the switching point where the mobility of water molecules starts to be high enough to effectively anneal the stacking faults on the laboratory time scale. This trend is even more pronounced at the reaction curves from 180 to 200K where the recrystallization clearly accelerates. Although a very rapid decomposition still produces a cubic component, the annealing quickly recovers most of the stacking faults to the thermodynamically favored hexagonal structure. It is worth mentioning that the switching point from where annealing start to dominate coincide with the change of the decomposition speed (Fig. 106) recorded on the reaction curves in this temperature range. Ice that is formed at about 210K generally should be defined as defective hexagonal since the observed ratio is almost from the very beginning just slightly greater than the ideal one. On closer inspection one can also notice that even for 245 and 250K some small number of stacking faults is still present. Since these experiments were stopped shortly after the end of the decomposition it is justify to assume that the last portions of formed ice did not have enough time to fully recover.

Aside from the approximate “cubicity” presented above, neutron diffraction offers also other interesting information like weight fractions of the crystal phases including both ices, particle size, averaged unit cell dimensions within the limits of a diffractometer and type cubic stacking sequences. Most of these additional parameters are not readily accessible through a standard Rietveld refinement due to its inability to deal with stacking faults. This problem has been solved by integrating a cubic/hexagonal stacking generator into a classical least squared refinement implemented in the programming package IGOR. In principles, the first module is used to generate a population of theoretical ice crystals by stacking hexagonal and cubic layers up to a given height. In the second step the program calculates diffraction patterns for each stacking sequence that are further refined to fit experimental patterns. For a more detailed description of this treatment the reader should refer to an introductory publication (Hansen et al., 2007) followed by two full papers (Hansen et al., 2008a), (Hansen et al., 2008b). The model was first tested for the case of cubic and stacking faulty hexagonal ices formed from different high pressure phases of ice

(1.3), but after some adjustments also clathrates could be treated. Unfortunately, up to now only a handful of available data (170 and 180K) have been analyzed.

The treatment still requires some additional work but is already able to return a significant amount of information that until now has been beyond reach of any previous study. For the first time it is possible to extract precise scaling factors for stacking faulty ice (Fig. 116A, B) formed upon decomposition of CO<sub>2</sub> clathrates. The overall shape

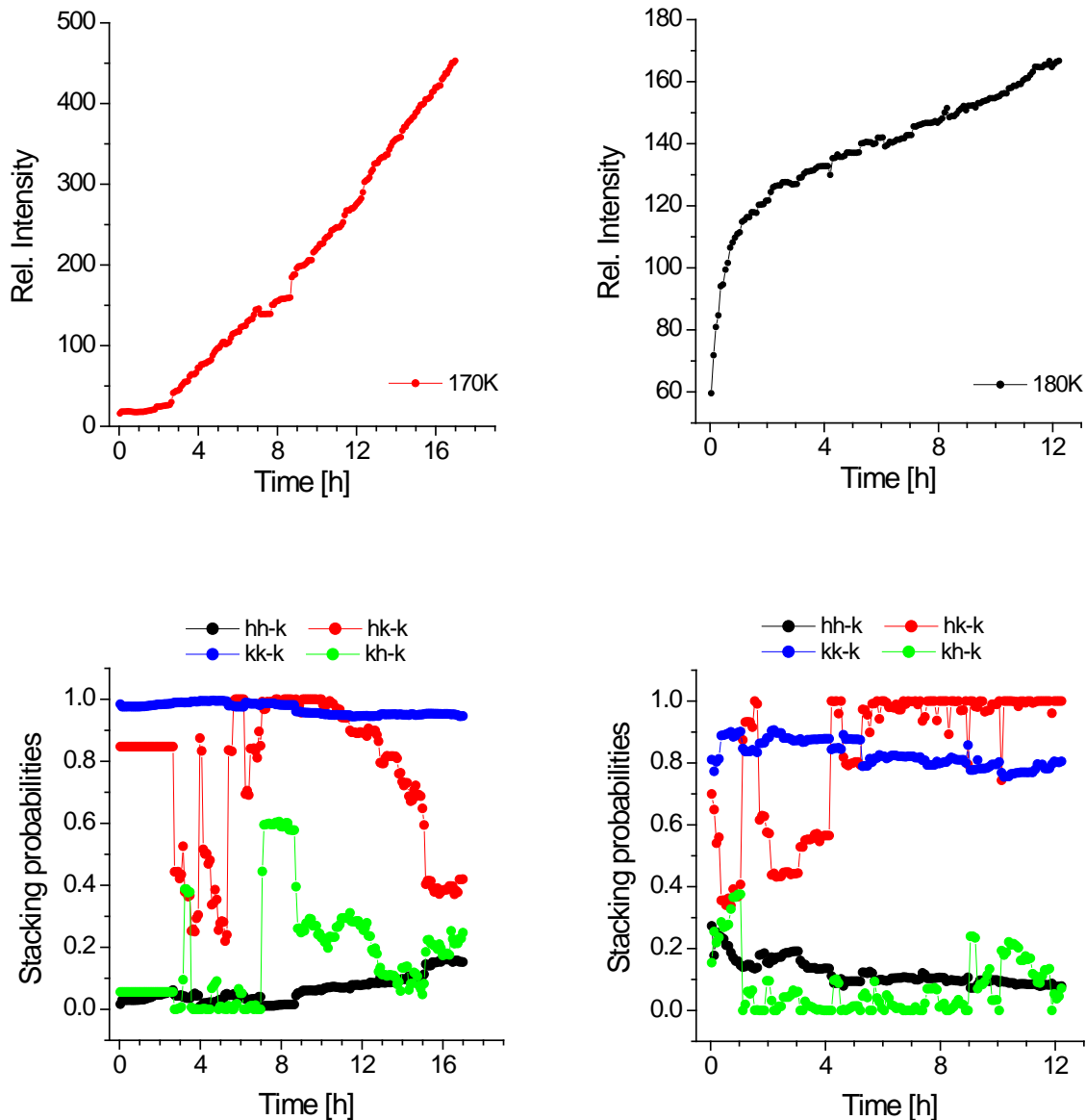


**Fig. 116)** First results from the modeling of the stacking faulty ice formed upon CO<sub>2</sub> clathrate decomposition. The first two plots show the scaling factor of ice reflections calculated for A) 170K and B) 180K. The distribution of cubic/hexagonal layers as a function of time in the C) 170K and D) 180K run expressed in probabilities of finding a cubic layer after two hexagonal (hh-k), two cubic (kk-k), hexagonal and cubic (hk-k) and cubic and hexagonal (kh-k) stacking.

of both presented curves for 170 and 180K is similar to those retrieved for clathrates in the standard refinement (Fig. 106) but a closer comparison must wait until the new data will be recalculated to weighted phase fractions. The new modeling offers also very unique insight in a distribution and evolution of cubic and hexagonal stacking sequence with time (Fig. 116C, D). In both analyzed experiments the probability of finding packets of cubic layers decreases with time, which generally reflects the annealing also observed in the  $I_{002}/I_{100}$  ratio (Fig. 115). Interestingly, a change towards shorter sequences is more pronounced on the lower temperature decomposition run. It should be pointed out that through such arrangement more possible diffusion pathways are introduced into the ice coating. A similar difference may be found in the probability to find a cubic layer after larger hexagonal packets. The dissociation at 180K favors such a situation quite in contrast to the 170K case where the sequence seems to be characterized by smaller cubic units. Unfortunately, due to the limited data quality and correlations between the parameters this picture is considerably blurred. Aside from the stacking distribution the model provides also very interesting information on the position of oxygen atoms in the layers reflected in the ratio of  $a$  and  $c$  of the elementary unit. As it can be seen below (Fig. 117A), for both experimental runs the  $a/c$  ratio evolves toward higher values approaching the ideal cubic value. The decomposition at 170K clearly shows initially a larger deviation from ideal

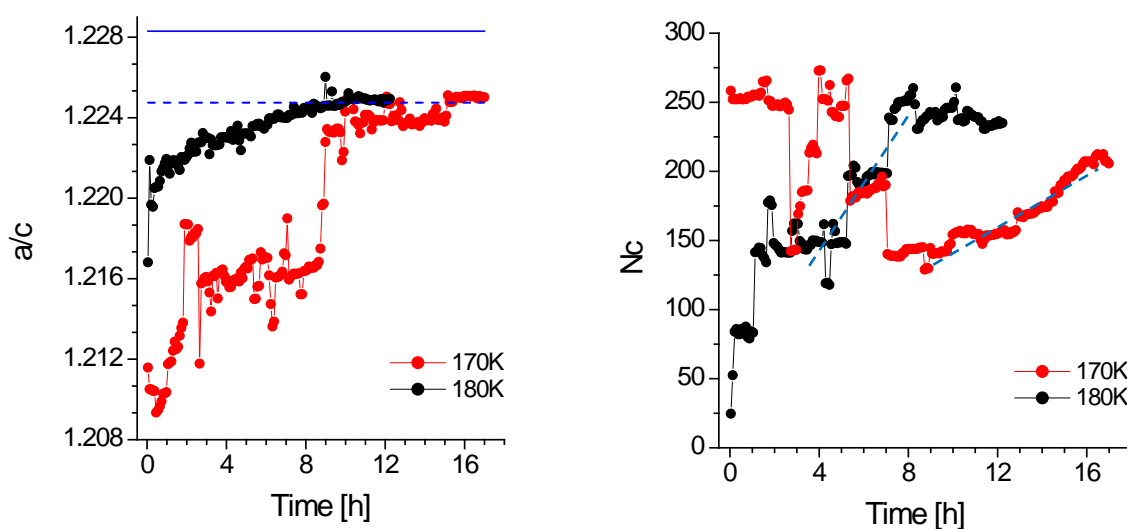


**Fig. 117)** Second set of data retrieved from the modeling. A) Evolution of the  $c/a$  ratio at 170 and 180K that clearly indicates a lower initial packing in formed ice and slow recovery with time. Blue dashed and solid lines mark the ideal packing for the cubic and hexagonal structures, respectively, B) First attempts to establish a change of the crystal size as a function of time. Unfortunately analyzed data have too low resolution for the smallest particles. The most credible fragments are marked by the dashed blue lines.

values than the 180K run but both of them eventually reach a similar plateau at about 1.2249. Interestingly this value is closer to the packing found in the ideal cubic (1.22475) not hexagonal ice (1.2283 - recalculated for a trigonal unit cell, based on: Röttger et al. 1994). This observation will be a subject of further investigations. The last information presented here, an evolution of the crystal size along the  $c$  axis (Fig. 117B) touches already the limits of our data that were taken not in the high resolution but high flux mode of D20 (favorable for kinetic studies). In these settings crystals smaller than  $\sim 140\text{\AA}$  are difficult to resolve, which is particularly well visible for the experiment at 170K. The upper limit on  $\sim 260\text{\AA}$  is set by the configuration of D20 (wavelength, take off angle, collimation). Even if the data are quite scattered, especially closer to the beginning of the runs, one can still see a trend for both experiments. The size increase is most pronounced for 180K, which is to be expected for a higher temperature experiment.

#### 4.3.4 Decomposition kinetics within Martian regolith pressure range

Experiments from this group (Fig. 102 - red dots) explore the decomposition process at target pressures between the stability boundary and 6mbar (0.6kPa) found at the surface. Surprisingly, some of the early runs follow unexpected kinetics that leads the decomposition to an abrupt slow down. This previously unknown phenomenon was further explored in a broad p-T range with the help of SEM and diffraction methods.

At higher decomposition pressures the driving force is visibly lower (Fig. 82), which should be also reflected in slower kinetics. As previously, aside from this p-T dependent parameter (4.3.3) the reactions are also strongly influenced by the interplay between the cubic ice formation and annealing. In order to show the role of the fugacity in the decomposition process it was necessary to find a temperature region where two other phenomena are balancing each other, thus decreasing their total impact on the reaction. The previously presented analysis suggests that the desired conditions may be found between 210 and 230K where freshly formed cubic ice is quickly transformed into the stacking faulty hexagonal one (Fig. 115) but the annealing still do not cause any noticeable anomaly like observed above 240K (Fig. 107). Surprisingly, a series of the decomposition runs at 220K did not show a regular deceleration of the decomposition as a function of increasing fugacity (Fig. 118). Instead, one can clearly observe anomalous curves at 450 and 600mbar (45 and 60kPa), that after a rapid dissociation abruptly slow down. The decomposition is still proceeding on but on much lower rate. The peak of the anomaly was found

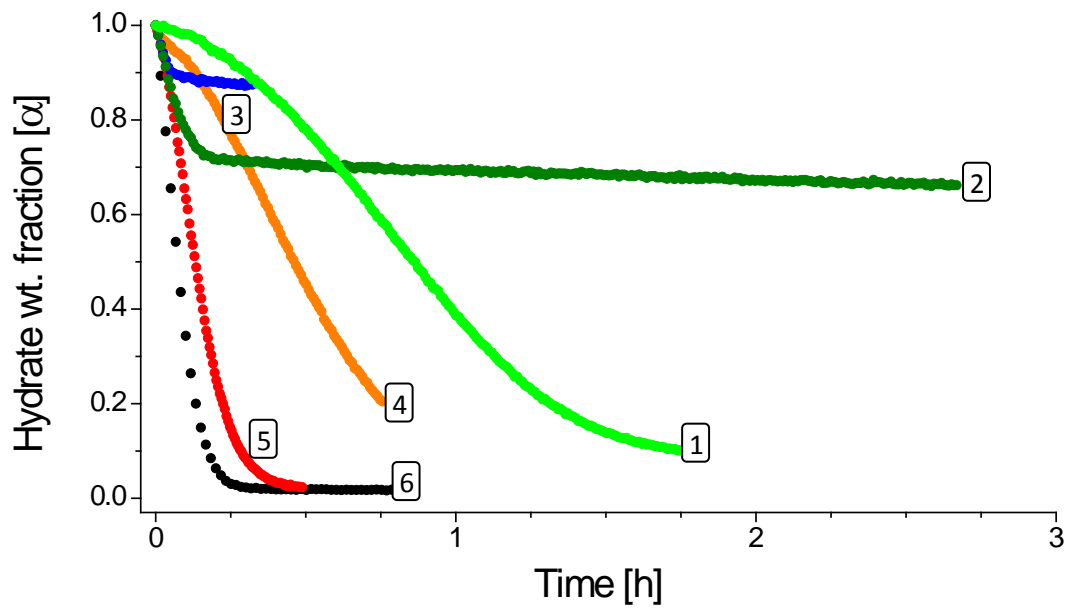


**Fig. 118)** Series of the decomposition experiments at 220K and pressure of: 1) 900mabr (90kPa), 2) 600mbar (60kPa), 3) 450mbar (45kPa), 4) 200mbar (20kPa), 5) 60mbar (6kPa) and 6) 6mbar (0.6kPa). The anomalous decomposition can be seen on the curves from 2 to 4. The strongest retardation is recorded for 450mbar (45kPa). CO<sub>2</sub> clathrates at 220K require ~1120mbar (112kPa) of gas for stabilization.

close to 450mbar (45kPa) where after ~30min as much as 87wt% of clathrates remains (Table 11). After a closer look one can also notice a rather unusually slow initial transformation at 200mbar (20kPa) that is most likely related to the same effect but in decreased form. Later, the reaction follows a typical sigmoid like curve similarly to unaffected runs at 900, 60 and 6mbar (90, 6 and 0.6kPa). The kinetic anomaly observed at the intermediate pressures creates quite a serious problem since there is no known mechanism that could cause it. The annealing that shows its strength at higher temperatures here is still too slow and its speed is unrelated to the driving force. The cubic or stacking faulty ice formation would lead to the accumulation of defects mostly at lower decomposition pressures, which still do not explain why the anomaly is found at the intermediate pressures. The time resolved stacking fault density evolution for the experiments at 220K (Fig. 119) not only does not show any unusually high perfection of ices in the anomalous runs but in fact indicate elevated values of the  $I_{002}/I_{100}$  ratio. It is particularly visible for the dissociation at 600mbar (60kPa) where the density of cubic stacking is the highest from all plotted runs. Interestingly the experiments at 60 and 6mbar (6 and 0.6kPa) that required the least time for the transformation show clearly the highest ice perfection.

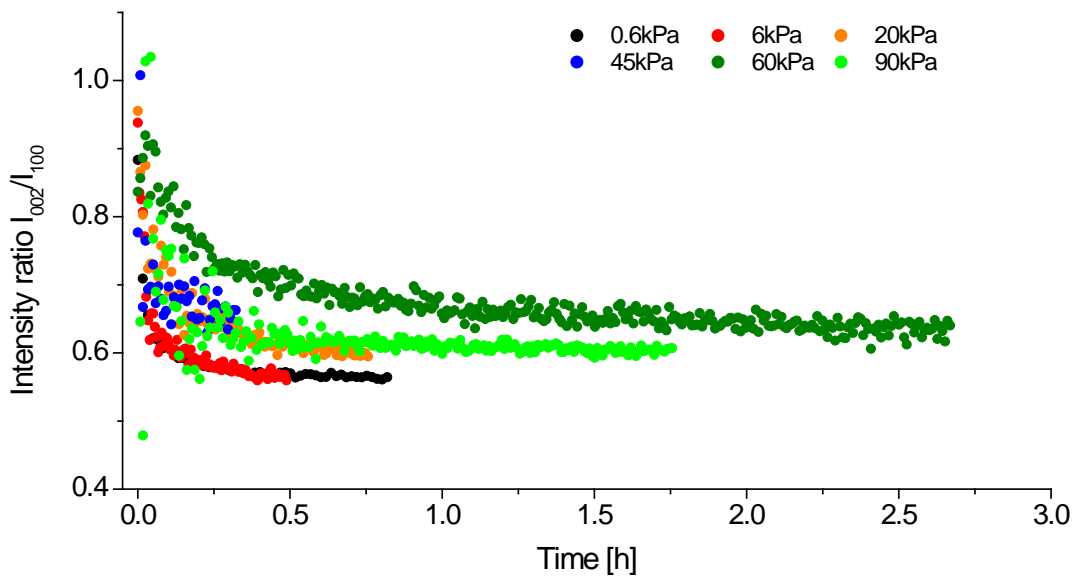


**Fig. 119)**  $I_{002}/I_{100}$  ratio for six experimental runs at 220K (The color coding is identical the one used in the figure 109). Two experiments at the lowest target pressures indicate the highest ice perfection in contrary to the anomalous runs that show elevated stacking fault densities. The lowest quality is found at 600mbar (60kPa).

Although the analysis presented above do not provide any firm connection between the ice coating and the origin of the kinetic anomaly, it is still reasonable to assume that this phenomenon is related to this layer. The quality of ice that was the key process in the

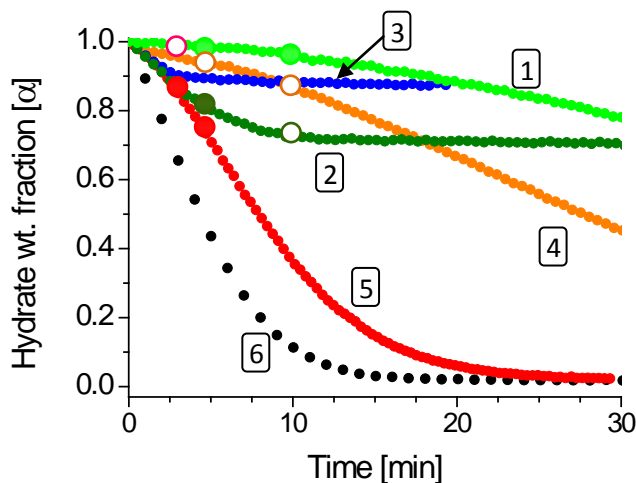


**Fig. 120)** Close up on the initial fragment of the decomposition experiments at 220K from the figure 109 (The numbering and color coding is kept identical to the original plot). The recovery point of the interrupted runs is marked by solid (analyzed under SEM) and open (not yet analyzed) large circles.

previous case (4.3.3) here seems to be of secondary importance affecting dissociation rates at later stages. An identification of the mechanism that leads to this anomalous decomposition requires additional information on surface microstructures that may be provided by SEM images taken at various stages of the reaction. Samples were obtained in a number of very short interrupted runs for selected target pressures (Fig. 120) believed to be characteristic for



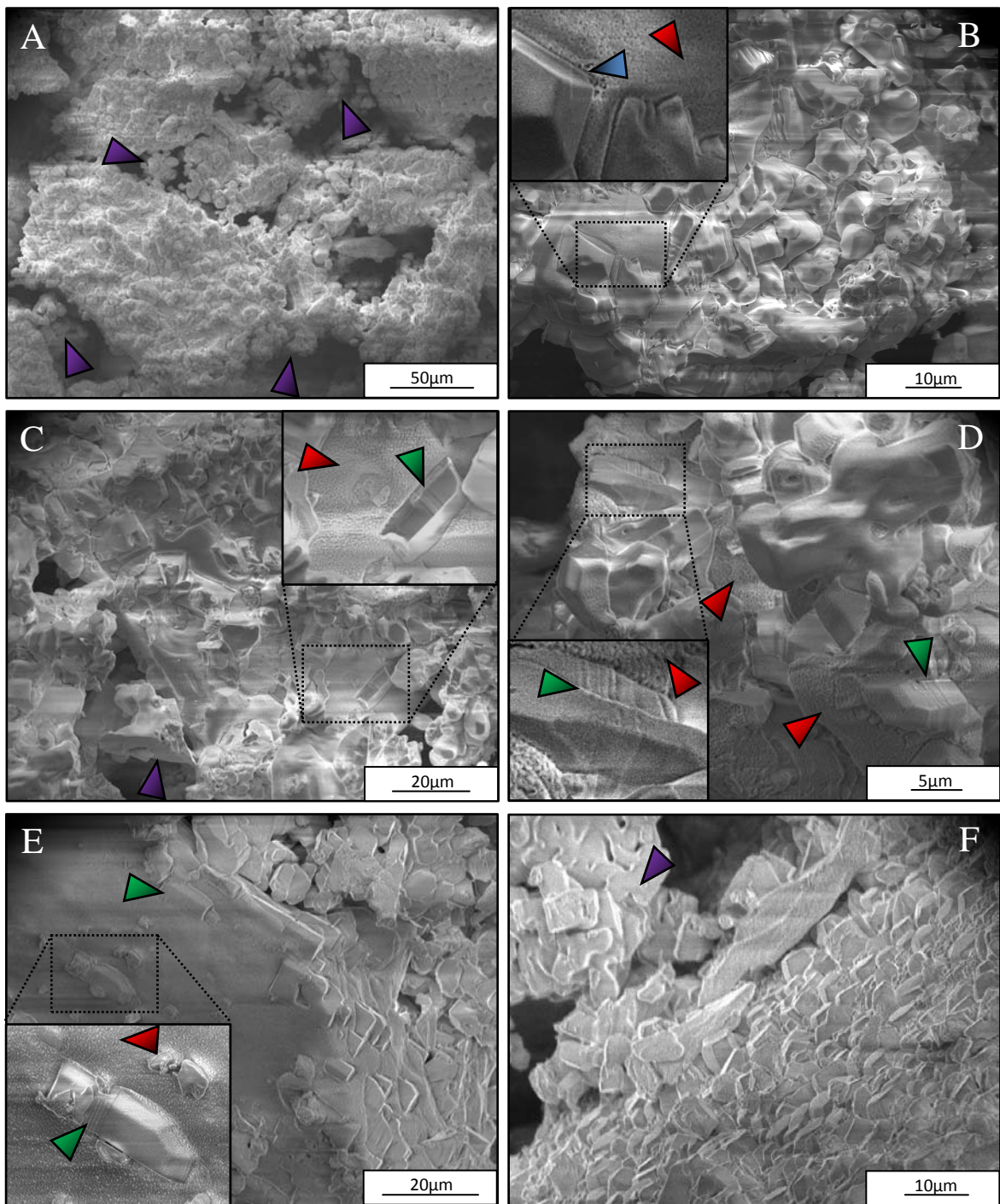


**Fig. 121)** SEM images (FEI Quanta 200FEG) from the sample recovered after 5 (A-D) and 10min (E-F) long decomposition at 220K and 900mbar (90kPa). A) General view on clathrate grains covered by ice crystals. Smaller hydrate particles that were also found in the starting material (Fig. 103C) fully transform into ice (Violet arrows) that fill pore spaces and/or stick to larger grains, B) Between fairly well developed ice crystals one can observe sub- $\mu$  porosity characteristic for clathrates (Red arrows), along the clathrate/ice interface one can observed a shallow depression (Blue arrow), C-E) A number of ice crystals shows signs of planar defects frequently observed on prismatic planes as characteristic kinks perpendicular to the  $c$  axis (Green arrows), E) After 10 minutes long reaction some areas still remain partially covered but F) the full coating becomes more common. Additional images can be found in the Appendix 10.

the pressure regions above within and under the kinetic anomaly. Unfortunately, this method that proved to be very effective in case of the formation experiments (4.2.2) here meets considerable technical difficulties and probing very fast decomposition experiments was found to be very challenging. Consequently, the shortest feasible runs were restricted to about two minutes. Although some of the interrupted runs still should be analyzed under SEM (Fig. 120), the gathered information appears sufficient for solving the issue of the discussed kinetic anomaly.

Images taken after 5 minutes long decomposition at 900mbar (90kPa) reveal a microstructure characteristic for the slow transformation (Fig. 121), which is in accordance with a shape of the recorded curve in this time period (Fig. 118). Ice crystals are well developed with frequently visible basal and prismatic planes (Fig. 121B-D). On close ups one can also notice some stacking faults appearing as striation/kinks perpendicular to the c axis (Fig. 121C-D). The average crystal size is about 5-10 $\mu\text{m}$  but also larger examples, up to 20 $\mu\text{m}$  are observed. The ice coverage is inhomogeneous and in a numerous places one can still observe an exposed clathrate surface with its characteristic sub- $\mu$  porosity (Fig. 121B-D). The commonly observed depression on the ice/clathrate interface (Fig. 121B) suggests an inward growth. A sample decomposed five minutes longer show fairly similar development (Fig. 121E) but in some places the coverage seems to be complete (Fig. 121F). Individual crystals still have well distinguishable faces and their arrangement in the

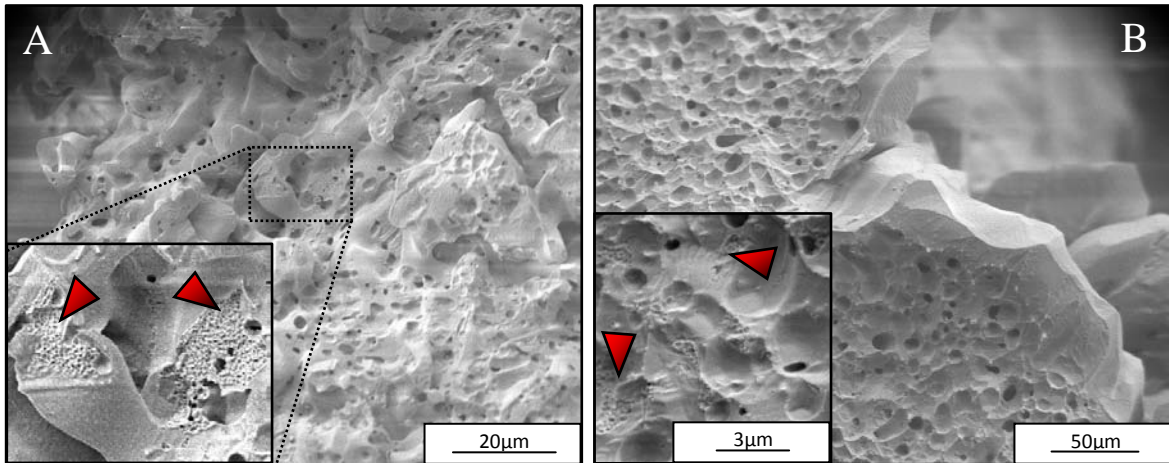


**Fig. 122)** Frozen-in visualization of the sample recovered at the end of the neutron diffraction experiment at 220K and 900mbar (90kPa). A) Slow recrystallization leads to a partial smoothing of the ice surface. The mantle is discontinued by multiple pores of different size, B) Broken surfaces reveal a foam like internal structure probably caused by the difference in the density between water ice and clathrate. At higher magnifications one can still find small patches of clathrates within the ice matrix and on fractured surfaces (Red arrows). Images taken with LEO 1530 Gemini.



cover does not create a continuous layer. The microstructure found in a sample recovered from an almost two hours long neutron experiment shows already quite advanced changes in the microstructure. Ice crystals at the surface are more rounded creating a smooth mantle discontinued by a large number of voids (Fig. 122A) that bears some resemblance to the one observed at higher temperatures e.g. (Fig. 112A). Another similarity is found in the foam like internal structure revealed on broken surfaces that cut through former clathrate particles (Fig. 122B). Small hydrate like inclusions with sub- $\mu$  porosity are found dispersed in the ice matrix and a few places at the surface where the coverage was mechanically

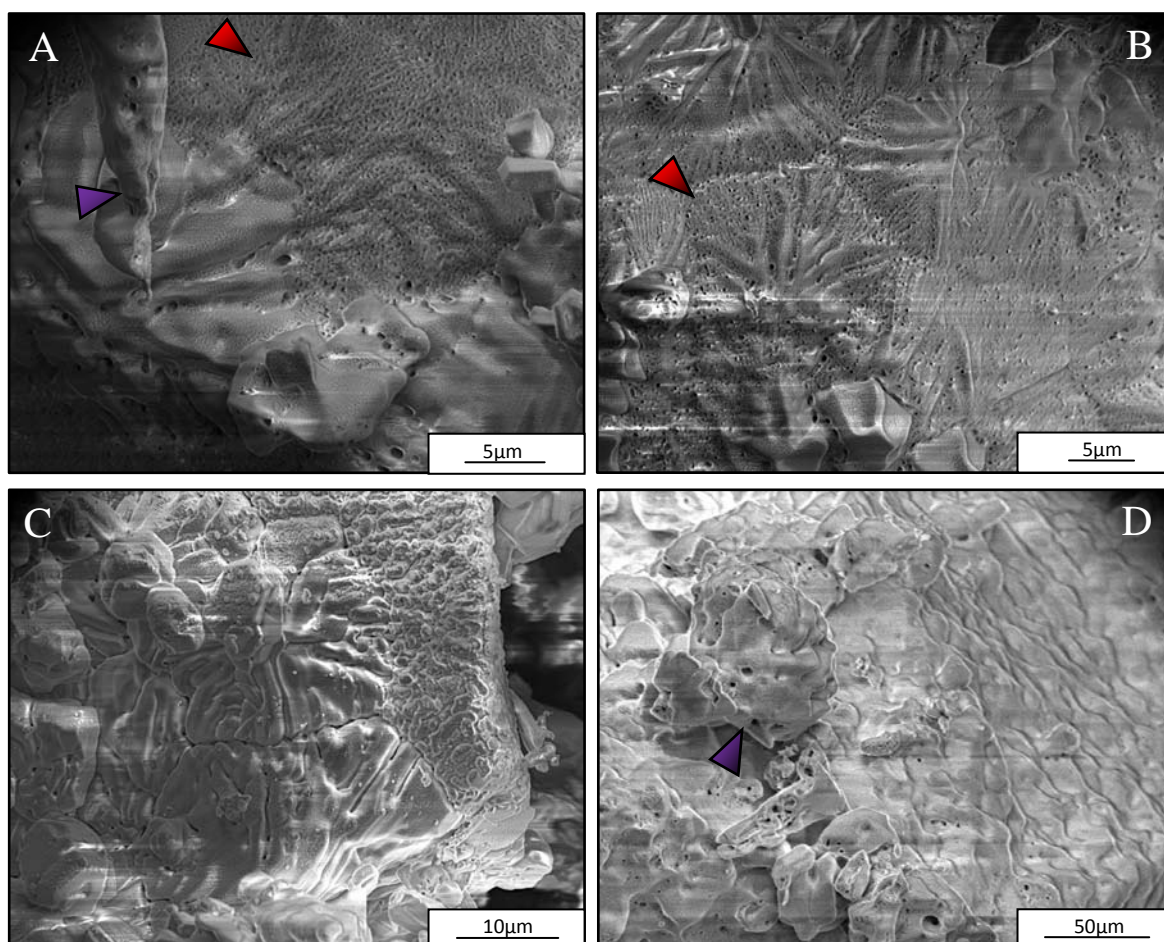


**Fig. 123)** Heterogeneous ice coating developed after 5min at 220K and 600mbar (60kPa). Fine clathrate detritus attached to the powder particles in all cases show nearly full surface transformation (Violet arrow) A) Ice crystallites cover only a small fragment of the hydrate particle (Red arrow) , B) At more advanced stage the coating is composed of ice crystals spreading across the hole surface. Near to the grain boundaries one can still see some remnants of clathrate surface between ice dendrites, C) Thickening ice film completely covers underlying clathrates but boundaries between individual crystals are still sharp, D) The final, fully developed coating retains traces of individual crystals but most of the fine details disappear in favor of a smooth, undulated surface. Images from FEI Quanta 200FEG. Other images from this experiment can be found in the Appendix 10.

removed during the sample handling.

Samples decomposed in the anomalous region (600mbar/60kPa), as it is to be expected, are characterized by different surface microstructures than those shown previously. The ice coverage is strongly heterogeneous. Images taken after a decomposition period of approximately 5 minutes represent a full spectrum of possible coatings, from very initial, fragmentary to fully developed, continuous layers (Fig. 123). Already at this point one can safely assume that in the mature state surface ice is very likely to provide much better protection for unstable clathrates than in case of the decomposition at 900mbar (90kPa). On closer inspection, the surface microstructure

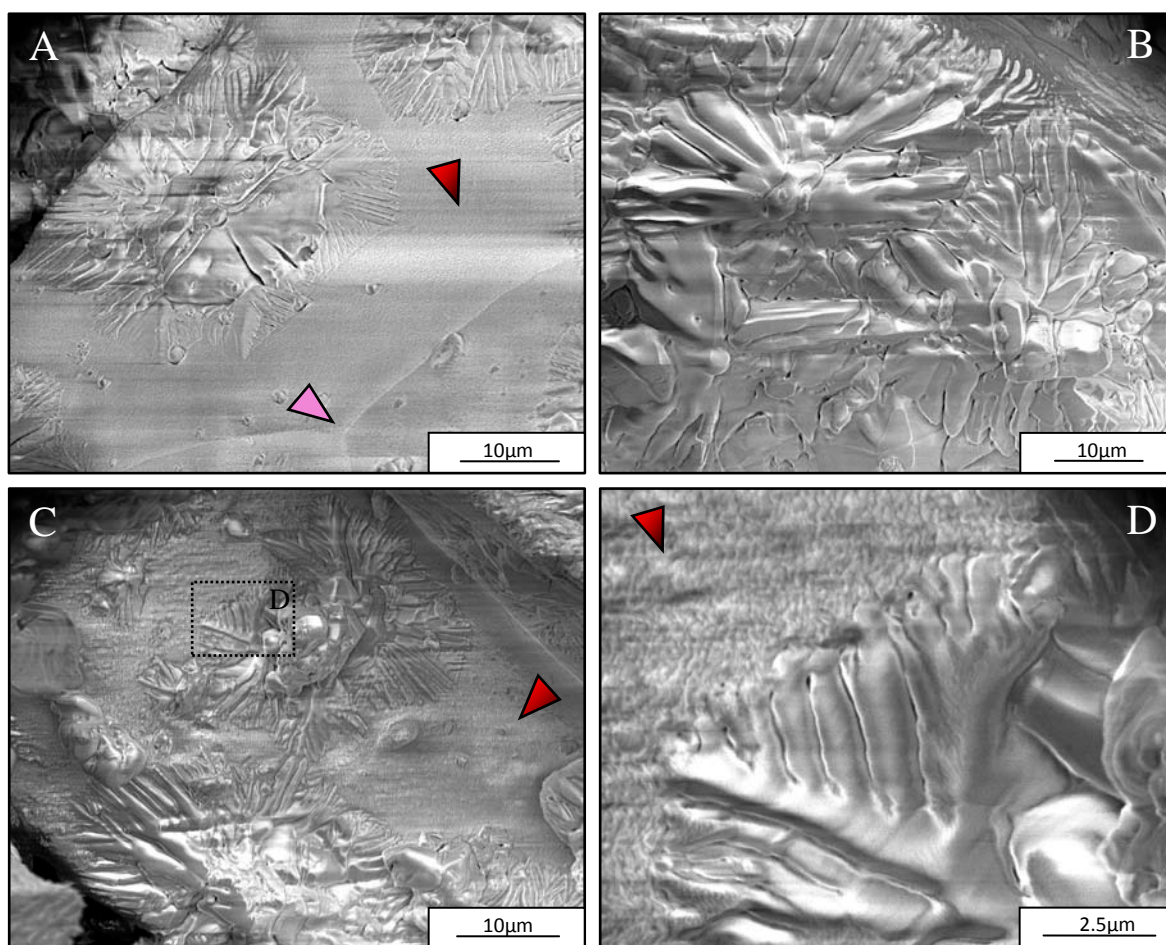


**Fig. 124)** Individual pancake like ice crystallites and their agglomerations found on clathrate surface (Red arrows) after 5min long decomposition at 220K and 600mbar (60kPa). A) Single ice crystallite with a well distinguishable central consolidated core and dendritically spreading fronts. At lower part of the image one can see also a triple junction between clathrate crystals (Pink arrow). B) Hydrate particle completely covered by a population of preferentially 2D ice crystallites, C) Two ice crystallites that indicate a mixed 3D/2D growth (central part from surrounded by a thin ice film), D) Magnification of the spreading front that reveals a complex dendritic development. Images from FEI Quanta 200FEG.

indicates a preferential fast, 2D growth, which is in agreement with a fast initial transformation shown in the neutron diffraction data (Fig. 120). Most of the observed crystallites have pancake or disk like shape (Fig. 124) where one can fairly easily distinguish centers from which ice grows in a dendritic manner. Some close-ups though suggest that some features are indeed single crystals (Fig. 124B, D). The typical size of the observed features is 15-20 $\mu\text{m}$ . Again, the sample recovered at the end of nearly 3 hours long neutron diffraction experiment reveals already advanced recrystallization of the ice layer (Fig. 125). One can still see some similarities with the full coverage observed after 5min (Fig. 123D) but ice crystals tend to be better developed in three dimensions (Fig. 125A). In spite of the coarsening, the ice layer seems to be very tight at the surface and only a handful of small pores could be found. Other interesting information is provided by broken surfaces (Fig. 125B) that cut through the powder particles containing still about 66wt% of clathrates. Remaining hydrates are clearly separated from the surrounding coating by a sharp interface. Ice layer has also characteristic foam like internal structure but it seem to be denser than in previous cases. Its thickness varies from one place to another hindering any reliable estimation.

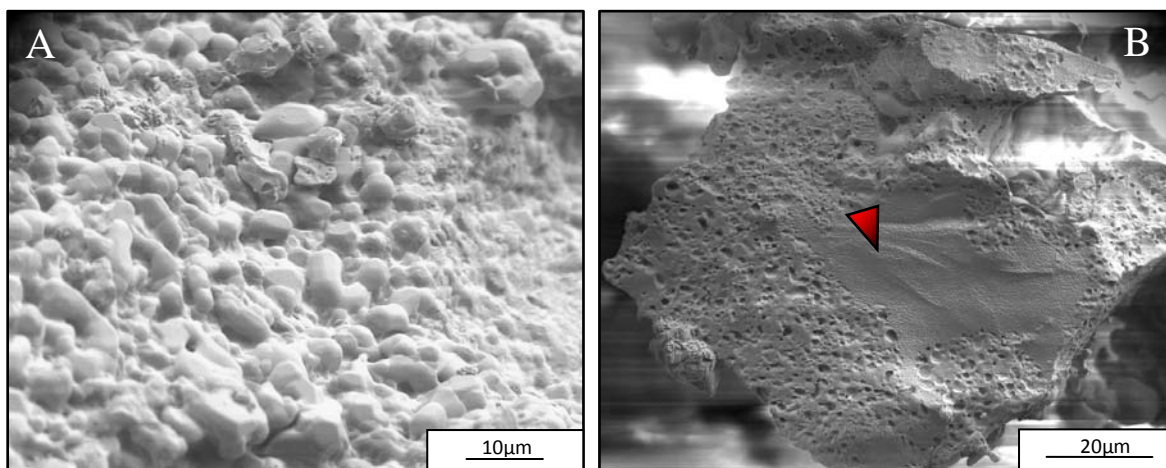


**Fig. 125)** Ice coating observed after nearly 3h of decomposition at 220K and 600mbar (60kPa). A) Partial coarsened surface ice is composed of a numerous idiomorphic small crystals with a diameter from 2 to 10 $\mu\text{m}$ . The layer is visually coarser than at the earlier stage (Fig. 123D), B) Surface of a broken particle that shows remaining clathrates (Red arrow) surrounded by an ice film with a characteristic foam like internal structure. Pictures taken with LEO 1530 Gemini.

A surface ice coating that is forming under even greater driving force than previously is not causing any apparent hindrance for decomposition (Fig. 120). It is rather surprising since one could expect an even more rapid coating formation as in the anomalous region



due to the rising driving force. Clathrates decomposed in two, 2 and 5 min. long runs performed at 220K and 60mbar (6kPa) surprisingly show yet another surface microstructure (Fig. 126). Clathrates dissociate rapidly along the grain boundaries cutting deeply into the powder particles (Fig. 126B). Since the transformation is also related to the volume decrease of  $\sim 13\%$  (see also. 1.1.2, page: 6) gaps that are formed between decaying hydrate crystals are considerably broad ( $0.5\text{-}3\mu\text{m}$ ). Remaining cores are gradually coated with an ice layer. Interestingly in spite of the formation of the ice shielding the reaction is not slowing down as it was observed in the anomalous region. This state is possibly a result of two parallel processes that support the dissociation. The first one, the leading process, exposes new clathrate surfaces to the surrounding gas as the decomposition quickly

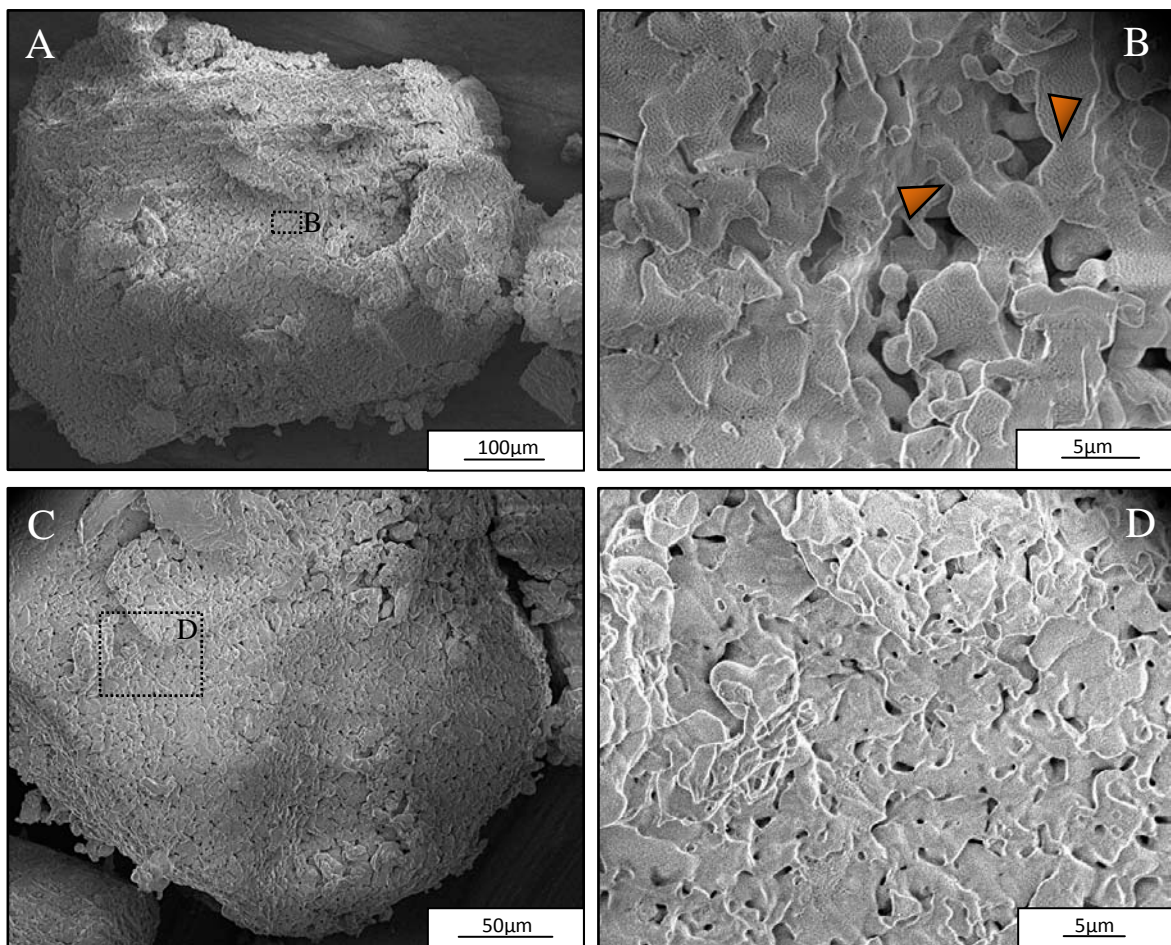


**Fig. 126)** Surface microstructure of clathrate powders decomposed at 220K and 60mbar (6kPa). Images from the sample recovered after 2min. (A, B) indicate that the dissociation preferentially progress along grain boundaries (examples - Orange arrows). Partially decomposed crystals still show only poorly developed ice film with a weak fabric of underlying sub- $\mu$  porosity. Slightly longer (5min) interrupted run (C, D) reveals more apparent ice coating surrounding remaining hydrate cores. Between those features one can observe a large number of pores. Images from FEI Quanta 200FEG.



progress inwards along the grain boundaries. The second one is related to the quality of the coating ice, its thickness and the size of remaining clathrate cores. Although the lowest density of cubic stacking (Fig. 119) for the runs from this pressure region (Fig. 120 curves 5,6) works against the dissociation, multiple SEM images suggest that the ice film is considerably thin. Initially, its thickness is on the order of a few microns. With the average size of remaining clathrate cores on the order of 5-10 $\mu$ m (Fig. 126B) there is not much of an available material to improve the thickness. Since the annealing and grain boundary reduction mechanisms (e.g. grain coarsening, Ostwald ripening) are still too slow to make the thin coating an effective barrier, the decomposition will transform remaining hydrates in a short period of time. This interesting observation will be more broadly discussed in the next subchapter. The final microstructure of both 60 and 6mbar runs (6 and 0.6kPa) unfortunately was not investigated but it is justified assuming its close resemblance to the one observed for the 245K and 250K decomposition runs (Fig. 112A, C) taking a correction for the faster annealing at those temperatures.

The interrupted runs clearly show how the decomposition speed and consequently the dimensionality of ice growth is important for the kinetic anomaly. The results suggest also that similar phenomena might be present in a wider temperature range. This intriguing possibility led to the second group of experiments at 200, 230, 240 and 250K that were attempting to localize the anomaly at higher and lower temperatures (Fig. 127). Decomposition target pressures were chosen with a guidance of the 220K series. At the lower temperature end (200K) the reaction was performed at 200mbar (20kPa), which lays close to the midpoint between the stability boundary at  $\sim$ 433mbar (43kPa) and 6mbar (0.6kPa) representing the Martian surface pressure. The reaction curve do not show any strong decomposition hindrance except the initial part resembles the situation from 220K 200mbar (20kPa) run. Unfortunately, a limited beam time did not allow for further studies of this temperature region. At higher temperatures, the anomalous kinetics was localized at pressures not far from the stability boundary that repeats the pattern observed at 220K. A pressure range where it appears seems to be related to the changes in the driving force and influence of the competing processes, namely the annealing and cubic ice formation. The first of the two, is likely to have a positive impact on the preservation thus extending the pressure region where the anomalous kinetic may occur. The second one, by introducing additional diffusion pathways accelerates gas transport through ice shielding, which results in a narrower pressure window.

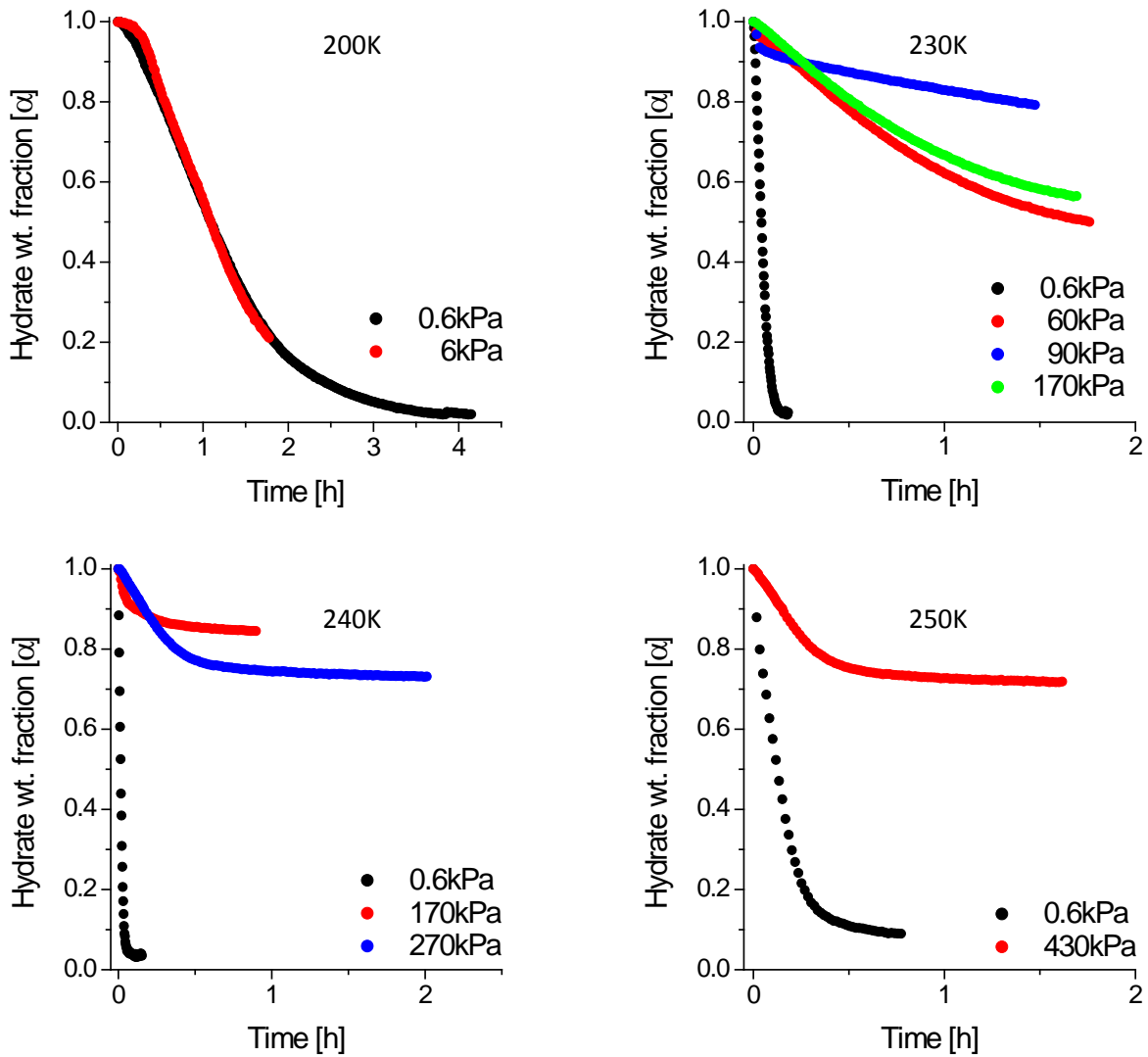


**Fig. 127)** Neutron diffraction decomposition runs at different target pressures for four selected temperatures.

#### 4.3.5 “Self-preservation” phenomenon

Anomalous decomposition kinetics reported at sub zero temperatures over the last few decades led many authors to formulate more or less complex definitions of the self-preservation effect giving various reasons for its existence e.g. (Davidson et al., 1986), (Handa, 1986), (Yakushev and Istomin, 1992), (Ershov and Yakushev, 1992), (Takeya et al., 2001), (Stern et al., 2001), (Stern et al., 2003), (Kuhs et al., 2004), (Takeya and Ripmeester, 2008). This lack of consistency could be searched among others in different clathrates preparation techniques, sample handling and experimental procedures. One should also note that most of the observations rely on analytical techniques that provide

only bulk information (DTA, volumetric/gas flow method, energy dispersive X-ray diffraction, neutron diffraction). Only a handful of studies combined with more detailed but localized cryo-SEM information (Stern et al., 2003), (Circone et al., 2003), (Kuhs et al., 2004) could give some insight on the relation of surface microstructures to the decomposition speed.

The preservation effect is generally considered to be restricted to the kinetic anomaly at temperatures between 240K and the melting point of ice at ambient pressure where clathrates decompose at much lower rates than expected from p-T conditions. The preservation phenomenon was found for clathrates of noble gases like krypton and xenon (Handa, 1986), methane and CO<sub>2</sub>. The most precisely studied CH<sub>4</sub>-H<sub>2</sub>O system (Stern et al., 2001), (Stern et al., 2003) show astonishingly complicated behavior of a preservation strength as a function of time (Fig. 128A). Synthetic clathrates used in these experiments showed a deviation from the expected transformation period even as great as a month. It is important to point out that in some of the experiments the dissociation rate was so low that they were interrupted before reaching full conversion. Moreover, there is good evidence that methane clathrates may stay in this metastable state for geological timescales trapped in permafrost (Yakushev and Istomin, 1992), (Yakushev and Chuvilin, 2000). Similar

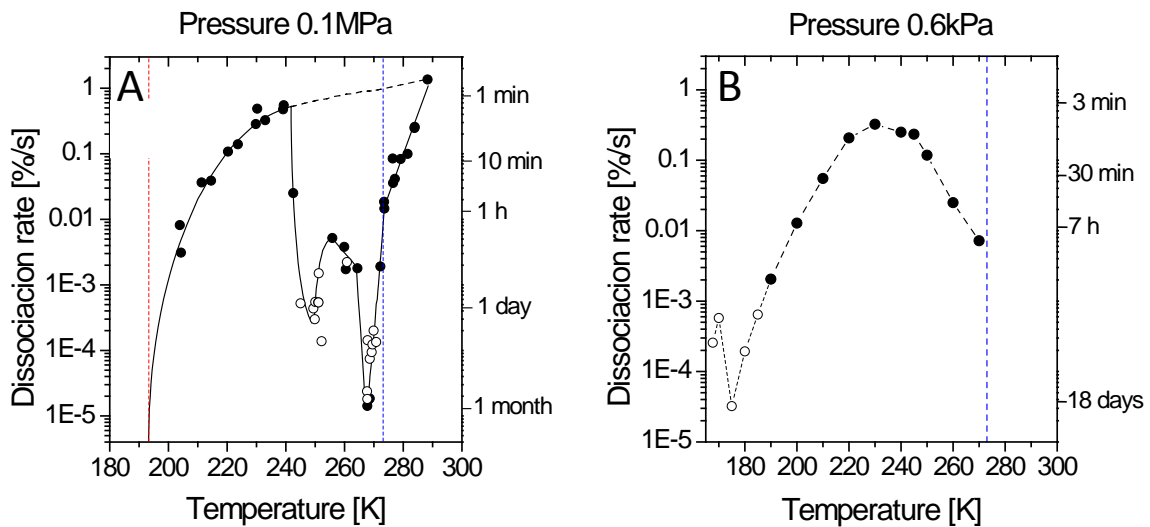


**Fig. 128)** Self-preservation phenomenon observed for A) methane (Stern et al., 2003) and CO<sub>2</sub> (right) clathrates at terrestrial and Martian conditions, respectively. Data points are taken at 50% transformation as proposed in (Stern et al., 2001). Open circles mark the runs that never reached 50% of the transformation. For CO<sub>2</sub> clathrates, the missing rates were calculated through a fitting of linear fragments of the reactions after 4h (177,7K, 180K) and 12h (175K) down to 50%. Exceptionally, the linear fit for the whole reaction was applied to 170K experiment. Red dashed line (A) - the stability boundary for the methane clathrates. Blue dashed line – melting point of water ice.

studies on CO<sub>2</sub> clathrates showed also the anomalous kinetics between 240K and the melting point of water at ambient pressure but no apparent variation of its strength was reported (Circone et al., 2003). Unfortunately a diagram similar to this for the methane clathrates was not published. For comparison, the reader will find here a plot based on the experimental work performed in frame of this thesis that presents the preservation effect at much higher driving force relevant to the Martian surface pressure (Fig. 128B). Yet, it should be clearly spelled out that this way of visualization is arbitrary by considering only one pressure niveau and also to some extent meaningless since it adopts a linear gradient that does not reflect changes in the decomposition rate. Perhaps, a better representation of the anomalous kinetic could be made by taking local derivatives of decomposition curves and plotting them in a 3D graph against wt. fraction and temperature. Most of the researchers agree that the preservation effect must be caused by an ice layer building on dissociating hydrates (Davidson et al., 1986), (Yakushev and Istomin, 1992), (Takeya et al., 2001). Although the ice layer buildup is a fact, its mechanical strength to withstand a considerable pressure difference between stabilized clathrates and surrounding gas was claim to be insufficient to cause the preservation effect (Stern et al., 2001), (Takeya et al., 2002), (Stern et al., 2003). Following this line of argumentation the reason for the self-preservation was searched in a change of clathrates physical chemistry (Stern et al., 2001). Yet, it should be clearly spelled out that the stability of the ice coating should not be considered in terms of a shear mechanical gas pressure but rather chemical activity at the ice/clathrate interface as shown in more recent studies (Kuhs et al., 2004). Moreover, they turned the attention on a “quality” of coating ice and for the first time qualitatively showed its relevance to the formation of the phenomenon (Fig. 114). The current thesis confirms this finding and additionally integrates it with the role of ice microstructures as it could be seen in the previous subchapters. The results coming from our experiments give a rise to a new definition of the self-preservation:

- The phenomenon is caused by an ice shielding developed on clathrate particles
- The dimensionality of ice growth and the nucleation density that are functions of a driving force controls the preservation effect at the initial decomposition stage
- The defectiveness of ice that is a function of temperature and time controls the strength of the self preservation effect on a longer time scale.

- A chance for clathrates to enter into the anomalous decomposition regime falls with decreasing particle and crystal size reflected in an outer and inner surface.

In practice, the phenomenon has two aspects, corresponding to high temperature (4.3.3) and intermediate pressure (4.3.4) anomaly. I propose to term both effects as a temperature and pressure dependent self-preservation, respectively. Both phenomena may exist in a pure form or act at the same time, thus amplifying the effect.

The temperature dependent self-preservation (Fig. 129) observed in the experiment relevant to the Martian atmospheric pressure starts around 240K but the preservation is still very weak. Its strength gradually increases toward higher temperatures (Fig. 128) as the stacking faulty ice annealing rate accelerates (Fig. 115). The maximum preservation effect is achieved close to the melting point of ice, for 270K (Fig. 107), (Fig. 128B). Available pathways for diffusion are restricted to a sluggish transport along crystal boundaries and even slower through the bulk. Assuming gas and self diffusion of water molecules to be similar one might expect about two orders of magnitude difference between both types of pathways (Mizuno and Hanafusa, 1987). In addition, the surface (boundary) diffusion may be gradually hindered by the progressing coarsening of ice crystals that accelerates toward higher temperatures (Fig. 112).

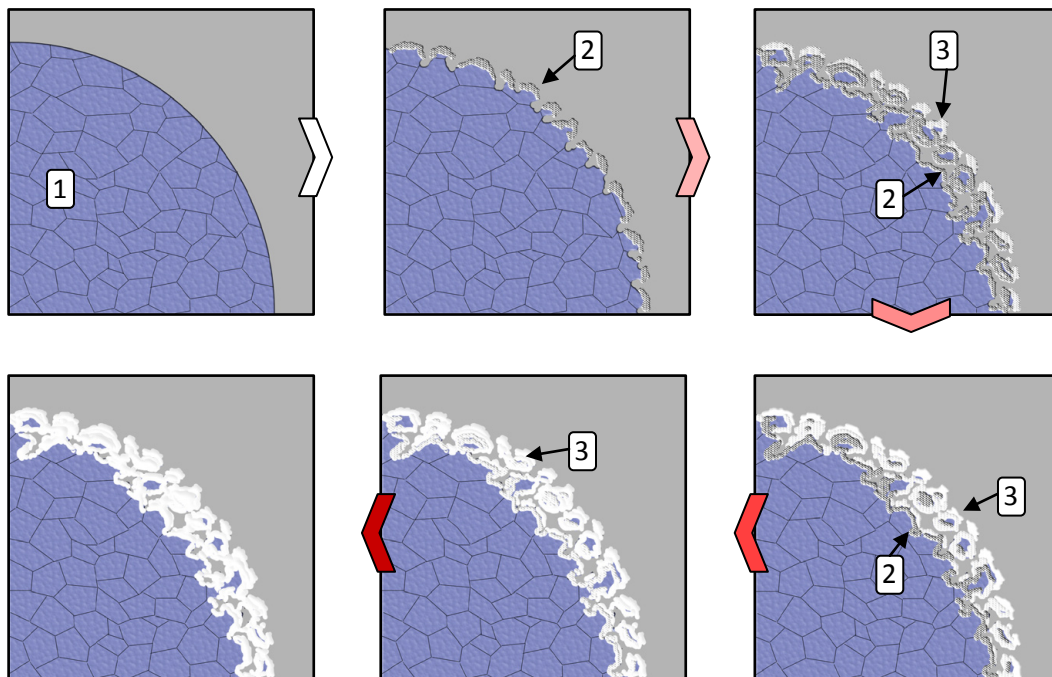


**Fig. 129)** Schematic development of the temperature dependent self-preservation. Initially, rapidly formed ice contains a considerable amount of stacking faults that are rapidly annealed. This process is followed by the grain size increase due to the coarsening. 1) Gas hydrate, 2) Stacking faulty Ih ice, 3) Annealed Ih ice.

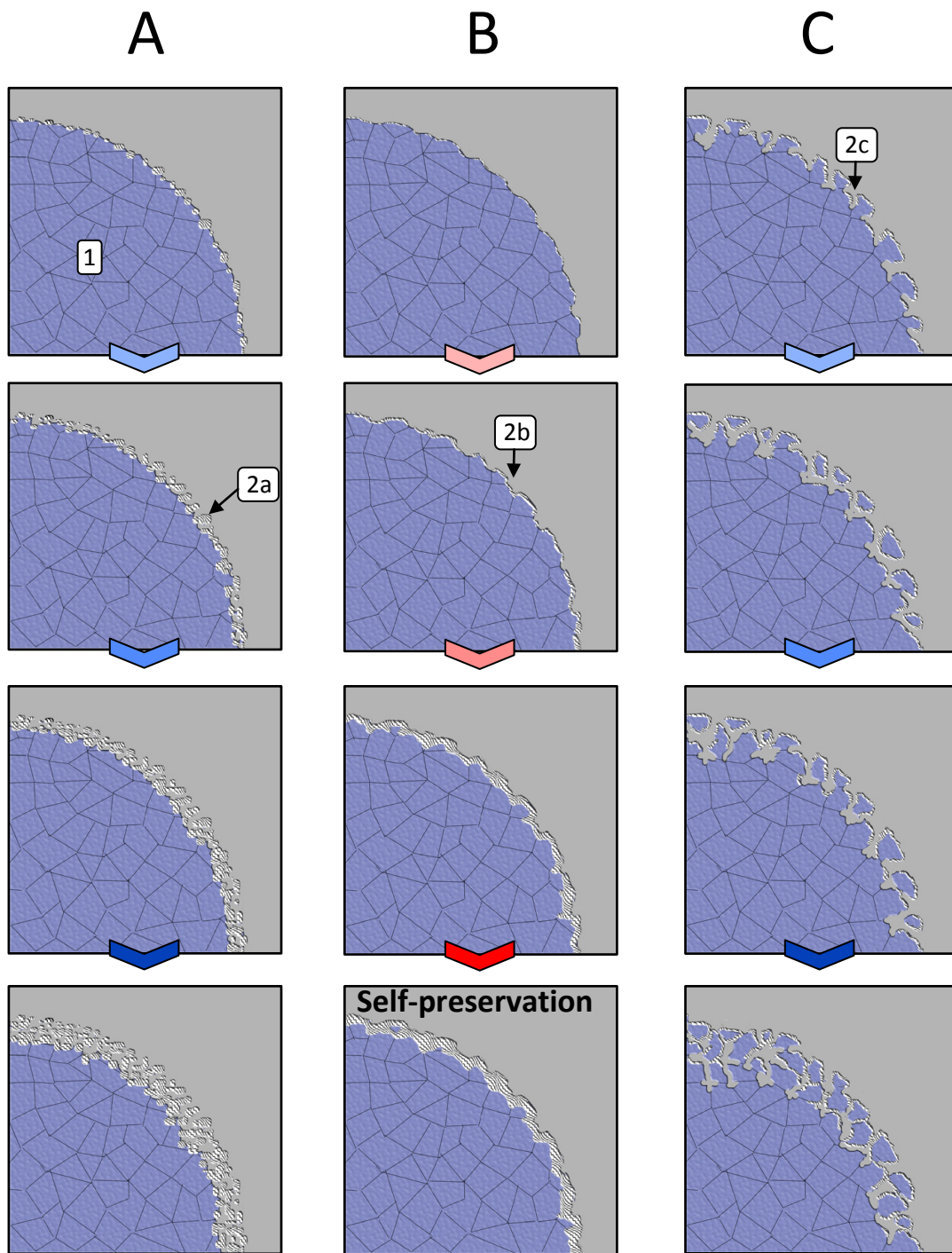


**Fig. 130** Evolution of the surface microstructure at three pressure regimes (See also Fig. 131): A) above, B) within the self-preservation zone and C) below (See also Fig. 122). 1) Gas hydrates, 2a) 3D stacking faulty Ih ice crystals, 2b) 2D fast growing defective Ih ice, 2c) Quick decomposition along grain boundaries.

The pressure dependent self-preservation is present in a wide temperature range from ~200 to 250K (Fig. 131) but one can assume that it also extends further toward the melting point of ice. This variant of the phenomenon is caused by the interplay between the



dimensionality of growing ice and decomposition speed that are related to the excess fugacity that drives the system (4.1). Another mechanism that might be also involved is a percolation of possible pathways for CO<sub>2</sub> that at a certain decomposition speed could lead to an abrupt reduction of a permeability of ice coating. Unfortunately, the presently available data do not provide enough support to confirm this intriguing idea. Interestingly, the excess fugacity and thus also indirectly pressure region, at which this aspect of the self-preservation occurs, is not constant in the investigated range but seems to spread towards higher temperatures (Fig. 131). This rough estimation should be revised in more detailed studies. At pressures above the anomalous zone ice do not form any substantial barrier for the decomposition due to the preferential 3D growth and poor packing of coating crystals (Fig. 130A). Within the self-preservation regime, fast 2D growth of stacking faulty hexagonal ice, quickly seals off unstable clathrates. The reaction is continued at much reduced rate through the diffusive transport (Fig. 130B). Attempts to test the effectiveness of this type of coating with the pVT method were unfortunately unsuccessful or still wait to be analysed. At higher driving force, below the anomalous zone, a complete ice coating layer is developed with a considerable difficulty due to the quickly progressing decomposition along grain boundaries. Ice that eventually covers clathrate particles is too thin and imperfect to create a considerable barrier for the diffusion.

At intermediate pressures and higher temperatures though, it is very likely that pressure and temperature dependent variants coexist together thus improving the self-preservation (Fig. 131). Such overlap might already, to some extent, affect the decomposition experiments at 240K/ 250K and higher target pressures (Fig. 127) but the limited duration of those runs is not sufficient to show both components at full strength. Intriguingly, such situation was most likely already recorded in the previous experiments on methane clathrates at 0.1Mpa (Stern et al., 2001) as the first dip at 248K (Fig. 128A) in the anomalous region. The increasing dissociation rate marks the moment where the pressure dependent mechanism is switched off. The second dip can be attributed to the pure temperature dependent phenomenon that requires higher temperatures to be effective on a short time scale. Although this speculative theory neatly explains the observed rates one should keep in mind that stacking faulty ice produced upon the decomposition of methane and CO<sub>2</sub> hydrates is not entirely identical (Kuhns et al., 2004) and therefore some more systematic studies of both kinetic anomalies for various clathrates are required.

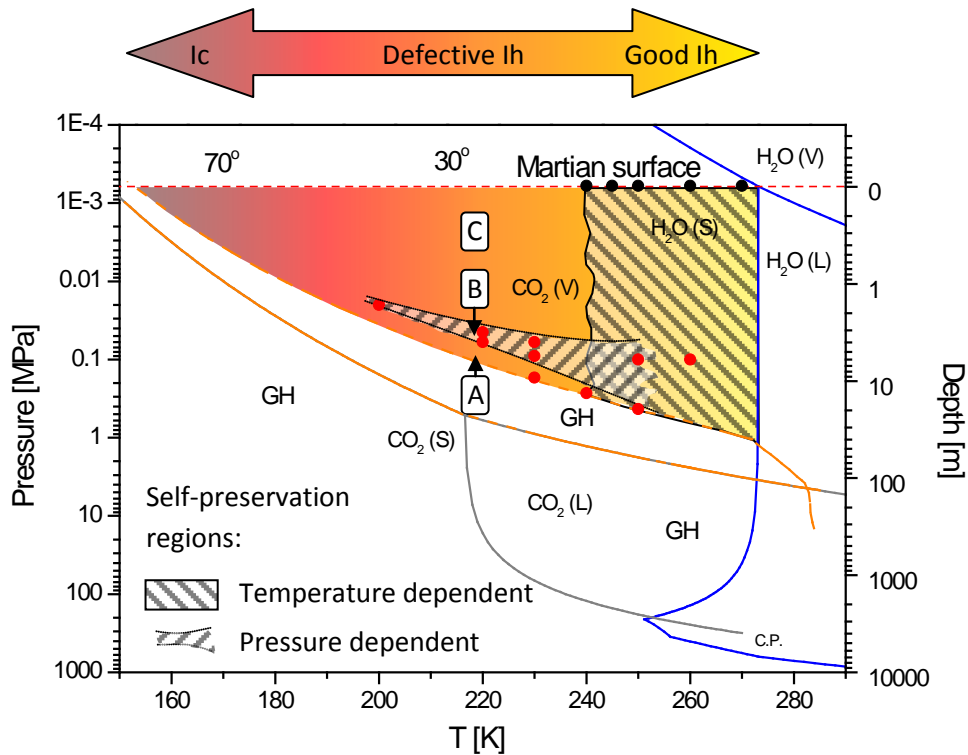


**Fig. 131)** Approximate position of two aspects of the self-preservation phenomenon on the phase diagram relevant to the Martian p-T conditions. Color gradient shows the transition from the cubic ice (Ic) to the well crystalline ice (Ih). Regions A-C corresponds to the microstructures presented on the Fig. 130.

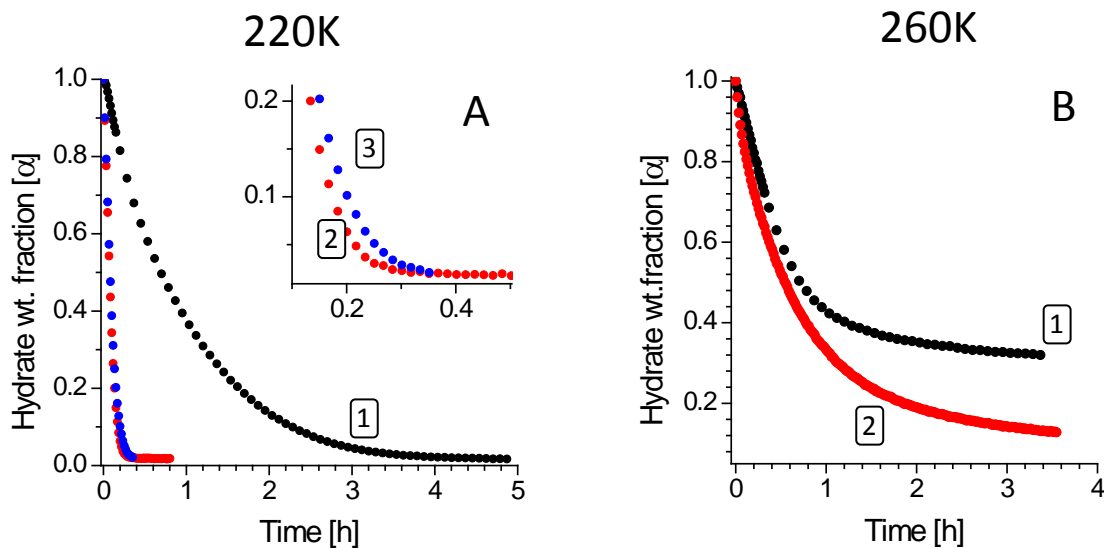


**Fig. 132)** Influence of the clathrate particle size on the decomposition process A) within and B) outside the self-preservation region. A) Decomposition experiments at 220K and 6mbar (0.6kPa) for three particle sizes: 1) consolidated core (Genov, 2005), 2) 250µm and 3) 350µm powders. B) CO<sub>2</sub> hydrate dissociation curves taken at 260K and 6mbar (0.6kPa) for 1) a consolidated sample (Genov, 2005) and 2) 250µm powder. Smaller SSA material (1) clearly shows larger persistency in comparison to fine particles (2).

As it could be already seen on a multiple examples, the self-preservation is a process that transforms a part of the clathrates to form a layer of protective ice. In such a case the phenomenon will be also influenced by the particle and crystal size of the starting material. Although these factors were not the main subject of this thesis still some useful information were acquired, also in the Martian context.

A handful of successful experimental runs with a different particle size of the starting material (powders and consolidated samples) performed in frame of this project show clearly that larger clathrate grains/pieces extend the transformation period (Fig. 132A) even if the favourable conditions for the anomaly are not met. The decomposition speed within the self-preservation region (Fig. 132B) clearly falls for larger particles, thus preserving a greater volume of hydrates outside their thermodynamic stability field. I also speculate that the size of individual crystal may similarly influence the decomposition kinetics. Some indirect evidence for this dependence may be found on some of the SEM

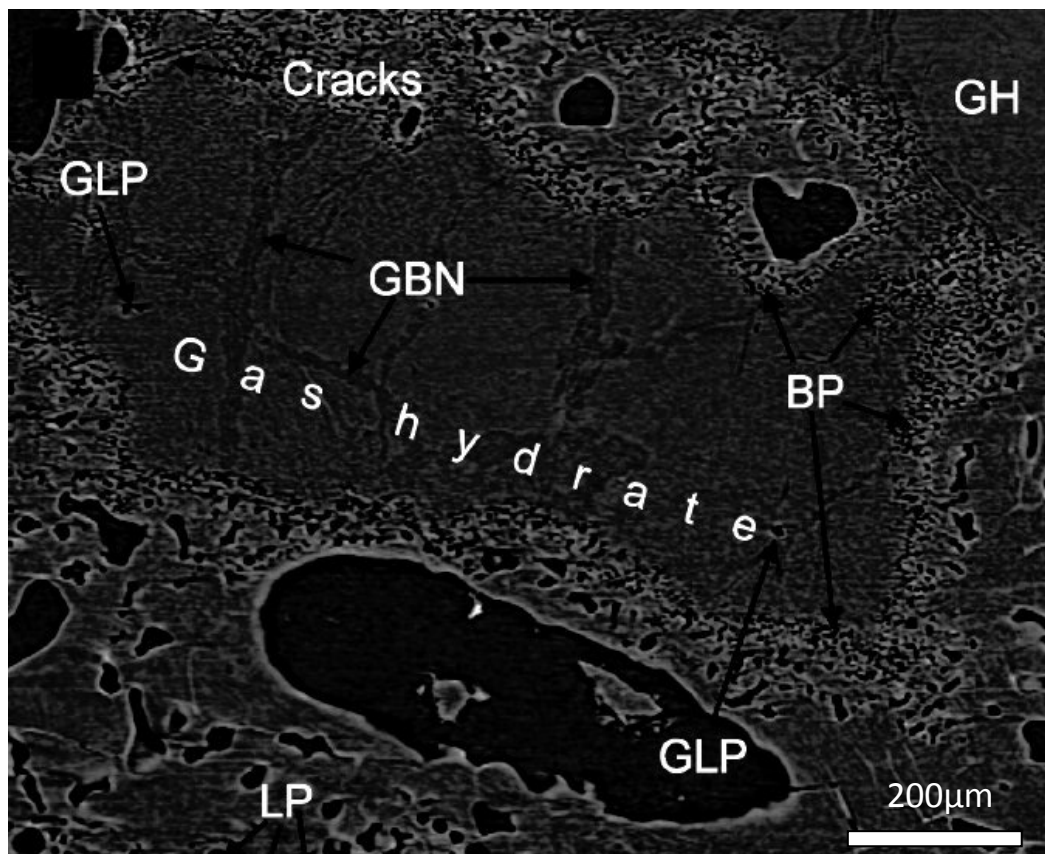


**Fig. 133)** Slice perpendicular to the sample from the x-ray density contrast tomography scan on a natural gas hydrate sample (GH) (mostly methane). Darker areas (GBN-grain boundary network) along grain boundaries correspond to progressing dissociation fronts. One can also clearly notice pores of different size in ice that surrounds clathrates. BP-boundary pores, GLP-gas hydrate large pores, LP-large pores, (Mursched et al., 2008)

images (Fig. 126) that suggest the decomposition along crystal boundaries. Interestingly, separate studies on the clathrate decomposition with x-ray tomography (Fig. 133) seem to support this conclusion. Image slices through the clathrate particles show quite clearly a density difference along grain boundaries that can be attributed to progressing dissociation fronts. The size of this additional, inner surface used for the decomposition is controlled by a crystal size that most likely evolves with time. Fine crystalline clathrates (10-15 $\mu\text{m}$  4.2.2) that used this thesis in this case would correspond to young deposits. More matured hydrates from natural deposits that had enough time for the recrystallization can reach even 600 $\mu\text{m}$  (Klapp et al. 2007).

The self-preservation is a fragile state that depends entirely on the sealing properties of the ice layer that can be melted or mechanically removed in natural geological processes. If it happens by crossing the melting point of ice, the dissociation is unavoidable. Since this process is endothermic, close to 237K some buffering may appear but eventually all clathrates will decompose. Below this temperature gas hydrates after a limited gas release will start to develop a new ice coating that in the favourable conditions may again hold the decomposition. If not, the remaining clathrates will undergo almost full transformation retaining about 1-2wt% of the intact compounds in form of inclusions dispersed in ice.

The self-preservation phenomenon itself and the two scenarios of its destruction create very intriguing possibilities for evolution scenarios involving gas hydrates especially those including episodes of a resurfacing through gas or liquid water + gas releases (Chapter 5).

#### 4.3.6 Kinetic metastability

A kinetic metastability is a known phenomenon for ices but for clathrates until now it was rather poorly explored and its possible applications not clearly spelled out. It can be defined as an absence of decomposition on a laboratory time scale that takes place at temperatures below ~160-170K. A good example of this phenomenon can be found in the experiment at 165K and 6mabr (0.6kPa) (Fig. 106) where CO<sub>2</sub> clathrates in spite of being unstable did not dissociate for more than three hours. Similar but not identical behavior was observed in a very recent campaign designed to study cubic ice Ic formation from Ne hydrates with a temperature ramping technique at 1bar (0.1MPa) (Fig. 134). Although the isothermal time steps in this method are considerably shorter than in the constant pressure and temperature runs in presented in this thesis, one can still notice that at the initial stage, up to 158K the hydrate wt. fraction is close to one. It is particularly interesting since Ne hydrates (sII) at this temperature range require about a few hundreds of bars of pressure to

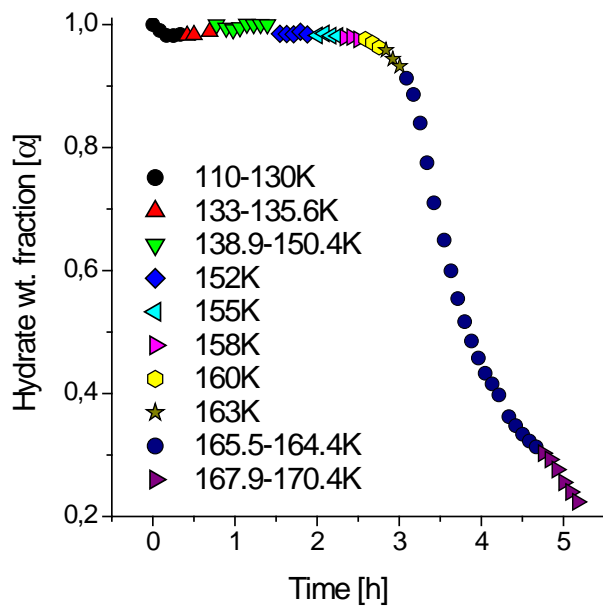


**Fig. 134)** Temperature ramping decomposition experiment on Ne clathrates. Initial variations in the scaling factor are most likely an artifact from the refinement. The dissociation starts significantly after crossing 160K.

be stable. In spite of this enormous driving force the decomposition becomes visible only after crossing 160K. Considerably smaller difference between the stability boundary and the target pressure in case of CO<sub>2</sub> clathrates shifts this critical temperature toward higher values. Interestingly this temperature range is quite similar to the stability limits of various recovered high pressure forms of ice that similarly to Ne clathrates recrystallize into the cubic form (Arnold et al., 1968). In case of ices this transformation was attributed to an increased mobility of water molecules, linked in ice-like structures to orientation defects called Bjerrum L- and D-defects (Woolridge et al., 1987). Since those defects are also likely to exist in gas hydrates (Davidson, 1973), it may well be that the onset of clathrate decomposition is related to the onset of appreciable Bjerrum defect mobility on the time-scale of the experiment. Yet, unlike in pure ices, the hydrate structure is likely to restrict the rotation of water molecules into cages by gas molecules trapped inside. This stabilizing effect towards somewhat higher temperatures should be particularly visible for larger molecules like CO<sub>2</sub>, which is in accordance with the observations presented earlier.

This phenomenon opens an interesting aspect of the persistence of clathrates at very low temperatures, which may be of interest not only for Mars but also for other planetary bodes (e.g. icy moons, comets) that fall within its temperature range.

# Chapter 5 – Possible role of clathrates on Mars and other planetary bodies

The theoretical considerations and experimental knowledge from the introductory chapters along with the results coming from this project give a firm ground for a discussion about the possible existence and active role of clathrates in geological and environmental processes, thus enabling a revision of published hypotheses. The experimental work on the decomposition process opens also some new possibilities that will be also considered here. Although this thesis was generally dedicated to the hydrates of CO<sub>2</sub> on Mars, the acquired information allow also expanding the discussion to other planetary bodies where different gas hydrates also are expected to exist.

## 5.1 Clathrates on Mars

As it could be seen in Chapter 2, essentially over the whole period of the modern space exploration of Mars, clathrates repeatedly appear in the various theories considering the surface geology, atmospheric gas composition and finally climate evolution. Until the detection of methane in the Martian atmosphere, the discussion about those compounds was related essentially only to CO<sub>2</sub>. Recently, a greater attention was placed on this new gas due to its biogenic affiliations. It is also worth noticing that even so, hydrates lately appear somewhat less frequently in the publications. One of the more apparent reasons that I could see for this situation may be perhaps a lack of additional data about gas compounds that did not allow for more critical assessment of their possible influence on the environment. The complicated, quite exotic physical-chemistry of gas hydrates certainly also does not add to their popularity. Finally, it is also hard not to notice that their strong presence in the “White Mars” scenario made them rather unpopular among the antagonist of this idea.

### 5.1.1 Polar regions

Polar caps from the beginning were considered as the most promising candidate for a place where clathrates could be found close or even at the surface (2.6.1). Following the thermodynamics of clathrates the abundance of major components, water ice in contact with gaseous or solid CO<sub>2</sub> may indeed lead to the nucleation and growth of hydrates. From



the kinetic point of view though, this becomes less obvious. The experiments exploring this issue were concentrated around two potential analogs for a temporary and permanent polar water ice, frost and ice spheres. The chosen materials (1.5 and 60 $\mu\text{m}$ ) have slightly different radius to the particles (2.5 and 100  $\mu\text{m}$ ) taken from the literature (Kieffer, 1990) but are close enough to be representative. Experimental work on the kinetics with the spherical material (Genov, 2005) was technically very difficult to follow on a longer time scale already at 193K. Even with the higher degree of transformation with frost, the lowest achievable temperature was 185K. It is worth noticing that this is still far from those observed at the surface of both polar caps. Even though, it was possible to get some insight on the transformation time at lower temperatures by a modeling with a JMAKGB and multistage Powder 2 (Genov, 2005). Relying only on the extrapolated diffusion coefficients ( $D = 2.68 \times 10^{-18} \text{ m}^2/\text{s}$  and  $8.45 \times 10^{-18} \text{ m}^2/\text{s}$ ) the half and total transformation time for ice spheres at 150K was estimated on 10 000 and 90 000 terrestrial years, respectively. Those preliminary results unfortunately do not include the nucleation and growth stage that is particularly important for small particles like frost that do not enter

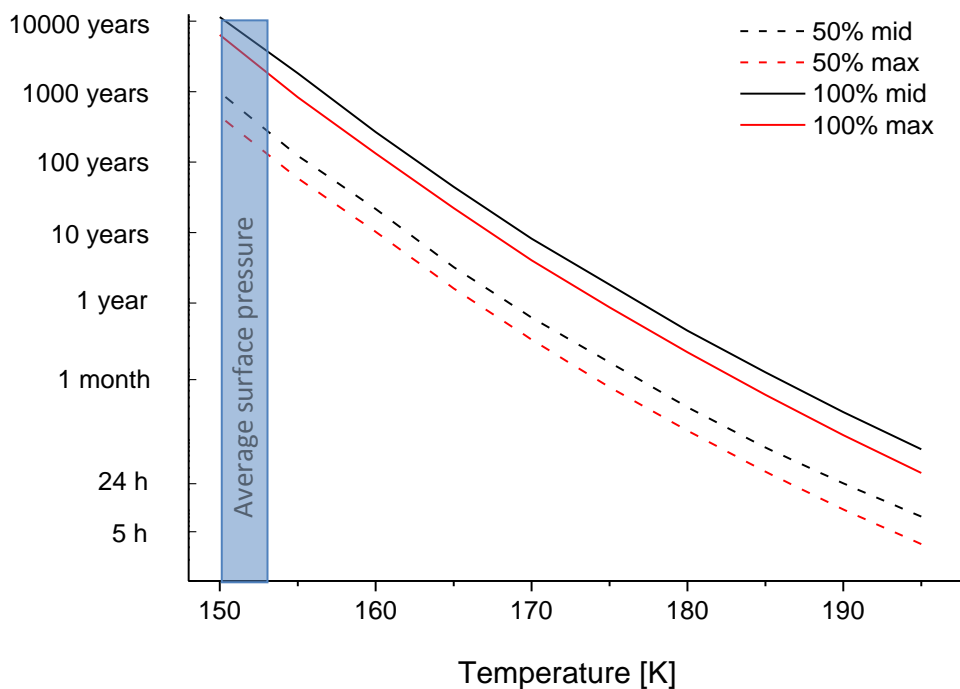


**Fig. 135)** Prediction time lines for the half (Dashed lines) and full transformation (Solid lines) of frost ( $r=1.5\mu\text{m}$ ) into  $\text{CO}_2$  clathrates. The notation “mid” and “max” refer to the driving force approximately in the middle of the  $\text{CO}_2(\text{V})$ -  $\text{H}_2\text{O}(\text{S})$  (Fig. 9), stability field and on the solid/volatile  $\text{CO}_2$  boundary, respectively. Parameters from “Frost” in Appendix 9.

into the diffusion controlled regime. The previous models assumed that the nucleation and growth stage is negligibly fast. Following this approach clathrates could quickly form if ice particles would be small enough. A general JMAK code in Powder 4 allows for a verification of this assumption. Down to ~195K the nucleation is indeed generally instantaneous. Towards even lower temperatures though, it becomes increasingly difficult. The change in the activation energy suggests that the nucleation is governed by a different process (Fig. 99) related to the mobility of water molecules that in this temperature region is decreased to such extent that the probability for embryos to exceed the critical size falls dramatically. Predicted time period needed for the half and full transformation for frost (Fig. 135) suggests that clathrates presently may not be formed in any significant quantities at the surface of polar ice. Although the transformation is still faster than in case of the spherical ice, gas hydrates still require a few thousands of terrestrial years for the full conversion. The negative impact of the annual and in particular diurnal temperature excursions is likely to be reduced by the kinetic metastability effect below 165K (4.3.6). Larger temperature excursion will lead to the decomposition.

The reader may notice that just a few degrees warmer environment speeds up the nucleation by at least an order of magnitude decreasing the importance of the time factor. Similar acceleration should be observed for diffusion controlled growth present for larger particles but unfortunately more precise timing is still not available. From our laboratory experience though I can roughly estimate that already at 180K the full transformation period enters in a terrestrial months - tens of years scale (depending on the size of ice particles). It is important to point out that with the temperature increase CO<sub>2</sub> pressure higher than atmospheric must be maintained to carry on the formation (Fig. 135). In order to meet these conditions substrates for clathrates must be sealed off from the atmospheric influence. The literature offers here two solutions: solid/volatile CO<sub>2</sub> burial e.g. (Jakosky et al. 1995), (Mellon, 1996), (Longhi, 2006) and basal melting of the temporary dry ice cap (Kurahashi-Nakamura and Tajika, 2006). This thesis is meant to check the viability of such mechanisms but their existence even in some limited form may be considered.

The first process is somewhat similar to the one known from the Terrestrial polar caps where air bubbles transform at certain depth into air hydrate (2.1). In the Martian environment it is already possible just a few meters below the surface as already noted in a number of publications (2.6.1). If the occurrence is close to the one known from the terrestrial caps then dispersed clathrate inclusions would occupy up to ~5 volume% of the

polar ice (S. Faria-personal communication) having only a minor influence on thermal gradients and mechanical properties of the caps. The burial of larger sheets of dry ice would deliver much greater volume of CO<sub>2</sub> (Longhi, 2006). This process presently seems to be rather limited judging on the ice flow that is too slow for buried larger quantities of solid CO<sub>2</sub> (Greve and Mahajan, 2004). Clathrates formed around the dry ice in such circumstances may form more or less continuous layer that could have already a considerable impact on the flow mechanics and thermal conductivity. Still, any effort to calculate this influence remains very speculative until more detailed information will be available. Unfortunately, presently published radar sounding data do not take clathrates into considerations (Picardi et al. 2005), (Plaut et al. 2007), (Seu et al. 2007). Certainly a limiting factor of the burial mechanism is a finite source of CO<sub>2</sub> during the formation. Consequently, the clathrate growth speed will gradually decelerate as gas is consumed until equilibrium is achieved. In this state gas hydrates may remain on geological timescales if tightly surrounded by ice as in case of the terrestrial analogs.

The other mechanism is much more intriguing since it offers a quasi constant supply of CO<sub>2</sub> to a potential formation zone placed deeper in the polar ice. Originally it was proposed for the atmospheric collapse at the end of the Noachian but I see also a way it could be adopted in present Mars. Presently such condition may exist at the base of temporary CO<sub>2</sub> caps yet not through a pressure melting suggested in the original paper (Kurahashi-Nakamura and Tajika, 2006) but due to insolation (Piqueux et al., 2003), (Kieffer et al., 2006). Here I would like to turn the attention of the reader to the Martian “spiders” phenomenon (Fig. 48) and the proposed process of its creation. I speculate that the basal sublimation that causes the buildup of pressure under the dry ice slab creates a good mechanism to pump CO<sub>2</sub> into the underlying layered polar deposits, mostly consisting of water ice. It is not difficult to notice that again suitable conditions for the formation are likely to be created. For natural pathways of such a transport I propose the layered interfaces of the polar deposits where gas molecules could be slowly transported in greater depths developing a clathrate layer under way. The efficiency of such a process remains speculative, since neither the excess fugacity nor the particle size/slab porosity is known. At lower latitudes of SPC and the whole NPC where the seasonal cap disappears completely during the spring and summer time one could expect also a gradual dissociation of gas hydrates eventually formed in this way. Areas with a persisting CO<sub>2</sub> cover, thus maintaining elevated pressure or temperature below 165K would tend to accumulate

clathrates.

Summarizing the discussion concerning a feasibility of the present formation of clathrates and potential mechanisms:

- It is very unlikely to find any significant volumes of clathrates formed in the ice-gas interaction anywhere at the surface due to the nucleation issue.
- Deeper in the ice caps and layered polar deposits clathrates formation is feasible but is limited by the accessibility of CO<sub>2</sub> and slow formation kinetics.
- Eventual gas hydrates are likely to be developed in form of dispersed crystals but continuous layers also cannot be excluded.
- Potential present delivery mechanisms of CO<sub>2</sub> into the polar ice are either of low efficiency (CO<sub>2</sub> burial) or speculative and restricted mostly to the southern polar cap (slow diffusive migration from the sublimating base of surface dry ice).
- Unstable clathrates below 165K are likely to not decompose on the scales of days, weeks due to the kinetic metastability phenomenon.

The project leaves still a few open questions that existed already at its beginning or came out during the last two years. One of them is the still unexplored possibility of clathrate condensation in the atmosphere or at the polar caps. The experiments performed in this and preceding thesis consider only a formation from gaseous CO<sub>2</sub> and Ih water ice. Another pending issue is an influence of cubic ice on the formation rates. Its presence already below 190K is generally not very surprising but up to now it was not considered in the Martian context. Since a chemical activity and vapor partial pressure at the surface of Ic ice is somewhat higher than in case of the regular Ih ice, I suspect that the transformation into clathrates may be increased. Similar acceleration might appear for heavily stacking faulty Ih ice where defects are likely to promote the nucleation at lower temperatures.

### 5.1.2 Regolith

A several kilometers thick regolith layer is another potential place where clathrates could be found. The thermodynamic stability boundary stretches at the depths from less than a meter at higher latitudes to about a kilometer at the equator assuming a lithostatic pressure build-up from the surface. For a regolith with open porosity those values should be increased accordingly (Longhi, 2006). Additionally, higher temperatures, especially at lower latitudes (Fig. 102) create very suitable conditions for the fast formation kinetics.

Yet, similarly to the polar regions at elevated temperatures one needs to supply CO<sub>2</sub> at sufficiently high pressure into region rich in solid or liquid H<sub>2</sub>O. Those rather straight forward conditions caused a vigorous discussion several years ago that should be seen as a struggle between the Blue and White model (2.5) that approach the initial CO<sub>2</sub> reservoir in different way. Consequently, as the effect of this polarized situation clathrates favored by the colder model were put in question along with liquid and solid CO<sub>2</sub> related processes (Stewart and Nimmo, 2002), (2.6.2). In light of present knowledge also expanded by this project, I find it important to reopen the discussion.

The main argument against widespread presence of clathrates was the lack of an efficient way to store of CO<sub>2</sub> within the regolith (Stewart and Nimmo, 2002). The authors assumed breccias' porosity to be globally connected and partially open in a vertical profile. An argument that was meant to support this speculation was found in an arbitrarily chosen permeability of the regolith compared to the one known from terrestrial firns. With this approach the removal of buried dry ice assumed as a representative CO<sub>2</sub> source was geologically very quick. In my opinion, proposed diffusion coefficient of 10<sup>-5</sup>-10<sup>-6</sup> m<sup>2</sup>/s (10<sup>-2</sup>-10<sup>-3</sup>m<sup>2</sup>/h) that may be true for partially open porosity most likely do not reflect the present and past situation due to the global presence of water ice in pore spaces e.g (Mitrofanov et al. 2002), (Boyton et al. 2002). Moreover, authors seem to also ignore the fact that the diffusion coefficient is temperature dependent and a direct application of the Terrestrial values may be wrong. Finally, I see no convincing argument supporting the discussed scenario as representative on a global scale. The lower limit for the transport through the water ice saturated regolith I propose on 10<sup>-11</sup>-10<sup>-18</sup> m<sup>2</sup>/h (273-150K) as derived from the Powder 4 model (Tab. 9), (Appendix 9). The optimal value would be about two orders of magnitude greater due to diffusion along grain boundaries. Since the presence of the water ice rich regolith was already suspected at that time e.g. (Jakosky et al. 1995), (Clifford and Parker, 2001) I find it quite surprising that this likely scenario was not considered.

With the new diffusion coefficients the retention of CO<sub>2</sub> and also other gases like CH<sub>4</sub>, H<sub>2</sub>S or SO<sub>2</sub> (2.6.2) e.g. 1) from the past epochs and in particular from 2) concentrated magmatic sources is no longer improbable. The present input of the first listed source is very speculative but it might be marginal since even such an impermeable ice layer is not able to completely halt the gas out transport over billions of years. The magmatic activity diminishing with time (2.5) will also decrease its contribution except more isolated still

active volcanic regions. Consequently, a potential global CO<sub>2</sub> reservoir stored in the regolith over the past epochs is likely to undergo a gradual depletion but definitely not at the rate proposed in the literature (Stewart and Nimmo, 2002). Therefore, I see no argument against the existence of clathrates within and at the bottom of the thickening cryosphere (Fig. 136). Their distribution and abundance in the mineral and ice matrix still remains speculative but I find it justifiable to compare to the terrestrial occurrences of massive deposits, veins or lenses related to geothermal sources (2.1). Disseminated deposits (generally of biogenic origin) most often found on Earth are less likely for CO<sub>2</sub> clathrates. The highest concentration of gas hydrates should be expected in a close proximity to possible gas sources (e.g. vicinity of the volcanic provinces, sub polar regions in the past). Other potential places may be related to tectonic zones that would cut through the permafrost causing buoyant gas to diffuse toward the surface. At such condition

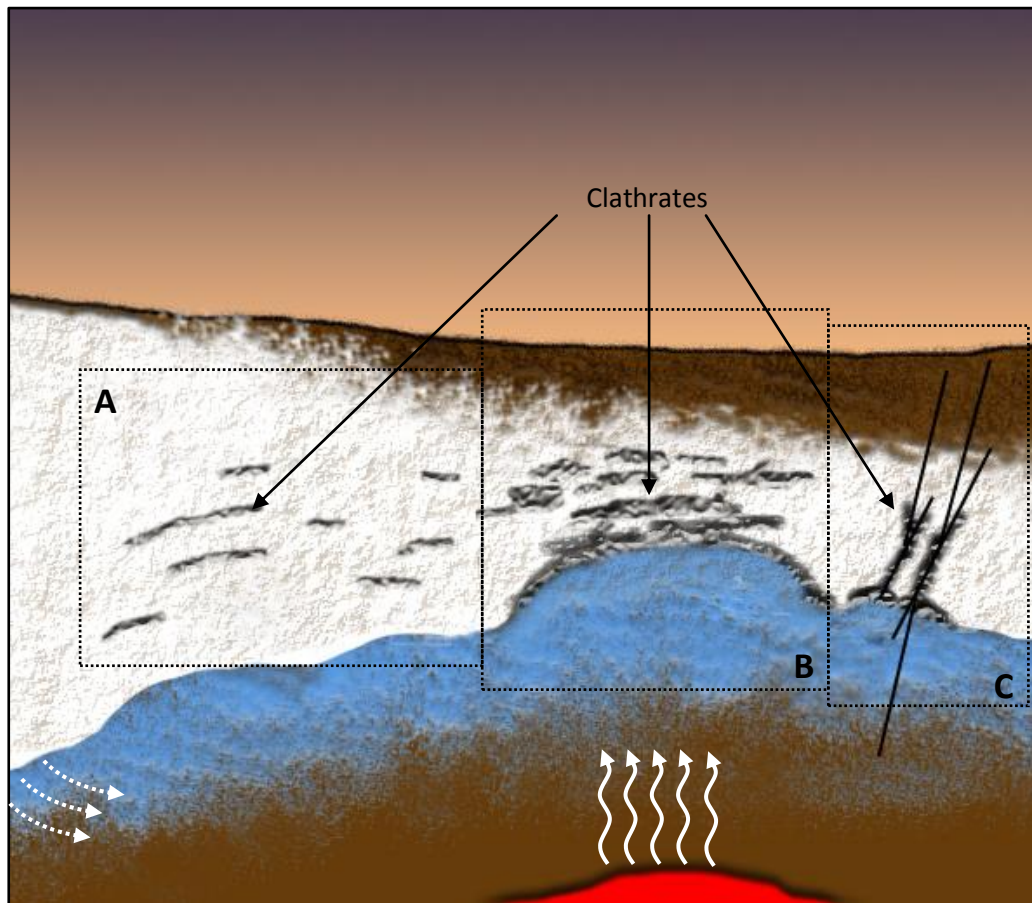


**Fig. 136)** Schematic representation of the possible clathrate occurrences in the present regolith. A) Dispersed lenses and bubbles trapped in the thickening cryosphere, B) Accumulation of clathrate veins, lenses and nodules close to gas sources, C) Impregnation of fractured, faulted zones. Dotted arrows mark an eventual transport of CO<sub>2</sub> from the polar caps. Solid arrows illustrate CO<sub>2</sub> rich fluids from magmatic sources.



clathrates would tend to grow in fractures wherever ice or water would be available at the proper p-T conditions. A small but still significant expansion upon growth is likely to cause a blockage similarly to the terrestrial pipelines clogging by gas hydrates. If this observation is correct then gas compounds could provide a good protection to the underlying gas reservoir. Possible larger accumulations of gas hydrates, like previously discussed (5.1.1), are likely to affect a regional/local thermal gradient. Recently, this effect has been also confirmed through numerical simulations (Kargel et al., 2007). In the regolith this effect gains a particular importance by moving the stability fields of liquids (H<sub>2</sub>O and eventually CO<sub>2</sub>) closer to the surface.

Summary:

- Regolith creates suitable conditions for geologically quick formation of gas hydrates.
- Gas out diffusion to the atmosphere is effectively slowed down by the regolith filled with water ice.
- The greatest concentrations of gas hydrates should be expected close to the potential gas sources and tectonically weakened zones.
- Larger concentrations of gas hydrates are likely to cause significant divergence in local and/or regional gradients moving underlying liquid/-s closer to the surface.

The reader may find above discussion rather general but I decided to keep the proposed scenarios as a flexible platform for a future discussion that would take into account the new diffusion coefficients.

### 5.1.3 Environmental impact of the formation and decomposition of gas hydrates

The existence of clathrates within the regolith and polar caps creates a wide range of new processes that could theoretically have a significant impact on the present and past Martian surface, atmosphere and even climate. Since most of the papers discussing such scenarios were relying almost exclusively on the thermodynamics (2.6) I find important to revise at least more controversial ideas where the formation and/or decomposition kinetics may have a significant impact.

The first very intriguing and probably the most speculative in this discussion is the possible formation of gas hydrates in the early Mars. Such a process at certain conditions would create an enormous sink for atmospheric gases that should be also considered in the

construction of evolutionary models. The most obvious candidate for greenhouse gases on Mars is of course CO<sub>2</sub> but even at high pressures it creates serious difficulties in maintaining the warm climate required for the “Blue Mars”. As it was discussed in the introductory part (2.5.1) the maximum considered initial CO<sub>2</sub> pressure in the warm model was set to 10bar (1MPa). At this point it is good to recall that liquid CO<sub>2</sub> appears at the surface already after crossing 5.11bar (0.51MPa) making it available also in “thicker” models (Manning et al. 2006). “White Mars” goes further in pressures up to 30bar (3MPa), (2.5.2). Temperatures achieved with different approaches were depending also on other parameters (2.5.1) but generally for e.g. 1.5bar (0.15MPa) gave ~214K (Kasting, 1991) and for 5bar (0.5MPa), ~215K (Manning et al. 2006) and ~273K (Pollack et al. 1987), respectively. Keeping in mind that those are averaged values, after a quick look at one of the phase diagrams in this thesis (Fig. 55, 102, 131) it becomes obvious that in all cases the formation of clathrates is unavoidable somewhere at the planet’s surface and subsurface. The process is prolonged in time, especially for less permeable ice where the diffusion limitation will appear but it will continue as long as there is water ice available at suitable p-T conditions. Close to the melting point of ice the kinetic is fast enough to effectively transform 1mm ice particles in a few weeks. Without the nucleation problem, much finer frost will need barely a few hours. Even at temperatures as low as 240K the reaction will proceed at a time scale of months or years depending on the specific surface area of ice. Consequently, the atmosphere draining may weaken the greenhouse effect but the influence remains very speculative. In the “White Mars” the kinetics at low temperatures may hinder the formation process. The thickness of the hydrate layer and its position in the vertical profile is likely to be controlled by the thermal gradient and decreasing global pressure and temperature. Clathrates destabilized eventually will return CO<sub>2</sub> back to the atmosphere on the time scale from days to months, as long as they are outside the self-preservation region (Fig. 122). If they enter into the anomalous state, gas can be stored within the hydrate lattice for geological time scales. More recently, some elements of the discussed scenario were also considered in a detailed work on the thermodynamic of the H<sub>2</sub>O-CO<sub>2</sub> system in the past and present Martian conditions (Longhi, 2000), (Longhi, 2006). All the theoretical models known to me that were trying to quantitatively reconstruct the evolution of the Martian atmosphere and climate to satisfy the “Blue Mars” scenario were ignoring the scenario above (2.5.1).

### Summary:

- Gas hydrates are likely to be present in the early Mars regardless the evolutionary pathway.
- Taking the “Blue Mars” scenario the formation is likely to be quick while in the “White Mars” it is sluggish.
- A general abundance of clathrates is still speculative but clathrates should be considered as a conceivable global sink for large volumes of atmospheric gases.
- The formation of clathrates should be also considered in terms of its possible influence on the climate and timing of the atmosphere collapse.

The gradual atmosphere cooling and its final collapse to the poles somewhere between the Noachian and Hesperian marks the beginning of a new period for gas hydrates. The formation is likely to be restricted to the polar caps and regolith similarly to the present situation but pressures larger than 6mbar (0.6kPa) and a still active volcanism is likely to modify the picture (5.1.1), (5.1.2) presented earlier in favor of clathrates. The transformation at the surface will be controlled by the sublimation pressure. As an example, at an approximate atmospheric pressure of ~500mbar (50kPa) (Carr, 1999), CO<sub>2</sub> gas hydrates could grow in the regions where temperatures do not exceed ~205K. The kinetics of the formation slows down considerably with the falling temperature and driving force from years to thousands of years for larger ice particles and days to months for frost. Below ~195K nucleation difficulties will appear as discussed previously (5.1.1). This limiting factor will gain on the importance along with the progressing cooling due to the atmosphere striping. According to some scientists the sublimation and deposition cycles of dry and water ices controlled by the orbital parameters create a convincing mechanism of CO<sub>2</sub> transfer into the regolith through the polar sheets and thus supporting clathrate formation within the caps (2.6.1). The diffusion constants of CO<sub>2</sub> molecules through water ice ( $10^{-9}$ - $10^{-10}$  m<sup>2</sup>/s) at 160K-180K (Kurahashi-Nakamura and Tajika, 2006) that were used to estimate the timescale of the percolation are about four orders of magnitude larger than those proposed in this thesis for the bulk. These values are still reasonable but then some limited porosity or cracks should be present in polar caps. Maintaining such pathways in a flowing ice might be difficult on a longer timescale. In another paper (Longhi, 2006) the percolation of volatile/liquid CO<sub>2</sub> through water ice was meant to be supported by growing clathrates that were supposed to improve the gas transport through a

volume decrease of about 20%. This incorrect and rather surprising idea most likely originates in the misleadingly interpreted density of clathrate compounds. Certainly the hydrogen bonded structure filled with gas will be always denser than water ice but it does not reflect the true volume change (1.1.2). The expansion of clathrate lattice of about 13% in comparison to pure water ice is likely to clog possible diffusion pathways, thus decreasing the permeability.

Summary:

- The formation of clathrates after the atmospheric collapse is likely to be similar to the present situation (5.1.1-5.1.2).
- Decreasing the availability of CO<sub>2</sub> over the Martian history controls the abundance of clathrates.
- Eventual warm periods are likely to accelerate the formation of clathrates and atmosphere draining with all its consequences.

Clathrates stored in the polar caps and regolith may buffer a considerable amount of CO<sub>2</sub> that during obliquity changes may be released to the atmosphere thus contributing to the temporary climate warming (2.6.3). I find the impact on the Martian climate and amount of gas involved in this process very speculative and additional data are indispensable to continue this discussion. By raising this issue I would like to turn the attention of the reader to another potential consequence that can be assessed with presently available data. The side effect of the periodic recycling of gas from decomposed clathrates may cause the alteration or even resetting of the isotopic ratios in the past Martian atmosphere (2.6.3). Clathrate incorporate all atmospheric gases according to their fugacity favoring heavier molecules that become enriched in the lattice. An influence of the formation process on the fractionation of isotopes exists but is very poorly investigated (1.1.5.2). Its effect for e.g. CO<sub>2</sub>, N<sub>2</sub>, Kr, Xe at the Martian p-T conditions is unknown. If a decomposed volume of gas hydrates is significant (Musslewhite and Swindle, 2001), then indeed atmospheric gases fractionated in various processes may be affected by atmospheric components preserved from past epochs. Although this project does not provide new information on this issue, I would like to quickly explore this idea with a newly developed CSMGem (Sloan and Koh, 2007) program that allows simulating compositions of mixed hydrates as a function of temperature. Unfortunately, as the package was created for oil industry applications thus the available non hydrocarbon gas feed composition has a

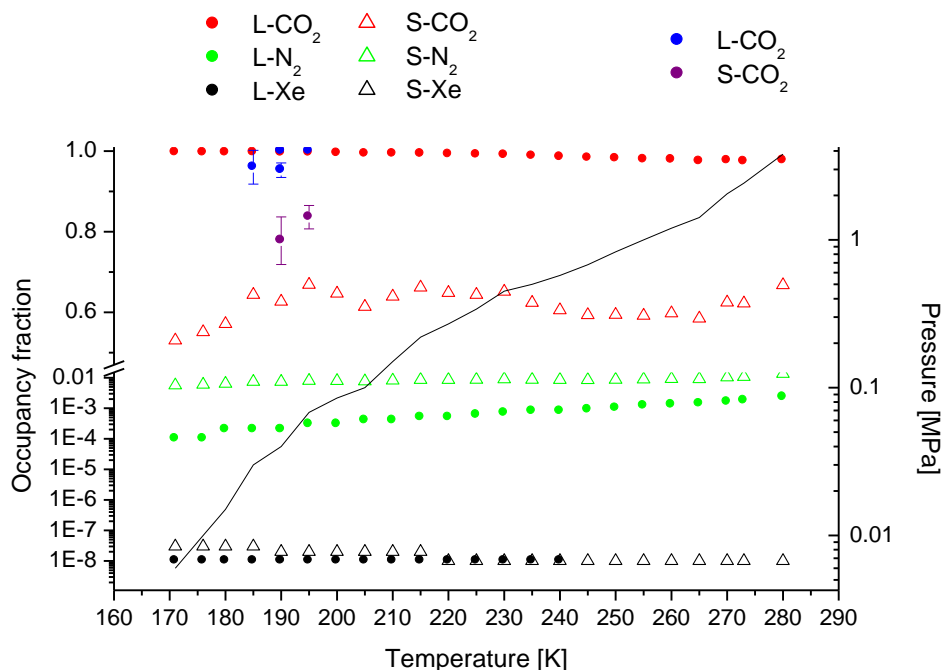


**Fig. 137)** Occupancy fraction for three gas species: CO<sub>2</sub>, N<sub>2</sub> and Xe in small (S) and large (L) cages of the theoretical mixed clathrates formed under in the present Martian atmosphere (CSMGem). The abundance of CO<sub>2</sub> in small cages shows a high sensitivity to change in pressure. The solid black line shows the formation pressure that roughly go through the middle of the H<sub>2</sub>O(S)-H-CO<sub>2</sub>(V) (Fig. 9) stability field. Due to internal issues within CSMGem some excursions from middle values were unavoidable. Blue (L) and violet (S) points correspond to the experimental data for pure CO<sub>2</sub> clathrates from Fig. 101 (right).

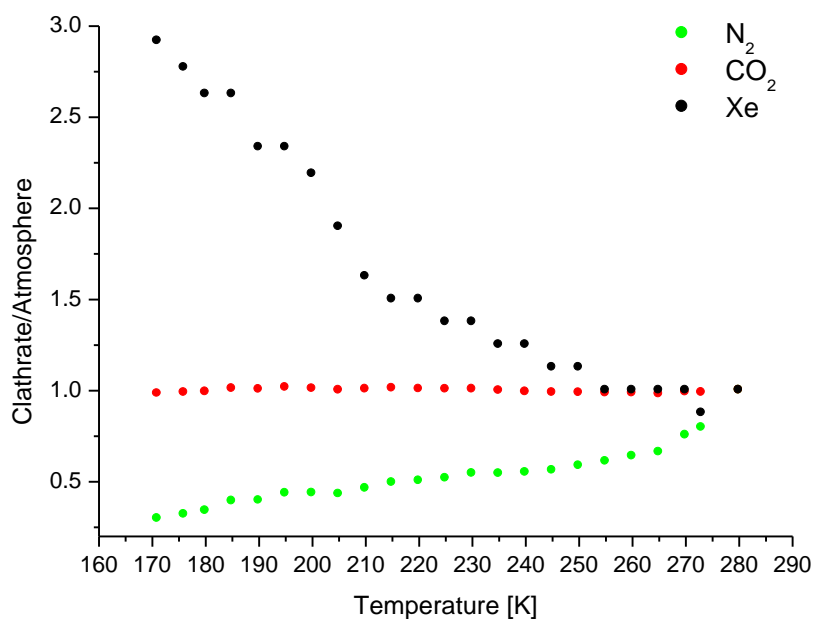


**Fig. 129)** Temperature dependent atmosphere fractionation by growing hydrates (CSMGem). Data were normalized to 280K.

limited choice. For this reason I had to limit the simulated Martian atmosphere to three gases: N<sub>2</sub>, Xe and CO<sub>2</sub>, where the first two were taken in their present abundance (Table 3) and CO<sub>2</sub> was recalculated to give a sum of 100%. Plotted cage occupancy for the simulated gas hydrates already at the first sight reveal an interesting dependence of all gases on changing p-T conditions (Fig. 128). CO<sub>2</sub> steadily substitutes N<sub>2</sub> in large cages toward lower temperatures reaching almost full occupancy at 190K. This value is in a good agreement with the pure CO<sub>2</sub> clathrates presented earlier (4.2.5). The abundance of nitrogen decreases also in smaller cavities but on the smaller rate. CO<sub>2</sub> occupy here only about 60% of cages with a visibly decreasing trend from about 185K. Unfortunately, internal limitations of CSMGem do not allow for tracing it to even lower temperatures. Experimentally established occupancy of smaller cages (4.2.5) shows values about 20% greater. Xe enters preferentially into small cages but below 180K it also contributes to large cavities. Interestingly, this trace gas becomes progressively enriched in the clathrate lattice (Fig. 129) reaching three times higher concentration than in the gas phase at 170K. N<sub>2</sub> shows the opposite trend but on smaller magnitude. On closer inspection one can also notice that CSMGem predicts a small depletion for CO<sub>2</sub> below ~185K. Clearly clathrates formed at the lower temperature end are likely to the greatest impact on the atmospheric chemical and isotopic composition. Although their abundance is limited by the sluggish kinetics even a small volume e.g. of 10-20mbar (1-2kPa) may already significantly affect atmospheric trace gases. To obtain a similar effect with clathrates formed at higher temperatures obviously greater volume must be decomposed.

With the above simulation I offer a quick guide for those scientists who evaluate volumes of CO<sub>2</sub> and other two gases that may be stored in clathrates formed at different p-T conditions. It becomes also possible to calculate the volume of hydrates subsequently released to the atmosphere. One should still keep in mind that more experimental evidences should be gathered to gain a confidence in these predictions. At this point is also worth mentioning that even if the mixed hydrates of a certain composition are thermodynamically preferred, there is always a risk that kinetic limitations like different diffusion rates of individual gases may change predicted occupancies. This issue is likely to be particularly pronounced at low temperatures and for large molecules like xenon. Although, some indirect evidences from terrestrial ice cores research support this idea, it remains still poorly investigated.



Summary:

- Clathrates show a potential to be enriched in heavier gases and perhaps also isotopes.
- Lower formation temperatures increase this effect.
- If the volume of gas from dissociating clathrates is substantial then the isotopic and chemical composition of the atmosphere may be indeed affected.
- The extend of this phenomenon would be related to the abundance of clathrates in the past epochs.

The decomposition of clathrates related to the liberation of large volumes of gas may create another effect worth considering, namely the ability of reshaping the planetary surface. This possibility has been extensively discussed in the literature (2.6.3) but the kinetics of the dissociation was very poorly explored. The published ideas should now be confronted with the results coming from this thesis. Here I would like to emphasize a possible role of both aspects of the self-preservation phenomenon (4.3.5) that can strongly alter the reaction rates. Although, gas hydrates can be destabilized in the number of processes (2.6.3) only a few of them can cause high decomposition rates that could have a major influence on the surface features.

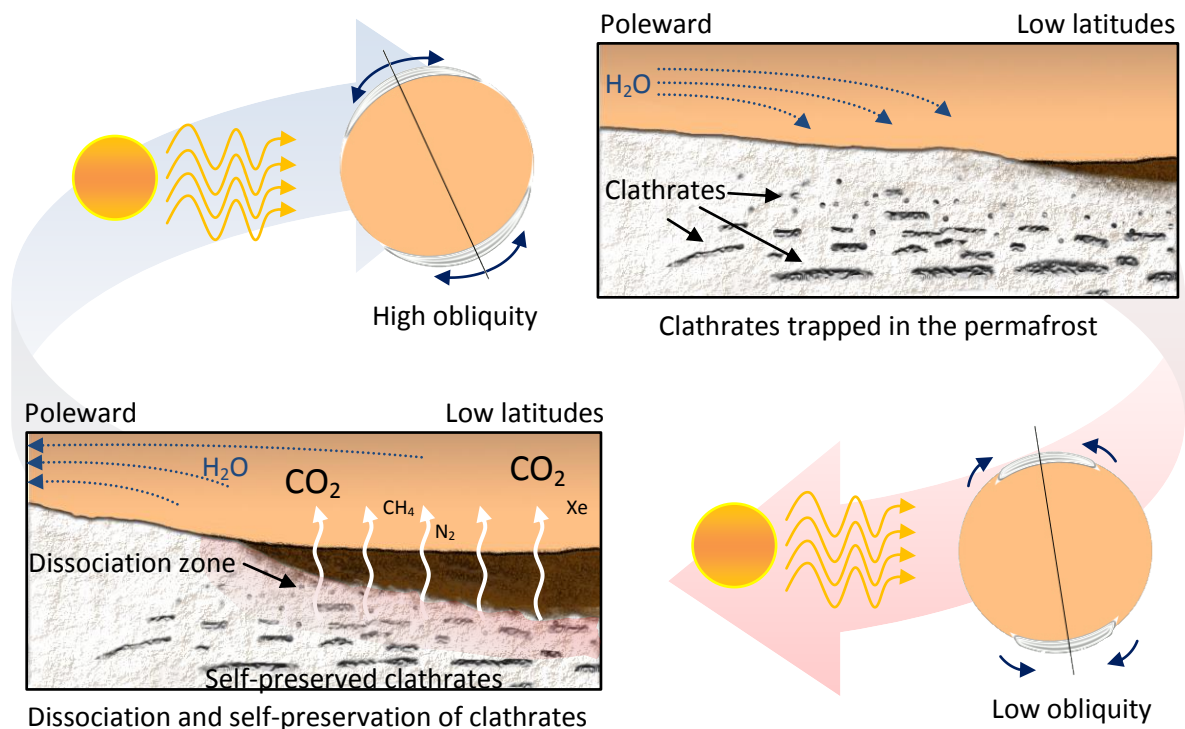
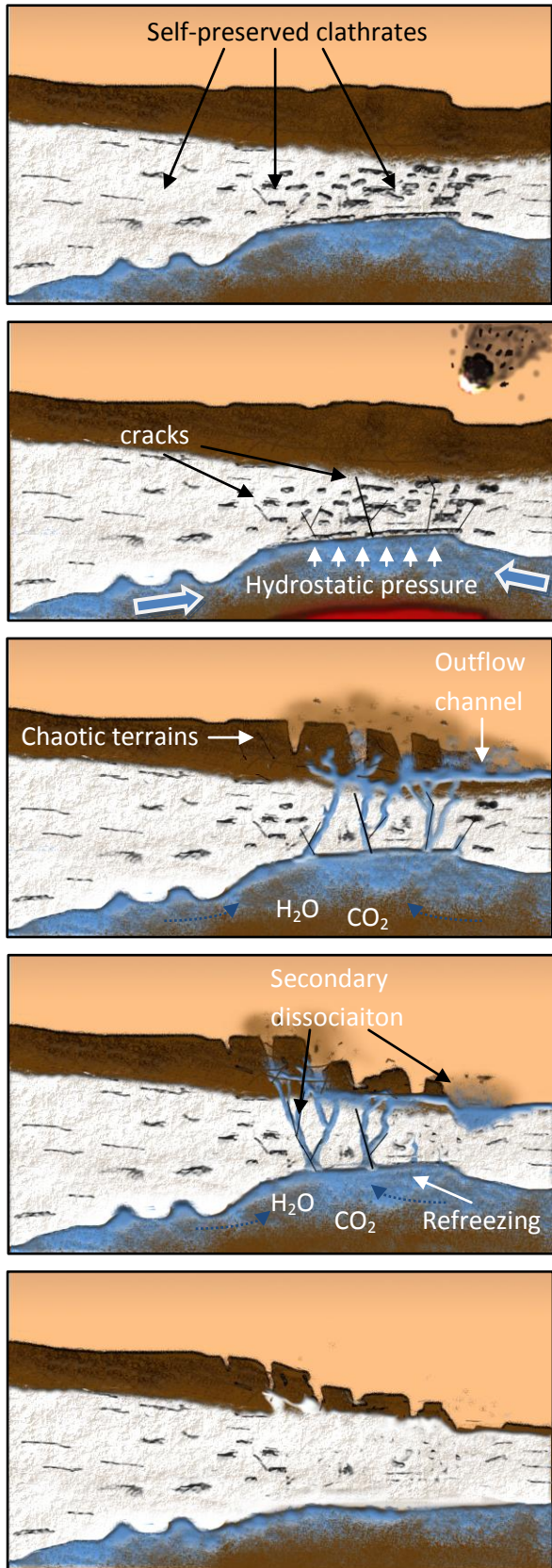


**Fig. 130)** Schematic representation of the sublimation and deposition cycles during high and low obliquity periods (General concept after Prieto-Ballesteros et al. 2006 expanded about the self-preservation phenomenon).

The obliquity cycles that are likely to control water sublimation and condensation between poles and equatorial regions certainly have a potential to destabilize clathrates trapped in the cryosphere. Slow expansion of the ice coverage at the surface and a possible thickening of the permafrost during high obliquity excursions may trap a certain volume of clathrates in form of e.g. lenses, layers and perhaps small inclusions (Fig. 130). During low obliquity periods sublimating ice may destabilize clathrates by the decompression and/or exposition to the atmosphere or causing dissociation at the rate corresponding to the local temperature. Shallow inclusions and smaller agglomerations are likely to be transformed into ice on a time scale from minutes/hours if exposed to the atmosphere. If some shielding is developed, the decomposition may take months/years depending on ice quality and sublimation rates. Larger bodies of clathrates destabilized deeper in the regolith below 220K are likely to share the same fate due to the increasing defects of the coating ice. The decomposition in this case might be extended in time to tens of years. The influence of the prolonged dissociation on the surface will be rather small. The only visible effect could be perhaps caused by the volume reduction during the transformation from hydrates to ice effecting in a limited ground subsidence. The decompression above 220K may lead gas hydrates into the self-preservation regime if required decomposition pressure and temperature are reached. Above 240K the phenomenon will occur in the whole pressure range. The temperature region where the self-preservation may occur corresponds to the depths roughly from hundreds of meters to a few kilometers. Clathrates surrounded by the ice film will continue to dissociate but on geological timescales (thousands, tens of thousands of years). The timing given in this subchapter is based on the laboratory experience and information found in the literature. For better constraints a model with predictive power is needed.

The fragile state of the self-preserved clathrates is an entry point for the discussion about one of the most spectacular surface features on Mars, namely outflow channels and their source regions. The origin of those features has been broadly discussed in the large number of theories related to liquid CO<sub>2</sub>, water and finally clathrates (see: 2.5.1, 2.5.2, 2.6.3). The common element of all of them is the formation through a catastrophic process. Interestingly, the decomposition of clathrates seems to repeatedly appear as a mechanism capable of disrupting an overlaying regolith e.g. (Clifford and Parker, 2001), (Rodriguez et al. 2005), (Rodriguez et al. 2006). Yet, as the reader saw in the previous section, clathrates in the “normal conditions” (outside the self-preservation – Fig. 131) decompose slowly



Self-preserved clathrates accumulated in the permafrost overlaying a water saturated regolith. Lower thermal conductivity of hydrates locally shifts up the ice/liquid water boundary.

Hydrostatic pressure buildup (e.g. thickening cryosphere, magmatism) or/and impacts weaken the overlaying permafrost. The self-preservation state is destroyed and clathrates begin to rapidly dissociate.

Pressurized liquids and gas quickly percolate to the surface through the shattered regolith. Undermined rocks start to collapse.

Water in primary pathways begin to freeze but new connection to the surface are formed through the secondarily destabilized clathrates

Depletion of semi stable clathrates and/or drop in the hydrostatic pressure ends the outflow. Affected region subsides due to the volume loss.

**Fig. 131)** Schematic presentation of a chaotic terrain formation and water release triggered by a rapid dissociation of self-preserved clathrates.

releasing stored gas over extended periods of time. This dissociation style may at most cause some strain in the regolith that would dissipate. In order to cause a massive gas release in a short period of time one has to destroy the ice shielding of self-preserved clathrates (Fig. 131). This can be done in two ways: 1) by melting (magmatism, water flow) or 2) through a mechanical cracking below the freezing point of water (tectonic activity, impacts). In the first case the decomposition is likely to be the most violent if only sufficient amount of heat will be provided to sustain positive temperatures. It may be achieved by a direct contact of water with the clathrates like in case the terrestrial analogs (2.1). Massive deposits of rapidly decomposing clathrates may be capable of disrupting perhaps even a regolith of a few kilometer (Max and Clifford, 2001). In the second case a rapid gas release will last as long as the new barrier is not formed. I speculate that the overpressure created in this way may be still sufficient to fracture a regolith already strained by e.g. melting of clathrates, thickening cryosphere, magmatic heating. The destruction of the plug allows pressurized liquid/-s to rapidly percolate toward the surface and form outflow channels. A local warming caused by escaping fluids may trigger additional secondary rapid decompositions. The greatest potential for the long lasting flow have certainly water but an initial presence of considerable amount of CO<sub>2</sub> gas or immiscible liquid CO<sub>2</sub> is also plausible. In fact their presence would considerably improve the short range flow and eroding power. The outflow would cease by a gradually reforming ice plug. Interestingly, the scenarios involving clathrates do not require any significant cavern system that would be difficult to maintain in brecciated regolith. The commonly observed subsidence may well be related to the missing or reduced volume after dissociated clathrates and removed water.

Certainly with the scenario proposed above I have not explored all possible implications of the self-preservation. One can build similar hypotheses for more specific geological settings (e.g. destabilization of clathrates along faulted zones by a recurring tectonic activity, magmatic intrusions, melting by brines). The main aim of this section was to demonstrate that clathrates need to be in a special state before causing a massive, fast dissociation. The self-preservation effect requires higher temperatures that are achievable at greater depths within the regolith. Also for this reason I find unlikely that smaller and shallower surface runoff features like gullies can be triggered by quickly decomposing clathrates. Neither temperatures nor pressures are sufficient to cause the anomalous state. A disruption of gas hydrates that perhaps remained from past epochs in the anomalous

state will decompose slowly as any other clathrates at these low temperatures.

Another issue that one should consider is a repeatability of the formation-decomposition process. If the conclusions from the previous subchapters are correct then the existence of such cycles, controlled by the expansion of the cryosphere and abundance of new deposits will diminish with time. Low atmospheric pressure and decaying gas supply in the regolith is likely to decrease the probability the reformation of clathrates close to the surface and within the regolith to the specific occurrences (5.1.1, 5.1.2). The sluggish kinetics at low temperatures is another important factor that gained on importance with time. Finally, thickening cryosphere may shift newly formed deposits to even greater depths where if destabilized may have a minimal or no influence on the surface.

Interestingly, this diminishing role of clathrates creates a considerable problem for the hypotheses that suggest them as an eventual origin and storage of methane (2.6.3). From the most often evoked locations the polar caps in my opinion are the least possible. The formation of mixed clathrates close to the surface is not only very difficult from the kinetic point of view but also supply of methane. It should be noticed that a hypothetical reservoir from the past epochs enclosed in clathrates is likely to be depleted after some obliquity changes. The present atmospheric methane content is far too low to be considered as a viable addition to recently formed hydrates. The chemical fractionation observed for xenon (Fig. 129) here cannot be applied since  $\text{CH}_4$  is considerably lighter. Much more probable source may be searched within the regolith but again the availability of methane is a crucial factor. One could consider here an episodic or constant inorganic and/or biogenic production. The isotopic composition of atmospheric methane was not measured yet and for now both options are still viable (Assuming that the hypothetical life on Mars affects isotopic ratios in a similar way to observed on Earth). The first type of the occurrence would likely involve massive deposit concentrated around the source while the second one could form mostly disseminated and layered accumulation similarly to the terrestrial examples (2.1). The decomposition kinetics of both types of the deposits is likely to be much different due to the relative particle size (4.3.5). Taking again the obliquity excursions as the main destabilizing factor dispersed deposits would gradually release stored methane in the contact with atmospheric gases (Fig. 130) as suggested in the literature (Prieto-Ballesteros et al. 2006). Much more difficult is recharging or this mechanism that requires ice/water vapor and an appropriate partial pressure of methane. Presently I do not see any potential mechanism that could help here. Concentrated deposits

might avoid these difficulties through a supply of gas and water rich fluids. Some weak evidences from the global mapping of methane also support more localized sources (Formisano et al. 2004). Yet, one should keep in mind that if the decomposition conditions reach the self-preservation region, resupplying of the atmosphere is likely to be halted.

Summary:

- Quasi cyclic obliquity excursions, local heat sources tectonic activity and brines are capable of destabilizing clathrates.
- At lower temperatures decomposition is governed by the slow kinetics and stacking faulty ice Ih or Ic.
- Self-preserved clathrates create a potential source for triggering large scale resurfacing processes.
- Mechanical removal of the ice protective layer below the freezing point of water will cause very rapid dissociation of preserved clathrates that will last as long as a new barrier is not formed.
- Melting of the ice that shields metastable gas hydrates is likely to be the strongest trigger.

## 5.2 Gas hydrates in the Solar System

The kinetic investigation presented in this thesis to some extent can be also applied to other planetary bodies where clathrates are suspect to exist and undergo the formation/decomposition at temperatures well below the melting point of ice. In this context I find the kinetic metastability and self-preservation most interesting but also the information on the quality of ice formed through the dissociation of clathrates may provide an additional tool for constraining clathrate related hypotheses.

A particularly good testing ground for above processes is a suggestion that decomposing clathrates of such gases like CO<sub>2</sub>, CH<sub>4</sub> and N<sub>2</sub> are responsible for the Enceladus' jets (Kieffer et al. 2006), (2.2). As could be seen on the Fig. 131 each phenomenon, the "quality" of water ice is prescribed to a certain temperature range characterized by different kinetics. The existence of jets already suggest that temperature inside the moon where a hypothetical clathrates reservoir might be is most likely above the kinetic metastability effect (<150-165K). Up to 240K the decomposition to vacuum unavoidably leads to the formation of cubic or stacking faulty ice that is incapable of creating any particular shielding effect. In addition, deformations caused by tidal forces



may mechanically remove formed ice. Consequently, if a hypothetical clathrate reservoir exists in this temperature range then one should expect a fairly weak but constant outgasing with periods of higher activity. The reservoir at even higher temperatures, above 240K, is likely to be influenced by the self-preservation mechanism. A considerably better ice protection would impede the gas flux through the "tiger strips". A mechanical removal of the protective layer would trigger periods of very high activity.

With this quick and robust kinetic test I wanted to demonstrate how with a very little effort one could try to constrain a presence of clathrates and their eventual role as an active element in dynamic processes even in such exotic places like Enceladus. This approach gives also some ideas about temperatures that cannot be accessed with direct methods. Certainly, one should also not forget that extraterrestrial environments may still hold some less understood mechanisms that can equally well explain observational data without any involvement of gas hydrates.

# Summary of the project and outlook

This thesis closes a six years long project that was targeting on the kinetics of growth and dissociation of CO<sub>2</sub> hydrates at temperatures and pressures relevant to the Martian surface and upper crust. The main motivation for this work was almost complete lack of information on the formation and decomposition rates well under the melting point of ice and a considerable demand of such data from the planetary science community.

The first part of the project was extensively exploring the formation kinetics in a solid H<sub>2</sub>O-volatile CO<sub>2</sub> system with respect to various driving forces, temperatures and SSA of starting ice (Genov, 2005). The experimental work was supported by two clathrate growth models: phenomenological Powder 2 (Genov et al., 2004) and Avrami based JMAKGB that enabled first predictions on formation timescales at the conditions relevant to the Martian polar caps. The calculations were still based only on the diffusion controlled stage. The initial nucleation and growth stage remained poorly constrained. A preliminary work performed on the decomposition kinetics confirmed the existence of the self-preservation anomaly above 240K. Later, a link between a temperature driven recrystallization from Ic to Ih (often referred as a ice perfection or “quality” of ice) and this phenomenon has been found (Kuhs et al., 2004).

The work presented in this thesis was carried on in the second part of the project. Missing information on the formation kinetics and crystal growth in the initial stage was successfully retrieved (Falenty et al., 2007) and introduced to the newest, Powder 4 program with its “Frost” module. It became possible to calculate formation timescales for small particles (<2 $\mu$ m) where the diffusion limited stage do not appear. The modeling also indicated an increasing nucleation problem below 190K. Preliminary attempts were made to establish occupancies of small and large cavities in clathrates formed at low temperatures. The extensive studies on the decomposition process at the Martian surface and subsurface conditions confirmed the importance of the “quality” of ice through a qualitative and quantitative stacking fault analysis (Hansen et al., 2007), (Hansen et al., 2008a), (Hansen et al., 2008b). A new variant of the self-preservation existing in a narrow p-T range below 240K has been discovered (Falenty and Kuhs, 2008). Its origin was linked to a surface microstructure of ice layer. At temperatures below 165K a kinetic metastability effect was found.

The information gathered throughout the whole duration of this project provides a

solid ground for the evaluation of Martian processes involving the formation or decomposition kinetics below the melting point of ice. The results of this project can be also applied, within the limits, to other planetary bodies where clathrates may form or decompose.

Definitely putting all observations to one consistent story was not a trivial task and still additional work need to be done:

- In the next step of the modeling of formation a polydispersity of ice should be introduced to better match natural situation.
- All formation experiments should be consistently fitted with the new Powder 4 model to refine obtained activation energies.
- It is advisable to perform a few formation experiments from frost at temperatures 165-185K to confirm the possible nucleation issue.
- There is a need of more extensive work on the cage filling issue for CO<sub>2</sub> and gas mixtures of the Martian composition.
- Formation of clathrates through a condensation from the gas phase should be investigated.
- Chemical fractionation of gases during the formation is a promising subject for further studies.
- Modeling approach for the decomposition still lacking but now it is within reach.
- Kinetic metastability requires more studies including, long experiments, different gases and gas mixtures.

# INDEX

- Acuña MH, Connerney JEP, Wasilewski, Lin RP, Anderson KA, Carlson CW, McFadden J, Curtis DW, Mitchell D, Reme H, Mazelle C, Sauvaud AJ, d'Uston C, Cros A, Medale JL, Bauer JL, Cloutier P, Mayhew M, Winterhalter D and Ness NF, *Magnetic field and plasma observations at Mars: Initial results of the Mars Global Surveyor mission*, *Science* **279** (5357), 1676-1680, 1998.
- Acuña MH, Connerney JEP, Ness NF, Lin RP, Mitchell D, Carlson CW, McFadden J, Anderson KA, Reme H, Mazelle C, Vignes D, Wasilewski P and Cloutier P, *Global distribution of crustal magnetization discovered by the Mars Global Surveyor MAG/ER experiment*, *Science* **284** (5415), 790-793, 1999.
- Adisasmito S, Frank RJ and Sloan ED, *Hydrates of carbon-dioxide and methane mixtures*, *Journal of Chemical and Engineering Data* **39** (1), 68-71, 1991.
- Agnor CB, Canup RM and Levison HF, *On the character and consequences of large impacts in the late stage of terrestrial planet formation*, *Icarus* **142** (1), 219-237, 1999.
- Aladko EY, Dyadin YA, Fenelonov VB, Larionov EG, Manakov AY, Mel'gunov MS and Zhurko FV, *Formation and decomposition of ethane, propane, and carbon dioxide hydrates in silica gel mesopores under high pressure*, *Journal of Physical Chemistry B* **110** (39), 19717-19725, 2006.
- Alavi S, Ripmeester JA and Klug DD, *Stability of rare gas structure H clathrate hydrates*, *Journal of Chemical Physics* **125** (10), art. no: 104501, 2006.
- Alibert Y and Mousis O, *Formation of Titan in Saturn's subnebula: constraints from Huygens probe measurements*, *Astronomy & Astrophysics* **465** (3), 1051-1060, 2007.
- Als-Nielsen Jens, J, *Diffraction, refraction and absorption of X-rays and Neutrons: A comparative exposition*, In: *Neutron and synchrotron radiation for condensed matter studies, vol.1, Theory, instruments and methods* (ed. J. Brauchel, JL. Hodeau, MS. Lehmann, JR. Regnard and C. Schlenker), EDP Sciences-Springer Verlag, Les Ulis, France, 1993.
- Als-Nielsen Jens and McMoorrow D, *Elements of Modern X-ray Physics*, Willey, New York, 2001.
- Anderson BJ, Radhakrishnan R, Baron Peters, Borghi GP, Tester JW and Trout BL, *Molecular simulations of gas hydrate nucleation*, In: *Physics and chemistry of ice* (ed. WF. Kuhs) 3-11, RSC Publishing, Cambridge, 2007.
- Anderson RC, Dohm JM, Golombek MP, Haldemann AFC, Franklin BJ, Tanaka KL, Lias J and Peer B, *Primary centers and secondary concentrations of tectonic activity through time in the western hemisphere of Mars*, *Journal of Geophysical Research – Planets* **106** (E9), 20563-20568, 2001.
- Anderson RC, Llamedo M, Tohidi B and Burgass RW, *Experimental measurement of methane and carbon dioxide clathrate hydrate equilibria in mesoporous silica*, *Journal of Physical Chemistry B* **107** (15), 3507-3514, 2003.
- Angell CA, In: *Water: A Comprehensive Treatise (Vo. 7)*, (ed. F. Franks), Plenum Press, New York, 1982.
- Angus S, de Reuck KM, Armstrong B, Craven RJ and Wagner W, *Carbon dioxide*, *International thermodynamic tables of the fluid state-3*, Pergamon, Oxford 1976.

- Anklam MR and Firoozabadi A, Driving force and composition for multicomponent gas hydrate nucleation from supersaturated aqueous solutions, *Journal of Chemical Physics* **121** (23), 11867-11875, 2004.
- Arkani-Hamed, *Paleomagnetic pole positions and pole reversals of Mars*, *Geophysical Research Letters* **28** (17), 3409-3412, 2001.
- Arkani-Hamed J and Boutin D, *Paleomagnetic poles of Mars: Revisited*, *Journal of Geophysical Research – Planets* **109** (E3), Art. No. E03011, 2004.
- Arkani-Hamed J, *Timing of the Martian core dynamo*, *Journal of Geophysical Research – Planets* **109** (E3), Art. No. E03006, 2004.
- Arkani-Hamed, *Magnetic crust of Mars*, *Journal of Geophysical Research – Planets* **110** (E8), Art. No. E08005, 2005.
- Atreya SK, Adams EY, Niemann HB, Demick-Montelara JE, Owen TC, Fulchignoni M, Ferri F, Wilson EH, *Titan's methane cycle*, *Planetary and Space Science* **54** (12), 1177-1187 Sp. Iss., 2006.
- Baker VR, Strom RG, Gulick VC, Kargel JS, Komatsu G and Kale VS, *Ancient oceans, ice sheets and the hydrological cycle on Mars*, *Nature* **352** (6336), 589-594, 1991.
- Baker VR, Strom RG, Dohm JM, Gulick VC, Kargel JS, Komatsu G, Ori GG and Rice JW, *Mars= Oceanus Borealis, ancient glaciers, and the megaoutflow hypothesis*, *Lunar and Planetary Science XXXI*, abstract nr: **1863**, 2000.
- Baker VR, *Water and the Martian landscape*, *Nature* **412** (6843), 228-236, 2001.
- Balme M, Mangold N, Baratoux D, Costard F, Gosselin M, Masson P, Pinet P and Neukum G, *Orientation and distribution of recent gullies in the southern hemisphere of Mars: Observations from High Resolution Stereo Camera/Mars Express (HRSC/MEX) and Mars Orbiter Camera/Mars Global Surveyor (MOC/MGS) data*, *Journal of Geophysical Research – Planets* **111** (E5), Art. No. E05001, 2006.
- Bandfield JL, Hamilton VE and Christensen PR, *A global view of Martian surface compositions from MGS-TES*, *Science* **287** (5458): 1626-1630, 2000.
- Bandfield JL, Glotch TD and Christensen PR, *Spectroscopic identification of carbonate minerals in the Martian dust*, *Science* **301** (5636), 1084-1087, 2003.
- Barrer RM and Ruzicka DJ, *Non-Stoichiometric Clathrate Compounds of Water Part 2.-Formation and Properties of Double Hydrates*, *Transactions of the Faraday Society* **58** (479), 2239-2252, 1962.
- Belosludov VR, Lavrentiev MY and Dyadin YA, *Theory of clathrates*, *Journal of Inclusion Phenomena and Molecular Recognition in Chemistry* **10** (4), 399-422, 1991.
- Belosludov RV, Kawazoe Y, Belosludov VR and Kuznetsov FA, *Role of guest molecules on the stability of different cage-like structures of large water clusters investigated by first-principle calculations*, *Proceedings of the Fourth International Conference on Gas Hydrates* 683-686, Yokohama, 2002.
- Benton MJ and Twitchett RJ, *How to kill (almost) all life: the end-Permian extinction event*, *Trends in Ecology & Evolution* **18** (7), 358-365, 2003.
- Berman DC and Hartmann WK, *Recent fluvial, volcanic, and tectonic activity on the Cerberus plains of Mars*, *Icarus* **159** (1), 1-17, 2002.

- Bertka CM and Fei YW, *Mineralogy of the Martian interior up to core-mantle boundary pressures*, Journal of Geophysical Research – Solid Earth **102** (B3), 5251-5264, 1997.
- Bibring JP, Langevin Y, Poulet F, Gendrin A, Gondet B, Berthe M, Soufflot A, Drossart P, Combes M, Bellucci G, Moroz V, Mangold N and Schmitt B, *Perennial water ice identified in the south polar cap of Mars*, Nature **428** (6983), 627-630, 2004.
- Blake DF, Allmandola L, Stanford S, Hudgins D and Freund F, *Clathrate formation in amorphous cometary ice analogs in vacuo*, Science **254** (5031), 548-551, 1991.
- Blichert-Toft J, Gleason JD, Telouk P and Albarede F, *The Lu-Hf isotope geochemistry of shergottites and the evolution of the Martian mantle-crust system*, Earth and Planetary Science Letters **173** (1-2), 25-39, 1999.
- Bodnar, RJ, *PTx phase equilibria in the H<sub>2</sub>O-CO<sub>2</sub>-Salt system at Mars near-surface conditions*, Lunar and Planetary Science XXXII, abstract nr: **1689**, 2001.
- Boynton WV, Feldman WC, Squyres SW, Prettyman TH, Bruckner J, Evans LG, Reedy RC, Starr R, Arnold JR, Drake DM, Englert PAJ, Metzger AE, Mitrofanov I, Trombka JI, d'Uston C, Wanke H, Gasnault O, Hamara DK, Janes DM, Marcialis RL, Maurice S, Mikheeva I, Taylor GJ, Tokar R and Shinohara C, *Distribution of hydrogen in the near surface of Mars: Evidence for subsurface ice deposits*, Science **297** (5578), 81-85, 2002.
- Brain DA and Jakosky BM, *Atmospheric loss since the onset of the Martian geologic record: Combined role of impact erosion and sputtering*, Journal of Geophysical Research – Planets **103** (E10), 22689-22694, 1998.
- Breuer D and Spohn T, *Early plate tectonics versus single-plate tectonics on Mars: Evidence from magnetic field history and crust evolution*, Journal of Geophysical Research – Planets **108** (E7), Art. No. 5072, 2003.
- Breuer D and Spohn T, *Viscosity of the Martian mantle and its initial temperature: Constraints from crust formation history and the evolution of the magnetic field*, Planetary and Science **54** (2), 153-169, 2006.
- Bridges NT and Lackner CN, *Northern hemisphere Martian gullies and mantled terrain: Implications for near-surface water migration in Mars' recent past*, Journal of Geophysical Research – Planets **111** (E9), 2006.
- Brightwell SN, Kargel JS and Titus TN, *Martian south polar deformation and sublimation processes*, Lunar and Planetary Science XXXIV, abstract nr: **2077**, 2003.
- Brunauer S, Emmett HP and Teller E, *Adsorption of gases in multi molecular layers*, Journal of the American Chemical Society **60**, 309-319, 1938
- Buffett B and Archer D, *Global inventory of methane clathrate: sensitivity to changes in the deep ocean*, Earth and Planetary Science Letters **227** (3-4), 185-199, 2004.
- Cabrol NA, Grin EA, Landheim R and McKay CP, *Cryovolcanism as a possible origin pancake-domes in the Mars 98 landing site area: Relevance for climate reconstruction and exobiology exploration*, Lunar and Planetary Science XXIX, abstract nr: **1249**, 1997.
- Cabrol NA and Grin EA, *Distribution, classification, and ages of Martian impact crater lakes*, Icarus **142** (1), 160-172, 1999.



- Cabrol NA and Grin EA, *Composition of the drainage network on early Mars*, *Geomorphology* **37** (3-4), 269-287, 2001.
- Carr MH and Clow GD, *Martian channels and valleys - their characteristics, distribution, and age*, *Icarus* **48** (1), 91-117, 1981.
- Carr MH, *Stability of streams and lakes on Mars*, *Icarus* **56** (3), 476-495, 1983.
- Carr MH, *Channels and valleys on Mars: Cold climate features formed as a result of a thickening cryosphere*, *Planetary and Space Science* **44** (11), 1411-1423, 1996.
- Carr MH, *Retention of an atmosphere on early Mars*, *Journal of Geophysical Research – Planets* **104** (E9), 21897-21909, 1999.
- Carr MH, *Martian oceans, valleys and climate*, *Astronomy & Geophysics* **41** (3), 20-26, 2000.
- Carr MH, *Elevations of water-worn features on Mars: Implications for circulation of groundwater*, *Journal of Geophysical Research – Planets* **107** (E12), Art. No. 5131, 2002.
- Cha SB, Ouar H, Wildeman TR and Sloan ED, *A 3RD-surface effect on hydrate formation*, *Journal of Physical Chemistry* **92** (23), 6492-6494, 1988.
- Chaix L, Ocampo J and Dominé F, *Adsorption of CH<sub>4</sub> on laboratory-made crushed ice and on natural snow at 77K. Atmospheric implications*, *Comptes rendus vol.* **322**, 609-616, 1996.
- Chakoumakos BC, Rawn CJ, Roninone AJ, Stern LA, Circone S, Kirby SH, Ishii Y, Hones CY and Toby BH, *Temperature dependence of polyhedral cage volumes in clathrate hydrates*, *Canadian Journal of Physics* **81** (1-2), 183-189, 2003.
- Chapman MG and Tanaka KL, *Related Magma–Ice Interactions: Possible Origins of Chasmata, Chaos, and Surface Materials in Xanthe, Margaritifer, and Meridiani Terrae, Mars*, *Icarus* **155** (2), 324-339, 2002.
- Chazallon B, Kuhs WF, *In situ structural properties of N<sub>2</sub>, O<sub>2</sub>, and air-clathrates by neutron diffraction*, *Journal of Chemical Physics* **117** (1), 308-320, 2002.
- Chen JH and Wasserburg GJ, *Formation ages and evolution of shergotty and its parent planet from U-Th-Pb systematics*, *Geochimica et Cosmochimica Acta* **50** (6), 955-968, 1986.
- Chevrier V and Mathé PE, *Mineralogy and Evolution of the surface of Mars: A review*, *Planetary and Space Science* **55** (3) 289-314, 2007.
- Chihaiia V, Adams S and Kuhs WF, *Molecular dynamics simulations of properties of a (001) methane clathrate hydrate surface*, *Chemical Physics* **317** (2-3), 208-225, 2005.
- Christensen PR, Bandfield JL, Hamilton VE, Ruff SW, Kieffer HH, Titus TN, Malin MC, Morris RV, Lane MD, Clark RL, Jakosky BM, Mellon MT, Pearl JC, Conrath BJ, Smith MD, Clancy RT, Kuzmin RO, Roush T, Mehall GL, Gorelick N, Bender K, Murray K, Dason S, Greene E, Silverman S and Greenfield M, *Mars Global Surveyor Thermal Emission Spectrometer experiment: Investigation description and surface science results*, *Journal of Geophysical Research – Planets* **107** (E12), 23823-23871, 2001.
- Christensen PR, *Formation of recent martian gullies through melting of extensive water-rich snow deposits*, *Nature* **422** (6927), 45-48, 2003.
- Christensen PR, Ruff SW, Ferguson RL, Knudson AT, Anwar S, Arvidson RE, Bandfield JL, Blaney DL, Budney C, Calvin WM, Glotch TD, Golombek MP, Gorelick N, Graff TG, Hamilton VE, Hayes A, Johnson JR,

- McSween HY, Mehall GL, Mehall LK, Moersch JE, Morris RV, Rogers AD, Smith MD, Squyres SW, Wolff MJ and Wyatt MB, *Initial results from the Mini-TES experiment in Gusev crater from the Spirit rover*, Science **305** (5685), 837-842, 2004.
- Chuvilin EM, Kozlova EV and Skolotneva TS, *Experimental simulation of frozen hydrate-containing sediments formation*, In: *Proceedings of the Fifth International Conference on Gas Hydrate*, v.5, 1540, Trondheim, Norway, 2005.
- Chuvilin EM, Petrakova SYu, Gureva OM and Istomin VA, *Formation of carbon dioxide gas hydrates in freezing sediments and decomposition kinetics of hydrates formed*, In: *Physics and chemistry of ice* (ed. WF. Kuhs) 147-154, RSC Publishing, Cambridge, 2007.
- Circone S, Stern LA, Kirby SH, Durham WB, Chakoumakos BC, Rawn CJ, Rondinone AJ and Ishii Y, *CO<sub>2</sub> hydrate: Synthesis, composition, structure, dissociation behavior, and a comparison to structure I CH<sub>4</sub> hydrate*, Journal of Physical Chemistry B **107** (23), 5529-5539, 2003.
- Circone S, Stern LA and Kirby SH, *The effect of elevated methane pressure on methane hydrate dissociation*, American Mineralogist **89** (8-9), 1192-1201, 2004.
- Clennell MB, Henry P, Hovland M, Booth JS, Winters WJ and Thomas M, *Formation of Natural Gas Hydrates in Marine Sediments: Gas Hydrate Growth and Stability Conditioned by Host Sediment Properties*, Annals of the New York Academy of Science, **912** (1), 887-896 et al. 2000.
- Clifford SM and Hillel D, *The stability of ground ice in the equatorial region of Mars*, Journal of Geophysical Research **88** (NB3), 2456-2474, 1983.
- Clifford SM, *Polar basal melting on Mars*, Journal of Geophysical Research-Solid Earth **92** (B9), 9135-9152, 1987.
- Clifford SM, *A model for the hydrologic and climatic behavior of water on Mars*, Journal of Geophysical Research-Planets **98** (E6), 10973-11016, 1993.
- Clifford SM and Parker TJ, *The evolution of the Martian hydrosphere: Implications for the fate of a primordial ocean and the current state of the northern plains*, Icarus **154** (1), 40-79, 2001.
- Colaprete A and Jakosky BM, *Ice flow and rock glaciers on Mars*, Journal of Geophysical Research-Planets **103** (E3), 5897-5909, 1998.
- Colaprete and Toon, *Carbon dioxide clouds in an early dense Martian atmosphere*, Journal of Geophysical Research-Planets **108** (E4), Art. No. 5025, 2003.
- Coleman NM, *Aqueous flows formed the outflow channels on Mars*, Lunar and Planetary Science XXXIII, abstract nr: **1059**, 2002.
- Coleman NM, Dinwiddie CL and Casteel K, *High outflow channels on Mars indicate Hesperian recharge at low latitudes and the presence of Canyon Lakes*, Icarus **189** (2), 344-361, 2007.
- Connerney JEP, Acuna MH, Ness NF, Spohn T, Schubert G, *Mars crustal magnetism*, Space Science Reviews **111** (1-2), 1-32, 2004.
- Costard F, Forget F, Mangold N, Mercier D and Peulvast JP, *Debris flows on Mars: Analogy with terrestrial periglacial environment and climatic implications*, Lunar and Planetary Science XXXII, abstract nr: **1534**, 2001.

- Costard F, Forget F, Mangold N, Peulvast JP, *Formation of recent Martian debris flows by melting of near-surface ground ice at high obliquity*, Science **295** (5552), 110-113, 2002.
- Craig H, Shoji H and Langway JR, *Nonequilibrium air clathrate hydrates in Antarctic ice: A paleopiezometer for polar ice caps*, Proceedings of the National Academy of Science U.S.A. **90**, 11416-11418, 1993.
- Crawford GD and Stevenson DJ, *Gas-Driven Water Volcanism and the Resurfacing of Europa*, Icarus **73** (1), 66-79, 1988.
- Cutts JA and Lewis BH, *Models of climate cycles recorded in Martian polar layered deposits*, Icarus **50** (2-3), 216-244, 1982.
- Davidson WD, *Clathrate Hydrates*. In: *Water - A Comprehensive Treatise* (ed. F. Franks) Vol. 2, Chapter 3, 115-234, Plenum Press, 1973.
- Davidson DW, Leaist DG and Hesse R, *O-18 enrichment in the water of a clathrate hydrate*, Geochimica et Cosmochimica Acta **47** (12), 2293-2295, 1983.
- Davidson DW, Garg SK, Gough SR, Handa YP, Ratcliffe CI, Ripmeester JA, Tse JS and Lawson WF, *Laboratory analysis of a naturally-occurring gas hydrate from sediment of the gulf of Mexico*, Geochimica et Cosmochimica Acta **50** (4), 619-623, 1986.
- de Forcrand R, *L'hydrate de xenon*, Comptes Rendus Hebdomadaires des Seances de l'Academie des Sciences **181**, 15-17, 1925.
- Deaton WM and Frost EM, *Gas Hydrates and Their Relation to the Operation of Natural-Gas Pipe Lines*, U.S. Bureau of Mines Monograph **8**, 27, OR Pipeline Research Council International Catalog No. L41020e, 1946.
- Delsemme AH and Miller DC, *Physico-chemical phenomena in comets II. Gas adsorption in snows of nucleus*, Planetary and Space Science **18** (5), 717-730, 1970.
- Delsemme AH and Wenger A, *Physico-chemical phenomena in comets I. Experimental study of snows in a cometary environment*, Planetary and Space Science **18** (5), 709-715, 1970.
- Delsemme AH, *Ice in comets*, Journal of Physical Chemistry **87** (21), 4214-4218, 1983.
- Dickens GR, Castillo MM and Walker JCG, *A blast of gas in the latest Paleocene: Simulating first-order effects of massive dissociation of oceanic methane hydrate*, Geology **25** (3), 259-262, 1997.
- Dickson JL, Head JW and Kreslavsky M, *Martian gullies in the southern mid-latitudes of Mars: Evidence for climate-controlled formation of young fluvial features based upon local and global topography*, Icarus **188** (2), 315-323, 2007.
- Dobrovolskis A and Ingersoll AP, *Carbon dioxide-water clathrate as a reservoir of CO<sub>2</sub> on Mars*, Icarus **26** (3), 353-357, 1975.
- Dohm JM, Ferris JC, Baker VR, Anderson RC, Hare TM, Strom GR, Barlow NG, Tanaka KL, Klemaszewski JE and Scott DH, *Ancient drainage basin of the Tharsis region, Mars: Potential source for outflow channel systems and putative oceans or paleolakes*, Journal of Geophysical Research-Planets **106** (E12), 32943-32958, 2001.
- Dominé F, Chaix L and Hanot L, *Reanalysis and new measurements of N<sub>2</sub> and CH<sub>4</sub> adsorption on ice and snow*, Journal of Colloid and Interface Science **227**, 104-110, 2000.

- Dominé F, Cabanes A, Taillandier AS and Legagneux L, *Specific surface area of snow samples determined by CH<sub>4</sub> adsorption at 77 K and estimated by optical, microscopy and scanning electron microscopy*, Environmental Science & Technology **35** (4), 771-780, 2001.
- Dreibus and Wänke, *Mars, a volatile-rich planet*, Meteoritics **20** (2), 367-381, 1985.
- Durham WB, *Factors affecting the rheologic properties of Martian polar ice*, First International Conference on Mars Polar Science, abstract nr: **3024**, 1998.
- Durham WB, Kirby SH and Stern LA, *The rheology of solid carbon dioxide: new measurements*, Lunar and Planetary Science XXX, abstract nr: **2017**, 1999.
- Durham WB, Kirby SH, Stern LA and Circone SC, *The rheology CO<sub>2</sub> clathrate hydrate and other candidate ices in the Martian polar caps*, Third Mars Polar Science Conference, abstract nr: 8132, 2003a.
- Durham WB, Stern LA and Kirby SH, *Ductile flow of methane hydrate*, Canadian Journal of Physics **81** (1-2), 373-380, 2003b.
- Dyadin YA, Zhurko FV, Bondaryuk IV and Zhurko GO, *Clathrate formation in water cyclic ether systems at high-pressure*, Journal of Inclusion Phenomena and Molecular Recognition in Chemistry **10** (1), 39-56, 1991.
- Dyadin YA, Larionov EG, Manakov AY, Zhurko FV, Aladko EY, Mikina TV and Komarov VY, *Clathrate hydrates of hydrogen and neon*, Mendeleev Communications **5**, 209-210, 1999.
- Elkins-Tanton LT, Zaranek SE, Parmentier EM and Hess PC, *Early magnetic field and magmatic activity on Mars from magma ocean cumulate overturn*, Earth and Planetary Science Letters **236** (1-2), 1-12, 2005a.
- Elkins-Tanton LT, Hess PC and Parmentier EM, *Possible formation of ancient crust on Mars through magma ocean processes*, Journal of Geophysical Research-Planets **110** (E12), Art. No. E12S01, 2005b.
- Englezos P and Hall S, *Phase-equilibrium data on carbon-dioxide hydrate in the presence of electrolytes, water-soluble polymers and montmorillonite*, Canadian Journal of Chemical Engineering **72** (5), 887-893, 1994.
- Ershov and Yakushev, *Experimental research on gas hydrate decomposition in frozen rocks*, Cold Regions Science and Technology **20** (2), 147-156, 1992.
- Falabella BJ and Vanpee M, *Experimental determination of gas hydrate equilibrium below ice point*, Industrial & Engineering Chemistry Fundamentals **13** (3), 228-231, 1974.
- Falenty A, Genov G and Kuhs WF, *From ice to CO<sub>2</sub> hydrates and back – study of nucleation and initial growth using scanning electron microscopy*, In: *Physics and chemistry of ice* (ed. WF. Kuhs) 171-179, RSC Publishing, Cambridge, 2007.
- Falenty A and Kuhs WF, *The formation and decomposition kinetics of gas hydrates at sub-zero temperatures*, Proceedings of the 6<sup>th</sup> International Conference on Gas Hydrates, Vancouver, British Columbia, Canada, 2008.
- Fassett CI and Head JW, *Valleys on Hecates Tholus, Mars: origin by basal melting of summit snowpack*, Planetary and Space Science **54** (4), 370-378, 2006.

- Fassett CI and Head JW, *Valley formation on martian volcanoes in the Hesperian: Evidence for melting of summit snowpack, caldera lake formation, drainage and erosion on Ceraunius Tholus*, *Icarus* **189** (1), 118-135, 2007.
- Fei YW and Bertka C, *The interior of Mars*, *Science* **308** (5725), 1120-1121, 2005.
- Feldman WC, Boynton WV, Tokar RL, Prettyman TH, Gasnault O, Squyres SW, Elphic RC, Lawrence DJ, Lawson SL, Maurice S, McKinney GW, Moore KR and Reedy RC, *Global distribution of neutrons from Mars: Results from Mars Odyssey*, *Science* **297** (5578), 75-78, 2002.
- Feldman WC, Prettyman TH, Maurice S, Plaut JJ, Bish DL, Vaniman DT, Mellon MT, Metzger AE, Squyres SW, Karunatillake S, Boynton WV, Elphic RC, Funsten HO, Lawrence DJ and Tokar RL, *Global distribution of near-surface hydrogen on Mars*, *Journal of Geophysical Research-Planets* **109** (E9), Art. No. E09006, 2004.
- Fenton LK and Herkenhoff KE, *Topography and stratigraphy of the northern Martian polar layered deposits using photogrammetry, stereogrammetry, and MOLA altimetry*, *Icarus* **147** (2), 433-443, 2000.
- Foley CN, Wadhwa M, Borg LE, Janney PE, Hines R and Grove TL, *The early differentiation history of Mars from W-182-Nd-142 isotope systematics in the SNC meteorites*, *Geochimica et Cosmochimica Acta* **69** (18), 4557-4571, 2005.
- Forget F, Haberle RM, Montmessin F, Levrard B and Head JW, *Formation of Glaciers on Mars by Atmospheric Precipitation at High Obliquity*, *Science* **311** (5759), 368-371, 2006.
- Formisano V, Atreya S, Encrenaz T, Ignatiev N and Giuranna M, *Detection of methane in the atmosphere of Mars*, *Science* **306** (5702), 1758-1761, 2004.
- Fouchet T, Lellouch E, Ignatiev NI, Forget F, Titov DV, Tschimmel M, Montmessin F, Formisano V, Giuranna A, Maturilli A and Encrenaz T, *Martian water vapor: Mars Express PFS/LW observations*, *Icarus* **190** (1), 32-49, 2007.
- Gaidos EJ, *Cryovolcanism and the recent flow of liquid water on Mars*, *Icarus* **153** (1), 218-223, 2001.
- Gay A, Lopez M, Cochonat P, Seranne M, Levache D and Sermondadaz G, *Isolated seafloor pockmarks linked to BSRs, fluid chimneys, polygonal faults and stacked Oligocene-Miocene turbiditic palaeochannels in the Lower Congo Basin*, *Marine Geology* **226** (1-2), 25-40, 2006.
- Genov G, Kuhs WF, Staykova DK, Goreshnik E and Salamatin AN, *Experimental studies on the formation of porous gas hydrates*, *American Mineralogist* **89** (8-9), 1228-1239, 2004.
- Genov G, PhD Thesis, *Physical processes of the CO<sub>2</sub> hydrate formation and decomposition at conditions relevant to Mars*, Georg-August-Universität Göttingen, 2005.
- Gessmann CK, Wood BJ, Rubie DC and Kilburn MR, *Solubility of silicon in liquid metal at high pressure: implications for the composition of the Earth's core*, *Earth and Planetary Science Letters* **184** (2), 367-376, 2001.
- Grasset O and Parmentier EM, *Thermal convection in a volumetrically heated, infinite Prandtl number fluid with strongly temperature-dependent viscosity: Implications for planetary thermal evolution*, *Journal of Geophysical Research-Solid Earth* **103** (B8), 18171-18181, 1998.
- Grauls D, *Gas hydrates: importance and applications in petroleum exploration*, *Marine and Petroleum Geology* **18** (4), 519-523, 2001.

- Greve R and Mahajan RA, *Influence of ice rheology and dust content on the dynamics of the north-polar cap of Mars*, *Icarus* **174** (2), 475-485, 2004.
- Gulick VC, Tyler D and McKay CP, *Episodic ocean-induced CO<sub>2</sub> greenhouse on Mars: Implications for fluvial valley formation*, *Icarus* **130** (1), 68-86, 1997.
- Haberle RM, Tyler D, McKay CP and Davis WL, *A model for the evolution of CO<sub>2</sub> in Mars*, *Icarus* **109** (1), 102-120, 1994.
- Haberle RM, McKay CP, Schaeffer J, Cabrol NA, Grin EA, Zent AP and Quinn R, *On the possibility of liquid water on present-day Mars*, *Journal of Geophysical Research-Planets* **106** (E10), 23317-23326, 2001.
- Hachikubo A, Kosaka T, Krylov A, Sakagami H, Minami H, Nunokawa Y, Yamashita S, Takahashi N, Shoji H, Khlystov O and Kalmychkov G, *Isotopic analyses of gas hydrate and dissolved gas in pore water in Lake Baikal*, *Preprints of the Annual Conference, Japanese Society of Snow and Ice* **2007**, 48, 2007.
- Hand KP, Chyba CF, Carlson RW and Cooper JF, *Clathrate hydrates of oxidants in the ice shell of Europa*, *Astrobiology* **6** (3), 463-482, 2006.
- Handa YP, *Calorimetric determinations of the compositions, enthalpies of dissociation, and heat-capacities in the range 85 to 270K for clathrate hydrates of xenon and krypton*, *Journal of Chemical Thermodynamics* **18** (9), 891-902, 1986.
- Handa YP and Stupin D, *Thermodynamic properties and dissociation characteristics of methane and propane hydrates in 70-angstrom-radius silica-gel pores*, *Journal of Physical Chemistry* **96** (21), 8599-8603, 1992.
- Hanel R, Conrath B, Flasar FM, Kunde V, Maguire W, Pearl J, Pirraglia J, Samuelson R, Herath L, Allison M, Cruikshank D, Gautier D, Gierasch P, Horn L and Koppany R, *Infrared observations of the saturnian system from Voyager-1*, *Science* **212** (4491), 192-200, 1981.
- Hansen TC, Falenty A and Kuhs WF, *Modeling of ice Ic of different origin and stacking-faulted hexagonal ice using neutron powder diffraction data*, In: *Physics and chemistry of ice* (ed. WF. Kuhs) 201-208, RSC Publishing, Cambridge, 2007.
- Hansen TC, Koza MM and Kuhs WF, *Formation and annealing of cubic ice, I Modelling of stacking faults*, *European Physical Journal*, in press, 2008a.
- Hansen TC, Koza MM and Kuhs WF, *Formation and annealing of cubic ice, II Kinetic study*, *European Physical Journal*, in press, 2008b.
- Hanumantha Rao Y, Subrahmanyam C, Rastogi A and Deka B, *Slope failures along the western continental margin of India: a consequence of gas-hydrate dissociation, rapid sedimentation rate, and seismic activity?*, *Geo-Marine Letters* **22** (3), 162-169, 2002.
- Harper CL, Nyquise LE, Bansal B, Weismann H and Shih CY, *Rapid accretion and early differentiation of Mars indicated by <sup>142</sup>Nd <sup>144</sup>Nd in SNC meteorites*, *Science* **267** (5195), 213-217, 1995.
- Hartmann WK and Neukum G, *Cratering chronology and the evolution of Mars*, *Space and Science Reviews* **96** (1-4), 165-194, 2001.
- Hartmann WK, *Martian Seeps and their Relation to Youthful Geothermal Activity*, *Space and Science Reviews* **96** (1-4), 405-410, 2001.



- Head JN, Melosh HJ and Ivanov BA, *Martian meteorite launch: High-speed ejecta from small craters*, *Science* **298** (5599), 1752-1756, 2002.
- Head JW, Kreslavsky M, Hiesinger H, Ivanov M, Pratt S, Seibert N, Smith DE and Zuber MT, *Oceans in the past history of Mars: Tests for their presence using Mars Orbiter Laser Altimeter (MOLA) data*, *Geophysical Research Letters* **25** (24), 4401-4404, 1998.
- Head JW, Hiesinger H, Ivanov MA, Kreslavsky MA, Pratt S and Thomson BJ, *Possible ancient oceans on Mars: Evidence from Mars Orbiter Laser Altimeter data*, *Science* **286** (5447), 2134-2137, 1999.
- Head JW, Neukum G, Jaumann R, Hiesinger H, Hauber E, Carr M, Masson P, Foing B, Hoffmann H, Kreslavsky M, Werner S, Milkovich S and van Gasselt S, *Tropical to mid-latitude snow and ice accumulation, flow and glaciation on Mars*, *Nature* **434** (7031), 346-351, 2005.
- Heldmann JL and Mellon MT, *Observations of Martian gullies and constraints on potential formation mechanisms*, *Icarus* **168** (2), 285-304, 2003.
- Hirai H, Uchihara Y, Nishimura Y, Kawamura T, Yamamoto Y and Yagi T, *Structural changes of argon hydrate under high pressure*, *Journal of Physical Chemistry B* **106** (43), 11089-11092, 2002.
- Hirai S, Okazaki K, Tabe Y and Kawamura K, *CO<sub>2</sub> clathrate-hydrate formation and its mechanism by molecular dynamics simulation*, *Energy Conversion and Management* **38** Suppl. S S301-S306, 1997.
- Hoefen TM, Clark RN, Bandfield JL, Smith MD, Pearl JC and Christensen PR, *Discovery of Olivine in the Nili Fossae Region of Mars*, *Science* **302** (5645) 627-630, 2003.
- Hoffman N, *White Mars: A new model for Mars' surface and atmosphere based on CO<sub>2</sub>*, *Icarus* **146** (2), 326-342, 2000a.
- Hoffman N, *Ideas about the surface runoff features on Mars*, *Science* **290** (5492), 711-711 2000b.
- Hoffman N, *Emplacement of a debris ocean on Mars by regional-scale collapse and flow at the crustal dichotomy*, *Lunar and Planetary Science XXXII*, abstract nr: **1584**, 2001a.
- Hoffman N, *The origin of pervasive layering on early Mars through impact/atmosphere feedback mechanisms*, *Lunar and Planetary Science XXXII*, abstract nr: **1582**, 2001b.
- Hoffman N, *Explosive CO<sub>2</sub>-driven source mechanisms for an energetic outflow "jet" at Aromatum Chaos, Mars*, *Lunar and Planetary Science XXXII*, abstract nr: **1257**, 2001c.
- Hoffman N, *CO<sub>2</sub> phase changes and flow mechanisms for non-aqueous "floods" on Mars*, *Lunar and Planetary Science XXXII*, abstract nr: **1588**, 2001d.
- Hoffman N, *Fresh polar channels on Mars as evidence of continuing CO<sub>2</sub> vapour-supported density flows*, *Lunar and Planetary Science XXXII*, abstract nr: **1271**, 2001e.
- Hoffman and Tanaka, *Co-existing "flood" and "volcanic" morphologies in Elysium as evidence for cold CO<sub>2</sub> or warm H<sub>2</sub>O outbursts*, *Lunar and Planetary Science XXXIII*, abstract nr: **1505**, 2002.
- Hoffman N, *Active Polar Gullies on Mars and the Role of Carbon Dioxide*, *Astrobiology* **2** (3), 313-323, 2002.
- Hoffman N, Kargel J and Tanaka K, *Basal melting of a CO<sub>2</sub>-rich icecap on Mars*, *Lunar and Planetary Science XXXIII*, abstract nr: **1509**, 2002.

- Hood LL, Young CN, Richmond NC and Harrison KP, *Modeling of major Martian magnetic anomalies: Further evidence for polar reorientations during the Noachian*, *Icarus* **177** (1), 144-173, 2005.
- Hovland M, Svensen H, Forsberg CF, Johansen H, Fichler C, Fossa JH, Jonsson R and Rueslatten H, *Complex pockmarks with carbonate-ridges off mid-Norway: Products of sediment degassing*, *Marine Geology* **218** (1-4), 191-206, 2005.
- Hurford TA, Helfenstein P, Hoppa GV, Greenberg R and Bills BG, *Eruptions arising from tidally controlled periodic openings of rifts on Enceladus*, *Nature* **447** (7142), 292-294, 2007.
- Hwang MJ, Wright DA, Kapur A and Holder GD, *An experimental-study of crystallization and crystal-growth of methane hydrates from melting ice*, *Journal of Inclusion Phenomena and Molecular Recognition in Chemistry* **8** (1-2), 103-116, 1990
- Iro N, Gautier D, Hersant F, Bockelee-Morvan D and Lunine JI, *An interpretation of the nitrogen deficiency in comets*, *Icarus* **161** (2), 511-532, 2003.
- Itoh H, Tse JK, Kawamura K, *The structure and dynamics of doubly occupied Ar hydrate*, *Journal of Chemical Physics*, **115** (20), 9414-9420, 2001.
- Jacobsen SB, *The Hf-W isotopic system and the origin of the earth and moon*, *Annual Review of Earth and Planetary Science* **33**, 531-570, 2005.
- Jagoutz E, *Chronology of SNC meteorites*, *Space Science Reviews* **56** (1-2), 13-22, 1991.
- Jakosky BM, Henderson BG and Mellon MT, *Chaotic obliquity and the nature of the Martian climate*, *Journal of Geophysical Research-Planets* **100** (E1), 1579-1584, 1995.
- Jakosky BM and Jones JH, *The history of Martian volatiles*, *Reviews of Geophysics* **35** (1), 1-16, 1997.
- Jakosky BM and Phillips RJ, *Mars' volatile and climate history*, *Nature* **412** (6843), 237-244, 2001.
- Jakosky BM, Mellon MT, Varnes ES, Feldman WC, Boynton WV and Haberle RM, *Mars low-latitude neutron distribution: Possible remnant near-surface water ice and a mechanism for its recent emplacement*, *Icarus* **175** (1), 58-67, 2005.
- Jeffrey AWA, Pflaum RC, McDonald TJ, Brooks JM and Kvenvolden KA, *Isotopic analysis of core gases at sites 565-570, Deep Sea Drilling Project, vol. 84, (ed. R. von Huene et al.), pp. 719-726, U.S. Government Printing Office, Washington, D. C., 1984.*
- Jenniskens P, Blake DF and Kouchi, *Amorphous water ice*, In: *Solar system ices* (ed. B. Schmitt et al.), 139-155, Kulwer Academic Publishers, Dordrecht, Netherlands, 1995.
- Johnson CL and Phillips RJ, *Evolution of the Tharsis region of Mars: insights from magnetic field observations*, *Earth and Planetary Science* **230** (3-4), 241-254, 2005.
- Johnson RE and Jesser WA, *O<sub>2</sub>/O<sub>3</sub> microatmospheres in the surface of Ganymede*, *Astrophysical Journal* **480** (1), L79-L82 Part 2, 1997
- Jöns HP, *Morphologic hints for CO<sub>2</sub> as active agent in Martian relief dynamics*, *Lunar and Planetary Science XXXII*, abstract nr: **1102**, 2001.
- Kahn R, *The evolution of CO<sub>2</sub> on Mars*, *Icarus* **62** (2), 175-190, 1985.

- Kargel JS and Lunine JI, *Clathrate hydrates on Earth and in the Solar System*, In: *Solar System Ices* (ed. B. Schmitt, C. De Bergh, M. Festou) 97-117, Kluwer Academic Publishers, Dordrecht, 1995.
- Kargel JS, *Possible composition of Martian polar caps and controls on ice-cap behavior*, First International Conference on Mars Polar Science, abstract nr: **3048**, 1998.
- Kargel JS, Kaye JZ, Head JW, Marion GM, Sassen R, Crowley JK, Ballesteros OP, Grant SA and Hogenboom DL, *Europa's crust and ocean: Origin, composition, and the prospects for life*, *Icarus* **148** (1), 226-265, 2000a.
- Kargel JS, Tanaka KL, Baker VR, Komatsu G, MacAyeal DR, *Formation and dissociation of clathrate hydrates on Mars: Polar caps, northern plains, and highlands*, *Lunar and Planetary Science XXXI*, abstract nr: **1891**, 2000b.
- Kargel JS and Tanaka KL, *The Martian south polar cap: glacial ice sheet of multiple interbedded ices*, *Lunar and Planetary Science XXXIII*, abstract nr: **1799**, 2002.
- Kargel JS, *Mars - a warmer wetter planet*, Praxis Publishing Ltd., Springer, 2004.
- Kargel JS, Furfaro R, Prieto-Ballesteros O, Rodriguez JAP, Montgomery DR, Gillespie AR, Marion GM, Wood SE, *Martian hydrogeology sustained by thermally insulating gas and salt hydrates*, *Geology* **35** (11), 975-978, 2007.
- Karunatillake S, Squyres SW, Taylor GJ, Keller JM, Gasnault O, Evans LG, Reedy RC, Starr R, Boynton W, Janes DM, Kerry KE, Dohm JM, Sprague AL, Hahn BC and Hamara D, *Composition of northern low-albedo regions of Mars: Insights from the Mars Odyssey Gamma Ray Spectrometer*, *Journal of Geophysical Research-Planets* **111** (E3), Art. No. E03S05, 2007.
- Kashchiev D and Firoozabadi A, *Driving force for crystallization of gas hydrates*, *Journal of Crystal Growth* **241** (1-2), 220-230, 2002a.
- Kashchiev D and Firoozabadi A, *Nucleation of gas hydrates*, *Journal of Crystal Growth* **243** (3-4), 476-489, 2002b.
- Kashchiev D and Firoozabadi A, *Induction time in crystallization of gas hydrates*, *Journal of Crystal Growth* **250** (3-4), 499-515, 2003.
- Kasting JF, *CO<sub>2</sub> condensation and the climate of early Mars*, *Icarus* **94** (1), 1-13, 1991.
- Kayen RE and Lee HJ, *Pleistocene slope instability of gas hydrate-laden sediment on the Beaufort Sea margin*, *Marine Georesources & Geotechnology* **10**, 125-141, 1991.
- Kelly JT, Dickson SM, Belknap DF, Barnhardt WA and Henderson M, *Giant sea-bed pockmarks-evidence for gas escape from Belfast bay, Maine*, *Geology* **22** (1), 59-62, 1994.
- Kennett JP, Cannariato KG, Hendy IL and Behl RJ, *Methane Hydrates in Quaternary Climate Change: The Clathrate Gun Hypothesis*, American Geophysical Union, Washington D.C., 2003.
- Kerr, *Planetary science - A dry view of Enceladus puts a damper on chances for life there*, *Science* **314** (5806), 1668-1668, 2006.
- Kieffer HH, Chase SC, Martin TZ, Miner ED, Palluconi FD, *Martian north pole summer temperatures - dirty water ice*, *Science* **194** (4271), 1341-1344, 1976.
- Kieffer HH, *H<sub>2</sub>O grain size and the amount of dust in Mars' residual north polar cap*, *Journal of Geophysical Research* **95** (B2), 1481-1493, 1990.

- Kieffer HH, *Annual punctuated slab-ice and CO<sub>2</sub> jets on Mars*, 2nd International Conference on Mars Polar Science and Exploration. Abstract nr: **4095**, 2000a.
- Kieffer HH, *Clathrates are not the culprit*, Science **287** (5459), 1753, 2000b.
- Kieffer HH, Christensen PR and Titus TN, *CO<sub>2</sub> jets formed by sublimation beneath translucent slab ice in Mars' seasonal south polar cap*, Nature **442** (7104) 793-796, 2006.
- Kieffer SW, Lu XL, Bethke CM, Spencer JR, Marshak S and Navrotsky A, *A clathrate reservoir hypothesis for Enceladus' south polar plume*, Science **314** (5806), 1764-1766, 2006.
- King, *Chemical applications of topology and group-theory. VI. Polyhedral water networks in clathrates and semiclathrates*, Theoretica Chimica Acta **25** (4), 309-318, 1972.
- Kipfstuhl S, Pauer F, Kuhs WF and Shoji H, *Air bubbles and clathrate hydrates in the transition zone of the NGRIP deep ice core*, Geophysical Research letters **28** (4), 591-594, 2001.
- Klapp SA, Klein H and Kuhs WF, *First determination of gas hydrate crystallite size distributions using high-energy synchrotron radiation*, Geophysical Research Letters **34** (13), L13608, doi: 10.1029/2006GL029134, 2007.
- Klaproth A, PhD Thesis, *Strukturuntersuchungen an Methan und Kohlenstoffdioxid-Clathrat-Hydraten*, Georg-August-Universität Göttingen, 2002.
- Klaproth A, Goreschnik E, Staykova D, Klein H and Kuhs WF, *Structural studies of gas hydrates*, Canadian Journal of Physics **81** (1-2), 503-518, 2003.
- Klaproth A, Techmer KS, Klapp SA, Musrshed MM, Kuhs WF, *Microstructure of gas hydrates in porous media*, In: *Physics and chemistry of ice* (ed. WF. Kuhs) 321-328, RSC Publishing, Cambridge, 2007.
- Kleine T, Mezger K, Munker C, Palme H and Bischoff A, *Hf-182-W-182 isotope systematics of chondrites, eucrites, and martian meteorites: Chronology of core formation and early mantle differentiation in Vesta and Mars*, Geochimica et Cosmochimica Acta **68** (13), 2935-2946, 2004.
- Kletetschka G, Wasilewski PJ and Taylor PT, *Mineralogy of the sources for magnetic anomalies on Mars*, Meteoritics & Planetary Science **35** (5), 895-899, 2000.
- Knauth LP and Burt DM, *Eutectic brines on Mars: Origin and possible relation to young seepage features*, Icarus **158** (1), 267-271, 2002.
- Koh CA and Sloan ED, *Natural gas hydrates: Recent advances and challenges in energy and environmental applications*, Aiche Journal **53** (7), 1636-1643, 2007.
- Komarov VY, Solodovnikov SF, Kurnosov AV, Kosyakov VI, and Manakov AY, *Design of tetrahedral frameworks as layered packings of uniform polyhedral cavities*, Journal of structural Chemistry **46**, Suppl. S181-S187, 2005.
- Komatsu G, Kargel JS, Baker VR, Strom RG, Ori GG, Mosangini C and Tanaka KL, *A chaotic terrain formation hypothesis: explosive outgas and outflow by dissociation of clathrate on Mars*, Lunar and Planetary Science XXXI, abstract nr: **1434**, 2000.
- Kordylewski I, Saner D and Lal R, *Atomic-force microscopy of freeze-fracture replicas of rat atrial tissue*, Journal of Microscopy-Oxford **173**, 173-181, part 3, 1994.

- Kosaka T, Ozeki T, Hachikubo A, Kida M, Krylov A, Sakagami H, Minami H, Nunokawa Y and Shoji H, *Isotopic fractionation of guest molecules at the formation of methane and ethane hydrates*, Preprints of the Annual Conference, Japanese Society of Snow and Ice **2007**, 50, 2007.
- Koster van Groos F and Guggenheim S, *What went wrong with the Mars Landing?*, Science **287** (5455), 973, 2000.
- Krasnopolsky V, Maillard JP and Owen TC, *Detection of methane in the Martian atmosphere: evidence for life?*, Icarus **172** (2), 537-547, 2004.
- Kreslavsky MA and Head JW, *Conditions and principal time scales for basal melting of Martian polar caps*, Lunar and Planetary Science XXXIII, abstract nr: **1779**, 2002.
- Kress ME and McKay CP, *Formation of methane in comet impacts: implications for Earth, Mars, and Titan*, Icarus **168** (2), 475-483, 2004.
- Kring DA and Cohen BA, *Cataclysmic bombardment throughout the inner solar system 3.9-4.0 Ga*, Journal of Geophysical Research-Planets **107** (E2), Art. No. 5009, 2002.
- Kuhs WF, Bliss DV and Finney JL. *High-resolution neutron powder diffraction study of ice Ic*, Le Journal de Physique Colloques **48**, VII<sup>th</sup> Symposium on the Physics and Chemistry of Ice, C1:631-636, 1987.
- Kuhs WF, Chazallon B, Radaelli PG and Pauer F, *Cage occupancy and compressibility of deuterated N-2-clathrate hydrate by neutron diffraction*, Journal of Inclusion Phenomena and Molecular Recognition in Chemistry **29** (1), 65-77, 1997.
- Kuhs WF, Genov G, Staykova DK and Hansen T, *Ice perfection and onset of anomalous preservation of gas hydrates*, Physical Chemistry Chemical Physics **6** (21), 4917-4920, 2004.
- Kuhs WF, Hensel E, Bartels H, *Gas pressure cells for elastic and inelastic neutron scattering*, Journal of Physics-Condensed Matter **17** (40), Sp. Iss. SI, S3009-S3015, 2005.
- Kuhs WF, Staykova DK and Salamatina AN, *Formation of methane hydrate from polydisperse ice powders*, 110 (26), 13283-13295, 2006.
- Kurahashi-Nakamura T and Tajika E, *Atmospheric collapse and transport of carbon dioxide into the subsurface on early Mars*, Geophysical Research Letters **33** (18), Art. No. L18205, 2006.
- Kurnosov A, Dubrovinsky L, Kuznetsov A and Dmitriev V, *High-pressure/high-temperature behavior of the methane-ammonia-water system up to 3 GPa*, Zeitschrift für Naturforschung Section B-A Journal of Chemical Sciences **61** (12), 1573-1576, 2006.
- Kvamme B, *Kinetics of hydrate formation from nucleation theory*, International Journal of Offshore and Polar Engineering **12** (4), 256-263, 2002.
- Kvenvolden KA, *Gas Hydrates-Geological perspective and global change*, Reviews of Geophysics **31** (2), 173-187, 1993.
- Kvenvolden KA and Lorenson TD, *A Global Inventory of Natural Gas Hydrate Occurrence*, poster USGS, <http://walrus.wr.usgs.gov/globalhydrate/>, 2000.
- Kvenvolden KA, *Gas hydrate and humans*, Annals of the New York Academy of Science **912**, 17-22, 2000.
- Lambert RSJ and Chamberlain VE, *CO<sub>2</sub> permafrost and Martian topography*, Icarus **34** (3), 568-580, 1978.

- Landry JC and England AW, *Far-infrared spectroscopy of CO<sub>2</sub> clathrate hydrate with Martian applications*, *Geophysical Research Letters* **21** (25), 2829-2832, 1994.
- Larionov EG, Aladko EY, Zhurko FV, Likhacheva AY, Ancharov A, Sheromov MA, Kurnosov AV, Manakov AY and Goryainov SV, *Clathrate hydrates of hexagonal structure III at high pressures: Structures and phase diagrams*, *Journal of Structural Chemistry* **46**, S54-S64 Suppl. S, 2005.
- Larson MA and Garside J, *Solute clustering in supersaturated solutions*, *Journal of Crystal Growth* **76** (1), 88-92, 1986.
- Larson SD, *Phase studies of the two-component carbon dioxide-water system, involving the carbon dioxide hydrate*, Ph.D. diss., University of Illinois, 1955.
- Lasaga AC, *Kinetic theory in earth science*, Princeton University Press, Princeton, New Jersey, 1997.
- Laskar J and Robutel P, *The chaotic obliquity of the planets*, *Nature* **361** (6413), 608-612, 1993.
- Laskar J, *A numerical experiment on the chaotic behavior of the Solar-System*, *Nature* **338** (6212), 237-238, 1989.
- Laskar J, Joutel F and Robutel P, *Stabilisation of the Earths obliquity by the Moon*, *Nature* **361** (6413), 615-617, 1993.
- Laskar J, Levrard B and Mustard JF, *Orbital forcing of the martian polar layered deposits*, *Nature* **419** (6905), 375-377, 2002.
- Lee DC and Halliday AN, *Core formation on Mars and differentiated asteroids*, *Nature* **388** (6645), 854-857, 1997.
- Lee KM, Lee H, Lee J and Kang JM, *CO<sub>2</sub> hydrate behavior in the deep ocean sediments; phase equilibrium, formation kinetics, and solubility*, *Geophysical Research Letters* **29** (21), 2034, 2002.
- Legagneux L, Cabanes A and Dominé F, *Measurement of the specific surface area of 176 snow samples using methane adsorption at 77K*, *Journal of Geophysical Research-Atmospheres* **107** (D17), 4335, 2002.
- Leighton RB and Murray BC, *Behavior of carbon dioxide and other volatiles on Mars*, *Science* **153** (3732), 136-144, 1966.
- Lekvam K and Ruoff P, *A reaction kinetic mechanism for methane hydrate formation in liquid water*, *Journal of American Chemical Society* **115** (19), 8565-8569, 1993.
- Lenardic A, Nimmo F and Moresi L, *Growth of the hemispheric dichotomy and the cessation of plate tectonics on Mars*, *Journal of Geophysical Research-Planets* **109** (E2), Art. No. E02003, 2004.
- Levrard B, Forget F, Montmessin F and Laskar J, *Recent ice-rich deposits formed at high latitudes on Mars by sublimation of unstable equatorial ice during low obliquity*, *Nature* **431** (7012), 1072-1075, 2004.
- Levrard B, Forget F, Montmessin F and Laskar J, *Recent formation and evolution of northern Martian polar layered deposits as inferred from a Global Climate Model*, *Journal of Geophysical Research-Planets* **112** (E6), Art. No. E06012, 2007.
- Lewis JS and Prinn RG, *Kinetic inhibition of CO and N<sub>2</sub> reduction in the solar nebula*, *Astrophysical Journal* **238** (1), 357-364, 1980.

- Li J and Agee CB, *Element partitioning constraints on the light element composition of the Earth's core*, *Geophysical Research Letters* **28** (1), 81-84, 2001.
- Lipenkov VY, *Air bubbles and air-hydrate crystals in the Vostok ice core*, In: *Physics of Ice Core Records* (ed. T. Hondoh) 327-358, Hokkaido University Press, Sapporo, 2000.
- Llamedo M, Anderson R and Tohidi B, *Thermodynamic prediction of clathrate hydrate dissociation conditions in mesoporous media*, *American Mineralogist* **89** (8-9), 1264-1270, 2004.
- Londono D, Finney JL, Kuhs WF, *Formation, stability, and structure of helium hydrate at high-pressure*, *Journal of Chemical Physics* **97** (1), 547-552, 1992.
- Longhi J, *Low-Temperature Phase Relations in the CO<sub>2</sub>-H<sub>2</sub>O System with Application to Mars*, *Lunar and Planetary Science XXXI*, abstract nr: **1518**, 2000.
- Longhi J, *Clathrate and ice stability in a porous martian regolith*, *Lunar and Planetary Science XXXII*, abstract nr: **1955**, 2001.
- Longhi J, *CO<sub>2</sub>-H<sub>2</sub>O Phase Equilibria: Residual Ice Layers and Basal Melting of the Martian Polar Ice Caps*, *Lunar and Planetary Science XXXX*, abstract nr: **1857**, 2004.
- Longhi J, *Phase equilibria in the system CO<sub>2</sub>-H<sub>2</sub>O I: New equilibrium relations at low temperatures*, *Geochimica et Cosmochimica Acta* **69** (3), 529-539, 2005.
- Longhi J, *Phase equilibrium in the system CO<sub>2</sub>-H<sub>2</sub>O: Application to Mars*, *Journal of Geophysical Research-Planets* **111** (E6), Art. No. E06011, 2006.
- Loveday JS, Nelmes RJ, Guthrie M, Klug DD and Tse JS, *Transition from cage clathrate to filled ice: The structure of methane hydrate III*, *Physical Review Letters* **87** (21), Art. No. 215501, 2001a.
- Loveday JS, Nelmes RJ, Guthrie M, Belmonte SA, Allan DR, Klug DD, Tse JS and Handa YP, *Stable methane hydrate above 2 GPa and the source of Titan's atmospheric methane*, *Nature* **410** (6829), 661-663, 2001b.
- Loveday JS and Nelmes RJ, *High-pressure neutron diffraction and models of Titan*, *High Pressure Research* **23** (1-2), 41-47, 2003.
- Loveday JS, Nelmes RJ, Klug DD, Tse JS and Desgreniers S, *Structural systematics in the clathrate hydrates under pressure*, *Canadian Journal of Physics*, **81** (1-2), 539-544, 2003.
- Luchitta BK, Ferguson HM and Summers C, *Sedimentary deposits in the northern lowland plains, Mars*, *Journal of Geophysical Research-Solid Earth* **91** (B13), E166-E174, 1986.
- Luchitta BK, *Mars and Earth - comparison of cold-climate features*, *Icarus* **45** (2), 264-303, 1981.
- Lunine JI and Stevenson DJ, *Thermodynamics of clathrate hydrate at low and high-pressure with application to the outer Solar-System*, *Astrophysical Journal Supplement Series* **58** (3), 493-531, 1985.
- Machida S, Hirai H, Kawamura T, Yamamoto Y and Yagi T, *A new high-pressure structure of methane hydrate surviving to 86 GPa and its implications for the interiors of giant icy planets*, *Physics of the Earth and Planetary Interiors* **155** (1-2), 170-176, 2006.
- Madden MEE, Ulrich SM, Onstott TC and Phelps TJ, *Salinity-induced hydrate dissociation: A mechanism for recent CH<sub>4</sub> release on Mars*, *Geophysical Research Letters* **34** (11), Art. No. L11202, 2007.



- Makogon YF, *Hydrates of hydrocarbons*, Pennwell, Tulsa, 1997.
- Makogon YF, Tsarev VP and Cherskii NV, Formation of large gas fields in lower temperature zones, *Doklady Akademii Nauk SSSR* **205** (3), 700-, 1972.
- Malin MC and Edgett KS, *Oceans or seas in the Martian northern lowlands: High resolution imaging tests of proposed coastlines*, *Geophysical Research Letters* **26** (19), 3049-3052, 1999.
- Malin MC and Edgett KS, *Evidence for recent groundwater seepage and surface runoff on Mars*, *Science* **288** (5475), 2330-2335, 2000.
- Malone RD, *Gas hydrates topical report*, DOE/METC/SP-218, U.S. Department of energy, April 1985.
- Manakov AY, Voronin VI, Kurnosov AV, Teplykh AE, Larionov EG and Dyadin YA, *Argon hydrates: Structural studies at high pressures*, *Doklady Physical Chemistry* **378** (4-6), 148-151, 2001.
- Mangold EN, Costard F, Forget F and Peulvast JP, Narrow gullies over high sand dunes on Mars: evidence for flows triggered by liquid water near surface, *Lunar and Planetary Science XXXIII*, abstract nr: **1215**, 2002.
- Mangold N, Maurice S, Feldman WC, Costard F and Forget F, *Spatial relationships between patterned ground and ground ice detected by the Neutron Spectrometer on Mars*, *Journal of Geophysical Research-Planets* **109** (E8), Art. No. E08001, 2004.
- Manning CV, McKay CP and Zahnle KJ, *Thick and thin models of the evolution of carbon dioxide on Mars*, *Icarus* **180** (1), 38-59, 2006.
- Mao WL, Mao HK, Goncharov AF, Struzhkin VV, Guo QZ, Hu JZ, Shu JF, Hemley RJ, Somayazulu M and Zhao YS, *Hydrogen clusters in clathrate hydrate*, *Science* **297** (5590), 2247-2249, 2002.
- Márquez A, Fernandez C, Anguita F, Farelo A, Anguita J and de la Casa MA, *New evidence for a volcanically, tectonically, and climatically active Mars*, *Icarus* **172** (2), 573-581, 2004.
- Márquez A, de Pablo MA, Oyarzun R and Viedma C, *Evidence of gully formation by regional groundwater flow in the Gorgonum-Newton region (Mars)*, *Icarus* **179** (2), 398-414, 2005.
- Maslin M, Owen M, Day S and Long D, *Linking continental-slope failures and climate change: Testing the clathrate gun hypothesis*, *Geology* **32** (1), 53-56, 2004.
- Masson P Carr MH, Costard F, Greeley R, Hauber E, Jaumann R, *Geomorphologic evidence for liquid water*, *Space Science Reviews* **96** (1-4), 333-364, 2001.
- Matson DL, Castillo JC, Lunine J and Johnson TV, *Enceladus' plume: Compositional evidence for a hot interior*, *Icarus* **187** (2), 569-573, 2007.
- Max MD, Dillon WP, Nishimura C and Hurdle BG, *Sea-floor methane blow-out and global firestorm at the K-T boundary*, *Geo-Marine Letters* **18** (4), 285-291, 1999.
- Max MD and Clifford SM, *The state, potential distribution, and biological implications of methane in the Martian crust*, *Journal of Geophysical Research – Planets* **105** (E2), 4165-4171, 2000a.
- Max MD and Clifford SM, *The initiation of Martian outflow channels through the catastrophic decomposition of methane hydrate*, *Lunar and Planetary Science XXXI*, abstract nr: **2094**, 2000b.

- Max MD and Clifford SM, *Initiation of Martian outflow channels: Related to the dissociation of gas hydrate?*, *Geophysical Research Letters* **28** (9), 1787-1790, 2001.
- Mayer E and Hallbrucker A, *Cubic ice from liquid water*, *Nature* **325** (6105), 601-602, 1987.
- Mazurenko LL, Soloviev VA, Gardner JM and Ivanov MK, *Gas hydrates in the Ginsburg and Yuma mud volcano sediments (Moroccan Margin): results of chemical and isotopic studies of pore water*, *Marine Geology* **195** (1-4), 201-210, 2003.
- McGovern PJ, Solomon SC, Smith DE, Zuber MT, Simons M, Wieczorek MA, Phillips RJ, Neumann GA, Aharonson O, Head JW, *Localized gravity/topography admittance and correlation spectra on Mars: Implications for regional and global evolution*, *Journal of Geophysical Research-Planets* **107** (E12), Art. No. 5136, 2002
- McKay CP and Smith HD, *Possibilities for methanogenic life in liquid methane on the surface of Titan*, *Icarus* **178** (1), 274-276, 2005.
- McLennan SM, *Crustal heat production and the thermal evolution of Mars*, *Geophysical Research Letters* **28** (21), 4019-4022, 2001.
- McMenamin DS and McGill GE, *Martian Glacial Morphology, Geomorphology, and Atmospheric Methane*, *Lunar and Planetary Science XXXVIII*, abstract nr: **1161**, 2007.
- Médar E and Grove TL, *Early hydrous melting and degassing of the Martian interior*, *Journal of Geophysical Research-Planets* **105** (E5), Art. No. E11003, 2006.
- Mellon MT, *Limits on the CO<sub>2</sub> content of the Martian Polar Deposits*, *Icarus* **124** (1), 286-279, 1996.
- Mellon MT and Phillips RJ, *Recent gullies on Mars and the source of liquid water*, *Journal of Geophysical Research-Planets* **106** (E10), 23165-23179, 2001.
- Mellon MT, Feldman WC and Prettyman TH, *The presence and stability of ground ice in the southern hemisphere of Mars*, *Icarus* **169** (2), 324-340, 2004.
- Melosh HJ, *Tectonic patterns on a reoriented planet*, *Icarus* **44** (3), 745-751, 1980.
- Melosh HJ and Vickery AM, *Impact erosion of the primordial atmosphere of Mars*, *Nature* **338** (6215), 487-489, 1989.
- Mendis DA and Ip WH, *Behavior of comet Kohutek (1973)*, *Nature* **249** (5457), 536-537, 1974.
- Meunier A, *Clays*, Springer Verlag, Berlin, 2005.
- Milkovich SM and Head JW, *North polar cap of Mars: Polar layered deposit characterization and identification of a fundamental climate signal*, *Journal of Geophysical Research-Planets* **109** (E8), Art. No. E01005, 2005.
- Miller SL, *The occurrence of gas hydrates in the Solar System*, *Proceedings of the national academy of science U.S.* **47** (11) 1798-1808, 1961.
- Miller SL, *Clathrate hydrates of air in Antarctic ice*, *Science* **165** (3892), 489-, 1969.
- Miller SL and Smythe WD, *Carbon dioxide in Martian ice cap*, *Science* **170** (3957), 531-533, 1970.
- Miller SL and Smythe WD, *Carbon dioxide clathrate in Martian ice cap*, *Science* **170** (3957), 531-533, 1970.

- Milton DJ, *Carbon-dioxide hydrate and floods on Mars*, Science **183** (4125), 654-656, 1974.
- Mitri G, Showman AP, Lunine JI and Lorenz RD, *Hydrocarbon lakes on Titan*, Icarus **186** (2), 385-394, 2007.
- Mitrofanov I, Anfimov D, Kozyrev A, Litvak M, Sanin A, Tret'yakov V, Krylov A, Shvetsov V, Boynton W, Shinohara C, Hamara D and Saunders RS, *Maps of subsurface hydrogen from the high energy neutron detector*, Mars Odyssey, Science **297** (5578), 78-81, 2002.
- Mitrofanov IG, Zuber MT, Litvak ML, Boynton WV, Smith DE, Drake D, Hamara D, Kozyrev AS, Sanin AB, Shinohara C, Saunders RS and Tret'yakov V, *CO<sub>2</sub> snow depth and subsurface water-ice abundance in the northern hemisphere of Mars*, Science **300** (5628), 2081-2084, 2003.
- Miyazaki K and Yasuoka K, Molecular dynamics simulation of dissociation and formation processes for methane hydrate, In: *Proceedings of the Fourth International Conference on Gas Hydrate*, 482-487, Yokohama, Japan, 2002.
- Mizuno Y and Hanafusa N, *Studies of surface-properties of ice using nuclear-magnetic-resonance*, Journal de Physique **48** (C-1), 511-517, 1987.
- Morgenstern A, Hauber E, Reiss D, van Gasselt S, Grosse G and Schirrmeyer L, *Deposition and degradation of a volatile-rich layer in Utopia Planitia and implications for climate history on Mars*, Journal of Geophysical Research-Planets **112** (E6), Art. No. E06010, 2007.
- Mori YH and Mochizuki T, *Dissolution of liquid CO<sub>2</sub> into water at high pressures: A search for the mechanism of dissolution being retarded through hydrate-film formation*, Energy Conversion and Management **39** (7), 567-578, 1998.
- Moudrakovski IL, Sanchez AA, Ratcliffe CI and Ripmeester JA, *Nucleation and growth of hydrates on ice surfaces: New insights from Xe<sup>129</sup> NMR experiments with hyperpolarized xenon*, Journal of Physical Chemistry B **105** (49), 12338-12347, 2001.
- Mousis O and Alibert Y, *Modeling the Jovian subnebula - II. Composition of regular satellite ices*, Astronomy & Astrophysics **448** (2), 771-778, 2006.
- Murray BC, Milton DJ, Cutts JA, Sharp RP, Soderblom LA and Leighton RB, *Geological framework of south polar region of Mars*, Icarus **17** (2) 328-345, 1972.
- Murray BJ, Knopf DA and Bertram AK, *The formation of cubic ice under conditions relevant to Earth's atmosphere*, Nature **434** (7030), 202-205, 2005.
- Murray BJ and Bertram AK, *Laboratory studies of the formation of cubic ice in aqueous droplets*, In: *Physics and chemistry of ice* (ed. WF. Kuhs) 3-11, RSC Publishing, Cambridge, 2007.
- Murshed, MM, Klapp SA, Enzmann F, Szeder T, Huthwelker T, Stampanoni M, Marone F, Hintermuller C, Bohrmann G, Kuhs WF and Kersten M, *Natural gas hydrate investigations by 1 synchrotron radiation X-ray cryo-tomographic microscopy (SRXCTM)*, Geophysical Research Letters, doi:10.1029/2008GL035460, in press. (accepted 12 November 2008)
- Musselwhite DS and Lunine JI, *Alteration of volatile inventories by polar clathrate formation on Mars*, Journal of Geophysical Research **100** (E11), 23301-23306, 1995.
- Musselwhite DS, Swindle TD and Lunine JI, *Liquid CO<sub>2</sub> breakout and the formation of recent small gullies on Mars*, Geophysical Research Letters **28** (7), 1283-1285, 2001.
- Musselwhite DS and Swindle JI, *Is Release of Martian Atmosphere from Polar Clathrate the Cause of the Nakhla and ALH84001 Ar/Kr/Xe Ratios?*, Icarus **154** (1), 207-215, 2001.

- Mustard JF, Cooper CD, Rifkin MK, *Evidence for recent climate change on Mars from the identification of youthful near-surface ground ice*, Nature **412** (6845), 411-414, 2001.
- Narita H, Azuma N, Hondoh T, Fujii M, Kawaguchi M, Mae SJ, Shoji H, Kameda T and Watanabe O, *Characteristics of air bubbles and hydrates in the Dome Fuji ice core, Antarctica*, Annals of Glaciology **28**, 207-210, 1999.
- Neukum G, Jaumann R, Hoffmann H, Hauber E, Head JW, Basilevsky AT, Ivanov BA, Werner SC, van Gasselt S, Murray JB, McCord T, *Recent and episodic volcanic and glacial activity on Mars revealed by the High Resolution Stereo Camera*, Nature **432** (7020), 971-979, 2004.
- Newman MJ and Rood RT, *Implications of solar evolution for Earth's early atmosphere*, Science **198** (4321), 1035-1037, 1977.
- Ng HJ, Robinson SB, *Hydrate formation in systems containing methane, ethane, propane, carbon-dioxide or hydrogen-sulfide in the presence of methanol*, Fluid Phase Equilibria **21** (1-2), 145-155, 1985.
- Niemann HB, Atreya SK, Bauer SJ, Carignan GR, Demick JE, Frost RL, Gautier D, Haberman JA, Harpold DN, Hunten DM, Israel G, Lunine JI, Kasprzak WT, Owen TC, Paulkovich M, Raulin F, Raaen E and Way SH, *The abundances of constituents of Titan's atmosphere from the GCMS instrument on the Huygens probe*, Nature **438** (7069), 779-784, 2005.
- Nimmo F and Stevenson DJ, *Influence of early plate tectonics on the thermal evolution and magnetic field of Mars*, Journal of Geophysical Research-Planets **105** (E5), 11969-11979, 2000.
- Nimmo F, Spencer JR, Pappalardo RT and Mullen ME, *Shear heating as the origin of the plumes and heat flux on Enceladus*, Nature **447** (7142), 289-291, 2007.
- Norman MD, *The composition and thickness of the crust of Mars estimated from rare earth elements and neodymium-isotopic compositions of Martian meteorites*, Meteoritic & Planetary Science **34** (3), 439-449, 1999.
- Notesco G, Laufer D, Bar-Nun A and Owen T, *An experimental study of the isotopic enrichment in Ar, Kr, and Xe when trapped in water ice*, Icarus **142** (1), 298-300, 1999.
- Notesco G and Bar-Nun A, *The effect of methanol clathrate-hydrate formation and other gas-trapping mechanisms on the structure and dynamics of cometary ices*, Icarus **148** (2), 456-463, 2000.
- Notesco G, Bar-Nun A and Owen T, *Gas trapping in water ice at very low deposition rates and implications for comets*, Icarus **162** (1), 183-189, 2003.
- Nyquist LE, Wooden J, Bansal B, Wiesmann H, McKay G and Bogard DD, *Rb-Sr age of the shergotty achondrite and implications for metamorphic resetting of isochron ages*, Geochimica et Cosmochimica Acta **43** (7), 1057-1074, 1979.
- Nyquist LE, Bogard DD, Shih CY, Greshake A, Stoffler D, Eugster O, *Ages and geologic histories of Martian meteorites*, Space Science Reviews **96** (1-4), 105-164, 2001.
- Ohmura R, Matsuda S, Uchida T, Ebinuma T and Narita H, *Phase equilibrium for structure-H hydrates at temperatures below the freezing point of water*, Journal of Chemical and Engineering Data **50** (3), 993-996, 2005.

- Ohno H, Lipenkov VY and Hondoh T, *Air bubble to clathrate hydrate transformation in polar ice sheets: A reconsideration based on the new data from Dome Fuji ice core*, *Geophysical Research Letters* **31** (21), Art. No. L21401, 2004.
- Okano Y and Yasuoka K, *Free-energy calculation of structure-H hydrates*, *Journal of Chemical Physics* **124** (2), Art. No. 024510, 2006.
- Ondreas H, Olu K, Fouquet Y, Charlou JL, Gay A, Dennielou B, Donval JP, Fifis A, Nadalig T, Cochonat P, Cauquil E, Bourillet JF, Le Moigne M and Sibuet M, *ROV study of a giant pockmark on the Gabon continental margin*, *Geo-Marine Letters* **25** (5), 281-292, 2005.
- Osegovic JP and Max MD, *Compound clathrate hydrate on Titan's surface*, *Journal of Geophysical Research-Planets* **110** (E8), Art. No. E08004, 2005.
- Østergaard KK, Anderson R, Llamedo M and Tohidi B, *Hydrate phase equilibria in porous media: effect of pore size and salinity*, *Terra Nova* **14** (5), 307-312, 2002.
- Owen T and Bar-Nun A, *Trapping of gases in water ice and consequences to comets and the atmospheres of the inner planets*, In: *Solar system ices* (ed. B. Schmitt et al.), 353-366, Kulwer Academic Publishers, Dordrecht, Netherlands, 1995.
- Paige DA, Herkenhoff KE and Murray BC, *Mariner-9 observations of the south polar-cap of mars - evidence for residual CO<sub>2</sub> frost*, *Journal of Geophysical Research-Solid Earth* **95** (B2), 1319-1335, 1990.
- Paige DA, *The thermal-stability of near-surface ground ice on Mars*, *Nature* **356** (6364), 43-45, 1992.
- Pang KD, Voga CC, Rhoads JW and Ajello JM, *Proceedings of 14<sup>th</sup> Lunar and Planet Science Conference* Houdson **14**, 592, 1983.
- Parker TJ, Saunders RS, Schneeberger DM, *Transitional morphology in west deuteronilus mensae, Mars - implications for modification of the lowland upland boundary*, *Icarus* **82** (1), 111-145, 1989.
- Parker TJ, Gorsline DS, Saunders RS, Pieri DC, Schneeberger DM, *Coastal geomorphology of the Martian northern plains*, *Journal of Geophysical Research-Planets* **98** (E6), 11061-11078, 1993.
- Parrish W, *Powder and related techniques: X-ray techniques*, In: *International tables for crystallography, Vol.C, Mathematical, physical and chemical tables* (ed. A.J.C. Wilson), Kulwer Academic Publisher, Dordrecht, Netherlands, 1992.
- Parsons JD, *Wet Evidence for a Dry Mars*, *Lunar and Planetary Science XXXII*, abstract nr: **1256**, 2001.
- Pavlov AK and Pavlov AA, *Atmospheric losses under dust bombardment in the ancient atmospheres*, *Earth, Moon and Planets* **76** (3), 157-183, 1998.
- Peale SJ, Schubert G and Lingfelter RE, *Origin of martian channels - clathrates and water*, *Science* **187** (4173), 273-274, 1975.
- Pellenbarg RE, Max MD and Clifford SM, *Methane and carbon dioxide hydrates on Mars: Potential origins, distribution, detection, and implications for future in situ resource utilization*, *Journal of Geophysical Research-Planets* **108** (E4), Art. No. 8042, 2003.
- Pepin RO, *Evolution of the Martian atmosphere*, *Icarus* **111** (2), 289-304, 1994.
- Peterson SW and Levy HA, *A single-crystal neutron diffraction of heavy ice*, *Acta Crystallographica* **10** (1), 70-76, 1957.

- Petrenko VF and Whitworth RW, *Physics of Ice*, Oxford University Press Inc., New York, 1999.
- Philips RJ, Zuber MT, Solomon SC, Golombek MP, Jakosky BM, Banerdt WB, Smith DE, Williams RM, Hynek BM, Aharonson O and Hauck SA, *Ancient Geodynamics and global-scale hydrology on Mars*, *Science* **291** (5513), 2587-2591, 2001.
- Picardi G, Plaut JJ, Biccari D, Bombaci O, Calabrese D, Cartacci M, Cicchetti A, Clifford SM, Edenhofer P, Farrell WM, Federico C, Frigeri A, Gurnett DA, Hagfors T, Heggy E, Herique A, Huff RL, Ivanov AB, Johnson WTK, Jordan RL, Kirchner DL, Kofman W, Leuschen CJ, Nielsen E, Orosei R, Pettinelli E, Phillips RJ, Plettemeier D, Safaeinili A, Seu R, Stofan ER, Vannaroni G, Watters TR, and Zampolini E, *Radar Soundings of the Subsurface of Mars*, *Science* **310** (5756), 1925-1928, 2005.
- Plaut JJ, Picardi G, Safaeinili A, Ivanov AB, Milkovich SM, Cicchetti A, Kofman W, Mouginito J, Farrell WM, Phillips RJ, Clifford SM, Frigeri A, Orosei R, Federico C, Williams IP, Nielsen E, Hagfors T, Heggy E, Stofan ER, Plettemeier D, Watters TR, Leuschen CJ and Edenhofer P, *Subsurface radar sounding of the south polar layered deposits of Mars*, *Science* **316** (5821), 92-95, 2007.
- Pollack JB, Kasting JF, Richardson SM and Poliakov K, *The case for a wet, warm climate on early Mars*, *Icarus* **71** (2), 203-224, 1987.
- Porco CC, Helfenstein P, Thomas PC, Ingersoll AP, Wisdom J, West R, Neukum G, Denk T, Wagner R, Roatsch T, Kieffer S, Turtle E, McEwen A, Johnson TV, Rathbun J, Veverka J, Wilson D, Perry J, Spitalo J, Brahic A, Burns JA, DelGenio AD, Dones L, Murray CD and Squyres S, *Cassini observes the active South Pole of Enceladus*, *Science* **311** (5766), 1393-1401, 2006.
- Prieto-Ballesteros O, Kargel JS, Fernandez-Sampedro M, Selsis F, Martinez ES and Hogenboom DL, *Evaluation of the possible presence of clathrate hydrates in Europa's icy shell or seafloor*, *Icarus* **177** (2), 491-505, 2005.
- Prieto-Ballesteros O, Kargel JS, Farén AG, Fernández-Remolar DC, Dohm JM and Amils R, *Interglacial clathrate destabilization on Mars: Possible contributing source of its atmospheric methane*, *Geology* **34** (3), 149-152, 2006.
- Rachold BV, Bolshiyakov DY, Grigoriev MN, Hubberten WH, Junker J, Kunitsky VV, Merker F, Overduin P and Schneider W, *Nearshore Arctic subsea permafrost in transition*, *EOS* vol. **88**, No: 13, 27 March 2007.
- Radhakrishnan R and Trout BL, *A new approach for studying nucleation phenomena using molecular simulations: Application to CO<sub>2</sub> hydrate clathrates*, *Journal of Chemical Physics* **117** (4), 1786-1796, 2002.
- Read PL and Lewis SR, *The Martian climate revisited. Atmosphere and environment of a desert planet*, Springer, Chichester, 2004.
- Rehder G, Kirby SH, Durham WB, Stern LA, Peltzer ET, Pinkston J and Brewer PG, *Dissolution rates of pure methane hydrate and carbon-dioxide hydrate in undersaturated seawater at 1000-m depth*, *Geochimica et Cosmochimica Acta* **68** (2), 285-292, 2004.
- Rempel AW and Buffett BA, *Formation and accumulation of gas hydrate in porous media*, *Journal of Geophysical Research-Solid Earth* **102** (B5), 10151-10164, 1997.
- Richardson HH, Wooldridge PJ and Devlin JP, *FT-IR spectra of vacuum-deposited clathrate hydrates of oxirane H<sub>2</sub>S, THF, and ethane*, *Journal of Chemical Physics* **83** (9), 4387-4394, 1985.

- Richter K, Hervig RL and Kring DA, *Accretion and core formation on Mars: Molybdenum contents of melt inclusion glasses in three SNC meteorites*, *Geochimica et Cosmochimica Acta* **62** (12), 2167-2177, 1998.
- Ringwood AE, *Composition of core and implications for origin of Earth*, *Geochemical Journal* **11** (3), 111-135, 1977.
- Ripmeester JA, Tse JS, Ratcliffe CI and Powell BM, A new clathrate hydrate structure, *Nature* **325** (6100), 135-136, 1987.
- Robinson DB and Metha BR, *Hydrates in the propane-carbon dioxide-water system*, *Journal of Canadian Petroleum Technology* **10** (1), 33-, 1971.
- Rodriguez JAP, Sasaki S, Kuzmin RO, Dohm JM, Tanaka KL, Miyamoto H, Kurita K, Komatsu G, Fairen AG, Ferris JC, *Outflow channel sources, reactivation, and chaos formation, Xanthe Terra, Mars*, *Icarus* **175** (1), 36-57, 2005.
- Rodriguez JAP, Kargel J, Crown DA, Bleamaster LF, Tanaka KL, Baker V, Miyamoto H, Dohm JM, Sasaki S and Komatsu G, *Headward growth of chasmata by volatile outbursts, collapse, and drainage: Evidence from Ganges chaos, Mars*, *Geophysical Research Letters* **33** (18), Art. No. L18203, 2006.
- Rogers D and Christensen PR, *Age relationship of basaltic and andesitic surface compositions on Mars: Analysis of high-resolution TES observations of the northern hemisphere*, *Journal of Geophysical Research-Planets* **108** (E4), Art. No. 5030, 2003.
- Röttger K, Endriss A, Ihringer J, Doyle S and Kuhs WF, *Lattice-constants and thermal-expansion of H<sub>2</sub>O and D<sub>2</sub>O ice Ih between 10 and 265 K*, *Acta Crystallographica Section B-Structural Science* **50** (6), 644-648, Part 6, 1994.
- Sakai H, Gamo T, Kim, ES, Tsutsumi M, Tanaka T, Ishibashi J, Wakita H, Yamano M and Oomori T, *Venting of carbon-dioxide rich fluid and hydrate formation in mid-Okinawa trough backarc basin*, *Science* **248** (4959), 1093-1096, 1990.
- Salamatin, AN and Kuhs WF, *Formation of porous gas hydrates*, *Proceedings of the 4-th International Conference on Gas Hydrates, Yokohama*, 766-770, 2002.
- Schicks JM, Luzi M, Erzinger J and Spangenberg E, *Clathrate hydrate formation and growth experimental observations versus predicted behavior*, In: *Physics and chemistry of ice* (ed. WF. Kuhs) 537-544, RSC Publishing, Cambridge, 2007.
- Schmitt B, *The formation and detectability of CO<sub>2</sub> clathrate hydrate on Mars*, *Mars Polar Science*, abstract nr: **4053**, 2000.
- Schorghofer N and Aharonson O, *Stability and exchange of subsurface ice on Mars*, *Journal of Geophysical Research-Planets* **110** (E5), Art. No. E05003, 2005.
- Schorghofer N, *Dynamics of ice ages on Mars*, *Nature* **449** (7159), 192-195, 2007.
- Segura TL, Toon OB, Colaprete A and Zahnle K, *Effects of large impacts on mars: implications for river formation*, *Lunar and Planetary Science XXXIII*, abstract no: **1900**, 2002a.
- Segura TL, Toon OB, Colaprete A and Zahnle K, *Environmental effects of large impacts on Mars*, *Science* **298** (5600), 1877-1980, 2002b.
- Seu R, Phillips RJ, Alberti G, Biccari D, Bonaventura F, Bortone M, Calabrese D, Campbell BA, Cartacci M, Carter LM, Catallo C, Croce A, Croci R, Cutigni M, Di Placido A, Dinardo S, Federico C, Flamini E, Fois F,



- Frigeri A, Fuga O, Giacomoni E, Gim YY, Guelfi M, Holt JW, Kofman W, Leuschen CJ, Marinangeli L, Marras P, Masdea A, Mattei S, Mecozzi R, Milkovich SM, Morlupi A, Mouginot J, Orosei R, Papa C, Paterno T, del Marmo PP, Pettinelli E, Pica G, Picardi G, Plaut JJ, Provenziani M, Putzig NE, Russo F, Safaeinili A, Salzillo G, Santovito MR, Smrekar SE, Tattarletti B and Vicari D, *Accumulation and erosion of Mars' south polar layered deposits*, *Science* **317** (5845), 1715-1718, 2007.
- Shean DE, Head JW, Fastook JL and Marchant DR, *Recent glaciation at high elevations on Arsia Mons, Mars: Implications for the formation and evolution of large tropical mountain glaciers*, *Journal of Geophysical Research-Planets* **112** (E3), Art. No. E03004, 2007.
- Sheehan W, *The Planet Mars: A history of Observation and Discovery*, The University of Arizona Press, Tucson, 1996. <http://www.uapress.arizona.edu/onlinebks/mars/contents.htm>
- Shih CY, Nyquist LE and Wiesmann H, *Samarium-neodymium and rubidium-strontium systematics of nakhlite Governador Valadares*, *Meteoritic & Planetary Science* **34** (4), 647-655, 1999.
- Shibley TH, Houtson MH, Buffler RT, Shaub FJ, McMillen KJ, Ladd JW and Worzel JL, *Seismic reflection evidence for the widespread occurrence of possible gas-hydrate horizons on continental slopes and rises*, *American Association of Petroleum Geologists Bulletin* **63** (12), 2204-2213, 1979.
- Sleep NH, *Martian plate-tectonics*, *Journal of Geophysical Research-Planets* **98** (E6), 5639-5655, 1994.
- Sloan DE, *Clathrate hydrates of natural gases (Second edition)*, Marcel Dekker Inc, New York, 1998.
- Sloan ED and Koh CA, *Clathrate Hydrates of Natural Gases, 3-rd Edition*, Taylor & Francis Group, LLC, Boca Raton, 2008.
- Smith DE, Zuber MT, Solomon SC, Phillips RJ, Head JW, Garvin JB, Banerdt WB, Muhleman DO, Pettengill GH, Neumann GA, Lemoine FG, Abshire JB, Aharonson O, Brown CD, Hauck SA, Ivanov AB, McGovern PJ, Zwally HJ and Duxbury TC, *The global topography of Mars and implications for surface evolution*, *Science* **284** (5419), 1495-1503, 1999.
- Smith DE, Zuber MT and Neumann GA, *Seasonal variations of snow depth on Mars*, *Science* **294** (5549), 2141-2146, 2001.
- Smith DH, Wilder JW, Seshadri K, *Methane hydrate equilibria in silica gels with broad pore-size distributions*, *AiChE Journal* **48** (2), 393-400, 2002.
- Smythe WD, *Spectra of hydrate frosts: Their application to the outer solar system*, *Icarus* **24** (4), 421-427, 1975.
- Sohl F, Schubert G and Spohn T, *Geophysical constraints on the composition and structure of the Martian interior*, *Journal of Geophysical Research-Planets* **110** (E12), Art. No. E12008, 2005.
- Solheim A and Elverhøi A, *Gas-related sea-floor craters in the Barents Sea*, *Geo-Marine Letters* **13** (4), 235-243, 1993.
- Solomatov VS, *Scaling of temperature-dependent and stress-dependent viscosity convection*, *Physics of Fluids* **7** (2), 266-274, 1995.
- Solomon SC, Aharonson O, Aurnou JM, Banerdt WB, Carr MH, Dombard AJ, Frey HV, Golombek MP, Hauck SA, Head JW, Jakosky BM, Johnson CL, McGovern PJ, Neumann GA, Phillips RJ, Smith DE and Zuber MT, *New Perspectives on Ancient Mars*, *Science* **307** (5713), 1214-1220, 2005.

- Span R and Wagner W, *A new equation of state for carbon dioxide covering the fluid region from the triple-point temperature to 1100 K at pressures up to 800 Mpa*, Journal of Physical and Chemical Reference Data **25** (6), 1509-1596, 1996.
- Spangenberg E, Kulenkampff J, Naumann R and Erzinger J, *Pore space hydrate formation in a glass bead sample from methane dissolved in water*, Geophysical Research Letters **32** (24), Art. No. L24301, 2005.
- Spangenberg E and Kulenkampff J, *Influence of methane hydrate content on electrical sediment properties*, Geophysical Research Letters **33** (24), Art. No. L24315, 2006.
- Spencer J and Grinspoon D, *Planetary science - Inside Enceladus*, Nature **445** (7126), 376-377, 2007.
- Spencer JR and Calvin WM, *Condensed O<sub>2</sub> on Europa and Callisto*, Astronomical Journal **124** (6), 3400-3403, 2002.
- Spohn T, Acuna MH, Breuer D, Golombek M, Greeley R, Halliday A, Hauber E, Jaumann R and Sohl F, *Geophysical constraints on the evolution of Mars*, Space Science Reviews **96** (1-4), 231-262, 2001.
- Squyres SW, *Urey prize lecture - Water on Mars*, Icarus **79** (2), 229-288, 1989.
- Staykova DK, Kuhs WF, Salamatin AN and Hansen T, *Formation of porous gas hydrates from ice powders: Diffraction experiments and multistage model*, Journal of Physical Chemistry B **107** (37), 10299-10311, 2003.
- Staykova DK, PhD Thesis, *Kinetic studies of methane-hydrate formation from ice Ih*, Georg-August-Universität Göttingen, 2004
- Stern LA, Kirby SH and Durham WB, *Peculiarities of methane clathrate hydrate formation and solid-state deformation, including possible superheating of water ice*, Science **273** (5283), 1843-1848, 1996.
- Stern LA, Circone S, Kirby SH and Durham WB, *Anomalous preservation of pure methane hydrate at 1 atm*, Journal of Physical Chemistry B **105** (9), 1756-1762, 2001.
- Stern LA, Circone S, Kirby SH and Durham WB, *Temperature, pressure, and compositional effects on anomalous or "self" preservation of gas hydrates*, Canadian Journal of Physics **81** (1-2), 271-283, 2003.
- Stevenson DJ, *Mars' core and magnetism*, Nature **412** (6843), 214-219, 2001.
- Stewart ST and Nimmo F, *Surface runoff features on Mars: Testing the carbon dioxide formation hypothesis*, Journal of Geophysical Research-Planets **107** (E9), Art. No. 5069, 2002.
- Stewart AJ, Schmidt MW, van Westeren W and Liebske C, *Mars: A new core-crystallization regime*, Science **316** (5829), 1323-1325, 2007.
- Steytler DC, Dore JC and Wright CJ, *Neutron-diffraction study of cubic ice nucleation in a porous silica network*, Journal of Physical Chemistry **87** (14), 2458-2459, 1983.
- Stofan ER, Elachi C, Lunine JI, Lorenz RD, Stiles B, Mitchell KL, Ostro S, Soderblom L, Wood C, Zebker H, Wall S, Janssen M, Kirk R, Lopes R, Paganelli F, Radebaugh J, Wye L, Anderson Y, Allison M, Boehmer R, Callahan P, Encrenaz P, Flamini E, Francescetti G, Gim Y, Hamilton G, Hensley S, Johnson WTK, Kelleher K, Muhleman D, Pailou P, Picardi G, Posa, Roth L, Seu R, Shaffer S, Vetrella S and West R, *The lakes of Titan*, Nature **445** (7123), 61-46, 2007.
- Takenouchi S and Kennedy GC, *Solubility of carbon dioxide in NaCl solutions at high temperatures and pressures*, American Journal of Science **263** (5), 445-454, 1965.

- Takeya S, Hori A, Hondoh T and Uchida T, *Freezing-memory effect of water on nucleation of CO<sub>2</sub> hydrate crystals*, Journal of Physical Chemistry B **104** (17), 4164-4168, 2000.
- Takeya S, Shimada W, Kamata Y, Ebinuma T, Uchida T, Nagao J and Narita H, *In situ X-ray diffraction measurements of the self-preservation effect of CH<sub>4</sub> hydrate*, Journal of Physical Chemistry A **105** (42), 9756-9759, 2001.
- Takeya S, Ebinuma T, Uchida T, Nagao J and Narita H, *Self-preservation effect and dissociation rates of CH<sub>4</sub> hydrate*, Journal of Crystal Growth **237**, 379-382, 2002.
- Takeya S and Ripmeester J, A, *Dissociation behavior of clathrate hydrates to ice and dependence on guest molecules*, Angewandte Chemie **47**, 1276-1279, 2008.
- Tanaka KL, Banerdt WB, Kargel JS and Hoffman N, *Huge, CO<sub>2</sub>-charged debris-flow deposit and tectonic sagging in the northern plains of Mars*, Geology **29** (5), 427-430, 2001.
- Tanaka KL, *Geology and insolation-driven climatic history of Amazonian north polar materials on Mars*, Nature **437** (7061), 991-994, 2005.
- Techmer KS, Heinrichs T and Kuhs WF, *Cryo-electron microscopic studies of structures and composition of Malik gas-hydrate-bearing samples*; In *Scientific Results from the Malik 2002 Gas hydrate Production Research Well Program, Mackenzie Delta, Northwest Territories, Canada*, ed. Dallimore SR and Collet TS, Geological Survey of Canada Bulletin **585**, 12.
- Teng H, Yamasaki A, Chun MK and Lee H, *Why does CO<sub>2</sub> hydrate disposed of in the ocean in the hydrate-formation region dissolve in seawater?*, Energy **22** (12), 1111-1117, 1997.
- Thomas PC, Malin MC, Edgett KS, Carr MH, Hartmann WK, Ingersoll AP, James PB, Soderblom LA, Veverka J and Sullivan R, *North-south geological differences between the residual polar caps on Mars*, Nature **404** (6774), 161-164, 2000.
- Thorsteinsson T, *Textures and fabric in the GRIP ice core, in relation to climate history and ice deformation*, Berichte zur Polarforschung **205**, Reports on Polar Research p.11, 1996.
- Tobie G, Lunine JI and Sotin C, *Episodic outgassing as the origin of atmospheric methane on Titan*, Nature **440** (7080), 61-64, 2006.
- Tohidi B, Anderson R, Clennell MB, Burgass RW and Biderkab AB, *Visual observation of gas-hydrate formation and dissociation in synthetic porous media by means of glass micromodels*, Geology **29** (9), 867-870, 2001.
- Toon OB, Pollack JB, Ward W, Burns JA and Bilski K, *The astronomical theory of climatic change on Mars*, Icarus **44** (3), 552-607, 1980.
- Touma J and Wisdom J, *The chaotic obliquity of Mars*, Science **259** (5099), 1294-1296, 1993.
- Treiman AH, *Geologic settings of Martian gullies: Implications for their origins*, Journal of Geophysical Research-Planets **108** (E4), Art. No. 8031, 2003.
- Tse JS, *Thermal-expansion of structure-H clathrate hydrates*, Journal of Inclusion Phenomena and Molecular Recognition in Chemistry **8** (1-2), 25-32, 1990.
- Tulk CA, Wright JF, Ratcliffe CI, and Ripmeester JA, *Storage and handling of natural gas hydrate, in Scientific Results from JAPEx/JNOC/GSC Mallik 2L-38 Gas Hydrate Research Well, Mackenzie Delta, Northwest Territories, Canada*, Geological Survey of Canada, Ontario, Canada **544**, 263-267, 1999.

- Uchida T, Ebinuma T, Takeya S, Nagao J and Narita H, *Effects of pore sizes on dissociation temperatures and pressures of methane, carbon dioxide, and propane hydrates in porous media*, Journal of Physical Chemistry B **106** (4), 820-826, 2002.
- Uchida T, Takeya S, Chuvilin EM, Ohmura R, Nagao J, Yakushev VS, Istomin VA, Minagawa H, Ebinuma T and Narita H, *Decomposition of methane hydrates in sand, sandstone, clays, and glass beads*, Journal of Geophysical Research-Solid Earth **109** (B5), Art. No. B05206, 2004.
- Udachin KA, Ratcliffe CI and Ripmeester JA, *Structure, composition, and thermal expansion of CO<sub>2</sub> hydrate from single crystal X-ray diffraction measurements*, Journal of Physical Chemistry B **105** (19), 4200-4204, 2001.
- Unruh CH and Katz DL, *Gas hydrate of carbon dioxide methane mixtures*, Translations of the American Institute of Mining and Metallurgical Engineers **186** (4), 83-86, 1949.
- Urquhart ML and Gulick VC, *Heat flow, thermal conductivity, and the plausibility of the "White Mars" hypothesis*, Lunar and Planetary Science XXXIII, abstract nr: **1680**, 2002.
- Villard P, *Sur quelques nouveaux hydrates de gaz*, Comptes Rendus vol. **106**, 1602-1603, 1888.
- Villard P, *Sur quelques nouveaux hydrates de gaz*, Comptes Rendus vol. **111**, 302-305, 1890.
- Villard P, *Combinaison de l'argon avec l'eau*, Comptes Rendus vol. **123**, 377-379, 1896.
- Vlahakis JG, Chen HS, Suwandi MS and Barduhn AJ, *The Growth rate of ice crystals: properties of carbon dioxide hydrate, A review of properties of 51 gas hydrates*, Syracuse University Research and Development report 830, prepared for US Department of the Interior, 1972.
- Vogt PR, Crane K, Sundvor E, Max MD and Pfirman SL, *Methane-generated (questionable) pockmarks on young, thickly sedimented oceanic-crust in the Arctic:-Vestnesa ridge, Fram strait*, Geology **22** (3), 255-258, 1994.
- Vos WL, Finger LW, Hemley RJ and Mao HK, *Novel H<sub>2</sub>-H<sub>2</sub>O clathrates at high-pressures*, Physical Review Letters **71** (19), 3150-3153, 1993.
- Wagner W and Pruss A, *International equations for the saturation properties of ordinary water substance – revisited according to the international temperature scale of 1990 (vol 16, PG 893, 1987)*, Journal of Physical and Chemical Reference Data **22** (3), 783-787, 1993.
- Wagner W, Saul A and Pruss A, *International Equations for the Pressure along the melting and along sublimation curve of ordinary water substance*, Journal of Physical and Chemical Reference Data **23** (3), 783-787, 1994.
- Waite JH, Niemann H, Yelle RV, Kasprzak WT, Cravens TE, Luhmann JG, McNutt RL, Ip WH, Gell D, De La Haye V, Muller-Wordag I, Magee B, Borggren N, Ledvina S, Fletcher G, Walter E, Miller R, Scherer S, Thorpe R, Xu J, Block B, Arnett K, *Ion Neutral Mass Spectrometer results from the first flyby of Titan*, Science **308** (5724), 982-986, 2005.
- Wänke H, *Constitution of terrestrial planets*, Royal Society (London), Philosophical Transactions, Series A, vol. **303**, no. 1477, 287-302, 1981.
- Weiss BP, Vali H, Baudenbacher FJ, Kirschvink JL, Stewart ST and Shuster DL, *Records of an ancient Martian magnetic field in ALH84001*, Earth and Planetary Science Letters **201** (3-4), 449-463, 2002.
- Wetherill GW, *Formation of the Earth*, Annual Review of Earth and Planetary Sciences **18**, 205-256, 1990.

- Wieczorek MA and Zuber TM, *Thickness of the Martian crust: Improved constraints from geoid-to-topography ratios*, Journal of Geophysical Research-Planets **109** (E1), Art. No. E01009, 2004.
- Williams DR, *Mars Fact Sheet*, National Space Science Data Center, NASA, 2004  
<http://nssdc.gsfc.nasa.gov/planetary/factsheet/marsfact.html>
- Wollan EO, Davidsohn WL and Shull CG, *Neutron diffraction study of the structure of ice*, Physical Review **75** (9), 1348-1352, 1949.
- Wooldridge PJ, Richardson HH and Devlin JP, *Mobile Bjerrum defects - a criterion for ice-like crystal-growth*, Journal of Chemical Physics **87** (7), 4126-4131, 1987.
- Wyatt MB and McSween HY, *Spectral evidence for weathered basalt as an alternative to andesite in the northern lowlands of Mars*, Nature **417** (6886), 263-266, 2002.
- Xu WY and Ruppel C, *Predicting the occurrence, distribution, and evolution of methane gas hydrate in porous marine sediments*, Journal of Geophysical Research-Solid Earth **104** (B3), 5081-5095, 1999.
- Yakushev, VS and Istomin VA, *Gas-Hydrates Self-Preservation Effect*, in: *Physics and Chemistry of Ice* (ed. N. Maeno and T. Hondoh), 136-139, Hokkaido Univ. Press, Sapporo, 1992.
- Yakushev VS and Chuvilin EM, *Natural gas and gas hydrate accumulations within permafrost in Russia*, Cold Region Science and Technology **31** (3), 189-197, 2000.
- Yin QZ, Jacobsen SB, Yamashita K, Blichert-Toft J, Telouk P and Albarede F, *A short timescale for terrestrial planet formation from Hf-W chronometry of meteorites*, Nature **418** (6901), 949-952, 2002.
- Yoder CF, Konopliv AS, Yuan DN, Standish EM and Folkner WM, *Fluid core size of Mars from detection of the solar tide*, Science **300** (5617), 299-303, 2003.
- Yokohata T, Odaka M and Kuramoto K, *Role of H<sub>2</sub>O and CO<sub>2</sub> ices in Martian climate changes*, Icarus **159** (2), 439-448, 2002.
- Zuber MT, *The crust and mantle of Mars*, Nature **412** (6843) 220-227, 2001.
- Zuber MT, Phillips RJ, Andrews-Hanna JC, Asmar SW, Konopliv AS, Lemoine FG, Plaut JJ, Smith DE and Smrekar SE, *Density of Mars' south polar layered deposits*, Science **317** (5845), 1718-1719, 2007.

# Appendices

Appendix 1 – Maps of Mars

Appendix 2 – ROC - A comparison between two diffraction patterns with and without a rocking oscillating collimator (ROC)

Appendix 3 – SEM images – Spherical ice

Appendix 4 – BET

Appendix 5 – SEM images - Interrupted runs-Formation at 193K 750mbar (75kPa) 30min run

Appendix 6 – Etching: Interrupted runs-Formation at 193K 750mbar (75kPa) 15min and 90min runs

Appendix 7 – SEM images - Interrupted runs-Formation at 193K 750mbar (75kPa) 90min run

Appendix 8 – Structural models

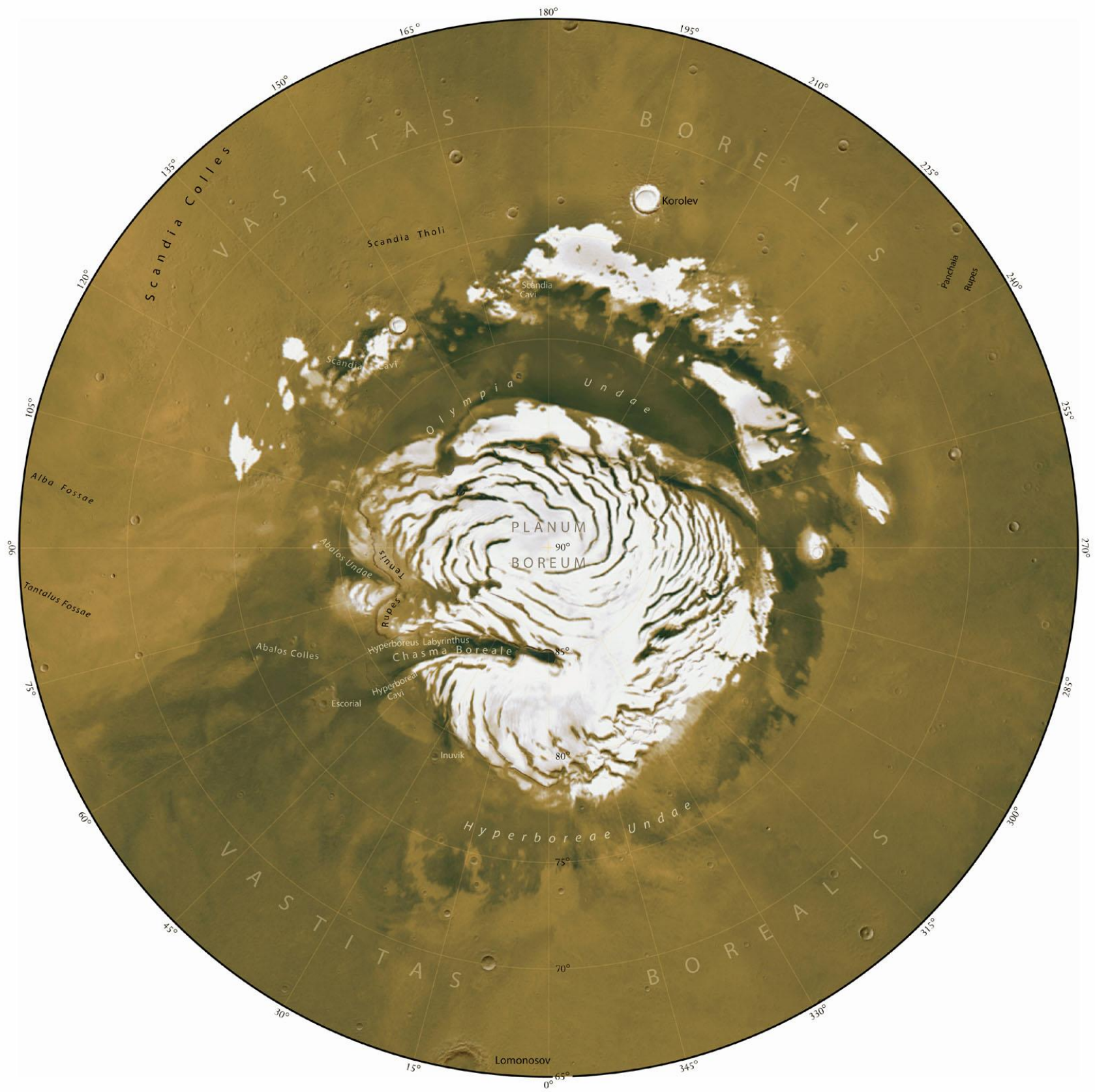
Appendix 9 – Selected diffraction patterns with Retveld fits

Appendix 10 – SEM images - Decomposition at 220K 600mbar (60kPa) 5min and 220K 900mbar (90kPa) 5-10min runs

Appendix 11 – “Frost” fitting parameters







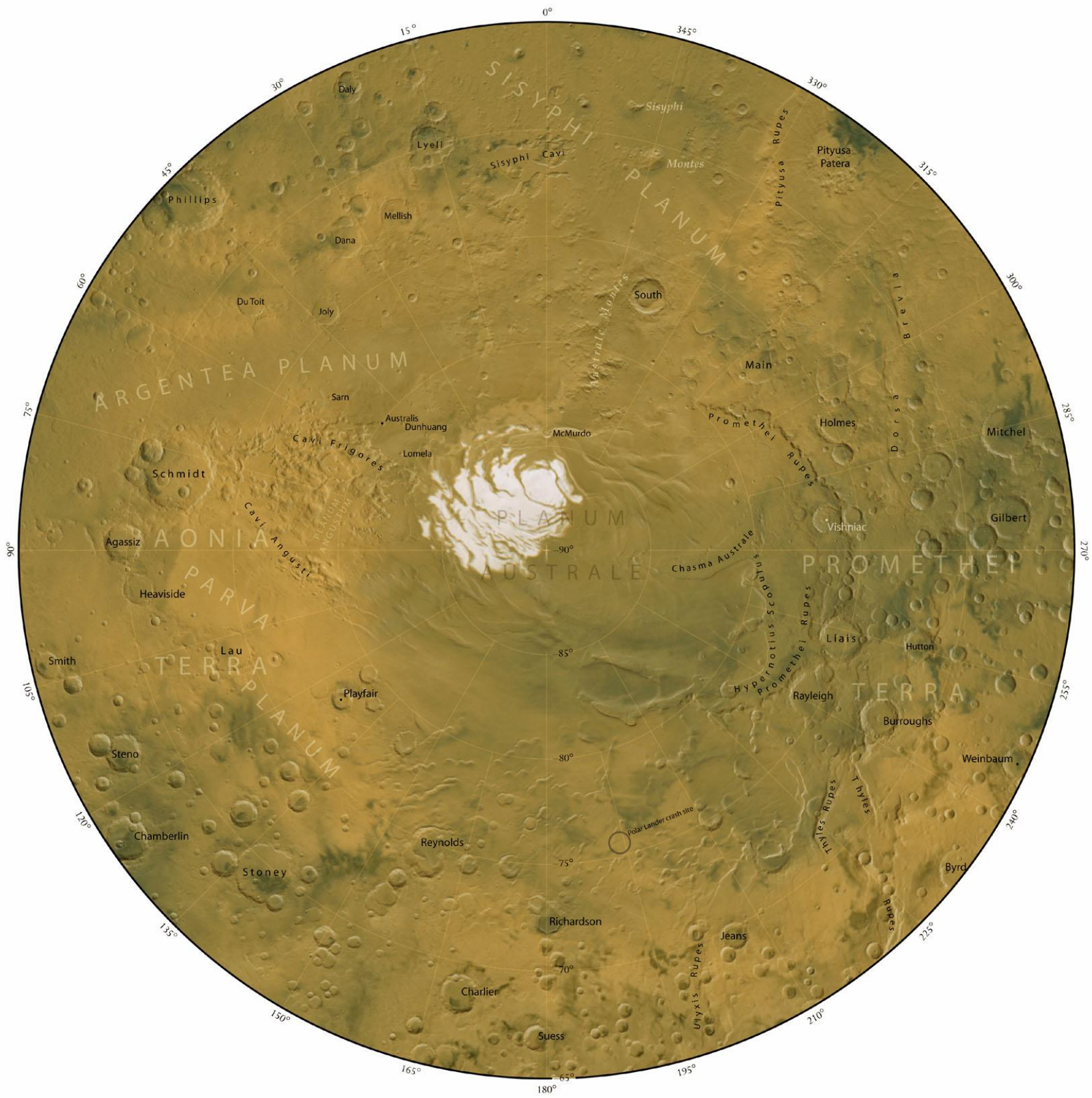
©Ralph Aeschliman

## The North Pole Quadrangle of Mars

Shaded Relief with Albedo Color

by  
 Ralph Aeschliman  
 Polar Stereographic projection





©Ralph Aeschliman

## The Australe Quadrangle of Mars

Shaded Relief with Albedo Color

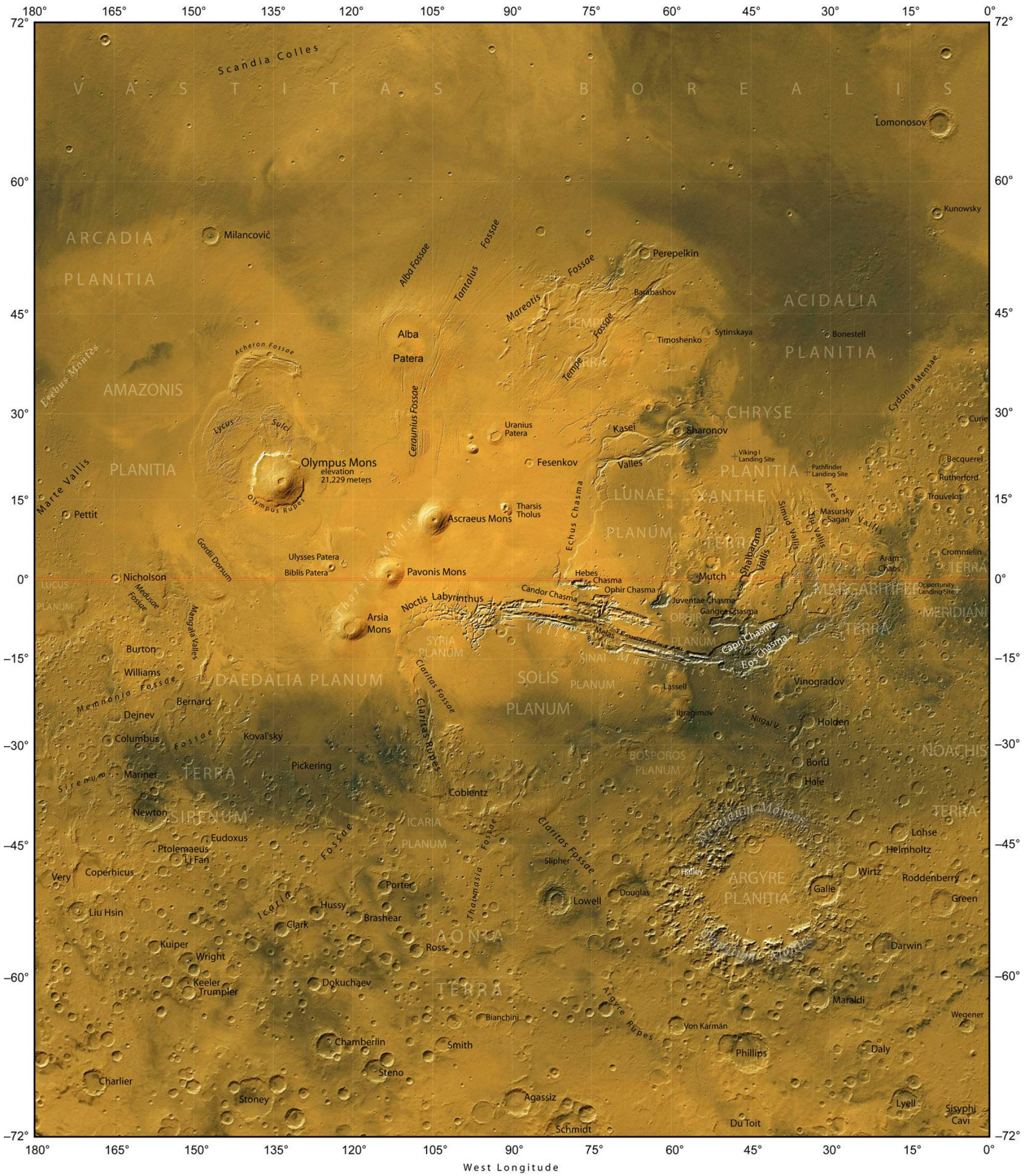
by

Ralph Aeschliman

Polar Stereographic projection



# The Western Hemisphere of Mars

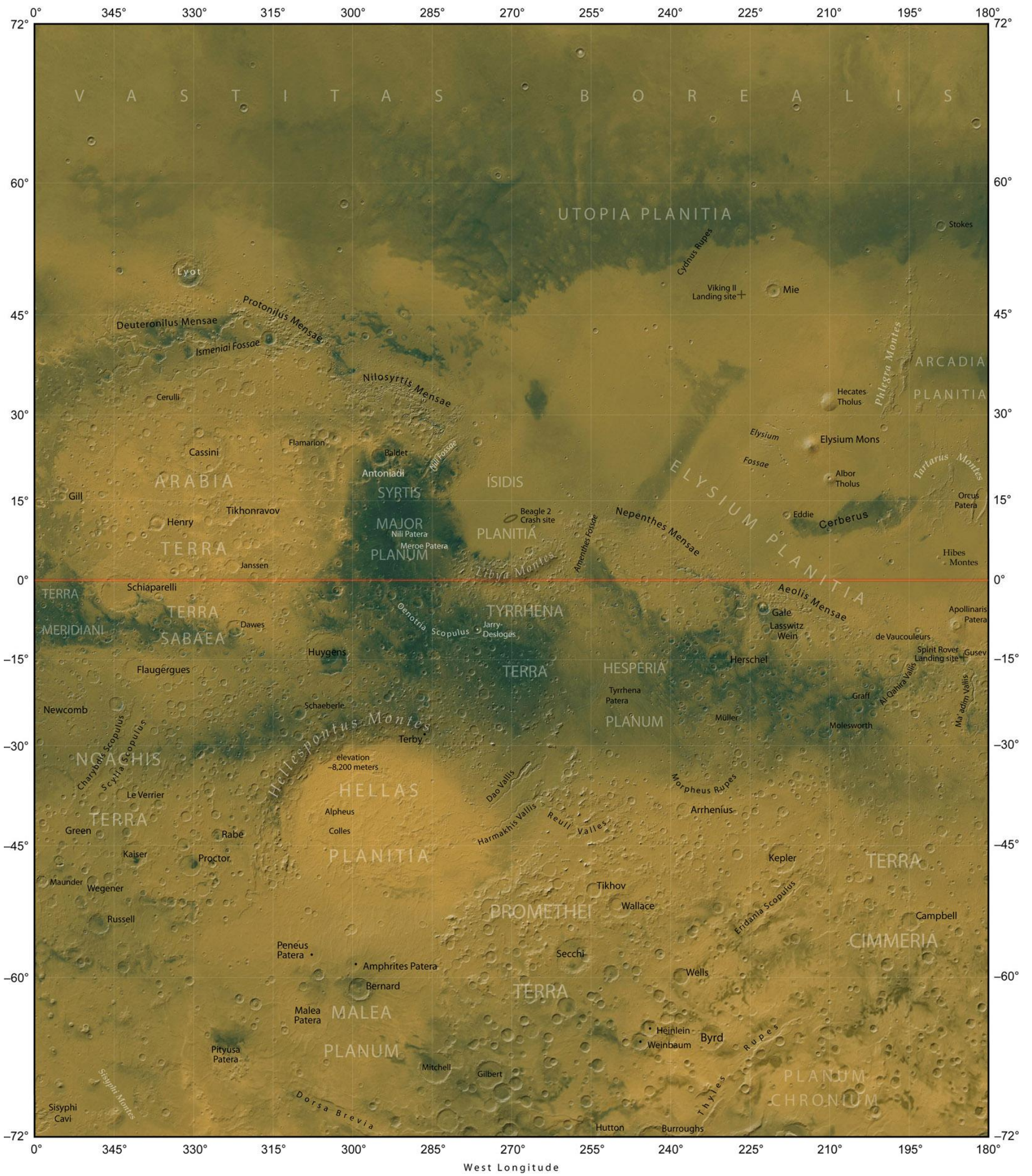


©Ralph Aeschliman

West Longitude  
Mercator Projection



# The Eastern Hemisphere of Mars



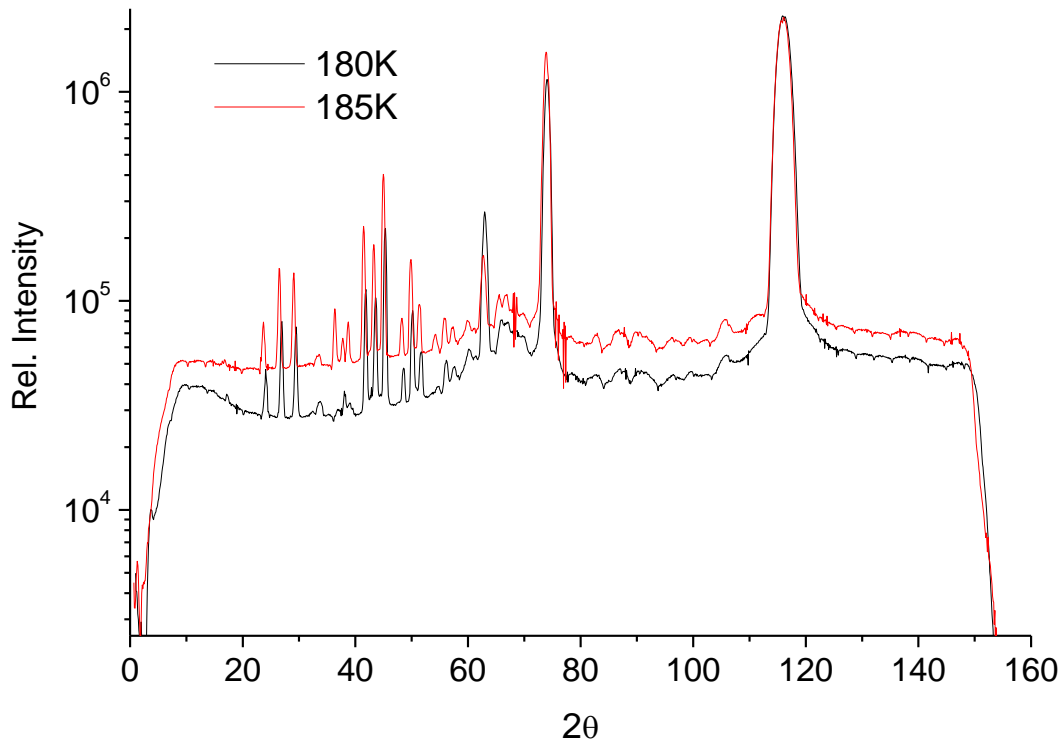
©Ralph Aeschliman

West Longitude  
Mercator Projection

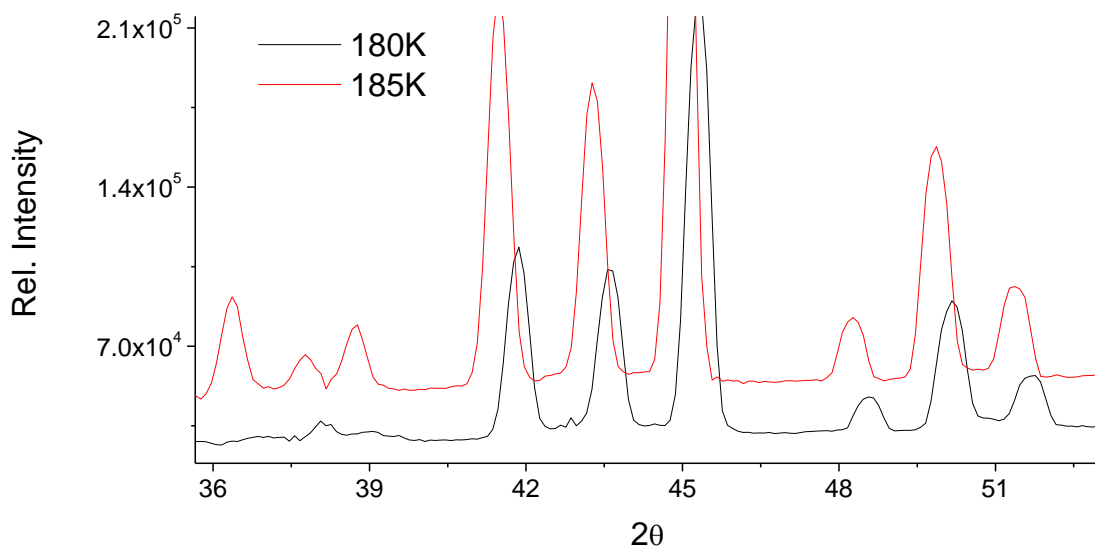


**Appendix 2:** Comparison\* between two diffraction patterns with (185K 0.6kPa) and without (180K 0.6kPa) the radial oscillating collimator.

Full diffraction pattern (Intensity in a log scale to emphasize different background shapes)



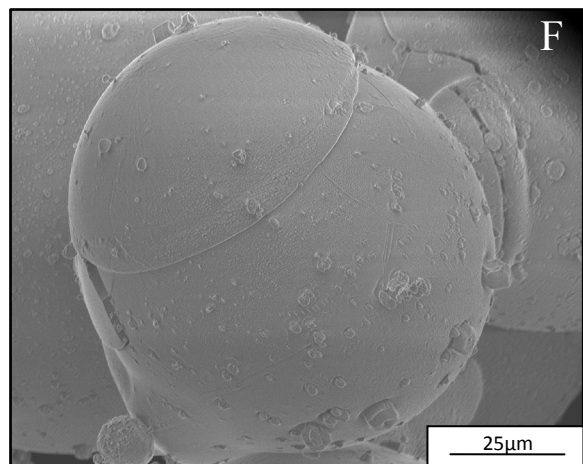
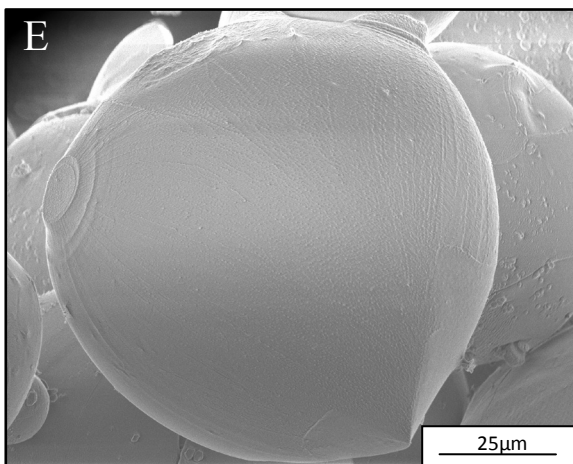
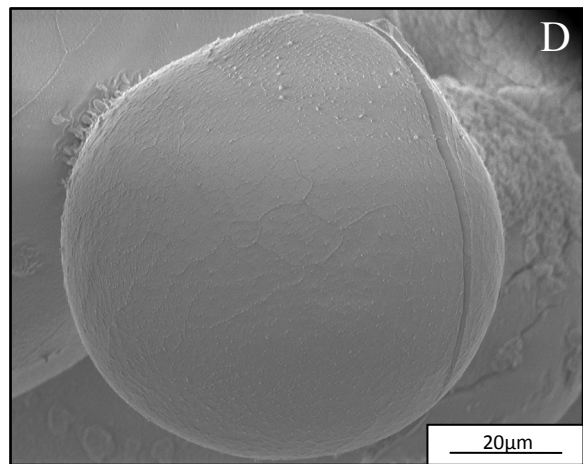
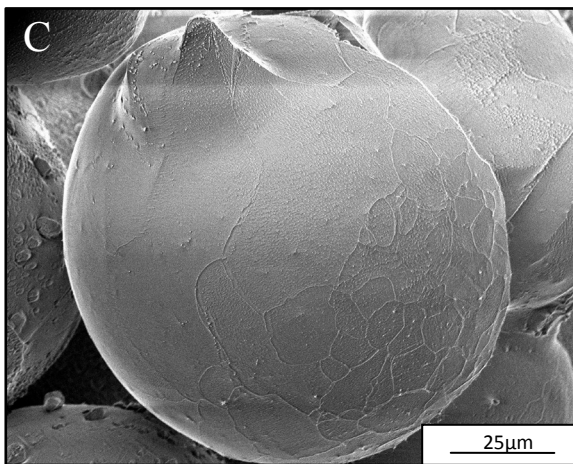
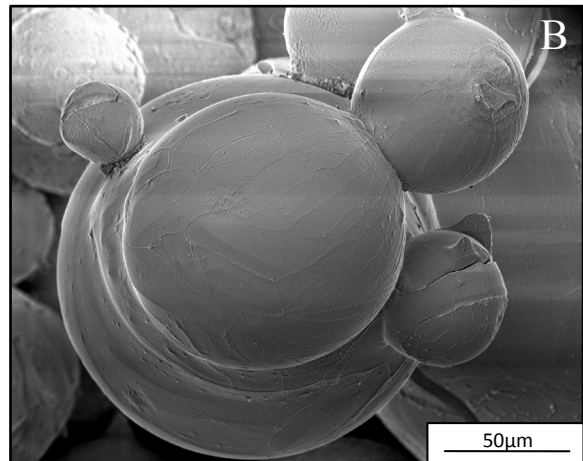
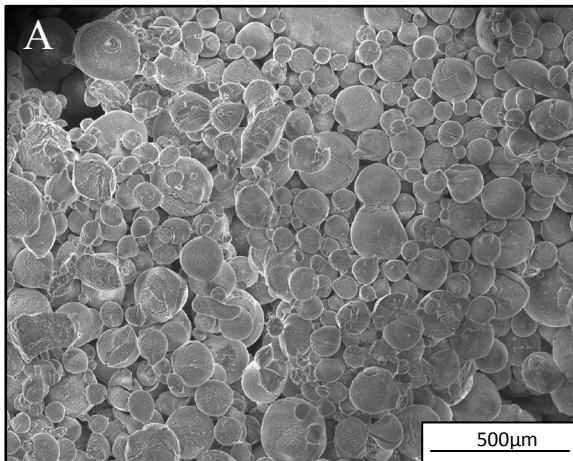
Close up on the high-resolution 2-theta region (Intensity in a linear scale)



\* The reader should be aware of a small difference in the lattice constant, zero shift and wavelength between both samples. Therefore corresponding reflections are slightly shifted. Ice fraction for both samples is also different.



**Appendix 3: Spherical ice**



Images taken with: FEI Quanta 200FEG





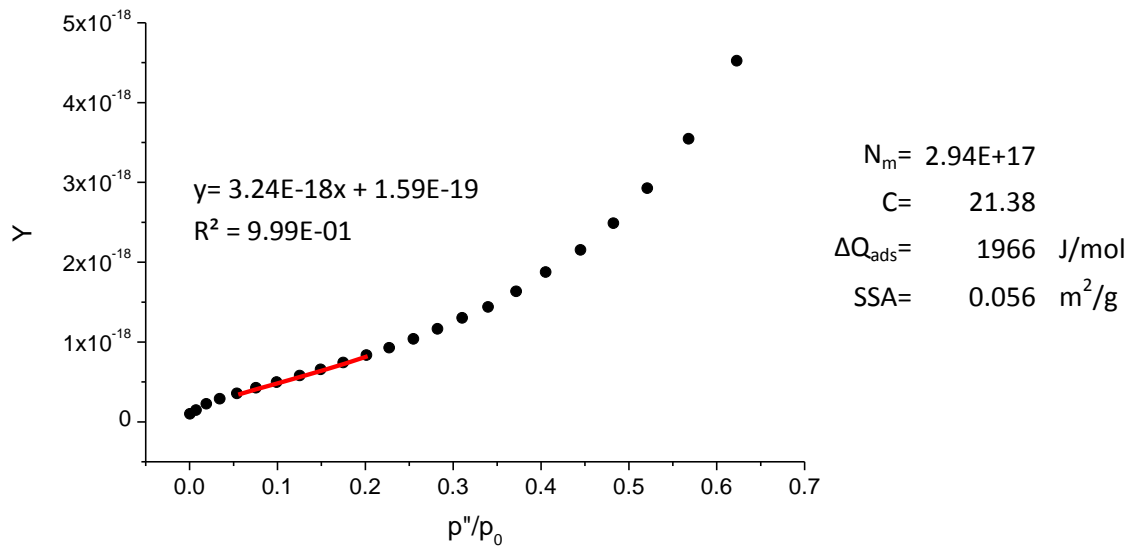
#### Appendix 4: BET measurement – Spherical ice

Large cell

Sample mass= 32.6g

No	p'	p''	n'	n''	n <sup>r</sup>	n <sub>ads</sub>	N <sub>ads/refill</sub>	N <sub>ads/acc</sub>	p''/p <sub>0</sub>	Y
1	0.2376	0.0247	0.019843	0.007604	0.005541	0.012239	2.26E+16	2.26E+16	0.001909	8.47078E-20
2	0.6276	0.112	0.052412	0.034479	0.025126	0.023474	4.33E+16	6.59E+16	0.008655	1.32525E-19
3	0.8962	0.266	0.074844	0.081888	0.059674	0.018082	3.34E+16	9.92E+16	0.020556	2.11492E-19
4	1.2185	0.4621	0.10176	0.142257	0.103666	0.019176	3.54E+16	1.35E+17	0.035711	2.75112E-19
5	1.6386	0.7158	0.136843	0.220358	0.16058	0.020151	3.72E+16	1.72E+17	0.055317	3.40866E-19
6	1.9477	0.996	0.162657	0.306618	0.223439	0.01662	3.07E+16	2.02E+17	0.076971	4.11911E-19
7	2.3126	1.3018	0.193131	0.400758	0.292042	0.015812	2.92E+16	2.32E+17	0.100603	4.8294E-19
8	2.7057	1.639	0.22596	0.504565	0.367688	0.013436	2.48E+16	2.56E+17	0.126662	5.65644E-19
9	2.9068	1.9488	0.242754	0.599937	0.437187	0.010505	1.94E+16	2.76E+17	0.150603	6.42923E-19
10	3.2968	2.282	0.275324	0.702512	0.511936	0.009999	1.84E+16	2.94E+17	0.176352	7.27709E-19
11	3.6312	2.62205	0.30325	0.807196	0.588222	0.007991	1.47E+16	3.09E+17	0.202631	8.22497E-19
12	3.9607	2.9583	0.330768	0.91071	0.663655	0.00828	1.53E+16	3.24E+17	0.228617	9.14048E-19
13	4.343	3.3135	0.362695	1.020058	0.74334	0.006292	1.16E+16	3.36E+17	0.256066	1.02489E-18
14	4.6803	3.6701	0.390863	1.129837	0.823338	0.004366	8.05E+15	3.44E+17	0.283624	1.15125E-18
15	5.0601	4.0337	0.422581	1.241771	0.904907	0.004148	7.65E+15	3.52E+17	0.311723	1.28829E-18
16	5.5071	4.4135	0.459911	1.358692	0.99011	0.006126	1.13E+16	3.63E+17	0.341074	1.42652E-18
17	5.9709	4.8282	0.498644	1.486358	1.083143	0.002397	4.42E+15	3.67E+17	0.373122	1.62059E-18
18	6.4384	5.263	0.537687	1.62021	1.180684	0.000619	1.14E+15	3.68E+17	0.406723	1.8608E-18
19	7.2049	5.7755	0.601699	1.777983	1.295657	0.0044	8.12E+15	3.77E+17	0.446329	2.1409E-18
20	7.5714	6.2593	0.632306	1.926921	1.404191	0.001043	1.92E+15	3.78E+17	0.483717	2.47562E-18
21	8.0798	6.7584	0.674764	2.080568	1.516158	-0.00161	-2.98E+15	3.75E+17	0.522287	2.91174E-18
22	8.9934	7.367	0.751061	2.267925	1.652689	-0.00071	-1.30E+15	3.74E+17	0.56932	3.53282E-18
23	9.9489	8.0776	0.830857	2.486683	1.812103	-0.00314	-5.79E+15	3.68E+17	0.624235	4.50941E-18

Fitted fragment in yellow



SSA recalculated to  $\Delta Q_{ads} = 2200 \text{ J/mol}$  gives:  $0.063 \text{ m}^2/\text{g}$ .

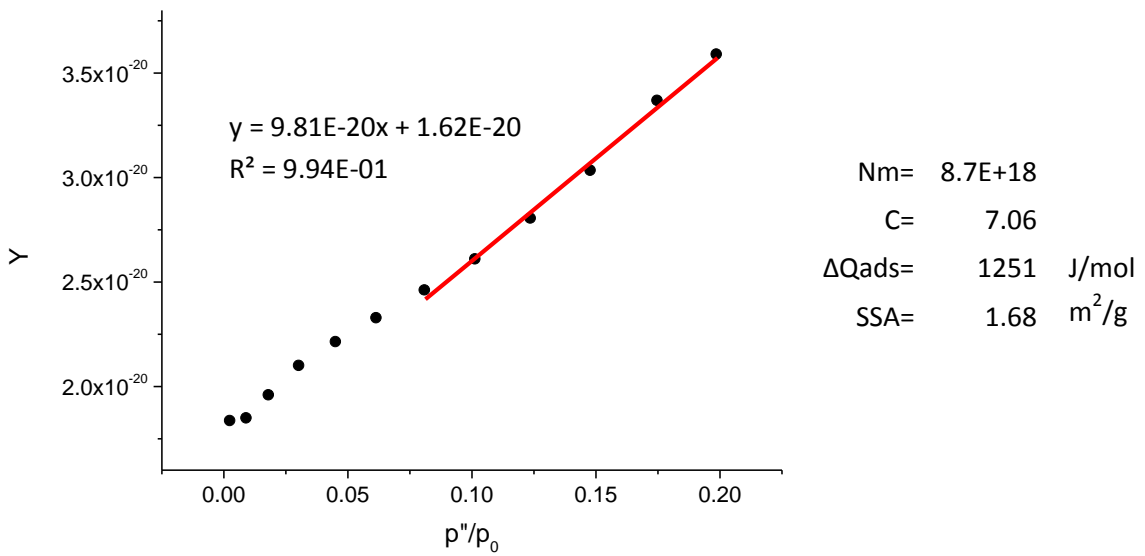
**Appendix 4: BET measurement – Frost**

Small cell

Sample mass= 4.47g

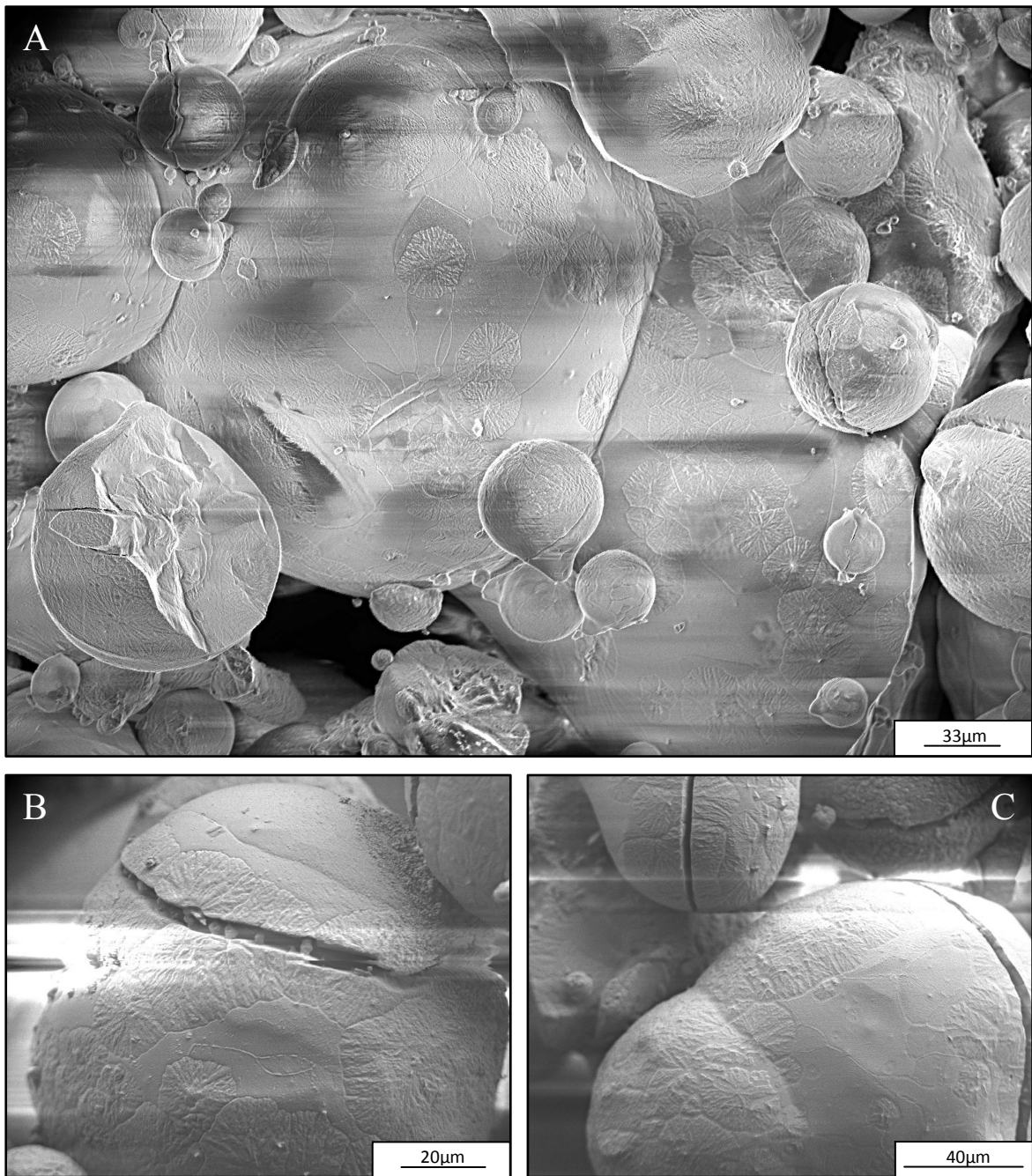
No	p'	p''	n'	n''	n <sup>l</sup>	n <sub>ads</sub>	N <sub>ads/refill</sub>	N <sub>ads/acc</sub>	p''/p <sub>0</sub>	Y
1	0.259	0.036	0.02165	0.010344	0.007333	0.011306	1.52E+17	1.52E+17	0.002782071	1.8316E-20
2	0.646	0.121	0.054042	0.034739	0.024625	0.026635	3.59E+17	5.11E+17	0.009343122	1.8451E-20
3	0.918	0.238	0.076796	0.068301	0.048416	0.033121	4.46E+17	9.57E+17	0.018369397	1.95465E-20
4	1.269	0.396	0.106126	0.113787	0.080659	0.040755	5.49E+17	1.51E+18	0.030602782	2.09561E-20
5	1.631	0.588	0.136443	0.168956	0.119767	0.048146	6.49E+17	2.16E+18	0.045440495	2.20892E-20
6	1.917	0.800	0.160335	0.229729	0.162846	0.050373	6.79E+17	2.83E+18	0.061785162	2.32396E-20
7	2.348	1.052	0.196424	0.302282	0.214276	0.056988	7.68E+17	3.60E+18	0.0812983	2.45713E-20
8	2.612	1.315	0.218509	0.377853	0.267845	0.054933	7.40E+17	4.34E+18	0.101622875	2.60549E-20
9	2.938	1.604	0.245781	0.460894	0.32671	0.052732	7.10E+17	5.05E+18	0.123956723	2.80082E-20
10	3.290	1.917	0.275219	0.550832	0.390464	0.051098	6.88E+17	5.74E+18	0.148145286	3.02958E-20
11	3.615	2.265	0.302416	0.650826	0.461346	0.042053	5.67E+17	6.31E+18	0.17503864	3.36421E-20
12	3.882	2.575	0.324777	0.739902	0.524488	0.046221	6.23E+17	6.93E+18	0.198995363	3.58508E-20

Fitted fragment in yellow



SSA recalculated to  $\Delta Q_{ads}$ =2200 J/mol gives: 1.89m<sup>2</sup>/g.

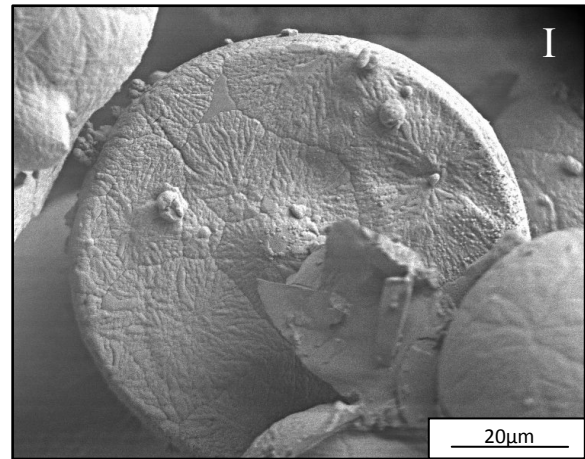
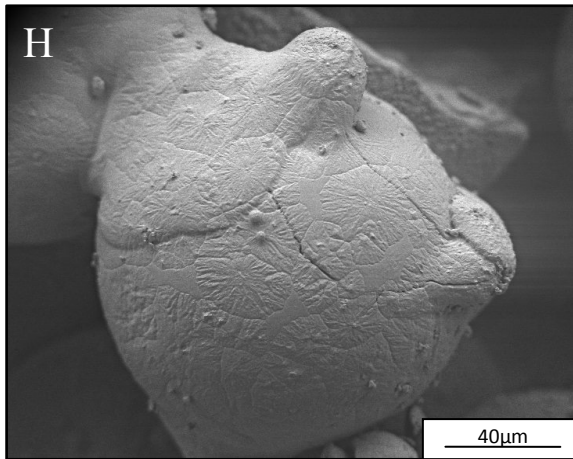
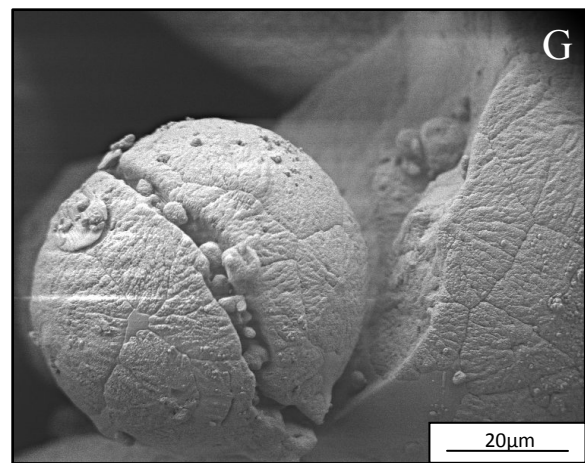
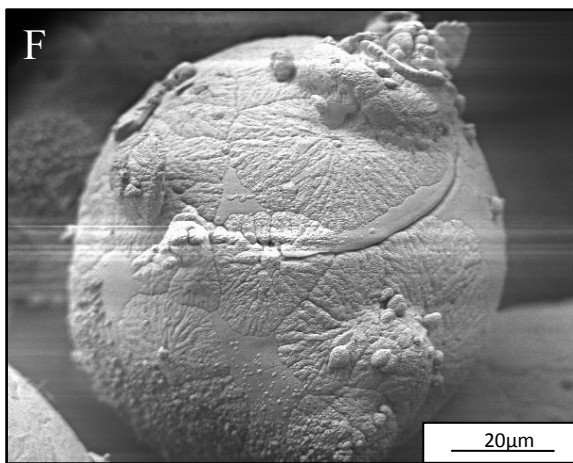
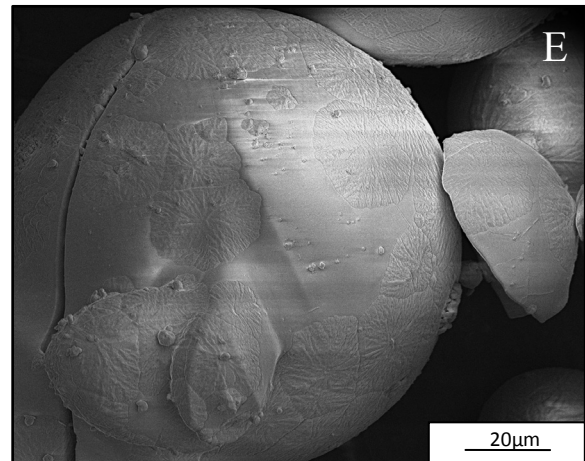
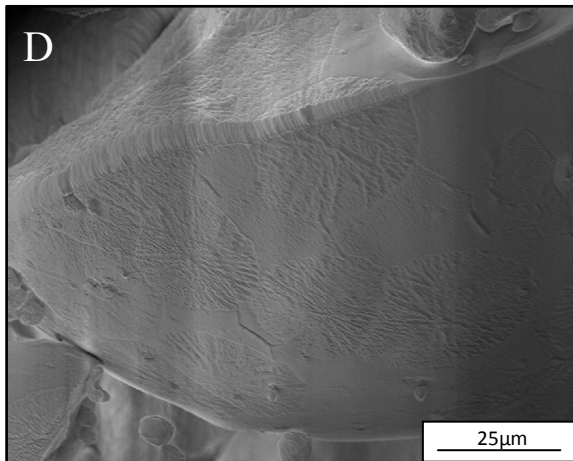
**Appendix 5: Interrupted runs-Formation at 193K 750mbar (75kPa) 30min run.**



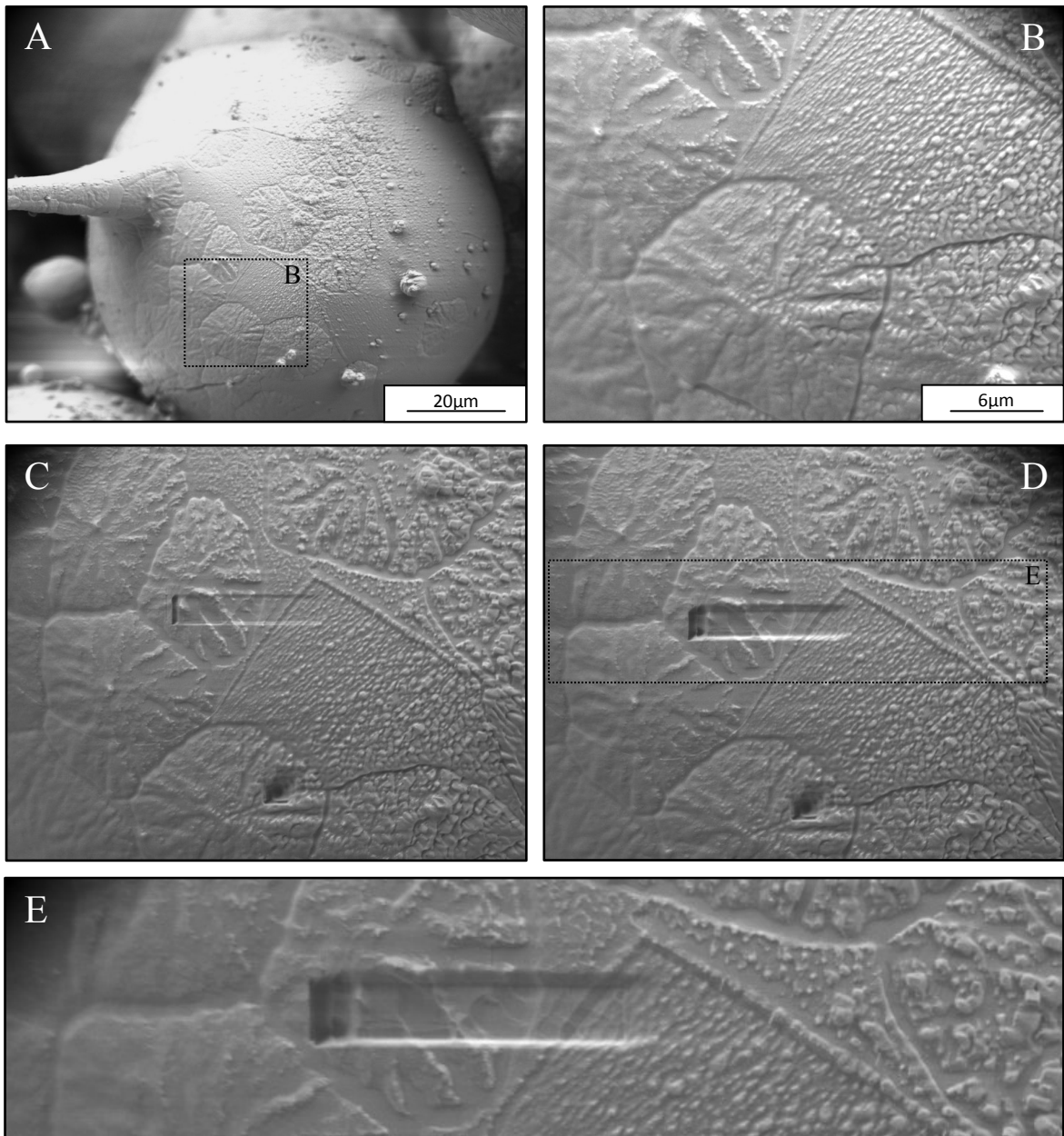
Images taken with: A, D, E) FEI Quanta 200FEG

B, C, F-I) LEO 1530 Gemini

**Appendix 5: Interrupted runs-Formation at 193K 750mbar (75kPa) 30min run.**



**Appendix 6:** Interrupted runs-Formation at 193K 750mbar (75kPa) 15min run.



Images taken with: LEO 1530 Gemini

Etching:

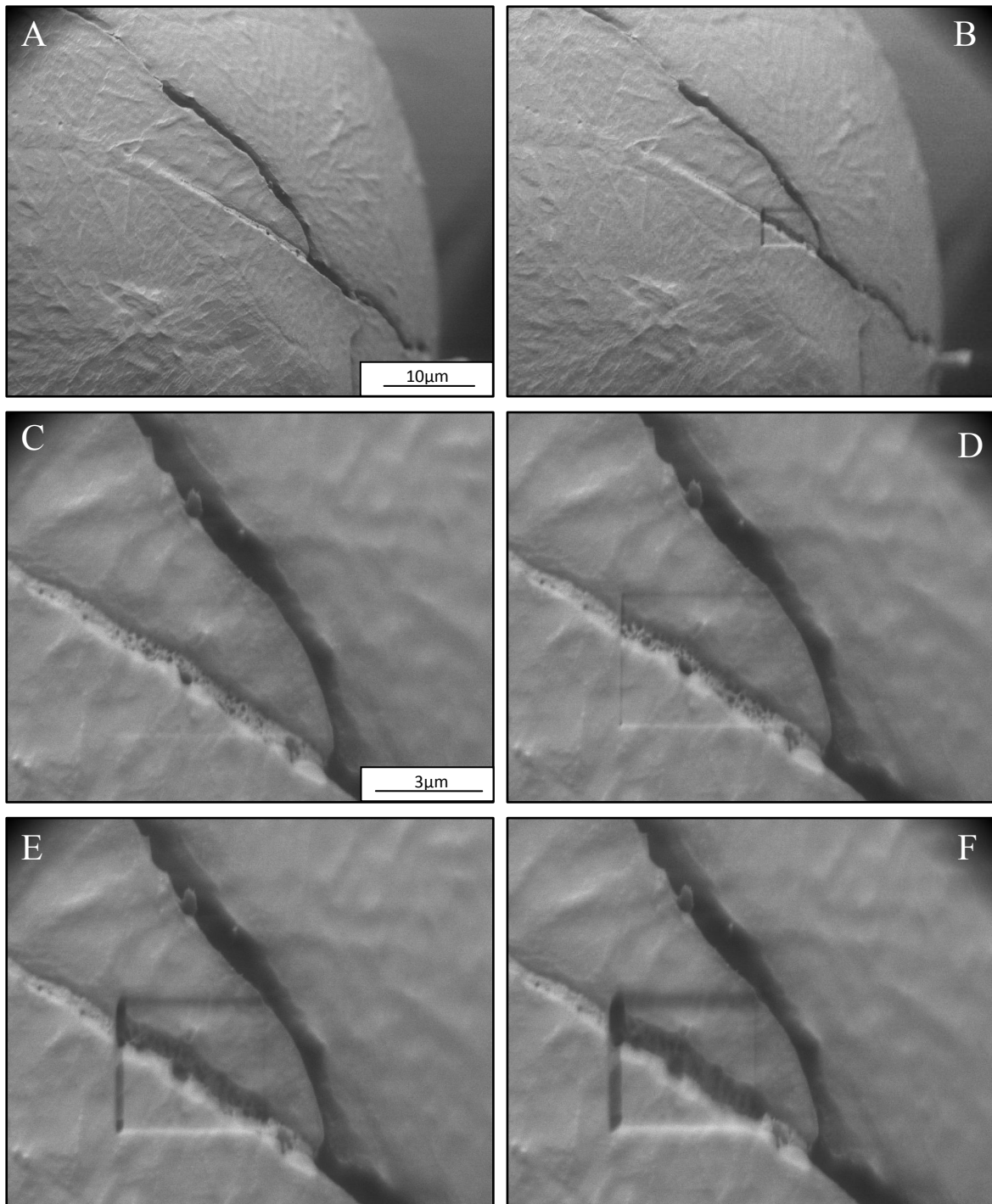
B) Start

C) 2min

D) 9min



**Appendix 6:** Interrupted runs-Formation at 193K 750mbar (75kPa) 90min run.



Images taken with: LEO 1530 Gemini

Etching:

A-B) Before and after

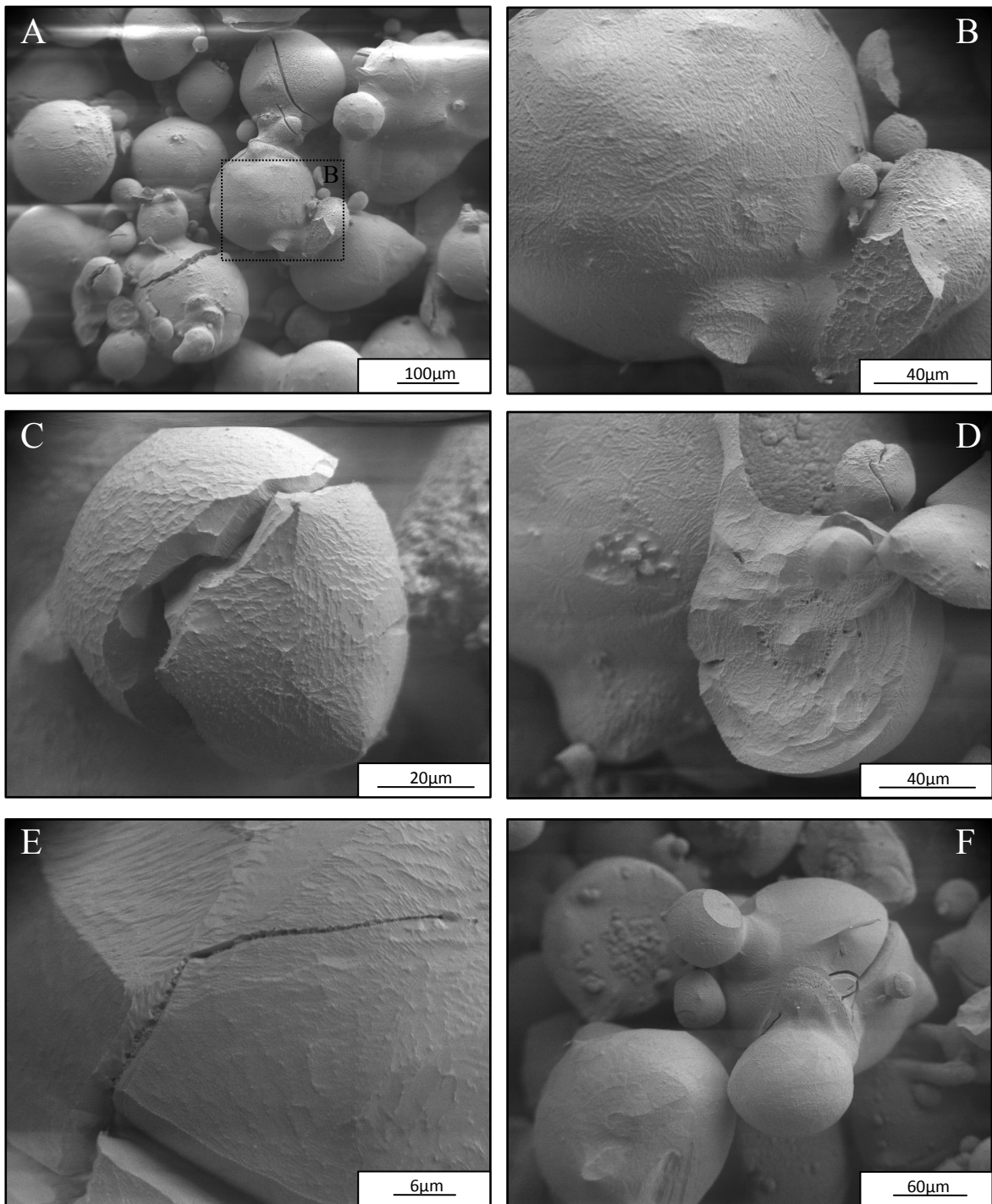
C) 1min

D) 2min

E) 4min

F) 6min

**Appendix 7: Interrupted runs-Formation at 193K 750mbar (75kPa) 90min run.**



Images taken with: LEO 1530 Gemini

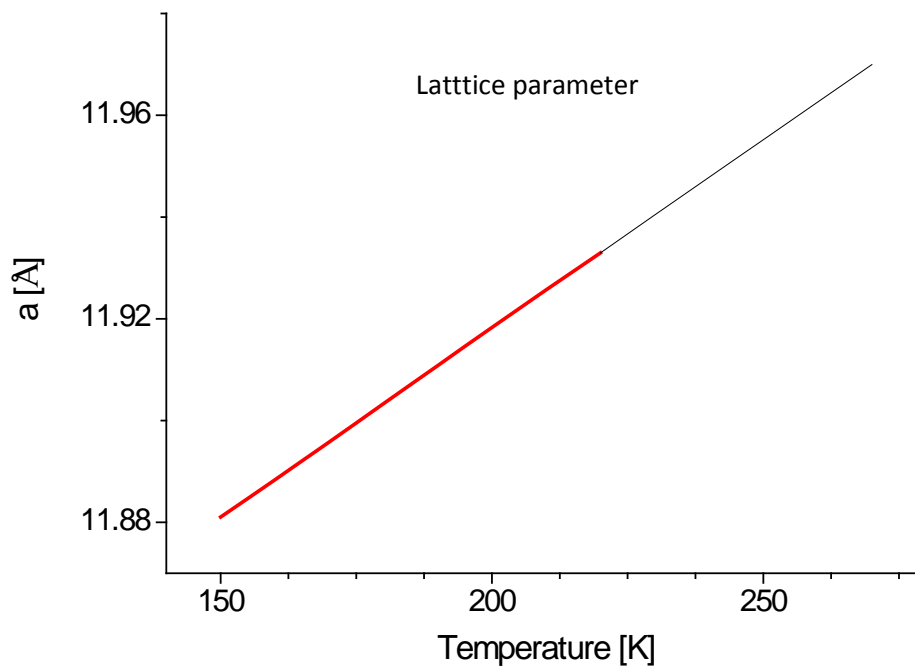


## Appendix 8: Structural models:

### 1) CO<sub>2</sub> Hydrate (Model modified after Klapproth, 2002)

*	name	type	fractional coordinates x,y,z			Mult	Occupancy	Uiso
1	O1	O	0.000000	0.308930	0.118200	24	1.0000	0.08620
2	O2	O	0.180430	0.180430	0.180430	16	1.0000	0.08620
3	O3	O	0.250000	0.000000	0.500000	6	1.0000	0.08620
4	D4	D	0.230320	0.230320	0.230320	16	0.4900	0.03660
5	D5	D	0.000000	0.434940	0.201600	24	0.4900	0.03660
6	D6	D	0.000000	0.377800	0.162900	24	0.4900	0.03660
7	D7	D	0.000000	0.318600	0.037630	24	0.4900	0.03660
8	D8	D	0.069120	0.263640	0.135500	48	0.4900	0.03660
9	D9	D	0.116760	0.228880	0.160700	48	0.4900	0.03660
10	O10	O	0.471000	0.909400	0.754500	48	0.2469	0.14247
11	C11	C	0.257400	0.500000	0.000000	12	0.4939	0.14247
12	C12	C	0.000000	0.000000	0.000000	2	0.5585	0.08130
13	O13	O	0.096600	0.000000	0.000000	12	0.1861	0.08130

Structure taken from the refinement of the decomposition run at 170K and 6mbar (0.6kPa)



150-223K - Polynomial function (Udachin et al., 2001)

$$a = 11.81945 - 9.08711 \times 10^{-5}T + 4.59676 \times 10^{-6}T^2 - 8.35548 \times 10^{-9}T^3$$

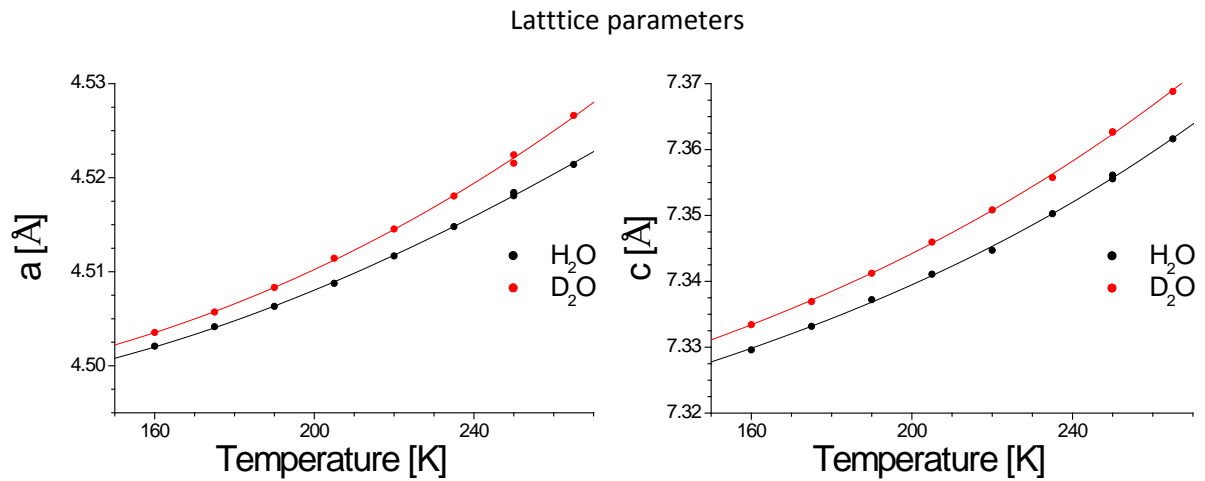
223-270K- Simplified linear extension (lattice most likely expands non-linearly closer to the melting point of ice)

$$a = 7.39472 \times 10^{-4}T + 11.77032$$

## Appendix 8: Structural models:

### 2) Water ice (Model modified after Röttger et al., 1994)

*	name	type	fractional coordinates x,y,z			Mult	Occupancy	Uiso
1	O1	O	0.333300	0.666700	0.063600	4	1.0000	0.02500
2	D1	O	0.333300	0.666700	0.199300	4	0.5000	0.02500
3	D2	O	0.453200	0.906400	0.016400	12	0.5000	0.02500



Experimental points (Röttger et al., 1994)

Polynomial polynomial fits for  $a$  and  $c$ :

$$a_{H_2O} = 4.5014 - 1.3738 \times 10^{-4}T + 9.9854 \times 10^{-7}T^2 - 7.27674 \times 10^{-10}T^3$$

$$a_{D_2O} = 4.4979 - 5.5859 \times 10^{-5}T + 4.9645 \times 10^{-7}T^2 - 4.58399 \times 10^{-10}T^3$$

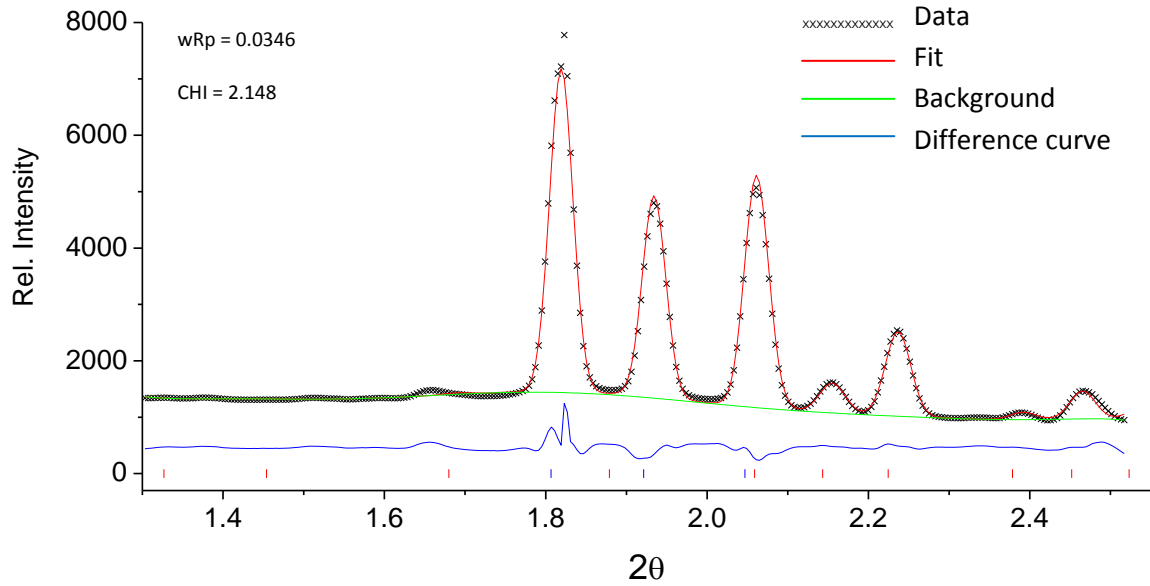
$$c_{H_2O} = 7.30039 + 2.20731 \times 10^{-4}T - 6.3993 \times 10^{-7}T^2 + 2.56758 \times 10^{-9}T^3$$

$$c_{D_2O} = 7.30466 + 1.80909 \times 10^{-4}T - 3.7561 \times 10^{-7}T^2 + 2.30109 \times 10^{-9}T^3$$

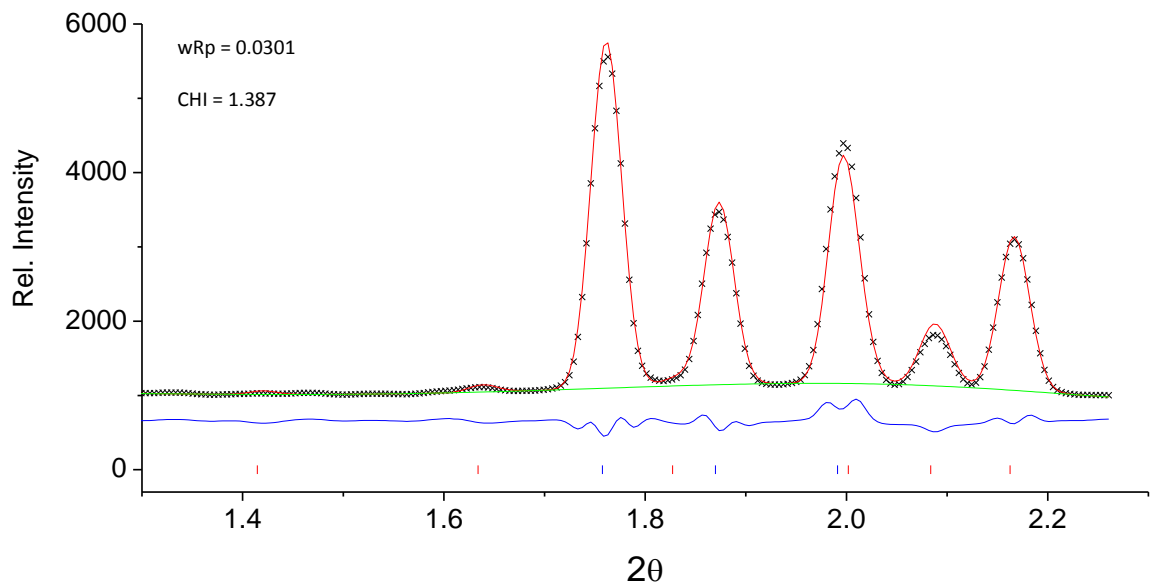
**Appendix 9:** Examples of diffraction patterns and Rietveld fits- Formation from ice spheres.

Formation from spheres at 193K 70kPa (X-ray diffraction)

Tickmarks: blue- Ih ice, red- Gas hydrate



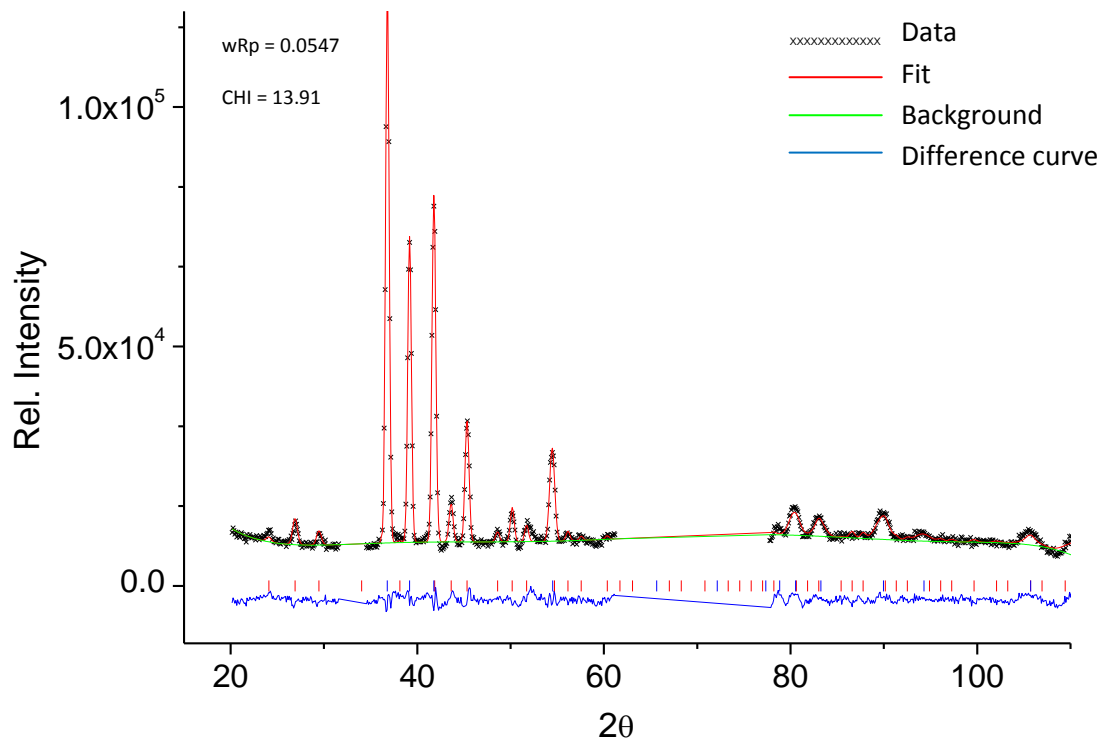
Formation from spheres at 223K 0.1MPa (X-ray diffraction)



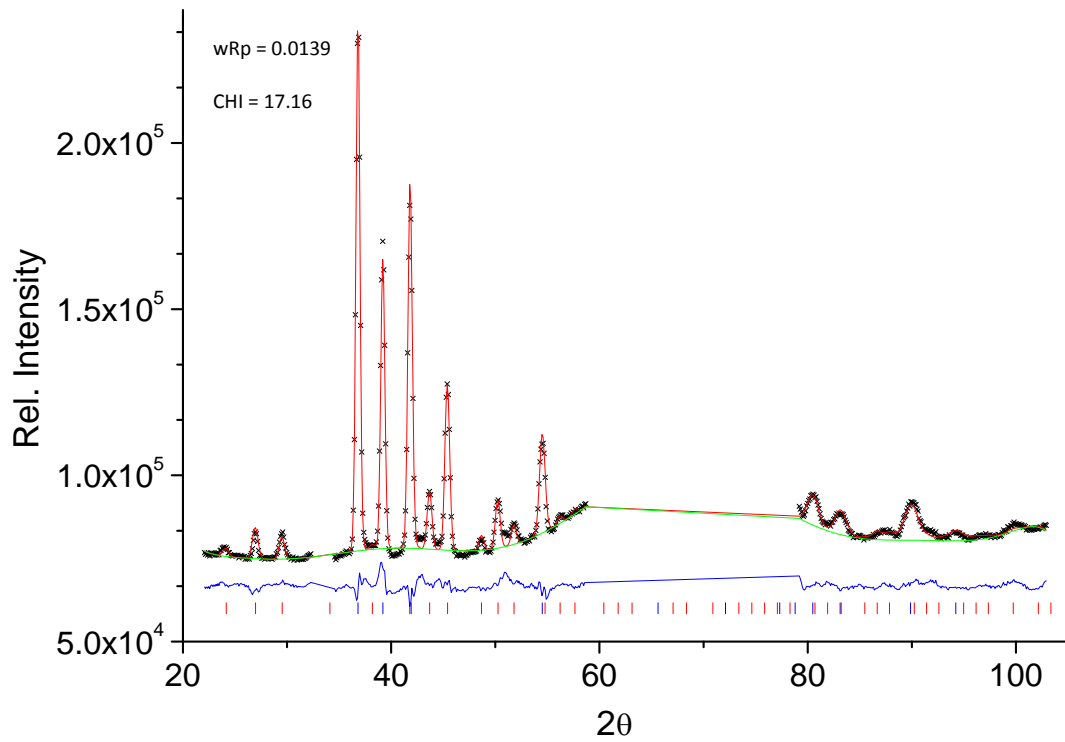


**Appendix 9:** Examples of diffraction patterns and Rietveld fits – Formation from frost.

Formation at 190K 36kPa AF (neutron diffraction, dataset: 366417)



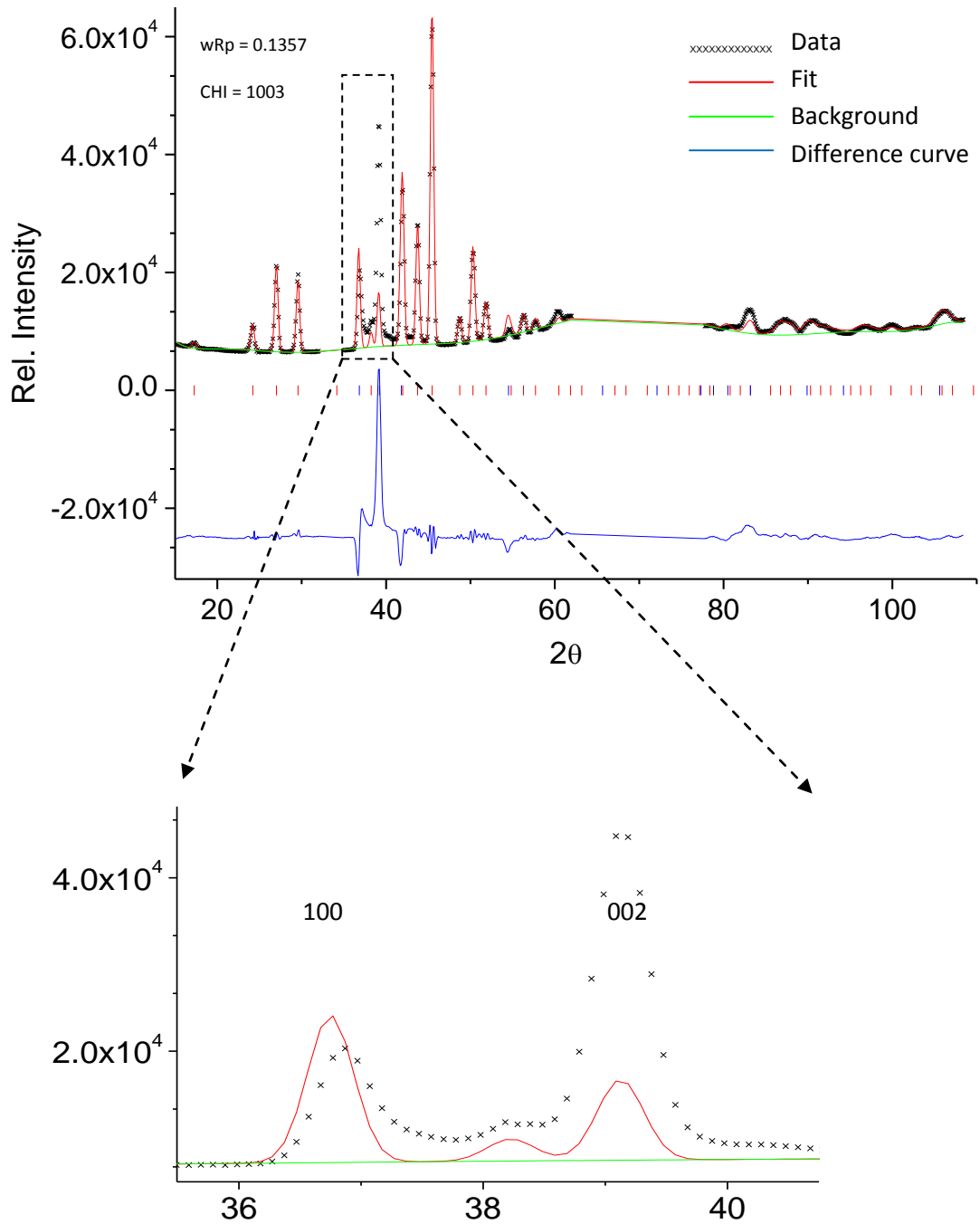
Formation at 190K 36kPa GG (neutron diffraction, dataset: 276856)



**Appendix 9:** Examples of diffraction patterns and Rietveld fits - Cubic ice.

Decomposition at 170K 0.6kPa after 16.34h (neutron diffraction, dataset: 317998), GSAS

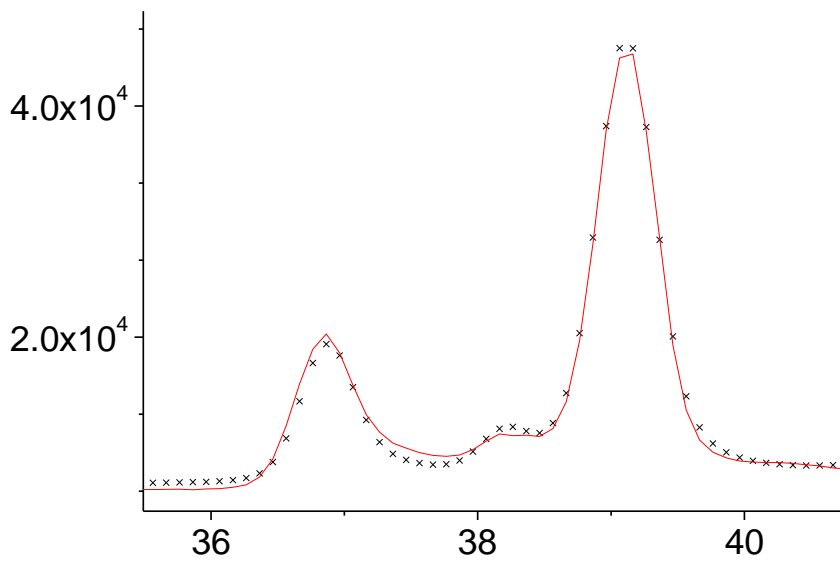
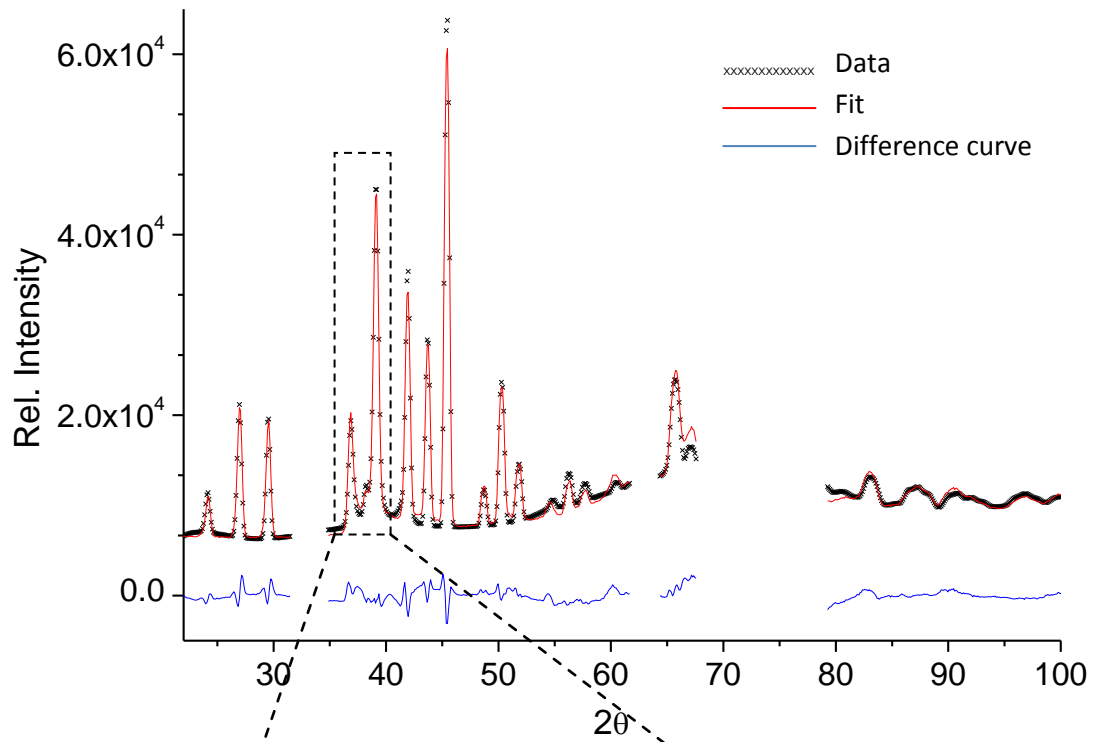
Tickmarks: blue- Ih ice, red- Gas hydrate



Standard Rietveld refinement with the Ih ice clearly does not fit to the experimental data.

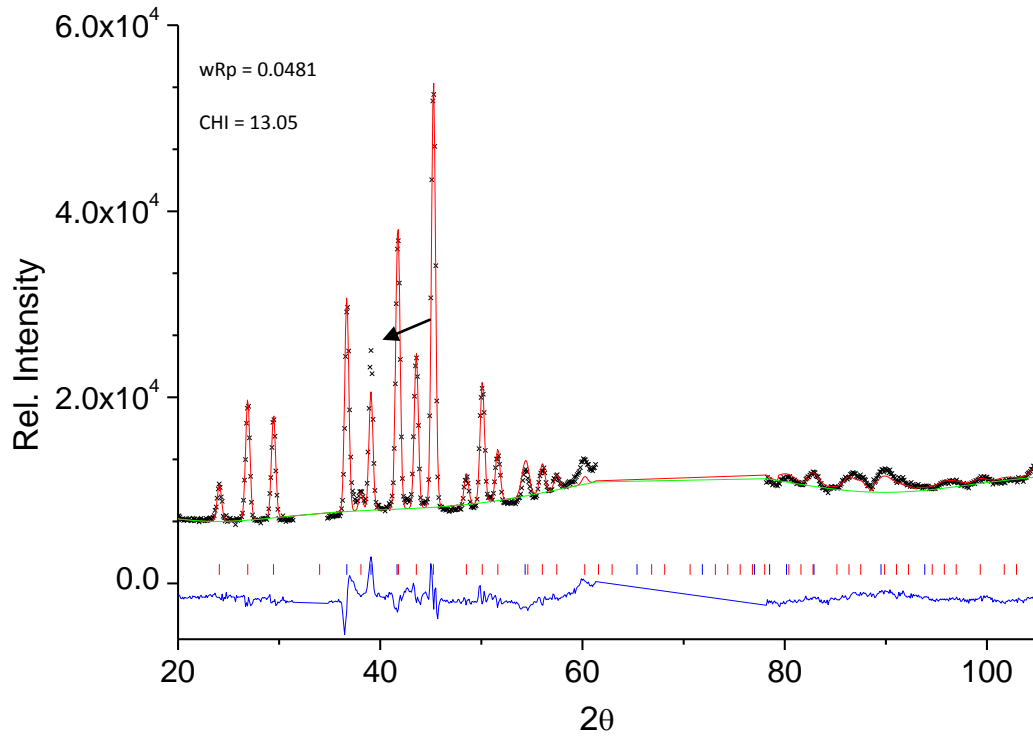
**Appendix 9:** Examples of diffraction patterns and Rietveld- Cubic ice

Decomposition at 170K 0.6kPa (neutron diffraction, dataset: 317998), Ic ice modeling (Hansen et al., 2008a), (Hansen et al., 2008b)

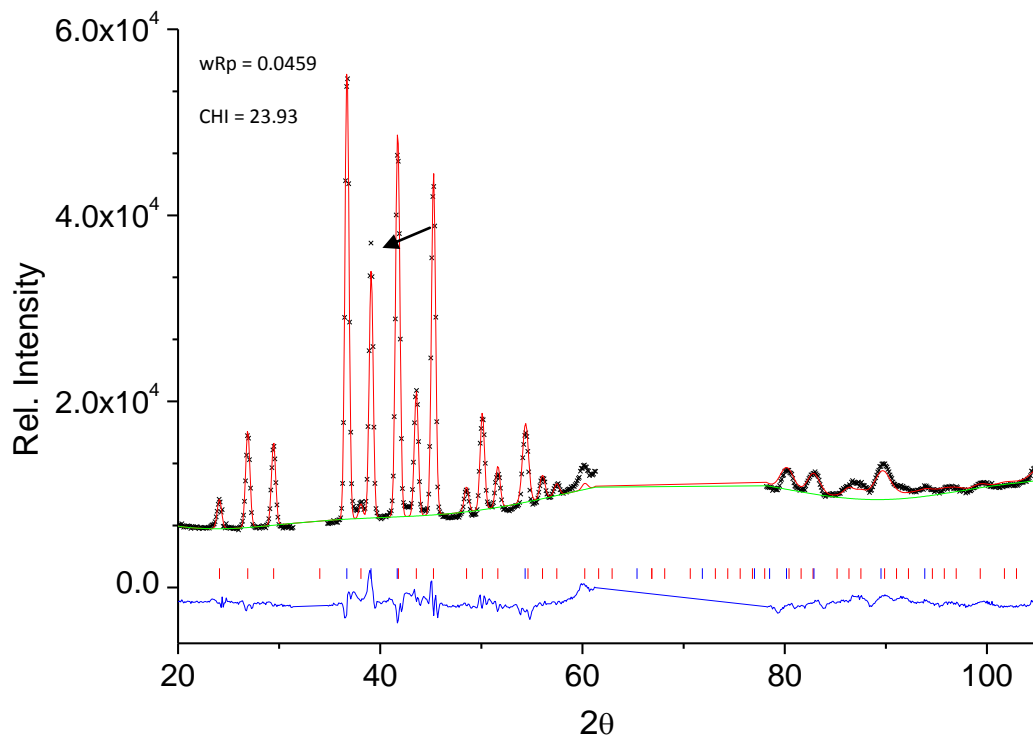


**Appendix 9:** Examples of diffraction patterns and Rietveld fits –defective ice at 220K

Decomposition at 220K 60kPa after 31min (neutron diffraction, dataset: 319056)

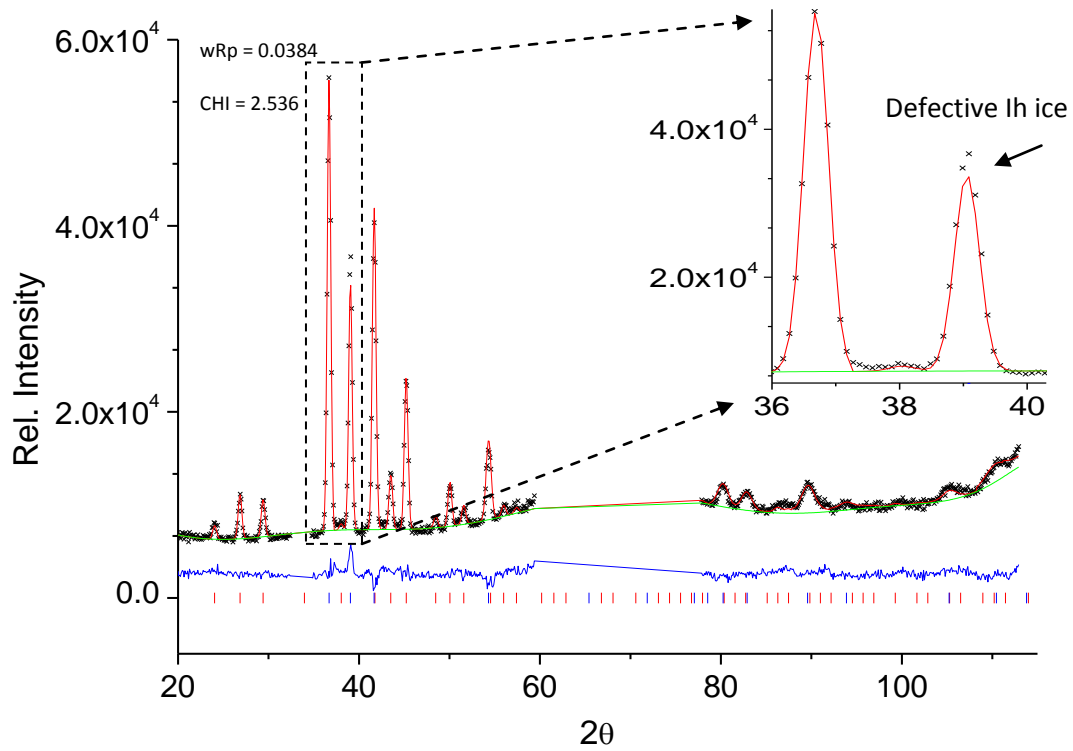


Decomposition at 220K 0.6kPa after 10.5min (neutron diffraction, dataset: 317500)

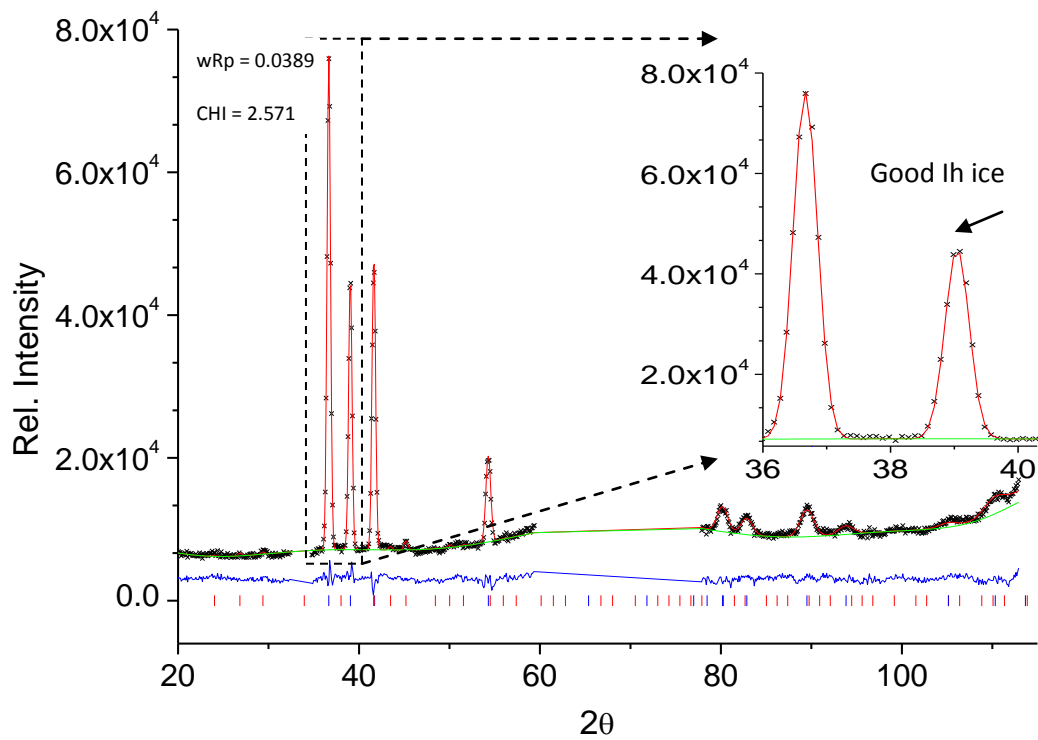


**Appendix 9:** Examples of diffraction patterns and Rietveld fits – Ice annealing

Decomposition at 240K 0.6kPa after 19 min (neutron diffraction, dataset: 318820)

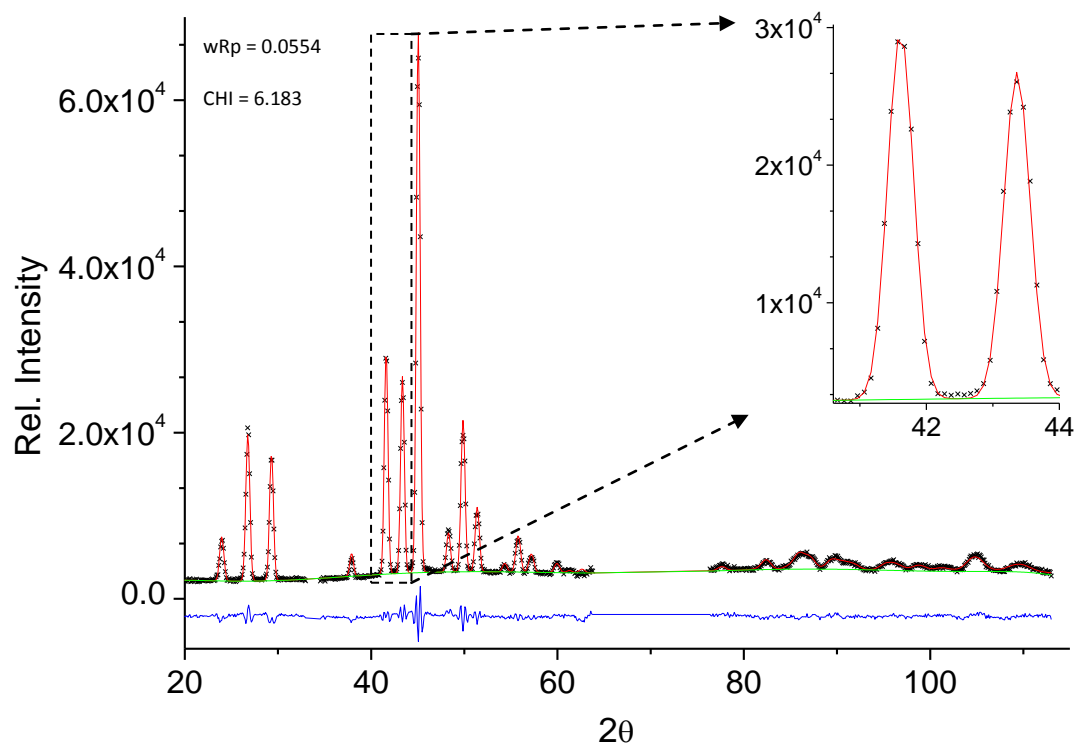


Decomposition at 240K 0.6kPa after 27min (neutron diffraction, dataset: 318868)



**Appendix 9:** Examples of diffraction patterns and Rietveld fits – temperature dependent Self-preservation

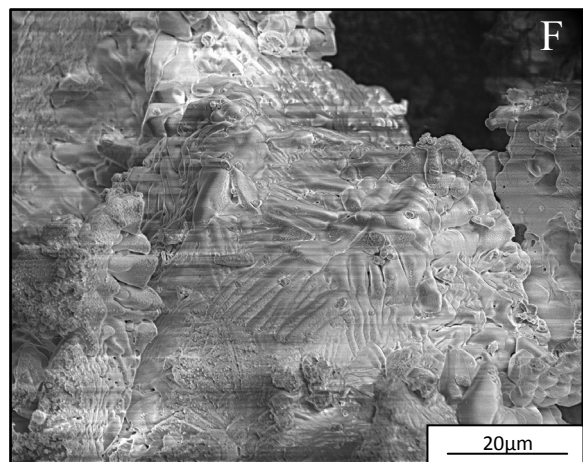
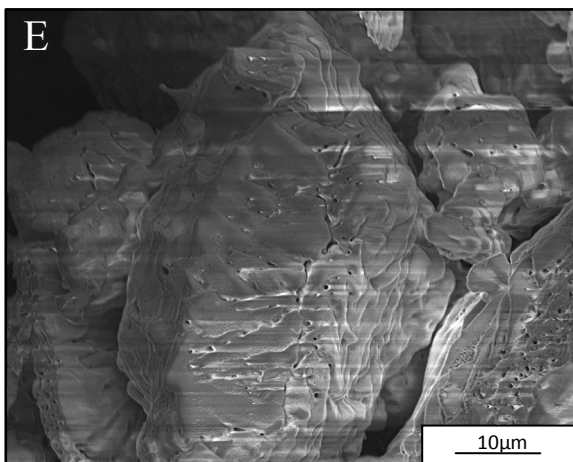
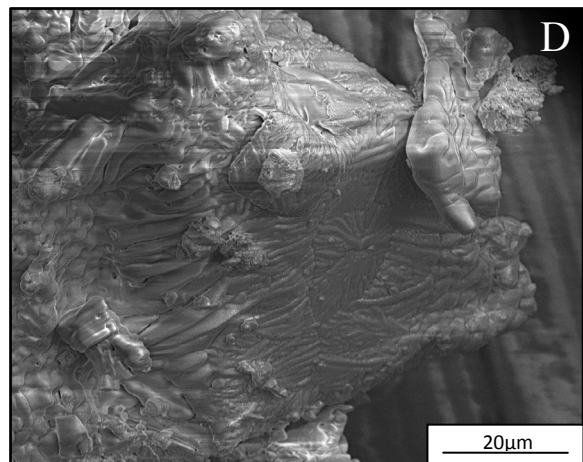
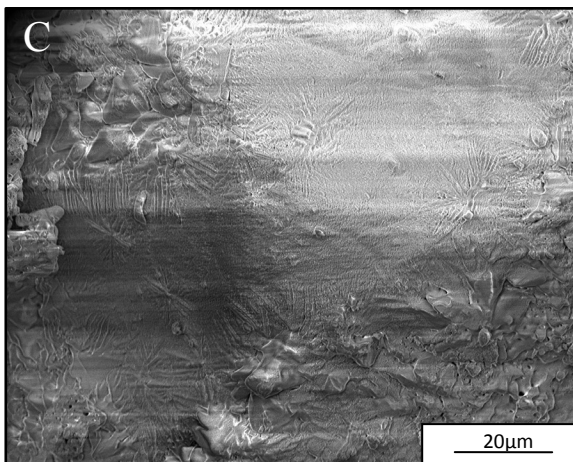
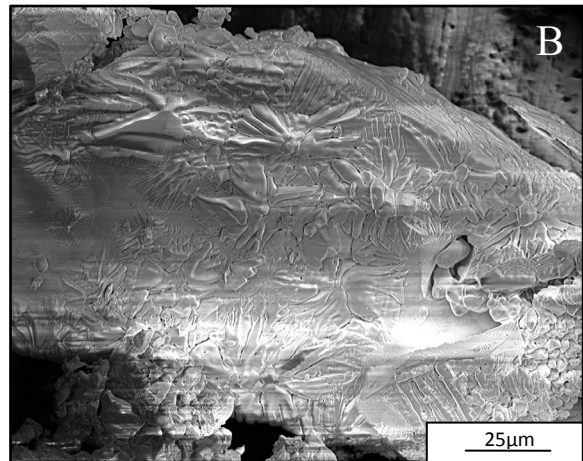
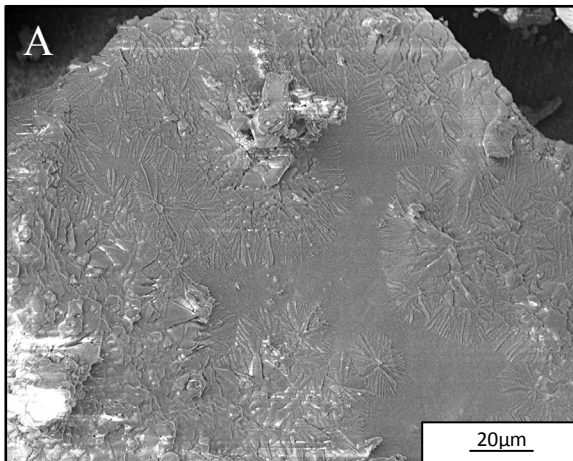
Decomposition at 270K 0.6kPa after 15s (neutron diffraction, dataset: 366862)





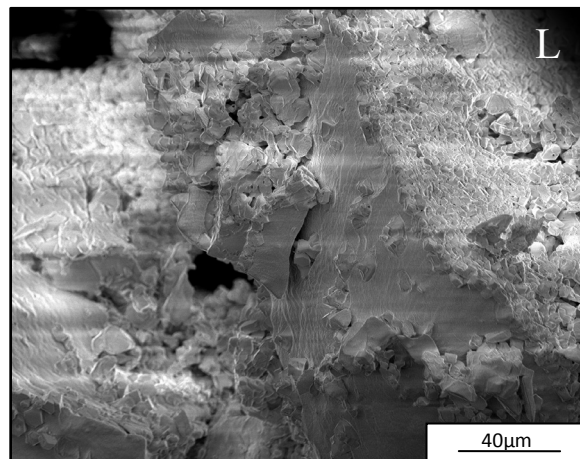
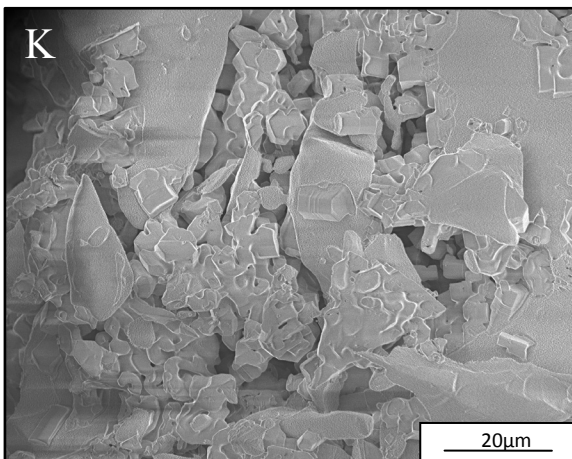
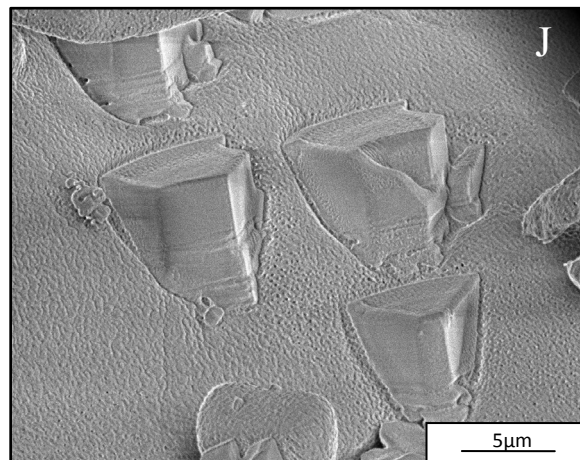
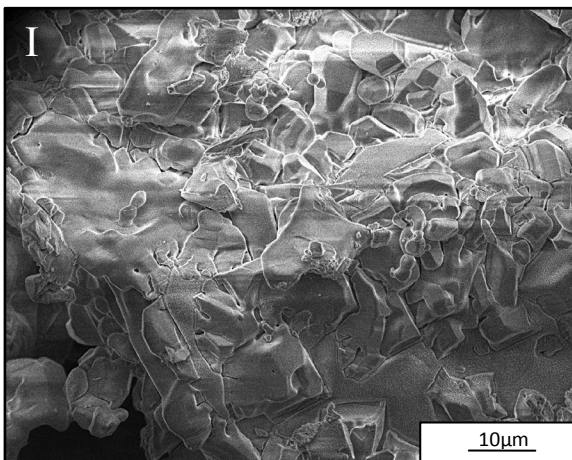
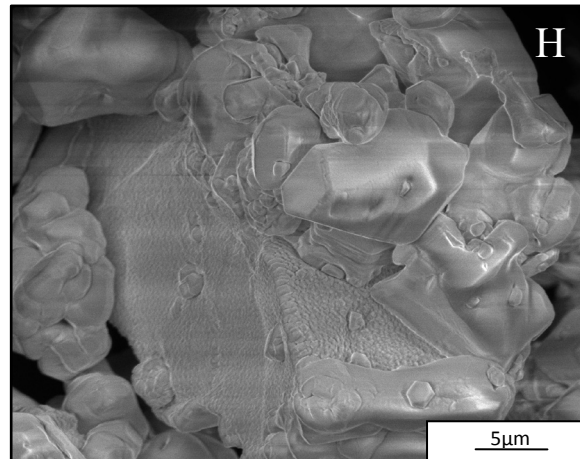
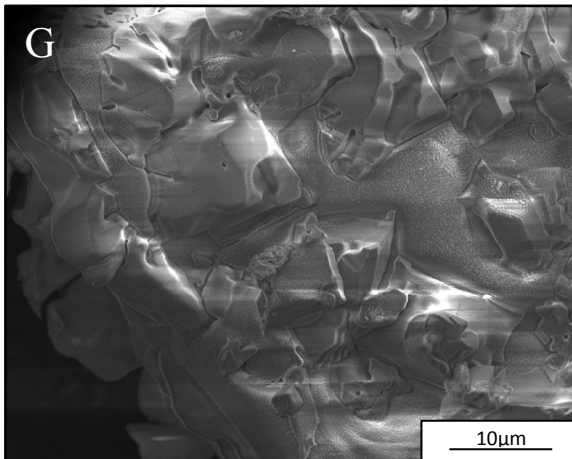


**Appendix 10:** Interrupted runs-Decomposition at 220K 600mbar (60kPa) 5min run.



Images taken with: FEI Quanta 200FEG

**Appendix 10:** Interrupted runs-Decomposition at 220K 900mbar (90kPa) 5-10min run.



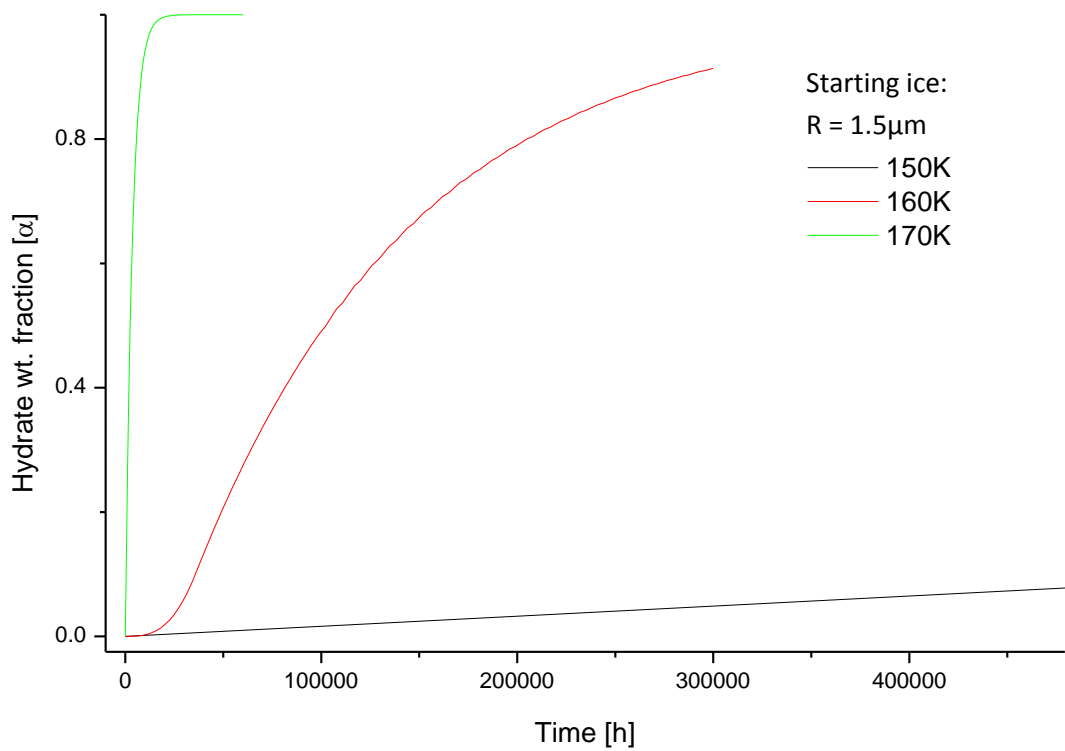
Images taken with: FEI Quanta 200FEG

G-I) 5min decomposition run

J-L) 10min decomposition run

**Appendix 11: “Frost” fitting parameters**

	$k_N$ [1/hm <sup>2</sup> ]	$k_G$ [m/h <sup>2/3</sup> ]	$k_S$ [1/h]
195	7.79E+09	7.98E-07	0.2203
190	2.36E+09	5.02E-07	0.06673
185	6.72E+08	3.08E-07	0.019
180	1.78E+08	1.84E-07	0.005033
175	4.37E+07	1.07E-07	0.001236
170	9.89E+06	5.98E-08	0.0002796
165	2.04E+06	3.24E-08	5.77E-05
160	3.85E+05	1.69E-09	1.09E-05
155	64400	8.45E-09	1.82E-06
150	9610	4.04E-09	2.72E-07



Formation curves generated by “Frost” module at three chosen temperatures and max fugacity (see Fig. 135).



# Acknowledgements

First of all I would like to thank my supervisor Prof. Dr. Werner F. Kuhs for great patience, and trusting in me. I could not forget to mention an excellent working climate and invaluable, countless discussions. It was a pleasure to work here.

Secondly I have to express my deepest gratitude to my wife who motivated me on every step to finish writing :)

I would like to thank Georgi Genov for introducing me to the experimental equipment, his technical and theoretical expertise in gas hydrates and a load of fun we had together.

Special thanks to Heiner Bartels not only for his for invaluable expertise but also for time we spent in Grenoble including 10h long car travels.

I would like to thank Klaus Haepe and Eberhard Hensel for the hardware and software support.

I am also thankful to Andrey Salamatin for the help and very valuable discussions on the Frost and Powder 4 models.

I am grateful to Thomas Hansen, for the help in performing the experiments on D20 and Ic/Ih modeling. I would like to also thank ILL for the beam time and support.

And not on the last place, I would like to thank all my colleagues from the Institute of Crystallography for the great working atmosphere.

This work was supported by the DFG grant **Ku 920/11**



## Lebenslauf

Name: Andrzej Falenty

Anschrift: Ginsterweg 8 app.44

Geburtstag: 30.10.1980

Geburtsort: Pruszków, Polen

Staatsangehörigkeit: Polnisch

Schulausbildung:

**2005-2008 Georg-August Universität – Göttingen (Deutschland);** GZG, Abteilung Kristallographie  
**Doktor Thesis:** "Formation and decomposition processes of CO<sub>2</sub> hydrates at conditions relevant to Mars"

**2002-2004 Warschauer Universität – Warschau (Polen);** Faculty of Geologie; Institute of Geochemistry, Mineralogy and Petrology **Diploma Thesis** about "Modelling of the mafic melt origin in the vicinity of Krakow, Poland" **Abschluß:** Magister of Geochemistry, Mineralogy and Petrology (MSc – Master of Science) with distinction "Summa Cum Laude"

**2001 / 2002 Georg-August Universität – Göttingen (Deutschland);** Faculties of Natural Sciences, Math and Informatics; Faculty of Geosciences Socrates-Erasmus five months scholarship

**1999-2002 Warschauer Universität – Warschau (Polen);** Faculty of Geology; Institute of Geochemistry, Mineralogy and Petrology **Abschluß:** Bachelor of Geochemistry, Mineralogy and Petrology **Note:** very good